Summer 8-24-2022

MECHANISMS AND ROLES OF DYNAMIC ACTIN ASSEMBLY AROUND DYSFUNCTIONAL MITOCHONDRIA

Tak Shun Fung
Dartmouth College, tak.shun.fung.gr@dartmouth.edu

“MECHANISMS AND ROLES OF DYNAMIC ACTIN ASSEMBLY AROUND DYSFUNCTIONAL MITOCHONDRIA”

A Thesis
Submitted to the Faculty
in partial fulfillment of the requirements for the
degree of
Doctor of Philosophy

in

Biochemistry and Cell Biology

by Tak Shun Fung

Guarini School of Graduate and Advanced Studies
Dartmouth College
Hanover, New Hampshire

August 2022

Examining Committee:

_____

(chair) Henry N. Higgs, Ph.D.

_____

James B. Moseley, Ph.D.

_____

Erik E. Griffin, Ph.D.

_____

Yasemin Sancak, Ph.D.

_____

F. Jon Kull, Ph.D.

Dean of the Guarini School of Graduate and Advanced Studies

Abstract

Possessing the ability to efficiently generate ATP required to sustain cellular functions, mitochondria are often considered the 'powerhouses of the cell'. However, our understanding of mitochondria in cell biology was further expanded when we recognized that communication between this unique organelle and the rest of the cell regulates cellular bioenergetics, metabolism and signaling processes such as mitophagy and apoptosis. Here, I investigate signaling between mitochondria and the actin cytoskeleton, and how this signaling regulates mitochondrial dynamics and cellular function. Specifically, I find that, upon mitochondrial dysfunction, actin polymerizes rapidly around the dysfunctional organelle, which we term 'acute damage-induced actin' (ADA). Hitherto, neither the mechanism of ADA activation nor the cellular role of ADA are well understood.

In this dissertation, I show that that two parallel signaling pathways are required for ADA: driven by calcium signaling and ATP depletion, respectively. In the first pathway, mitochondrial calcium efflux through the sodium/calcium exchanger NCLX leads to elevation of cytosolic calcium, activating protein kinase C (PKC)-β. PKC-β activation in turn activates the Rac-GEF Trio, leading to activation of the Rho family GTPase Rac, the WAVE complex, and finally the actin-polymerizing Arp2/3 complex. Simultaneously, ATP depletion caused by mitochondrial dysfunction activates the energy sensor AMPK. AMPK activates in turn the Cdc42 GEF Fgd1, the Rho-family GTPase Cdc42, and finally a specific family of actin-polymerizing formin proteins, FMNL formins. Both FMNL formins and Arp2/3 s are to assemble mitochondrially-associated actin filaments.

Next, I elucidated roles for ADA in mitochondrial and cellular dynamics, finding three distinct ADA effects. First, ADA stimulates glycolysis in multiple cell types, including mouse embryonic fibroblasts (MEFs) and cytotoxic T lymphocytes (CTLs). Second, ADA inhibits a specific form of mitochondrial dynamics we term 'circularization'. Third, ADA delays mitochondrial recruitment of the E3 ubiquitin ligase, Parkin, which delays mitophagy. Taken together, I propose that ADA is an acute mechanism for sensing and responding to mitochondrial damage, by promoting re-establishment of ATP production and giving the cell a 'pause' for recovery before the damaged organelle is permanently cleared.

Acknowledgements

I would like to thank my thesis advisor Dr. Henry Higgs, Dr. Higgs has been incredibly supportive throughout my graduate career. He has helped me in multiple ways, developing me as a thinking and curious scientist. It was great learning from Dr. Higgs how to frame questions, troubleshoot assays and analyze results critically. Every discussion we had was fruitful and I came out with more exciting plans and hypotheses to test for the next experiments. For all these years, thank you!

I would also like to thank my thesis committee members Dr. James Moseley and Dr. Erik Griffin for all the advice and discussions. The scrutiny and comments lead my project into interesting avenues. Thank you as well to my external examiner Dr. Yasemin Sancak, an outstanding scientist whose work I admire and will continue to follow throughout my career.

Thank you to all past and present members of the Higgs Lab members. Especially Raj, whom I worked with extensively, a fantastic colleague and a real friend. And also to all scientific collaborators involved in my project for their invaluable help, teaching me that science is a cross-discipline and international endeavor.

Last but not least, I would like to thank my family - my parents and my brother. Even though I am away for my studies, your love, support and encouragement helped me more than you will ever know.

Table of contents

Abstract ii

Acknowledgements iii

Table of contents iv

List of illustrations vii

List of tables x

Glossary xi

Notes on the format of this thesis xiv

Chapter I: Introduction 1

1.1 The actin cytoskeleton 2

1.1.1 Proteins controlling actin dynamics 3

1.1.2 Proteins controlling actin organization 5

1.1.3 Myosins 6

1.1.4 More about the WAVE regulatory complex 7

1.1.5 More about FMNL family formins 7

1.2 The mitochondrion: a unique organelle 9

1.2.1 Mitochondria possess two membranes with specific characteristics 9

1.2.2 Mitochondria possess its own genome 10

1.2.3 Mitochondria dynamics 11

1.3 Cellular bioenergetics: a primer 14

1.3.1 Glycolysis: oxygen independent ATP production 15

1.3.2 The tricarboxylic acid cycle (TCA) cycle 17

1.3.3 Oxidative phosphorylation: oxygen dependent ATP production 19

1.3.4 Complexes of the electron transport chain (ETC) 20

1.3.5 Energy sensing in the cell: AMPK and glycolytic enzymes 25

1.3.6 Shifting between glycolysis and oxidative phosphorylation 27

1.3.7 Calcium signaling in mitochondria 29

1.3.8 The mitophagy process: PINK1/Parkin dependent clearance 32

1.4 Actin and mitochondria coming together: what we know so far 34

1.4.1 Mitochondrial division and the formin INF2 34

1.4.2 Actin inhibiting microtubule-based mitochondrial motility 35

1.4.3 Mitochondrially-associated actin in interphase and mitotic cells 35

1.4.4 Actin and mitochondrial dysfunction, mitophagy 36
1.4.5 Actin and glycolysis 36
Chapter II: Distinguishing acute damage-induced actin from other forms of mitochondrially-associated actin 62
2.1 Abstract 64
2.2 Introduction 65
2.3 Results 66
2.3.1 Distinct actin polymerization mechanisms induced by mitochondrial depolarization or cytoplasmic calcium 67
2.3.2 Spontaneous mitochondrial depolarization triggers Arp2/3 complex-mediated actin clouds 68
2.3.3 Actin polymerization is not required for depolarization-induced mitochondrial shape change 69
2.3.4 Mitochondrial shape changes depend on the IMM protease Oma1 71
2.4 Discussion 73
2.5 Materials and Methods 76
Chapter III: Unravelling the mechanism for rapid actin assembly after CCCP-induced mitochondrial damage 102
3.1 Abstract 104
3.2 Introduction 105
3.3 Results 107
3.3.1 Rac-activated WAVE regulatory complex activates Arp2/3 complex during ADA 107
3.3.2 Calcium-stimulated PKC activates Rac during ADA 108
3.3.3 A parallel pathway involving AMPK and FMNL formins is necessary for ADA 110
3.3.4 ADA inhibition accelerates mitochondrial shape changes upon CCCP treatment 113
3.4 Discussion 115
3.5 Material and Methods 119
Chapter IV: Mitochondrial-associated actin regulates glycolysis in mitochondrial dysfunction 156
4.1 Abstract 158

4.2 Introduction 159
4.3 Results 161
4.3.1 ADA is required for rapid up-regulation of glycolysis upon oxphos inhibition 162
4.3.2 ETC protein depletion causes mitochondrially-associated actin filaments and actin-dependent glycolytic activation 165
4.3.3 ADA-dependent glycolytic activation in effector $CD8^+$ T cells 166
4.4 Discussion 168
4.5 Materials and Methods 172
Chapter V: Peri-mitochondrial actin delays Parkin recruitment in damaged mitochondria 207
5.1 Abstract 209
5.2 Introduction 210
5.3 Results 212
5.3.1 ADA disrupts ER-mitochondrial contact 212
5.3.2 ADA delays Parkin recruitment to depolarized mitochondria 213
5.3.3 Galactose-primed cells have sustained ADA and delayed Parkin recruitment 214
5.3.4 Myosin VI, N-WASP, Spire1C and mDia formins are not required for ADA 216
5.4 Discussion 218
5.5 Material and Methods 220
Chapter VI: Future directions 254
Chapter VII: Literature cited 256

List of illustrations

Figure 1.1: Actin-based structures, viewed from above the cell. 38

Figure 1.2: Actin-based cellular structures viewed in cross section. 40

Figure 1.3: Proteins controlling actin dynamics. 41

Figure 1.4: Actin nucleation and elongation factors. 42

Figure 1.5: Actin-organizing proteins, and myosins. 44

Figure 1.6: Mitochondria and their dynamics. 45

Figure 1.7: The ten steps of glycolysis in the cytosol. 47

Figure 1.8: The traditional and non-canonical TCA cycle. 49

Figure 1.9: The biochemical assay by Racker and Stoeckenius. 51

Figure 1.10: The mitochondrial ETC in metazoans. 52

Figure 1.11: The Q cycle in complex III. 53

Figure 1.12: AMPK regulation in the cell. 54

Figure 1.13: PINK1/Parkin mitophagy. 55

Figure 1.14: Actin and mitochondrial division. 56

Figure 1.15: Actin and mitochondrial motility. 57

Figure 1.16: Two types of actin-induced by mitochondrial damage. 58

Figure 2.1. Distinct actin structures assemble in response to two stimuli: increased cytoplasmic calcium and mitochondrial depolarization. 83

Figure 2.2: Actin polymerization accompanying transient depolarization of a sub-set of mitochondria in the absence of CCCP. 85

Figure 2.3: Depolarization-induced mitochondrial shape changes in U2-OS cells. 87

Figure 2.4: Effect of latrunculin A and Arp2/3 complex inhibition on depolarization-induced mitochondrial shape changes. 89

Figure 2.5: Role of Oma1 in depolarization-induced mitochondrial shape change. 91

Figure S2.1: Actin and mitochondrial dynamics upon ionomycin and CCCP treatments. 93

Figure S2.2: Actin dynamics upon CCCP treatment in control and INF2 KD cells. 94

Figure S2.3: Depolarized mitochondria with circular matrix and intact OMM. 96

Figure S2.4: Effect of Drp1 KD on CCCP induced actin clouds and mitochondrial shape change. 98

Figure S2.5: Effect of Opa1 KD on CCCP-induced actin burst and mitochondrial morphology. 100

Figure 3.1. WAVE activates Arp2/3 complex during ADA. 129

Figure 3.2. Rac and Cdc42 activation during ADA. 131

Figure 3.3. Cytoplasmic calcium increase stimulated by mitochondrial depolarization. 133
Figure 3.4. Protein kinase C activation of the Rac GEF Trio during ADA. 135
Figure 3.5. AMPK activation by LKB during ADA. 136
Figure 3.6. FMNL formins are required for ADA. 137
Figure 3.7. ADA accelerates mitochondrial circularization. 139
Figure S3.1. ADA induction by metformin treatment. 141
Figure S3.2. NPF Knock-outs. 142
Figure S3.3. Rho GTPase activation in ADA. 144
Figure S3.4. Cytoplasmic calcium increase stimulated by CCCP and histamine. 145
Figure S3.5. Protein Kinase C activation of Rac through the Rac GEF Trio. 147
Figure S3.6. AMPK activation, Fgd1 phosphorylation and Cdc42 activation during ADA. 149
Figure S3.7. FMNL formins and ADA. 151
Figure 4.1: ADA in multiple cell types. 181
Figure 4.2: ADA stimulation by mitochondrial depolarization or ETC inhibition. 182
Figure 4.3: ADA is required for glycolytic activation upon mitochondrial perturbation in MEFs. 184
Figure 4.4: Actin assembly in ETC protein depleted cells. 186
Figure 4.5: Effector T lymphocytes (T_{eff}) require ADA for glycolytic activation. 188
Figure S4.1: Line scans of ADA MEFs. 190
Figure S4.2: Oligomycin-induced ADA in MEFs. 191
Figure S4.3: ATP levels changes by complex I or III inhibition. 192
Figure S4.4: Changes in ECAR in MEFs after mitochondrial inhibitor treatments. 194
Figure S4.5: Effect of NCLX inhibition on CCCP- and oligomycin-activated glycolysis. 195
Figure S4.6: Changes in lactate production induced by mitochondrial inhibitors and hypoxia in MEFs. 197
Figure S4.7: Cytoplasmic ATP changes induced by ATP synthase inhibition. 199
Figure S4.8: ADA and mitochondrial depolarization in EtBr-treated cells. 200
Figure S4.9: Changes in lactate production in EtBr or NDUFS4 KO MEFs. 202
Figure S4.10: Actin assembly in Leigh syndrome fibroblasts. 203
Figure S4.11: Effect of CK666 on ADA and glycolytic activation in T_{eff}. 204
Figure S4.12: Effect of CK666 on hypoxia-induced lactate production in T_{eff}. 206

Figure 5.1: ADA transiently disrupts MERCs. 228
Figure 5.2: ADA delays mitochondrial Parkin recruitment in CK666 treated and FMNL family KD U2-OS cells. 230
Figure 5.3: ADA delays mitochondrial Parkin recruitment in WRC KD and VAP-B OE U2-OS cells. 232
Figure 5.4: Parkin recruitment is inhibited by dynamic actin in EtBr-treated MEF. 234
Figure 5.5: ADA is sustained in galactose-grown HeLa cells. 235
Figure 5.6: Parkin recruitment is delayed in galactose-grown cells. 236
Figure 5.7: PDA in HEK-293 and HeLa cells. 238
Figure 5.8: Myosin VI silencing does not affect ADA in U2-OS cells. 240
Figure S5.1: ADA does not inhibit protein arrival or mitochondrial-lysosomal interactions. 242
Figure S5.2: VAP-B OE does not inhibit ADA. 244
Figure S5.3: ADA delays mitochondrial Parkin recruitment in CK666 treated and FMNL family KD in HeLa cells. 245
Figure S5.4: Bioenergetic profiling of glucose versus galactose-grown cells. 247
Figure S5.5: ADA is sustained in galactose-grown U2-OS cells. 249
Figure S5.6: Spire1 KD does not inhibit ADA in U2-OS cells. 250
Figure S5.7: mDia family silencing does not inhibit ADA in U2-OS cells. 252

List of tables

Table 1.1: NPFs for Arp2/3 complex activation	59
Table 1.2: 15 mammalian formins	60
Table 1.3: The 13 protein-coding mitochondrial genes, and the ETC subunits they encode	61
Table 3.1: List of pharmacological treatments and their effects.	153
Table 3.2: Oligonucleotides used for CRISPR KO and siRNA silencing in human and murine cell lines.	154
Table 5.1: Parkin recruitment times after CCCP-depolarization	253

Glossary

2-DG	2-Deoxy-D-glucose
AA	Antimycin A, compound for complex III inhibition
ADA	Acute damage-induced actin
ADP	Adenosine diphosphate
AMP	Adenosine monophosphate
AMPK	AMP-activated protein kinase
Arp2/3 complex	Actin promoting factor
ATP	Adenosine triphosphate
BFP	Blue fluorescent protein
CCCP	Carbonyl cyanide m-chlorophenyl hydrazone, protonophore
CD3	Cluster of differentiation 3
CD28	Cluster of differentiation 28
Cdc42	Cell division control protein 42 homolog, Rho family GTPase
CGP37157	NCLX inhibitor
CIA	Calcium induced actin
CK666	Arp2/3 complex inhibitor
CL	Cardiolipin
Cos-7	Monkey kidney fibroblast-like cell
CRISPR/Cas9	Gene editing system
CTL	Cytotoxic T lymphocyte/$CD8^+$ T lymphocyte
DAPI	4′,6-diamidino-2-phenylindole, fluorescent dye for DNA
DMSO	Dimethyl sulfoxide
Drp1	Dynamin-related protein 1, GTPase for mitochondrial division
ECAR	Extracellular acidification rate (mpH/min)
ECM	Extracellular matrix
ER	Endoplasmic reticulum
EtBr	Ethidium bromide
ETC	Electron transport chain
FAD/$FADH_2$	Flavin adenine dinucleotide (oxidized/reduced forms)
FCCP	Carbonyl cyanide 4-(trifluoromethoxy)phenylhydrazone, protonphore
Fis1	Mitochondrial fission 1 protein
FMN/$FMNH_2$	Flavine Mononucleotide (oxidized/reduced forms)
FMN1/2	Formin-1/-2, founding family of ‘formins’
FMNL	Formin-Like Protein

FRET	Fluorescence resonance energy transfer
F-tractin	Cytoplasmic actin filament reporter, expressing the neuronal inositol 1,4,5-triphosphate 3-kinase A actin-binding domain
GFP	Green fluorescent protein
GAPDH	Glyceraldehyde 3-phosphate dehydrogenase
HeLa	Human cervical carcinoma cell, derived from Henrietta Lacks, an African-American mother of five and cancer patient
IMM	Inner mitochondrial membrane
IMS	Intermembrane space
INF2	Inverted formin 2
Iono	Ionomycin, a calcium ionophore
IP_3R	Inositol trisphosphate receptor
KD	Protein knock-down
KO	Protein knock-out
LatA	Latrunculin A, actin assembly inhibitor
MCU	Mitochondrial calcium uniporter
MDV	Mitochondrial-derived vesicle
MEF	Mouse embryonic fibroblast
MERC	Mitochondrial-ER contact site
Mff	Mitochondrial fission factor
MiD49/51	Mitochondrial dynamics proteins of 49 and 51 kDa
Mito	Mitochondria
mPTP	Mitochondrial permeability transition pore
mtDNA	Mitochondrial DNA
NAD^+/NADH	Nicotinamide adenine dinucleotide (oxidized/reduced forms)
$NADP^+$/NADPH	Nicotinamide adenine dinucleotide phosphate (oxidized/reduced forms)
NCLX	Mitochondrial $Na^+/Ca^{2+}/Li^+$ exchanger
NPF	Nucleation promoting factor, Arp2/3 complex activator
OCR	Oxygen consumption rate (pmol/min)
OE	Protein over-expression
OFP	Orange fluorescent protein
Oligo	Oligomycin, compound to inhibit ATP synthase
Oma1	Metalloprotease-Related Protein 1, mitochondrial protease
OMM	Outer mitochondrial membrane
Opa1	Optic atrophy-1, mitochondrial dynamin like GTPase

Oxphos	Oxidative phosphorylation
PDA	Prolonged damaged-induced actin
PFA	Paraformaldehyde
PFK	Phosphofructokinase
P_i	Phosphate ion
PIP_3	Phosphatidylinositol (3,4,5)-triphosphate
PI3K	Phosphoinositide 3-kinase
PKCβ	Protein kinase C-β
PM	Plasma membrane
pmf	Proton motive force (mV)
Rac	Rac family small GTPase
RFP	Red fluorescent protein
ROI	Region of interest
ROS	Reactive oxygen species
Rot	Rotenone, compound to inhibit complex I
rRNA	Ribosomal ribonucleic acid
s.d.	Standard deviation
s.e.m./SEM	Standard error of mean
siRNA	Small interfering RNA
TCA cycle	Tricarboxylic acid cycle
T_{eff}	Effector $CD8^+$ T cell
TME	Tumor microenvironment
TMRE	Tetramethylrhodamine, ethyl ester
Tom20	Translocase Of Outer Mitochondrial Membrane 20
TRITC-Phalloidin	Fluorescent actin filament dye
tRNA	Transfer ribonucleic acid
$T_{1/2}$	Reaction half-life (min/sec)
UQ/UQH_2	Ubiquinone/Ubiquinol (oxidized/reduced forms)
U2-OS	Human bone osteosarcoma epithelial cell, derived from a 15-year-old, white female cancer patient
VDAC	Voltage-Dependent Anion Channel
WRC	WAVE regulatory complex
WT	Wild-type
$\Delta\psi_m$	Mitochondrial membrane potential (mV)

NOTES ON THE FORMAT OF THIS THESIS

Portions of the text and figures in Chapters I-V have been previously published or submitted in the following journals:

Chapter I : Introduction

Fung TS, Chakrabarti R, Higgs HN. Emerging roles for actin in nuclear and mitochondrial function. *Under revision at Nat Rev Mol Cell Biol.* 2022

Chakrabarti R*, Kage F*, **Fung TS***, Liu A, Higgs HN. Actin interactions with mitochondria: multiple roles for multiple situations. *Under revision at J Cell Sci*. 2022

*: These authors contributed equally to this work

Chapter II: Distinguishing acute damage-induced actin from other forms of mitochondrially-associated actin

Fung TS, Ji WK, Higgs HN, Chakrabarti R. Two distinct actin filament populations have effects on mitochondria, with differences in stimuli and assembly factors. J Cell Sci. 2019 Sep 23;132(18):jcs234435. doi: 10.1242/jcs.234435. PMID: 31413070; PMCID: PMC6765187.

Chapter III: Unravelling the mechanism for rapid actin assembly after CCCP-induced mitochondrial damage

Fung TS[*], Chakrabarti R[*], Kollasser J, Rottner K, Stradal TEB, Kage F, Higgs HN. Parallel kinase pathways stimulate actin polymerization at depolarized mitochondria. Curr Biol. 2022 Apr 11;32(7):1577-1592.e8. doi: 10.1016/j.cub.2022.02.058. Epub 2022 Mar 14. PMID: 35290799; PMCID: PMC9078333.

*: These authors contributed equally to this work

Chapter IV: Mitochondrial-associated actin regulates glycolysis in mitochondrial dysfunction

Chakrabarti R*, **Fung TS***, Kang T, Elonkirjo PW, Suomalainen A, Usherwood EJ, Higgs HN. Mitochondrial dysfunction triggers actin polymerization necessary for rapid glycolytic activation. bioRxiv 2022.06.03.494723; doi: 10.1101/2022.06.03.494723. *Accepted in J Cell Biol.*

*: These authors contributed equally to this work

Chapter V: Peri-mitochondrial actin delays Parkin recruitment in damaged mitochondria

Fung TS, Chakrabarti R, Higgs HN. Acute actin polymerization at depolarized mitochondria delays Parkin recruitment. *Manuscript in preparation.*

Chapter 1:

Introduction

1.1 The actin cytoskeleton:

Actin (a 42kDa monomeric protein) is universally abundant in all eukaryotes, ranging from 50μM to 200μM in mammalian cells [1-3]. First discovered in muscle and described as far back as 1887, actin was successfully purified in 1942 [4]. The actin cytoskeleton provides animal cells, which lack a cell wall, with a structural framework – allowing them to change their shape, migrate, exchange material and adapt to their immediate environment [5]. On top of that, the actin cytoskeleton also provides scaffolds for protein and cargo transport within the cell [6], making it a dynamic and versatile system and crucial for health and physiology. A general biophysical function of actin is to generate force, which it does in two fundamentally different ways: 1) by filament growth to push material forward; or 2) as a substratum for myosin motor proteins, which provide a pulling force.

There are six actin genes in humans, four α-actin in various types of muscle, and two non-muscle actins, β-actin and γ-actin [7]. Our focus here is on non-muscle cells. β- and γ-actin are identical in all but four amino acids.

Interestingly, actin belongs in the same super-family as the glycolytic enzyme hexokinase, with both proteins binding to adenosine triphosphate (ATP) in a central cleft [7]. A recent paper found that the yeast hexokinase Glk1 polymerizes into filaments to inhibit its hexokinase activity after a nutrient shift [8]. Actin as a monomer is not an effective ATPase, but once it polymerizes into a filament, ATP hydrolysis efficiency increases [9].

In cells, the basic building block of the actin cytoskeleton are not actin monomers but rather actin filaments, double-stranded helical (right-handed twist) polymers (7nm in diameter) [10]. The actin filament is polar, meaning there are two different ends - called the barbed and the pointed end respectively [7]. Each actin subunit adds 2.7nm in length to a filament [7].

There are two distinct phases to actin polymerization: nucleation and elongation. Nucleation requires monomers to sequentially dimerize then trimerize, both steps being unfavorable. The trimeric actin ‘seed’ can elongate rapidly to generate the actin filament. Thus, actin filament assembly is limited by the nucleation phase, with dimerization the

most unfavorable step [5]. During elongation, the barbed end is the more dynamic end, having on-rates and off-rates ~10 fold faster than the pointed end [11].

One key feature of actin is how quickly it transitions between monomers and filaments - being able to generate and disassembly extensive filament networks within seconds to minutes [12-14]. Therefore, to achieve the rapid and precise mobilization of the actin cytoskeleton for specific purposes, cells possess a myriad of actin-associated proteins that regulate the location and structure of actin networks. **Figures 1.1** and **1.2** showcase a bird's eye view and a cross section of a mammalian cell, giving a taste of the diversity in cellular actin-associated structures.

1.1.1 Proteins controlling actin dynamics

To control actin polymerization and depolymerization, cells rely on a number of actin-binding proteins (**Figure 1.3** and **Figure 1.4**) [5, 15]. An overall picture of cellular actin dynamics is that several of these proteins essentially prevent spontaneous nucleation (profilin, thymosin) and elongation (capping protein). Nucleation factors allow filament creation when and where needed.

Elongation factors allow extended filament growth where appropriate. Depolymerization factors (cofilin, working with other proteins) accelerate filament disassembly,

1) Nucleation factors, which initiate new filaments from monomers. Three important nucleation factor classes are:

    a. Arp2/3 complex. "Arps" are actin related proteins that share between 17% and 52% sequence with actin. There are 11 Arps in eukaryotes. Arp2 and Arp3 combine with 5 other subunits to form the Arp2/3 complex, which acts as a barbed end nucleus and remains at the pointed end after nucleation. The complex is inactive and requires two activators: 1) a nucleation promoting factor (NPF; **Table 1.1**) and 2) the side of a pre-existing filament.

        This second activator results in a highly characteristic 70˚ branch upon Arp2/3-mediated nucleation. Mammalian NPFs include WASP/N-WASP, Scar/WAVE (explained more in the later **section 1.1.4**), WASH, WHAMM, and Dip/WISH. Cortactin is another Arp2/3 complex-binding protein that reinforces branches. There are multiple instances of Arp2/3

complex-induced actin networks assembling around mitochondria (**section 1.4**). In these cases, actin polymerizes in a dense 'cloud' that surrounds the mitochondrion. Cortactin can also be found around mitochondria. In mouse embryonic fibroblasts (MEFs), knocking out cortactin elongates mitochondria length [16].

b. Formins represent a diverse protein family (15 in mammals) [17] that promote nucleation and remain at the barbed end during elongation [18]. Structurally, formins are defined by the eponymous formin homology (FH) domains 1 and 2. Most formins are dimers, and the FH2 domains regulate nucleation and processively move with the growing barbed end of an actin filament during elongation. FH1 domains bind profilin-bound actin monomers and delivery them onto the growing filament. One key difference between formin- and Arp2/3 complex-mediated actin assembly is that formins generate linear actin filaments. Examples include mDia1, mDia2, INF2, FMNL (explained more in **section 1.1.5**), and FMN2 (**Table 1.2**).

c. Tandem WH2 domain-containing proteins. The exact mechanism of actin assembly for this class of actin polymerizing factors is still poorly understood, but they promote nucleation and elongation [19]. Examples include Spire1/2, Cordon Bleu (Cobl), and leiomodin (Lmod).

   Of note, mitochondrially-localized Spire1C (an isoform of Spire1) is reported to participate in calcium-induced mitochondrial division alongside formin INF2 [20].

2) Elongation factors either allow or inhibit barbed end growth in cells:

   a. Capping proteins bind tightly to barbed ends and stops elongation. The major capping protein is a hetero-dimer and is expressed in all eukaryotes [7]. Capping proteins can be counter-acted by the next two protein classes.

   b. Formins. After nucleating a filament, the formin remains at the growing barbed end, allowing elongation even in the presence of capping protein.

c. Ena/VASP proteins. Similar to formins, these proteins bind near the barbed end, antagonizing capping proteins. Mammals have three such proteins: VASP, Mena and EVL. Ena/VASP proteins can be found in focal adhesions, stress fibers, lamellipodial and filopodia [21].

3) Profilin is a small (13kDa protein) and abundant protein that binds actin monomers. Most unpolymerized actin is profilin-bound. Profilin plays a number of important roles. Profilin-bound monomers cannot nucleate, and only add to the barbed end (and not to the pointed). Profilin also accelerates recharging of depolymerized actin with ATP [22, 23]. In addition to its other functions, profilin can bind most formins, and works together with formins to accelerate elongation. The three mammalian profilins are: PFN1, 2 and 3.

4) Thymosins are very small (~5kDa) proteins that bind actin monomers and "sequester' actin, preventing nucleation or addition to either end. Thymosins have shown to be at higher concentration than actin in some cell types, but are somewhat mysterious due to their small size [24]. Mammals possess at least three thymosins: thymosin β4 (*TMSB4* gene), the best characterized; thymosin β10 (*TMSB10*); and thymosin β10 (*TMSB15*).

5) Cofilin is largely associated with depolymerization. Cofilin preferentially binds to ADP(adenosine diphosphate)-actin sections of filaments, generally near the pointed end [7]. Cofilin-mediated severing in these regions is often an important step in filament depolymerization and cofilin works with other proteins in this role, including cyclase-associated protein (CAP), twinfilin, coronin and Aip1. Sometimes, however, cofilin-mediated severing promotes actin polymerization by creating new barbed ends. Cofilin phosphorylation inhibits actin binding [25, 26]. There are three mammalian cofilins: Cofilin1, Cofilin2 and Destrin. Mitochondrially-associated cofilin1 might modulate mitochondrial dynamics [27, 28].

1.1.2 Proteins controlling actin organization

A number of actin-binding proteins organize filaments, including (**Figure 1.5A-C**):

1) Arp2/3 complex. This nucleation factor automatically causes filament branching when it nucleates, through its ability to bind both pointed ends and filament sides.

Repeated Arp2/3-mediated nucleation leads to tree-like 'dendritic networks' that can be extensive and dense, such as those found in the lamellipodia [29], or in a more limited manner around endosomes [30].

2) Crosslinking and bundling proteins. These proteins bind two actin filaments to create networks or bundles. α-actinin and filamin favor networks, while fascin creates parallel bundles. Filament spacing by fascin is tight (~8nm [31]); while spacing by α -actinin (~35nm [32]) or filamin (~80nm[33]) are wider. FMNL formins can also bundle filaments [34], as well as some gelsolin family proteins, IQGAP1, EPS8 and paladin.
3) ERM proteins (ezrin, radixin and moesin) link actin filaments to the plasma membrane [35]. I-BAR proteins such as IRSp53, MTSS1, IRTKSS, ABBA and Pinkbar can also serve this function.
4) Tropomyosins bind along the actin filament and modulate filament stability through interactions with myosins or other actin-binding proteins (**Figure 1.3**). Mammals have four tropomyosin genes with multiple splice variants, leading to a diversity that is poorly understood [36].

1.1.3 Myosins

The wide variety of myosin motors serve three general purposes (**Figure 1.5D-F**):

1) Cargo transport. Some myosins travel along an actin filament, towing cargo behind [37]. Examples are the myosin I, myosin V, myosin VI and myosin 19 classes. All myosins except myosin VI move toward the barbed end.
2) Actin network contraction by the myosin II class, which forms bi-polar filaments, pulling actin filaments in opposite directions [38]. There are > 10 'muscle' myosins that assemble sarcomeric structures in specific muscle types. Mammals also have three non-muscle myosin IIs: NMIIA, NMIIB and NMIIC [39], important for contractile structures like the cytokinetic ring, stress fibers and retraction fibers.
3) Load-resisting anchors. In some situations, myosins maintain cellular structure in the face of a significant counter force. Examples include myosin I, myosin II, myosin VI, and myosin 19 [40, 41].

1.1.4 More about the WAVE regulatory complex

The ubiquitously expressed WAVE regulatory complex (WRC) is an important NPF, that activates the Arp2/3 complex [42]. NPFs (including WAVEs, WASP/N-WASP, WASH, WHAMM and DIP/WISH) contain a carboxy-terminal WCA (WASP Homology 2 (WH2)-central-acidic) domain [43] necessary for Arp2/3 complex activation. The WRC is a five subunit complex of ~400kDa [44]. In mammals, the subunits are WAVE (containing the WCA), Sra1, Nap1/Hem2 (or hematopoietic-specific Hem1), Abi1/2 and HSPC300. There are three WAVE genes, *WAVE1*, *2* and *3*. with WAVE2 being the most widely expressed. Interestingly, removal of any single WRC subunit often eliminates the expression of all other subunits [45].

WAVE's WCA is sequestered in the complex [46]. The Rho-family GTPase Rac1 activates WAVE by releasing the WCA [47]. Aside from Rac1, phospholipids like phosphatidylinositol (3,4,5)-triphosphate (PIP_3) and a number of transmembrane proteins can promote further activation [48, 49] or recruit WRC to specific membranes. Phosphorylation in the WCA domain also provides additional fine tuning [50].

The WRC is widely known to promote lamellipodia formation at the leading edge [51, 52] but we recently found that the WRC can also be found near mitochondria. WRC activity triggers 'acute damage-induced actin' (ADA) after mitochondrial dysfunction (**Chapter III**).

Mutations of the WRC have been implicated in many different diseases, including neurological disorders, immune deficiencies and cancer progression [42]. Other non-canonical roles of WRC (or through individual subunits) are being determined as well. Recently, it was shown that Hem1 on its own can bind to mTORC2. In $CD4^+$ T cells, Hem1 lost disrupted both WRC function and cellular growth through the phosphoinositide 3-kinase (PI3K)/AKT/mTORC2 pathway, leading to immunodeficiencies [53]. Abi1 can also work independently as a signal transducer in Ras-mediated cell transformation [54] or as an activator of another NPF, N-WASP [55].

1.1.5 More about FMNL family formins

FMNLs represent a distinct formin sub-family, with three mammalian FMNLs: FMNL1, FMNL2 and FMNL3. Biochemically, FMNLs are weak nucleators but they are proficient in filament elongation and bundling [56-59]. FMNLs are N-terminally myristolyated and

localize preferentially to the plasma membrane and the Golgi [60, 61]. FMNL2 and FMNL3 are found in filopodia and interact with the actin-bundler fascin [62-65]. High activities of FMNL2 and FMNL3 are linked to poor prognosis in cancer patients and increased probability of metastasis [66-68].

Strikingly, knocking out FMNL2/3 in melanoma and fibroblasts limits cell migration and lamellipodia structure [60], suggesting that lamellipodial actin assembly requires the coordinated action of the Arp2/3-complex and FMNL formins. We hypothesize that something similar occurs around mitochondria for ADA (**Chapter III**).

1.2 The mitochondrion: a unique organelle

While mitochondria are commonly called 'powerhouses of the cell' and ATP production is perhaps the most critical function of the organelle, the organelle also provides a host of other functions related to apoptosis [69-71], calcium signaling and buffering [72-74], immune defence [75-77], generation of metabolic derivatives for macromolecule synthesis [78-80], lipid synthesis and exchange [81, 82], amongst others. In addition, maintenance of mitochondrial health is now appreciated as crucial to overall cellular homeostasis, especially in long-lived cells like neurons, and pathways for mitochondrial disposal by mitophagy are important processes. For these reasons, mitochondrial biology is a subject of intense interest.

1.2.1 Mitochondria possess two membranes with specific characteristics

Mitochondria contain two lipid membranes that are distinct from each other [83]. The OMM is lipid-rich, highly fluid and relatively permeable to low-molecular weight solutes (< 5kDa) [84]. In rat liver cells, the phospholipid composition of the OMM is 44-59% phosphatidylcholine (PC), 20-35% phosphatidylethanolamine (PE), 5-20% phosphatidylinositol (PI) and the rest consisting of phosphatidylserine (PS), phosphatidic acid (PA), cardiolipin (CL) and lysophospholipids [82, 85]. The outer mitochondrial membrane (OMM) participates in mitochondrial signaling and provides a platform for receptors and tethering proteins [86, 87].

In contrast, the inner mitochondrial membrane (IMM) folds to form a unique architecture consisting of invaginations called cristae (**Figure 1.6A, B**), is protein-rich and crucial for metabolism, hosting complexes vital for mitochondrial respiration [88-90]. The lipid composition of IMM in rat liver cells consists of 38-45% PC, 32-39% PE, 14-23% CL, 2-7% PI with the remaining mostly consisting of PS, PG and lysophospholipids [82, 85]. CL is selectively abundant in the IMM and is a negatively charged (-2) lipid that stabilizes the membrane morphology [82]. On the other hand, sphingolipids and cholesterol are not major constituents of mitochondria [82].

Between the OMM and IMM lies a constricted region called the intermembrane space (IMS) and the interior of the mitochondrion is called the matrix.

1.2.2 Mitochondria possess its own genome

The mitochondrion is the only metazoan organelle with its own genome, called the 'nucleoid' or mitochondrial DNA (mtDNA), located in the matrix. Mammalian mtDNA is a ~16kb circular double-strand structure that encodes 13 protein-coding genes, 22 tRNAs and two ribosomal RNAs (rRNAs) (**Table 1.3**) [91].

All the other ~1400 mitochondrial proteins, however, are encoded by nuclear genes and are imported into the mitochondria through elaborate machineries [92]. PGC1α is a key transcriptional regulator that promotes gene expression to supply mitochondrial proteins during organelle biogenesis [93]. Laudable efforts have been made to characterize the full mitochondrial proteome, with the MitoCarta initiative [94] and the MITOMICS dataset [95] being valuable resources. Interestingly, the mRNAs of mitochondria proteins are enriched on the OMM, suggesting translation at close proximity before eventual import [96].

Each mitochondrion possesses multi-copies of mtDNA. How the copies are distributed is still unknown. However, regulation of mtDNA replication and distribution are less rigorous compared with the nuclear genome [97]. The mtDNA replisome is required for mtDNA synthesis and consists of three components: 1) The mitochondrial polymerase γ (Pol γ) (encoded by the *POLG* gene). Pol γ contains two subunits, a catalytic subunit (POLG1) and a processivity subunit (POLG2) [98]. 2) A helicase known as Twinkle [99], and 3) A single-stranded DNA binding protein [100].

Besides replication, the mitochondrial transcription factor A (TFAM) [101] packages mtDNA into a nucleoid and facilitates transcription [101, 102]. All the proteins of the mtDNA replisome and transcription are nuclear-encoded.

Similar to nuclear DNA, mtDNA is prone to damage from environmental factors or replication mistakes. Mitochondria possess corrective abilities like short and long patch base excision repair (BER) or single-strand break (SSB) repair [103]. However, unlike the nuclear genome, double-stranded breaks (DSBs) of the mtDNA result in rapid degradation rather than serious repair attempts [104, 105]. Due to the existence of disorders linked to mtDNA, engineering the mitochondrial genome offers therapeutic promise [106].

Why do mitochondria need its own genome? Currently, the answers are still speculative, but all proteins encoded in the mitochondria are relatively hydrophobic. Delivering these hydrophobic proteins to mitochondria is avoided by their local synthesis [107].

1.2.3 Mitochondrial dynamics

Mitochondria in cells are not static, uniform 'pill-shaped' structures (**Figure 1.6C-E**). Instead, they exhibit dynamic behaviors (also known as 'mitochondrial dynamics'). Directed movement of mitochondria (called 'mitochondrial transport') is important for organelle distribution [108], especially true for polarized cells like neurons, which need to deliver mitochondria across long distances in the axons [109, 110].

In addition, the mitochondrial network undergoes constant remodelling that is balanced by two counteracting processes, mitochondrial division and fusion [111, 112]. Division splits one mitochondrion into two [113]; while fusion does the opposite and combines mitochondria together [114, 115]. Both division and fusion have distinct molecular mechanisms and signaling cues [116-118]. Remodeling of the cristae represents another form of mitochondrial dynamics [119].

1.2.3a Mitochondrial division/fission

Two major ways of mitochondrial division are recently characterized (**Figure 1.6F, G**). They can occur either at the middle of the organelle (midzone) or at the periphery [120].

The main, central protein facilitating division is a dynamin-related GTPase, Drp1 [121]. Drp1 is a cytosolic protein that needs to be recruited by OMM-bound adaptor proteins such as mitochondrial fission factor (Mff), mitochondrial dynamics proteins of 49 kDa and 51 kDa (MiD49/51) [122-125]. Both Mff and MiD49/51 recruit and bind Drp1 independently of one another [126]. Mitochondrial fission protein 1 (Fis1), on the other hand – although a known receptor of Drp1 in yeast [127] - has a more debatable role as an adaptor for Drp1 in mammalian cells [128-131].

Midzone and peripheral divisions are both Drp1-dependent, but the receptor differs. Fis1 regulates midzone division while Mff mediates peripheral division. Midzone division is also associated to healthier mitochondria, while periphery division is driven by a stress response, like an accumulation of reactive oxygen species (ROS) for example.

A majority of mitochondrial division events (~88% of events in Cos-7 cells [132], mainly midzone divisions [120]) occur at mitochondrial-endoplasmic reticulum (ER) contact sites (MERCs), which mark regions of Drp1 recruitment [133]. Here, we define a MERC to be a temporally stable regions with less than 30nm of resolvable distance between the two parties [134, 135]. Elegant studies in MERCs revealed that the ER wraps itself around the mitochondrion before constriction and final scission [132]. Interestingly, during midzone division, mtDNA synthesis occurs at the same MERCs prior to division [136].

Besides the ER, contact with two other organelles may contribute to mitochondrial division: lysosomes [137-139] and Golgi-derived vesicles [140]. The Higgs lab and others have also shown that actin plays a role in mitochondrial division, likely related to MERCs, and will be discussed in **section 1.4.1**.

What are the functional roles of mitochondrial division? Firstly, division is required for segregating mitochondria population between mother and daughter cells [141, 142]. Mitochondrial division is also important in neurons, where smaller mitochondria are transported from the soma out to the neurites [143, 144]. A recent report also suggested that mitochondrial division distributes mitochondrial RNA granules [145] across the mitochondrial network. Lastly, mitochondrial division is essential for mitochondrial quality control through mitophagy. Surprisingly however, in certain mitophagic situations, division can be Drp1-independent [146, 147]. The budding of mitochondrial-derived vesicles (MDVs) for cargo degradation does not require Drp1 either [148].

1.2.3b Mitochondrial damage and circularization

Mitochondrial damage through the loss of mitochondrial membrane potential is thought to result in massive division known as mitochondrial 'fragmentation'. Morphologically, the entire mitochondrial population converts from an elongated network to small discrete units. While most studies observe this fragmentation after long periods of damage (in hours of protonophore treatment) [149, 150], there are several reports of fragmentation within minutes, acting in an actin-dependent manner [16, 151, 152]. In contrast however, several other detailed studies, including my own work, suggest something different [153-156].

In the early stages of mitochondrial damage by uncouplers (within 30 min), we and others observe that mitochondria do not divide. Instead, the IMM re-organizes itself to form a 'donut' morphology under confocal imaging. An elegant electron microscopy study found that the IMM is reorganized extensively during circularization while the OMM remains intact [156]. We term this phenomenon 'mitochondrial circularization' (**Chapter II and III**). Circularization is Drp1-independent [154, 156]. Importantly, we found that circularization does not require actin either (**Chapter II**), and is in fact inhibited by actin.

1.2.3c Mitochondrial fusion

As mitochondrial fusion is not the major theme for this thesis, it is only briefly described. Successful mitochondrial fusion is a two-step process where opposite OMMs and IMMs fuse sequentially [114, 157] . Fusion of the OMM relies on dynamin GTPases Mitofusin1 and 2 (Mfn1/2) [158]; while IMM fusion is dependent on a dynamin-like GTPase Opa1 and CL [159, 160]. Mitochondrial fusion is essential for cellular survival [161-163], preserving mitochondrial DNA (mtDNA) integrity [164, 165] and safeguards the genome from mutations [166]. Recent research has found that mitochondrial fusion can occur at the same MERCs where the division machineries are found [167]**.**

It is worth noting that mitochondrial membrane potential ($\Delta\psi_m$) is essential for fusion [150]. A mitochondrion without membrane potential cannot fuse. Hence, if a mitochondrion is partially depolarized (with ~50% membrane potential assessed by TMRE staining in live-cell imaging), it will attempt to fuse with healthy counterparts to regain its membrane potential [167].

Taken together, mitochondrial fusion is instrumental in maintaining cellular health. The current consensus is that hyperconnected mitochondria are associated with higher respiration rates [150, 168-170], increased ATP production [171, 172] and considered advantageous to cells with high energy demands [173].

1.3 Cellular bioenergetics: a primer

All living cells require a constant supply of energy with the common currency being ATP. In healthy cells, ATP concentration is maintained around 10-fold higher than ADP, which is orders of magnitude away from the hydrolysis reaction equilibrium [174]. Hence, achieving and maintaining this healthy ADP/ATP ratio requires constant ATP production, largely through carbohydrate (glucose) and/or fat (fatty acid) oxidation [91, 175]. Regulation of these processes is critical and energy-sensing proteins like AMPK and several glycolytic enzymes are sensitive to fluctuations in cytosolic ADP/ATP ratio. AMPK will be further elaborated in **section 1.3.5**.

The second thing to consider is how cells store and transfer electrons. Catabolic pathways converting food (like glucose) into energy are essentially a flow of electrons down an energy gradient [175]. In many situations, the terminal electron acceptor is often oxygen, which is reduced to H_2O. Important intracellular electron carriers and redox intermediaries includes:

1) NAD^+ (nicotinamide adenine dinucleotide)/NADH (reduced) pool –associated with ATP production.
2) $NADP^+$ (nicotinamide adenine dinucleotide phosphate)/NADPH (reduced) – associated with macromolecule synthesis or photosynthesis in plants.
3) reduced glutathione/oxidized glutathione (GSH/GSSG) – associated with redox stress.
4) ubiquinone/ubiquinol (reduced) (UQ/UQH_2) - mobile electron carriers within the IMM.

These electron carriers are highly compartmentalized in cells. For example, neither NAD^+/NADH nor $NADP^+$/NADPH are capable of crossing subcellular membranes [176, 177]. Therefore, spatial and temporal control of electron carriers is important issues, as the imbalance of these species are implicated in conditions like cancer [178] and aging [179]. Given that changes to ADP/ATP or electron carriers are highly dynamic (within seconds or minutes), targeted fluorescent probes are now used to assess local levels of ATP [180], ADP/ATP [181] or NAD^+/NADH [182-184] in real time.

Below, I will elaborate on ATP production, starting with glucose metabolism and glycolysis.

1.3.1 Glycolysis: oxygen independent ATP production

Glycolysis is one of the first metabolic pathway elucidated (**Figure 1.7**) [185] and refers to the splitting of one glucose molecule into two molecules of pyruvate, the terminal product. In humans, the normal fasting plasma glucose is maintained at 3.9-5.5mM (70-100mg/dL) [186, 187]. Glucose transporters (GLUT – 14 proteins identified for humans [188]) facilitate the glucose uptake in cells, with GLUT1-4 being the most commonly expressed [189].

Once inside the cell, glucose breakdown requires ten biochemical reactions, all in the cytosol. ATP is initially consumed in early steps (the investment phase) before net ATP production is realized in the latter steps (the payoff phase) [185]. It might seem counter intuitive why ATP should be consumed first, but there are good reasons for this [185]. Firstly, phosphorylation of glucose to glucose 6-phosphate generates a negatively-charged molecule that traps glucose for further processing [185]. Secondly, glycolysis relies on substrate-level phosphorylation. Phosphorylated metabolites, like 1,3-bisphosphoglycerate, transfer their phosphoryl (PO_3) group to ADP to produce ATP [185]. For complete glycolysis, 2 net ATP molecules and 2 NADH reducing equivalents are released for every glucose molecule.

The third step of glycolysis, phosphofructokinase (PFK), is often considered the rate limiting step and is a focus of regulation. PFK is also a key sensor of the ADP/ATP ratio, with AMP allosterically activating and ATP allosterically inhibiting [190], allowing rapid response to changing cellular ATP. In **section 1.3.5,** I will discuss other glycolytic regulatory mechanisms.

1.3.1a What to do with NADH?

Tracing the flow of electrons, NAD^+ accepts electrons from glyceraldehyde 3-phosphate dehydrogenase (GAPDH- step six) [175]. Cytosolic NADH can be subsequently imported into the mitochondria through shuttle pathways (e.g. the malate-aspartate shuttle [191]) and combine with the mitochondrial NAD^+/NADH pool. During rapid glycolysis, however, this mechanism can be insufficient. A buildup of intracellular NADH (reductive stress) is undesirable as it inhibits GAPDH activity and slows down glycolysis [192]. In the next section. We will learn another mechanism to convert NADH to NAD^+.

1.3.1b Pyruvate: Metabolite at a crossroad

After glycolysis, pyruvate has two major fates, which is largely dependent on oxygen availability, glycolytic rate and other factors. In the presence of oxygen, pyruvate is translocated into the mitochondria and utilized in the tricarboxylic acid (TCA) cycle (described in **section 1.3.2**). In the absence of oxygen, pyruvate becomes an electron acceptor [185], converting lactate by lactate dehydrogenase to regenerate NAD^+[175, 193]. For some proliferating cancer cells, the pressure to recover NAD^+ can even overcome ATP demands to drive high glycolytic output [178].

Like NADH, lactate accumulation is undesirable, and cytosolic lactate (and protons) translocate into the extracellular environment through monocarboxylate transporters (MCT) [194, 195]. There is a misconception that lactate in the circulation is a metabolic 'waste product' [196], when in fact, it is actually a valuable carbon substrate. Lactate is utilized as fuel in different contexts, for example by regulatory T cells in the tumor microenvironment (TME) [197], by neurons during periods of high energy demand [198], and by cardiac muscle at all times [199]. Moreover, lactate is now known as a key signaling molecule [200] and even regulates gene expression through histone lactylation [201].

Besides pyruvate to lactate conversion, other metabolic pathways to regenerate NAD^+ are also available in the cytosol to buffer reductive stress during hypoxia [202].

1.3.1c Glycolysis beyond ATP production

Cells use glycolysis for purposes beyond ATP production. Stimulated with growth factors, cells consume high amounts of glucose to support biosynthesis in different ways [79, 203]:

1) Glucose 6-phosphate channels into the pentose phosphate pathway as a building block for nucleotide synthesis [79].
2) NADH can be converted to NADPH for anabolic reactions through cytosolic or mitochondrial NAD kinases [204, 205].
3) Fructose 6-phosphate is a precursor for UDP-N-acetylglucosamine (UDP-GlcNAc) [206, 207], an essential component for protein post-translational modification [208].

1.3.1d Glucose and fructose: A tale of two carbohydrates

Apart from glucose, fructose is another major dietary carbohydrate in the modern world [209]. Metabolism of fructose by ketohexokinase-c eventually produces glyceraldehyde and dihydroxyacetone phosphate [210], which enter glycolysis at the ATP payoff phase. This finding has raised health concerns, since fructose breakdown bypasses the regulatory PFK step [209]. Excess glucose- or fructose-derived energy is converted to fatty acids in the liver and stored as triglycerides in white adipocytes. Therefore, carbohydrate consumption is now linked with increasing rates of worldwide obesity [211] and the prevalence of non-alcoholic fatty liver disease [209].

1.3.2 The tricarboxylic acid cycle (TCA) cycle

In terms of ATP generation. Mitochondria use a series of redox reactions to drive ADP phosphorylation. The following reactions take place either in the mitochondrial matrix or across the IMM. The realization that mitochondria participate in oxygen-dependent ATP production came in the late 1940s, through biochemical assays (with isolated rat liver mitochondria) done by Albert Lehninger [212, 213]. Metabolites like pyruvate, are funneled into the TCA cycle to facilitate ATP production.

After glycolysis, cytosolic pyruvate is imported into the mitochondrial matrix, converted either to acetyl coenzyme A (acetyl-CoA) through pyruvate dehydrogenase or into oxaloacetate by pyruvate carboxylase [214] and enters one of the most well-described pathways of metabolism – the TCA cycle (also known as the citric acid cycle or the Krebs cycle) (**Figure 1.8A**) [215]. This hallmark finding was first introduced in the 1930s by Sir Hans Krebs, who performed a good portion of the work on pigeon breast muscle [216].

The TCA cycle consists of eight reactions [217]. In the canonical first step, citrate synthase combines the two carbons of acetyl-CoA with the four carbons of oxaloacetate to form citrate. In the next seven steps, citrate is progressively catabolized, generating reducing equivalents (three NADH and one $FADH_2$), as well as one GTP, while two CO_2 are released to regenerate oxaloacetate [217]. Isocitrate decarboxylation by isocitrate dehydrogenase is the rate limiting step [218]. In addition, several key enzymes are calcium-activated: pyruvate dehydrogenase [219], isocitrate dehydrogenase and α-ketoglutarate [220].

In the presence of oxygen, NADH and $FADH_2$ are the electron sources for the electron transport chain (ETC – **section 1.3.3b**). One step in the TCA cycle, succinate dehydrogenase, is also a component of the respiratory chain (Complex II) and supplies its $FADH_2$-derived electrons directly [221].

1.3.2a The TCA cycle: beyond generating reducing equivalents

Mirroring glycolysis, ATP production is one of the many functions of the TCA cycle. Multiple TCA intermediates are employed as signaling molecules or building blocks for anabolic processes [222] :

1) Oxaloacetate is involved in the synthesis of aspartate, a precursor of pyrimidine bases and asparagine [223, 224].
2) α-ketoglutarate can be converted to glutamate [79], which in turn, be used for synthesizing non-essential amino acids like proline [205].
3) Citrate exported from the mitochondrion through the citrate/malate antiporter (**Figure 1.8B**) [225] is cleaved by cytosolic ATP citrate lyase (ACL) into acetyl-CoA and oxaloacetate [226, 227].
   Acetyl-CoA is further used for fatty acid synthesis [228] or imported into the nucleus for histone acetylation [229, 230].
   Oxaloacetate, on the other hand, is converted into malate, re-enters the mitochondria and fed back into the TCA cycle [225]. Highly proliferating cells like embryonic stem cells engage this non-canonical TCA loop. In contrast, terminally differentiated cells (e.g. differentiated myotubes) prefer the conventional TCA cycle [225].

Taken together, TCA cycle intermediates are not single-use molecules but actively branch off for diverse functions - supporting the notion that metabolic networks are constantly multitasking to maintain cell viability [175]. Experimental techniques to track metabolites, like fluorescent reporters [231] or stable isotope tracing [232, 233] are currently used to determine the spatiotemporal fate of these metabolites.

1.3.3 Oxidative phosphorylation: oxygen dependent ATP production

1.3.3a The chemiosmotic theory

Peter Mitchell, a British biochemist and Nobel laureate, was the person who brought about a paradigm shift in the field of cellular bioenergetics. In his time, how ATP forms from the oxidation of food in the mitochondria was still a mystery. To solve this puzzle, Mitchell proposed in his 1961 seminal paper [234] that the link between oxidation and ATP synthesis is a proton gradient: the redox energy derived from reducing equivalents (like NADH) is used to generate a proton electrochemical gradient across a membrane, which in turn, drives ATP synthesis.

Mitchell's scheme is referred to as the 'chemiosmotic theory'; and he coined the phrase 'protonmotive force' (pmf or Δp) to describe this proton electrochemical gradient [235].

It is astonishing to note that when he proposed this idea, there were still no experimental findings to support the hypothesis [236]. However, he persisted and wrote two privately published books, elaborating and refining the details of the chemiosmotic theory [235, 237].

Unsurprisingly, the chemiosmotic theory caused controversy in the field, and was not accepted until critical studies confirmed its basic principles. One of the most important biochemical study was conducted in 1974 by Racker and Stockenius (**Figure 1.9**) [238], where they found that ATP synthase can indeed utilize a bacteriorhodopsin-driven proton gradient to produce ATP. Mitchell would later go on to win the Nobel Prize in Chemistry in 1978 for revolutionizing the field of cellular bioenergetics [239].

1.3.3b The proton circuit in the mitochondria and oxidative phosphorylation

Nowadays, we have a much better understanding of the mechanism behind mitochondrial chemiosmosis [221, 240]. The pmf across the IMM is maintained through the ETC (or respiratory chain), which comprises of four large protein complexes I-IV (**Figure 1.10**). Complexes, I, III and IV possess the ability to translocate protons out of the matrix [240], while Complex II does not. The driving force for proton translocation is oxidation of TCA-derived NADH and $FADH_2$, with the electrons passed between complexes (I→III→IV or II→III→IV) to the terminal electron acceptor, oxygen, to form water [240].

The pmf (expressed in mV) is a function of two components, ΔpH: the pH gradient across the membrane (a concentration term, defined as the pH_{IMS} minus the pH_{matrix}) and $\Delta\psi_m$: the mitochondrial membrane potential across the membrane (an electrical term) [91, 240, 241], where:

$$pmf = \Delta\psi_m - 61\,\Delta\text{pH}$$

In mitochondria isolated from rat livers, the overall pH of the matrix is around 7.5-8.2 while the pH of the IMS is around 7, giving an ΔpH ranging from -0.5 to -1.2 pH units. Meanwhile, the $\Delta\psi_m$ measures around 150 to 180mV; giving an overall pmf from 180 to 220mV [241]. The pmf in a single mitochondrion is surprisingly dynamic, local variations in pH [242] and $\Delta\psi_m$ [243] have been observed between cristae.

To generate ATP, protons re-enter the matrix through ATP synthase, driving phosphorylation of ADP into ATP. Hence, the process of harnessing the pmf for ATP production is called 'oxidative phosphorylation'.

Other proton re-entry pathways are also available, which make up the proton 'leak' component [244, 245]. Even in healthy mitochondria, a basal amount of leakage helps relieve the pmf [246]. The uncoupling protein 1 (UCP1) in brown adipocytes [247] and the ADP/ATP carrier (AAC) [248] are alternate proton re-entry pathways. Both can be activated by fatty acids, superoxide or lipid peroxidation products [246].

1.3.4 Complexes of the electron transport chain (ETC)

Here we shall briefly review some key aspects of each individual complex of the ETC. More on this topic can be found in [91, 221, 249]:

Two key electron carries in the ETC are ubiquinone (UQ) [250] and cytochrome c. UQ is a lipid-soluble organic molecule that is reduced by either complex I or complex II to form ubiquinol (UQH_2). UQH_2 diffuse in the IMM to complex III, which is oxidized back to UQ [250]. Cytochrome c is a protein bound peripherally to the IMS face of the IMM, and shuttles electrons from complex III to complex IV.

1.3.4a Complex I

The function of mitochondrial complex I is to couple electron transfer from NADH to UQ with proton movement. Bovine mitochondrial complex I contains 45 subunits and a combined mass of ~980kDa [221], and is an L-shaped structure, divided into a

hydrophobic module and an hydrophilic arm [251]. Seven of the complex I subunits are encoded by mtDNA, and are all found in the hydrophobic domain [221]. The hydrophilic arm is the region where NADH is oxidized. At the base of the hydrophilic domain, a tightly but non-covalently bound flavin mononucleotide (FMN) cofactor accepts electrons from NADH and reduces to $FMNH_2$. The electrons from reduced FMN are then transferred up a series of nine iron-sulfur (Fe-S) centers - moving towards the hydrophobic module and the IMM. The final and exact site of electron transfer to UQ is still in debate but it is thought to happen at a crucial N2 Fe-S center (with a UQ binding chamber proposed) [252]. This binding chamber is strategically positioned close to the inner leaflet of the IMM (~30 Angstroms between UQ binding and IMM) [221].

How complex I couples redox reactions with proton transport is still an unresolved question [91]. One explanation is that during electron transfer, conformational changes in the hydrophilic arm is 'sensed' by the hydrophobic region for proton translocation [221].

Rotenone, a potent complex I inhibitor, prevents the transfer of electrons from the N2 Fe-S center to UQ [251]. Structural analysis reveals that rotenone binds to a pocket very close to the N2 Fe-S center, at a distance around 10.1 Angstroms away [251].

Complex I is also a major center of ROS formation in the ETC [253], which occurs at the FMN region in the hydrophilic arm. Even at basal condition, fully reduced FMN leaks electrons to nearby oxygen to produce $O_2^{\bullet -}$ [254]. This situation is exacerbated if rotenone inhibits complex I and reduced FMN passes on electrons to nearby oxygen instead to produce high quantities of ROS [255]. Other inhibitors, like mucidin [256] or metformin [257], can inhibit complex I without forming ROS, although the mechanism for metformin action is still an active investigation [258].

Complex I deficiency is linked to the pathogenesis of multiple diseases and disorders, including Parkinson's disease [259], T cell exhaustion [260] and cardiovascular failures [261].

1.3.4b Complex II

The function of complex II is to transfer electrons from $FADH_2$ to UQ, and is thus a second route to introduce electrons to the ETC. Complex II is unique in the ETC for three reasons. Firstly, none of its four subunits in mammals are encoded by mtDNA. Secondly,

complex II is the only enzyme in the TCA cycle (succinate dehydrogenase). Thirdly, complex II does not translocate protons across the IMM like the other complexes do.

It was recently found that under hypoxic stress or complex III/IV inhibition, complex II works in reverse to oxidize UQH_2 back to UQ while reducing fumarate to succinate [262]. This reversed complex II activity enables complex I to continue depositing electrons into the ETC to regenerate mitochondrial NAD^+. Succinate is now regarded as a key signaling metabolite [250]. The accumulation of succinate have various effects on cellular function, including T cell proliferation, brown adipocyte differentiation, amongst others [250, 263].

1.3.4c Complex III

Complex III consists of 11 subunits (one encoded by mtDNA) and catalyzes UQH_2 and cytochrome c reduction, while moving four protons from the matrix to the IMS. The mechanism was first proposed by Mitchell and is known as the 'Q cycle' (**Figure 1.11**) [264, 265]. Complex III contains two catalytic sites, one called the Q_p site and resides close to the IMS. The other is called the Q_n site, which is situated close to the lumen. A unique Fe-S protein called the 'Rieske protein' is also loosely tethered to complex III in the IMS and haem C of cytochrome c.

Various compounds inhibit complex III function, including antimycin A, myxothiazol and stigmatellin. Antimycin A binds to the Q_n site and prevents the formation of an radical intermediate $UQ^{\bullet -}$ (ubisemiquinone), thereby blocking reduction of UQ into UQH_2 [91]. In contrast, myxothiazol blocks the Q_p site while stigmatellin blocks the transfer of electrons to the Rieske protein [91].

Antimycin A treatment is a potent trigger for complex III-mediated ROS generation [255]. By blocking Q_n site activity, $UQ^{\bullet -}$ starts accumulating at the Q_p site, leaking electrons to nearby oxygen to generate $O_2^{\bullet -}$ [254]. $O_2^{\bullet -}$ is released from complex III on both sides of the IMM [254]. ROS formation for Myxothiazol is context dependent, experiments have shown that it can induces ROS formation on its own [266] but also inhibit ROS during hypoxia [267]. Stigmatellin, on the other hand, has an inhibitory effect on H_2O_2 production from complex III [268].

1.3.4d Complex IV

Complex IV the last complex in the ETC, consisting of 13 subunits (three encoded by mtDNA). It accepts two electrons from cytochrome c to reduce O_2 to H_2O [269], coupled with protons pumping out into the IMS. How this coupling occur is still poorly understood.

What is known however, is that electrons are first passed from cytochrome c to a bimetallic copper center (Cu_A) and subsequently to a haem a_3/Cu_B catalytic site, which serves as the center for oxygen reduction. As for proton transport, there are two putative proton routes (called the D- and the K- channels, after a critical Asp and Lys residue respectively) that connect the mitochondrial matrix to the catalytic site /Cu_B and the IMS. It is still unknown which path protons take to exit into the IMS. Overall, eight protons are utilized from the mitochondrial matrix for each O_2, four protons end up in H_2O and four are pumped across the IMM [249].

A recent report suggested that metformin can inhibit complex IV activity (~20% reduction) in liver models [270].

1.3.4e ATP synthase

The mitochondrial F_0F_1-ATP synthase is a remarkable nanomachine consisting of 16 subunits (two encoded by mtDNA [271]). Detailed explanation here is beyond the scope of this thesis but excellent resources are available [272, 273]. Briefly, ATP synthase consist of two functional domains, the membrane-intrinsic F_0 sector (in the IMM) and the membrane-extrinsic F_1 sector (in the matrix). The two domains are connected by central and periphery stalks. The F_1 domain is the catalytic part of the enzyme, and phosphorylates ATP from ADP and P_i. On the other hand, the F_0 part contains a motor, which generates rotary action using the pmf. The rotational energy of the F_0 motor is transmitted to the catalytic F_1 domain through the central stalk, which is physically attached to the F_0 motor. Meanwhile, the peripheral stalk acts as a stator to hold sections of the F_1 domain static relative to the rotary elements of the complex [274].

In the mitochondria, ATP synthase dimerizes at the highly curved base of the cristae ridge [275]. There is evidence to suggest that these dimers contribute to IMM folding and cristae formation [276]. Oligomycin, a potent inhibitor of the ATP synthase [277, 278]

binds to the F_o domain of the complex, although the exact binding site(s) is still an area of investigation [279].

1.3.4f Organization of ETC complexes

On the IMM, the ETC complexes can function independent of one another. However, curiously enough, complex I, III and IV organize themselves together into a supramolecular assembly known as the 'respirasome'[280, 281], containing all the necessary mobile electron carriers UQ/UQH_2 and cytochrome c to facilitate efficient electron transfer. The exact reasonings for forming the respirasome is still an area of active research, some hypotheses being:

1) A respirasome offers a favorable way to select out ETC complexes from the protein-rich IMM and stabilize them on the membrane.
2) To reduce the chance of unfavorable and irreversible aggregation with other unrelated protein, preventing erroneous degradation of ETC complexes [280].
3) To minimize the diffusion distances for UQ/UQH_2 and cytochrome *c* (also known as substrate channeling) [280], increasing catalysis efficiency [249, 282].

In mammalian cells, the respirasome occupies the planar, straight surfaces of the mitochondrial cristae [283]. Therefore, respirasome function is closely tied to IMM integrity. Remodeling of the IMM can lead to instabilities of the supercomplexes, bringing about undesirable effects on respiratory functions and overall cellular health [284].

There is no known experimental evidence yet to suggest that complex II forms a supercomplex in mammalian systems. However, a very recent preprint reports that the respiratory supercomplex purified from *Tetrahymena thermophila* (a unicellular eukaryote) contained all four members of the ETC (I-IV) [285]. This gives rise to the possibility that complex II can indeed assemble as a part of the respirasome given the right conditions.

1.3.4g Oxygen: indispensable but in excess?

Since oxygen is essential for oxidative phosphorylation, it might be worthwhile to consider how this important molecule factors into cell culture experiments. As a matter of fact, standard, routine cell culture have oxygen levels drastically different from their *in vivo* tissue sources [286]. Apart from the pulmonary veins in the lungs, most human

tissues contain oxygen levels (5-10%) which are much lower compared to atmospheric air (21%) [286].

To make matters worse, cells are grown in supraphysiological levels of glucose (10 - 25mM glucose in standard media solutions, which is 2-5 fold more than fasting plasma glucose!), we might be observing molecular changes (or missing key observations) for cells that have rewired their biological behaviors based off an abundance of oxygen and nutrients. In the future, more physiological media [287, 288] and cell culture conditions might be beneficial in helping us make the next important discoveries in cell biology.

1.3.4h A quick note about protonophores

To disrupt the pmf, many studies employ mitochondrial uncouplers like carbonyl cyanide m-chlorophenylhydrazone (CCCP) [289], or carbonilcyanide p-triflouromethoxyphenylhydrazone (FCCP) [290] as pharmacological treatments. Dinitrophenol (DNP), another protonophore, was once used for weight loss in the 1930s [291] but was banned due to dangerous hyperthermic effects [292-294]. Sorafenib, an FDA-approved cancer drug, also disrupts mitochondrial pmf [295].

These compounds dissipate the pmf across the inner mitochondrial membrane in seconds (also called 'mitochondrial depolarization') [156, 295-297]. CCCP and FCCP have at least two other effects: 1) they cause the TCA cycle and the ETC to operate and consume substrates (including oxygen) at their maximum rates, representing an 'out of control' respiration [240, 298, 299]; and 2) they cause ATP synthase to work 'in reverse', hydrolyzing ATP to pump protons out of the matrix to recover the pmf, even draining glycolytically generated ATP if required [91, 300-302].

We used to think of protonophores' action as a black box in the past, where protons are indiscriminately transported across the IMM. However, a recent breakthrough study found that this is not the case. Instead, these protonophores depolarize the IMM by binding and activating the proton leak channels. AAC and UCP1 are both stimulated by protonophores to allow proton re-entry [303].

1.3.5 Energy sensing in the cell: AMPK and glycolytic enzymes

Regulation of glycolysis and oxidative phosphorylation is dependent on the energetic state of the cell. How do cells sense energetic changes in the cytoplasm and respond? Several key metabolic enzymes are sensitive to cytosolic ADP/ATP ratio.

1.3.5a AMPK

One key enzyme is the AMP-activated protein kinase (AMPK) (**Figure 1.12**) [304]. AMPK in mammals exist as a heterotrimeric complex including a catalytic α subunit and two regulatory subunits: β and γ. Multiple isoforms exist in mammals for each subunit, two α (α_1, α_2), two β (β_1, β_2) and three γ subunits (γ_1, γ_2, γ_3) [305].

AMPK is activated by phosphorylation of the 'activation loop' of the α subunit, mainly at a highly conserved Thr172 [306]. The major upstream kinase targeting Thr172 is the liver kinase B1 (LKB1 or STK11) [307].

Aside from the α subunit, the other interesting part is the γ subunit, which contains the regulatory adenine nucleotide-binding sites [304, 308]. In a state where cells are well-fed, ATP is bound to the γ subunit, clamping the kinase in an inactive conformation [309]. However, when there is an energy shortage and ADP accumulates, cytosolic adenylate kinases catalyze phosphate transfer from one ADP to another, producing one ATP and one AMP [174]. AMP outcompetes ATP on the γ subunit [310, 311], triggering a conformational change of the whole complex [174] for three effects [308]: 1) it makes AMPK more susceptible to LKB1 phosphorylation at Thr172. 2) it decreases the rate of dephosphorylation of Thr172 by phosphatases. 3) it allosterically activates phosphorylated AMPK. These three mechanisms act synergistically, making AMPK sensitive to even small increases in AMP.

Apart from AMP activation, AMPK can be activated through calcium signaling. Increased cytosolic calcium activates the calcium-sensitive kinase CaMKK2, which phosphorylates AMPK at Thr172 [312, 313].

1.3.5b AMPK and mitochondria

Activation of AMPK enables the cell to initiate transcriptional changes and fine-tune its bioenergetics [304]. Recently, it was found that AMPK also modulates mitochondrial dynamics [314]. Mitochondrial dysfunction causes AMPK to phosphorylate the Drp1 receptor Mff on the OMM, driving Drp1 recruitment and mitochondrial division.

AMPK is also an important kinase for mitophagy [315]. AMPK phosphorylates the serine/threonine kinase ULK1, which subsequently phosphorylates the E3 ubiquitin ligase Parkin, activating Parkin for downstream mitophagy (see **section 1.3.8**). It should be noted that AMPK activation in this context is rapid, occurring within two minutes of

CCCP treatment. We found that this rapid AMPK activation is also crucial for ADA around depolarized mitochondria (**Chapter III**).

1.3.5c Other energy-sensing enzymes in the cell

AMPK aside, three other metabolic enzymes respond to ATP levels independently [174]:

1) Phosphofructokinase (PFK), which is allosterically activated by AMP and inhibited by ATP to regulate glycolysis.
2) Glycogen phosphorylase, which is responsible in the breakdown of glycogen, the storage form of glucose. Glycogen phosphorylase is activated by ↑ADP/ATP ratio
3) Fructose-1,6-bisphosphatase (FBPase), which is involved in the *de novo* synthesis of glucose (gluconeogenesis) in the liver and reverses the PFK step. The reactions of FBPase and PFK are distinct from one other. FBPase is inhibited with ↑ADP/ATP ratio.

1.3.6 Shifting between glycolysis and oxidative phosphorylation: an open mystery still

1.3.6a The Pasteur effect

How and why cell shifts between glycolysis to oxidative phosphorylation is still poorly understood. The detailed experiments of Louis Pasteur (19^{th} century) showed that baker's yeast ferment simple sugars (like glucose) to produce ethanol in the absence of oxygen [316, 317] but the presence of oxygen suppressed fermentation. Hence, he identified, rightly, that cells would convert glucose to ethanol (or lactate in humans) as a response to hypoxia. The metabolic switches – shifting from respiration to fermentation/glycolysis during hypoxia and high oxygen tension inhibiting glycolysis became collectively known as the 'Pasteur effect'.

Currently, it is known that any conditions causing defects in mitochondrial ATP production (ETC inhibition, loss of $\Delta\psi_m$ etc.) accelerates glycolysis [91]. One physiological situation where metabolic switching matters is the tumor microenvironment (TME), where immune cells must survive [318, 319].

Interestingly, by studying Pasteur's original findings, Otto Warburg made his own ground-breaking and profound contribution years later.

1.3.6b The Warburg effect: past and present

In the 1920s, Warburg observed that cultured tumor tissues have high, abnormal rates of glucose utilization and lactate secretion, even in the presence of abundant oxygen [320]. This propensity of cancer cells to preferentially rely on anaerobic metabolism became known as the 'Warburg effect' [321] or 'aerobic glycolysis' [322].

Warburg himself concluded that mitochondria in cancer cells were 'impaired' [323, 324], since oxygen could no longer suppress glycolysis anymore [325]. Thus, this phenomenon can be considered a 'weakening' of the Pasteur effect [326].

In one of his later papers, Warburg further suggested that transformation of a normal cell to a cancerous cell happens in two-stages [323]. The first stage occurs when normal cells encounter irreversible respiration injury, setting them on the path to become cancerous. The second phase of carcinogenesis represents a period of adaptation for the injured cells to maintain their viability - cells which could not adapt die from a lack of energy while others succeed by replacing ATP production from respiration to glycolysis [327].

His conclusion has been a topic of controversy since, not least because his own experiments [328] and by other laboratories [329] revealed persistent oxygen consumption in tumor tissues; suggesting that cancer cells' mitochondria might not be totally impaired after all.

Today, the current consensus is that the Warburg effect should be more broadly defined. It is certainly true that cancer cells employ glycolytic metabolism even under high oxygen tension. For example, lung tumors in the airway are highly glycolytic during tumorigenesis [330, 331]. However, apart from injuries to mitochondria [332-334] (which might impact its oxygen-sensing capacity [335, 336]), the Warburg effect can be considered a 'damage' to the proper regulations of glycolysis [329] or cytosolic oxygen-sensing pathways [337-339].

1.3.6c Cancer metabolism: an ongoing investigation

In one sense, Warburg correctly inferred that cancer cells adapt readily for survival. In fact, cancer cells will do whatever is necessary to gain a metabolic advantage. In certain tumors, active mitochondria operate together with accelerated glycolysis [340]; while in other situations, slow-growing cancer cells might prefer oxidative phosphorylation and faster proliferative cells more glycolytic [340].

Hence, to address the unresolved puzzle of Warburg's observation - a better understanding of the metabolic flexibility in cancer cells [203] and the metabolic regulation of host immunity [341, 342] are crucial, allowing better diagnostics and more precise treatments [343]. For example, teasing out the metabolic effects of immunotherapies like programmed cell death protein 1 (PD-1) blockade [344] is currently a hot topic of research [345, 346].

How does ADA around mitochondria influence cellular metabolism? In **Chapter IV** of this dissertation, we will explore this question. Our findings suggest that actin assembly upon mitochondrial dysfunction stimulates a 'glycolytic switch', adding mechanistic insight to one part of the Pasteur effect.

1.3.7 Calcium signaling in mitochondria

The late Nobel laureate Otto Loewi once remarked: "Ja Kalzium, das ist alles.", which is roughly translated as "Yes, calcium is universal" [347]. Intracellular calcium is a vital signaling ion. Excitable cells like neurons [348] and pancreatic β-cells [349] release neurotransmitters or insulin after extracellular calcium influx through voltage-gated calcium channels. For most other cell types, a number of receptor-activated pathways trigger ER calcium release into the cytosol through ER-localized inositol-trisphosphate receptors (IP_3Rs) [350, 351] or ryanodine receptors in skeletal and cardiac muscles [352]. It is likely that ryanodine receptor-like pathways exist in many cells, but are poorly characterized.

Mitochondria have also been regarded as important regulators of intracellular calcium signaling after it was first demonstrated that isolated mitochondria could accumulate calcium [353].

1.3.7a The cytosol is a calcium 'desert'

In a 'resting' cell, mitochondrial and cytosolic free calcium levels are approximately 0.1μM. Stimuli that trigger increased cytosolic calcium also often induce a mitochondrial calcium rise [351, 354, 355], bringing ions in either from the extracellular medium (1.8 mM) or from the ER (250-600 μM) [356, 357]. Calcium ionophores like ionomycin induces both calcium influx from the extracellular space and triggers significant ER calcium release [12, 358, 359], while agonists like histamine activate ER calcium release through IP_3Rs.

From the numbers, there is an ~18,000-fold difference in calcium between the extracellular environment and the cytosol; and a ~5,000-fold difference between the ER lumen and cytosol. Cells maintain a low basal intracellular calcium concentration (a calcium 'desert') for good reasons. One important reason is that calcium, unlike magnesium, do not bind water tightly and readily precipitates out as calcium phosphate [360]. This precipitation is detrimental to the cell and it invests a significant amount of energy to regulate cytoplasmic calcium levels through ion channels (pumps and exchangers) [361]. Also, many magnesium-requiring enzymes (like actin) bind calcium with higher affinity than they do magnesium, leading to altered activity. The ATP-dependent pumps maintaining the calcium gradient include SERCA (ER) [362, 363], the PMCA pump (plasma membrane, PM) [364], and the Na^+/K^+-ATPase (PM, which indirectly powers calcium efflux through the Na^+/Ca^{2+} exchanger NCX in the PM) [365].

In addition to these pumps, the mitochondria help sequester any excess cytosolic calcium, having a buffering capacity of ~0.2 to 2μM in isolated brain mitochondria [366]. Interestingly, the mitochondrion stores a portion of its calcium as solid-phase calcium phosphate (or organo-phosphate) granules [367]. The estimated concentration of calcium in these granules is around 1.9 M [367], which makes the mitochondria a vital reservoir of calcium apart from the ER.

Mitochondria cannot buffer calcium indefinitely though and overaccumulation causes opening of mitochondrial permeability transition pores (mPTPs) [368]. Once assembled, this nonspecific channel allows hydrophilic molecules up to 1500 Da to pass [369, 370], swelling and rupturing the organelle which eventually leads to cell necrosis [371]. The molecular identity of this pore is still unknown.

Mitochondria also accept calcium from the ER through MERCs [372-375]. Various extracellular stimuli (e.g. hormones, growth factors, neurotransmitters) can induce ER calcium release [376], along with signals originating from the mitochondria. ROS released from mitochondria is shown to trigger IP_3R-mediated calcium efflux, which then gets imported into the mitochondria at MERCs [377].

How does calcium transport across the OMM and IMM to enter the mitochondrial lumen? Crossing the OMM is generally unproblematic, as this membrane is permeable to cations like calcium. The main entry point through the OMM involves the 30-35kDa

voltage-dependent anion channel (VDAC) [378], which contains calcium binding sites and does not restrict calcium movement. [379-381].

1.3.7b IMM calcium entry

Once inside the IMS, calcium must transverse the IMM which is a selective membrane impermeable to even the smallest cation (the proton) [84]. The molecular identity of the IMM calcium channel was unknown for many years [382, 383]. The breakthrough came in the early 2010s through careful studies by several groups [384-386]. Nowadays, we know that a multiprotein channel called the 'mitochondrial uniporter channel' is responsible for IMM calcium entry.

This channel is made up of several proteins. The channel-forming protein is the mitochondrial calcium uniporter (MCU), containing two transmembrane domains (TM1 and TM2). Four MCU proteins assemble the tetrameric pore [387].

Other subunits include:

1) The essential mitochondrial response element (EMRE) [388], a scaffolding protein that helps to stabilize the tetrameric pore.
2) The mitochondrial calcium uniporter regulator 1 (MCUR1) [389].
3) The mitochondrial calcium uptake 1,2 and 3 (MICU1/2/3) [390-392]. To function, MICU1 forms a homodimer or heterodimer with either MICU2 or MICU3 [393]. MICU3 is a brain-specific isoform [394]. MICUs interact electrostatically with MCU in the IMS [395] and binds to local calcium using EF hands [393]. At low calcium levels, MICUs physically occlude the MCU pore to prevent cation entry [387]. Conversely, at high calcium concentrations, MICUs dissociate from the MCU, opening the pore. Therefore, mitochondrial calcium uptake is regulated by the calcium-sensing MICUs.

1.3.7c IMM calcium efflux

The major IMM calcium release pathway that is applicable to this thesis is the mitochondrial $Na^+/Ca^{2+}/Li^+$ exchanger (NCLX). The molecular discovery of NCLX occurred roughly the same time as for MCU [396].

This exchanger has been suggested to import 3 Na^+ for each Ca^{2+} exit [397]. Regulation of NCLX is still poorly understood but mitochondrial membrane potential and phosphorylation of the exchanger are required [398]. A loss of $\Delta\psi_m$ has been associated

with the inhibition of NCLX but NCLX phosphorylation by protein kinase A (PKA) can override this $\Delta\psi_m$-induced inhibition of NCLX [399].

Hence, calcium efflux via NCLX has been shown in hypoxic experiments [267] and ischemic models [400] where the IMM depolarizes. In our context, we found that calcium efflux by NCLX after CCCP treatment is an initial trigger for ADA (**Chapter III**).

One important method to interrogate NCLX activity is through the small molecule inhibitor CGP37157 [397, 401]. Although CGP37157 is considered a selective and potent inhibitor, there are studies suggesting that it possess off-target effects on PM calcium transporters and channels [397, 402].

1.3.7d Mitochondrial calcium and respiration

How does mitochondrial Ca^{2+} regulate cellular metabolism? Firstly, Ca^{2+} activates several key enzymes of the TCA cycle (**Figure 1.8**), which increases their affinities for substrates to drive an efficient TCA cycle [220, 403]. Hence, MCU-mediated Ca^{2+} uptake has been demonstrated to stimulate ATP synthesis [394]. In addition, reports also suggest that complexes I, III, IV [404] and the ATP synthase [405] increase their activities in the presence of Ca^{2+}, but the exact mechanisms for these situations are still unclear.

1.3.8 The mitophagy process: PINK1/Parkin dependent clearance

Cellular health is tightly linked to mitochondrial health. When mitochondria get damaged, proper clearance of is required to maintain homeostasis. The mitochondrial turnover process is called 'mitophagy', which is a specific form of autophagy [406, 407]. In a canonical mitophagy model, loss of membrane potential causes stabilization of the serine/threonine kinase PINK1 on the OMM (**Figure 1.13**) [406, 408]. PINK1 then phosphorylates both ubiquitin [409, 410] and the E3 ubiquitin ligase Parkin [411-413], causing Parkin recruitment to ubiquitinate a number of OMM substrates. Next, autophagy receptors including p62, NBR1, NDP52, optineurin (OPTN) and TAX1BP1 bind ubiquitinated OMM proteins [406, 414] and tether the organelle with the autophagosome for engulfment [415]. The completed autophagosome is then delivered to the lysosome for degradation [415].

Besides mitophagy, PINK1/Parkin also drive MDV budding for organelle removal [416]. Defects in PINK1/Parkin have been implicated in immune deficiency disorders [417] and

neurodegenerative diseases [418]. How actin plays an active role in PINK1/Parkin mitophagy are described in **section 1.4.4** and **Chapter V**.

Other mitophagy models that do not involve PINK1/Parkin include the OMM proteins FUNDC1 [419] or BNIP3/NIX [420].

1.4 Actin and mitochondria coming together: what we know so far

The attention to actin and mitochondria has significantly increased over the course of the past 20 years. It is now established that actin participates in mitochondrial biology in a variety of contexts, which we divide into four categories:

1) To stimulate mitochondrial division
2) To induce or inhibit mitochondrial motility
3) As actin clouds in interphase and mitotic cells
4) In several stages of the mitochondrial damage response

1.4.1 Mitochondrial division and the formin INF2

A role for actin in mitochondrial fission was first suggested almost 20 years ago [154], with the molecular players starting to emerge in recent years. In our current mechanism (**Figure 1.14**), an ER-bound isoform of the formin INF2 nucleates a meshwork of cytosolic actin filaments [12, 421, 422], some of which interact with mitochondria. A second actin polymerization factor, the mitochondrially-bound Spire1C, might also be involved in this actin assembly [20]. Notably, Arp2/3 complex is not required for mitochondrial fission through this mechanism (**Chapter II**). Myosin II also plays a role here [1, 423], and the actin bundler fascin has been linked to INF2-polymerized actin in cancer cells [424].

We refer to this INF2-mediated polymerization as 'calcium-induced actin' (CIA) because it is triggered by increased cytoplasmic calcium. CIA brings about mitochondrial division in two ways. First, CIA stimulates ER-to-mitochondrial calcium transfer, through stabilized MERCs. The increased mitochondrial matrix calcium causes IMM constriction in a Drp1-independent manner [12]. Second, CIA stimulates Drp1 recruitment to mitochondria [12, 425, 426]. Biochemically, Drp1 binds actin filaments and actin synergizes with Mff to promote Drp1 GTPase activity [3, 427]. In cells, actin-stimulated Drp1 oligomerization may be initiated on the ER, which contains a population of ER-localized Mff [425]. The current model is that CIA may help in both recruitment and oligomerization of Drp1 - either on the ER or on actin filaments - before Drp1 finally translocate onto the mitochondria for constriction.

Interestingly, two distinct 'types' of mitochondrial division were recently identified: 'midzone' division occurs in healthy mitochondria, whereas 'peripheral' division occurs in damaged mitochondria. Midzone division is dependent on associated ER and INF2, but not for division at the periphery (**Figure 1.6F, G**) [120].

1.4.2 Actin inhibiting microtubule-based mitochondrial motility

Mitochondrial distribution and motility are largely driven by kinesin- or dynein-motors moving along microtubules (**Figure 1.15**) [110]. These motors link up with the mitochondria through two intermediaries: Milton (also called TRAK) and Miro. Regulation of mitochondrial movement is important. A recent study identified that increased cytoplasmic glucose causes post-translational modification of Milton by N-acetylglucosamine (O-GlcNAcylation) [428]. Modified Milton recruits and binds to FHL2. This Milton-FHL2 complex promotes actin polymerization around the mitochondria, thereby arresting microtubule-based movement. While this actin bears some resemblance to cycling peri-mitochondrial actin (**section 1.4.3**) or ADA, its assembly mechanisms apart from FHL2 are still unknown.

1.4.3 Mitochondrially-associated actin in interphase and mitotic cells

Some cultured cells during interphase display 'clouds' of actin filaments around a sub-set of mitochondria (**Figure 1.15**) [429], with the cloud dynamically circling around the cell within 15 min. Presence of the cloud correlates with increased Drp1-dependent mitochondrial fission but these mitochondria often re-fuse after the actin cloud passes. This actin cloud is Arp2/3 complex dependent [429].

During the mitotic stage, another actin cloud develops which possess greater speed and actin density than interphase clouds. Mitotic clouds makes a full revolution in 6 min [430] and restricts mitochondrial motility. However, in a minority of cases (13%), a mitochondrion can break free and propel away with an actin 'tail' (~250 nm/sec). Morphologically, this Arp2/3 complex-dependent tail contains two main strands that are helically entwined, similar to the distinctive tails behind Rickettsia at a specific stage in its infection cycle [431]. While this actin-based motility is not important for overall symmetrical distribution of mitotic mitochondria, it does increase mixing of mitochondrial populations.

1.4.4 Actin and mitochondrial dysfunction, mitophagy

Rapid actin polymerization (within 5mins of treatment) around damaged mitochondria, which we call ADA (acute damage-induced actin), was first described in mouse embryonic fibroblasts [16] using the protonophore FCCP (**Figure 1.16**) and forms the central theme of this dissertation.

At the beginning of this project, the distinction between CIA (**section 1.4.1**) and ADA was murky. In **Chapters II** and **III**, we shall discuss how CIA and ADA are fundamentally different from each other. Although cytoplasmic calcium is involved in both actin responses, calcium alone is necessary but insufficient for ADA, and a parallel signaling pathway is required (**Chapter III**). The comparison between CIA and ADA highlights the point that cellular actin is polymerized based on distinct signaling cues to promote unique functional outcomes.

Apart from CCCP, we found that other stimuli like ETC inhibitors and hypoxia can generate ADA (**Chapters IV**). ADA is crucial for a variety of cellular dynamics - mitochondrial circularization (**Chapter II and III**), metabolic shift to glycolysis (**Chapter IV**) and Parkin recruitment (**Chapter V**).

After ADA, a second round of peri-mitochondrial actin polymerization, which we term "PDA" (prolonged damage-induced actin) occurs after 1-2 hours of persistent $\Delta\psi_m$ loss [432, 433]. The functions of PDA is distinct from ADA. Firstly, it prevents re-fusion of damaged mitochondria with healthy ones [432]. Myosin VI-mediated actin cages isolate damaged mitochondria from neighboring populations [432] and the caged mitochondria are sealed for destruction in mitophagy. Secondly, PDA also disperses mitoaggregates for efficient autophagosomal engulfment [433]. PDA is currently known to be N-WASP, Arp2/3 complex and formin(s) dependent.

1.4.5 Actin and glycolysis

Two examples of actin-mediated glycolytic regulation have recently been revealed.

In the first example, aldolase A is inactive when bound to cortical actin at the plasma membrane. Stimulation with insulin, however, activates the PI3K signaling cascade, eventually activating both Rac1 and WRC, remodelling the actin cytoskeleton and disassembles the cortical actin network to release aldolase A. Once released from actin, aldolase is activated [434].

In the second example, cells in a stiff extracellular matrix (ECM) experience high physical tension and remodel their actin cytoskeleton to build stress fibers, shifting their metabolism toward glycolysis. Stress fibers help sequester an E3 ubiquitin ligase called TRIM21. Under normal circumstances, TRIM21 targets PFK for ubiquitination and degradation. With TRIM21 immobilized on stress fibers, excess PFK elevates glycolysis. Cancer cells like non-small-cell lung carcinomas maintain these actin stress fibers (even on a soft ECM) to sustain high glycolytic rates [435].

In **Chapter IV** of my thesis, we found that in addition to stress fibers and cortical actin, ADA is a potential driver of glycolysis. Unlike the pre-existing models, the glycolytic activation we observe is rapid, occurring within 5-min of mitochondrial dysfunction. ADA-mediated glycolysis is particularly crucial for cells in physiology (5mM glucose) or hypoglycemic (<2mM glucose) and hypoxic (1% O_2) conditions.

The exact mechanisms for this effect are still unknown. And we speculate whether the abovementioned models [434, 435] or Arp2/3 complex-dependent glucose uptake [436] might be responsible. However, our finding has opened new avenues to explore. Simply, cells have devised multiple ways to accelerate glycolysis by remodeling their intracellular actin cytoskeletal landscape.

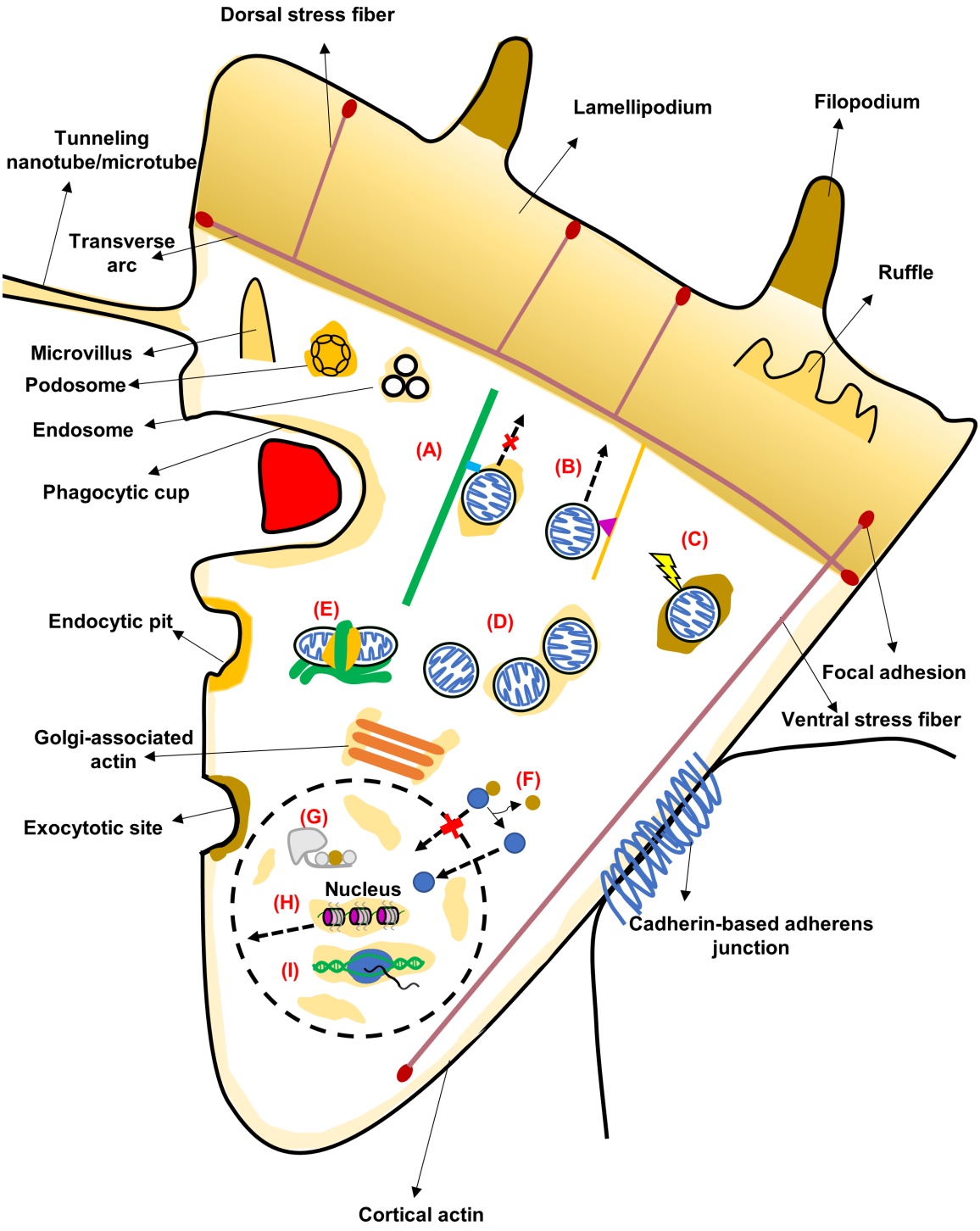
Dorsal stress fiber
Lamellipodium
Filopodium
Tunneling nanotube/microtube
Transverse arc
Ruffle
Microvillus
Podosome
Endosome
Phagocytic cup
(A)
(B)
(C)
(D)
(E)
(F)
(G)
(H)
(I)
Endocytic pit
Focal adhesion
Ventral stress fiber
Golgi-associated actin
Exocytotic site
Nucleus
Cadherin-based adherens junction
Cortical actin

Figure 1.1: Actin-based structures, viewed from above the cell. A hypothetical mammalian cell, migrating toward the top of the page and attached to a second cell on the right. Cellular structures/processes known to use actin are labeled by name, with actin indicated by brown shading. Actin-based functions that are somewhat distinct from the canonical functions are denoted by letters. (**A**) Actin assembly around mitochondria, inhibiting microtubule-mediated mitochondrial translocation (microtubule in green, kinesin in blue). (**B**) Myosin-based mitochondrial motility along an actin filament. Myosin in purple. (**C**) Actin polymerization around a damaged mitochondrion (ADA), which induces several downstream responses. Damage indicated by lightning bolt. (**D**) 'Cycling' actin polymerization around several mitochondria. (**E**) CIA: calcium-activated actin polymerization by the ER-bound formin INF2 (ER in green). Actin plays a major role in regulating cell dynamics in the nucleus too, which are beyond the scope of this dissertation. (**F**) MRTFA (Myocardin Related Transcription Factor A, blue circle) nuclear entry, regulated by actin monomer binding. In the nucleus, the MRTFA-Serum response factor (SRF) complex is a major transcription factor. (**G**) Actin monomer as part of a chromatin remodeling complex. (**H**) Actin-based motility of chromatin toward the nuclear periphery. (**I**) Actin involvement in transcription regulation.

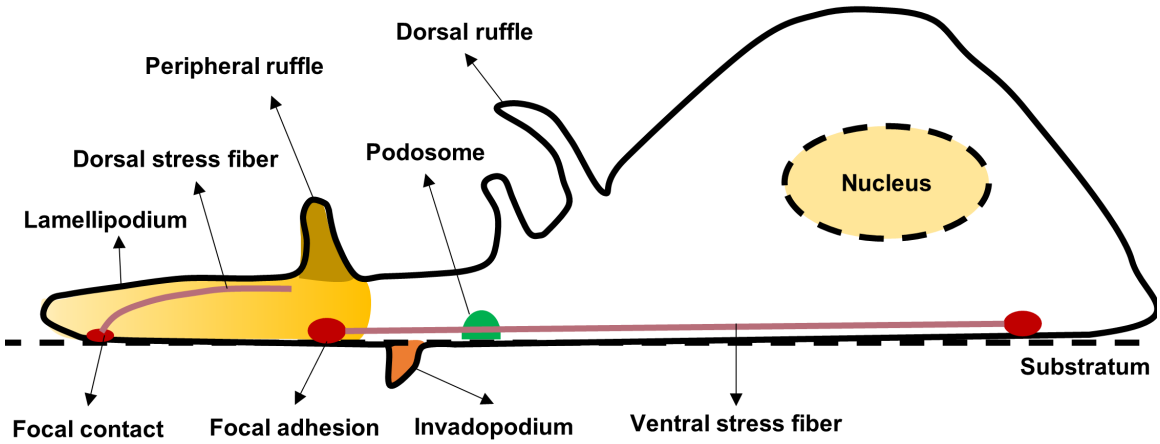

Figure 1.2: Actin-based cellular structures viewed in cross section. A side view of a cell, emphasizing several points: ruffles are dorsal structures; peripheral ruffles and dorsal ruffles are distinct structures; podosomes and invadopodia are ventral; the lamellipodium is weakly attached to the substratum. Ventral stress fibers are attached at both ends to focal adhesions, whereas dorsal stress fibers are only attached to focal contacts near the leading edge. Important organelles like mitochondria, ER and Golgi are not shown. Figure adapted from [437].

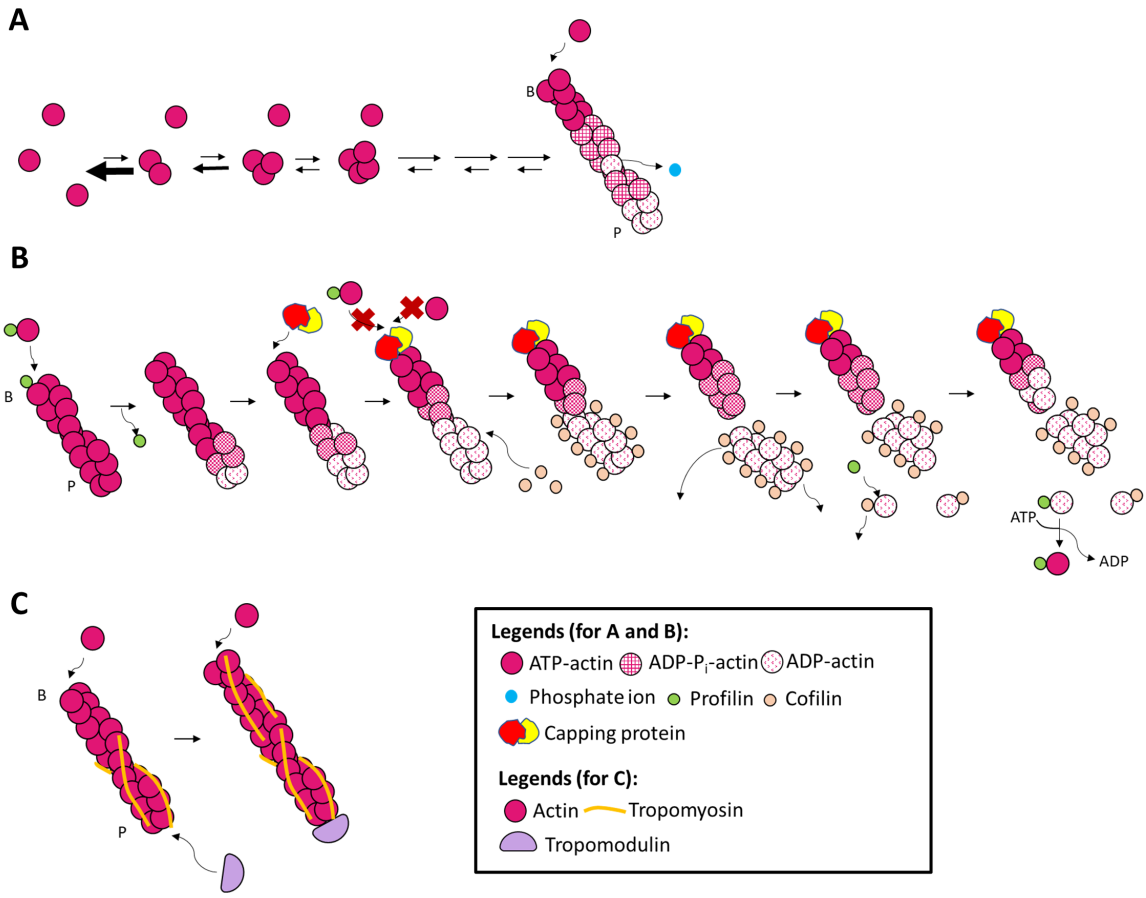

Figure 1.3: Proteins controlling actin dynamics. A) Polymerization of actin alone. The two initial steps of actin polymerization (dimerization and trimerization) are unfavorable, and collectively called 'nucleation'. Subsequent monomer additions (elongation) are much more favorable. In cells, monomer addition occurs preferentially at the filament barbed end, rather than the pointed end. ATP hydrolysis by the actin subunit is generally slower than the polymerization rate, resulting in an ATP-rich region at the barbed end and an "ADP-P_i" rich region (P_i = phosphate) in the middle of the filament. P_i release is slower, resulting in an "ADP" region at the pointed end. B – barbed end. P - pointed end. **B)** Three abundant proteins that are central to cellular actin dynamics. 1) profilin binds actin monomers, allowing them to add to barbed ends but not pointed ends. 2) Capping protein binds the barbed end, blocking elongation. 3) Cofilin binds ADP-bound filament regions near the pointed end, resulting in filament severing. 4) the severed filament releases ADP-bound actin monomers from both the barbed and pointed ends. 5) Profilin re-binds the ADP-bound actin monomer, and cofilin releases. 6) Profilin accelerates nucleotide exchange on actin, resulting in ATP re-charging. **C)** Tropomyosins bind along the actin filament. Tropomodulins bind at pointed ends of tropomyosin-bound filaments, capping these ends. Nucleotide dynamics are not shown in this panel, for simplicity.

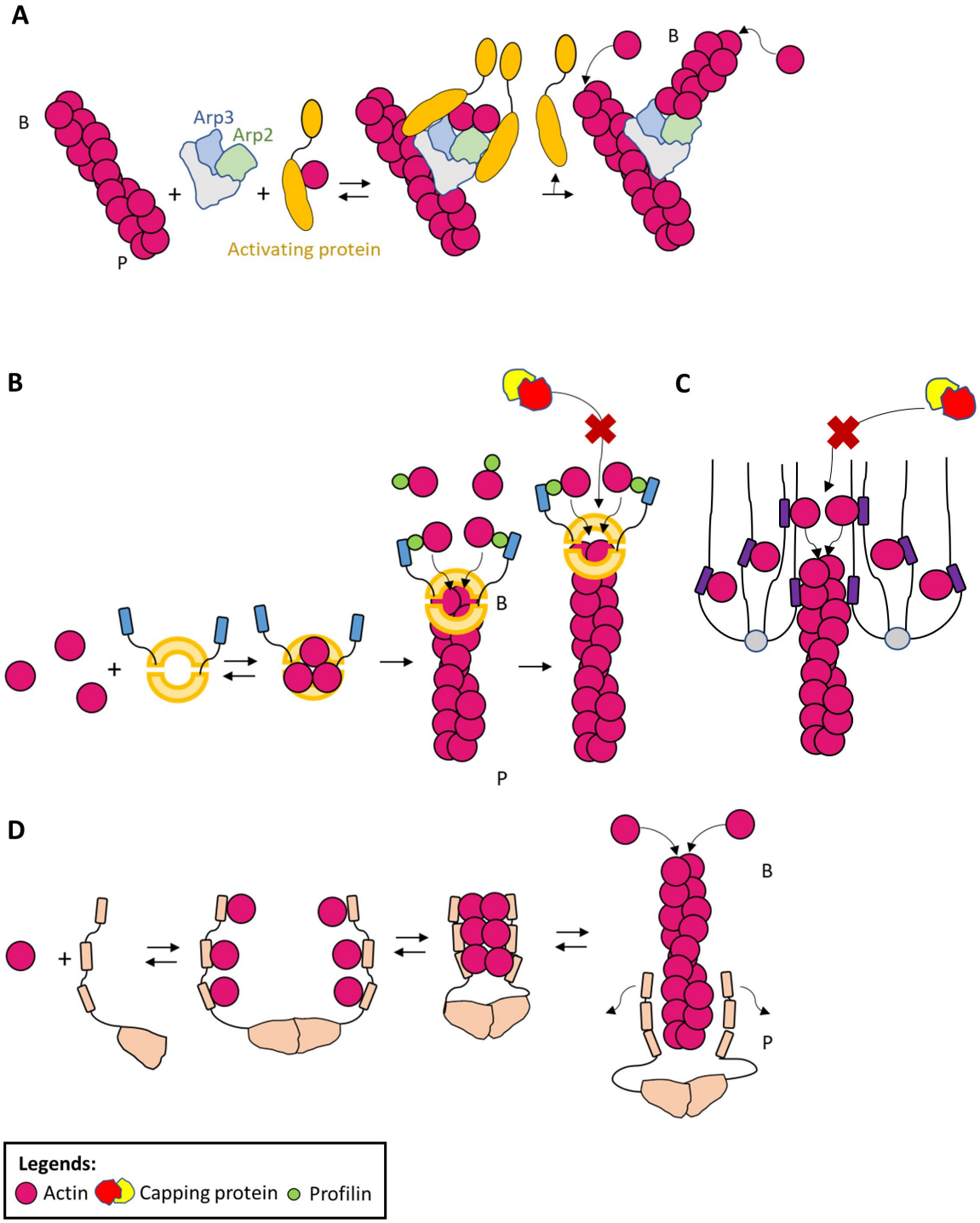
A
B
Arp3
Arp2
Activating protein
P
B
B
C
P
D
B
P
Legends:
Actin
Capping protein
Profilin

Figure 1.4: Actin nucleation and elongation factors. A) Arp2/3 complex-mediated nucleation, requiring both an activating protein (bound to an actin monomer) and an existing actin filament for activation, resulting in a branched filament. B - barbed end. P - pointed end. **B)** Formin-mediated nucleation, with the formin remaining at the barbed end, and working with profilin in filament elongation, while blocking capping protein access. **C)** Ena/VASP proteins at barbed end, mediating elongation while blocking capping protein access. **D)** Tandem WH2 motif-containing protein nucleating a filament, then releasing. There are several open questions with these proteins, including if/how fast they release from the pointed end, and whether they are able to interact with barbed ends as well.

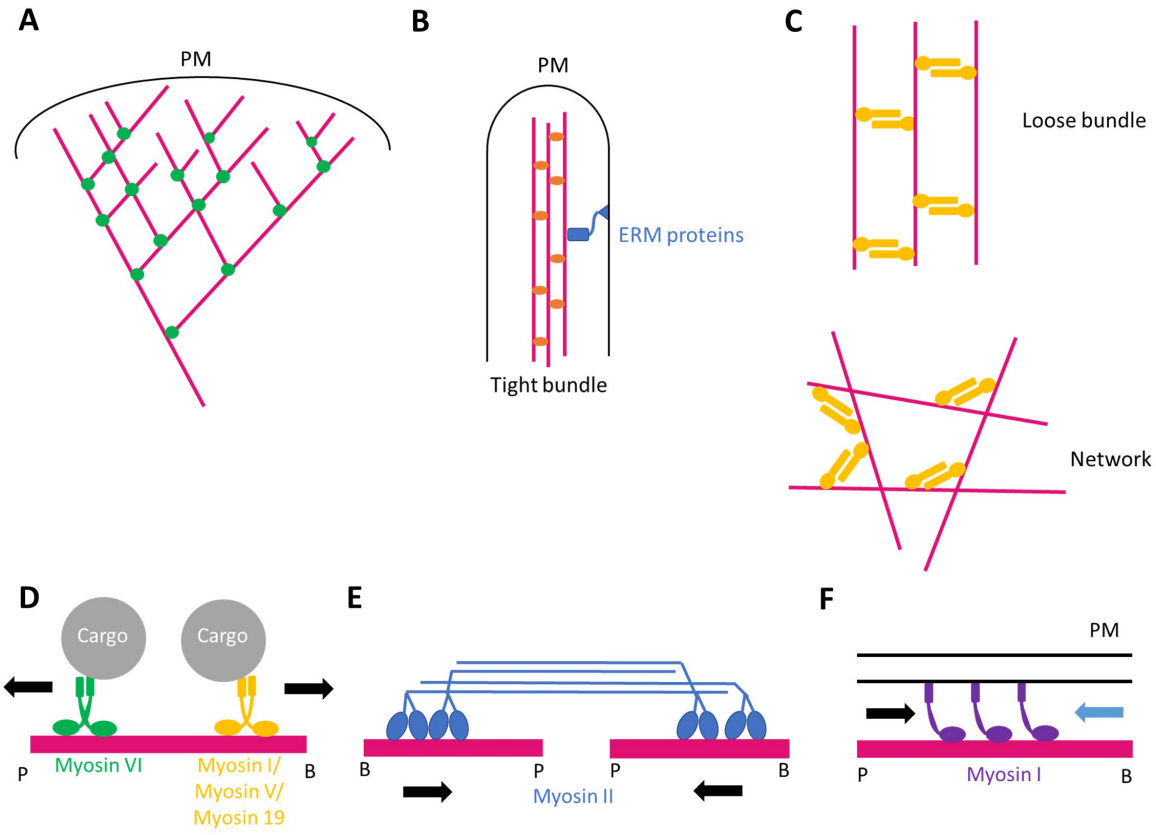

Figure 1.5: Actin-organizing proteins, and myosins. **A)** Dendritically branched network assembled by Arp2/3 complex. **B)** Fascin-mediated filament bundle in a filopodium, linked to the plasma membrane (PM) by an ERM protein. Barbed ends are toward the filopodial tip. **C)** Filaments crosslinked by α-actinin, into either a loose bundle (top) or a network (bottom). **D)** Myosin-mediated cargo translocation, either toward the barbed end (myosin I, V, myosin 19) or pointed end (myosin VI). B – barbed end. P – pointed end. **E)** Contraction of anti-parallel actin filaments by the myosin II oligomer, causing the actin filaments to move in the direction of the black arrows. **F)** Myosin I as a static tether, resisting a counter-acting force. Direction of myosin force is black arrow, direction of counter-force is blue arrow.

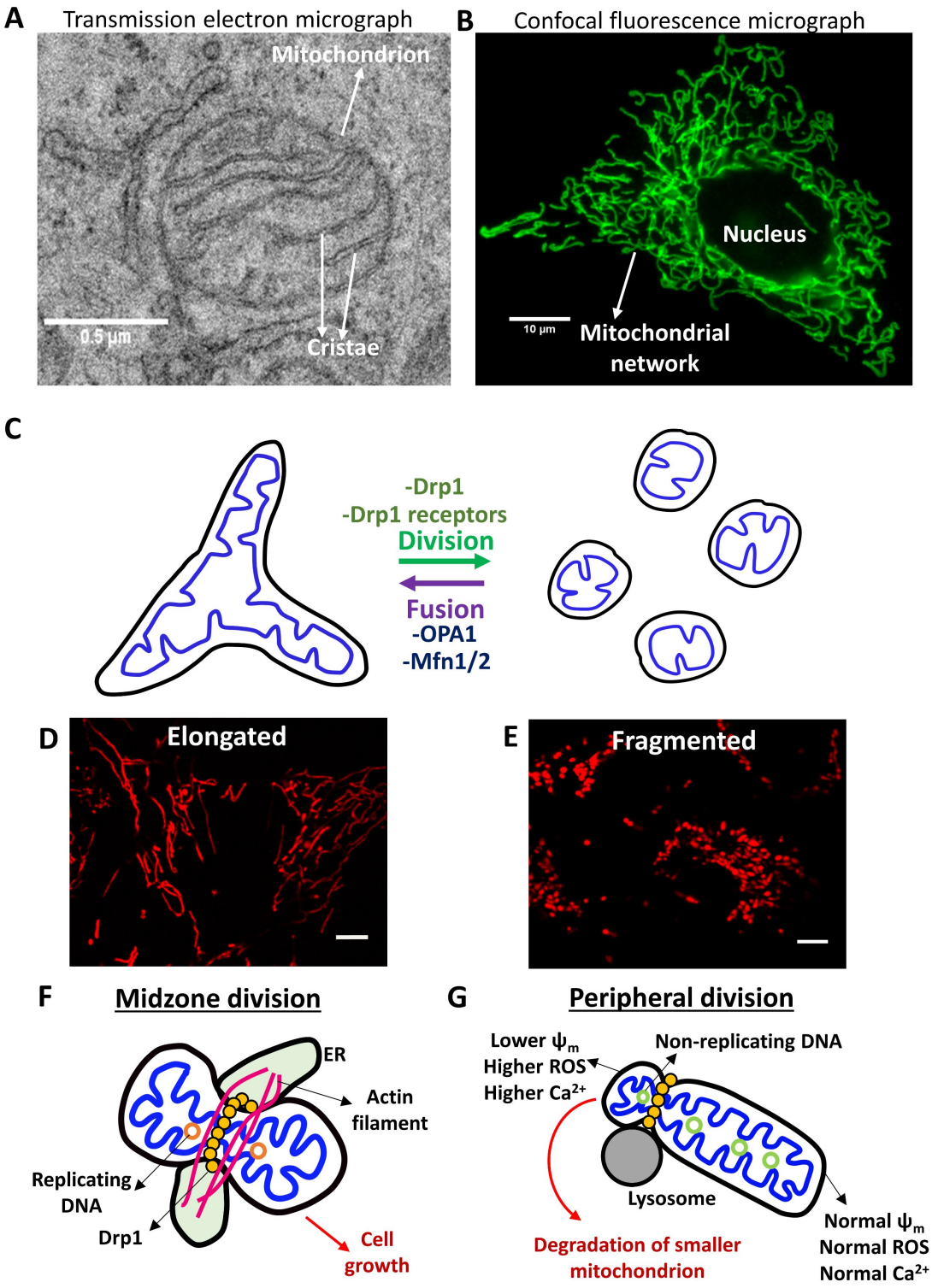
A
Transmission electron micrograph
Mitochondrion
0.5 µm
Cristae
B
Confocal fluorescence micrograph
Nucleus
10 µm
Mitochondrial network
C
-Drp1
-Drp1 receptors
Division
Fusion
-OPA1
-Mfn1/2
D
Elongated
E
Fragmented
F
Midzone division
ER
Actin filament
Replicating DNA
Drp1
Cell growth
G
Peripheral division
Lower ψm
Higher ROS
Higher Ca2+
Non-replicating DNA
Lysosome
Degradation of smaller mitochondrion
Normal ψm
Normal ROS
Normal Ca2+

Figure 1.6: Mitochondria and their dynamics. A) A transmission electron micrograph of a single mitochondrion in human osteosarcoma U2-OS cell. This image is from a thin section (~50nm in thickness). Therefore, the 'spherical' or 'ovoid' appearance is likely an artifact due to sample preparation for electron microscopy imaging, and the full mitochondrion is probably much longer (see panel **B**). **B)** A confocal fluorescence micrograph of a mouse embryonic fibroblast (MEF) with a mitochondrially-targeted green fluorescent protein, showing that mitochondria can exist as a branched network. **C)** Model of mitochondrial dynamics in the cell. Mitochondria are dynamic organelles that divide and fuse according to cellular needs. Both division and fusion require distinct molecular partners. **D) and E)** Confocal fluorescence micrographs of U2-OS cells expressing a mitochondrially-targeted red fluorescent protein. Scale bars: 5μm. **D)** the mitochondrial morphology is elongated. **E)** the mitochondrial morphology is fragmented. Corresponds to (**C**). Scale bar: 5μm. **F) and G)** Drp1-dependent mitochondrial division comes in at least two distinct flavors. For midzone division (**F**), the event is associated with the ER, replicating mtDNA and actin filaments. Midzone division is vital to maintain cellular homeostasis and cell growth. **G)** For peripheral division, mitochondrial stressors like a drop in mitochondrial membrane potential (ψ_m) trigger the asymmetrical division which is assisted by lysosome recruitment. After division, the smaller unit is targeted for organelle clearance. **(A)**: image courtesy of Dr. S. Kamerkar (Higgs lab, Dartmouth College) and Dr. R.V. Stan (Department of Biochemistry and Cell Biology, Dartmouth College). **(C)**: Adapted from [438]. **(F)** and **(G)**: Adapted from [439].

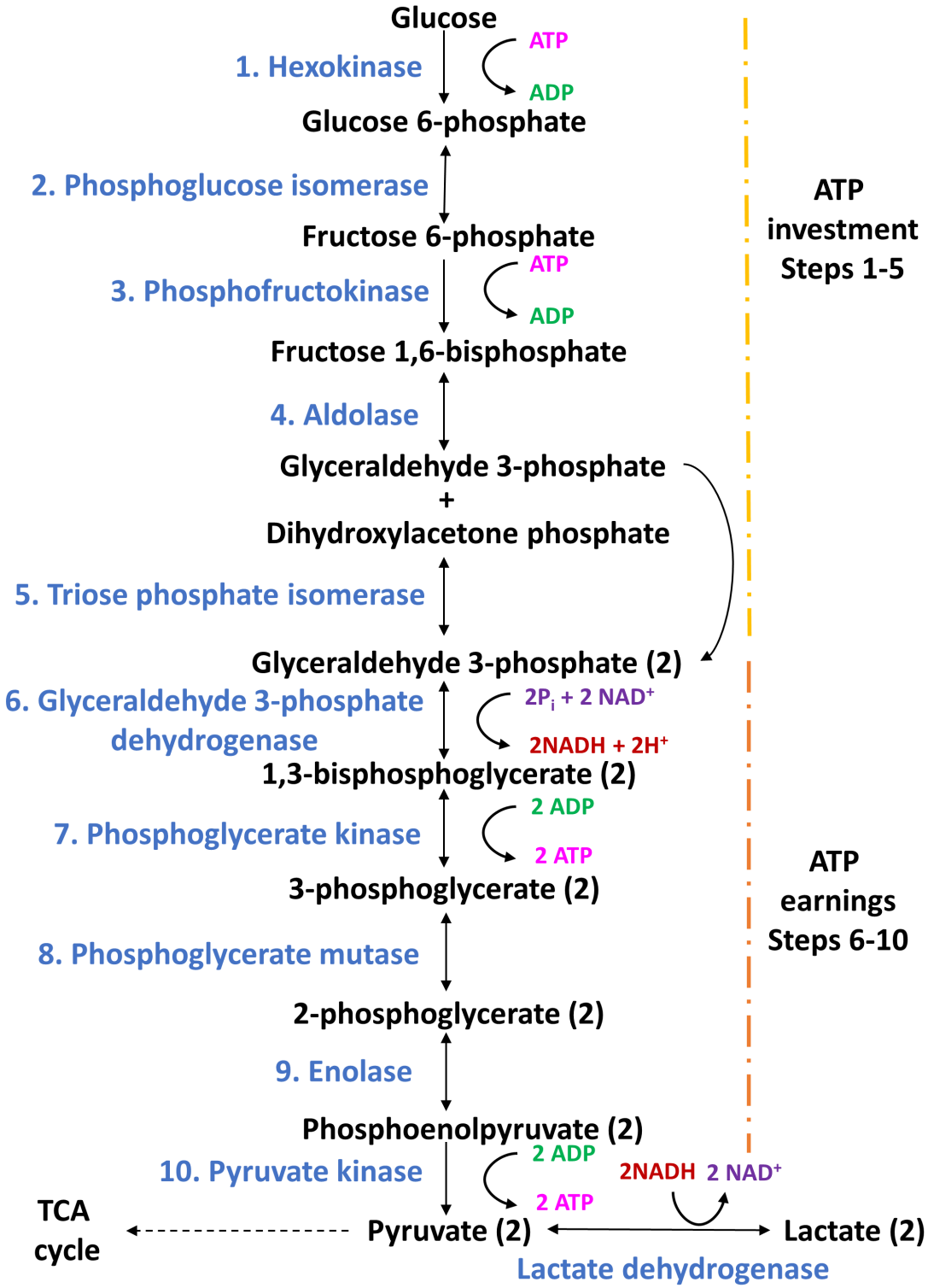
Glucose
1. Hexokinase
ATP
ADP
Glucose 6-phosphate
2. Phosphoglucose isomerase
Fructose 6-phosphate
3. Phosphofructokinase
ATP
ADP
Fructose 1,6-bisphosphate
4. Aldolase
Glyceraldehyde 3-phosphate
+
Dihydroxylacetone phosphate
5. Triose phosphate isomerase
Glyceraldehyde 3-phosphate (2)
6. Glyceraldehyde 3-phosphate dehydrogenase
2Pi + 2 NAD+
2NADH + 2H+
1,3-bisphosphoglycerate (2)
7. Phosphoglycerate kinase
2 ADP
2 ATP
3-phosphoglycerate (2)
8. Phosphoglycerate mutase
2-phosphoglycerate (2)
9. Enolase
Phosphoenolpyruvate (2)
10. Pyruvate kinase
2 ADP
2 ATP
TCA cycle
Pyruvate (2)
2NADH
2 NAD+
Lactate (2)
Lactate dehydrogenase
ATP investment Steps 1-5
ATP earnings Steps 6-10

Figure 1.7: The ten steps of glycolysis in the cytosol. Cells initially invest ATP to generate glycolytic intermediates before receiving a 'payoff' later in the process. One glucose molecule generates a net product of 2 ATP, 2 reducing equivalents (NADH) and 2 pyruvate molecules. Steps 1 (hexokinase), 3 (phosphofructokinase) and 10 (pyruvate kinase) are irreversible reactions. Pyruvate after glycolysis has two fates, lactate production or import into the mitochondria for further processing in the TCA cycle. Glycolytic intermediates can be diverted for other cellular purposes. For example, as building blocks for biosynthesis or signaling molecules. To regenerate NAD^+, pyruvate can be converted to lactate. Figure adapted from [185].

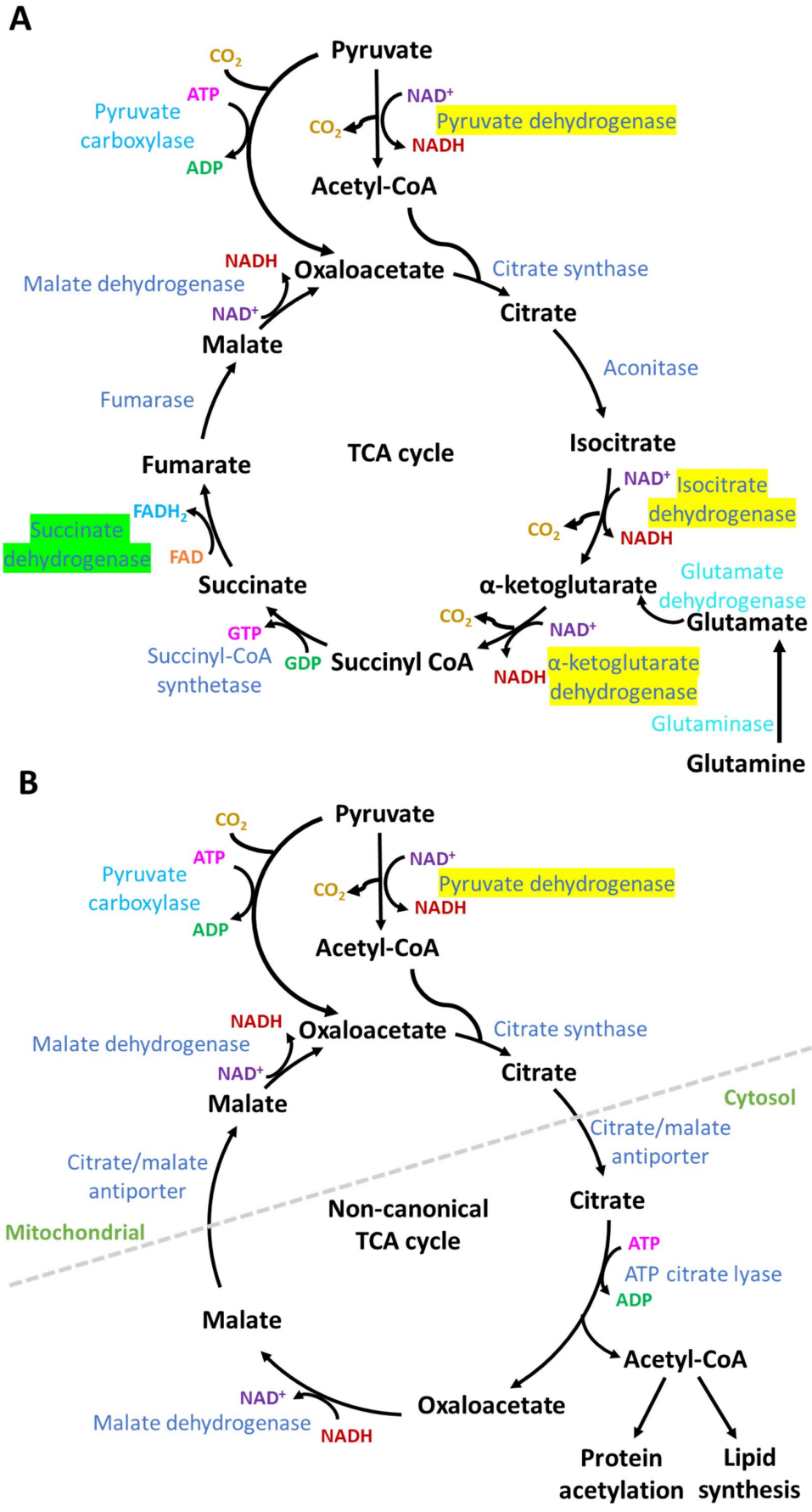
A
Pyruvate
CO2
ATP
Pyruvate carboxylase
ADP
NAD+
CO2
Pyruvate dehydrogenase
NADH
Acetyl-CoA
NADH
Malate dehydrogenase
Oxaloacetate
Citrate synthase
NAD+
Citrate
Malate
Aconitase
Fumarase
Isocitrate
TCA cycle
Fumarate
NAD+
Isocitrate dehydrogenase
CO2
NADH
FADH2
Succinate dehydrogenase
FAD
α-ketoglutarate
Glutamate dehydrogenase
Succinate
CO2
NAD+
Glutamate
GTP
Succinyl-CoA synthetase
GDP
Succinyl CoA
NADH
α-ketoglutarate dehydrogenase
Glutaminase
Glutamine
B
Pyruvate
CO2
ATP
Pyruvate carboxylase
ADP
NAD+
CO2
Pyruvate dehydrogenase
NADH
Acetyl-CoA
NADH
Malate dehydrogenase
Oxaloacetate
Citrate synthase
NAD+
Citrate
Malate
Cytosol
Citrate/malate antiporter
Citrate/malate antiporter
Citrate
Non-canonical TCA cycle
Mitochondrial
ATP
ATP citrate lyase
ADP
Malate
Acetyl-CoA
NAD+
Malate dehydrogenase
NADH
Oxaloacetate
Protein acetylation
Lipid synthesis

Figure 1.8: The traditional and non-canonical TCA cycle. A) In the mitochondrial matrix, pyruvate is converted into acetyl-CoA [440] before entering the eight chemical reactions of the TCA cycle, centered on the cyclic catabolism and recovery of citrate. Alternately, pyruvate can be converted directly into oxaloacetate [441]. The reducing equivalents released are the fuel for the ETC afterwards. For a complete catalytic cycle, three NADH, 1 $FADH_2$ along with one GTP are produced. Enzymes which are sensitive to mitochondrial calcium are highlighted in yellow. Succinate dehydrogenase (in green) is also a step in the ETC (complex II). Metabolite intermediates of the TCA cycle can be diverted for other cellular purposes. For example, as building blocks for biosynthesis or signaling molecules. Glutamine enters the TCA cycle by conversion to glutamate by glutaminase, and subsequently to α-ketoglutarate by glutamate dehydrogenase or other mitochondrial aminotransferases (whole process called 'glutaminolysis' [442]). **B)** In addition to the traditional TCA cycle, a non-canonical citrate cycle exists for fast proliferating cells [225]. The citrate/malate uniporter shuttles and exchanges metabolites into the cytosol for processing. It is still unclear what the exact roles of this alternate TCA cycle are and how the setup affects cellular bioenergetics [443]. What is clear is that NADH or $FADH_2$ generating steps in the mitochondria are bypassed and NAD^+ is replenished in the cytosol instead. **(A)**: Adapted from [444]. **(B)**: Adapted from [225].

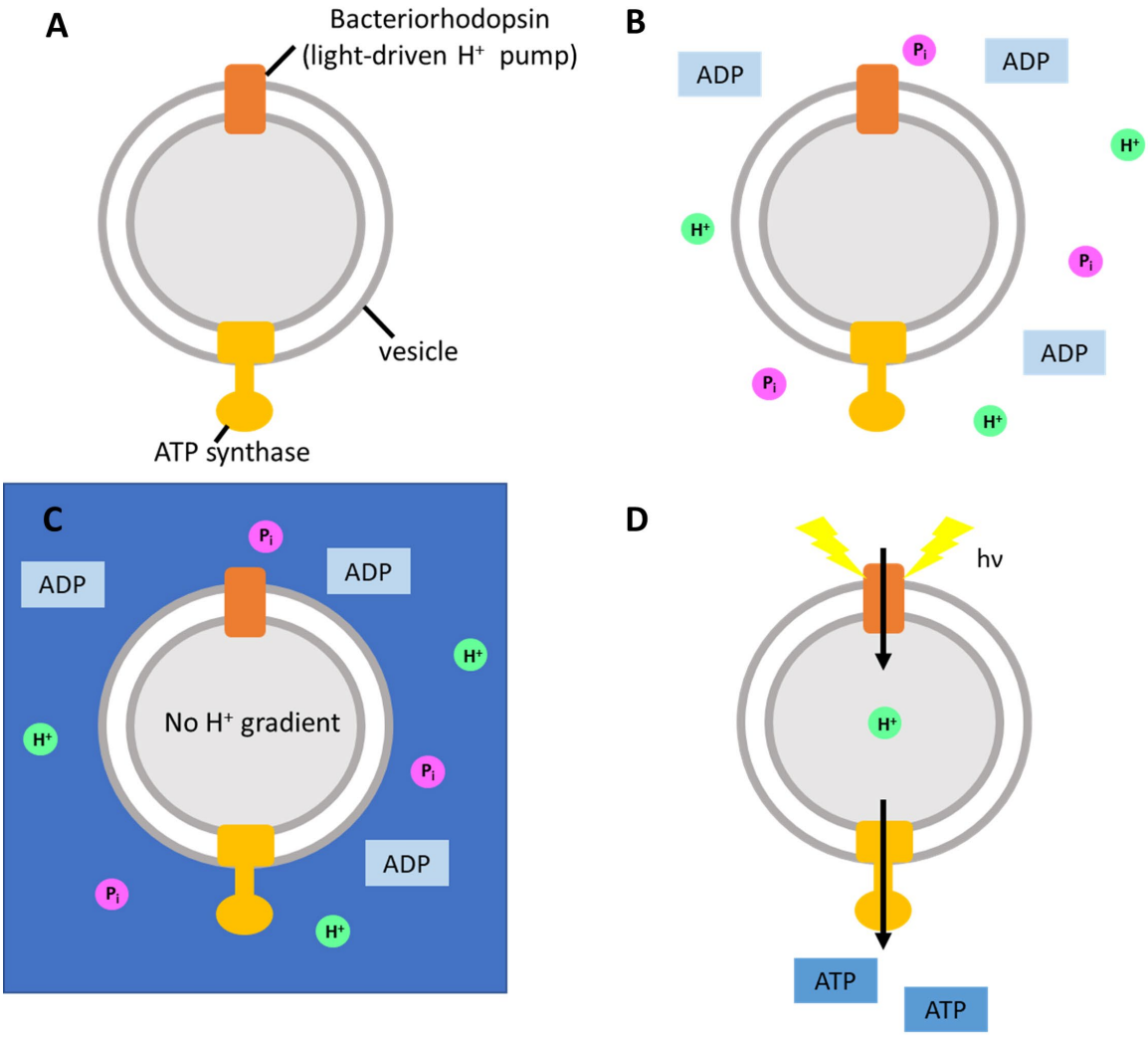

Figure 1.9: The biochemical assay by Racker and Stoeckenius [238] that confirmed Mitchell's chemiosmotic theory. A) ATP synthase and bacteriorhodopsin are incorporated into the same membrane vesicle. **B)** ADP and P_i are added to the outside of the vesicles. **C)** In the dark, no ATP is synthesized. **D)** In the presence of light, bacteriorhodopsin pumps protons into the vesicle and the proton gradient across the membrane is utilized by ATP synthase to produce ATP. Figure adapted from [249].

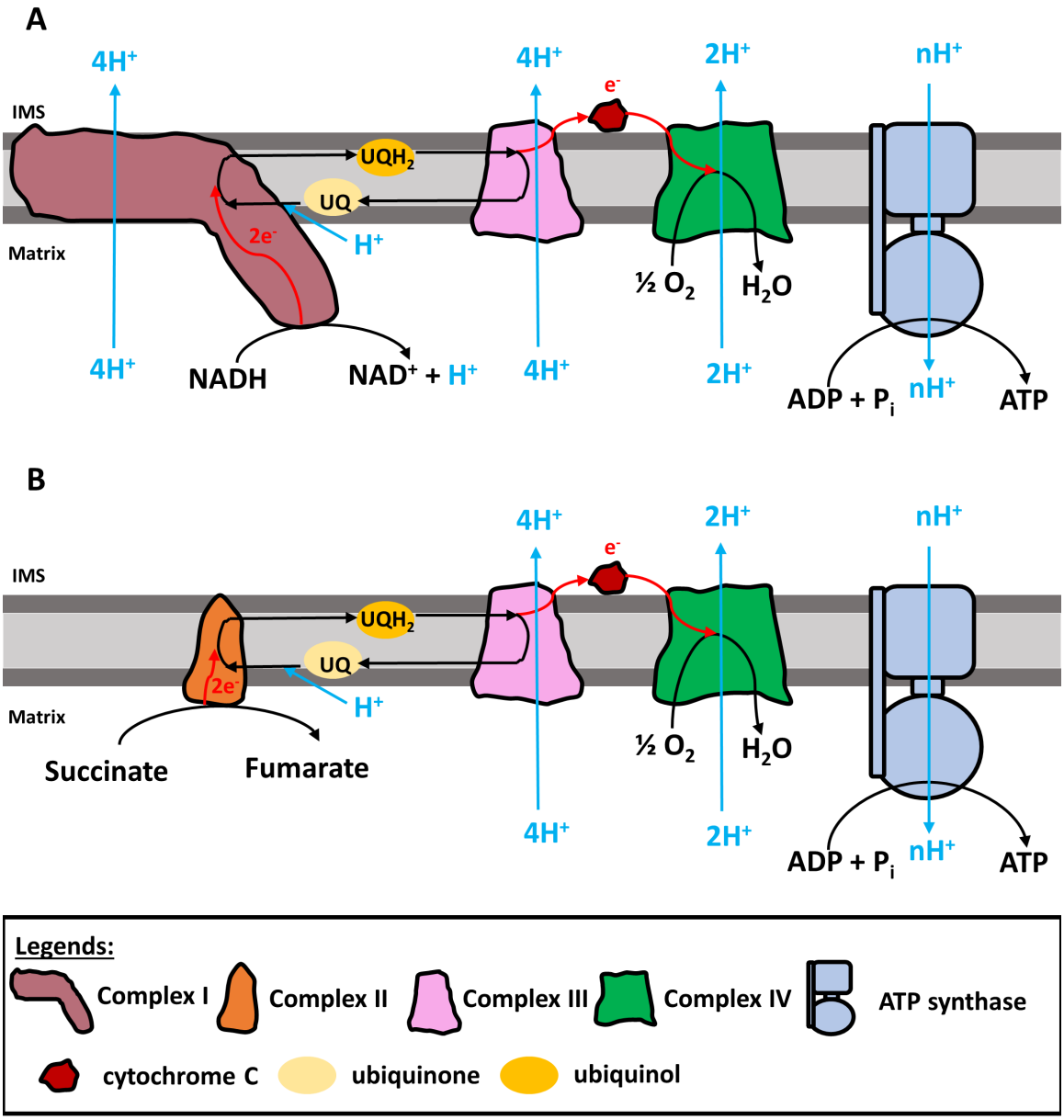

Figure 1.10: The mitochondrial ETC in metazoans. A) Pathway of electron transfer for NADH. Complex I translocates four protons for two electrons donated from NADH oxidation. Electrons from complex I are carried by the ubiquinone (UQ)/ubiquinol (UQH_2) pool at the hydrophobic core of the IMM. Electrons at complex III are transferred to cytochrome c. Each cytochrome c shuttles one electron from complex III to IV, where oxygen is the terminal acceptor electrons. pmf across the IMM drives ATP production through ATP synthase. **B)** Same as **(A)** but complex II shown instead of complex I. Complex II is incapable of transporting protons across the IMM. Figure adapted from [91].

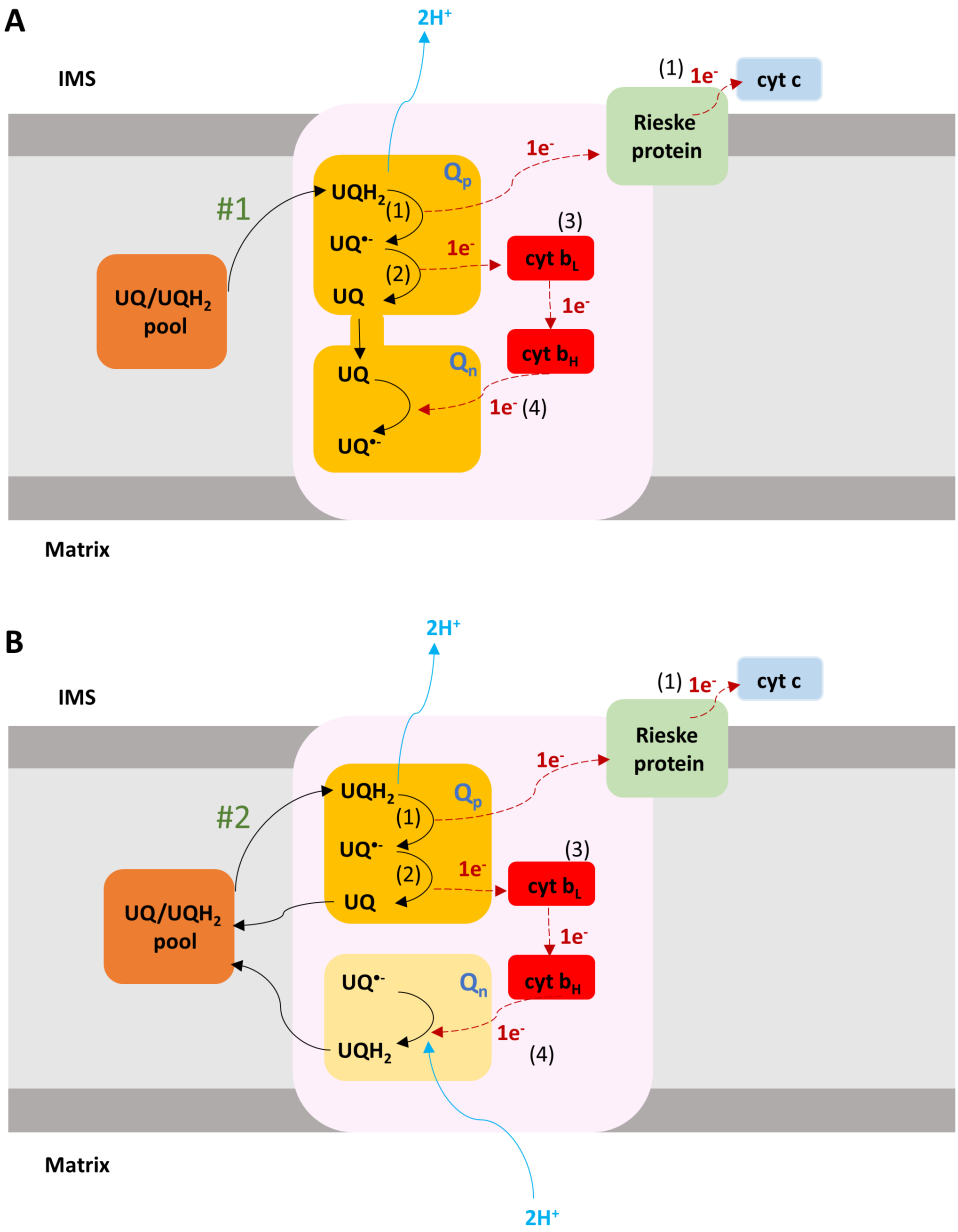

Figure 1.11: The Q cycle in complex III. A) The first UQH_2 comes into the Q_p site where it donates one electron to the Rieske protein, generating $UQ^{\bullet-}$ and releasing protons into the IMS (1). Next, $UQ^{\bullet-}$ donates the second electron to cyt b_L to become UQ (2). UQ moves into the Q_n site while cyt b_L transfers the electron to cyt b_H (3). At the Q_n site, cyt b_H reduces UQ back into $UQ^{\bullet-}$ (4). **B)** The second UQH_2 comes into the Q_p site and does the same as the first UQH_2 – donating one electron to the Rieske protein and cyt b_L each (1-2). Here the UQ returns to the general pool instead of transport into the Q_n site. cyt b_L follows the same steps to transfer electron to cyt b_H. The $UQ^{\bullet-}$ at the Q_n site then accepts the electron, along with 2 protons from the matrix to regenerate UQH_2 (4). Afterwards, this UQH_2 returns to the general pool as well. Figure adapted from [91].

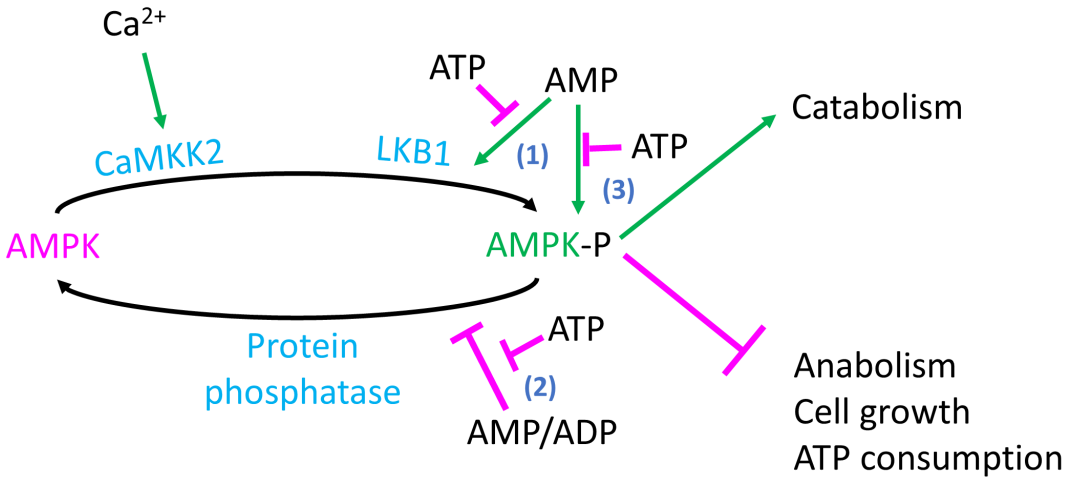

Figure 1.12: AMPK regulation in the cell. AMPK can be activated by upstream kinase CaMKK2 or LKB1. Phosphorylated AMPK regulates catabolic and anabolic reactions. AMP has three general effects on AMPK: 1) it makes AMPK more susceptible to LKB1; 2) it inhibits protein phosphatase from dephosphorylating AMPK and 3) allosterically activates AMPK further after phosphorylation. ATP antagonizes all three effects. Figure adapted from [174].

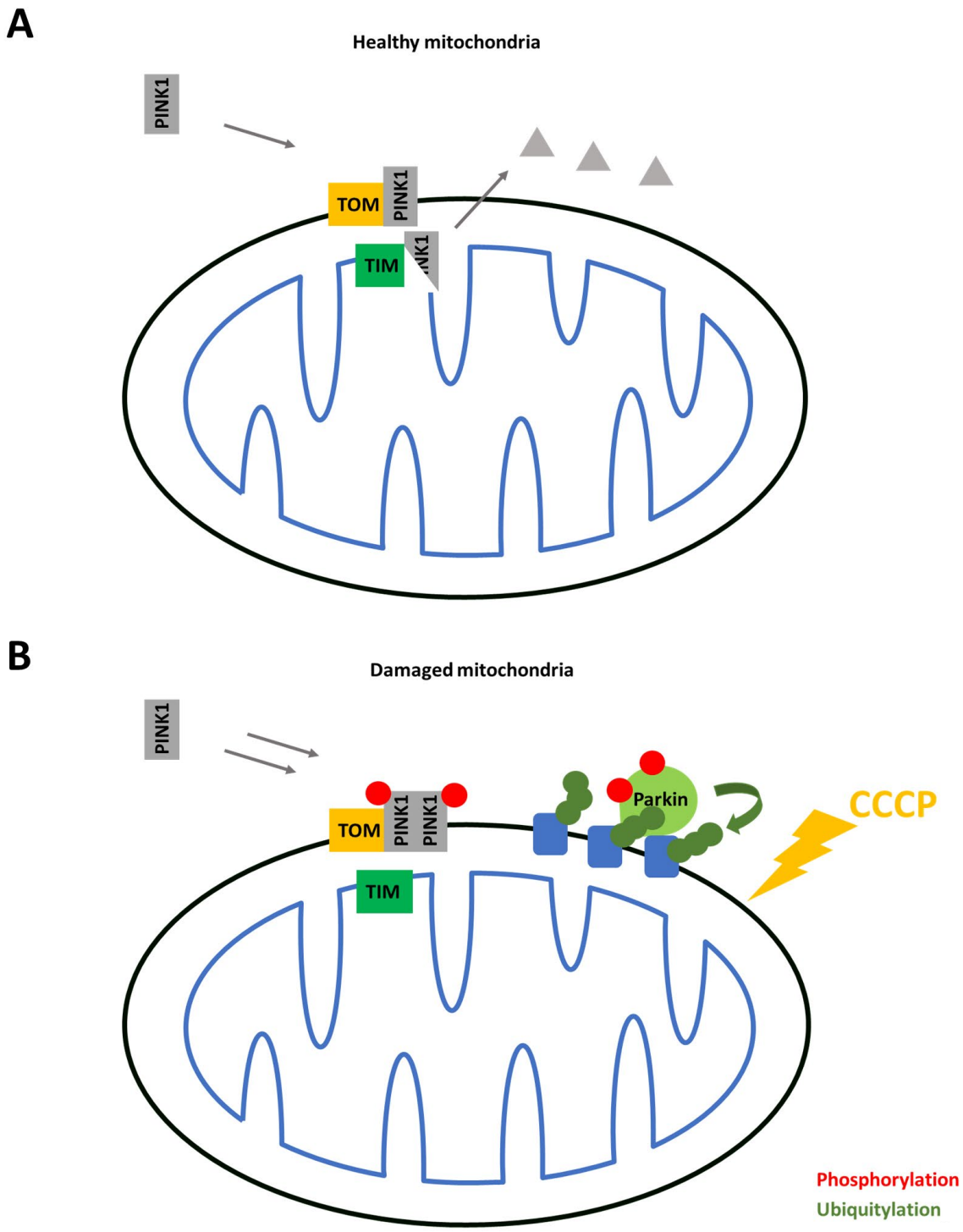

Figure 1.13: PINK1/Parkin mitophagy. A) In healthy conditions, PINK1 is recruited to the mitochondrion but gets imported into the IMM where it is cleaved by mitochondrial protease presenilin-associated rhomboid-like protein (PARL) [445] and degraded. **B)** When mitochondria are damaged, however, PINK1 stabilizes on the OMM, driving E3 ubiquitin ligase Parkin recruitment and phosphorylation. Once activated, Parkin ubiquitinate OMM substrates to tag the organelle for clearance by mitophagy.

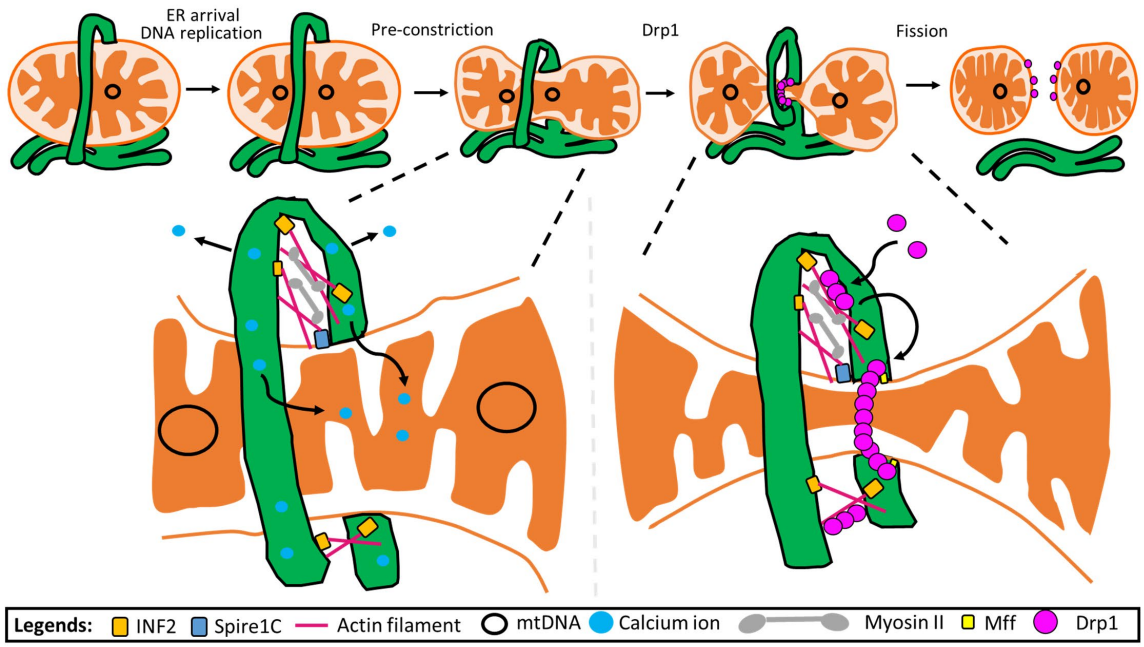

Figure 1.14: Actin and mitochondrial division. The top row shows a progression of mitochondrial division at MERCs. The mitochondrial genome replicates at the contact site, followed by Drp1-independent pre-constriction. Drp1 is then recruited, followed by fission. The bottom row shows models for actin involvement at two fission steps. At the left: actin polymerized by ER-bound INF2 (calcium-induced actin, CIA) and mitochondrially-bound Spire 1C leads to enhanced ER-mitochondrial contact in a myosin II-dependent manner. Enhanced organelle-organelle contact allows more efficient calcium transfer from ER to mitochondria, leading to "pre-constriction" of both IMM and OMM (driven by IMM constriction). At the right, the actin filaments bind Drp1, allowing transfer of these small oligomers to OMM receptors for further oligomerization, leading to full ring assembly and OMM constriction.

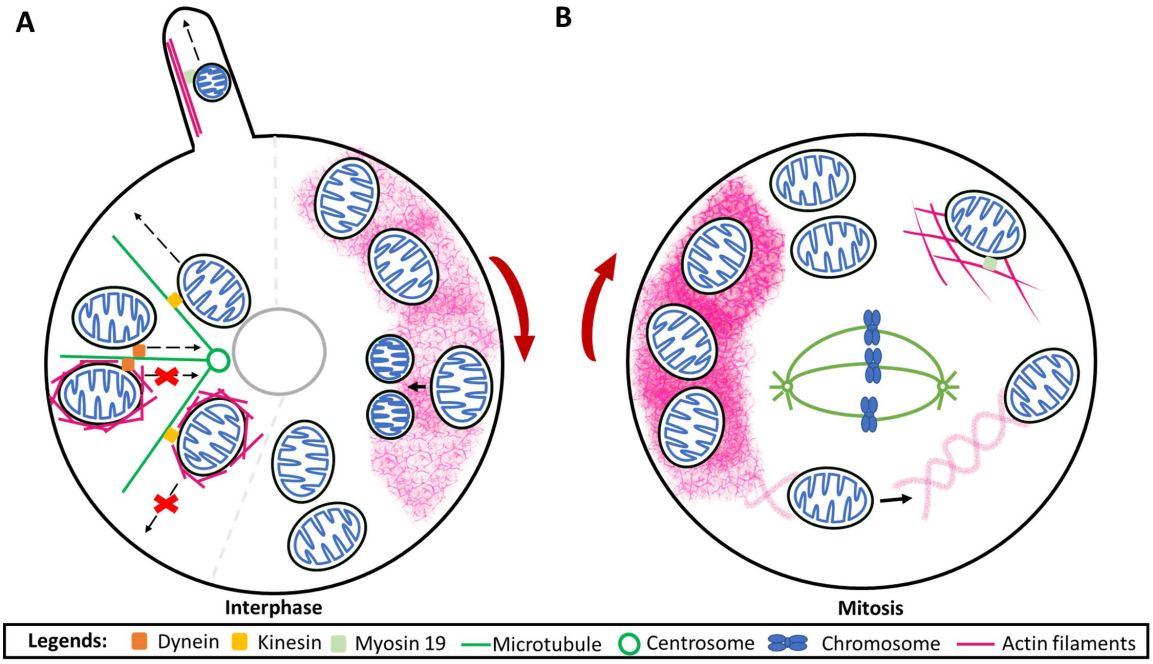

Figure 1.15: Actin and mitochondrial motility. A) Interphase cell. *Left*: Increased O-GNAcylation of the protein Milton leads to actin recruitment around mitochondria, resulting in inhibition of kinesin-mediated (yellow) or dynein-mediated (orange) mitochondrial transit along microtubules. Center/top: myosin 19 can mediate mitochondrial motility toward filopodial tips. Given the narrow filopodial diameter (100-200 nm), it is unclear how mitochondria adapt for this transit. *Right*: actin clouds assemble around sub-sets of mitochondria, with the cloud moving between mitochondria in a uniform direction over time (here shown clockwise). The actin cloud does not enhance mitochondrial motility, but does correspond to an increase in mitochondrial division. **B)** Mitotic cell. *Left*: the actin cloud shown in the interphase cell can transition to a mitotic actin cloud, which increases in both filament density and speed of rotation around the cell. As with interphase clouds, the associated mitochondria are less motile. However, the clouds can give rise to helical actin 'tails', which cause rapid (250 nm/sec) translocation of the associated mitochondrion to randomize mitochondrial inheritance. *Right*: a network of actin filaments assembles throughout the mitotic cytoplasm (outside of the spindle zone), which results in myosin 19-mediated mitochondrial tethering to the network, allowing appropriate mitochondrial distribution to daughter cells.

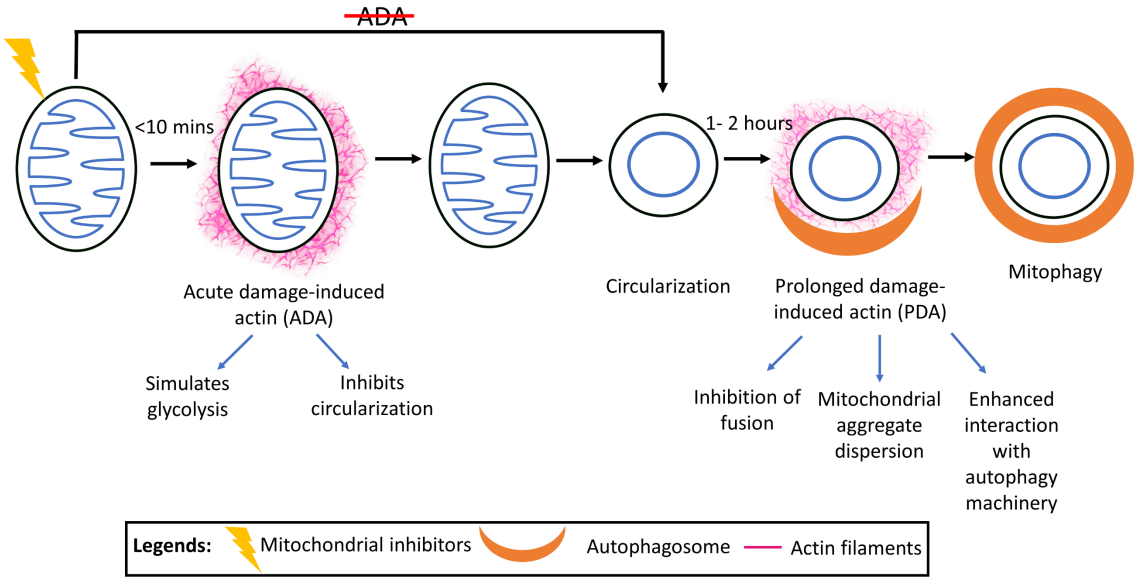

Figure 1.16: Two types of actin-induced by mitochondrial damage. Treatment with a number of mitochondrial inhibitors (CCCP, antimycin, rotenone, oligomycin, hypoxia, metformin) leads to rapid actin polymerization around the mitochondrion (ADA), which has two effects: glycolytic stimulation, and inhibition of IMM rearrangements ('circularization'). ADA is transient, and circulation ensues after actin depolymerization. After approximately 1 hr, a second round of actin polymerization occurs (PDA), which has three demonstrated effects that favor mitophagy: 1) inhibition of fusion, even if the damaged mitochondrion repolarizes; 2) dispersal of mitochondrial aggregates; and 3) recruitment of core autophagy components. The roles and mechanisms of action for ADA is the focus of the thesis.

Table 1.1: NPFs for Arp2/3 complex activation

NPF	# members*	Regulation	Role
WASP	2 (*WAS, WASL*)	Cdc42 [446, 447], PIP2 [446, 447], Nck [448], tyrosine phosphorylation [449]	Filopodia [450], phagocytosis [451], immune synapse [452], podosomes [453], invadopodia [454], endocytosis [455], pathogen motility [456, 457], prolonged mitochondrial damage (PDA) [432]
WAVE	3 (*WASF1, WASF2, WASF3*)	Rac1[48, 458, 459], PIP_3[48, 51], tyrosine/serine phosphorylation [48, 50], IRSp53 [460], Nck [461]	Lamellipodia [43, 462], cell migration [52, 462, 463], acute mitochondrial dysfunction (ADA) (**Chapter III**)
WASH	1 (*WASHC1*)	WASH regulatory complex [464, 465], USP7 deubiquitylation [466]	Endosome formation [464], sorting and transport [464, 467-469], autophagosome formation [470, 471]
WHAMM	1 (*WHAMM*)	Rab1 [472]	ER-Golgi transport [473], Golgi organization [473], autophagosome formation [474]
JMY	1 (*JMY*)	DNA damage [475]	Cell motility [476], vesicle trafficking [477], Oocyte division [478], Autophagosome formation [479, 480], transcription [476, 481, 482], neurite outgrowth [483]
DIP**	1 (*NCKIPSD*)	Phosphorylation [484, 485]	Lamellipodia [486, 487], endocytosis [488]
Cortactin	2 (*CTTN, HS1*)	Tyrosine/Serine phosphorylation [489-494], lysine acetylation [495], Nck [496]	Invadopodia formation [489], Cell- cell adhesion [497], lamellipodia [498], immunological synapse [499, 500], mitochondrial division [16]

*Number (names) of distinct genes in mammals.

**only NPF that can induce un-branched filaments through Arp2/3 complex [501].

Table 1.2: 15 mammalian formins (Adapted from [4])

Full name	**# members (human isoforms)**	**Associated structures or processes**	**Associated diseases**
Dia (Diaphanous)	3 (*Dia1, Dia2, Dia3*)	Stress fibers [18], contractile ring [502], microtubule stabilization [503], cell migration [504]	Deafness [505], diabetic retinopathy [506], microcephaly syndrome [507]
Daam (Disheveled-associated activators of morphogenesis)	2 (*Daam1, Daam2*)	Planar cell polarity [508], axonal growth cone [509]	Unknown
FMNL/FRL (Fromin-related proteins identified in leukocytes)	3 (*FMNL1, FMNL2, FMNL3*)	Cell migration [56], cell-cell contact [510], acute mitochondrial dysfunction (ADA) (**Chapter III**)	Cancer metastasis [511]
INF ('inverted' formins)	2 (*INF1, INF2*)	Calcium-induced actin (CIA), mitochondrial division [12], nuclear actin [512]	Focal segmental glomerulosclerosis [513], Charcot-Marie-Tooth disease [514]
FHOD (Formin homology domain containing proteins)	2 (*Fhod1, Fhod3*)	Stress fibers [515]	Cardiac disorders [516]
Delphilin	*GRID2IP*	Purkinje cells [517]	Unknown
FMN (the founding family of 'formins')	2 (*FMN1, FMN2*)	Oogenesis [518], DNA damage response [519]	Polydactyly [520], intellectual disability [521]

Table 1.3: The 13 protein-coding mitochondrial genes, and the ETC subunits they encode (Adapted from [522])

Protein	Gene name	Complex
NADH dehydrogenase 1	*MT-ND1*	I
NADH dehydrogenase 2	*MT-ND2*	I
NADH dehydrogenase 3	*MT-ND3*	I
NADH dehydrogenase 4	*MT-ND4*	I
NADH dehydrogenase 4L	*MT-ND4L*	I
NADH dehydrogenase 5	*MT-ND5*	I
NADH dehydrogenase 6	*MT-ND6*	I
Cytochrome B	*MT-CYB*	III
Cytochrome C oxidase I	*MT-CO1*	IV
Cytochrome C oxidase II	*MT-CO2*	IV
Cytochrome C oxidase III	*MT-CO3*	IV
ATP synthase 6	*MT-ATP6*	V
ATP synthase 8	*MT-ATP8*	V

Chapter II:

Distinguishing acute damage-induced actin from other forms of mitochondrially-associated actin

Chapter II

Two distinct actin filament populations have effects on mitochondria, with differences in stimuli and assembly factors

Tak Shun Fung[1], Wei-Ke Ji[2], Henry N. Higgs[1,3] & Rajarshi Chakrabarti[1,3]

[1]Department of Biochemistry and Cell Biology, Geisel School of Medicine at Dartmouth, Hanover NH 03755

[2]Department of Biochemistry and Molecular Biology, School of Basic Medicine and the Collaborative Innovation Center for Brain Science, Tongji Medical College, Huazhong University of Science and Technology, Wuhan, China

The text and data here are adapted or reproduced in full from the manuscript published in *J Cell Sci*.

(DOI: https://doi.org/10.1242/jcs.234435)

T.S.F. and R.C. designed and performed experiments, interpreted and analyzed data, and wrote the manuscript.

H.N.H. supervised the project, designed experiments, interpreted and analyzed data, and wrote the manuscript.

W.-K.J. interpreted and analyzed data for **Figure S2.4A**.

Conceptualization: T.S.F., H.N.H., R.C.; Methodology: T.S.F., R.C.; Software: T.S.F., R.C.; Validation: T.S.F., R.C.; Formal analysis: T.S.F., W.-K.J., R.C.; Investigation: T.S.F., R.C.; Writing - original draft: T.S.F., H.N.H., R.C.; Writing - review & editing: T.S.F., H.N.H., R.C.; Visualization: T.S.F., H.N.H., R.C.; Supervision: H.N.H.; Project administration: H.N.H.; Funding acquisition: H.N.H.

2.1 Abstract

Recent studies show that mitochondria and actin filaments work together in two contexts: (1) increased cytoplasmic calcium induces cytoplasmic actin polymerization that stimulates mitochondrial fission and (2) mitochondrial depolarization causes actin assembly around mitochondria, with roles in mitophagy. It is unclear whether these two processes utilize similar actin assembly mechanisms. Here, we show that these are distinct actin assembly mechanisms in the acute phase after treatment (<10 min). Calcium-induced actin assembly is INF2 dependent and Arp2/3 complex independent, whereas depolarization-induced actin assembly is Arp2/3 complex dependent and INF2 independent. The two types of actin polymerization are morphologically distinct, with calcium-induced filaments throughout the cytosol and depolarization-induced filaments as 'clouds' around depolarized mitochondria. We have previously shown that calcium-induced actin stimulates increases in both mitochondrial calcium and recruitment of the dynamin GTPase Drp1 (also known as DNM1L). In contrast, depolarization-induced actin is temporally associated with extensive mitochondrial dynamics that do not result in mitochondrial fission, but in circularization of the inner mitochondrial membrane (IMM). These dynamics are dependent on the protease Oma1 and independent of Drp1. Actin cloud inhibition causes increased IMM circularization, suggesting that actin clouds limit these dynamics.

2.2 Introduction

Mitochondria have traditionally been viewed as energy-generating organelles, through oxidation of metabolic substrates and creation of a proton gradient across the inner mitochondrial membrane (IMM), with the subsequent passage of protons back into the matrix being coupled to ATP synthesis [212, 523]. However, it is increasingly clear that mitochondria communicate frequently with the rest of the cell and are therefore important signaling organelles. For example, mitochondrial release of cytochrome c triggers cell death [71], mitochondrially-generated reactive oxygen species activate hypoxia-related genes [524, 525] and mitochondrial heat shock proteins promote cytosolic calcium-mediated signaling [73, 74]. Mitochondria also participate in innate immunity by serving as platforms for downstream signaling to facilitate anti-microbial host cell responses [76]. Finally, changes in the IMM proton gradient have immediate signaling effects, with IMM depolarization causing stabilization of the PINK1 protein kinase, whose downstream targets include the PARKIN E3 ubiquitin ligase [406]. Mitochondrial depolarization also activates an IMM protease, Oma1, which proteolytically cleaves the dynamin-family GTPase Opa1 [526-528].

A growing number of studies suggests that actin polymerization participates in mitochondrial communication and dynamics. During apoptosis, both a C-terminal actin fragment [529] and the actin-binding protein cofilin translocate to mitochondria, with evidence that translocation of active cofilin is important for downstream cytochrome c release and apoptotic response [530]. Inhibition of ATP synthase by oligomycin results in mitochondrial fission, which is attenuated by the actin polymerization inhibitors cytochalasin D or latrunculin A [154]. In another study, actin and myosin II were shown to play a role in translocation of the dynamin GTPase Drp1 to mitochondria, resulting in mitochondrial fission [531].

We have previously found that elevated cytosolic calcium activates the endoplasmic reticulum (ER)-bound formin INF2, which stimulates actin polymerization that leads to mitochondrial fission [3, 12, 422, 425, 426]. INF2-mediated actin polymerization stimulates constriction of both mitochondrial membranes during fission: IMM constriction is enhanced by increased calcium transfer from ER to mitochondrion, and OMM constriction is enhanced by increased Drp1 recruitment. This pathway also

requires non-muscle myosin II [12, 423] , and the mitochondrially-bound SPIRE 1C protein might also participate [20].

A somewhat different type of mitochondrially-associated actin polymerization has been reported in several studies. Dissipation of the mitochondrial proton gradient using the uncoupler FCCP causes rapid accumulation of an extensive cloud of actin filaments around depolarized mitochondria [20]. Similar actin clouds were observed in both unstimulated cells and cells treated with the uncoupler CCCP and were shown to be dependent on both Arp2/3 complex and formin activity [429, 432]. On a similar time scale as actin cloud formation, mitochondria become less elongated, consistent with an increase in mitochondrial fission [20, 429]. At a later stage after mitochondrial depolarization, a second wave of actin polymerization encircles depolarized mitochondria, and is proposed to prevent their fusion with other mitochondria in a myosin VI-dependent manner [432].

These studies raise a question concerning actin polymerization and mitochondrial function. Are there multiple ways in which actin interacts with mitochondria, or do these studies represent variations on a common actin polymerization pathway? Our present work attempts to clarify this issue. We show that calcium-induced actin polymerization is INF2-dependent and Arp2/3-independent, whereas depolarization-induced actin polymerization is Arp2/3-dependent and INF2-independent. Although both processes are rapid, calcium-induced actin polymerization is faster than depolarization-induced actin polymerization in U2-OS cells and is less tightly associated with mitochondria. Spontaneous mitochondrial depolarization causes Arp2/3-dependent actin polymerization around the depolarized mitochondria similar to that of CCCP-induced actin filaments. While mitochondrial depolarization results in extensive mitochondrial shape changes on a similar time course to actin polymerization, these shape changes are not dependent on actin polymerization or Arp2/3 complex. In fact, the shape changes are due to IMM dynamics and are dependent on the IMM protease Oma1. Inhibition of actin cloud assembly causes an increase in CCCP-induced mitochondrial shape changes, suggesting that actin clouds inhibit these shape changes. In summary, we show that two distinct types of actin filaments, differing in morphology and assembly mechanisms, have differing effects on mitochondria.

2.3 Results

2.3.1 Distinct actin polymerization mechanisms induced by mitochondrial depolarization or cytoplasmic calcium

We compared the actin bursts stimulated by the calcium ionophore ionomycin with those induced by the mitochondrial depolarizer CCCP in U2-OS cells, using live-cell imaging of actin filaments (GFP-F-tractin) and mitochondrial matrix (mito-BFP). In serum-containing medium, 4μM ionomycin treatment results in a transient increase in cytoplasmic calcium, with a $T_{1/2}$ of <5 sec and a return to baseline within 2 min [12], while 20μM CCCP causes mitochondrial depolarization within 30 sec and persisting for at least 10 min, as measured by the polarization marker tetramethylrhodamine methyl ester (20nM TMRE) [296] (**Figure S2.1A**). Both stimuli induce transient actin polymerization responses that differ in morphology and kinetics. Morphologically, ionomycin-induced actin polymerization occurs throughout the cytosol, whereas CCCP-induced actin polymerization occurs as "clouds" that are closely associated with mitochondria (**Figure 2.1A; Figure S2.1B**). These features are best appreciated in a medial Z-plane, (**Figure S2.1B**), due to less interference from basal actin stress fibers. However, actin polymerization in response to both stimuli is apparent at the basal surface as well (**Figure 2.1A**). Kinetically, ionomycin-induced actin dynamics are more rapid than those induced by CCCP (**Figure 2.1B**), both in the polymerization ($T_{1/2}$ actin polymerization values: 12.2 ± 5.9 sec and 133 ± 78.1 sec respectively) and depolymerization phases ($T_{1/2}$: 29.4 ± 12.9 sec and 79.31 ± 38.9 sec respectively) (**Figure S2.2A**).

We next examined the actin assembly factors required for ionomycin- and CCCP-induced actin polymerization. Past results have shown that ionomycin-induced actin polymerization requires the formin INF2 [12-14, 426]. However, INF2 is not required for CCCP-induced actin polymerization, tested using either CRISPR-mediated INF2 KO (**Figure 2.1C**) or siRNA-induced INF2 knock-down (**Figure S2.2B, C**). Control experiments show that ionomycin-induced actin polymerization is abolished in INF2 KO cells (**Figure S2.2D**). These results show that INF2 is not required for depolarization-induced actin polymerization.

Arp2/3 complex has been shown to contribute to mitochondrially-associated actin polymerization in HeLa cells in the absence of stimulation [429], and to actin polymerization that occurs after prolonged CCCP treatment [432]. We used the Arp2/3 complex inhibitor CK666 to test Arp2/3 complex involvement in the rapid actin bursts induced by ionomycin and CCCP. A 30-min pre-treatment with 100μM CK666 abolishes the CCCP-induced actin burst (**Figure 2.1D**), while having no clear effect on the ionomycin-induced actin burst (**Figure 2.1E**).

These results show that actin polymerization induced by increased cytoplasmic calcium and by mitochondrial depolarization differ in three ways: kinetically, morphologically, and in nucleation mechanism. Calcium-induced actin polymerization is INF2-dependent and Arp2/3 complex-independent, whereas depolarization-induced actin polymerization is Arp2/3 complex-dependent and INF2-independent.

2.3.2 Spontaneous mitochondrial depolarization triggers Arp2/3 complex-mediated actin clouds

Mitochondria periodically undergo transient depolarization in the absence of uncoupler treatment [532]. We asked whether actin polymerization faithfully accompanies such transient depolarization in U2-OS cells, using TMRE. Occasional loss of TMRE fluorescence occurs in sub-populations of mitochondria (**Figure 2.2A**). These depolarization events are generally transient, having a mean duration of 143.7 ± 106.5 sec (**Figure 2.2E**). Actin polymerization accompanies the majority (87.3% ± 6.3) of depolarization events (**Figure 2.2A-C**), with an appreciable lag between depolarization and actin polymerization, taking an average time of 129.8 ± 95.0 sec (**Figure S2.2E**). The actual polymerization $T_{1/2}$ (measured from the first detectable polymerization) is 57.2 ± 54.1 sec (**Figure S2.2F**).

We asked whether Arp2/3 complex is involved in actin polymerization induced by spontaneous mitochondrial depolarization. To this end, we pre-treated U2-OS cells with CK666 for 30 min prior to imaging. Spontaneous depolarization of sub-populations of mitochondria still occurs in CK666 pretreated cells, similar to control cells (**Figure 2.2A**). In fact, the frequency of spontaneous depolarization events is somewhat higher in CK666-treated cells (**Figure 2.2D**), while the average duration of depolarization events is not significantly different (**Figure 2.2E**). CK666 treatment, however, strongly reduces the actin polymerization events that occur after spontaneous depolarization (**Figure 2.2A-**

C). These results further support the finding that the actin polymerization occurring around depolarized mitochondria is mediated by Arp2/3 complex in U2-OS cells.

2.3.3 Actin polymerization is not required for depolarization-induced mitochondrial shape change

In addition to inducing actin polymerization, CCCP-triggered mitochondrial depolarization induces rapid mitochondrial shape changes (**Figure 2.1A**). While these shape changes have often been described as mitochondrial fragmentation [149, 533], there is also evidence for other changes such as circularization [154, 155]. Using the mitochondrial matrix marker mito-BFP in live-cell microscopy, we observe extensive rearrangement of the matrix compartment, that can occur at any point along the mitochondrion, including at mitochondrial branches (**Figure 2.3A**). The end result of these rearrangements is circularization of the mitochondrion. In the absence of CCCP, circularization occurs in a sub-set of depolarized mitochondria, typically those that have been depolarized for a prolonged period (**Figure 2.3B, C**).

We also used dual-color live-cell imaging to observe the dynamics of both the OMM (Tom20-GFP) and the matrix (Mito-dsRed) in the same cell. Interestingly, the matrix marker undergoes circularization, while the OMM marker remains intact across the center of this circularized region (**Figure 2.3B**). This result is consistent in all cases analyzed (**Figure S2.3A**) and is similar to those previously reported by others [156], suggest that the IMM is the primary membrane undergoing rearrangement during depolarization-induced mitochondrial circularization.

To verify this result, we used fixed cell microscopy, first fixing cells with glutaraldehyde. Upon CCCP treatment for 20 min, numerous circular mitochondria are observed (**Figure 2.3C**). The mitochondrial matrix marker (transfected mito-GFP) displays a characteristic hollow donut shape, while the OMM marker (anti-Tom20 is intact throughout the circle. A similar pattern occurs upon formaldehyde fixation, although OMM staining is less regular in this case (**Figure S2.3B**). Using an antibody against the beta subunit of ATP synthase (an IMM protein) shows a similar result, although the ATP synthase staining is more irregular than the GFP matrix protein (**Figure S2.3C**).

We asked whether actin polymerization is required for these mitochondrial shape changes, quantifying shape change as the number of circular matrix structures ('centroids') present per overall mitochondrial area at specific timepoints after CCCP addition. Interestingly, while the actin sequestering drug latrunculin A eliminates CCCP-induced actin polymerization (**Figure 2.4A**), it does not inhibit mitochondrial rearrangement (**Figure 2.4B, C**). In fact, the number of CCCP-induced centroids is moderately increased by 500nM LatA treatment. Similarly, Arp2/3 complex inhibition by CK666 also increases CCCP-induced mitochondrial shape change (**Figure 2.4D, E**). CCCP-induced mitochondrial shape change also occurs in INF2-KO cells (**Figure S2.3D**). Finally, we examined the presence of actin filaments around mitochondria at the time of circularization for CCCP-treated cells. Of 96 circularization events examined, actin polymerization preceded 93 of these events, but had fully depolymerized prior to circularization for 85 events. These results suggest that actin polymerization is not required for the acute mitochondrial shape changes that occur upon CCCP treatment, and may even be inhibitory to these shape changes.

We also assessed whether mitochondrial fission was up-regulated during the early stages of CCCP-induced mitochondrial depolarization. For this purpose, we used a live-cell assay to quantify fission rate [12, 425, 426], because fixed-cell methods to assess fission based on change in mitochondrial length are confounded by the apparent length change induced by circularization. Our results suggest that CCCP treatment does not increase the number of fission events in the first 30 min, contrary to the fission increase induced by ionomycin (**Figure S2.4A**). In addition, we evaluated the effect of Drp1 depletion on CCCP-induced actin clouds and mitochondrial circularization. Drp1 suppression by siRNA has no clear effect on actin cloud assembly (**Figure S2.4B, C**), and causes a slight increase in mitochondrial circularization both prior to and at all time points during CCCP treatment (**Figure S2.4D, E**). The constitutive nature of the circularization increase suggests that acute CCCP induced mitochondrial shape changes are not due to Drp1 dependent mitochondrial dynamics. The increase in circularization upon Drp1-KD might be explained by a constitutive elevation in Opa1 processing (**Figure S2.4B**). Combined, these results suggest that the major morphological change to mitochondria in response to depolarization is remodeling of the IMM, resulting in circular mitochondria in which the OMM remains intact.

2.3.4 Mitochondrial shape changes depend on the IMM protease Oma1

Since CCCP-induced mitochondrial shape change appears to be due largely to IMM rearrangement, we asked which IMM proteins could be mediating these changes. One candidate is the IMM dynamin family protein Opa1, since Opa1 mediates fusion of IMM [534], is important for cristae structure [535-537], and also might play a role mitochondrial fission [535]. Opa1 can be proteolytically processed by two IMM proteases, Oma1 and Yme-1, with consequences for both mitochondrial fission/fusion balance and for cristae ultrastructure [438]. Five distinct bands for Opa1 can be resolved by SDS-PAGE, resulting both from splice variation and differential proteolytic processing (**Figure 2.5A**).

CCCP treatment induces Opa1 proteolytic processing on a similar time scale to both actin polymerization and mitochondrial rearrangement, with increases in short Opa1 bands (S3, S4, S5) within 5 min, and almost complete disappearance of long forms (L1 and L2) by 30 min (**Figure 2.5A, B**), similar to past results [526-528]. CK666 treatment causes accelerated CCCP-induced Opa1 proteolytic processing (**Figure 2.5C**). Conversely, CCCP-induced Opa1 processing is abolished upon siRNA-mediated KD of Oma1 (**Figure 2.5A, B**), similar to past results [526, 538]. In contrast, Yme1 KD has no effect on depolarization-induced Opa1 processing (**Figure 2.5A**). Therefore, we reasoned that Oma1 processing of Opa1 might be involved in mediating depolarization-induced mitochondrial shape changes.

We assessed the effect of Oma1-KD or Opa1-KD on CCCP-induced actin polymerization and mitochondrial shape changes. CCCP-induced actin polymerization is unaffected by either Oma1-KD (**Figure 2.5D**) or Opa1-KD (**Figure S2.5A, D**). Due to the highly fragmented mitochondria resulting from Opa1-KD (**Figure S2.5C**), it is difficult to assess the role of Opa1 in CCCP-induced mitochondrial shape change. In contrast, mitochondria in Oma1-KD cells are similar in morphology to those in control cells, allowing examination of shape change upon CCCP treatment. Oma1-KD cells fail to undergo significant CCCP-induced shape changes, as judged by quantifying circularization for 20 min after stimulation (**Figure 2.5E**). In addition, the increase in CCCP-induced circles caused by CK-666 treatment is strongly suppressed by Oma1-KD (**Figure 2.5F**). As a further test of this effect, we mixed control cells (transfected with a GFP-mito marker) and Oma1-KD cells (transfected with a Ds-red mito marker) and

imaged the two cell types in the same field upon CCCP treatment. While mitochondria in the control cells undergo CCCP-induced shape changes, mitochondria in the Oma1-KD cells do not (**Figure 2.5F**).

These results suggest that the rapid changes in mitochondrial morphology induced by CCCP are due to changes in IMM structure through Oma1-mediated proteolysis, rather than through actin-mediated effects on the OMM.

2.4 Discussion

A growing number of studies show that actin can functionally interact with mitochondria [12, 20, 154, 422, 426, 429, 432, 529-531]. In this paper we show that there are at least two distinct types of mitochondrially-associated actin, differing in cellular stimulus, assembly mechanism, and functional consequences. Mitochondrial depolarization triggers assembly of a dense cloud of actin filaments around the depolarized mitochondria, whereas increased cytosolic calcium triggers actin polymerization throughout the cytosol. Both actin filament populations are transient, with the calcium-induced actin being more rapid both in assembly and disassembly. Depolarization-induced actin is Arp2/3 complex-dependent and INF2-independent, while calcium-induced actin is INF2-dependent and Arp2/3 complex-independent. Inhibition of depolarization-induced actin polymerization causes a greater degree of Oma1-dependent mitochondrial shape change, suggesting that actin polymerization inhibits these changes. Inhibition of calcium-induced actin polymerization causes reduced mitochondrial calcium entry and Drp1 recruitment, with downstream inhibition of mitochondrial fission, which we have shown previously [12, 422].

Several studies have shown similar types of actin clouds to those that we observe after depolarization [20, 429, 432]. In two cases, these clouds were triggered after mitochondrial depolarization [20, 432], while in one case the clouds assembled without stimulation, were not associated with depolarization, and progressed in a cyclic pattern around the cell [429]. Both the depolarization-induced and the depolarization-independent clouds were blocked by Arp2/3 complex inhibition [429, 432]. Therefore, multiple mechanisms may exist to activate Arp2/3 complex around mitochondria. In addition, these studies show formins are involved in Arp2/3 complex-mediated actin assembly around mitochondria [429, 432]. In our work, we find that INF2 is not the responsible formin in the case of depolarization-induced clouds. Mammals possess 15 distinct formin proteins [17, 539], and it will be interesting to identify which formin(s) participate(s) in actin cloud assembly.

One question concerns the activation mechanisms for INF2 and Arp2/3 complex in these processes. We recently showed that cytosolic calcium activates INF2 through a mechanism involving HDAC6-mediated deacetylation of actin [540]. The mechanism by which mitochondrial depolarization activates Arp2/3 complex is less clear. Arp2/3

complex is directly activated by members of the nucleation-promoting factor (NPF) family, which includes WASP/N-WASP, WAVE proteins, WASH, Dip/WISH, WHAMM, JMY, and cortactin [541]. The NPF responsible for depolarization-induced Arp2/3 complex activation has yet to be identified. WHAMM is an attractive candidate, being recruited to early autophagosomes to promote Arp2/3 complex activity during starvation-induced non-specific autophagy [474]. Since long-term CCCP incubation leads to mitophagy and an overall increase in autophagosomes [151, 413, 542-544]. WHAMM may also regulate actin clouds around mitochondria. JMY is another strong candidate, due to its role in autophagosome formation after cell stress [545]. Finally, previous results show that downregulation of cortactin results in elongated and interconnected mitochondria [20], so cortactin is also a candidate Arp2/3 complex activator.

Another question is how IMM depolarization can activate the NPF involved in actin cloud assembly. One protein activated by depolarization is the IMM protease Oma1, but we show that neither Oma1 suppression, nor suppression of the Oma1 substrate Opa1, inhibits actin cloud assembly. Another interesting candidate to relay the depolarization signal might be the protein kinase PINK1, which is stabilized on the outer mitochondrial membrane (OMM) of depolarized mitochondria [412]. An important role of PINK1 is to initiate PARKIN-mediated mitophagy by phosphorylating both PARKIN and ubiquitin [406, 546, 547]. PINK1 is expressed in U2-OS cells [548] while PARKIN has not been detected [549], so it is possible that stabilized PINK1 phosphorylates other substrates that control Arp2/3 complex activation. Candidates include the recently discovered PINK1 substrate Paris [550], or possibly direct phosphorylation of an NPF.

A third question concerns the roles for actin clouds around mitochondria. There is evidence that actin filaments are involved in mitochondrial quality control [20, 432]. A recent paper [432] showed evidence that “cages” of actin and myosin VI assembled around CCCP-depolarized mitochondria and inhibited mitochondrial fusion after CCCP wash-out. These cages assemble later (approximately 2 hrs) than the actin clouds shown here. Since mitochondrial fusion has been shown to require membrane potential [150, 534, 551], and mitochondria remain depolarized for at least 10 min after CCCP treatment in U2-OS cells (**Figure S2.1A**), it is unlikely that the rapidly-assembled actin clouds act as a mitochondrial fusion barrier.

Another possibility is that actin polymerization mediates changes in mitochondrial morphology, since CCCP treatment results in significant changes in mitochondrial structure on a similar time course as actin cloud assembly. However, we find that these rapid mitochondrial shape changes still occur under conditions that prevent actin cloud assembly. In fact, the shape changes are actually increased in the absence of actin clouds. Possibly, actin clouds serve to confine the depolarized mitochondria in order to reduce mitochondrial dynamics.

Our work provides insights into the mechanisms behind these shape changes. A number of studies suggest that depolarization-induced shape changes are the result of massive mitochondrial fragmentation, which are generally observed after mitochondria have been depolarized for an hour or longer [149, 151, 533, 552]. However, others show that in the first 20 min of depolarization the major change in mitochondria is circularization, which is due to changes in the IMM but not the OMM [154-156].

Our live-cell imaging agrees with these observations, showing that the IMM circularizes while the OMM remains intact. IMM circularization depends upon Oma1 and is independent of Drp1. The exact nature of the IMM dynamic rearrangements leading to circularization remain to be determined, but it is our impression that the matrix compartment seems to "split" in most cases to form the circle. We also show that inhibition of Arp2/3 complex increases the rate of Oma1 mediated Opa1 processing after mitochondrial depolarization. It is therefore possible that signaling occurs in both directions in this system, with mitochondrial depolarization triggering cytosolic Arp2/3 complex activation, and the resulting actin clouds inhibiting Oma1 activity. Subsequent actin cloud disassembly might then allow Oma1 to mediate IMM rearrangement. While Opa1 is likely to be the relevant Oma1 substrate in these rearrangements, other Oma1 substrates have been identified as well, including PINK1 [553]; C11orf83 [554] and even Oma1 itself [555]. Reciprocal communication from and to the mitochondrial matrix, through actin polymerization, could serve as another form of interaction between the mitochondrion and its cellular environment.

2.5 Materials and Methods

Cell culture

Wild Type (WT) and INF2-KO Human osteosarcoma U2-OS cells were grown in DMEM (Corning, 10-013-CV) supplemented with 10% newborn calf serum (Hyclone, SH30118.03) at 37°C with 5% CO_2. Cell lines were routinely tested negative for mycoplasma contamination using Universal Mycoplasma detection kit (ATCC, 30-1012K) or LookOut Mycoplasma Detection Kit (Sigma-Aldrich, MP0035). The INF2-KO U2-OS cell line made by CRISPR-Cas9 is described elsewhere [12].

DNA transfections

For plasmid transfections, cells were seeded at $4x10^5$ cells per well in a 35 mm dish ~ 16 hours before transfection. Transfections were performed in OPTI-MEM media (Gibco, 31985062) with 2µl Lipofectamine 2000 (Invitrogen, 11668) per well for 6 hours, followed by trypsinization and re-plating onto glass-bottomed dishes (MatTek Corporation, P35G-1.5-14-C) at ~$3.5x10^5$ cells per well. Cells were imaged ~16-24 hours after transfection.

The following expression constructs were used: Mito-DsRed and mito-BFP, previously described [423], consisting of amino acids 1-22 of *S.cerevisiae* COX4 N-terminal to the respective fusion protein. GFP-F-tractin was a gift from Clare Waterman and Ana Pasapera (NIH, Bethseda, MD) and described in [556]. GFP-Mito was purchased from Clontech (pAcGFP1-Mito, #632432) and consists of the mitochondrial targeting sequence derived from the precursor of subunit VIII of human cytochrome c oxidase. Tom20-GFP was made by restriction digest of Tom20 from Tom20-mCherry (a gift from Andrew G York, NIH, Bethseda, MD) with NheI and BamHI; and cloned into eGFP-N1 (Clontech) and is previously described in [12]. Mito-R-GECO1 (Addgene, #46021) is previously described in [557]. H2B-mCherry (Addgene # 20972) is previously described in [558].

The following amounts of DNA were transfected per well (individually or combined for cotransfection): 500ng for Mito-BFP, Mito-DsRed, GFP-Mito, Mito-R-GECO1, H2B-mCherry and GFP-F-tractin and 600ng for Tom20-GFP construct.

For siRNA transfections, 10^5 cells were plated on a 35 mm dish and 2µl RNAimax (Invitrogen, 13778) with 63pmol siRNA were used per well. Cells were analyzed 96 hours post siRNA transfection. For live-cell imaging, plasmids containing fluorescent markers were transfected into siRNA-treated cells 18-24 hrs prior to imaging, as described above. All siRNAs were purchased from IDT Inc, including: human INF2 (custom synthesized, HSS.RNAI.N001031714.12.7., 5'-GGAUCAACCUGGAGAUCAUCCGC-3'); human Oma1 (hs.Ri.OMA1.13.1, 5'-

GGAUAUUCAGGGUCAAAUGUACAUGAUUUGACCCUG-3'); human Yme1l1 (hs.Ri.YME1L1.13.1, 5'-GGUGGAGGAAGCUAAACAAGAAUUA-3'); human Opa1 (hs.Ri.OPA1.13.1, 5'-CCACAGUGGAUAUCAAGCUUAAACA-3'); human Drp1 (custom synthesized, HSC.RNAI.N005690.12.1, 5′-GCCAGCUAGAUAUUAACAACAAGAA-3′); and negative control (#51-01-14-04, 5'-CGUUAAUCGCGUAUAAUACGCGUAU-3').

Antibodies

Anti-INF2 (rabbit polyclonal against amino acids 941-1249 of human INF2) was described in [559] and used at 3.75 μg/mL. Anti-Opa1 (BD Biosciences, 612606, mouse monoclonal, clone 18/OPA1) was used at 1:2000. Anti-Oma1 (Santa Cruz Biotechnology, sc-515788, mouse monoclonal, clone H-11/OMA1) was used at 1:500. Anti-tubulin (Sigma-Aldrich, T9026, mouse, clone DM1- α) was used at 1:10,000 dilution. Anti-GAPDH (Santa Cruz Biotechnology, sc-365062, G-9, mouse) was used at 1:1500. Anti-Tom20 (Abcam, ab78547) was used at 1:500 for immunofluorescence. Anti-ATP synthase beta monoclonal antibody (Invitrogen, A-21351, mouse, 3D5AB1) was used at 1:500 for immunofluorescence. Secondary antibodies used for westerns were: goat anti-mouse IgG horseradish peroxidase (HRP) conjugate (Bio-rad, 1705047) at 1:2000 and goat anti-rabbit IgG HRP conjugate (Bio-rad, 1706515) at 1:5000. For immunofluorescence, we used goat anti-rabbit IgG Texas red secondary (Vector Laboratories, TI-1000) was used at 1:500, and horse anti-mouse IgG Fluorescein secondary (Vector Laboratories, FI-2000) was used at 1:500.

Western blot analysis

Cells from a 35 mm dish were trypsinized, pelleted by centrifugation at 300xg for 5 min, and resuspended in 400μl 1 X DB (50mM Tris-HCl, pH 6.8, 2mM EDTA, 20% glycerol, 0.8% SDS, 0.02% Bromophenol Blue, 1000mM NaCl and 4M Urea). Proteins were separated by SDS-PAGE in a BioRad mini gel system (7 X 8.4 cm) and transferred onto polyvinylidene fluoride membrane (EMD Millipore, IPFL00010). The membrane was blocked with TBS-T (20mM Tris-HCl, pH 7.6, 136mM NaCl and 0.1% Tween-20) containing 3% BSA (VWR Life Science, VWRV0332) for 1 hour, then incubated with primary antibody solution at 4°C overnight. After washing with TBS-T, the membrane was incubated with HRP-conjugated secondary antibody for 1 hour at 23˚C. Signals were detected by chemiluminescence. For western blots of Opa1, samples were prepared and separated by SDS-PAGE on a Hoefer SE600 (14 cm X 14 cm) apparatus and transferred using a Hoefer transfer apparatus. The rest of the procedure was similar to as listed above.

Immunofluorescence

U2-OS-WT cells ($1x10^5$, either transfected with mito-GFP or untransfected) were plated on Mat-Tek dishes (MatTek Corporation, P35G-1.5-14-C) 16 hours prior to fixation and staining. Cells were treated with DMSO or 20 uM CCCP for 20 min at 37˚C/5% CO_2, washed twice in PBS (23˚C)

and fixed in either 1% glutaraldehyde (EMS, 16020) prepared in BRB80 buffer (80 mM PIPES pH 6.9, 1mM $MgCl_2$, 1mM EGTA) or 4% prewarmed paraformaldehyde (EMS, 15170) in PBS for 10 min or 20 min respectively. The glutaraldehyde-fixed samples were additionally washed with $NaBH_4$ (1mg/ml in PBS; 3 X 10 min each) prior to permeabilization. The cells were then permeabilized in 0.1% Triton X-100 in PBS for 10 min and blocked in PBS + 10% calf serum for 30 min. These cells were then stained with Tom 20 antibody and/or ATP-synthase (mitochondria), appropriate secondary antibodies and DAPI (nucleus) in PBS + 1% calf serum and imaged by Dragonfly 302 spinning disk confocal (Andor Technology) CFI Plan Apochromat Lambda 100X/1.45 NA oil in PBS on the Mat-Tek dish. Z-stacks were taken from the basal region to the apical top at 0.4μm step size. Maximum intensity projections were generated from z-stack images and background subtracted in ImageJ Fiji (rolling ball 20.0).

Live imaging by confocal microscopy and Airyscan microscopy

All live cell imaging was conducted in DMEM (Gibco, 21063-029) with 25mM D-glucose, 4mM L-glutamine and 25mM Hepes, supplemented with 10% newborn calf serum, hence referred to as "live cell imaging media". Cells (~$3.5x10^5$) were plated onto MatTek dishes 16hrs prior to imaging. Medium was preequilibrated at 37°C and 5% CO_2 before use.

For confocal microscopy, dishes were imaged using the Dragonfly 302 spinning disk confocal (Andor Technology) on a Nikon Ti-E base and equipped with an iXon Ultra 888 EMCCD camera, a Zyla 4.2 Mpixel sCMOS camera, and a Tokai Hit stage-top incubator set at 37°C. A solid-state 405 smart diode 100 mW laser, solid state 560 OPSL smart laser 50 mW laser, and solid state 637 OPSL smart laser 140 mW laser were used. Objectives used were the CFI Plan Apochromat Lambda 100X/1.45 NA oil (Nikon, MRD01905) for all drug treatment live-cell assays; and CFI Plan Apochromat 60X/1.4 NA oil (Nikon, MRD01605) to observe transient depolarization events during live-cell imaging. Images were acquired using Fusion software (Andor Technology, version 2.0.0.15). For actin burst and TMRE quantifications, cells were imaged at a single confocal slice at the medial region, approximate 2μm above the basal surface, to avoid stress fibers. To observe mitochondrial morphological changes, cells were imaged at a single confocal slice at the basal surface.

For ionomycin treatments, cells were treated with 4μM ionomycin (Sigma-Aldrich I0634, from 1mM stock in DMSO) at the start of the 5^{th} image frame (~1 min, time interval set at 15sec) during imaging and continued for another 5-10 mins. INF2 KO cells were used as a negative control. For Carbonyl cyanide 3-chlorophenylhydrazone (CCCP) (Sigma-Aldrich, C2759) treatments, cells were treated with 20μM CCCP (from a 100mM stock in DMSO) at the start of the 5^{th} frame (~1 min, with time interval set at 14sec or 15sec) during imaging and continued for another 15-20mins. Equal volume DMSO (Invitrogen, D12345) was used as the negative control. For

Tetramethylrhodamine ethyl ester perchlorate (TMRE) (Sigma-Aldrich, 87917) staining before CCCP treatment, cells were loaded with 20 nM TMRE (from a 30mM stock in DMSO) for 30 minutes in live cell imaging media. Cells were subsequently washed twice with live-cell media and fresh live-cell media was added prior to imaging. During imaging, cells were treated with 20μM CCCP at the start of the 5th frame (~1 min, with time interval set at 15sec) and continued for another 15-20mins. As a negative control, equal volume DMSO was added during imaging (in place of CCCP) for cells loaded with 20nM TMRE.

To observe transient depolarization in U2-OS cells in the absence of CCCP, cells were loaded with 20nM TMRE (with or without CK666) for 30 minutes in live cell imaging media at 37°C and 5% CO_2. CK666 and TMRE treated cells were rinsed twice with fresh live cell medium and 50μM CK666 containing live cell medium was added prior to imaging. Single field confocal imaging in the medial region was conducted at 1.2sec time interval and continued for 1000 frames (20mins). To visualize more cells in the field, the 60X/1.4NA objective was used. Equal volume DMSO was used as a negative control in place of CK666 while retaining TMRE. To observe mitochondrial rearrangements after transient depolarization, multiple field confocal imaging with the 100X/1.4NA objective was conducted in the basal region at 6sec time interval and continued for 200 frames (20mins).

For Latrunculin A (LatA) (Millipore Sigma, 428021) coupled with CCCP treatment, cells were treated with live-cell media containing 500nM LatA (from a 1mM stock in DMSO) and 20μM CCCP simultaneously at the start of the 5th frame (1 min, time interval set at 15sec). Imaging was continued for 10-20mins. Cells treated with DMSO (replacing LatA) and 20μM CCCP simultaneously were the positive control; while cells treated with 500nM LatA and DMSO (replacing CCCP) simultaneously were used as the negative control.

For CK666 (Sigma-Aldrich, SML006) pretreatment before CCCP addition, cells were pretreated with 1mL of live-cell media containing 100μM CK666 (from a 20mM stock in DMSO) for 30 min before the start of imaging. During imaging, cells were treated with 1mL live cell media containing 40μM CCCP at the start of the 5th frame (1 min, time interval set at 15sec). Imaging was continued for 15-20mins with cells in media containing a final concentration of 20μM CCCP and 50μM CK666. Control cells were pretreated with equal volume DMSO (replacing CK666) and stimulated with 20μM CCCP during imaging; and as a negative control, cells were pretreated with 100μM CK666 and equal volume DMSO (replacing CCCP) was added during imaging.

For CK666 pretreatment before ionomycin addition, cells were pretreated with 1mL of live-cell media containing 100μM CK666 for 30 mins. After which, cells were directly taken for imaging. During imaging, cells were treated with 1mL of live cell media containing 8μM ionomycin at the start of the 5th frame (1 min, time interval set at 15sec). Imaging continued for 5-10mins with cells

in media containing a final concentration of 4μM ionomycin and 50μM CK666. Control cells were pretreated with equal volume DMSO (replacing CK666) and stimulated with 4μM ionomycin during imaging; and as a negative control, cells were pretreated with DMSO (replacing CK666) and additional DMSO (replacing ionomycin) was added during imaging.

For Airyscan imaging, dishes were imaged on the LSM 880 equipped with a 100X/1.4 NA Apochromat oil objective using the Airyscan detectors (Carl Zeiss Microscopy). The Airyscan uses a 32-channel array of GaAsP detector configured as 0.2 airy units per channel. Cells were imaged with the 488nm laser and Band Pass (BP) 420-480/BP 495-620 filter for GFP, 561nm laser and BP 495-550/Long Pass 570 filter for RFP. For live-cell microscopy, WT U2-OS cells were co-transfected with 500ng of Mito-DsRed and 600ng Tom20-GFP while INF2 KO cells were co-transfected with 500ng Mito-R-GECO1 and 600ng Tom20-GFP. All imaging conducted at 37°C and 5% CO_2, with a single basal slice acquired at a frame interval of 4.1sec. Images were subsequently processed using Zen2 software. Raw data were processed using Airyscan processing with Zen Black software (Carl Zeiss, version 2.3).

For mixing experiment, control cells were transfected with 500ng Mito-Ds-Red and Oma1 KD cells were transfected with 500ng Mito-BFP 72 hours post knock down. After four hours transfection, control cells were mixed with Oma1 KD cells in a 1:2 (control : Oma1 KD) volume ratio. Mixed cells were re-plated onto MatTek dishes at ~$3.5x10^5$ cells per dish and allowed to adhere for ~18 hours. During live-cell imaging with CCCP, fields were selected with both Oma1 KD and control cells visible.

Quantification from live-cell imaging experiments

Unless otherwise stated, all image analysis was performed on ImageJ Fiji (version 1.51n, National Institutes of Health). Cells that shrunk during imaging or exhibited signs of phototoxicity like blebbing or vacuolization were excluded from analysis.

Actin burst measurements. Mean actin fluorescence was calculated by selecting two region of interests (ROIs) (for ionomycin treatments) per cell or one ROI per cell (for CCCP treatments). The ROI selected for CCCP encompass the entire area at the height of actin assembly after CCCP treatment. Fluorescence values for each time point (F) were normalized with the mean initial fluorescence before drug treatment (first four frames – F_0) and plotted against time as F/F_0. For DMSO control or cells that did not exhibit actin burst, ROI was selected as the bulk region of the cytoplasm containing mitochondria using the Mito-BFP channel.

Centroid measurements. Every eight frame was analyzed (2 min intervals). Imaging fields were coded and scrambled by one investigator (TSF) and given to the other investigator (RC) for blind analysis. Centroid were counted manually for every time point. To normalize the data, the number

of centroids was divided by the total mitochondrial area in the field (μm^2). The results were then decoded by the first investigator.

Mitochondrial division rate measurements. Mitochondrial division rate was described in detail previously [426]. Suitable ROIs were selected based on whether individual mitochondria were resolvable and did not leave the focal plane. One ROI was selected per cell. Files of the ROIs were coded and scrambled by one investigator (RC) and analyzed for division by a second investigator (WKJ) in a blinded manner. The second investigator scanned the ROIs frame by frame manually for division events and determined total mitochondrial length in the ROI using the ImageJ macro, Mitochondrial Morphology. The results were then returned to the first investigator for decoding.

Depolarization measurements. Mean TMRE fluorescence was calculated from the entire mitochondrial area determined in the Mito-BFP channel, for which the fluorescent intensity did not change appreciably during imaging. TMRE fluorescence values for each time point (F) were normalized with the mean initial fluorescence before drug treatment (first four frames – F_0) and plotted against time as F/F_0.

Transient depolarization events in untreated cells are defined as an abrupt loss in mitochondrial TMRE fluorescence signal that persist for ≥ 30 seconds without an appreciable decrease in fluorescence signal of the Mito-BFP marker. Individual transient depolarization events were manually identified by scrolling through images frame by frame. Clear increase in actin fluorescence signal after transient depolarization were considered as "$\Delta\psi_m$ followed by actin assembly"; while depolarization events that demonstrated no appreciable actin fluorescence increase were considered as "$\Delta\psi_m$ followed by no actin assembly". To determine the frequency of depolarization, the total number of depolarization events was normalized to the total cell count and the total duration of the imaging (min). For depolarization duration, suitable ROIs were selected for mitochondria which underwent depolarization. TMRE fluorescence values for each time point were normalized to the mean initial fluorescence (ten frames before transient depolarization) and plotted against time. Depolarization events that occurred 16 minutes into imaging and did not recover at the end of 20 minutes imaging were separately noted.

$T_{1/2}$ analysis of actin assembly and disassembly. Mean actin fluorescence was calculated by selecting one region of interest (ROI) (for ionomycin and CCCP treatments). The ROI selected for CCCP encompass the entire cell area at a medial cell section, whereas for ionomycin treatment one ROI at peri-nuclear region (free from stress fibers for all time frame) per cell was selected. Fluorescence values for each time point (F) were normalized with the mean initial fluorescence before drug treatment (first thirty frames – F_0) and plotted against time as F/F_0. Half-max value was calculated after establishing the peak value and the time determined from the ascending slope (actin assembly) for each cell. For actin disassembly, the time (s) was determined for the half max value

from the descending slope and deducted from the peak time. For ionomycin analysis all the cells were used for assembly, peak and disassembly calculations. For CCCP. 5 cells were removed for disassembly calculations because of stress fiber interference. Number of individual cells: 18 (ionomycin) and 25 (CCCP/ actin assembly & actin peak); 20 (CCCP actin disassembly). Data compiled from three independent experiments.

Statistical analysis and graph plotting softwares

All statistical analyses and p-value determination were conducted using GraphPad Prism QuickCalcs or GraphPad Prism 8 (version 8.2.0, GraphPad Software). To determine p-values, an unpaired Student's t test was performed between two groups of data, comparing full datasets stated in the figure legends. For p-values in multiple comparisons (unpaired), Sidak's multiple comparisons test and Dunnett's multiple comparison test were performed in GraphPad Prism 8. Average p-values were calculated with multiple t-tests (without correction) in GraphPad Prism 8. All graphs, along with their standard error of mean (SEM) were plotted using Microsoft Excel for Office 365 (version 16.0.11231.20164, Microsoft Corporation), with the exception of scatter plots. **Figures 2.2E, S2.2A, S2.2E, S2.2F** were plotted with GraphPad Prism 8 and **Figure S2.4A** was plotted with KaleidaGraph (version 4.01, Synergy Software).

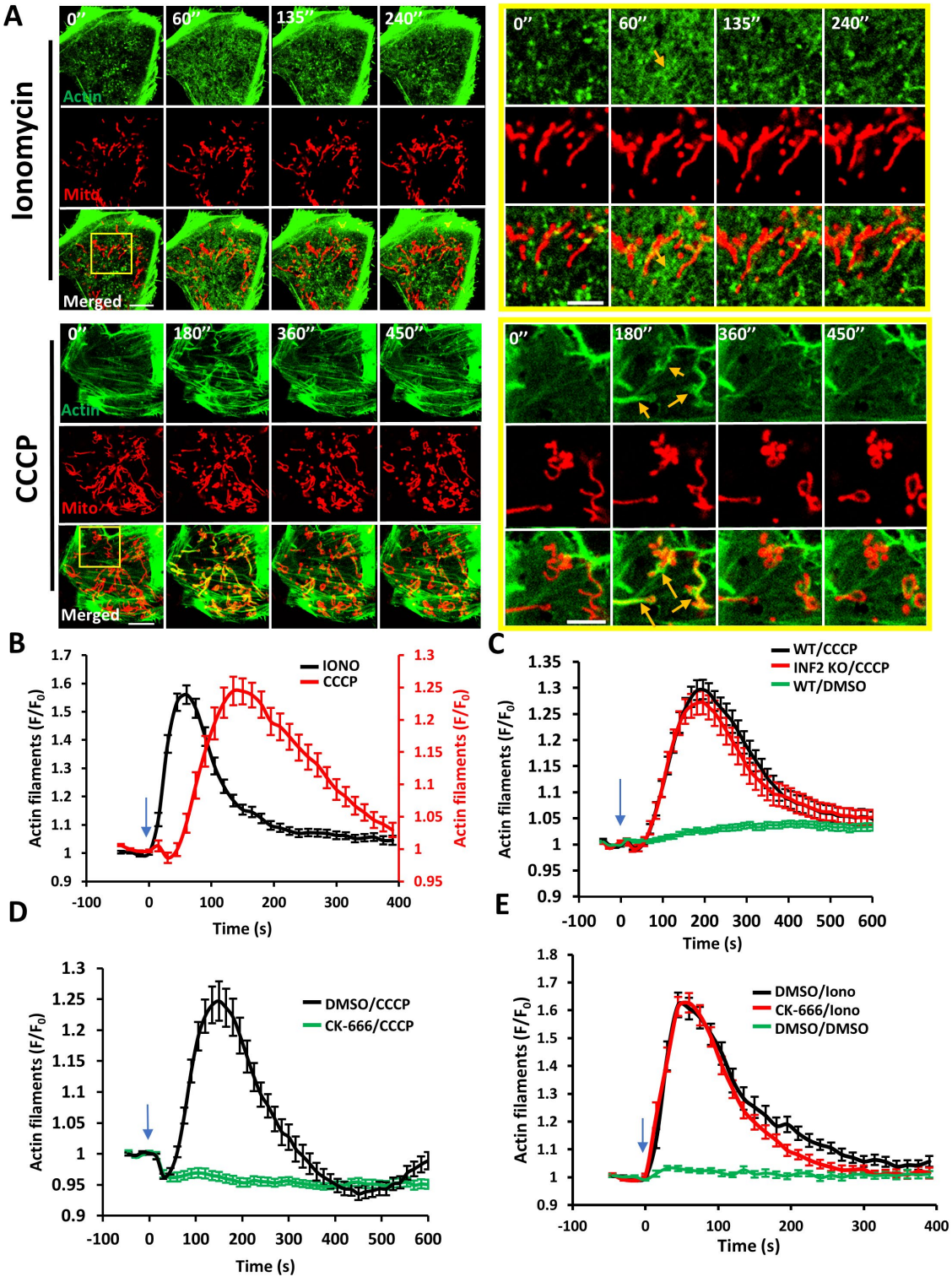
A
Ionomycin
0''
60''
135''
240''
Actin
Mito
Merged
CCCP
180''
360''
450''
B
IONO
CCCP
Actin filaments (F/F0)
Time (s)
C
WT/CCCP
INF2 KO/CCCP
WT/DMSO
D
DMSO/CCCP
CK-666/CCCP
E
DMSO/Iono
CK-666/Iono
DMSO/DMSO

Figure 2.1. Distinct actin structures assemble in response to two stimuli: increased cytoplasmic calcium and mitochondrial depolarization. **A)** Time-lapse image montage of ionomycin-induced (top) and CCCP-induced (bottom) actin polymerization for U2-OS cells transfected with GFP-F-tractin (green) and mito-BFP (red). Imaging conducted at the basal cell surface. Ionomycin or CCCP added at time point 0. Scale bar: 10μm. Inset scale bar: 5μm. Orange arrow shows actin assembly in both cases. **B)** Comparison of ionomycin-induced and CCCP-induced actin polymerization time course for U2-OS cells. Data from three experiments. N = 30 cells/60 ROIs for ionomycin (4 μM) treatment, 27 cells/27 ROIs for CCCP (20 μM) treatment. 15 sec intervals. Blue arrow denotes drug addition. Error bar, ±SEM. **C)** CCCP-induced actin polymerization in U2-OS-WT and U2-OS-INF2-KO cells. Data from three experiments. N=35 cells for WT, 39 cells for INF2 KO and 35 cells for WT cells stimulated with DMSO. 14 sec intervals. Blue arrow denotes CCCP addition. Error bar, ±SEM. **D)** Effect of Arp2/3 complex inhibition on CCCP-induced actin polymerization. U2-OS cells were treated with either DMSO or 100μM CK-666 for 30 min, then stimulated with 20μM CCCP (blue arrow). Data from three experiments. N=35 cells/35 ROIs for DMSO/CCCP, 41/41 for CK-666/CCCP. 15 sec intervals. Error bar, ±SEM. **E)** Effect of Arp2/3 complex inhibition on ionomycin-induced actin polymerization. U2-OS cells were treated with either DMSO or 100μM CK-666 for 30 minutes, then stimulated with DMSO or 4μM ionomycin (blue arrow). Data from three experiments. N=23 cells/46 ROI for DMSO/Iono, 25/50 for CK-666/Iono and 20/40 for DMSO/DMSO. 15 sec intervals. Error bar, ±SEM.

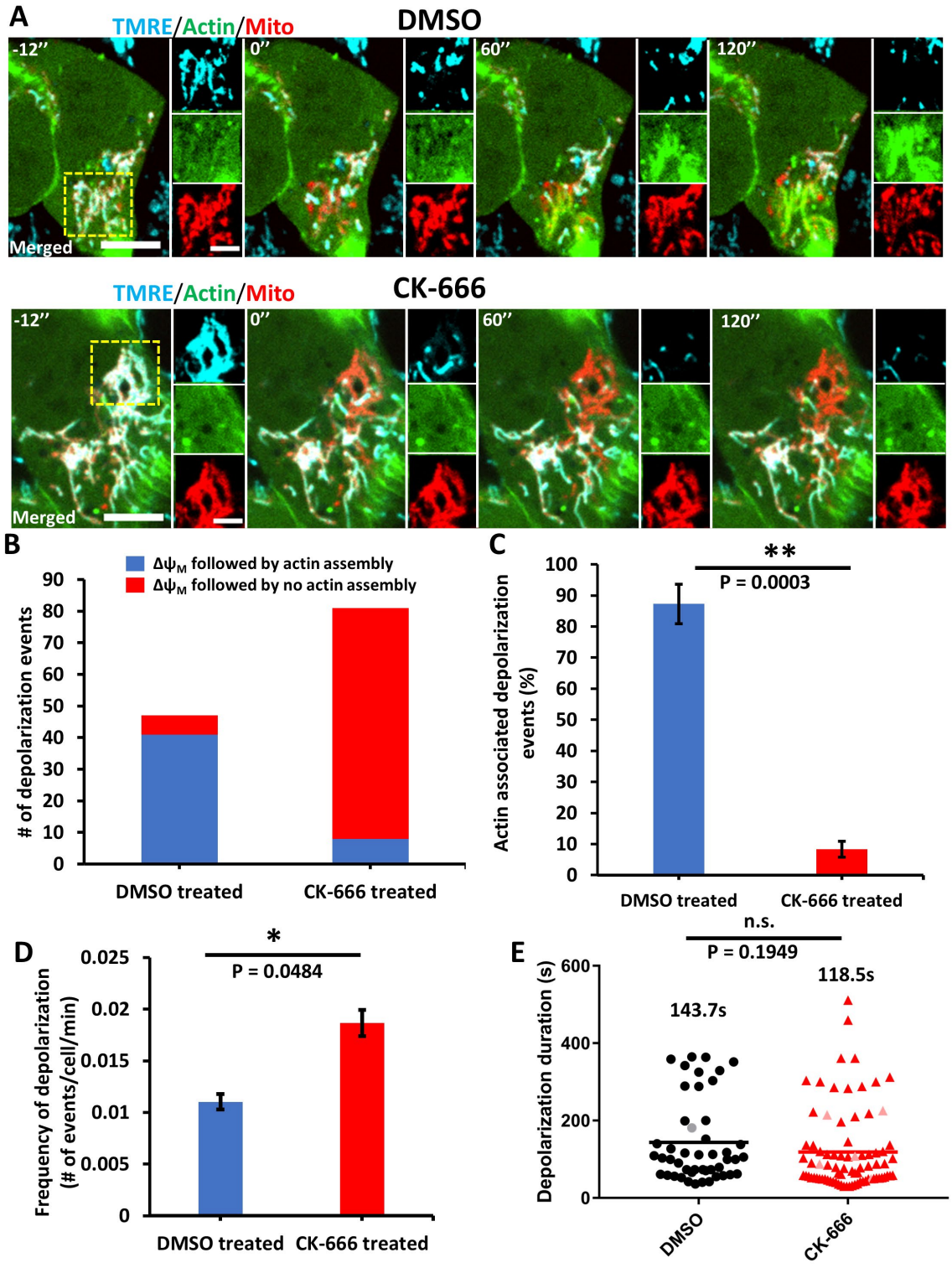
A
TMRE/Actin/Mito
DMSO
-12''
0''
60''
120''
Merged
TMRE/Actin/Mito
CK-666
-12''
0''
60''
120''
Merged
B
ΔψM followed by actin assembly
ΔψM followed by no actin assembly
# of depolarization events
DMSO treated
CK-666 treated
C
**
P = 0.0003
Actin associated depolarization events (%)
DMSO treated
CK-666 treated
D
*
P = 0.0484
Frequency of depolarization (# of events/cell/min)
DMSO treated
CK-666 treated
E
n.s.
P = 0.1949
143.7s
118.5s
Depolarization duration (s)
DMSO
CK-666

Figure 2.2: Actin polymerization accompanying transient depolarization of a sub-set of mitochondria in the absence of CCCP. A) Time-lapse image montages of changes in mitochondrial polarization (TMRE, blue) and actin polymerization (GFP-F-tractin, green) in U2-OS cells in the absence of uncoupler treatment. A mitochondrial matrix marker (Mito-BFP, red) is also included. Top panels show a control cell (DMSO) and bottom panels show a CK-666-treated cell (100 μM CK-666 for 30 min before imaging, and 50μM during imaging). Time 0 denotes start of a depolarization event. Panels to right of each time point denote zooms of boxed regions. Scale bars:10μm (5 μm for inset). **B)** Graph of spontaneous depolarization events associated with actin polymerization, in either control (DMSO) or CK-666-treated cells. Total numbers from 3 experiments (20 min imaging per cell, 1.2 sec intervals): DMSO, 213 cells, 47 depolarization events (41 events accompanied by actin assembly); CK-666, 217 cells, 81 depolarization events (8 events accompanied by actin assembly). **C)** Graph of % depolarization events accompanied by actin polymerization for DMSO versus CK-666 treatment, from same data as panel B. Student's unpaired t-test: $p = 0.0003$. Error bar: ±SEM. **D)** Graph of depolarization frequency for DMSO versus CK-666 treatment, from data set described in panel B. Student's unpaired t-test: $p = 0.0484$. Error bar: ±SEM. **E)** Scatter plot of depolarization duration, from data set described in (**B**). Mean depolarization durations: DMSO group (black line), 143.7 sec ± 106.5 sec; CK-666 group (red line), 118.5 sec ± 104.4 sec (standard deviation). Gray and pink points represent depolarization events that occurred after 16 minutes of imaging time and failed to repolarize at the end of the 20minutes imaging period. Student's unpaired t-test: $p = 0.1949$.

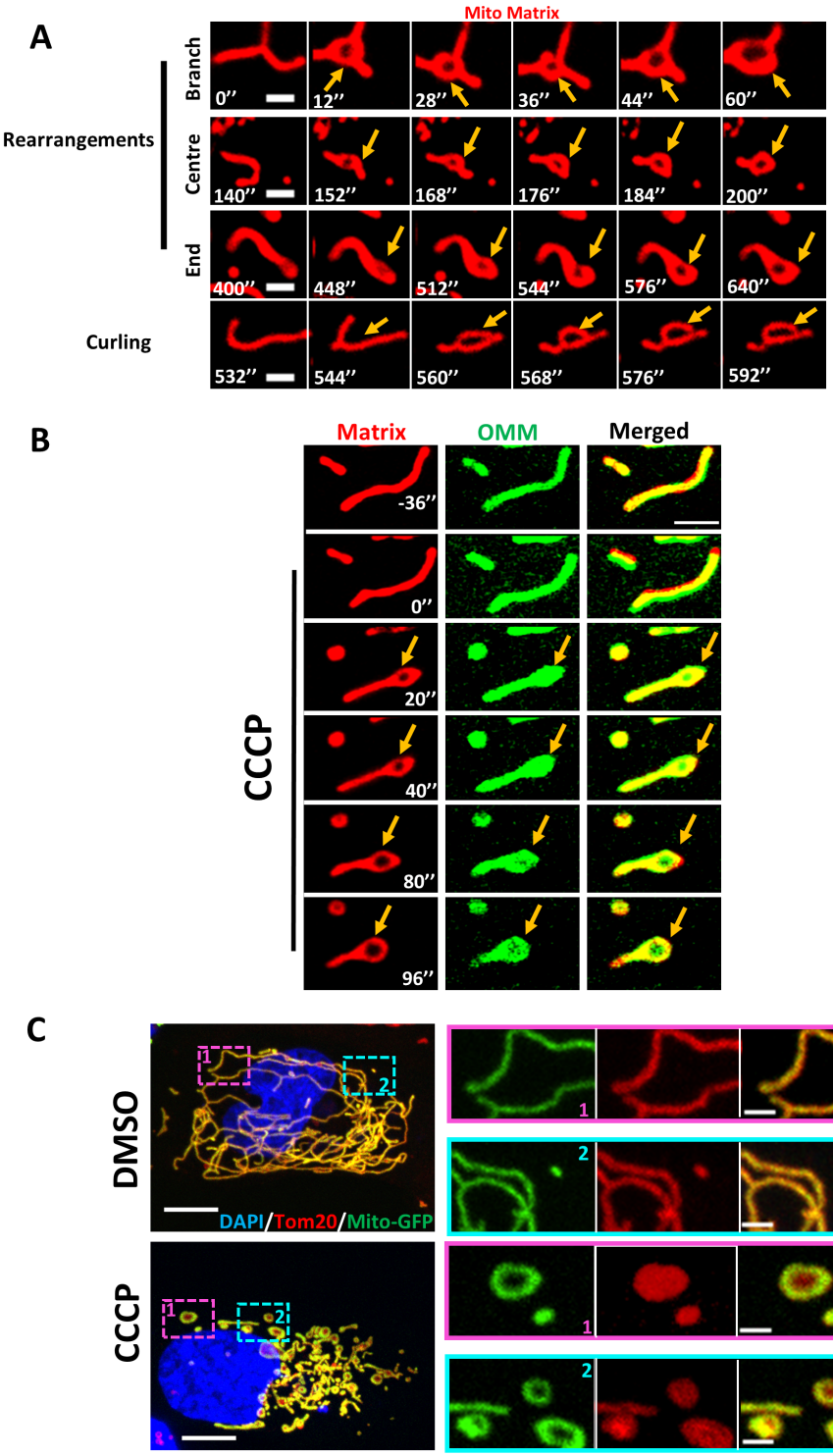
A
Mito Matrix
Rearrangements
Branch
Centre
End
Curling
0''
12''
28''
36''
44''
60''
140''
152''
168''
176''
184''
200''
400''
448''
512''
544''
576''
640''
532''
544''
560''
568''
576''
592''
B
Matrix
OMM
Merged
CCCP
-36''
0''
20''
40''
80''
96''
C
DMSO
CCCP
DAPI/Tom20/Mito-GFP
1
2

Figure 2.3: Depolarization-induced mitochondrial shape changes in U2-OS cells. **A)** Examples of mitochondrial matrix dynamics after depolarization, leading to circularization. Three examples of matrix rearrangement and one example in which the mitochondrion curls back on itself to form the circle. U2-OS cells were transfected with the mitochondrial matrix marker mito-DsRed and treated with 20μM CCCP at time point 0. Confocal imaging was conducted at the basal region of the cell at 4 sec intervals, starting 10 frames before CCCP treatment. Scale bar: 2μm. **B)** Dynamics of the OMM and mitochondrial matrix upon depolarization. U2-OS cell transfected with Mito-DsRed (red) and Tom20-GFP (green) was treated with 20μM CCCP at time point 0. Airyscan images (basal region) were acquired at 4 sec intervals starting 10 frames before CCCP treatment. Scale bar: 2.5μm. **C)** Maximum intensity projections of glutaraldehyde-fixed U2-OS cells (transfected with GFP-Mito, green) after treatment with either DMSO (top) or 20μM CCCP (bottom) for 20 min. Cells were stained with anti-Tom20 (OMM, red) and DAPI (nucleus, blue). Z stacks were taken at step size of 0.4μm. Zooms show representative examples of mitochondrial circularization after CCCP treatment. Scale bars: 10μm and 2μm (inset).

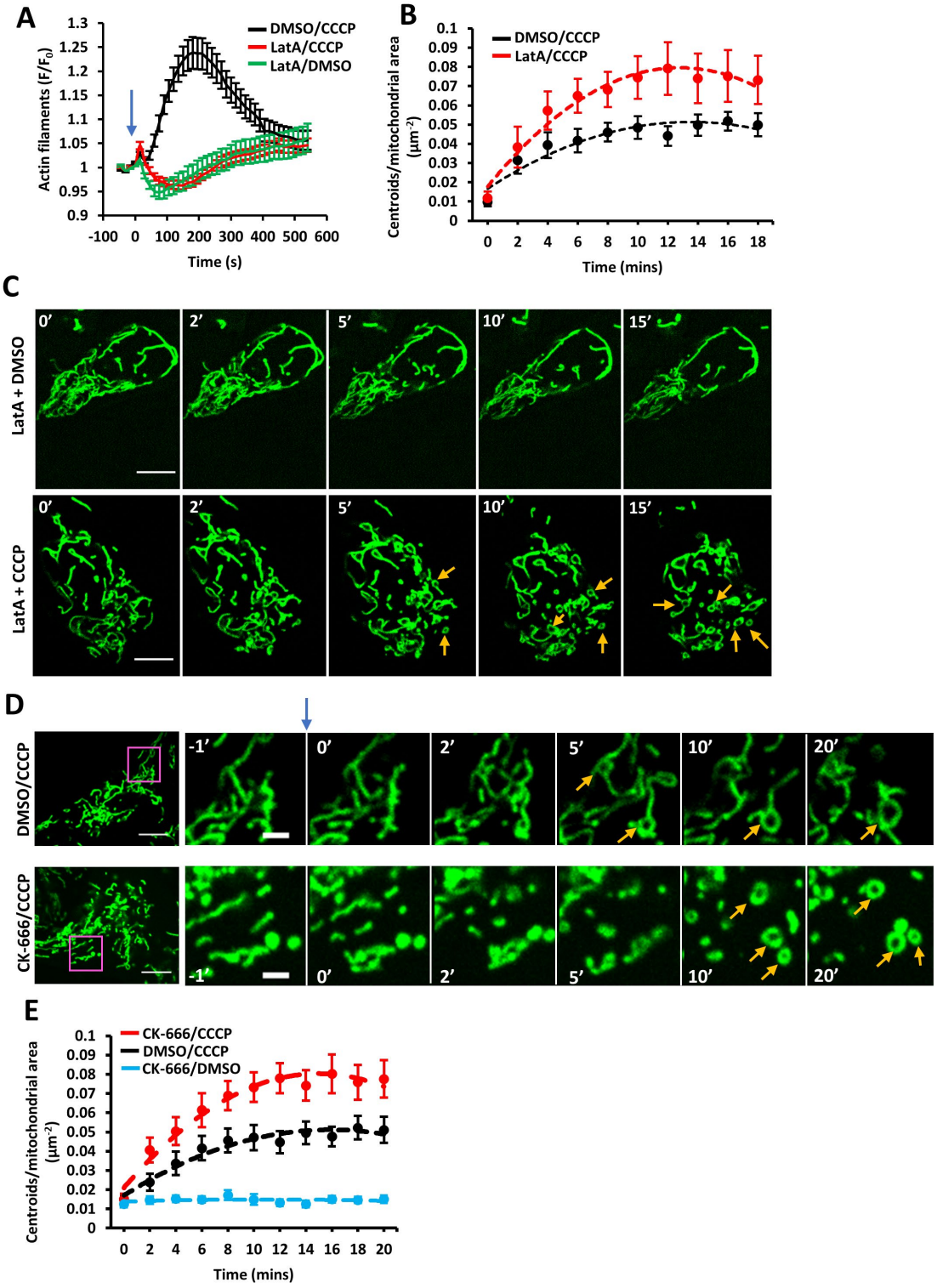
A
Actin filaments (F/F0)
DMSO/CCCP
LatA/CCCP
LatA/DMSO
Time (s)
B
Centroids/mitochondrial area (µm-2)
DMSO/CCCP
LatA/CCCP
Time (mins)
C
LatA + DMSO
LatA + CCCP
0′
2′
5′
10′
15′
D
DMSO/CCCP
CK-666/CCCP
-1′
0′
2′
5′
10′
20′
E
Centroids/mitochondrial area (µm-2)
CK-666/CCCP
DMSO/CCCP
CK-666/DMSO
Time (mins)

Figure 2.4: Effect of latrunculin A and Arp2/3 complex inhibition on depolarization-induced mitochondrial shape changes. A) Effect of LatA on CCCP-induced actin polymerization. U2-OS cells were treated with combinations of LatA (500 nM) and CCCP (20μM) at time 0 (blue arrow). Confocal images (medial section) were acquired at 15 sec intervals starting four frames before treatment. Data from three experiments. N=23 cells/23 ROIs for LatA/DMSO, 38/38 for LatA/CCCP and 31/31 for DMSO/CCCP. Error bar, ±SEM. **B)** Effect of LatA on CCCP-induced mitochondrial matrix circularization ('centroids'). U2-OS cells transfected with mito-BFP and GFP-F-tractin. CCCP (20μM) added at time point 0, simultaneous to LatA addition (500 nM). Data from three experiments. N= 17 cells/3702 μm^2 total mitochondrial area for DMSO/CCCP control cells; 18 cells /3823 μm^2 for LatA/CCCP. Error bars, ±SEM. Average p values for time points four mins after treatment is 0.0204 ± 0.0179 for DMSO versus LatA. **C)** Time-course montage of LatA-treated cells under control conditions (DMSO treatment, top) or CCCP treatment (20 μM, bottom). U2-OS cells, transfected with F-tractin (not shown) and mito-BFP (green), treated with 500nM LatA and CCCP or DMSO simultaneously at 0 min. Confocal images (basal section) acquired at 15 sec intervals starting four frames before treatment. Yellow arrows denote centroids (circular mitochondrial matrix). Time in min. Scale bar: 10μm. **D)** Time-course montage of CCCP-induced mitochondrial matrix circularization in the absence (top) or presence (bottom) of CK-666 pre-treatment. U2-OS cells transfected with GFP-F-tractin (not shown) and mito-BFP (green) were treated with DMSO or CK-666 (100μM) for 30 minutes before stimulation with 20μM CCCP at time point 0 (blue arrow). Confocal images (basal section) were acquired at 15 sec intervals starting four frames before CCCP treatment. Yellow arrows denote centroids (circular mitochondrial matrix). Time in min. Scale bar: 10μm. Inset scale bar: 2.5μm. **E)** Graph of change in mitochondrial matrix circularization (defined as centroids per total mitochondrial area in the region of interest) from time-courses taken as described in (**A**). Data from three experiments. Conditions tested: CK-666 pre-treatment followed by CCCP stimulation (N= 46 cells/8539 μm^2 total mitochondrial area); DMSO pretreatment, CCCP stimulation (58 cells/11473 total mitochondrial area); and CK-666 pre-treatment/DMSO stimulation (36 cells/6655 total mitochondrial area). Error bars, ±SEM.

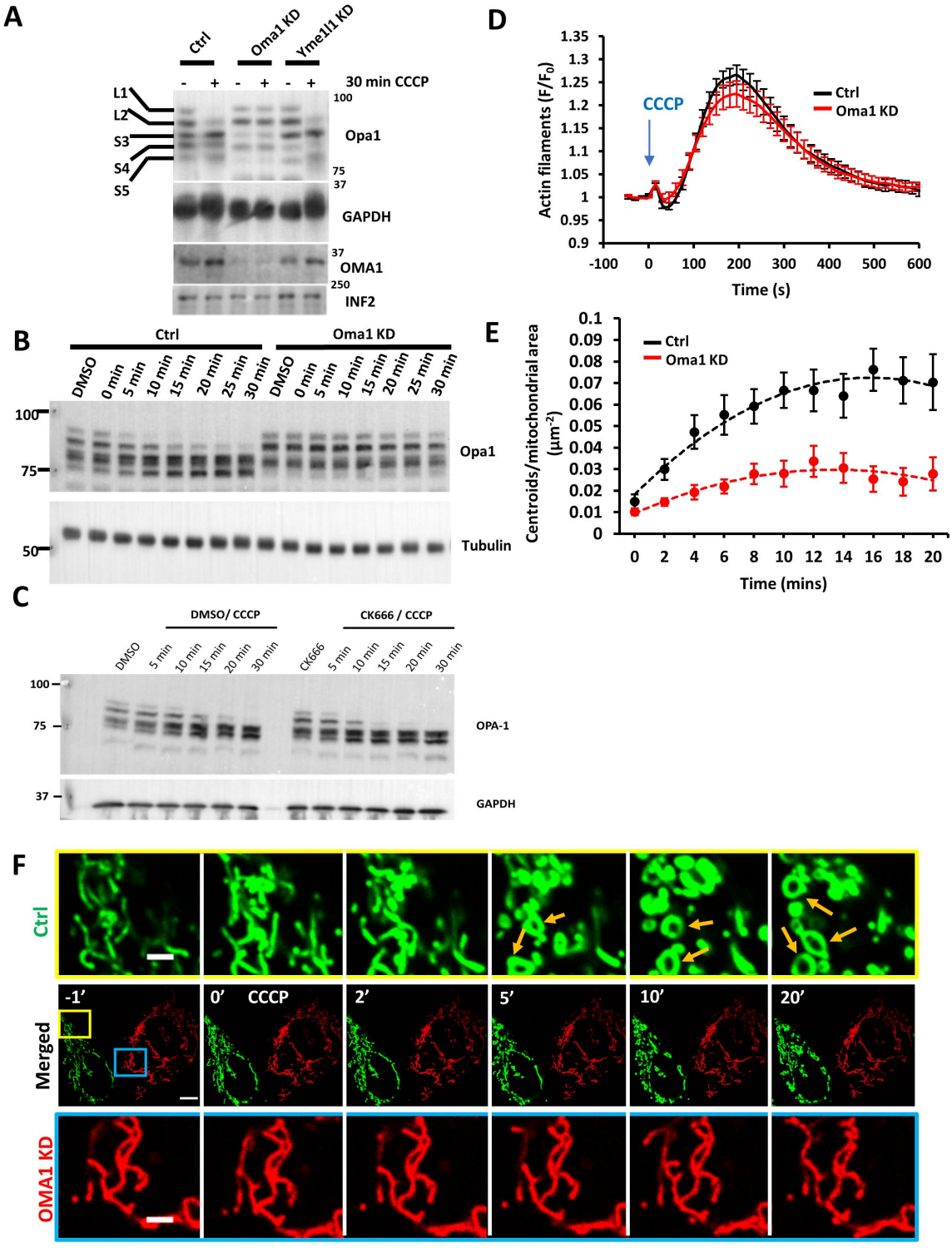
A
Ctrl
Oma1 KD
Yme1l1 KD
30 min CCCP
L1
L2
S3
S4
S5
Opa1
GAPDH
OMA1
INF2
B
Ctrl
Oma1 KD
DMSO
0 min
5 min
10 min
15 min
20 min
25 min
30 min
Opa1
Tubulin
C
DMSO/ CCCP
CK666 / CCCP
CK666
OPA-1
GAPDH
D
CCCP
Ctrl
Oma1 KD
Actin filaments (F/F0)
Time (s)
E
Centroids/mitochondrial area (µm-2)
Time (mins)
F
Ctrl
Merged
OMA1 KD
-1'
0'
CCCP
2'
5'
10'
20'

Figure 2.5: Role of Oma1 in depolarization-induced mitochondrial shape change. A) Western blot of Opa1 and Oma1 in control, Oma1 KD and Yme1 KD U2-OS cells before and after treatment with 20μM CCCP for 30 mins. The positions of the five Opa1 forms (L1, L2, S1-3) are indicated. GAPDH, INF2 loading control. **B)** Western blot of Opa1 in control and Oma1 KD U2-OS cells during time course of CCCP treatment (20μM). Tubulin, loading control. **C)** Western blot of Opa1 in control and CK666 treated U2-OS-WT cells during time course of CCCP treatment (20μM). GAPDH, loading control. **D)** CCCP-induced actin polymerization for control and Oma1 KD U2-OS cells, transfected with GFP-F-tractin and mito-BFP, and stimulated with 20μM CCCP (blue arrow). Data from three experiments. N=40 cells/40 ROIs for scrambled control, 28/28 for Oma1 KD. Error bar, ±SEM. **E)** Change in mitochondrial matrix circularization ('centroids') over time for control and Oma1-KD U2-OS cells transfected with mito-BFP and GFP-F-tractin. CCCP (20μM) added at time point 0. Data from three experiments. N= 36 cells/4733 μm^2 total mitochondrial area for control cells; 53 cells /9519 μm^2 for OMA1 KD cells. Error bars, ±SEM. **F)** Time-course montage of CCCP-induced mitochondrial shape change (yellow arrows) in control (green) and Oma1-KD U2-OS cells (red), imaged in the same field. Control cells (scrambled siRNA) were transfected with Mito-GFP while Oma1-KD cells were transfected with Mito Ds-Red. The two cell populations were trypsinized, mixed, and plated 24 hr before imaging. Confocal images (basal cell section) were acquired at 15 sec intervals starting four frames before CCCP treatment. 20μM CCCP added at time point 0. Time in min. Scale bar: 10μm. Inset scale bar: 2.5μm.

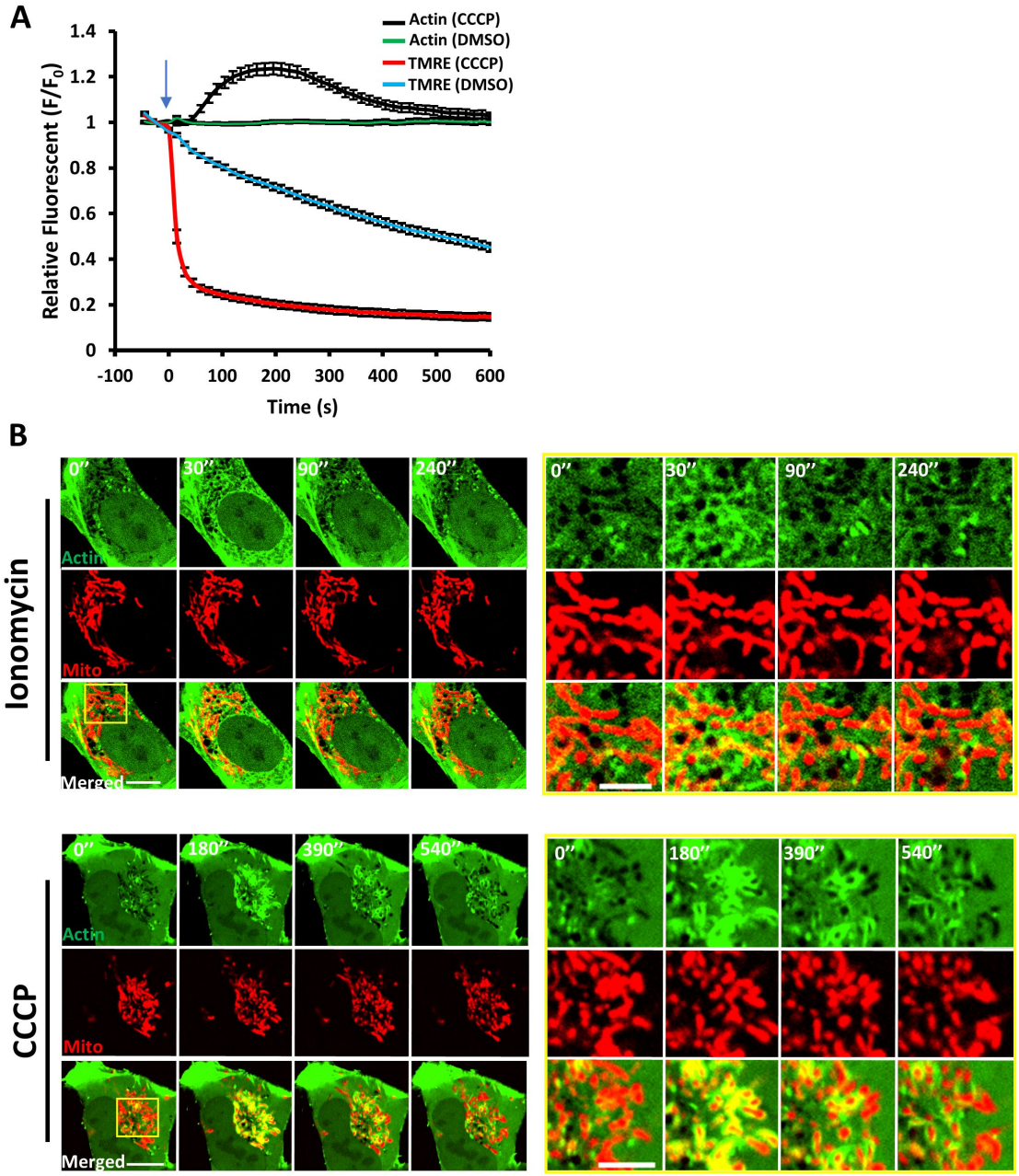

Figure S2.1: Actin and mitochondrial dynamics upon ionomycin and CCCP treatments. **A)** CCCP-induced actin polymerization and mitochondrial depolarization in U2-OS cells. Cells transfected with GFP-F-tractin and mito-BFP, stained with 20 nM TMRE for 30 min, and stimulated with 20μM CCCP or DMSO at 0 sec (blue arrow). Confocal images (medial section) acquired at 15 sec intervals starting four frames before CCCP treatment. F-tractin and TMRE intensity quantified. Data from three experiments. N=40 cells/40 ROIs for CCCP, 33/33 for DMSO. Error bar, ±SEM. **B)** Time-lapse image montage of ionomycin-induced (top) and CCCP-induced (bottom) actin polymerization for U2-OS cells transfected with GFP-F-tractin (green) and mito-BFP (red). Imaging conducted at a medial cell section. Ionomycin or CCCP added at time point 0. Scale bar: 10μm. Inset scale bar: 5μm.

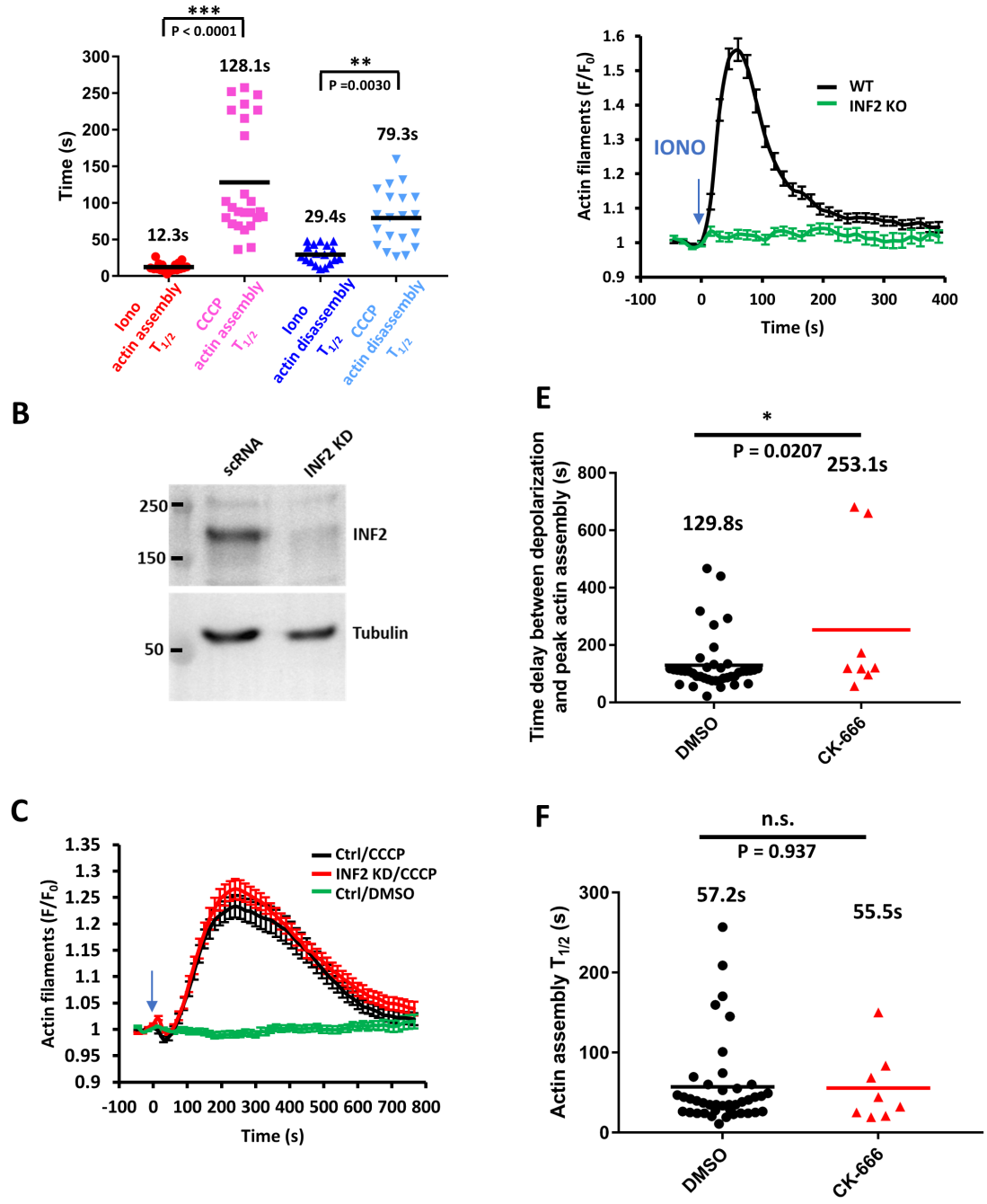
A
***
P < 0.0001
**
P =0.0030
128.1s
79.3s
29.4s
12.3s
Time (s)
Iono actin assembly T1/2
CCCP actin assembly T1/2
Iono actin disassembly T1/2
CCCP actin disassembly T1/2
B
scRNA
INF2 KD
250
150
50
INF2
Tubulin
C
Ctrl/CCCP
INF2 KD/CCCP
Ctrl/DMSO
Actin filaments (F/F0)
Time (s)
D
WT
INF2 KO
IONO
Actin filaments (F/F0)
Time (s)
E
*
P = 0.0207
253.1s
129.8s
Time delay between depolarization and peak actin assembly (s)
DMSO
CK-666
F
n.s.
P = 0.937
57.2s
55.5s
Actin assembly T1/2 (s)
DMSO
CK-666

Figure S2.2: Actin dynamics upon CCCP treatment in control and INF2 KD cells. A) Scatter plots of actin stimulation and recovery half-times for ionomycin and CCCP treatments in U2-OS-WT cells imaged at 1.4 sec/frame. Number of individual cells: 18 (ionomycin) and 25 (CCCP/ actin assembly); 20 (CCCP actin disassembly). Data compiled from three independent experiments. P value (unpaired) using Sidak's multiple comparisons test. Error, Standard deviation. **B)** Western blot for INF2 of control (scrambled siRNA) and INF2-KD cells. Tubulin, loading control. **C)** Graph of CCCP-induced actin polymerization for control (scrambled siRNA) and INF2-KD U2-OS cells. Cells were transfected with GFP-F-tractin and mito-BFP, then stimulated with DMSO or 20μM CCCP (blue arrow). Confocal images (medial section) acquired at 15 sec intervals starting four frames before CCCP treatment. Data from three experiments. N= 67 cells/67 ROIs for control/CCCP, 53/53 for INF2 KD/CCCP, and 26/26 for control/DMSO. Error bar, ±SEM. **D)** Graph of ionomycin-induced actin polymerization for U2-OS-WT and INF2-KO cells. Cells transfected with GFP-F-tractin and mito-BFP, then stimulated with 4μM ionomycin (blue arrow). Confocal images (medial section) acquired at 15 sec intervals starting four frames before ionomycin treatment. Data from three experiments. N = 30 cells/60 ROIs for WT cells, 27/54 for INF2 KO cells. Error bar, ±SEM. **E)** Lag between mitochondrial depolarization and actin assembly during spontaneous depolarization events. From the same data set described in **Figure 2.2**. Student's unpaired t-test. **F)** Scatter plots of actin stimulation during spontaneous depolarization events. U2-OS cells transfected with GFP-F-tractin and mito-BFP, stained with 20 nM TMRE for 30 min, then imaged by confocal microscopy for 20 min. From the same data set described in **Figure 2.2**. Student's unpaired t-test.

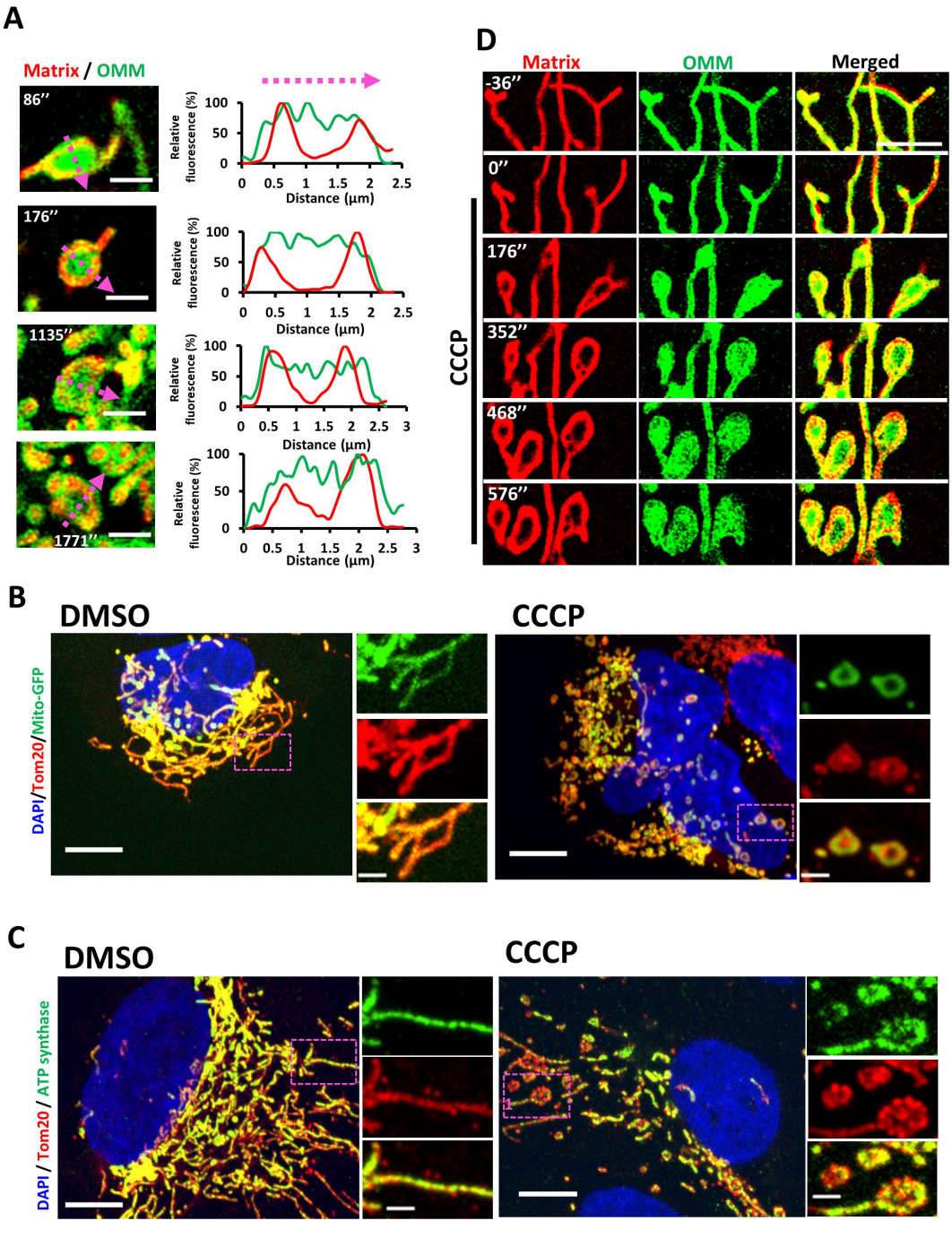
A
Matrix / OMM
86''
176''
1135''
1771''
Relative fluorescence (%)
Distance (μm)
D
Matrix
OMM
Merged
-36''
0''
176''
352''
468''
576''
CCCP
B
DMSO
CCCP
DAPI/Tom20/Mito-GFP
C
DMSO
CCCP
DAPI / Tom20 / ATP synthase

Figure S2.3: Depolarized mitochondria with circular matrix and intact OMM. A) Four examples of CCCP-induced mitochondrial shape changes. U2-OS cells transfected with Mito-DsRed (matrix, red) and Tom20-GFP (OMM, green) and stimulated with 20μM CCCP at time point 0. Airyscan microscopy images (basal cell section) acquired at 4.2 sec intervals starting ten frames before CCCP treatment. Single time points at time of matrix circularization shown (time (sec) after CCCP addition shown in upper left). Scale bar: 2μm. On right, line scans for matrix and OMM taken along the magenta line, showing reduced signal for the matrix marker but not for OMM marker. **B)** Maximum intensity projections of paraformaldehyde-fixed U2-OS cells (expressing the matrix marker mito-GFP, green) after treatment with either DMSO (top) or 20μM CCCP (bottom) for 20 min. Cells were stained for OMM using anti-Tom20 (red) and nucleus using DAPI (blue). Z stacks were taken at step size of 0.4μm. Representative examples of mitochondrial circularization after CCCP treatment are zoomed in. Scale bars: 10μm and 2μm (insets). **C)** Maximum intensity projections of paraformaldehyde fixed U2-OS cells after treatment with either DMSO (top) or 20μM CCCP (bottom) for 20 min. Cells were stained for the IMM with ATP synthase (green), OMM with anti-Tom20 (red) and DAPI (blue) for nucleus. Z stacks were taken at step size of 0.4μm. Representative examples of mitochondrial circularization after CCCP treatment are zoomed in. Scale bar: 10μm and inset 2μm. **D)** Dynamics of the OMM and mitochondrial matrix upon CCCP treatment in INF2-KO cells. INF2-KO U2-OS cell transfected with Mito-R-GECO1 (red) and Tom20-GFP (green) was treated with 20μM CCCP at time point 0. Airyscan images (basal region) acquired at 4 sec intervals starting 10 frames before CCCP treatment. Scale bar: 5μm.

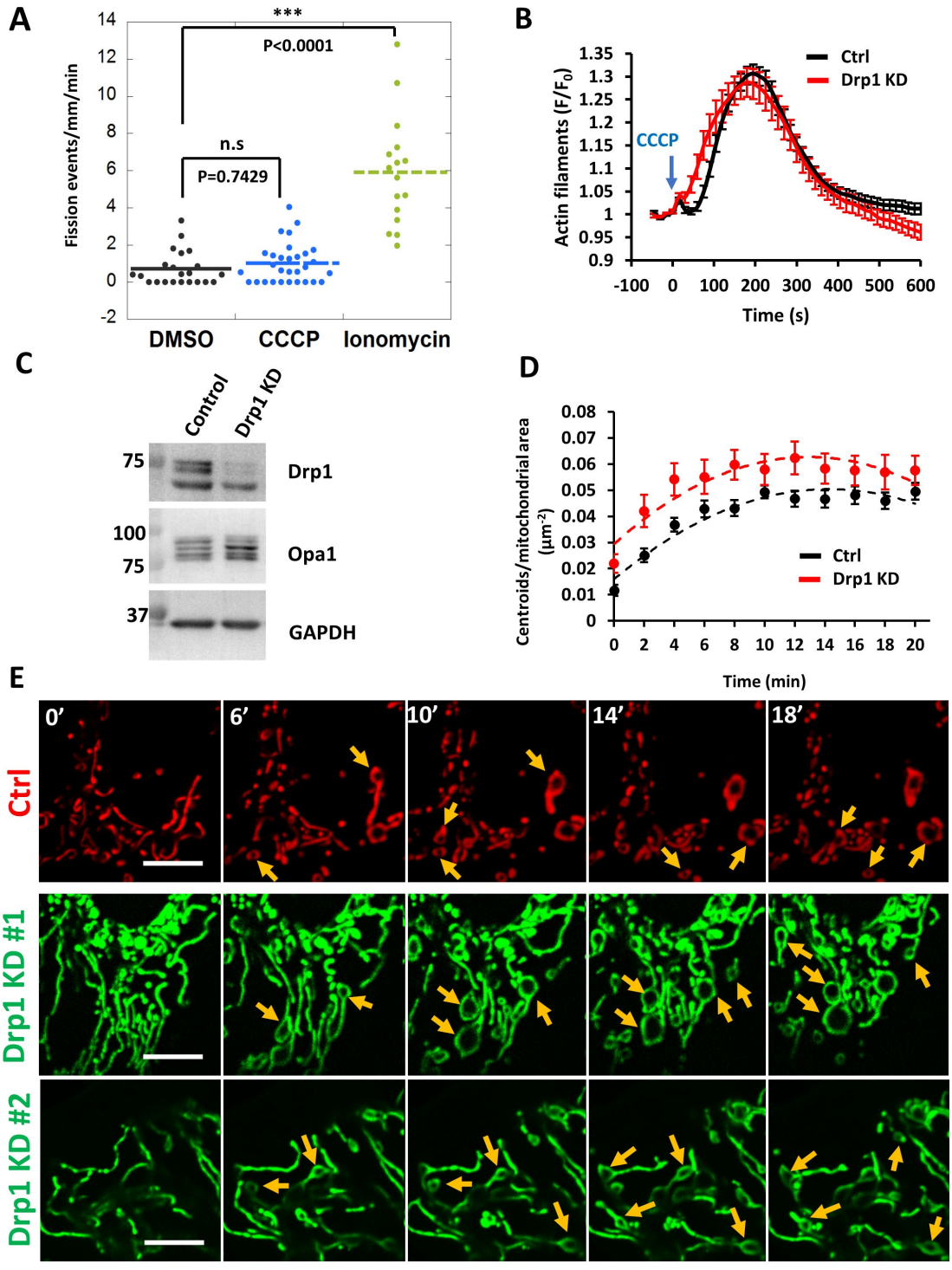
A
***
P<0.0001
n.s
P=0.7429
Fission events/mm/min
DMSO
CCCP
Ionomycin
B
Ctrl
Drp1 KD
CCCP
Actin filaments (F/F0)
Time (s)
C
Control
Drp1 KD
75
Drp1
100
75
Opa1
37
GAPDH
D
Centroids/mitochondrial area (µm-2)
Ctrl
Drp1 KD
Time (min)
E
0'
6'
10'
14'
18'
Ctrl
Drp1 KD #1
Drp1 KD #2

Figure S2.4: Effect of Drp1 KD on CCCP induced actin clouds and mitochondrial shape change. A) Quantification of mitochondrial fission rate in U2-OS cells, using ROIs from live-cell movies of mitochondrial matrix marker (mito-BFP) treated with DMSO, 4 μM ionomycin (10 mins) or 20μM CCCP (30 min). N = 22 cells, 2590.5 μm mitochondrial perimeter (DMSO), 16 cells, 3093.7 μm mitochondrial perimeter (ionomycin), 30 cells, 3999.5 μm mitochondrial perimeter (CCCP). Each point represents one ROI per cell. Compiled from two independent experiments. Dunnett's multiple comparisons test (unpaired): DMSO vs CCCP, p=0.7429 and DMSO vs Ionomycin, p <0.0001 **B)** Effect of Drp1 depletion on CCCP-induced actin polymerization. CCCP-induced actin polymerization for control and Drp1-KD U2-OS cells, transfected with GFP-F-tracin and mito-BFP, stimulated with 20μM CCCP (blue arrow) and imaged at 15 sec intervals. Data from three experiments. N=40 cells/40 ROIs for scrambled control, 41/41 for Drp1 KD. Error bar, ±SEM. **C)** Western blot analysis of Drp1 and Opa1 in control (scrambled siRNA) and Drp1 KD U2-OS cells. GAPDH, loading control. **D)** Change in mitochondrial matrix circularization ('centroids') over time for control and Drp1-KD U2-OS cells transfected with mito-BFP and GFP-F-tractin. CCCP (20μM) added at time point 0. Data from three experiments. N= 71 cells/8217.2 μm2 total mitochondrial area for control cells; 45 cells /6557.3 μm2 for OMA1 KD cells. Error bars, ±SEM. **E)** CCCP induced mitochondrial shape changes in Drp1 KD cells. Time-lapse image montage of CCCP-induced mitochondrial shape change in control (top, red) and Drp1 KD cells (middle, bottom, green) transfected with mito-BFP. Imaging conducted at a basal cell section. CCCP added at time point 0. Scale bar: 10μm.

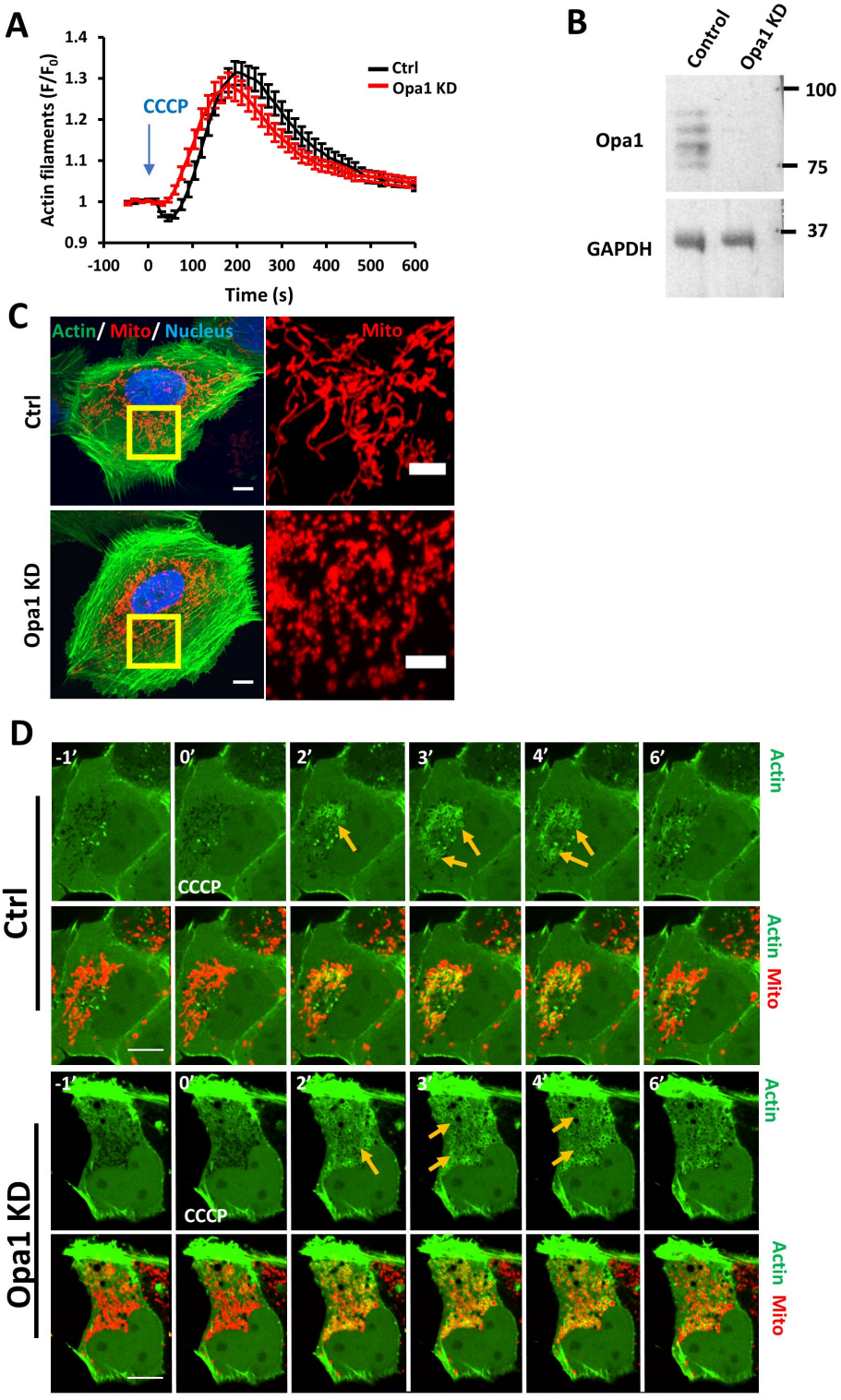
A
Actin filaments (F/F0)
Time (s)
CCCP
Ctrl
Opa1 KD
B
Control
Opa1 KD
Opa1
GAPDH
100
75
37
C
Actin/ Mito/ Nucleus
Mito
Ctrl
Opa1 KD
D
-1'
0'
2'
3'
4'
6'
CCCP
Actin
Actin Mito
Ctrl
Opa1 KD

Figure S2.5: Effect of Opa1 KD on CCCP-induced actin burst and mitochondrial morphology. A) CCCP-induced actin polymerization for control and Opa1-KD U2-OS cells, transfected with GFP-F-tracin and mito-BFP, stimulated with 20μM CCCP (blue arrow) and imaged at 15 sec intervals. Data from three experiments. N=23 cells/23 ROIs for scrambled control, 27/27 for Opa1 KD. Error bar, ±SEM. **B)** Western blot analysis of Opa1 in control (scrambled siRNA) and Opa1 KD U2-OS cells. GAPDH, loading control. **C)** Maximum intensity projection of control U2-OS cells (scrambled siRNA) and Opa1 KD U2-OS cells transfected GFP-Ftractin, mitoBFP and H2B-mCherry. Z sections were selected based on actin and imaged at 0.4 μm step size. Scale bar: 10μm and inset scale bar: 5μm. **D)** Time-course of CCCP induced actin polymerization for control and Opa1 KD U2-OS cells transfected with GFP-F-tractin (green) and mito-BFP (red). Confocal images from from a medial cell section. CCCP added at time point 0. Time in minutes. Scale bar: 10μm. Yellow arrows denote actin assembly around mitochondria.

Chapter III:

Unravelling the mechanism for rapid actin assembly after CCCP-induced mitochondrial damage

Chapter III

Parallel kinase pathways stimulate actin polymerization at depolarized mitochondria

Tak Shun Fung[1,†], Rajarshi Chakrabarti[1,†], Jana Kollasser[2], Klemens Rottner[2,3], Theresia E. B. Stradal[2], Frieda Kage[1] & Henry N. Higgs[1,*]

[1]Department of Biochemistry and Cell Biology, Geisel School of Medicine at Dartmouth College, Hanover NH, USA

[2]Department of Cell Biology, Helmholtz Centre for Infection Research, Inhoffenstrasse 7, 38124 Braunschweig, Germany

[3]Division of Molecular Cell Biology, Zoological Institute, Technische Universität Braunschweig, Spielmannstrasse 7, 38106 Braunschweig, Germany

[†]These authors contributed equally to this work

The text and data here are adapted or reproduced in full from the manuscript published in *Curr Biol.*

(DOI: https://doi.org/10.1016/j.cub.2022.02.058)

T.S.F. and R.C. designed and performed experiments, interpreted and analyzed data, and wrote the manuscript.

J.K. made and characterized CRISPR/Cas9 NPF KO cell lines in **Figure 3.1** and **Figure S3.2**.

K.R. and T.E.B.S provided NPF KO cell lines, gave critical feedback and revised the manuscript.

F.K. designed and performed experiments in **Figure 3.1**, **Figure 3.2, Figure 3.7I** and **Figure S3.2**, interpreted and data, and wrote the manuscript.

H.N.H. supervised the project, designed experiments, interpreted and analyzed data, and wrote the manuscript.

Conceptualization, R.C., T.S.F., and H.N.H.; Methodology, R.C., T.S.F., F.K., J.K., K.R., T.E.B.S., and H.N.H.; Investigation, R.C., T.S.F., F.K., and J.K.; Visualization, R.C., T.S.F., F.K., and J.K.; Funding acquisition: K.R., T.E.B.S., and H.N.H.; Project administration, H.N.H.; Supervision, K.R., T.E.B.S., and H.N.H.; Writing – original draft, R.C., T.S.F., and H.N.H.; Writing – review & editing, R.C., T.S.F., F.K., K.R., T.E.B.S., and H.N.H.

3.1 Abstract

Mitochondrial damage (MtD) represents a dramatic change in cellular homeostasis, necessitating metabolic changes and stimulating mitophagy. One rapid response to MtD is rapid peri-mitochondrial actin polymerization, termed ADA (acute damage-induced actin). The activation mechanism for ADA is unknown. Here, we use mitochondrial depolarization or the complex I inhibitor metformin to induce ADA. We show that two parallel signaling pathways are required for ADA. In one pathway, increased cytosolic calcium activates in turn PKC-β, Rac, WAVE regulatory complex, and Arp2/3 complex. In the other pathway, a drop in cellular ATP activates in turn AMPK (through LKB1), Cdc42, and FMNL formins. We also identify putative guanine nucleotide exchange factors for Rac and Cdc42, Trio and Fgd1 respectively, whose phosphorylation states increase upon mitochondrial depolarization and whose suppression inhibits ADA. The depolarization-induced calcium increase is dependent on the mitochondrial sodium-calcium exchanger NCLX, suggesting initial mitochondrial calcium efflux. We also show that ADA inhibition results in enhanced mitochondrial shape changes upon mitochondrial depolarization, suggesting that ADA inhibits these shape changes. These depolarization-induced shape changes are not fragmentation but a circularization of the inner mitochondrial membrane, dependent on the inner mitochondrial membrane protease Oma1. ADA inhibition increases proteolytic processing of an Oma1 substrate, the dynamin GTPase Opa1. These results show that ADA requires the combined action of Arp2/3 complex and formin proteins to polymerize a network of actin filaments around mitochondria, and that the ADA network inhibits the rapid mitochondrial shape changes that occur upon mitochondrial depolarization.

3.2 Introduction

Dynamic actin polymerization is a vital component of many cellular processes, including cell motility, cytokinesis, endocytosis, vesicle transport and others[5, 30]. Often, the actin filaments created are transient, polymerizing and depolymerizing on a timescale of minutes. These filaments can be used as substrates for myosin-mediated force production, or can generated force on their own through polymerization.

One recently identified population of actin filaments polymerizes around damaged mitochondria (**Chapter II**) [16, 560], which we refer to as acute damage-induced actin (ADA). ADA is transient, being triggered within 2 min of stimulation and being fully depolymerized in 10 min (**Chapter II**) [560]. One function of ADA is to inhibit mitochondrial rearrangements after damage, potentially allowing a chance for recovery (**Chapter II**) [560].

How is ADA activated? Cellular actin structures require an actin polymerization factor to initiate new actin filaments. Two major actin polymerization factors are the Arp2/3 complex and the formin family. Arp2/3 complex is required for ADA (**Chapter II**) [560]. Arp2/3 complex consists of seven proteins, including two actin-related proteins, and typically nucleates new actin filaments as branches from the sides of existing "mother" filaments, itself remaining at the slow-growing "pointed" end of the new actin filament and crosslinking this end to the side of the mother filament [5]. Arp2/3 complex alone is inactive, but is activated by binding to a nucleation promoting factor (NPF) [561]. Seven NPF families exist in mammals, including WASP/N-WASP, WAVE/Scar, WASH, WISH/DIP, WHAMM, JMY [541, 562, 563]. The Arp2/3 complex-binding protein cortactin has weak NPF activity biochemically, but its cellular interaction with Arp2/3 complex may serve more to prolong branched filament lifetime [564]. Up-stream activators of NPFs include Rho family GTPases, polyphosphoinositides, adaptor proteins, and protein kinases. Importantly for the current work, WAVE is a sub-unit of a multi-protein complex called the WAVE Regulatory complex (WRC), and activation of the complex is mediated by the Rac sub-family of Rho GTPases [565].

While Arp2/3 complex is clearly required for ADA, it is possible that formin proteins contribute as well, given the cooperation between Arp2/3 complex and formins in other actin-based processes [60, 63]. Formin proteins nucleate actin by a fundamentally different mechanism than Arp2/3 complex, remaining at the rapidly-growing barbed end

of the filament and mediating filament elongation [18]. Two mechanisms by which formins and Arp2/3 complex can work together are: 1) formin nucleation of the mother filaments used for subsequent Arp2/3 complex-mediated branched filament polymerization; and 2) formin binding to new barbed ends created by Arp2/3 complex-mediated nucleation, allowing these ends to elongate by protecting them from capping protein.

There are 15 formin proteins in mammals, segregating into seven sub-groups phylogenetically [17]. Presently, no formin protein has been identified as being involved in ADA. The formin INF2 has been shown to play roles in mitochondrial division [12], and is activated by increased cytoplasmic calcium in a process we call CIA (calcium-induced actin) [12-14]. INF2, however, is not required for ADA [560].

The signaling pathway leading from mitochondrial damage to ADA is unknown. What signal(s) is/are transmitted across both the inner and outer mitochondrial membranes to activate ADA? What intermediate factors are required between this/these signal(s) and Arp2/3 complex activation? In this work, we show that ADA is mediated by two parallel signaling pathways. One pathway is initiated by calcium efflux from the mitochondrion, triggering a protein kinase C-dependent pathway that activates Arp2/3 complex. The second pathway is mediated by decreased ATP, which initiates an AMP-dependent protein kinase (AMPK) pathway leading to activation of the FMNL family of formins. Thus, ADA represents a highly regulated process whereby Arp2/3 complex and formins work together for rapid actin network assembly.

3.3 Results

We have previously shown that CCCP treatment rapidly stimulates ADA in U2-OS cells (**Chapter II**) [560], and use CCCP treatment in the current work to elucidate the signaling pathway leading from mitochondrial depolarization to ADA. Given that CCCP is a relatively harsh cellular treatment, depolarizing mitochondria in seconds (**Chapter II**) [560], we sought other means of inducing mitochondrial dysfunction that would relate to a more physiologically-relevant situation. The antidiabetic drug metformin inhibits complex 1 of the electron transport chain [257, 566, 567]. If ADA is stimulated by a disruption in the mitochondrial electrochemical gradient, metformin should have a similar effect to CCCP. Indeed, we find that metformin treatment stimulates ADA in mouse embryonic fibroblasts (MEFs), with peak stimulation at 20 min (**Figure S3.1**). These results suggest that ADA is induced by mitochondrial dysfunction.

3.3.1 Rac-activated WAVE regulatory complex activates Arp2/3 complex during ADA

An important question is how depolarization is signaled so quickly across two membranes to activate ADA. We started our investigation of the ADA pathway by asking which NPF is responsible for Arp2/3 complex activation, screening NPF knock-out (KO) cell lines for the ADA response using a fixed-cell assay in which ADA is stimulated by the mitochondrial uncoupler carbonyl cyanide m-chlorophenyl hydrazine (CCCP) for 1 min. KO lines used were derived from either NIH 3T3 (WRC, WASH, WHAMM and JMY, **Figure S3.2A**) or MEF cells (N-WASP, cortactin) [456, 568]. The paralogous WRC subunits Nap1 and Hem1 were gene-edited by CRISPR, resulting in markedly diminished expression of all other WRC subunits (**Figure S3.2A**), causing a functional loss of the entire complex.

While WT cells are 98.6 ± 1.3% positive for mitochondrially-associated actin after 1-min CCCP treatment, WRC KO cells display only 18.4 ± 10.6% (**Figure 3.1A, B**). In contrast, JMY, WHAMM, WASH, cortactin and N-WASP KO cells display ADA comparable to WT cells (**Figure 3.1B, C; Figure S3.2B**). Two other independent WRC KO lines display similar ADA reduction, while additional cell lines of WASH, WHAMM and JMY KO do not affect ADA (**Figure S3.2C**). WRC KO reduces ADA at multiple time points (**Figure S3.2D**), showing that its effect is not simply to delay ADA.

To further assess the importance of WRC for ADA, we used live-cell microscopy in U2-OS or HeLa cells knocked-down (KD) for the WRC subunit Nap1, which has been reported to cause reduction of all other WRC subunits [55, 569, 570] (**Figure S3.2E, F**). In both cell types, WRC KD significantly reduces ADA (**Figure 3.1D, E; Figure S3.2G**). We also examined WRC and Arp2/3 complex localization during ADA. Both the Abi1 subunit of WRC and the Arpc5 subunit of Arp2/3 complex accumulate around mitochondria after CCCP stimulation in MEF cells (**Figure 3.1F**).

We conducted further tests of cortactin's potential importance to ADA, since a previous publication showed a modest decrease in the percentage of cortactin KD cells displaying ADA [16]. Cortactin suppression has no clear effect on the ADA time course in U2-OS cells (**Figure S3.2H-J**). However, cortactin accumulates with actin around mitochondria during ADA, similar to Arp2/3 complex and WRC (**Figure 3.1F**). We conclude that cortactin may act with Arp2/3 complex during ADA, but that WRC is the key NPF.

WRC is activated by the Rac family of Rho GTPases [565], so we tested the effect of CCCP on Rac activity in U2-OS cells. CCCP treatment for 2 min causes a 2.4-fold increase in the level of active Rac (**Figure 3.2A, B**), while levels of active RhoA are unchanged (**Figure S3.3A, B**). We then examined ADA in MEFs lacking all three Rac proteins (Rac1 genetically removed, Rac2 and -3 not expressed) [571], using the fixed-cell ADA assay. Control cells give a robust response to CCCP, going from 0.6 ± 1.1% to 100% ADA-positive cells without and with CCCP, respectively, while only 6.8 ± 1.2% of CCCP-treated Rac1 KO MEFs display ADA (**Figure 3.2C, D**). As a further test, we transfected the T17N dominant-negative (DN) constructs of Rac1, 2 and 3 into U2-OS cells and examined ADA in the live-cell assay. While Rac1-DN partially inhibits ADA, co-expression of Rac1-3 DN constructs causes near-complete ADA inhibition (**Figure 3.2E; Figure S3.3C**). In contrast, a RhoA-DN construct has no effect on ADA (**Figure 3.2E; Figure S3.3C**). These results support a model in which Rac activates WRC which activates Arp2/3 complex during ADA.

3.3.2 Calcium-stimulated PKC activates Rac during ADA

What might be the stimulus leading to Rac activation during ADA? To address this issue, we asked whether rapid changes in known second messengers such as calcium might occur upon ADA induction. CCCP treatment causes a rise in cytoplasmic calcium prior to

ADA (**Figure 3.3A; Figure S3.4A**). This calcium rise is comparatively small compared to that of other known cytoplasmic stimuli such as histamine (**Figure S3.4A-C**).

To test whether calcium plays a role in ADA, we pre-treated U2-OS cells with BAPTA-AM, a cytosolic calcium chelator. BAPTA-AM causes a reduction in ADA (**Figure 3.3B, C**). Another cytosolic calcium sequestration strategy, over-expression of the cytosolic calcium probe Cyto-R-GECO, has a similar effect (**Figure S3.4D**). These results suggest that an increase in cytosolic calcium is required for ADA.

We next examined the source of this cytosolic calcium increase, with two prime candidates being the endoplasmic reticulum (ER) and the extracellular space [572]. Neither chelation of extracellular calcium with EGTA (**Figure S3.4E**) nor depletion of ER calcium stores with thapsigargin (**Figure S3.4F, G**) has a clear effect on ADA.

We also examined mitochondria as a possible calcium source, since there is evidence for a considerable amount of 'solid-phase' calcium that can be solubilized by depolarization [573], and another mitochondrial inhibitory treatment, hypoxia, causes mitochondrial calcium release through the sodium-calcium exchanger NCLX[267] . Treatment with the small molecule NCLX inhibitor CGP37157 (hereafter called CGP) causes significant ADA reduction (**Figure 3.3D, E**), while having no effect on ionomycin-stimulated actin polymerization (**Figure S3.4H**). CGP also blocks the CCCP-induced increase in cytosolic calcium (**Figure S3.4I**). Suppression of NCLX by siRNA has a similar inhibitory effect on ADA as CGP treatment (**Figure S3.4J**), while suppression of the mitochondrial calcium channel MCU has no effect (**Figure S3.4K, L**). These results suggest that NCLX-mediated calcium release from mitochondria initiates ADA.

We next asked what calcium effectors act in ADA, with one possibility being the conventional protein kinase C (cPKC) family [574]. Treatment of U2-OS cells with the cPKC inhibitor Go6976 significantly reduces ADA (**Figure 3.4A**). Combined RNAi-mediated suppression of cPKC-βI and -βII also causes significant ADA reduction, whereas suppression of cPKC-α has no apparent effect (**Figure 3.4B**). We conclude that PKC-β is the relevant calcium effector in ADA.

In addition to inhibiting ADA, PKC inhibition also reduces CCCP-induced Rac activation (**Figure 3.2A, B**), suggesting that PKC activates Rac. Rho-family GTPase activation is often mediated by guanine nucleotide exchange factors (GEFs), and at least 14 Rac GEFs

have been identified[575]. To identify the Rac-GEF downstream of cPKC-β in ADA, we conducted comparative phospho-proteomics of MEFs under three conditions: DMSO-treated for 2 min, CCCP-treated for 2 min, and CCCP- treated for 2 min after pre-treatment with Go6976. The Rac-GEF Trio is significantly increased in phosphorylation on S2634 by CCCP treatment, while phosphorylation of none of the other 13 Rac GEFs changes in a similar manner (**Figure S3.5A**). This change in Trio phosphorylation is abrogated by Go6976 (**Figure S3.5B**). Trio KD suppresses ADA (**Figure 3.4C-E**). In sum, our data suggest that ADA is activated by the following pathway: increased cytosolic calcium>>PKC-beta >>Trio>>Rac>>WRC>>Arp2/3 complex.

One puzzling result is that, although thapsigargin pre-treatment does not affect ADA (**Figure S3.4F, G**), ER-derived calcium accounts for a major portion of the CCCP-induced increase in cytoplasmic calcium. Two results support this claim. First, ER calcium decreases rapidly upon CCCP treatment in a manner abolished by CGP pre-treatment (**Figure S3.5C**), suggesting that mitochondrial calcium release triggers additional ER calcium release. Second, thapsigargin pre-treatment strongly reduces the CCCP-induced cytoplasmic calcium increase (**Figure S3.5D**). These results could suggest that the ER-derived calcium release is an independent effect of CCCP, and not required for ADA. A second possibility is that the rise in cytoplasmic calcium caused by thapsigargin pre-treatment is sufficient to activate Rac prior to CCCP treatment. Indeed, published results show that thapsigargin-mediated increase in cytosolic calcium activates Rac[576]. We confirmed this possibility by measuring active Rac levels during thapsigargin treatment and subsequent CCCP treatment (**Figure S3.5E**).

Our conclusion from these experiments is that initial calcium efflux from CCCP-treated mitochondria causes a quantitatively greater calcium efflux from ER, which causes Rac activation. This Rac activation is prolonged, which enables CCCP to stimulate ADA even after prior thapsigargin treatment. However, while Rac activation through this mechanism is necessary for ADA, it is not sufficient. A parallel required pathway is discussed in the next section.

3.3.3 A parallel pathway involving AMPK and FMNL formins is necessary for ADA

We wondered is why ADA is not activated by other stimuli that raise cytosolic calcium, such as ionomycin or histamine. Previous studies have shown that these stimuli activate

actin polymerization through the formin INF2 [12-14], but that these responses are not Arp2/3 complex-dependent (**Chapter II**) [560].

One possibility is that ADA requires a second activation signal to work in tandem with the calcium increase. An attractive candidate for such a signal is a drop in ATP, since treatments that compromise mitochondria are likely to cause this effect. Indeed, treatment of U2-OS cells or MEFs with CCCP for 2 min results in ~ 13 and 40% drops in total cellular ATP, respectively (**Figure 3.5A**). Reduction in cellular ATP can in turn lead to increased AMP, and activation of the AMP-activated protein kinase (AMPK) through phosphorylation of T172 on the α-subunit [311]. AMPK has also been shown to enrich on mitochondria in some circumstances [577]. In both U2-OS cells and MEFs, phospho-T172-AMPK levels increase within 1 min of CCCP treatment (**Figure 3.5B; Figure S3.6A**), similar to recently published results [315]. Suppression of the AMPK-α subunit significantly reduces ADA (**Figure 3.5C, D; Figure S3.6B**).

Two kinases can phosphorylate AMPK T172: liver kinase B1 (LKB1) and calcium calmodulin-dependent protein kinase kinase β (CaMKK2) [311]. Suppression of LKB1 inhibits ADA and reduces CCCP-induced AMPK phosphorylation (**Figure 3.5E; Figure S3.6B**). In contrast, the small molecule CaMKK2 inhibitor STO-609 has little effect on either ADA or AMPK phosphorylation (**Figure S3.6C, D**). Likewise, neither BAPTA-AM chelation of cytosolic calcium nor Go6976 inhibition of PKC inhibits AMPK phosphorylation (**Figure S3.6D, E**), suggesting that AMPK activation is independent of PKC-β. We conclude that AMPK activation through LKB1 constitutes an independent pathway required for ADA.

AMPK might work with PKC-β to stimulate ADA by 1) contributing to Arp2/3 complex activation through Rac/WRC, or 2) contributing to a parallel signaling pathway. Interestingly, AMPK suppression does not reduce CCCP-mediated Rac activation (**Figure 3.2A, B**). However, AMPK has been shown to activate Cdc42 [578], so we tested Cdc42 for a role in ADA. CCCP treatment causes an increase in active Cdc42 levels, that is inhibited by AMPK suppression but not by PKC inhibition (**Figure 3.2A, B**). Both the T17N dominant-negative Cdc42 construct (**Figure 3.2E; Figure S3.3C**) and the small molecule Cdc42 inhibitor ML141 (**Figure 3.6A**) inhibit ADA. We conclude that there are two parallel pathways for ADA: PKC activation of Rac and AMPK activation of Cdc42.

To identify the Cdc42 GEF which might lay between AMPK and Cdc42, we took a similar phosphoproteomic approach as used for Rac GEF identification. Disappointingly, our phosphoproteomic dataset did not reveal significant phosphorylation changes in any of the 19 known Cdc42 GEFs. However, we had learned from our assays of Cdc42 activity that there is a high background of active Cdc42 in MEFs cultured in the presence of serum, which is reduced significantly by serum starvation overnight (**Figure S3.6F**). For this reason, we repeated the phosphoproteomics experiment in serum-starved cells. Under these conditions, one Cdc42 GEF, Fgd1, displays a highly significant phosphorylation increase on S207 upon 2 min CCCP stimulation (**Figure 3.6B; Figure S3.6G**). Suppression of Fgd1 inhibits ADA (**Figure 3.6C; Figure S3.6H**), suggesting that Fgd1 is the relevant Cdc42 GEF regulating ADA.

We next addressed the downstream targets of Cdc42. Cdc42 activates actin polymerization through several pathways, including the Arp2/3 complex NPF N-WASP and the FMNL family of formins [447, 579]. Our NPF KO screen suggests that N-WASP is not required for ADA (**Figure 3.1C**). We therefore tested the three FMNL formins for potential roles in ADA.

Western blot analysis reveals that U2-OS cells express detectable levels of FMNL1 and FMNL3, while FMNL2 is undetectable (**Figure S3.7A**). Nonetheless, any low level of FMNL2 should be suppressed with the siRNA used here, as shown for U2-OS cells over-expressing GFP-tagged FMNL2 (**Figure S3.7B**). KD of either FMNL1 or FMNL3 results in partial reduction of ADA, while combined FMNL1/FMNL3 KD reduces ADA to near-baseline levels (**Figure 3.6D, E**). KD of FMNL2 alone, or in combination with FMNL1 or FMNL3, results in smaller decreases in ADA (**Figure S3.7C**). These results suggest that, in addition to Arp2/3 complex, activity of both FMNL1 and FMNL3 is required for a full ADA response in U2-OS cells.

We also tested FMNL KD in HeLa cells, which also display ADA but express predominately FMNL1 and FMNL2, with lower levels of FMNL3 (**Figure S3.7D**). FMNL1 KD in HeLa cells results in partial reduction of ADA, but FMNL2 KD does not (**Figure 3.6F**). Combined depletion of FMNL1 and FMNL2 reduces ADA to near-baseline levels (**Figure 3.6F, G**). Thus, at least two FMNL proteins appear to be required for the full ADA response in HeLa cells as well.

The effect of FMNL formin KD could suggest a wide-spread defect in actin polymerization, and not a specific role in ADA. To test this possibility, we examined the effect of FMNL KD on calcium-induced actin polymerization, which is similar to ADA in its rapid and transient activation but which we and others have shown to be dependent on the formin INF2 but independent of Arp2/3 complex (**Chapter II**) [12, 560]. FMNL KD has no significant effect on calcium-induced actin polymerization (**Figure S3.7E**), suggesting that FMNL KD is not causing a wide-spread defect in actin polymerization.

3.3.4 ADA inhibition accelerates mitochondrial shape changes upon CCCP treatment

CCCP treatment induces significant shape changes to mitochondria. While these changes have often been referred to as fragmentation, the acute shape changes (within 30 min) occurring upon mitochondrial depolarization have been shown to be independent of mitochondrial division, and instead involve rearrangements of the mitochondrial inner membrane [154, 156, 560]. We refer to these shape changes as 'circularization', because the mitochondrion converts from an elongated to a circular state (**Chapter II**) [560].

Our previous work in U2-OS cells showed that Arp2/3 complex inhibition by CK666 treatment causes increased CCCP-induced circularization, suggesting that ADA suppresses circularization (**Chapter II**) [560]. Here, we tested the acute mitochondrial response to CCCP in MEFs. In the absence of CK666, CCCP causes an increase in circularization over a 20 min time period, to a lower circle density than previously observed in U2-OS cells (0.03 circles/mm^2 versus 0.05 circles/mm^2 for U2-OS cells (**Chapter II** [560], **Figure 3.7A, B; Figure S3.7F**). Live-cell imaging shows that these events are due to mitochondrial rearrangement, rather than mitochondrial division. Longer CCCP treatments result in punctate mitochondria (**Figure S3.7G**), similar to previous studies [125, 130, 143, 580-582]. CK666 treatment increases mitochondrial circularization approximately 5-fold in the first 20 min (**Figure 3.7A, B**), a much greater change than observed for U2-OS cells. We had previously shown that CCCP-induced circularization was inhibited by knock-down of the inner mitochondrial membrane protease Oma1 in U2-OS cells (**Chapter II**) [560]. We extend this result by showing that that Oma1 knock-down inhibits circularization in MEFs treated with CCCP and CK666 (**Figure 3.7C, D; Figure S3.7H**).

We previously reported that ADA also inhibits CCCP-induced proteolytic processing of the dynamin-family GTPase Opa1 in U2-OS cells (**Chapter II**) [560]. Opa1 is a transmembrane protein on the inner mitochondrial membrane, and acts in mitochondrial dynamics and maintenance of cristae integrity. Proteolytic processing by Oma1 or other proteases releases Opa1 into the inter-membrane space, acting as a regulatory mechanism for Opa1-mediated functions [438]. We examined Opa1 proteolytic processing in MEFs upon CCCP treatment in the absence or presence of CK666. CCCP alone causes a gradual shift in Opa1 bands, eliminating the two non-proteolyzed 'long' forms (L1 and L2) and increasing the three proteolytic product 'short' forms (S1, S2 and S3) over a 60-min time period, as been previously shown [583]. ADA inhibition by CK666 accelerates these changes (**Figure 3.7E, F**). These data suggest that ADA exerts an inhibitory effect on Opa1 processing.

To test whether both branches of the ADA signaling pathway are required for circularization inhibition, we tested the effect of siRNA-mediated suppression of FMNL formins in U2-OS cells. Similar to CK666 treatment, FMNL1/3 KD results in increased CCCP-induced circularization, an effect not enhanced by CK666 addition (**Figure 3.7G, H**). These results suggest that ADA inhibits the acute mitochondrial rearrangements induced by CCCP.

3.4 Discussion

The combination of these results suggests that two parallel pathways are required for ADA activation: one pathway through increased cytosolic calcium, resulting in Arp2/3 complex activation; and the other through altered ATP levels, resulting in FMNL formin activation (**Figure 3.7I**). Both pathways utilize protein kinases (PKC and AMPK) downstream of the initial signal, and use Rho family GTPases (Rac and Cdc42) as activators of the actin polymerization factors. We also identify the putative GEF proteins responsible for GTPase activation (Trio and Fgd1). Finally, we show that inhibition of ADA increases the mitochondrial shape changes that occur in the first 20 min after mitochondrial depolarization.

One interesting question pertains to the nature of the cooperation between FMNL formins and Arp2/3 complex in actin polymerization during ADA. These two polymerization factors are known to act together in other actin-based structures, such as filopodia and lamellipodia [60, 63]. The nature of their combined action in ADA is unclear at present, but possibilities include: 1) FMNL-mediated nucleation of 'mother filaments' required for Arp2/3 complex activation; and 2) FMNL-mediated barbed end binding of Arp2/3 complex-nucleated filaments, allowing prolonged filament elongation. Biochemical studies suggest that FMNL formins are comparably weak actin nucleators, but effectively mediate actin filament elongation [58, 584, 585]. In addition, FMNL formins can bundle actin filaments [584, 585]. Given the fact that the ADA actin filaments appear to be densely packed around mitochondria, their bundling activity may be relevant here.

Another question pertains to the apparent requirement for two FMNL formins in ADA. Previous studies have shown FMNL formins to have diverse roles. FMNL2 and 3 play roles in lamellipodia and filopodia assembly [63, 64, 586], while FMNL1 has been shown to act in maintenance of centrosome polarity[587]. In addition, all three FMNLs appear to act at the Golgi [586, 588]. One possibility is that there are two different functions for FMNL formins during ADA, dependent on FMNL1 and FMNL2/3, respectively.

The source of the calcium for PKC activation is another interesting question. Two inhibitors of the mitochondrial Na^+/Ca^{2+} exchanger NCLX inhibit ADA, the small molecule CGP37157, and siRNA-mediated NCLX suppression. CGP also inhibits the CCCP-induced cytoplasmic calcium increase. These results suggest that calcium release from the mitochondrion is involved in ADA activation. However, CCCP also causes a

drop in ER calcium level, and prior treatment with thapsigargin eliminates the CCCP-induced increase in cytoplasmic calcium. These results suggest that CCCP triggers ER calcium release, and that this release is the biggest contributor to increased cytoplasmic calcium. We postulate that release of a small amount of mitochondrial calcium induces a larger release of ER calcium, analogous to the process known as calcium-induced calcium release during muscle contraction and neuronal conduction, whereby calcium influx from the extracellular space triggers additional calcium release from the endoplasmic reticulum/sarcomeric reticulum [589]. Calcium-induced calcium release also is likely to occur in a variety of other cell types [590, 591], but we are not aware of prior reports that mitochondrial calcium release can trigger a similar phenomenon.

We identify Trio and Fgd1 as being the putative GEFs for Rac and Cdc42 activation, respectively, during ADA. Trio has been shown to play important roles in cell migration, particularly during neuronal development, osteoclast differentiation, and endothelial growth[592-594]. Fgd1 acts in Cdc42-dependent cargo assembly at the Golgi [595, 596], and mutations in Fgd1 lead to X-linked faciogenital dysplasia [597]. The potential roles for these GEFs in ADA constitute novel functions for these proteins. As yet, it is not clear whether these GEFs are recruited to damaged mitochondria. Another interesting question is whether these are the sole GEFs responsible for ADA in all cell types, given the wide range of GEF expression and the possibility of compensation between GEFs.

We also show that the phosphorylation states of these GEFs are significantly altered by the 2-min CCCP treatment used to induce ADA, with phosphorylation of S2634 of Trio and S207 of Fgd1 being increased by the treatment. Both residues lie in regions predicted to be disordered in the protein, and not in the catalytic Dbl homology domain of the GEF. It is possible that phosphorylation of these residues promotes an interaction that brings the GEF to the mitochondrion. Indeed, although S207 has not been identified as a phosphorylation site in Fgd1, a neighboring residue, S205, has been identified in a patient with Aarskog-Scott syndrome[598], an X-linked developmental disorder resulting in craniofacial dysmorphism. The disease-linked mutation, S205I, results in reduced EGF-stimulated migration, Fgd1 translocation to the plasma membrane, and phosphorylation [599]. For Trio, S2634 has been identified eight times thus far in high-throughput screens [600], but no information on its functional significance is available. An alternate possibility is that these phosphorylation changes are not related to the activation or

recruitment of Trio or Fgd1 during ADA. Specific phosphorylation effects for both GEFs will need to be tested in the future.

We show in this work and in a previous paper (**Chapter II**) [560] that ADA inhibits the rapid mitochondrial shape changes (circularization) that occur in response to CCCP. This inhibition is temporary, and after the ADA filaments depolymerize mitochondria change shape substantially. Circularization within the first 20 min of CCCP treatment is largely due to inner mitochondrial membrane reorganization (**Chapter II**) [154, 156, 560], and we have previously shown in U2-OS cells that they depend on the inner mitochondrial membrane protease Oma1 (**Chapter II**) [560], a result we extend to MEFs. We also show here that ADA inhibition results in a dramatic increase in CCCP-induced circularization in MEFs, much greater than we previously observed in U2-OS cells[560]. It is unclear why ADA would have a differential ability to inhibit circularization in the two cell types. Inhibition of either Arp2/3 complex or FMNL formins accelerates CCCP-induced mitochondrial shape changes, suggesting that both signaling pathways are involved. In addition to inhibiting mitochondrial circularization, ADA also inhibits Opa1 processing upon mitochondrial depolarization. Opa1 processing might be linked to IMM changes leading to circularization, but other Oma1 substrates such as PGAM5 might also be involved [601].

Importantly, the mitochondrial shape changes we observe in the first 20 min of CCCP treatment are not due to mitochondrial division (**Chapter II**) [560]. While several other groups have found the same division-independent shape changes in early time points after mitochondrial depolarization [154, 156], it is commonly believed that mitochondrial depolarization results in rapid mitochondrial fragmentation or fission. Many of the studies reporting fragmentation are either observing cells after prolonged depolymerizer treatment (>1 hr) [149, 582, 602]. Our main point here is that, while mitochondria may fragment at longer time points after mitochondrial depolarization, the circularization that occurs within the first 20 min of depolarization are not due to extensive mitochondrial division.

ADA is the first of several stages at which actin polymerization is needed after loss of mitochondrial membrane potential, with at least two other temporally-distinct actin filament populations assembling around depolarized mitochondria at different times and for different purposes. All are Arp2/3-dependent. A second round of actin polymerization

occurs 1-2 hours after the initial depolarization, and is dependent on Parkin recruitment to mitochondria as well as on N-WASP and myosin 6 [433, 603]. This second round of actin polymerization appears to facilitate mitophagy in two ways: by preventing re-fusion of damaged mitochondria with healthy ones [603] and by dispersing clumps of damaged mitochondria [433]. In addition, Arp2/3 complex-mediated actin filaments clearly play other roles in autophagosome assembly several hours after mitochondrial depolarization. It is unclear how many roles these filaments play at this point, but three NPFs have been shown to mediate these functions: WHAMM, JMY, and WASH [480, 604, 605]. The speed of the ADA pathway (activated within 2 min) and its reliance on both WAVE-activated Arp2/3 complex and FMNL formins, makes it distinct from these subsequent pathways.

ADA is also distinct from another actin polymerization pathway that impacts mitochondria, CIA. It is interesting that increased cytosolic calcium is an activating factor in both ADA and CIA, with it being the apparent sole activator in CIA [12-14]. The cytosolic calcium increase that stimulates ADA is significantly lower than that which stimulates CIA, possibly explaining why CIA is not activated by ADA stimuli.

Recently, other mitochondrially-associated actin polymerization processes have been identified that require Arp2/3 complex. In interphase cells, transient “waves” of actin polymerization can occur, cycling through the cytoplasm over time [429]. In mitotic cells, two distinct types of actin polymerize in association with mitochondria, with one of these being Arp2/3 complex-dependent [430]. It is unclear whether either of these Arp2/3 complex-dependent actin polymerization processes is similar to ADA. The interphase actin waves are not associated with mitochondrial dysfunction. The mitotic actin polymerization appears to function in mitochondrial motility, while ADA actually inhibits mitochondrial dynamics (**Chapter II**) [560]. The signaling pathways and Arp2/3 complex NPFs required for these two actin-based processes are unknown, and it will be interesting to see how they might relate to ADA.

3.5 Material and Methods

Cell culture

Wild-type human osteosarcoma U2-OS (U2-OS-WT) and human cervical cancer HeLa cells were procured from American Type Culture Collection (ATCC) and grown in DMEM (Corning, 10-013-CV) supplemented with 10% newborn calf serum (Hyclone, SH30118.03) for U2-OS or 10% fetal bovine serum (Sigma-Aldrich F4135) for HeLa, at 37°C with 5% CO_2. NIH 3T3 fibroblasts (ATCC CRL-1658) and Mouse Embryonic Fibroblasts (MEFs) for CRISPR NPF KOs were grown in DMEM (4.5 g/L glucose, Invitrogen), 10% FCS (Sigma), 2 mM L-glutamine (Thermo Fisher Scientific), 1% non-essential amino acids (Gibco) and 1 mM sodium pyruvate (Gibco). For all other purposes, MEFs were grown in DMEM with 10% fetal bovine serum. Cell lines were tested every 3 months for mycoplasma contamination using Universal Mycoplasma detection kit (ATCC, 30-1012K) or MycoAlert Plus Mycoplasma Detection Kit (Lonza, LT07-701). Cell lines were used no more than 30 passages.

Generation of NPF KO lines

NIH 3T3 cells were genome-edited using the CRISPR/Cas9 technology. Selected guide RNAs were cloned into pSpCas9(BB)-2A-Puro (Addgene plasmid ID: 48139) and transfected overnight with JetPrime transfection reagent (PolyPlus) according to the manufacturer's instructions. The following day, cells were replated into medium supplemented with 3 µg/ml puromycin. After 3 days of puromycin selection, cells were counted and diluted into 96-well plates at a density of app. 0.5 cells per well in order to generate clonal lines. Nap1 (NCKAP1) was eliminated using the CRISPR-guideRNA 5'-GACGCCCCGGTCGTTGAGGA-3'. As the hematopoietic version of Nap1, Hem1 (NCKAP1L), showed low levels of compensatory expression upon Nap1 loss (not shown), targeting of the *Hem1* gene was additionally performed in Nap1 KO cells using CRISPR-guide RNA 5'-CTCACGATCCTGAATGACCG-3'. Respective guide RNAs for other NPF knockout lines were: WHAMM (5'-TGGCTGGGTTCCGCTGCGTG-3'), JMY (5'-GGAGACACTCGAGTCCGACT-3'), and WASH (5'-GCGACGAGAGGAGGCAATCC-3'). These guides were expressed by transfection of pSpCas9(BB)-2A-GFP (Addgene plasmid ID: 48138) using X-tremeGENE following the manufacturer's recommended protocol. Isolation of clonal cell lines was achieved by flow cytometry of single GFP-positive cells into 96-well plates. All CRISPR clones were initially screened for the absence of respective protein expression by western blotting and positive clones were further validated for loss-of-function mutations by sequencing of respective genomic loci. Most CRISPR/Cas-9-modified cell lines will be additionally characterized elsewhere[606] (Kollasser et al., in preparation).

N-WASP KO cells (kindly provided by Frank Pui-Ling Lai, University of Hong Kong) were obtained following immortalization and Cre-recombinase-mediated deletion of respective, *loxP* site-flanked allele [456] in MEFs derived from mice backcrossed to C57BL/6J. Cortactin KO [568] and Rac1 KO [571] cells were published previously.

DNA transfections, plasmids, and siRNA

For plasmid transfections, cells were seeded at 4×10^5 cells per well in a 35 mm dish at ~16h before transfection. Transfections were performed in OPTI-MEM medium (Gibco, 31985062) using lipofectamine 2000 (Invitrogen, 11668) as per manufacturer's protocol, followed by trypsinization and re-plating onto glass-bottom dishes (MatTek Corporation, P35G-1.5-14-C) at $\sim1\times10^5$ cells per well. Cells were imaged ~16–24 h after transfection.

GFP-F-tractin plasmid were gifts from C. Waterman and A. Pasapera (National Institutes of Health, Bethesda, MD) and were on a GFP-N1 backbone (Clonetech), as described previously [556]. Mito-DsRed and mito-BFP (GFP-N1 backbone) constructs were previously described [560] and consist of amino acids 1–22 of *S. cerevisiae* COX4 N terminal to the respective fusion protein. Tom20–GFP was made by restriction digest of Tom20 from Tom20–mCherry (a gift from Andrew G. York, NIH, Bethseda, MD) with NheI and BamHI, and then cloned into eGFP–N1 (Clontech). GFP–mito was purchased from Clontech (pAcGFP1-Mito, #632432) and consists of the mitochondrial targeting sequence derived from the precursor of subunit VIII of human cytochrome c oxidase. TagBFP2-C1 (termed 'Cyto-BFP') as a general marker to label the cytosol was a gift from J. Lippincott-Schwartz (Janelia Research Campus, VA). Cyto-R-GECO1 (K_d = 0.48 μM for calcium) constructs were gifts from Y.M. Usachev (University of Iowa Carver College of Medicine, Iowa City, IA) and have been described previously[607]. ER-GCaMP6-150 (K_d = 150 μM for calcium) was described previously[356] and is available from Addgene (86918). GFP-ArpC5, GFP-Abi1 and GFP-Cortactin have been previously described[55, 568, 608]. HA-RhoA T17N, HA-RhoB T17N, HA-Rac1 T17N, HA-Rac2 T17N, HA-Rac3 T17N and HA-Cdc42 T17N were procured from UMR cDNA Resource Center. The following amounts of DNA were transfected per well (individually or combined for co-transfection): 500 ng for mito–BFP, mito–DsRed, GFP-mito, GFP–F-tractin, Cyto-BFP, and cyto-R-GECO, GFP-ArpC5, GFP-Abi1, GFP-Cortactin, HA-RhoA T17N, HA-RhoB T17N, HA-Rac1 T17N, HA-Rac2 T17N, HA-Rac3 T17N and HA-Cdc42 T17N; 800 ng for ER-GCAMP.

For all siRNA transfections, 1×10^5 cells were plated onto a 35mm dish and 2μl RNAimax (Invitrogen, 13778) with 63pmol siRNA were used per well. Cells were analyzed 72-96 hrs post siRNA transfection. For live-cell imaging, plasmids containing fluorescent markers were transfected into siRNA-treated cells 18–24 hrs prior to imaging, as described above. All siRNAs used are listed in **Table 3.2**.

Western blotting

For preparation of whole cell extracts of MEFs and NIH 3T3 cells for KO characterization, cells were washed 3x with ice-cold PBS, lysed using SDS-lysis-buffer (2% SDS, 10% glycerol, 63 mM Tris-HCl pH 6.8, 0.01% bromophenol blue, 5% β-mercaptoethanol), boiled for 5 min at 95°C and sonicated to shear genomic DNA. Western blotting was carried out according to standard techniques and chemiluminescence signals were obtained upon incubation with ECL Prime Western Blotting Detection Reagent (GE Healthcare) and were recorded with ECL Chemocam imager (Intas).

For probing protein levels and AMPK phosphorylation in U2-OS, HeLa or MEF extracts, cells from a 35mm dish were trypsinized, pelleted by centrifugation at 300 g for 5 min and resuspended in 400µl of 1× DB (50mM Tris-HCl, pH 6.8, 2mM EDTA, 20% glycerol, 0.8% SDS, 0.02% Bromophenol Blue, 1M NaCl, 4M urea). Proteins were separated by SDS-PAGE in a Bio-Rad mini-gel system (7×8.4cm) and transferred onto polyvinylidene fluoride membrane (EMD Millipore, IPFL00010). The membrane was blocked with TBS-T (20 mM Tris-HCl, pH 7.6, 136 mM NaCl, 0.1% Tween-20) containing 3% BSA (VWR Life Science, VWRV0332) for 1h, then incubated with primary antibody solution at 4°C overnight. After washing with TBS-T, the membrane was either incubated with HRP-conjugated secondary antibody or fluorescently tagged Li-COR antibody for 1h at 23°C. Signals were detected by chemiluminescence or using Li-COR fluorescent imager. Western procedure for pull-down assays of active Rho family GTPases is described separately in that section.

Antibodies and reagents

GAPDH (Calbiochem; clone 6C5; #CB1001; 1:10,000; mouse monoclonal) and (Santa Cruz: clone C9; sc-365062; 1:1500; mouse monoclonal), a-Tubulin (Synaptic Systems; clone 3A2; #302117; 1:50,000; mouse monoclonal) and (Sigma-Aldrich; clone DM1-α; T9026; 1:10,000; mouse monoclonal), Sra-1 (clone 4955B; 1:10,000; rabbit polyclonal)[571], Nap1 (clone 4953B; 1:5000; rabbit polyclonal)[571] and (Proteintech; 12140-1-AP; 1: 1000; rabbit polyclonal), Abi1 (clone E3B1; 1:2000; rabbit polyclonal) (*46*), pan-WAVE (clone 5502; 1:1000; rabbit polyclonal) (*46*)**,** WHAMM (Abcam; ab122572; 1:500; rabbit polyclonal), WASH (kindly provided by Alexis Gautreau, École Polytechnique, France; 1:1000; rabbit polyclonal), and JMY (kindly provided by Jan Faix, Hannover Medical School, Germany; 1:500; rabbit polyclonal). Actin (Millipore; clone C4; MAB1501; 1: 1000; mouse monoclonal) and Myosin IIA (CST; #3403; 1:1000; rabbit polyclonal). FMNL1 (1:1000; rabbit polyclonal) (*47*). FMNL2 (Sigma-Aldrich HPA005464; 1:1500; mouse monoclonal). FMNL3 (1:1000; guinea pig polyclonal)[58] and mDia1 (1:1000; chicken polyclonal)[63]. Cortactin (Upstate 05-180; 1:1000; mouse monoclonal). LKB1 (CST; #3047; 1:1000; rabbit polyclonal). Phospho-AMPKα (Thr172) (CST;#2535; 1:1000; clone 40H9;

rabbit monoclonal). AMPKα (CST; #2532; 1:1000; rabbit polyclonal). RhoA (CST; #2117; 1:1000; rabbit monoclonal). Rac1 (BD Transduction Laboratories; Cat No. 610651; 1:500; mouse monoclonal). Cdc42 (CST; #2466; 1:500; rabbit monoclonal). Trio (Abcam; ab194364; 1:1000; mouse polyclonal). Opa1 (BD biosciences; #612606; 1:2000; mouse monoclonal; clone 18/OPA1). OMA1 (Santa Cruz: clone H-11/OMA1; sc-515788; 1: 500; mouse monoclonal). For ECL: HRP-conjugated secondary antibodies used were anti-mouse IgG (Dianova; #115-035-062; 1:10,000; goat) and (Bio-Rad; 1705047; 1:2000; goat), anti-rabbit IgG (Dianova; #111-035-045; 1:10,000; goat) and (Bio-Rad; 1706515; 1:5000; goat), anti-guinea pig IgG (Jackson Immuno Research Laboratories; #106-035-003; 1:5000; goat) and anti-Chicken/Turkey IgG (Invitrogen; #613120; 1:5000; Rabbit). Li-COR antibodies used were: anti-rabbit IRDye 800CW (#926-32211; 1:15000; goat) and anti-mouse IRDye 680RD (#926-68070; 1:15000; goat). For pharmacological treatments, concentration and time are listed in **Table 3.1**.

Immunofluorescence

NPF KO cells were seeded subconfluently in 1 mL medium onto glass coverslips (15 mm) coated with 25 µg/ml fibronectin (Sigma, 10838039001), and allowed to adhere overnight. The following day, cells in 12 well dishes (Sarstedt) containing 1 ml medium each were treated by the addition of 1 ml of prewarmed and pH-equilibrated medium containing 40 µM CCCP (Sigma, C2759) (freshly added before the treatment, final concentration 20 µM CCCP) for the indicated time. Volume equivalent DMSO was used as a control. Cells were then fixed with a mixture of prewarmed 4% PFA (Electron Microscopy Sciences, 15710)/PBS supplemented with 0.25% glutaraldehyde (Electron Microscopy Sciences, 16020) for 20 min at room temperature, enabling optimal preservation of the actin cytoskeleton. Cells were washed with PBS and then permeabilized with 0.1% Triton-X100/PBS for 1 min, and again washed with PBS three times. Prior to antibody staining, cells were blocked with 5% horse serum in 1% BSA/PBS for ~30 min. Primary Tom20 antibody (Abcam, ab78547) was diluted 1:250 in 1% BSA/PBS. Coverslips were incubated on a drop of antibody solution on parafilm in a wet chamber for 1 h. Secondary antibody against Tom20 (Alexa Fluor 594-coupled anti-rabbit; Invitrogen #A11037; 1:200) was mixed with Alexa Fluor 488-conjugated phalloidin (1:400) and incubated for 45 min. Coverslips were mounted on glass slides using ProLong Gold antifade mounting media (Invitrogen #P36930).

Microscopy

Microscopy of fixed samples was performed on an inverted Axiovert S100TV (Carl Zeiss) epifluorescence microscope equipped with electronic shutters (Uniblitz Electronic 35 mm including driver Model VMMD-1, BFI Optilas), a filter wheel (LUDL Electronic products LTD), filter cubes (Chroma Technology Corp. Rockingham), and epifluorescence illumination (light

source HXP 120, Zeiss). Imaging was performed using a 100x/1.4-NA plan apochromatic oil objective. Images were acquired with a back-illuminated, cooled, charge-coupled-device (CCD) camera (CoolSnap HQ2, Photometrics) driven by VisiView software (Visitron Systems).

Live cell imaging was conducted in DMEM (Gibco, 21063-029) with 25 mM D-glucose, 4 mM L-glutamine and 25 mM Hepes, supplemented with 10% newborn calf serum. Cells (~$3.5x10^5$) were plated onto MatTek dishes 16 hrs prior to imaging. Medium was pre-equilibrated at 37°C and 5% CO_2 before use. Dishes were imaged using the Dragonfly 302 spinning disk confocal (Andor Technology) on a Nikon Ti-E base and equipped with an iXon Ultra 888 EMCCD camera, a Zyla 4.2 Mpixel sCMOS camera, and a Tokai Hit stage-top incubator set at 37°C. A solid-state 405 smart diode 100 mW laser, solid state 560 OPSL smart laser 50 mW laser, and solid state 637 OPSL smart laser 140 mW laser were used. Objectives used were the CFI Plan Apochromat Lambda 100X/1.45 NA oil (Nikon, MRD01905) for all drug treatment live-cell assays. Images were acquired using Fusion software (Andor Technology, version 2.0.0.15). For actin burst imaging, cells were imaged at a single confocal slice at the medial region, approximate 2 μm above the basal surface, to avoid stress fibers. For centroid observation, cells were imaged at a single confocal slice at the basal region. For CCCP treatments, cells were treated with 20μM CCCP at the start of the fifth frame (~1 min, with time interval set at 15s) during imaging and continued for another 9 min. Equal volume DMSO (Invitrogen, D12345) was used as negative control.

Pull down assays for active Rho family GTPases

For active Rac1, Cdc42, and RhoA pull down, GST fusions of PAK-PBD (residues 70-117; Addgene 12217), WASP-CRIB (residues 228-298, Addgene 30113), or Rhotekin-RBD (residues 7-89, Addgene 15247) were produced in Rosetta2 cells and purified/immobilized on glutathione Sepharose (GE Biosciences) in Buffer A (10 mM Tris-Cl pH 8, 50 mM NaCl, 1 mM DTT, 1 mM EDTA, 0.05% thesit and protease inhibitors [Leupeptin (2 μg/ml) /aprotinin (10 μg/ml), Calpeptin 1 μg/ml, Pepstatin A 1 μg/ml, Benzamidine 1 mM]).

Cell lysates from U2-OS cells were prepared as follows. Control, Go6976 (20 μM/ 1 hr) -treated, or AMPK KD cells (1 X 10^7 cells on 10 cm plate) were treated with either DMSO or CCCP (20 μM) for 2 min and immediately lysed with 1 ml of ice-cold lysis buffer (25 mM Tris-Cl pH 7.5, 10 mM $MgCl_2$, 150 mM NaCl, 5% (W/V) Sucrose, 1% NP-40 alternative (Calbiochem, 492016), 10mM NaF and protease inhibitors as above). The lysate was centrifuged immediately at 300xg / 4˚C for 5 min and supernatants collected. Glutathione Sepharose beads coupled to 30 mg of the indicated GST fusion were added to this ~1 mL volume (from a 10 mg/mL stock of protein/bead suspension), and the mixture rotated at 4˚C for 1 hr. The beads were then centrifuged, washed once in lysis buffer and resuspended in 30 ml of 1X Laemmli sample buffer (BioRad, 161-0747),

boiled immediately for 5 min and run on 12.5% SDS-PAGE gels. The proteins were then transferred onto PVDF membrane using western blot buffer (25 mM Tris-Cl pH8.3, 192 mM Glycine and 15% methanol) at 350 mA for 1 hr, followed by the relevant primary and secondary antibodies and visualization on the Li-COR Odyssey. For active Cdc42 pull-down experiments, the respective cells were serum starved for 18 hours prior to processing as outlined above, due to the high level of active Cdc42 in cells cultured in our standard medium containing 10% NCS. Under these serum-free conditions, only 1μM CCCP is used for stimulation, with Go6976 concentration remaining at 20μM. For thapsigargin-treated U2-OS cells, cell lysates were collected at indicated time and a positive control with CCCP (20 μM/ 2min) after 10 min Thapsigargin pre-treated was performed.

ATP assays from cell extracts

A luciferase-based assay was used (BMR service, University of Buffalo, SUNY, A-125). MEFs or U2-OS cells were plated at 1×10^6 cells per well in 60mm cell culture dishes and incubated for two days, resulting in 5.75 x 10^6 and 1.80 x 10^6 cells/dish for MEFs and U2-OS, respectively. On the day of extraction, cells were given fresh live-cell media (DMEM (Gibco, 21063-029) with 25 mM D-glucose, 4 mM L-glutamine and 25 mM Hepes, supplemented with 10% newborn calf serum) and treated with 20μM CCCP for 2 min. Cells were lysed immediately with 10% TCA and washed 3 times with 1:1 ether pre-saturated in TE (10mM Tris-HCl and 1mM EDTA, pH 8) for sample deproteinization. Samples were diluted 8-fold in water and ATP assay then followed manufacturer's instructions. The luminescence intensity was measured in a microplate reader (BioTek Synergy Neo2 multi-mode plate reader). A standard curve with ATP standards ranging from 0 -10μM was plotted for every experiment. The mM value of ATP determined in each assay was converted to a mM cellular value using the cell number stated above and an estimated cellular volume of 6 pL, obtained for Cos7 cells[609]. Scatter plots were plotted (with s.d.) in GraphPad Prism 9 (version 9.2.0, GraphPad Software). Each point indicates individual well measurements with 3 and 5 independent experiments performed for U2-OS and MEF respectively.

Phosphoproteomics

MEFs (1 x 10^7 cells) were plated on 10 cm plates 24 hrs before stimulation. Two different methods for stimulation were used. In Method 1, cells were kept in normal medium (DMEM+10% NCS) and stimulated with either 20μM CCCP or DMSO control for 2 min. In Method 2, cells were washed in serum-free DMEM 6 hrs post-plating, incubated in serum-free medium overnight, and stimulated with either 1μM CCCP or DMSO control for 2 min. Subsequent procedures were the same. Following respective treatments, cells were quickly washed with 15 ml of PBS and rapidly extracted with 1mL of extraction buffer (10 mM Tris-HCl

pH 7.5, 150 mM NaCl, 4% SDS, 10 mM DTT). Lysates were quickly boiled for 5 min and then frozen prior to the phospho-proteomic work-up and analysis, which was conducted at the IDeA National Resource for Quantitative Proteomics (University of Arkansas, Little Rock AR).

Proteins were reduced, alkylated, and purified by chloroform/methanol extraction prior to digestion with sequencing grade trypsin and LysC (Promega). The resulting peptides were labeled using a tandem mass tag 10-plex isobaric label reagent set (Thermo), then enriched using High-Select TiO2 and Fe-NTA phosphopeptide enrichment kits (Thermo) following the manufacturer's instructions. Both enriched and un-enriched labeled peptides were separated into 46 fractions on a 100 x 1.0 mm Acquity BEH C18 column (Waters) using an UltiMate 3000 UHPLC system (Thermo) with a 50 min gradient from 99:1 to 60:40 buffer A:B ratio under basic pH conditions, then consolidated into 18 super-fractions (Buffer A = 0.1% formic acid, 0.5% acetonitrile. Buffer B = 0.1% formic acid, 99.9% acetonitrile. Both buffers adjusted to pH 10 with ammonium hydroxide). Each super-fraction was then further separated by reverse phase XSelect CSH C18 2.5 μm resin (Waters) on an in-line 150 x 0.075 mm column using an UltiMate 3000 RSLCnano system (Thermo). Peptides were eluted using a 75 min gradient from 98:2 to 60:40 buffer A:B ratio. Eluted peptides were ionized by electrospray (2.2 kV) followed by mass spectrometric analysis on an Orbitrap Eclipse Tribrid mass spectrometer (Thermo) using multi-notch MS3 parameters. MS data were acquired using the FTMS analyzer in top-speed profile mode at a resolution of 120,000 over a range of 375 to 1500 m/z. Following CID activation with normalized collision energy of 31.0, MS/MS data were acquired using the ion trap analyzer in centroid mode and normal mass range. Using synchronous precursor selection, up to 10 MS/MS precursors were selected for HCD activation with normalized collision energy of 55.0, followed by acquisition of MS3 reporter ion data using the FTMS analyzer in profile mode at a resolution of 50,000 over a range of 100-500 m/z.

Proteins were identified and reporter ions quantified by searching the UniprotKB database using MaxQuant (Max Planck Institute) with a parent ion tolerance of 3 ppm, a fragment ion tolerance of 0.5 Da, a reporter ion tolerance of 0.001 Da, trypsin/P enzyme with 2 missed cleavages, variable modifications including oxidation on M, Acetyl on Protein N-term, and phosphorylation on STY, and fixed modification of Carbamidomethyl on C. Protein identifications are accepted if they could be established with less than 1.0% false discovery. Proteins identified only by modified peptides were removed. Protein probabilities were assigned by the Protein Prophet algorithm[610]. TMT MS3 reporter ion intensity values are analyzed for changes in total protein using the unenriched lysate sample. Phospho(STY) modifications are identified using the samples enriched for phosphorylated peptides. The enriched and un-enriched samples are multiplexed using two TMT10-plex batches, one for the enriched and one for the un-enriched samples.

Following data acquisition and database search, the search results were normalized using an in-house ProteiNorm app, a user-friendly tool for a systematic evaluation of normalization methods, imputation of missing values and comparisons of different differential abundance methods[611]. ProteiNorm evaluates popular normalization methods including log2 normalization (Log2), median normalization (Median), mean normalization (Mean), variance stabilizing normalization (VSN)[612], quantile normalization (Quantile, https://www.bioconductor.org/packages/release/bioc/html/preprocessCore.html), cyclic loess normalization (Cyclic Loess)[613], global robust linear regression normalization (RLR)[614], and global intensity normalization (Global Intensity)[614]. The individual performance of each method can be evaluated by comparing of the following metrices: total intensity, Pooled intragroup Coefficient of Variation (PCV), Pooled intragroup Median Absolute Deviation (PMAD), Pooled intragroup estimate of variance (PEV), intragroup correlation, sample correlation heatmap (Pearson), and log2-ratio distributions.

The normalized data is imported into ProteoViz to perform statistical analysis using Linear Models for Microarray Data (limma) with empirical Bayes (eBayes) smoothing to the standard errors[613, 615]. A similar approach is used for differential analysis of the phosphopeptides, with the addition of a few steps. The phosphosites are filtered to retain only peptides with a localization probability > 75%, filter peptides with zero values, and log2 transformed. Limma is also used for differential analysis. Proteins and phosphopeptides with an FDR-adjusted p-value < 0.05 and an absolute fold change > 2 are considered significant.

For full phosphoproteomics dataset results, kindly consult the ProteomeXchange Consortium[616] via the PRIDE[617] partner repository with the dataset identifier PXD031699 and 10.6019/PXD031699.

Immunofluorescence NPF screens

Imaging fields for control (WT) or NPF KOs were coded and scrambled by one investigator (FK) on ImageJ Fiji (version 1.51n, National Institutes of Health) and given to the other investigator (TSF) for blind analysis. Cells with actin clouds were scored by visual analysis for the presence or absence of actin assembly. The results were then decoded by the first investigator and the analysis was expressed as a percentage of the total cell count from all images. Bar graphs with their standard deviations (s.d.) were generated using Prism Graphpad version 9.2.0.

Quantification from live-cell imaging

Unless otherwise stated, all image analysis was performed on ImageJ Fiji (version 1.51n, National Institutes of Health). Cells that shrunk during imaging or exhibited signs of

phototoxicity such as blebbing or vacuolization were excluded from analysis (maximal amount 10% for any treatment).

ADA. Quantification methods for actin assembly after CCCP treatment were previously described[560]. For each cell, one ROI was chosen which encompasses the entire area of ADA around mitochondria after drug addition. Fluorescence values for each time point (F) were normalized with the mean initial fluorescence before drug treatment (first four frames−F_0) and plotted against time as F/F_0. For DMSO control or cells that did not exhibit actin burst, the ROI was selected as the bulk region of the cytoplasm containing mitochondria using the mito–BFP channel. For WRC KD in U2-OS and HeLa cells (**Figure 3.1E; Figure S3.2G**), imaging fields for control (ctrl/CCCP and ctrl/DMSO) or WRC KDs were coded and scrambled by one investigator (F.K.) and given to the other investigator (T.S.F.) for blind analysis. The results were then decoded by the first investigator. For FMNL double KD in U2-OS and HeLa cells (**Figure 3. 6E, F; Figure S3.7C**), imaging fields for control or FMNL double KDs were coded and scrambled by one investigator (T.S.F.) and given to the other investigator (R.C.) for blind analysis. The results were then decoded by the first investigator.

Ionomycin. Quantification methods for actin assembly after ionomycin treatment were previously described [12]. For each cell, one or two ROIs are picked. Fluorescence values for each time point (F) were normalized with the mean initial fluorescence before drug treatment (first four frames−F_0) and plotted against time as F/F_0.

Cytoplasmic and ER calcium. Quantification methods for calcium changes after CCCP or histamine treatment were previously described [12]. For each cell, one ROI was chosen to encompass the perinuclear cytosol or the entirety of the endoplasmic reticulum. Fluorescence values for each time point (F) were normalized with the mean initial fluorescence before drug treatment (first four frames−F_0) and plotted against time as F/F_0.

Mitochondrial centroids. Centroids were counted manually for every time-point (2min interval for 20mins in live-cell imaging for U2-OS; indicated time-points for fixed MEFs). To normalize the data, the number of centroids was divided by the total mitochondrial area in the imaging field (μm^2). Number of cells in each field was also recorded. For live-cell U2-OS imaging dataset, images were coded and scrambled by one investigator (T.S.F.) and given to the other investigator (R.C.) for blind analysis. The results were then decoded by the first investigator.

Statistical analysis and graph plotting software

All statistical analyses and P-value determinations were performed using GraphPad Prism QuickCalcs or GraphPad Prism 9 (version 9.2.0, GraphPad Software). To determine P-values, an unpaired Student's t-test was performed between two groups of data, comparing full datasets. For

P-values in multiple comparisons (unpaired; one or two-way ANOVA), Tukey's multiple comparisons test was performed in GraphPad Prism 9. All scatter plots were created with GraphPad Prism 9. Curve fitting (**Figure 3.7F**) was done with a smoothing spline curve set to four knots with GraphPad Prism 9. Live-cell actin burst, along with the standard errors of the mean (s.e.m.) were plotted using Microsoft Excel for Office 365 (version 16.0.11231.20164, Microsoft Corporation).

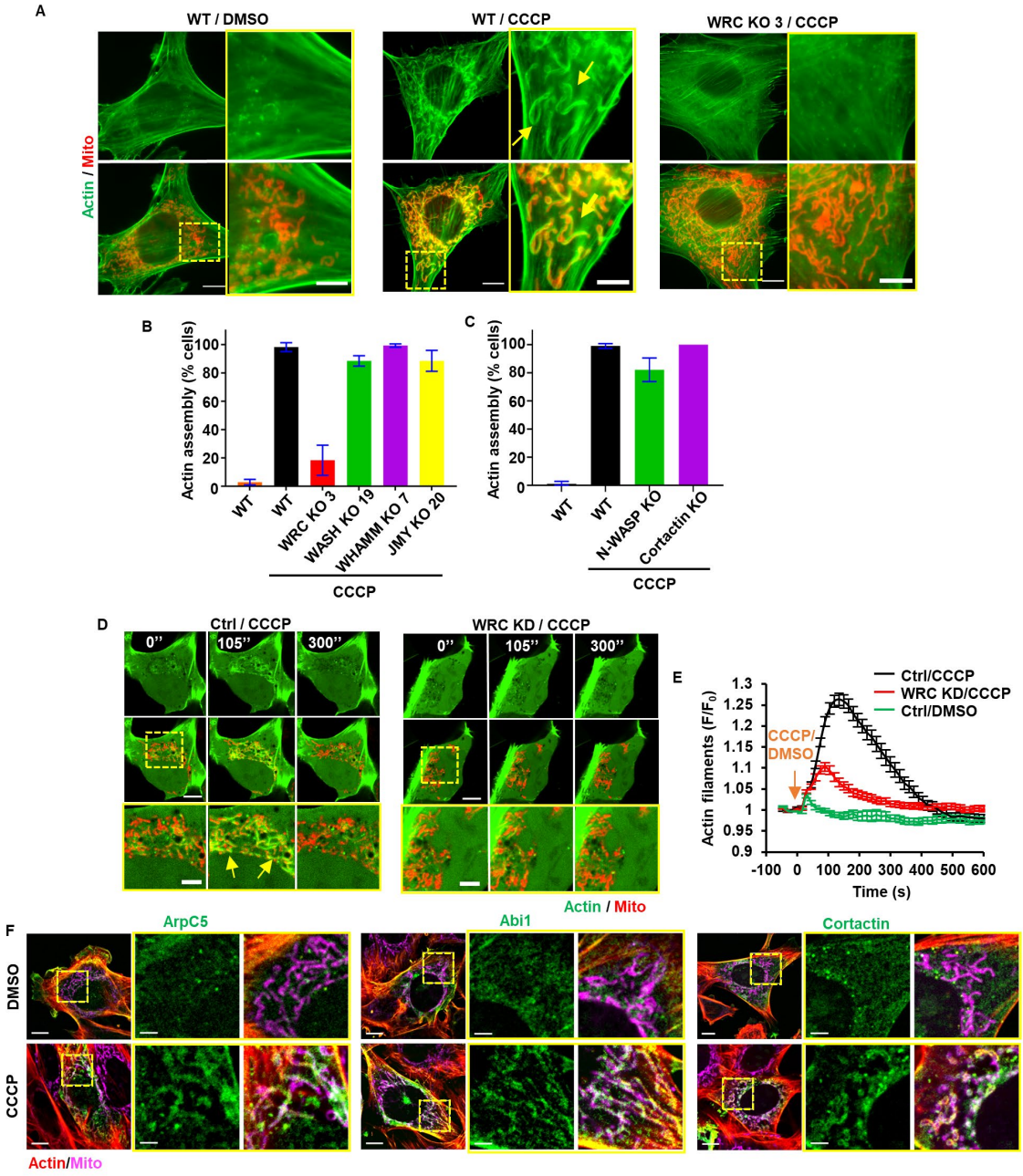
A
WT / DMSO
WT / CCCP
WRC KO 3 / CCCP
Actin / Mito
B
Actin assembly (% cells)
WT
WT
WRC KO 3
WASH KO 19
WHAMM KO 7
JMY KO 20
CCCP
C
Actin assembly (% cells)
WT
WT
N-WASP KO
Cortactin KO
CCCP
D
Ctrl / CCCP
WRC KD / CCCP
0''
105''
300''
Actin / Mito
E
Ctrl/CCCP
WRC KD/CCCP
Ctrl/DMSO
CCCP/DMSO
Actin filaments (F/F0)
Time (s)
F
ArpC5
Abi1
Cortactin
DMSO
CCCP
Actin/Mito

Figure 3.1: WAVE activates Arp2/3 complex during ADA. A) Images of actin (green)/mitochondria (red) in fixed NIH 3T3 cells (wild-type or WAVE regulatory complex (WRC) KO) treated with DMSO or CCCP for 1 min. Arrows: mitochondria-associated actin. Bars: 10 μm (full cell) and 5 μm (insets). **B)** Graph of % NIH 3T3 cells displaying mitochondrially-associated actin. Additional KO clones are presented in **Figure S3.2C**. **C)** Graph of % MEFs displaying mitochondrially-associated actin assembly in either DMSO or CCCP treatment for 1 min. **D)** Images from live U2-OS cells (Ctrl or WRC KD) transfected with markers for actin filaments (GFP-F-tractin, green) and mitochondria (mito-BFP, red), then stimulated with CCCP at time 0 (0 sec). 105" represents optimal stimulation time point for Ctrl (in sec). Arrows: mitochondria-associated actin. Images at bottom are zooms of boxed regions. Bars: 10 μm (full cell) and 5 μm (insets). **E)** Graph quantifying actin polymerization in control or WRC KD U2-OS cells upon CCCP treatment. **F)** Enrichment of GFP-Arpc5, GFP-Abi1, and GFP-cortactin (green) and actin filaments (red) around mitochondria (magenta) upon 1 min CCCP stimulation. Bars: 10 μm (full cell) and 3 μm (inset). Error bars in s.d. (**B, C**) or s.e.m. (**E**). See also **Figure S3.1** (metformin experiment), **Figure S3.2**, **Table 3.1** for pharmacological treatment conditions, **Table 3.2** for oligonucleotides used for CRISPR KO and siRNA knock downs.

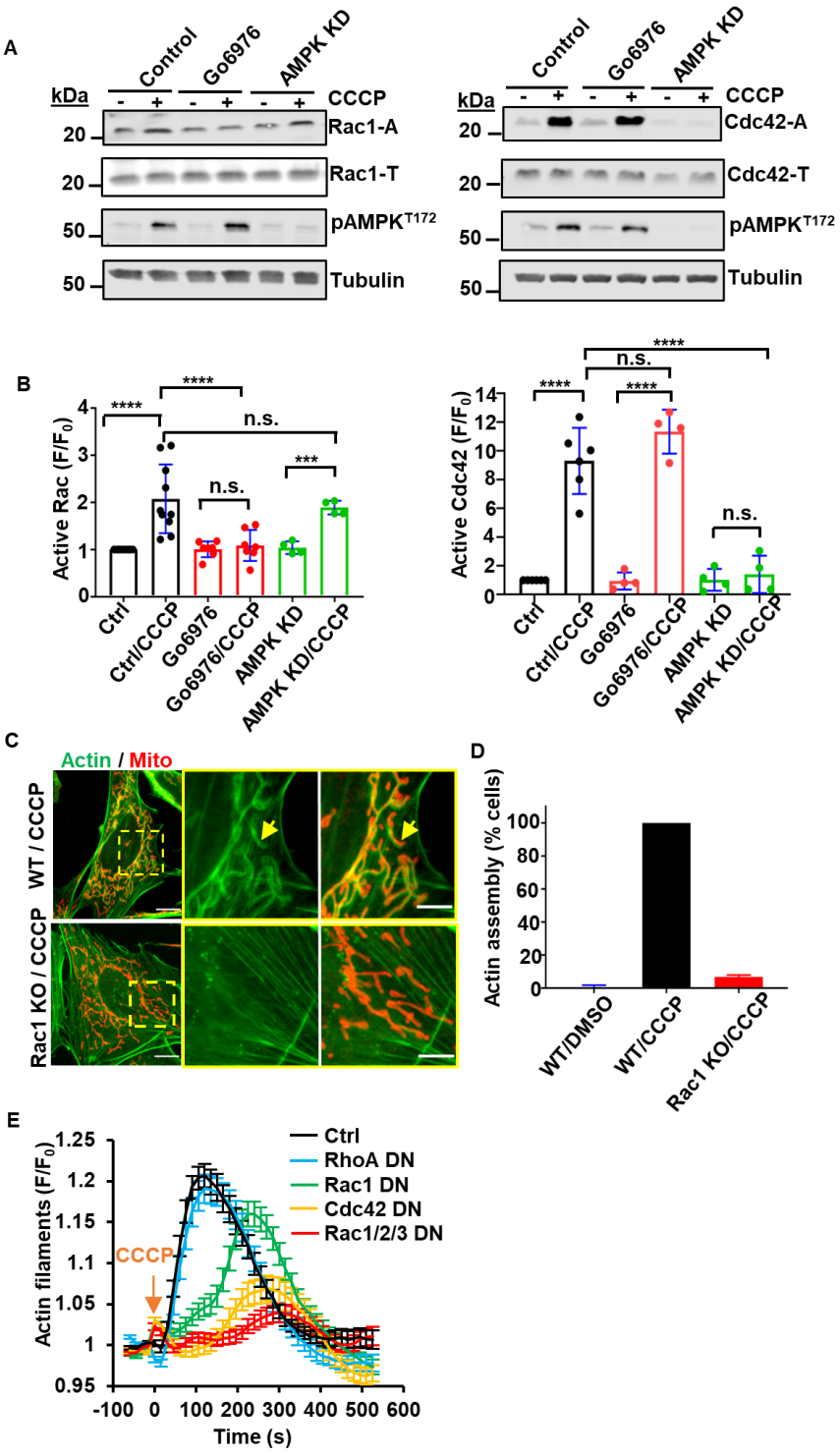
A
Control
Go6976
AMPK KD
kDa
CCCP
Rac1-A
Rac1-T
pAMPK^{T172}
Tubulin
Cdc42-A
Cdc42-T
B
Active Rac (F/F$_0$)
Active Cdc42 (F/F$_0$)
Ctrl
Ctrl/CCCP
Go6976
Go6976/CCCP
AMPK KD
AMPK KD/CCCP
n.s.
C
Actin / Mito
WT / CCCP
Rac1 KO / CCCP
D
Actin assembly (% cells)
WT/DMSO
WT/CCCP
Rac1 KO/CCCP
E
Actin filaments (F/F$_0$)
Ctrl
RhoA DN
Rac1 DN
Cdc42 DN
Rac1/2/3 DN
CCCP
Time (s)

Figure 3.2: Rac and Cdc42 activation during ADA. A) Pull-downs of active Rac (left) or Cdc42 (right) from U2-OS cells stimulated 2 min with CCCP after pre-treatment with DMSO, Go6976, or AMPK KD. Rac1-A and Cdc42-A, active proteins; Rac1-T and Cdc42-T, total proteins in extract. T172P-AMPK (phosphorylated AMPK) in extract also shown, along with tubulin (loading control). **B)** Graphs quantifying active Rac (left) or Cdc42 (right) for indicated conditions. **C)** Images of actin/mitochondria in fixed MEFs stimulated with CCCP for 1 min. Top, WT; bottom, Rac1 KO. Arrows: mitochondria-associated actin. Bars: 10 μm (full cell) and 5 μm (insets). **D)** Graph of % MEFs showing mitochondrially-associated actin. **E)** Actin polymerization upon CCCP treatment in U2-OS cells expressing dominant-negative constructs of indicated GTPases. Images in Figure **S3.3C**. ***: $p < 0.05$; ****: $P < 0.002$; n.s. > 0.05 by one-way ANOVA using Tukey's multiple comparisons test. Error bars in s.d. (**B**) and s.e.m. (**E**). See also **Figure S3.3**, **Table 3.1** and **Table 3.2**.

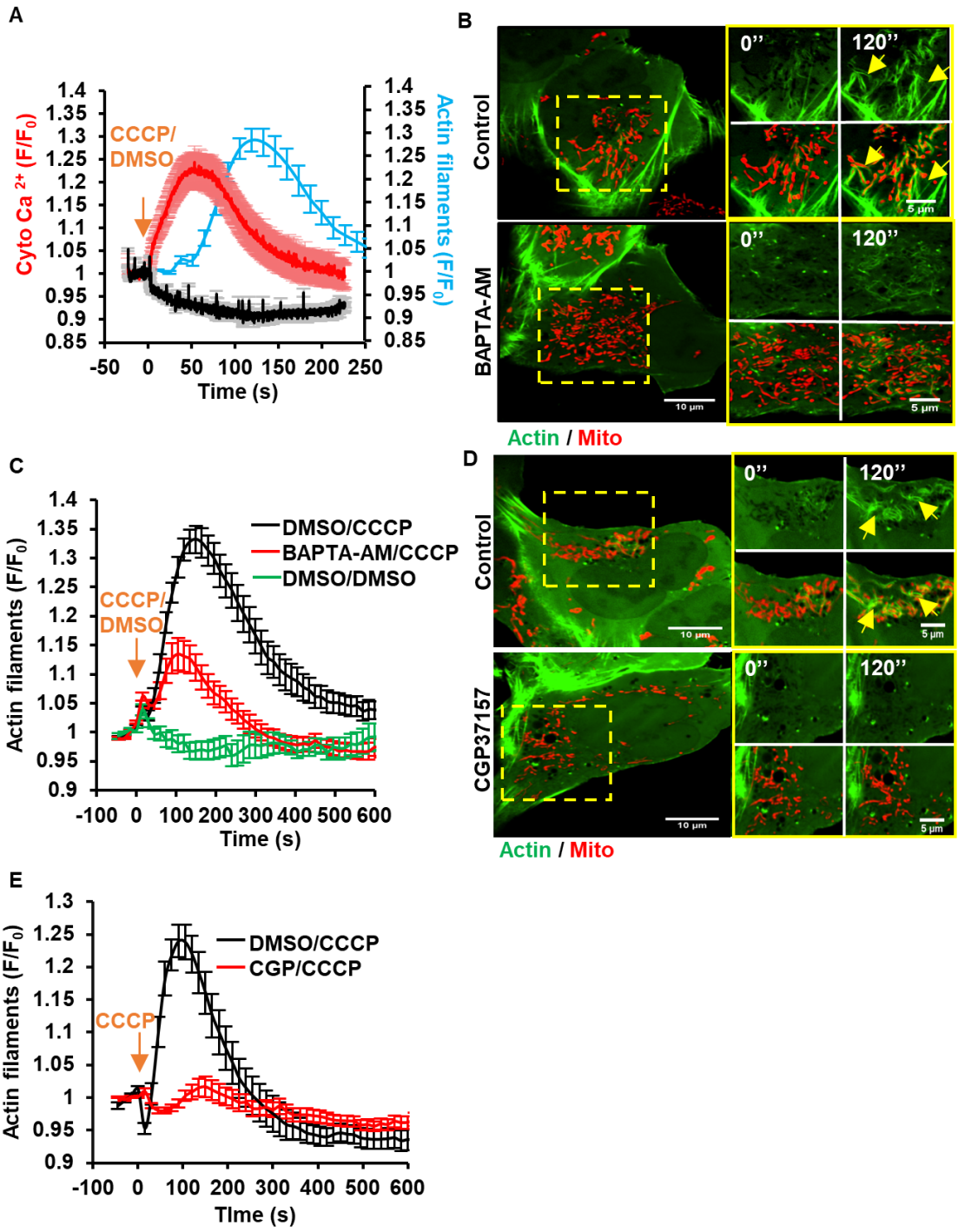
A
Cyto Ca 2+ (F/F0)
Actin filaments (F/F0)
CCCP/
DMSO
Time (s)
B
Control
BAPTA-AM
0''
120''
10 μm
5 μm
Actin / Mito
C
Actin filaments (F/F0)
DMSO/CCCP
BAPTA-AM/CCCP
DMSO/DMSO
CCCP/
DMSO
Time (s)
D
Control
CGP37157
0''
120''
10 μm
5 μm
Actin / Mito
E
Actin filaments (F/F0)
DMSO/CCCP
CGP/CCCP
CCCP
TIme (s)

Figure 3.3: Cytoplasmic calcium increase stimulated by mitochondrial depolarization. A) Change in cytoplasmic calcium (red-CCCP/Black-DMSO) and actin filaments (blue) in live U2-OS cells upon CCCP treatment. Cytoplasmic calcium images in **Figure S3.4A**. **B)** Images of live U2-OS cells transfected with markers for actin filaments (green) and mitochondria (red), stimulated with CCCP at time 0 (0") after DMSO (control) or BAPTA-AM pre-treatment. Images at right: zooms of boxed regions. 120" represents optimal stimulation time point for control (in sec). Arrows indicate mitochondrially-associated actin. **C)** Graph of actin polymerization in control or BAPTA-AM pre-treated U2-OS cells upon CCCP. **D)** Images from live U2-OS cells transfected with markers for actin filaments (green) and mitochondria (red) and stimulated with CCCP at time 0 (0") after DMSO (control) or CGP37157 pre-treatment. Images at right are zooms of boxed regions. 120" represents optimal stimulation time point for control (in sec). Arrows indicate mitochondrially-associated actin. **E)** Graph of actin polymerization in control or CGP37157 pre-treated U2-OS cells upon CCCP. All error bars in s.e.m. See also **Figure S3.4**, **Table 3.1** and **Table 3.2**.

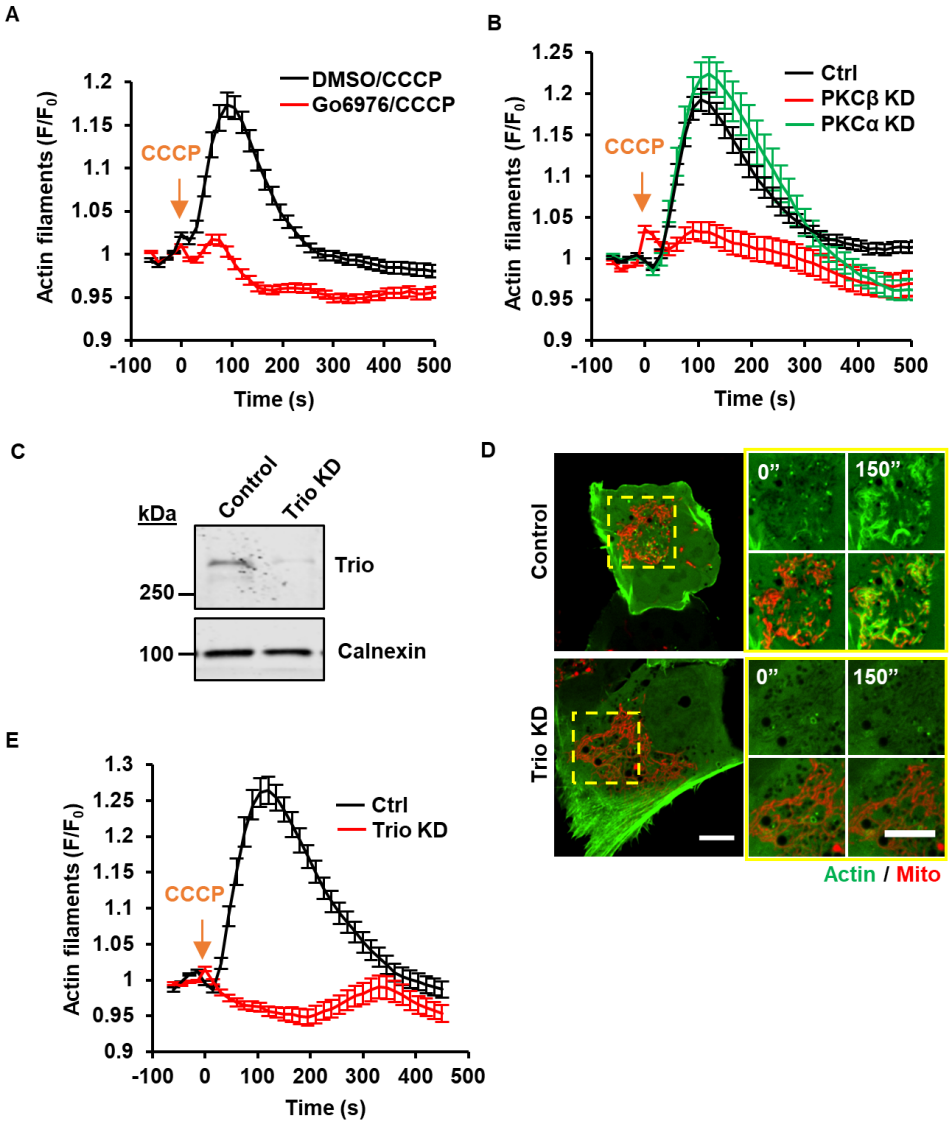

Figure 3.4: Protein kinase C activation of the Rac GEF Trio during ADA. A) Effect of pre-treatment with the PKC inhibitor Go6976 on CCCP-induced actin polymerization in live U2-OS cells. **B)** Graph of actin polymerization in U2-OS cells upon CCCP treatment after knock-down of cPKCβ (both βI and βII) or cPKCα. **C)** Western blot of Trio KD. Calnexin is used as loading control. **D)** Images from live U2-OS (Ctrl siRNA or Trio KD) transfected with markers for actin filaments (GFP-F-tractin, green) and mitochondria (mito-BFP, red) and stimulated with CCCP at time 0 (0”). 150” represents optimal stimulation time point for control (in sec). Images at right: zooms of boxed regions. Bars: 10 μm (full cell) and 10 μm (insets). **E)** Graph of actin polymerization in control or Trio KD U2-OS cells upon CCCP. All error bars in s.e.m. See also **Figure S3.5, Table 3.1** and **Table 3.2**.

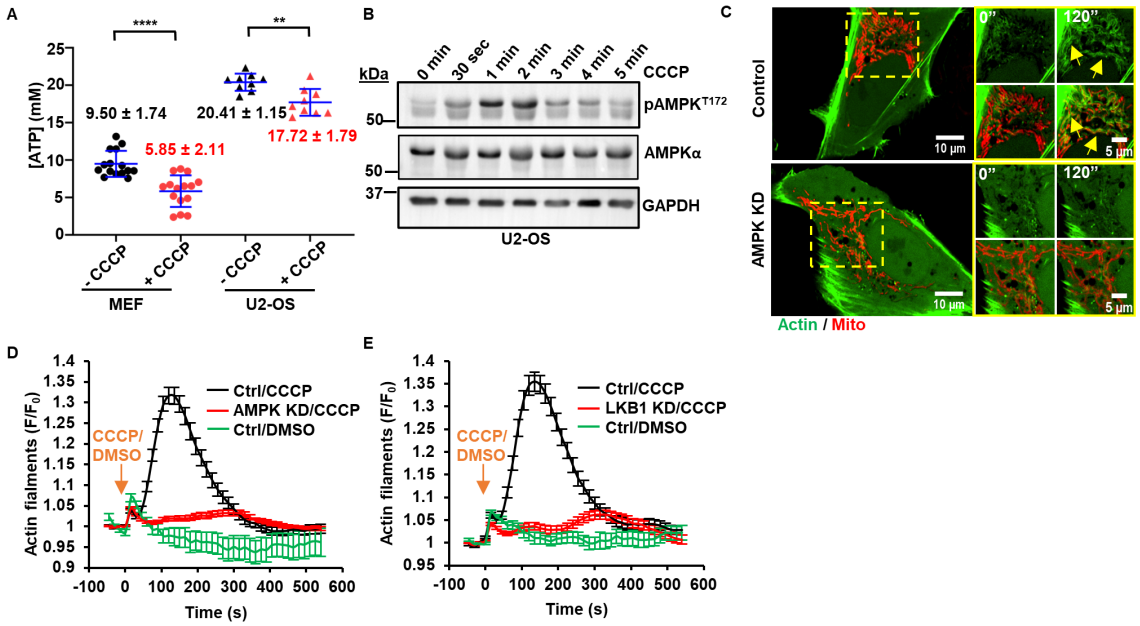

Figure 3.5: AMPK activation by LKB during ADA. A) ATP levels in U2-OS and MEF cells either without or with CCCP treatment (2 min). Data represent 15 and 9 independent points from five and three experiments, for MEFs and U2-OS, respectively. **B)** Western of T172P-AMPK changes (p-AMPK) upon CCCP treatment in U2-OS cells. **C)** Images from live U2-OS (Ctrl siRNA or AMPK KD) transfected with markers for actin filaments (GFP-F-tractin, green) and mitochondria (mito-BFP, red) and stimulated with CCCP at time 0 (0"). 120" represents optimal stimulation time point for control (in sec). Arrows: mitochondria-associated actin. Images at right: zooms of boxed regions. Bars: 10 µm (full cell) and 5 µm (insets). **D)** Graph of actin polymerization in control or AMPK KD U2-OS cells upon CCCP. **E)** Graph of actin polymerization in control or LKB1 KD U2-OS cells upon CCCP. **: P = 0.0016 ;****: P < 0.0001 using unpaired two-tailed Student's t-test. Error bars in s.d. (**A**) and s.e.m. (**D, E**). See also **Figure S3.6**, **Table 3.1** and **Table 3.2**.

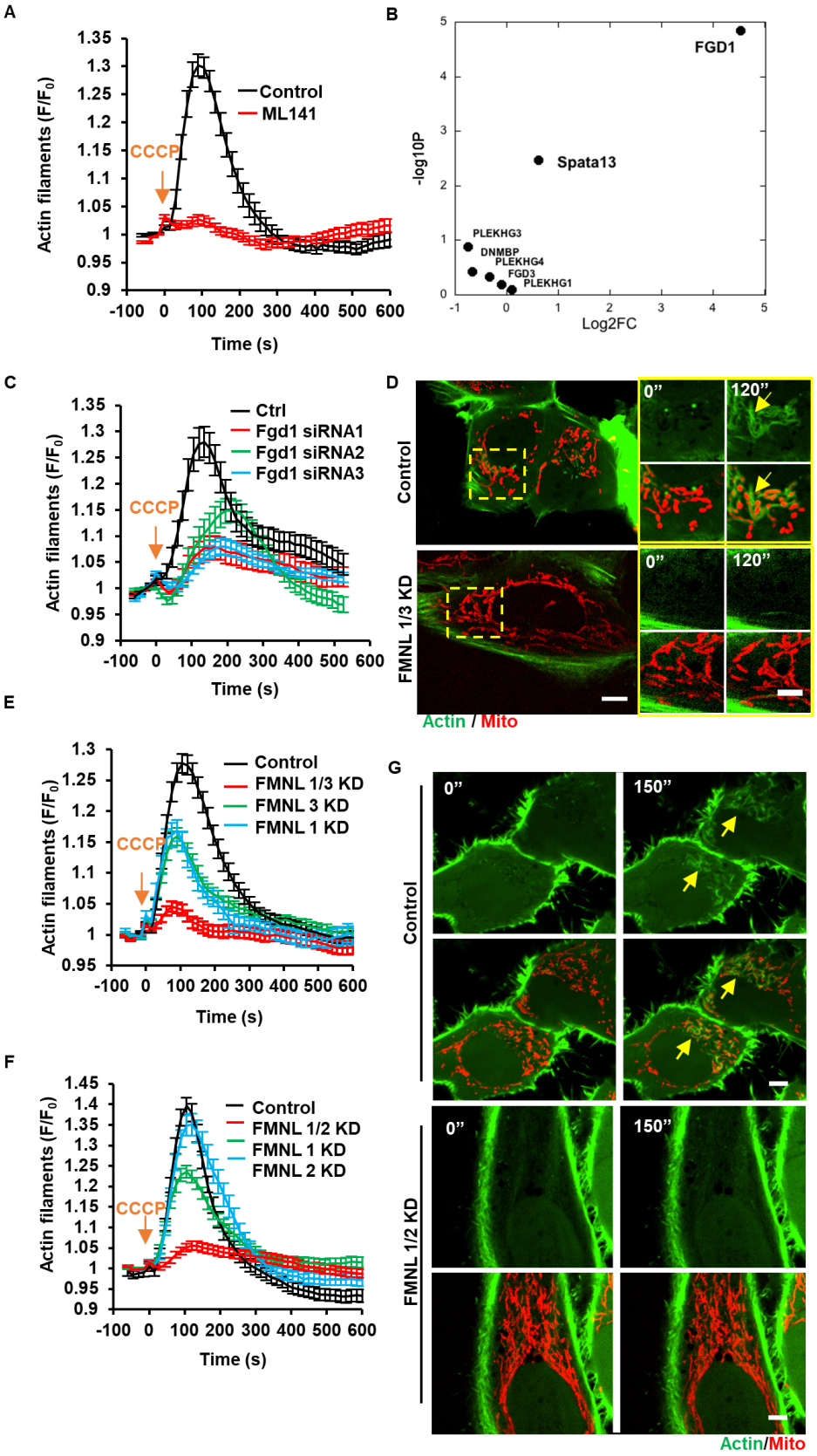
A
Actin filaments (F/F0)
Time (s)
Control
ML141
CCCP
B
-log10P
Log2FC
FGD1
Spata13
PLEKHG3
DNMBP
PLEKHG4
FGD3
PLEKHG1
C
Actin filaments (F/F0)
Time (s)
Ctrl
Fgd1 siRNA1
Fgd1 siRNA2
Fgd1 siRNA3
CCCP
D
Control
FMNL 1/3 KD
0"
120"
Actin / Mito
E
Actin filaments (F/F0)
Time (s)
Control
FMNL 1/3 KD
FMNL 3 KD
FMNL 1 KD
CCCP
F
Actin filaments (F/F0)
Time (s)
Control
FMNL 1/2 KD
FMNL 1 KD
FMNL 2 KD
CCCP
G
Control
FMNL 1/2 KD
0"
150"
Actin/Mito

Figure 3.6: FMNL formins are required for ADA. A) Graph of actin polymerization in ctrl or ML141 pre-treated U2-OS cells upon CCCP treatment. **B)** Phospho-proteomic analysis of Cdc42 GEFs. MEFs were treated with DMSO or with CCCP under protocol 2 (see Methods) and then analyzed for phosphorylation differences on Cdc42 GEFs. Plot represents the log2 change in phosphorylation with CCCP treatment versus the P value of the difference (expressed as -log10). The seven Cdc42 GEFs with detectable phosphorylation are shown, no phosphorylation detected for ARHGEF4, ARHGEF9, ARHGEF15, ARHGEF26, FGD2, FGD4, MCF2, MCF2L, PLEKHG48, RASGRF2. Full phosphoproteomics data can be found online (PRIDE-PXD031699). **C)** Graph of actin polymerization in ctrl or Fgd1 KD (treated with different siRNAs) U2-OS cells upon CCCP treatment. Images in **Figure S3.6H**. **D)** Images from live U2-OS (Ctrl siRNA or FMNL 1/3 KD) transfected with markers for actin filaments (GFP-F-tractin, green) and mitochondria (mito-BFP, red) and stimulated with CCCP at time 0 (0"). 120" represents optimal stimulation time point for control (in sec). Arrows: mitochondria-associated actin. Images at right: zooms of boxed regions. Bars: 10 μm (full cell) and 5 μm (insets). **E)** Graph of actin polymerization in control or various FMNL KD U2-OS cells upon CCCP. **F)** Graph of actin polymerization in ctrl HeLa cells or various FMNL KD upon CCCP treatment. **G)** Images from live HeLa cells (Ctrl siRNA or FMNL 1/2 KD) transfected with markers for actin filaments (GFP-F-tractin, green) and mitochondria (mito-BFP, red) and stimulated with CCCP at time 0 (0"). 150" represents optimal stimulation time point (in sec). Arrows: mitochondria-associated actin. Bars: 5 μm. All error bars in s.e.m. See also **Figure S3.6**, **Figure S3.7**, **Table 3.1** and **Table 3.2**.

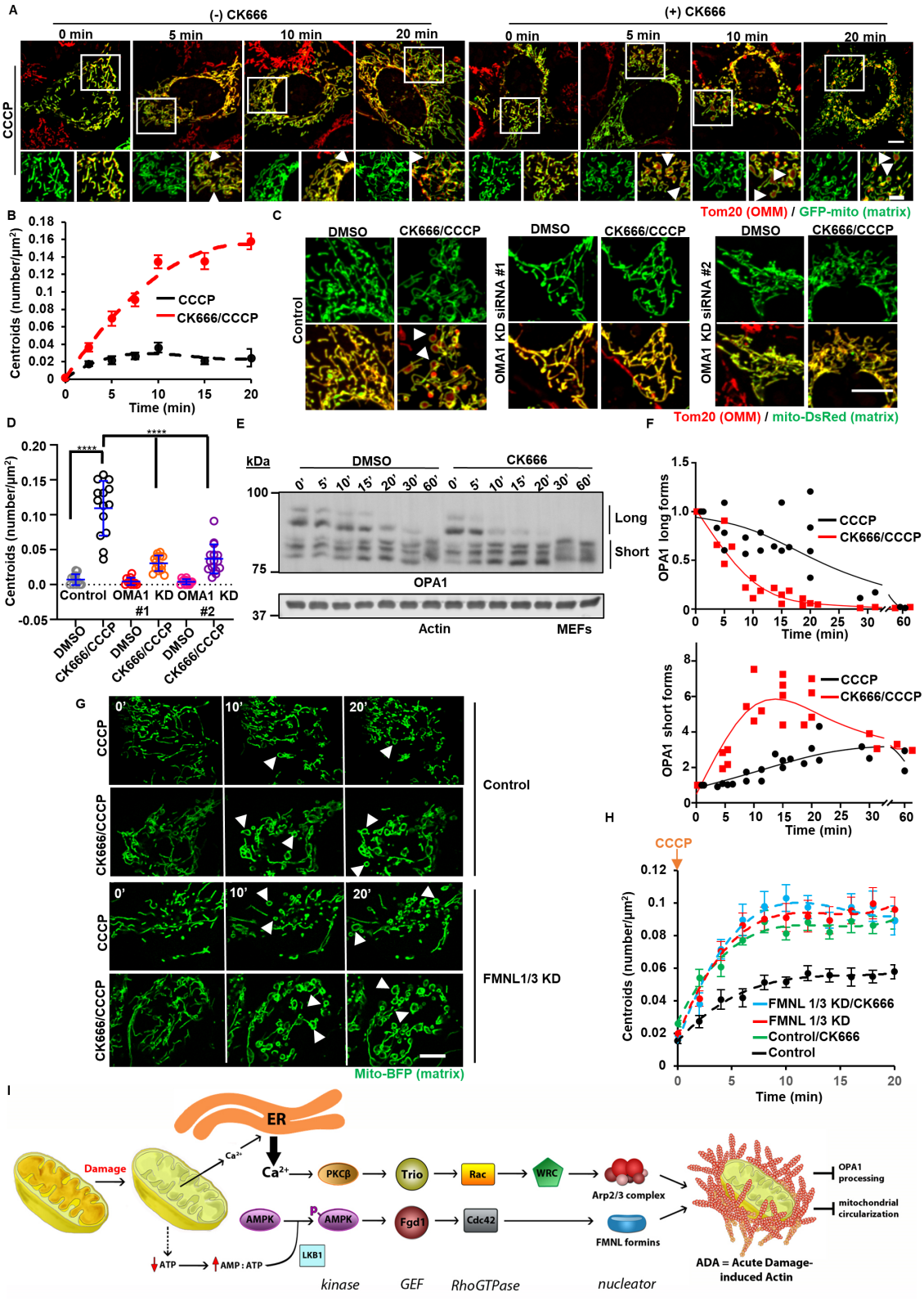
A
(-) CK666
(+) CK666
0 min
5 min
10 min
20 min
CCCP
Tom20 (OMM) / GFP-mito (matrix)
B
Centroids (number/µm²)
Time (min)
CCCP
CK666/CCCP
C
DMSO
CK666/CCCP
Control
OMA1 KD siRNA #1
OMA1 KD siRNA #2
Tom20 (OMM) / mito-DsRed (matrix)
D
Centroids (number/µm²)
Control
OMA1 KD #1
OMA1 KD #2
E
kDa
DMSO
CK666
Long
Short
OPA1
Actin
MEFs
F
OPA1 long forms
OPA1 short forms
Time (min)
G
Control
FMNL1/3 KD
Mito-BFP (matrix)
H
CCCP
Centroids (number/µm²)
FMNL 1/3 KD/CK666
FMNL 1/3 KD
Control/CK666
Control
I
ER
Damage
Ca2+
PKCβ
Trio
Rac
WRC
Arp2/3 complex
AMPK
Fgd1
Cdc42
FMNL formins
LKB1
ATP
AMP : ATP
OPA1 processing
mitochondrial circularization
ADA = Acute Damage-induced Actin
kinase
GEF
RhoGTPase
nucleator

Figure 3.7: ADA accelerates mitochondrial circularization. A) Micrographs of mitochondrial matrix (Mito-GFP, green) and outer mitochondrial membrane (Tom20 immunofluorescence, red) in fixed MEFs treated with CCCP after 30 minutes of CK666 pre-treatment for indicated times, compared to control (CCCP alone without CK666 pre-treatment). Arrows: circularized mitochondria. Bars: 10 μm (full cell) and 5 μm (insets). **B)** Plot of change in mitochondrial matrix circularization (defined as centroids per total mitochondrial area) between pre-treatment with CK666 followed by CCCP (CK666/CCCP) or CCCP alone from fixed MEFs as in panel **A**. Double-Y plot of same data in **Figure S3.7F**. **C)** Micrographs of mitochondrial matrix (Mito-DsRed, green) and outer mitochondrial membrane (Tom20 immunofluorescence, red) in fixed MEFs with 30min CK666 pre-treatment followed by CCCP for 15 minutes (CK666/CCCP), compared to DMSO addition for 15 minutes without CK666 pre-treatment. Scrambled siRNA (control) or OMA1 siRNA #1 and #2 cells. Arrows: circularized mitochondria. Scale bar: 10 μm. **D)** Change in mitochondrial matrix circularization between CK666/CCCP treatment or DMSO in control or Oma1 siRNA #1 and #2. **E)** Western blot showing representative time course of Opa1 processing after CCCP treatment with or without 30 min CK666 pre-treatment in MEFs. Actin, loading control. **F)** Quantification of the long forms or the short forms of Opa1 from two or more biological replicates, similar to panel **E**. Values normalized to time 0. **G)** Micrographs of time course of mitochondrial matrix (Mito-BFP, green) changes in control or FMNL 1/3 KD U2-OS cells with CCCP alone or 30 minutes CK666 pre-treatment followed by CCCP (CK666/CCCP) for indicated times (mins). Arrows: circularized mitochondria. Bars: 10 μm. **H)** Plot of change in mitochondrial matrix circularization between CK666 pre-treatment before CCCP or CCCP alone from live-cell WT or FMNL 1/3 KD U2-OS samples in **G**. **I)** Model of the ADA pathway. Dissipation of the mitochondrial proton-motive force by CCCP triggers two parallel pathways. PATHWAY 1: calcium efflux through the sodium-calcium exchanger NCLX triggers additional calcium release from ER. Increased cytoplasmic calcium activates protein kinase C-β (PKCβ), which phosphorylates the Rac-GEF Trio, activating Rac which in turn activates the WAVE regulatory complex (WRC), which activates Arp2/3 complex. PATHWAY 2: decreased cytoplasmic ATP leads to LKB1 phosphorylation of AMP-dependent protein kinase (AMPK), which in turn phosphorylates the Cdc42-GEF Fgd1, activating Cdc42 which activates formins of the FMNL family. Actin assembly delays Opa1 processing and mitochondrial circularization.****: $P < 0.0001$ by one-way ANOVA using Tukey's multiple comparisons test. Error bars in s.e.m (**B, H**) and s.d. (**D**). See also **Figure S3.7**, **Table 3.1** and **Table 3.2**.

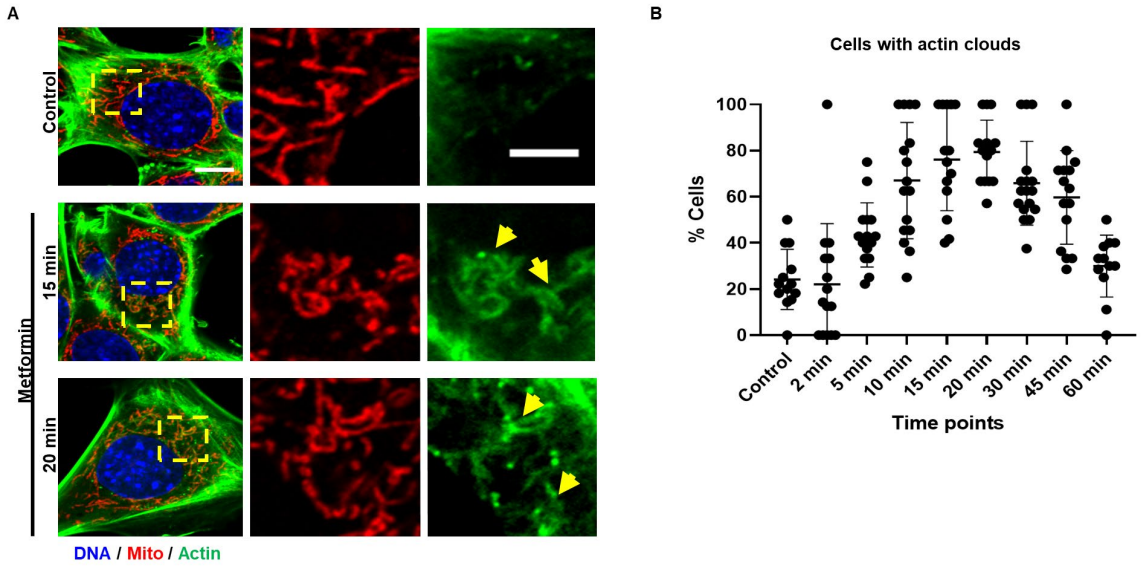

Figure S3.1: ADA induction by metformin treatment. A) Images of actin (GFP-F-tractin, green) and mitochondria (Tom20, red) in fixed MEFs treated with 20mM metformin for indicated times, compared to control (without treatment). Arrows: mitochondria-associated actin. Bars: 10 µm (full cell) and 5 µm (insets). **B)** Graph of % MEF cells displaying mitochondrially-associated actin. Each point represents an individual field of view (FOV). Error bars in s.d.

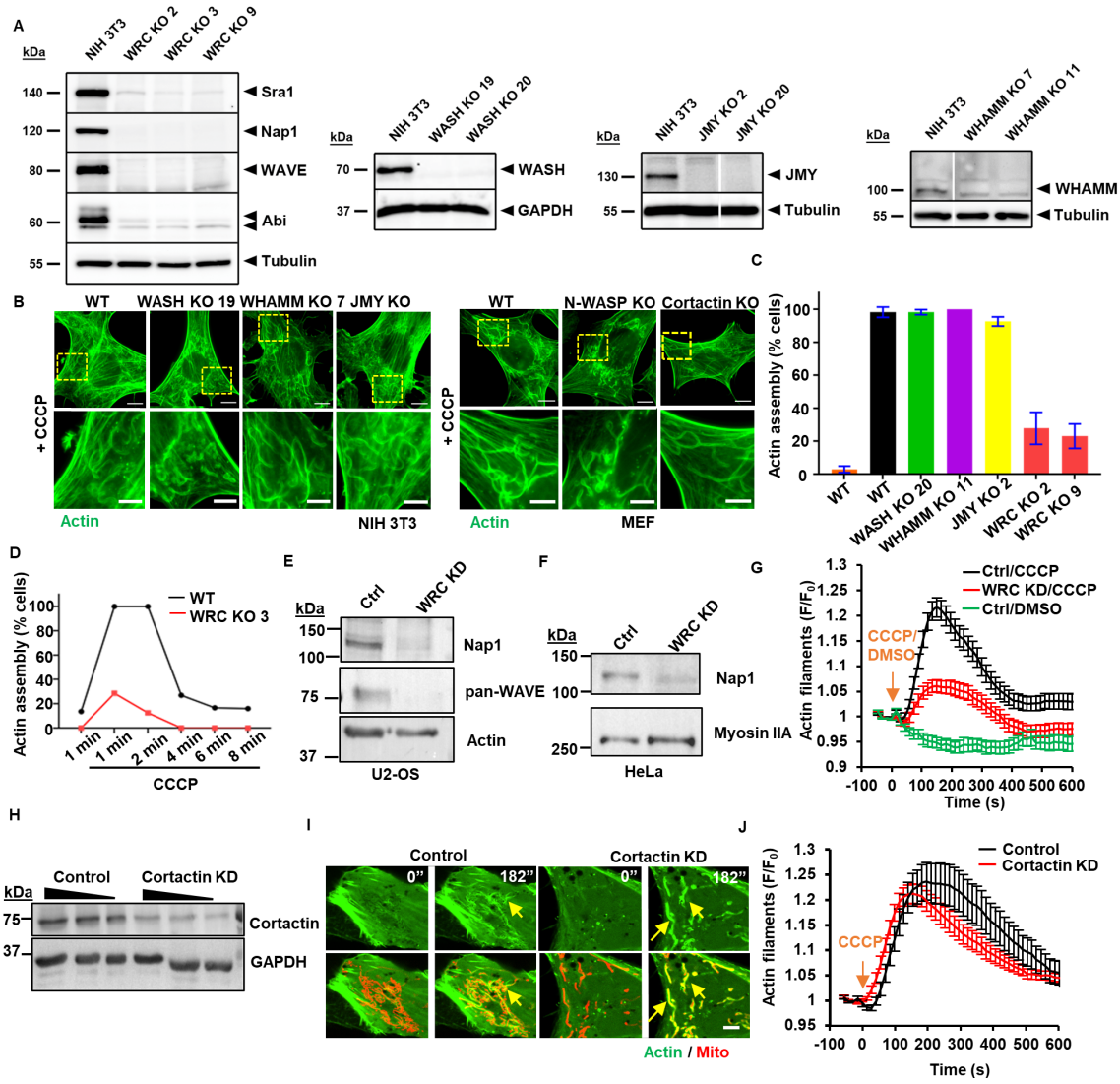
A
kDa
NIH 3T3
WRC KO 2
WRC KO 3
WRC KO 9
140
120
80
60
55
Sra1
Nap1
WAVE
Abi
Tubulin
NIH 3T3
WASH KO 19
WASH KO 20
70
37
WASH
GAPDH
NIH 3T3
JMY KO 2
JMY KO 20
130
55
JMY
Tubulin
NIH 3T3
WHAMM KO 7
WHAMM KO 11
100
55
WHAMM
Tubulin
B
WT
WASH KO 19
WHAMM KO 7
JMY KO
+ CCCP
Actin
NIH 3T3
WT
N-WASP KO
Cortactin KO
+ CCCP
Actin
MEF
C
Actin assembly (% cells)
WT
WT
WASH KO 20
WHAMM KO 11
JMY KO 2
WRC KO 2
WRC KO 9
D
Actin assembly (% cells)
WT
WRC KO 3
1 min
1 min
2 min
4 min
6 min
8 min
CCCP
E
kDa
Ctrl
WRC KD
150
100
75
37
Nap1
pan-WAVE
Actin
U2-OS
F
kDa
Ctrl
WRC KD
150
100
250
Nap1
Myosin IIA
HeLa
G
Actin filaments (F/F0)
Ctrl/CCCP
WRC KD/CCCP
Ctrl/DMSO
CCCP/
DMSO
Time (s)
H
Control
Cortactin KD
kDa
75
37
Cortactin
GAPDH
I
Control
Cortactin KD
0"
182"
0"
182"
Actin / Mito
J
Actin filaments (F/F0)
Control
Cortactin KD
CCCP
Time (s)

Figure S3.2: NPF Knock-outs. A) Western blots of CRISPR KO lines for WRC, WASH, WHAMM and JMY in NIH 3T3 cells. **B)** Images showing CCCP-induced mitochondrially-associated actin for the indicated fixed NIH 3T3 (left) or MEF (right) KO lines (1 min CCCP treatment). Images at bottom are zooms of boxed regions. Scale bars: 10μm (whole cell), 5μm (inset). **C)** Graph showing the % cells displaying mitochondrially-associated actin for the indicated NIH 3T3 lines that are either mock-treated (DMSO, first WT bar) or CCCP-treated for 1 min (all other bars). **D)** Kinetics of ADA in response to CCCP in either WT (black) or WRC KO3 (red) NIH 3T3 cells. Percentage of cells with actin assembly shown. **E)** Western blots of U2-OS transfected with siRNA against the WRC subunit Nap1. Pan-WAVE antibody (recognizes all three WAVE proteins) is shown to demonstrate its loss upon Nap1 KD. Actin is used as loading control. **F)** Westerns of Nap1 KD in HeLa. Myosin IIA is used as loading control. **G)** Graph of actin polymerization in control or WRC KD HeLa cells upon CCCP. **H)** Western blot showing cortactin KD in U2-OS cells. GAPDH is used as loading control. **I)** Images from live U2-OS cells either with control (left) or cortactin KD (right), transfected with markers for actin filaments (GFP-F-tractin, green) and mitochondria (mito-BFP, red) and stimulated with CCCP at time 0 (0"). Arrows: mitochondria-associated actin. Scale bar: 5 μm. **J)** Graph of actin polymerization in control or cortactin KD U2-OS cells upon CCCP. Errors bars in s.e.m. See also **Table 3.1**, **Table 3.2**.

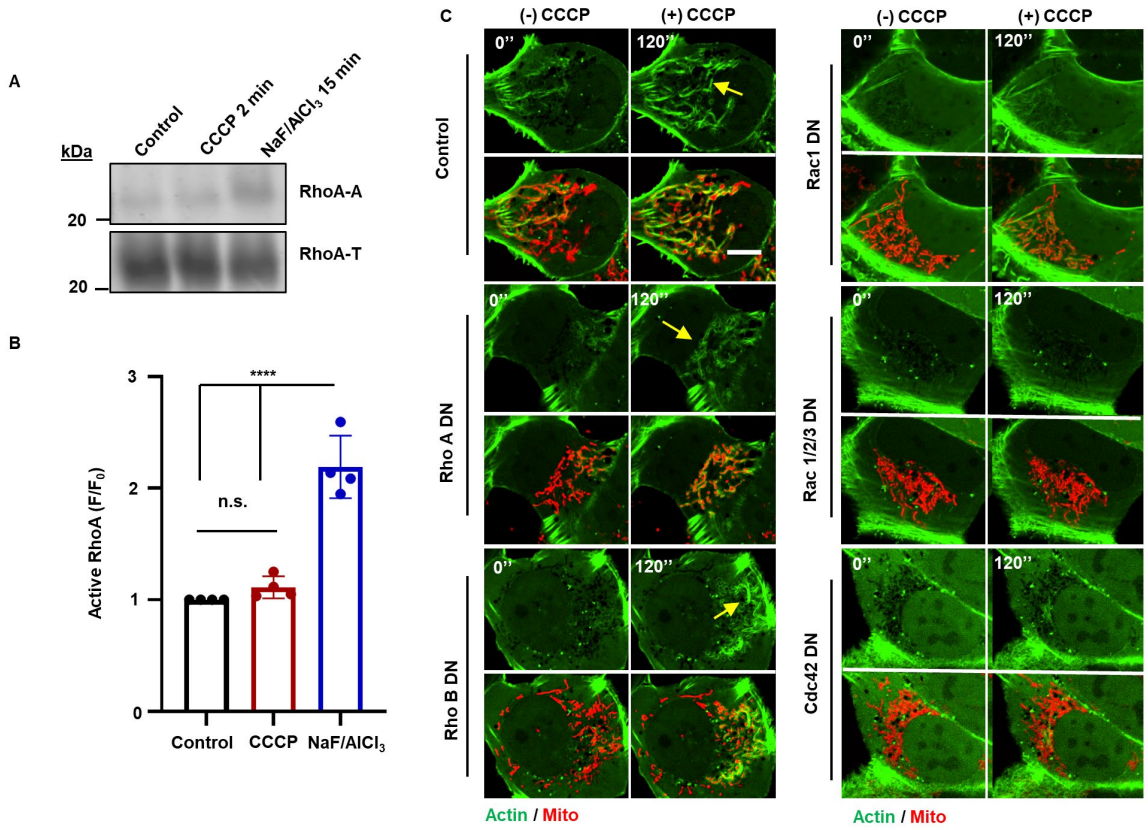

Figure S3.3: Rho GTPase activation in ADA. A) Pull-downs of active RhoA from U2-OS cells on GST-RBD beads after either 2 min CCCP treatment or 15 min $NaF/AlCl_3$ treatment (positive control). RhoA-A, active RhoA; RhoA-T, total RhoA in lysates. **B)** Graph quantifying active RhoA band intensity as a function of total Rho for the indicated conditions. **C)** Representative images of effects of dominant-negative Rho family GTPases on CCCP-induced actin polymerization in live U2-OS cells transfected with markers for actin filaments (GFP-F-tractin, green) and mitochondria (mito-BFP, red). Arrows: mitochondria-associated actin. Scale: 10 µm. Error bars in s.d. n.s. : $P > 0.05$; ****: $P < 0.0001$ using unpaired two-tailed Student's t-test.

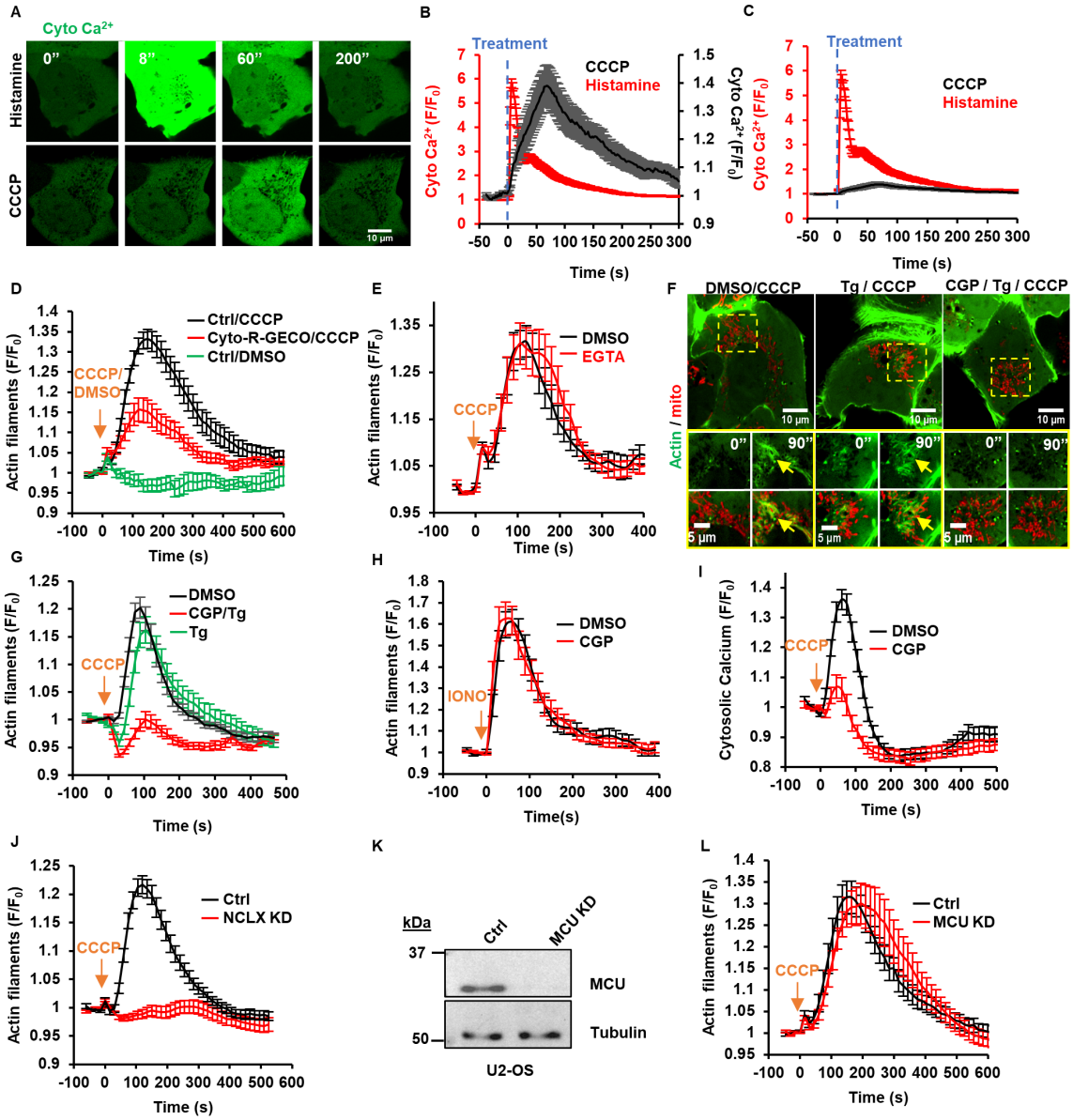
A
Cyto Ca2+
Histamine
CCCP
0”
8”
60”
200”
10 µm
B
Treatment
CCCP
Histamine
Cyto Ca2+ (F/F0)
Time (s)
C
Treatment
CCCP
Histamine
Cyto Ca2+ (F/F0)
Time (s)
D
Ctrl/CCCP
Cyto-R-GECO/CCCP
Ctrl/DMSO
CCCP/ DMSO
Actin filaments (F/F0)
Time (s)
E
DMSO
EGTA
CCCP
Actin filaments (F/F0)
Time (s)
F
DMSO/CCCP
Tg / CCCP
CGP / Tg / CCCP
Actin / mito
0”
90”
10 µm
5 µm
G
DMSO
CGP/Tg
Tg
CCCP
Actin filaments (F/F0)
Time (s)
H
DMSO
CGP
IONO
Actin filaments (F/F0)
Time(s)
I
DMSO
CGP
CCCP
Cytosolic Calcium (F/F0)
Time (s)
J
Ctrl
NCLX KD
CCCP
Actin filaments (F/F0)
Time (s)
K
kDa
Ctrl
MCU KD
37
50
MCU
Tubulin
U2-OS
L
Ctrl
MCU KD
CCCP
Actin filaments (F/F0)
Time (s)

Figure S3.4: Cytoplasmic calcium increase stimulated by CCCP and histamine. A) Images from live U2-OS cells transfected with a cytosolic calcium probe (cyto-R-GECO) and stimulated with either histamine or CCCP at 0 sec. **B)** Graph of change in cytoplasmic calcium signal upon histamine or CCCP treatment. Scales different for histamine stimulation (red, left axis) and CCCP stimulation (black, right axis). **C)** Same data as panel **B**, but plotted on a single-Y graph to better display the difference between histamine-induced and CCCP-induced changes in cytosolic calcium. **D)** Graph of CCCP-induced actin polymerization in U2-OS cells transfected with a cytosolic calcium probe (cyto-R-GECO) or with Cyto-BFP (Ctrl). **E)** Effect of EGTA pre-addition to the medium on CCCP-induced actin polymerization in U2-OS cells. **F)** Images from live U2-OS cells transfected with markers for actin filaments (GFP-F-tractin, green) and mitochondria (mito-BFP, red) and stimulated with CCCP at time 0 (0") after 10 min DMSO or thapsigargin (Tg) treatment. Right-most panels show cells treated with CGP37157 (CGP) 30 min prior to Tg treatment. Images below are zooms of boxed regions. Arrows: mitochondria-associated actin. 90" represents near-optimal stimulation time point for DMSO/CCCP (in sec). **G)** Graph of CCCP-induced actin polymerization in conditions described in **(F)**. **H)** Effect of CGP37157 pre-treatment on ionomycin-stimulated actin assembly in U2-OS cells. **I)** Effect of CGP37157 pre-treatment on CCCP-stimulated cytosolic calcium increase (measured in live U2-OS cells with cyto-R-GECO). **J)** Graph of actin polymerization in control or NCLX KD U2-OS cells upon CCCP. **K)** Western blots of MCU KD in U2-OS. Tubulin is used as loading control. **L)** Graph of actin polymerization in control or MCU KD U2-OS cells upon CCCP. All error bars in s.e.m. See also **Table 3.1** and **Table 3.2.**

A

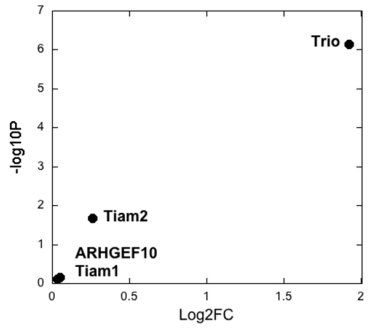

B

		CCCP vs DMSO		CCCP/Go6976 vs CCCP	
Rac GEF	Position	Log2FC	P adjust	Log2FC	P adjust
ARHGEF10	S7	0.05135384	0.69598771	0.0429123	0.657138633
TIAM1	S231	0.03614524	0.77275203	0.02121072	0.823716698
TIAM2	T147	0.26226315	0.0208356	-0.4035277	0.000778066
Trio	S2634	1.92203775	7.161E-07	-1.0195486	1.98937E-05

C

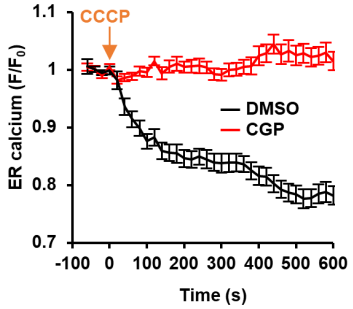

D

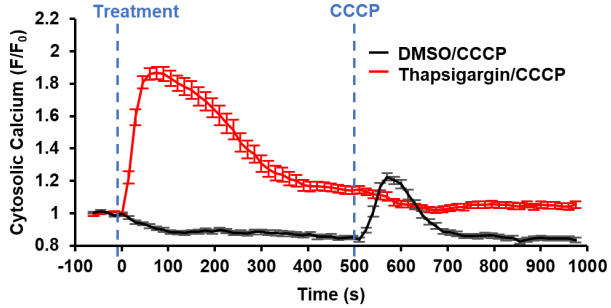

E

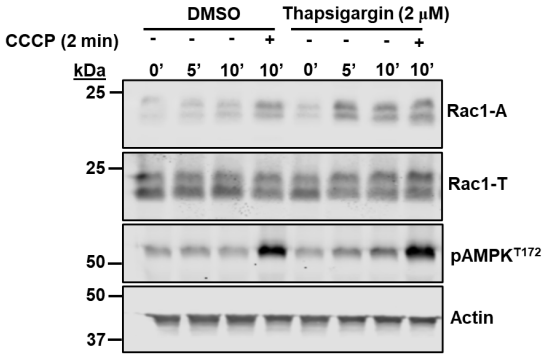

Figure S3.5: Protein Kinase C activation of Rac through the Rac GEF Trio. A) Phospho-proteomic analysis of Rac GEFs. MEFs were treated with DMSO or with CCCP under protocol 1 (see Methods) and then analyzed for phosphorylation differences on Rac GEFs. Plot represents the log2 change in phosphorylation with CCCP treatment versus the P value of the difference (expressed as -log10). The four Rac GEFs with detectable phosphorylation are shown. No phosphorylation detected for DOCK3, DOCK10, FGD5, MCF2, PLEKHG6, PREX1, PREX2, RASGRF2, VAV1, VAV2. Full phosphoproteomics data can be found online (PRIDE-PXD031699). **B)** Table of phospho-proteomics results for Rac-GEFs in MEFs treated with DMSO (negative control), CCCP, or CCCP + Go6976. **C)** ER calcium (gCAMP-150 calcium sensor) changes upon CCCP treatment in U2-OS cells pre-treated with CGP37157 or DMSO for 30 min. **D)** Cytoplasmic calcium (cyto-R-GECO) changes upon thapsigargin or DMSO pre-treatment, followed by CCCP treatment. **E)** Western blots of Rac activation in thapsigargin treatment after indicated treatment (in min). A positive control with 20μM CCCP was performed. T172P-AMPK (phosphorylated AMPK) in extract also shown, along with actin (loading control). All error bars in s.e.m. See also **Table 3.1** and **Table 3.2**.

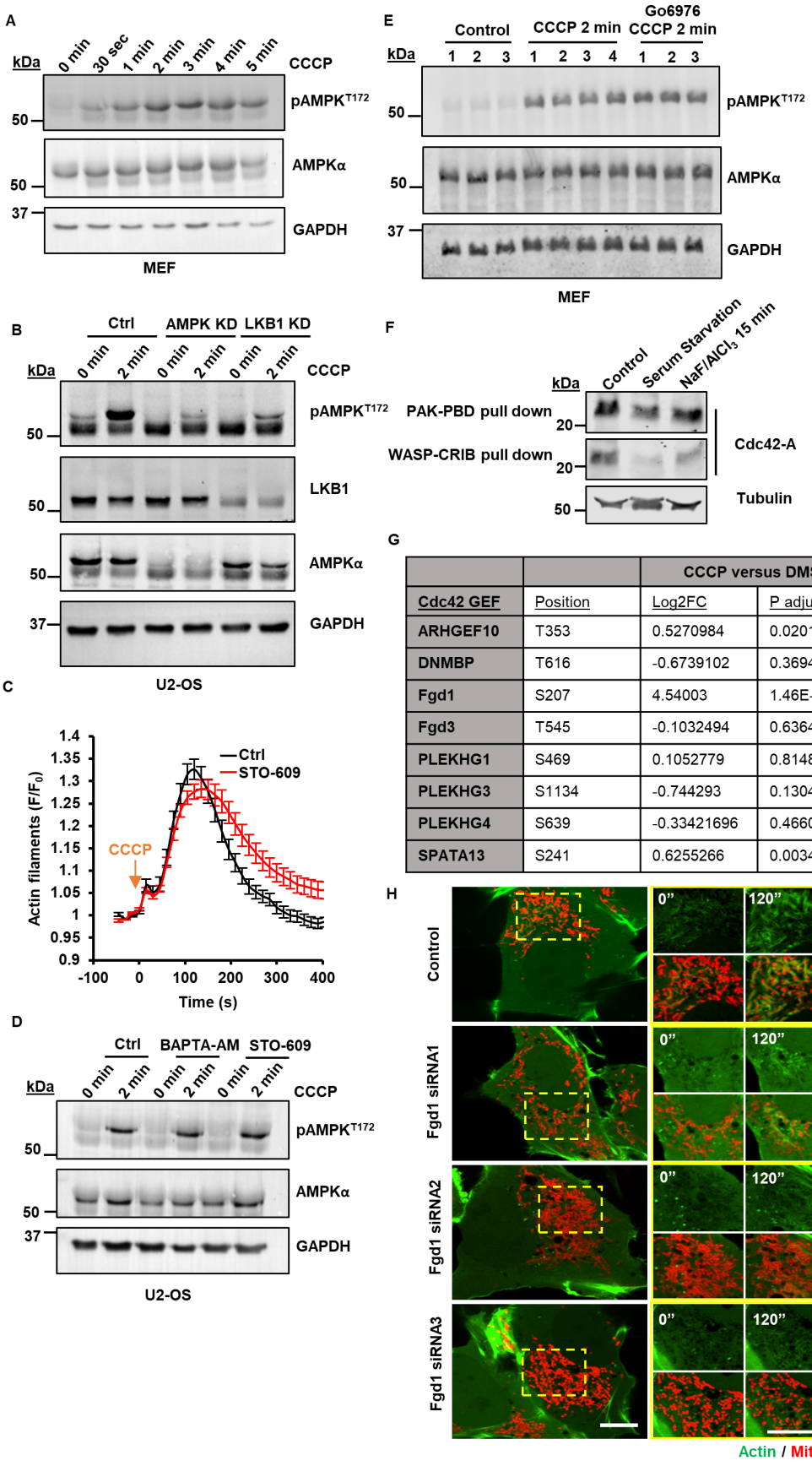

		CCCP versus DMSO	
Cdc42 GEF	Position	Log2FC	P adjust
ARHGEF10	T353	0.5270984	0.02015311
DNMBP	T616	-0.6739102	0.369415
Fgd1	S207	4.54003	1.46E-05
Fgd3	T545	-0.1032494	0.6364094
PLEKHG1	S469	0.1052779	0.81482421
PLEKHG3	S1134	-0.744293	0.1304867
PLEKHG4	S639	-0.33421696	0.46605283
SPATA13	S241	0.6255266	0.00343765

Figure S3.6. AMPK activation, Fgd1 phosphorylation and Cdc42 activation during ADA. A) Western of T172P-AMPK changes (p-AMPK) upon CCCP treatment in MEFs. **B)** Western of AMPK KD (AMPKαI and αII) and LKB1 KD in U2-OS, also showing effects on T172P-AMPK levels. **C)** Graph of change in actin polymerization in U2-OS cells upon CCCP treatment in control or STO-609 pre-treated cells. **D)** Western showing effect of pre-treatment with the CaMKK2 inhibitor STO-609 or with BAPTA-AM on T172P-AMPK levels before and after CCCP treatment. **E)** Western showing effect of pre-treatment with the cPKC inhibitor Go6976 on T172P-AMPK levels after CCCP treatment in MEFs. Numbers (1, 2, 3, 4) indicate biological replicates. **F)** Western blots of Cdc42 activation (using either PAK or WASP pull-down) in conditions after serum starvation for 18 hr or $NaF/AlCl_3$ treatment for 15 min. Tubulin is used as loading control. **G)** Table of phospho-proteomics results for Cdc42-GEFs in MEFs treated with DMSO (negative control) or CCCP. Full phosphoproteomics data can be found online (PRIDE-PXD031699). **H)** Images from live U2-OS (Ctrl siRNA or Fgd1 siRNA1-3) transfected with markers for actin filaments (GFP-F-tractin, green) and mitochondria (mito-BFP, red) and stimulated with CCCP at time 0 (0"). 120" represents optimal stimulation time point for control (in sec). Images at right: zooms of boxed regions. Bars: 10 μm (full cell) and 10 μm (insets). All error bars in s.e.m. See also **Table 3.1** and **Table 3.2**.

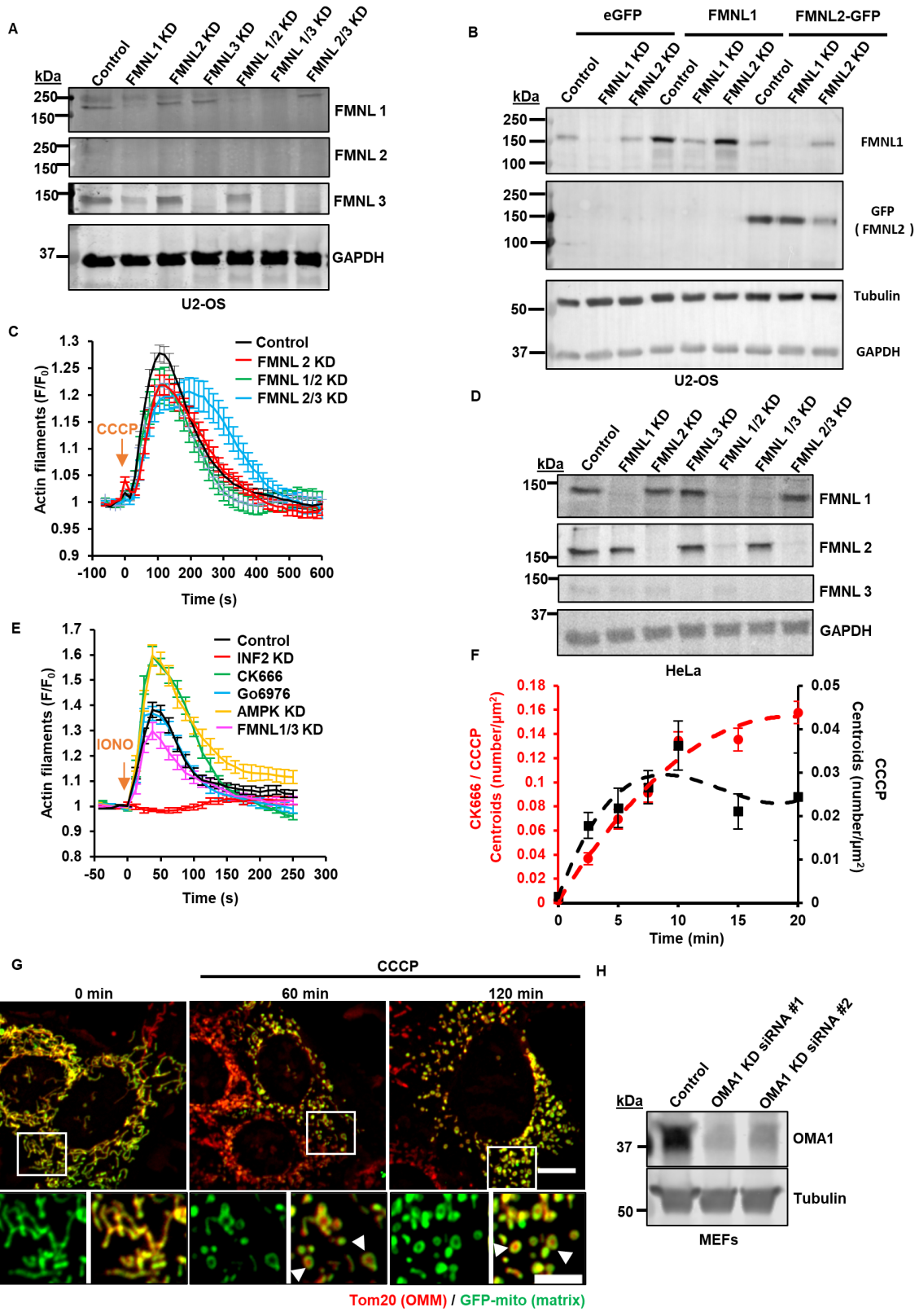
A
Control
FMNL1 KD
FMNL2 KD
FMNL3 KD
FMNL 1/2 KD
FMNL 1/3 KD
FMNL 2/3 KD
kDa
250
150
FMNL 1
FMNL 2
FMNL 3
37
GAPDH
U2-OS
B
eGFP
FMNL1
FMNL2-GFP
FMNL1
GFP (FMNL2)
Tubulin
GAPDH
U2-OS
C
Control
FMNL 2 KD
FMNL 1/2 KD
FMNL 2/3 KD
CCCP
Actin filaments (F/F0)
Time (s)
D
FMNL 1
FMNL 2
FMNL 3
GAPDH
HeLa
E
Control
INF2 KD
CK666
Go6976
AMPK KD
FMNL1/3 KD
IONO
Actin filaments (F/F0)
Time (s)
F
CK666 / CCCP
Centroids (number/μm²)
CCCP
Time (min)
G
CCCP
0 min
60 min
120 min
Tom20 (OMM) / GFP-mito (matrix)
H
Control
OMA1 KD siRNA #1
OMA1 KD siRNA #2
OMA1
Tubulin
MEFs

Figure S3.7. FMNL formins and ADA. A) Western blots of FMNL formins in U2-OS cells. GAPDH is used as loading control. **B)** Western blot for FMNL1 and FMNL2 (GFP) in U2-OS cells transfected with either eGFP-alone, untagged FMNL1, or FMNL2-GFP and treated with siRNA for FMNL1 and FMNL2 for 96 hours. Tubulin and GAPDH are used as loading controls. **C)** Graph of change in actin polymerization in ctrl U2-OS cells versus FMNL2 KD alone or in combo with FMNL1 and FMNL3 KD upon CCCP treatment. **D)** Westerns of FMNL formins in HeLa cells and effects of KD on their levels. GADPH is used as loading control. **E)** Effect of CK666, Go6976 treatments or AMPK KD, FMNL 1/3 KD and INF2 KD on ionomycin-stimulated actin assembly in U2-OS cells. **F)** Double-Y axis plot of the same data as in **Figure 3.7B**, to convey the change in circularization that occurs upon CCCP treatment alone. **G)** Micrographs of mitochondrial matrix (GFP-mito, green) and outer mitochondrial membrane (Tom20 immunofluorescence, red) in fixed MEFs treated with CCCP for 60 or 120 min. Arrows: circularized/fragmented mitochondria. Bars: 10 μm (full cell) and 5 μm (insets). **H)** Western blot for OMA1 KD in MEFs. Tubulin is used as loading control. All error bars in s.e.m. See also **Table 3.1** and **Table 3.2**.

Table 3.1: List of pharmacological treatments and their effects.

Reagent	Conc./ Pre-treatment Time	Target/Purpose
Metformin	20mM – added for various time-points before fixation	ADA stimulation
BAPTA-AM	10μM/ 15 min	Calcium chelation
CGP37157	80μM/ 1 hour	NCLX inhibitor
Go6976	20μM/ 1 hour	PKC kinases inhibitor
EGTA	5mM/ 10 min	Calcium chelation
Thapsigargin	2μM/ 10 min	ER calcium release
CK666	100μM/ added simultaneously with CCCP 100μM/ 30 min pre-treatment before CCCP addition for mitochondrial circularization experiments only (Fig 7; and Fig S7F)	Arp2/3 complex inhibitor
STO-609	10μM/ 1 hour	CaMKK2 inhibitor
ML141	25μM/1 hour	Cdc42 inhibitor
Ionomycin	4μM – added during live-cell imaging	Calcium ionophore
Histamine	100μM – added during live-cell imaging	ER calcium release
CCCP	20μM – added during live-cell or for various time-points before fixation	ADA stimulation

Table 3.2. Oligonucleotides used for CRISPR KO and siRNA silencing in human and murine cell lines.

REAGENT or RESOURCE	SOURCE	IDENTIFIER
Nap1 CRISPR-guideRNA 5'-GACGCCCCGGTCGTTGAGGA-3'	This paper	N/A
Hem1 CRISPR-guideRNA 5'-CTCACGATCCTGAATGACCG-3'	This paper	N/A
WHAMM CRISPR-guideRNA 5'-TGGCTGGGTTCCGCTGCGTG-3'	This paper	N/A
JMY CRISPR-guideRNA 5'-GGAGACACTCGAGTCCGACT-3'	This paper	N/A
WASH CRISPR-guideRNA 5'-GCGACGAGAGGAGGCAATCC-3'	This paper	N/A
siRNA negative control 5′-CGUUAAUCGCGUAUAAUACGCGUAU-3′	IDT	Cat#51-01-14-04
siRNA against human FMNL1 5'- GTGGTACATTCGGTGGATCATGTTCTCCACCGAA T-3'	IDT	hs.Ri.FMNL1.13.5
siRNA against human FMNL2 5'-CATGATGCAGTTTAGTAA-3'	IDT	hs.Ri.FMNL2.13.1
siRNA against human FMNL3 5'- GCATCAAGGAGACATATGA-3'	Ambion	Cat#s40551
siRNA against human Cortactin 5'- ACAAGACCGAATGGATAAGTCAGCT-3'	IDT	Custom-made
siRNA against human INF2 5'- GAGCGGAUGAUCUCCAGGUUGAUCCCU-3'	IDT	Custom-made
siRNA against human Nap1 (termed 'WRC KD') 5'- AAUACGCUUUACCAAGUCAAUUGUU-3'	IDT	hs.Ri.NCKAP1.13. 1

REAGENT or RESOURCE	SOURCE	IDENTIFIER
siRNA against human PKCα 5’- GUCAACAGUAUGAAGGAUUCUGACC-3’	IDT	hs.Ri.PRKCA13.1
siRNA against human PKCα 5’-GAUGAAGACGAGCUAUUUCAGUCTA-3’	IDT	hs.Ri.PRKCA13.2
siRNA against human PKCβ 5’-AUCAUUUACCGUGACCUAAAACUTG-3’	IDT	hs.Ri.PRKCB13.1
siRNA against human PKCβ 5’-AUAUCUUCUUUGAAUGCUAAGCATG-3’	IDT	hs.Ri.PRKCB13.2
siRNA against human PKCβ 5’-GAUAUCAAAGAGCAUGCAUUUUUCC-3’	IDT	hs.Ri.PRKCB13.3
siRNA against human MCU 5’- TAATTGACACTTTAGATTATCTCTT-3’	IDT	hs.Ri.MCU.13.1
siRNA against human AMPKαI/II	Santa Cruz	Cat#sc-45312
siRNA against human LKB1 5’- GGGUACUUCUGUCAGCUGAUUGACG-3’	IDT	hs.Ri.STK11.13.1
siRNA against human NCLX 5’-GAAUUUGGAGUGAUUCACCUGAAAA-3’	IDT	hs.Ri.SLC8B1.13.3
siRNA against human Trio 5’-AACACCAACUUCAGAUAAUAAAATT-3’	IDT	hs.Ri.TRIO.31.1
siRNA against human Fgd1 5’-GCCCUUCAAUUCUAUCAAUCACCAAACGC-3’	IDT	hs.Ri.FGD1.13.1
siRNA against human Fgd1 5’-AGACCGAUACCUCAUACUAUUCAAC-3’	IDT	hs.Ri.FGD1.13.2
siRNA against human Fgd1 5’-AGUCAAUACUUGAACUCCCAUCACG-3’	IDT	hs.Ri.FGD1.13.3
siRNA against mouse OMA1 5'-GACCUUUUCCUUAUUACGCAACUTT-3'	IDT	mm.Ri.Oma1.13.3
siRNA against mouse OMA1 5'-GUGGACCUUUUCCUUAUUACGCAAC-3'	IDT	mm.Ri.Oma1.13.7

Chapter IV:

Mitochondrial-associated actin regulates glycolysis in mitochondrial dysfunction

Chapter IV

Mitochondrial dysfunction triggers actin polymerization necessary for rapid glycolytic activation

Rajarshi Chakrabarti[1,†], **Tak Shun Fung**[1,†], Taewook Kang[2], Pieti W. Elonkirjo[3], Anu Suomalainen[3], Edward J. Usherwood[2] & Henry N. Higgs[1,]

[1]Department of Biochemistry and Cell Biology, Geisel School of Medicine at Dartmouth College, Hanover NH, USA

[2]Department of Microbiology and Immunology, Geisel School of Medicine at Dartmouth College, Hanover NH, USA

[3]Stem Cells and Metabolism Research Program, Faculty of Medicine, University of Helsinki, Finland

[†]These authors contributed equally to this work

The text and data here are adapted or reproduced in full from the manuscript uploaded in biorxiv and accepted in *J Cell Biol*.

(DOI: https://doi.org/10.1101/2022.06.03.494723)

T.S.F. and R.C. designed and performed experiments, interpreted and analyzed data, and wrote the manuscript.

T.K. prepared effector T cells, interpreted and analyzed data for **Figure 4.5**, **Figure S4.11-12**.

P.W.E prepared and isolated human patient fibroblast samples, interpreted and analyzed data for **Figure 4.4I** and **Figure S4.10**.

E.J.U and A.S designed experiments, provided critical feedback and revised the manuscript.

H.N.H. supervised the project, designed experiments, interpreted and analyzed data, and wrote the manuscript.

Conceptualization, R.C., T.S.F., and H.N.H.; Methodology, R.C., T.S.F., T.K., P.W.P., A.S., E.J.U., and H.N.H.; Investigation, R.C., T.S.F., T.K., and P.W.P.; Visualization, R.C., T.S.F., T.K., and P.W.P.; Funding acquisition: A.S., E.J.U., and H.N.H.; Project administration, H.N.H.; Supervision, A.S., E.J.U., and H.N.H.; Writing – original draft, R.C., T.S.F., and H.N.H.; Writing – review & editing, R.C., T.S.F., T.K., P.W.P., A.S., E.J.U, and H.N.H.

4.1 Abstract

Mitochondrial damage represents a dramatic change in cellular homeostasis, necessitating rapid responses. One rapid response is peri-mitochondrial actin polymerization, termed ADA (acute damage-induced actin). The consequences of ADA are not fully understood. Here we show that ADA is necessary for rapid glycolytic activation upon inhibition of mitochondrial ATP production in multiple cells, including mouse embryonic fibroblasts and effector $CD8^+$ T lymphocytes, for which glycolysis is an important source of ATP and biosynthetic molecules. Treatments that induce ADA include CCCP, antimycin A, rotenone, oligomycin, and hypoxia. The Arp2/3 complex inhibitor CK666 or the mitochondrial sodium-calcium exchanger (NCLX) inhibitor CGP37157, applied simultaneously with the ADA stimulus, inhibit both ADA and the glycolytic increase within 5-min, suggesting that ADA is necessary for glycolytic stimulation. Two situations causing chronic reductions in mitochondrial ATP production, ethidium bromide treatment (to deplete mitochondrial DNA) and mutation to the NDUFS4 subunit of complex 1 of the electron transport chain, cause persistent peri-mitochondrial actin filaments of similar morphology to ADA. Both peri-mitochondrial actin loss and a 20% ATP decrease occur within 10 min of CK666 treatment in NDUFS4 knock-out cells. We propose that ADA is necessary for rapid glycolytic activation upon mitochondrial impairment, to re-establish ATP production.

4.2 Introduction

Mitochondrial damage represents an acute cellular stress, compromising ATP production and the balance of several key metabolites, as well as a rise in reactive oxygen species in some situations[618, 619]. Cells respond in many ways to mitochondrial damage, including up-regulating glycolysis and mitochondrial destruction by mitophagy [406, 620]. These responses require extensive communication between mitochondria and the rest of the cell, and defects in these responses are linked to multiple pathologies such as Parkinson's.

One response is ADA (acute damage-induced actin), resulting in a dense actin filament network surrounding the mitochondrion[560] [16]. This actin network is dependent on Arp2/3 complex, and has morphological similarities to other Arp2/3 complex-dependent mitochondrial polymerization events that occur in interphase [429] and mitotic cells [430]. ADA is distinct, however, from another population of actin filaments that influences mitochondria, which we call CIA (calcium-induced actin). CIA is not dependent on Arp2/3 complex, but instead on the formin INF2, which is activated by increased cytoplasmic calcium [12-14, 426]. A consequence of CIA is increased mitochondrial division, through two mechanisms: 1) increased ER-to-mitochondrial calcium transfer, leading to increased inner mitochondrial membrane (IMM) dynamics; and 2) increased recruitment of the mitochondrial division factor Drp1 to the outer mitochondrial membrane (OMM), leading to increased OMM dynamics [12].

The function of ADA is at present unclear. One study suggests that ADA increases mitochondrial division [16]. Our previous data, however, suggest that ADA actually decreases the extensive mitochondrial dynamics that occur in the acute stages of mitochondrial depolarization [560, 621]. We also show that these mitochondrial dynamics are more consistent with changes to IMM morphology, driven by the IMM protease Oma1, than they are with mitochondrial division. These findings are in line with several previous studies [153, 154, 156]. The acute mitochondrial changes induced by depolarization are independent of Drp1 [156, 560].

Here, we provide evidence for a second function for ADA: stimulation of the rapid increase in glycolysis that occurs after mitochondrial ATP production is compromised. This effect on glycolysis occurs upon a variety of treatments, including hypoxia. Based

on these results, we postulate that ADA represents an acute response to maintain cellular ATP levels in the face of mitochondrial dysfunction.

4.3 Results

To begin our investigation into the function of ADA, we first asked whether ADA is a common cellular response, both in terms of cell type and in terms of the nature of the mitochondrial assault. ADA is rapidly and transiently induced by CCCP, a mitochondrial depolarizer, in multiple cell lines including mouse embryonic fibroblasts (MEFs), U2-OS, HeLa and Cos-7 cells (**Figure 4.1**). In all cases, maximum actin polymerization occurs within 4 min, and actin is largely depolymerized in 10 min. Closer examination shows that actin accumulates around most but not all mitochondria, in both live-cell imaging of multiple cell types (**Figure. 4.1A**) and fixed-cell imaging of MEFs (**Figure S4.1**). The actin-free mitochondria are frequently smaller, which may be due to CCCP-induced circularization that has been previously identified [153, 154, 156] and that we have shown to be inhibited by ADA (**Chapter II & III**) [560, 621].

Treatment with CK666, an Arp2/3 complex inhibitor [622], inhibits ADA in all cell types tested (**Figure 4.1B**), similar to our previous results in U2-OS cells (**Chapter II & III**) [560, 621] and to the actin "waves" recently shown in interphase and mitotic cells [429, 430]. ADA does not appear to drive directional mitochondrial motility, and the actin polymerization rarely extends appreciably beyond the mitochondrion, in contrast to the motility-inducing actin 'tails' previously shown to assemble from actin clouds in mitotic cells [430].

Since CCCP is a relatively harsh treatment, resulting in complete mitochondrial depolarization in seconds, we tested two electron transport chain (ETC) inhibitors: antimycin A (Complex III) and rotenone (Complex I), which cause partial depolarization, as measured by tetramethylrhodamine ethyl ester (TMRE) (**Figure 4.2A**). ADA is induced within 3 min for both antimycin A and rotenone, in a CK666-inhibitable manner (**Figure 4.2B, C**). Importantly, CK666 effectively inhibits ADA when added simultaneously to the ADA stimulus, suggesting that the effect of Arp2/3 complex inhibition is on the acute ADA response. We also examined the effect of the ATP synthase inhibitor oligomycin on ADA, which causes a slight increase in mitochondrial polarization over 5 min (**Figure S4.2A**). Oligomycin stimulates ADA in a CK666-inhibitable manner (**Figure S4.2B, C**). This result suggests that ADA is not triggered by decreased mitochondrial polarization.

Another deleterious treatment is hypoxia, which depletes a necessary substrate for Complex IV of the ETC. Upon exposure to hypoxia (1% oxygen), morphologically similar actin filaments to those generated by the ADA treatments arise within 30 min (**Figure 4.2D, E**). Hypoxia-induced actin polymerization is inhibited by CK666 (**Figure 4.2D, E**). These results show that ADA is a rapid response to multiple acute treatments that inhibit oxidative phosphorylation (oxphos), including chemical treatments (CCCP, antimycin A, rotenone, oligomycin) and oxygen deprivation (hypoxia).

4.3.1 ADA is required for rapid up-regulation of glycolysis upon oxphos inhibition

What might be the function of ADA? Since ADA is stimulated by treatments that inhibit oxphos, we asked whether inhibiting ADA would have an impact on cytoplasmic ATP levels. For these experiments, we used the GO-ATeam1 ATP biosensor [623] in live MEFs. To inhibit ADA, we used CK666 added simultaneously to the stimulus, decreasing the possibility of longer-term CK666 effects. We conducted the experiment at two glucose concentrations: 25 mM, which is the concentration in DMEM but is ~5-fold higher than serum glucose; and 2 mM, which is hypoglycemic compared to serum but is similar to the extracellular glucose concentration a number of environments, including solid tumors [20] and in the brain [624]. ADA occurs in MEFs in hypoglycemic conditions (**Figure S4.2D**), similar to our earlier results in 25 mM glucose (**Figure 4.1A, B**).

At 2 mM glucose, there is a 20% drop in ATP within 2 min of mitochondrial depolarization by CCCP. Simultaneous addition of CK666 increases the ATP drop to >30% (**Figure 4.3A; Figure S4.3A**). Biochemical assays of whole-cell ATP levels show similar results (**Figure S4.3B**). The effects of antimycin A or rotenone on ATP levels are slower than for CCCP, with the rotenone effect being negligible (**Figure 4.3 B; Figure S4.3C**). However, CK666 addition causes significant additional drops in cytosolic ATP for both antimycin A and rotenone treatment at 2 mM glucose (**Figure 4.3B; Figure S4.3C**). At 25 mM glucose, CK666 has a non-significant effect on ATP levels when added with CCCP, antimycin A or rotenone (**Figure S4.3D, E**). Treatment with CK666 alone does not have a significant effect on ATP levels at either glucose concentration (**Figure 4.3A, B; Figure S4.3D, E**). These experiments suggest that ADA is necessary to maintain cellular ATP levels upon oxphos inhibition when glucose is limited.

Inhibition of oxphos causes an increase in glycolysis to make up for decreased ATP production [625, 626]. Changes in glycolysis can be assayed by changes in extracellular acidification rate (ECAR), an indirect measure of lactate production [627]. Treatment of MEFs with CCCP causes a rapid ECAR spike followed by prolonged ECAR elevation in both 2 mM and 25 mM glucose medium (**Figure 4.3C; and Figure S4.4A**). The initial ECAR spike occurs at the first measurable timepoint after CCCP addition (3-min). Antimycin A and rotenone also induce ECAR increases, but not as rapidly as CCCP (**Figure 4.3D, E; Figure S4.4B, C**).

For all three treatments, addition of CK666 simultaneously with the treatment suppresses the ECAR increase in 2 mM glucose (**Figure 4.3C-E**) but not in 25 mM glucose (**Figure S4.4A-C**). Titrating the glucose concentration, we find significant effects of CK666 on ECAR occur at 5 mM glucose and below for CCCP treatment, for both the initial effect (3 min, **Figure 4.3F; Figure S4.4D**), or at 40 min after treatment (**Figure S4.4E, F**). These results show that Arp2/3 complex-mediated actin polymerization is necessary for up-regulation of glycolysis upon inhibition of oxphos.

Given that CK666 is added at the same time as CCCP, and inhibits both ADA and the initial ECAR increase by CCCP (both occurring within 4-min), it is likely to us that ADA is the relevant population of actin filaments responsible for the ECAR increase. However, Arp2/3 complex plays roles in many cellular processes, so a more specific link between ADA and the glycolytic increase is needed. We have previously shown that the initial step in CCCP-triggered Arp2/3 complex activation is a rise in cytoplasmic calcium, dependent upon the mitochondrial sodium-calcium exchanger NCLX [621]. We asked whether the NCLX inhibitor CGP37157 would affect the CCCP-induced glycolytic response. When applied simultaneously with CCCP, CGP37157 lowers ECAR to a similar extent as CK666 (**Figure S4.5A**). Oligomycin also potently increases ECAR [628]. We tested the effects of CK666 and CGP37157 on oligomycin-stimulated ECAR at 2 mM glucose. Similar to their effects with CCCP, both CK666 and CGP37157 inhibit the oligomycin-stimulated ECAR increase (**Figure S4.5B**). These results suggest that ADA is the relevant Arp2/3 complex-dependent actin population that stimulates glycolysis, as opposed to another Arp2/3 complex-dependent process.

In contrast to its effects on ECAR, the effects of CK666 on oxygen consumption rate (OCR) are minimal for CCCP, antimycin A, and rotenone. As expected [240], CCCP increases OCR, while antimycin A and rotenone decrease OCR (**Figure S4.5C-E**). Simultaneous treatment with CK666 has no clear effect on OCR under any conditions (**Figure S4.5C-E**). These results show that CK666 affects the activation of glycolysis, rather than altering oxidative phosphorylation.

As a second method to assess glycolysis over a longer time period, we assayed lactate in the culture medium. At 2 mM glucose, lactate levels are significantly elevated by CCCP, antimycin A or rotenone treatment over a 5-hr time course, but simultaneous addition of CK666 suppresses this increase (**Figure S4.6A**). In contrast, the effect of CK666 at 25 mM glucose is comparatively mild (**Figure S4.6B**).

We also used the lactate assay to assess the effect of CK666 on glycolysis under hypoxic conditions (1% oxygen). At 2 mM glucose, CK666 inhibits lactate production 2.21-fold under hypoxic conditions (**Figure 4.3G**, 5-hr timepoint) but only 1.15-fold in normoxia (**Figure S4.6C**). At 25 mM glucose, lactate production is similar in the presence or absence of CK666 in normoxic or hypoxic conditions (**Figure S4.6D, E**). These results suggest that Arp2/3 complex-mediated actin polymerization is important for the up-regulation of glycolysis under hypoxic conditions.

Finally, we examined the effect of oligomycin on ATP levels and ECAR at both 25 mM and 2 mM glucose in MEFs. At 25 mM glucose, oligomycin treatment for 10 min causes a 10.16 ± 8.3 % increase in cytoplasmic ATP, which is brought back to baseline by CK666 addition (1.0 ± 1.1 %) (**Figure S4.7A**). At 2 mM glucose, oligomycin causes a 3.4 ± 5.4 % decrease in cytoplasmic ATP (**Figure S4.7B**). Even this small change in cytoplasmic ATP is sufficient to cause significant activation of AMP-dependent protein kinase (AMPK) (**Figure S4.7C**), which we have shown to be an initial step in ADA activation [621]. In low glucose, CK666 addition to oligomycin causes further reduction of ATP level, to 19.7 ± 7.5 % (**Figure S4.7B**). These results suggest that glycolysis supplies the vast majority of ATP at either 25 or 2 mM glucose, but that Arp2/3 complex-mediated actin is required for optimal glycolysis under low glucose conditions when mitochondrial ATP synthesis is inhibited. The Seahorse assays suggest that the relevant Arp2/3 complex-mediated actin is ADA, based on its inhibition by both CK666 and CGP37157 (**Figure S4.5B**).

4.3.2 ETC protein depletion causes mitochondrially-associated actin filaments and actin-dependent glycolytic activation

We tested whether longer-term reduction of mitochondrial oxphos induced an ADA-like response. One method for inducing chronic oxphos reduction is depletion of mitochondrial DNA (mtDNA), which in mammals contains genes encoding essential subunits of Complex I, III, IV, and V [629]. Treatment with a low-dose of ethidium bromide (EtBr) causes mtDNA depletion [630]. EtBr treatment of MEFs causes progressive mitochondrial depolarization over several days, with complete depolarization (comparable to CCCP) by 10 days (**Figure 4.4A; Figure S4.8A**). During this time, mitochondria adopt a circular conformation (**Figure S4.8B**). ADA-like filaments arise around mitochondria by day 2, and are still present after 10 days (**Figure 4.4B, C**; **Figure S4.8B**). Although this mitochondrially-associated actin is persistently present over multiple days (**Figure S4.8B**), it is inhibited within 5 min of CK666 treatment (**Figure S4.8C**). This result suggests that the mitochondrially-associated actin filaments in these cells are dynamic, turning over with a half-life of less than 5 min.

We examined the effect of these peri-mitochondrial actin filaments on glycolysis in EtBr-treated MEFs, testing lactate production in cells treated for either 4 and 10 days (EtBr-4 and EtBr-10 cells, respectively), and comparing to control cells treated with uridine only (control) for 10 days. In medium containing 2 mM glucose, lactate production is elevated in both EtBr-4 and EtBr-10 cells compared to control (**Figure 4.4D; Figure S4.9A-C**). Treatment with CK666 reduces this lactate to control levels for both EtBr-4 and EtBr-10 (**Figure 4.4D; Figure S4.9A-C**).

Another method for chronically reducing oxphos is knock-out of the NDUFS4 subunit of Complex I, which is associated with approximately 5% of autosomal recessive cases of the neurometabolic disorder Leigh syndrome [631, 632]. Mice with NDUFS4 KO in neurons and glia display progressive encephalopathy that resembles the disease phenotype [633]. Examination of NDUFS4 KO MEFs reveals ADA-like peri-mitochondrial actin accumulation in the majority of cells (**Figure 4.4E, F**). Similar to mtDNA-depleted cells, this ADA-like actin is largely removed within 10 min of CK666 treatment (**Figure 4.4E, F**). These results suggest that longer-term inhibition of oxphos also leads to accumulation of actin around mitochondria.

We tested cytoplasmic ATP levels in NDUFS4 KO cells using the GO-ATeam1 sensor, suspecting that inhibition of ADA-like filaments would cause decreased ATP, similar to the mitochondrial poisons. In medium containing 2 mM glucose, treatment with CK666 causes an approximate 20% reduction in ATP levels in 10 min (**Figure 4.4G**), a similar time course to actin removal. In comparison, WT MEFs do not experience a significant ATP drop over 60 min of CK666 treatment (**Figure 4.4G**), similar to our earlier results. In terms of lactate production, NDUFS4 KO cells display characteristics similar to cells depleted of mitochondrial DNA. In medium containing 2 mM glucose, lactate production is significantly higher for these cells than WT MEFs, but is brought down to similar levels as WT MEFs by addition of CK666 (**Figure 4.4 H; Figure S4.9D**). In 25 mM glucose, CK666 treatment causes no significant change in lactate production for NDUFS4 cells (**Figure S4.9E**), again showing that the Arp2/3 complex-dependent effect on glycolysis does not occur under hyperglycemic conditions.

We also examined fibroblasts from Leigh syndrome patients for ADA-like actin accumulation around mitochondria. Cells from two patients with defined mutations were examined, in addition to cells from two control subjects. The two patient lines display a significant increase in the percentage of cells displaying peri-mitochondrial actin (**Figure 4.4I; Figure S4.10**), suggesting a similar situation to that in NDUFS4 KO cells.

These results suggest that, similar to the acute treatments, Arp2/3 complex-dependent actin polymerization is necessary for optimal glycolytic capability in cells that have chronic mitochondrial dysfunction. These cells also maintain polymerized actin around their mitochondria.

4.3.3 ADA-dependent glycolytic activation in effector $CD8^+$ T cells

T cells undergo a dramatic metabolic change upon activation from naïve T cells to effector T cells (T_{eff}), up-regulating glycolysis while also still using oxidative phosphorylation for significant ATP production [634-637]. Glycolytic activation is important for T_{eff} proliferation and the elaboration of effector functions to kill target cells [638, 639]. To test the importance of ADA in T cells, we isolated $CD8^+$ T cells from the spleens of naïve mice, and activated them to T_{eff} *in vitro* with anti-CD3 and anti-CD28 antibodies. Treatment with CCCP, antimycin A, rotenone or hypoxia causes mitochondrially-associated actin polymerization in the majority of T_{eff}, in a manner that is inhibited by CK666 (**Figure 4.5A, B; Figure S4.11A**).

We then tested the effect of CK666 on glycolysis in T_{eff}, using ECAR as a readout. At both 2 mM and 25 mM glucose, ECAR is stimulated by CCCP, antimycin A, and rotenone (**Figure 4.5C-E; Figure S4.11B-D**). Interestingly, the ECAR response to antimycin A or rotenone treatment is rapid in T_{eff}, in contrast to the slow response in MEFs. At 2 mM glucose, CK666 significantly inhibits the ECAR increase stimulated by all three treatments (**Figure 4.5C-E**), while the effects on OCR are unchanged (**Figure S4.11E-G**). At 25 mM glucose, simultaneous CK666 treatment reduces this ECAR increase slightly in all cases (**Figure S4.11B-D**).

T cells often encounter a hypoxic environment in solid tumors, and can be out-competed by highly glycolytic cancer cells under these conditions [20, 640]. We therefore tested the effect of hypoxia on glycolysis in T_{eff}, using lactate production as a readout. At 2, 5 and 25 mM glucose, CK666 inhibits lactate production 2.32-, 1.75-, and 1.33-fold, respectively, under hypoxic conditions (**Figure 4.5F**; and **Figure S4.12A, B**, 6-hr timepoints). These results show that Arp2/3 complex-mediated actin polymerization stimulates glycolysis in T_{eff} upon treatments that compromise mitochondrial ATP production, with the effect being more pronounced at lower glucose concentration.

4.4 Discussion

In this paper, we show that actin polymerization is rapidly stimulated around mitochondria in response to multiple treatments that compromise mitochondrial ATP synthesis, including mitochondrial uncoupling (CCCP), inhibition of the electron transport chain (antimycin A, rotenone), inhibition of ATP synthase (oligomycin), and hypoxia. We refer to this actin accumulation as ADA, with the filaments being tightly apposed to the mitochondrion. A similar morphology of mitochondria-associated actin occurs under more chronic treatments that reduce mitochondrial oxidative phosphorylation, including mitochondrial DNA depletion, knock-out of the NDUFS4 subunit of complex 1 of the electron transport chain, and cells from Leigh syndrome patients. In all cases, inhibition of a key actin polymerization factor needed for ADA, Arp2/3 complex, inhibits the compensatory increase in glycolytic rate that occurs upon inhibition of mitochondrial ATP production. These results suggest that glycolysis is activated by peri-mitochondrial actin polymerization in response to decreased mitochondrial ATP synthesis.

The mechanism by which mitochondrial dysfunction induces ADA is intriguing. In response to CCCP, actin accumulates within 1-min and peaks by 4-min in multiple cell types. In the more chronic forms of mitochondrial dysfunction (EtBr treatment to deplete mtDNA, NDUFS4 KO, Leigh Syndrome cells), the peri-mitochondrial filaments are eliminated within 5 minutes of Arp2/3 complex inhibition, suggesting that this is not a pool of stably polymerized actin but is constantly turning over. We have previously shown that CCCP-induced ADA requires two parallel signaling pathways, one induced by increased cytoplasmic calcium, which activates Arp2/3 complex; and the other through AMPK activation, which activates the FMNL family of formins [621]. One possibility is that mitochondrial depolarization is the initiating stimulus of these events. However, we show here that ADA-inducing stimuli span a wide range in terms of effects on mitochondrial polarization, including oligomycin, which causes slight hyper-polarization. Our current data might suggest that a decrease in mitochondrial ATP production capacity is a key signal. Even those stimuli that cause low changes in overall cytoplasmic ATP levels, such as oligomycin, cause significant and rapid AMPK activation, which might suggest an ability to detect ATP locally around mitochondria.

Another question concerns whether the mitochondrially-associated actin filaments induced during ADA are the cause of the glycolytic increase. While Arp2/3 complex mediates many actin-dependent cellular processes [30, 641], three items suggest that ADA specifically contributes to glycolytic activation. First, inhibition of the mitochondrial sodium-calcium antiporter NCLX by CGP37157 inhibits the glycolytic increase caused by either CCCP or oligomycin stimulation. We have previously shown that NCLX mediates an important initial step in the ADA activation pathway [621]. Second, the effects of both NCLX or Arp2/3 complex inhibition (by CGP37157 or CK666) on glycolysis occur within 4-min, because simultaneous addition of these compounds with CCCP inhibit the CCCP-induced ECAR increase at the first time point measured. While effects on other processes such as lamellipodia or endocytosis on this time scale are certainly possible, it is more likely to us that the inhibition of ADA de novo is the relevant event. Third, there is a strong inhibitory effect of CK666 on glycolytic activation by mitochondrial inhibitors in T_{eff}, which have a limited number of existing actin-based structures. However, a role for other Arp2/3 complex-dependent actin processes in the rapid glycolytic activation we observe here cannot be ruled out.

The target linking Arp2/3 complex-mediated actin polymerization to this glycolytic increase is unclear, but a number of links between glycolysis and actin have previously been made. One study showed that aldolase was inhibited by an interaction with actin, and that insulin stimulation caused actin depolymerization and aldolase activation [642]. Intriguingly, this insulin-stimulated aldolase activation was inhibited by CK-666, suggesting a more complicated mechanism than simply actin depolymerization. Whether this insulin-mediated glycolytic activation is related to the effects we observe is unclear, considering the different time courses of the responses (minutes for the effects reported here versus hours for the insulin effect). Another glycolytic enzyme that might be regulated by ADA is phosphofructokinase (PFK), whose degradation has recently been shown to be regulated by the E3 ubiquitin ligase TRIM21, itself being activated upon release from stress fibers [435]. Again, it is not clear that the effects reported here follow this mechanism, both in terms of speed of response and the fact that stress fibers are fundamentally different from Arp2/3 complex-dependent structures [5]. In budding yeast, a number of glycolytic enzymes appear to bind and be activated by actin [643], but links with Arp2/3 complex-mediated actin have not been made.

The effect of ADA on glycolysis is particularly important at lower glucose concentrations. While normal blood glucose ranges from 4-6 mM, lower glucose concentrations are common in peripheral tissues. In particular, neuronal cells experience steady-state glucose levels of 2.4 mM, which rapidly drop to below 1 mM during ischemia [624]. The tumor micro-environment also can experience extracellular glucose levels below 1 mM, and competition for glucose between cancer cells and tumoricidal T_{eff} compromises anti-tumor effects [20, 640]. Rapid cellular proliferation and poor vascular supply lead to hypoxia in tumors, compromising mitochondrial function. Induction of ADA in infiltrating T cells might be therefore crucial in maintaining T cell viability and anti-tumor immunity.

Glycolytic activation is one of at least two functions of ADA. We have previously shown that ADA inhibits the mitochondrial re-organization that occurs downstream of depolarization (**Chapter II & III**) [560, 621]. This re-organization occurs within the first 30 min after depolarization, and involves a circularization of the mitochondrion, rather than mitochondrial division [153, 154, 156]. We showed that circularization depends upon the inner mitochondrial membrane protease Oma1 (**Chapter II & III**) [560, 621], one of whose substrates is Opa1 [438]. Inhibition of ADA enhances Opa1 processing as well as circularization (**Chapter II & III**) [560, 621], suggesting that ADA might be able to exert some form of regulatory control over Oma1. The purpose of these shape changes are unclear, but may be a prelude to mitophagy. In this respect, ADA might serve as a temporary brake on responses to mitochondrial damage, increasing glycolytic rate to maintain ATP levels and delaying the mitophagic response. It is not clear whether the mitochondrial circularization we observe upon EtBr treatment represents a similar process to the rapid circularization induced by mitochondrial depolarization.

The exact organization of the actin filaments induced during ADA is unclear, but the staining intensity suggests them to be bundles of filaments or tightly-packed networks. The fact that Arp2/3 complex is required for ADA would suggest that a dendritic network might be present [641]. Similar Arp2/3 complex-dependent actin structures, termed actin 'clouds' have been observed around mitochondria in mitotic [430] and interphase cells [429] in the absence of treatment with mitochondrial-compromising drugs. These actin clouds cycle in waves around the cell, making a full rotation within 15 minutes. In contrast, we have previously shown ADA to be dependent on the WAVE family of

Arp2/3 complex activators [621], while WAVE1 knock down does not inhibit mitotic actin clouds [430]. It is possible, though, that ADA and actin clouds have overlapping functions, and it would be interested to determine whether actin clouds are associated with increased glycolysis.

Another type of recently-identified mitochondrial actin structure is termed actin 'tails', which develop from actin clouds during mitosis and increase mitochondrial motility, to favor homogenous distribution of mitochondria between daughter cells [430]. ADA differs from actin tails in that it does not extend to micron lengths from the mitochondrion. In addition, we have not observed an increase in mitochondrial motility during ADA. In fact, we have previously shown that ADA suppresses mitochondrial dynamics (**Chapter II**) [560].

In addition to the rapid effects on actin and glycolysis upon treatment with mitochondrial inhibitors, cells that are chronically compromised for mitochondrial function also have peri-mitochondrial actin. Arp2/3 complex inhibition eliminates this peri-mitochondrial actin in 5-min in ethidium bromide-treated cells. In NDUFS4-KO cells, Arp2/3 complex inhibition eliminates peri-mitochondrial actin and causes a substantial ATP drop in 10-min (the first time point we tested). Thus, these cells appear to continuously polymerize actin around their compromised mitochondria, perhaps to continuously stimulate glycolysis.

Finally, ADA is not the only Arp2/3 complex-dependent process in which actin polymerizes around damaged mitochondria. A second phase of actin polymerization occurs 1-2 hrs post-damage, which appears to function in the mitophagic process [433, 603]. In addition, we have previously mentioned in this discussion the Arp2/3 complex-dependent mitochondrial actin polymerization identified around apparently un-damaged mitochondria at interphase [429] and during mitosis [16, 430], which possess a number of differences to ADA. Our conclusion at present is that multiple mechanisms for Arp2/3 complex-mediated actin polymerization around mitochondria exist, activated by distinct mechanisms for distinct purposes. One purpose of ADA is to promote rapid glycolytic up-regulation in the face of mitochondrial dysfunction, in order to maintain cellular ATP levels.

4.5 Materials and Methods

Cell culture

Wild-type human osteosarcoma U2-OS and human cervical cancer HeLa cells were procured from American Type Culture Collection (ATCC) and grown in DMEM (Corning, 10-013-CV) supplemented with 10% newborn calf serum (NCS) (Hyclone, SH30118.03) for U2-OS or 10% fetal bovine serum (FBS) (Sigma-Aldrich F4135) for HeLa. Primate *Cercopithecus aethiops* Cos-7 cells were procured from ATCC (CRL-1651) and grown in DMEM with 10% FBS. Wild-type mouse embryonic fibroblasts (MEFs) were a gift from David Chan (previously described [125], while NDUFS4 KO MEFs were a gift from Yasemin Sancak (University of Washington, Seattle). MEFs were grown in DMEM with 10% FBS. Cell lines are cultivated at 37°C with 5% CO_2 and were tested every 3 months for mycoplasma contamination using Universal Mycoplasma detection kit (ATCC, 30-1012K) or MycoAlert Plus Mycoplasma Detection Ki (Lonza, LT07-701). Cell lines were used no more than 30 passages.

Mice and $CD8^+$ T cells

Female wild-type C57BL/6NCrl mice were obtained from Charles River Laboratories. Mouse $CD8^+$ T cells were isolated from the mouse spleens using EasySep™ Mouse $CD8^+$ T Cell Isolation Kit (STEMCELL Technologies, 19853A) according to manufacturer instructions. Isolated $CD8^+$ T cells were stimulated for 2 days in 24 well culture plates coated overnight with 10µg/mL anti-CD3 antibody (clone 145-2C11, BioXCell) and 5µg/mL soluble anti-CD28 (clone 37.51, BioXCell) antibody with 25U/mL recombinant human IL-2 (National Cancer Institute) in the medium. RPMI 1640 with L-Glutamine (Corning, 10-040-CV) supplemented with 10% FBS (HyClone, SH30541.03), 10mM HEPES (Corning Cellgro, 25-060-Cl), 1x non-essential amino acids (Corning Cellgro, 25-025-Cl), 1mM sodium pyruvate (Corning Cellgro, 25-000-Cl), and 44µM 2-Mercaptoethanol (Fisher Scientific, 03446I-100) was used for T cell stimulation and culture until the cells were harvested for experiments.

EtBr treatment of MEFs

This treatment followed published protocols showing mtDNA depletion [630]. 2×10^4 MEFs were plated directly onto Mat-tek imaging dishes and incubated in DMEM + 10% FBS overnight. 24 hours later, overnight media was replaced either with EtBr-containing media (DMEM + 10% FBS + 0.2 µg/ml EtBr (VWR life science, X328) + 50 µg/ml uridine) or control media (DMEM + 10% FBS + 50 µg/ml uridine). At designated times, cells were stained with TMRE to record mitochondrial membrane potential, following which they were fixed and stained for actin (TRITC-phalloidin), mitochondria (Tom-20) and nuclear DNA (DAPI).

Human control and Leigh syndrome fibroblasts

All the culture cell materials from study subjects were collected with informed consent of the parents or the patient, following the recommendation from the Helsinki University Hospital ethical review board. The control cell lines originate from subjects eventually deemed not to manifest a mitochondrial disease.

The fibroblast cultures, previously immortalized by retroviral transduction of E6/E7 proteins of human papilloma virus, were cultivated at 37°C with 5% CO_2 in DMEM (Dulbecco's Modified Eagle's Medium, Lonza Cat. #BE12-614F) with 10% fetal bovine serum albumin (Gibco, Cat. #11550356), 1 X GlutaMAX Supplement (Gibco, Cat. #35050061) 50 mg/l uridine (Calbiochem Cat. #6680) and 50 U/ml penicillin/streptomycin antibody (Gibco, Cat. #15070063) with media change in three day intervals. Cells were passaged after reaching 80% confluency by washing with PBS (Dulbecco's Phosphate Buffered Saline, Sigma-Aldrich, Cat. #D8537-6X500ML) and incubating in 1 X trypsin-EDTA (Gibco, Cat. #15400-054) in 37°C for 3 min prior to replating on two fresh 10 cm dishes. Cell lines were used no more than 30 passages.

DNA transfections and plasmids

For plasmid transfections, cells were seeded at 4×10^5 cells per well in a 35 mm dish at ~16 hours before transfection. Transfections were performed in OPTI-MEM medium (Gibco, 31985062) using lipofectamine 2000 (Invitrogen, 11668) as per manufacturer's protocol, followed by trypsinization and re-plating onto glass-bottomed dishes (MatTek Corporation, P35G-1.5-14-C) at $\sim1\times10^5$ cells per well. Cells were imaged ~16–24 h after transfection.

GFP-F-tractin plasmid were gifts from C. Waterman and A. Pasapera (National Institutes of Health, Bethesda, MD) and were on a GFP-N1 backbone (Clonetech), as described previously [556]. Mito-DsRed construct was previously described [423] and consist of amino acids 1–22 of *S. cerevisiae* COX4 N terminal to the respective fusion protein. ATP FRET sensor GoATeam1 was a gift from Hiromi Imamura (Kyoto University) and is described elsewhere [180]. The following amounts of DNA were transfected per well (individually or combined for co-transfection): 500 ng for Mito–DsRed, GFP–F-tractin and GoATeam1.

Immunofluorescence

For all cell types and conditions, cells were fixed with 1% glutaraldehyde (Electron Microscopy Sciences, 16020) for 10 mins and subsequently washed three times with sodium borohydride (Fisher Chemical, S678)(1mg/ml, 15 mins interval) and then permeabilized with 0.25% TritonX-100 for 10 min. After permeabilization, they were washed thrice again with PBS and incubated in blocking buffer (10% NCS in PBS) for 30 min. The cells were then incubated with anti-Tom20

(Abcam, ab78547 1:500) antibody prepared in 0.1% blocking solution for 90 min. Following PBS washes, the cells were incubated with secondary antibody against Tom20 (Alexa Fluor 488-coupled anti-rabbit; Invitrogen #A11037; 1:200) mixed with TRITC-phalloidin (Sigma, P1951 1:400), 1X DAPI (Sigma, D9542) and incubated for 60 min. The cells were then washed with PBS, resuspended in 2 ml PBS and imaged on the same or following day.

Drug treatment. For drug treatments with MEFs, cells were seeded onto Mat-tek dishes at 200,000 cells/well and incubated at 37°C incubator overnight. Cells were fixed after 3mins treatment with 20μM CCCP (Sigma, C2759), 20μM CCCP + 100μM CK666 (Sigma, SML0006) simultaneously, 25μM antimycin A (Sigma; A8674), 25μM antimycin A + 100μM CK666 simultaneously, 50μM rotenone (Sigma; R8875), 50μM rotenone + 100μM CK666 simultaneously in serum-containing culture DMEM. For oligomycin treatments, cells were fixed after 5mins treatment with 1.5μM oligomycin (Sigma; 75351) or 1.5μM oligomycin + 100μM CK666 simultaneously in serum-free 2mM glucose DMEM. For EtBr and NDUFS4 KO MEFs, cells were treated with 100μM CK666 for 10 mins before fixation with glutaraldehyde. For human fibroblasts, cells were seeded onto μ-slide 8 well (ibidi, 80826) at 200,000 cells/well and incubated at 37°C incubator overnight. Cells were fixed without treatment to identify actin structures around mitochondria.

For drug treatments with effector T cells (T_{eff}), cells were seeded onto Mat-tek dishes at 200,000 cells/well in serum-free (low glucose) DMEM medium (Agilent Seahorse XF DMEM; 103575-100) supplemented with 4mM L-glutamine, 1mM sodium pyruvate with 2mM D-glucose and allowed to adhere for 1 hour. Cells were fixed after 3mins treatment with 1μM CCCP, 1μM CCCP + 100μM CK666 simultaneously; or 5mins treatment with 2.5μM antimycin A, 2.5μM antimycin A + 100μM CK666 simultaneously, 5μM rotenone, 5μM rotenone + 100μM CK666 simultaneously. A control for no treatment was also performed.

Hypoxia. For hypoxia treatments, WT-MEF cells were seeded onto Mat-tek dishes at 200,000 cells/well and incubated at 37°C incubator overnight. Serum free DMEM medium was placed in the hypoxia chamber (InvivO2; BAKER; 94% N_2, 5% CO_2, 1% O_2 at 37°C) overnight for equilibration. The following day, the Mat-tek dishes were washed twice with pre-warmed serum free DMEM. 2 ml of pre-equilibrated serum free DMEM (with DMSO, or CK666) were added to respective plates and quickly placed in the hypoxia chamber. 30 min later, the cells were fixed with glutaraldehyde and washed three times with PBS in the chamber before being taken out on the bench for downstream processing.

For effector T cells in hypoxia, serum free (low glucose) DMEM (Gibco, A1443001) with 2 mM D-glucose, 4 mM L-glutamine, 1mM sodium pyruvate was placed in the hypoxia chamber for equilibration overnight. The following day, cells were seeded onto a poly-D-lysine coated 8 well

chamber slide (Ibidi, 80821) at 500,000 cells/well in low glucose and allowed to adhere in normoxia condition at 37°C for 1 hour. Next, the slide was brought into the hypoxia chamber and the pre-existing medium was substituted for the hypoxic medium containing either 100μM CK666 or DMSO. 1 hour later, the cells were fixed with glutaraldehyde and washed thrice with PBS before they were taken out of the chamber for sodium borohydride washes and subsequent steps.

Antibodies and Western blotting

Anti-actin (mouse; mab1501R; Millipore) used at 1:1,000. Anti-phospho-AMPKα (Thr172) (CST;#2535; clone 40H9; rabbit monoclonal) was used at 1:1000. Li-COR secondary antibodies used were: anti-rabbit IRDye 800CW (#926-32211; 1:15000; goat) and anti-mouse IRDye 680RD (#926-68070; 1:15000; goat). For probing protein levels and AMPK phosphorylation in cell extracts, cells from a 35mm dish were trypsinized, centrifuged at 300 g for 5 min and resuspended in 400μl of 1× DB (50mM Tris-HCl, pH 6.8, 2mM EDTA, 20% glycerol, 0.8% SDS, 0.02% 784 Bromophenol Blue, 1M NaCl, 4M urea). Proteins were then separated by 10% SDS-PAGE in a Bio-Rad mini-gel system (7×8.4cm) and transferred onto polyvinylidene fluoride membrane (EMD Millipore, IPFL00010). The membrane was blocked with TBS-T (20 mM Tris-HCl, pH 7.6, 136 mM NaCl, 0.1% Tween-20) containing 3% BSA (VWR Life Science, VWRV0332) for 1h, then incubated with primary antibody solution at 4°C overnight. After washing with TBS-T, the membrane was incubated with fluorescently tagged Li-COR antibody for 1h at 23°C. Signals were detected by Li-COR fluorescent imager.

Microscopy

Both fixed and live sample dishes were imaged using the Dragonfly 302 spinning disk confocal (Andor Technology) on a Nikon Ti-E base and equipped with an iXon Ultra 888 EMCCD camera, a Zyla 4.2M pixels CMOS camera, and a Tokai Hit stage-top incubator set at 37°C. A solid-state 405 smart diode 100 mW laser, solid state 560 OPSL smart laser 50 mW laser, and solid state 637 OPSL smart laser 140 mW laser were used. Objectives used were the CFI Plan Apochromat Lambda 100X/1.45 NA oil (Nikon, MRD01905) for all drug treatment in live-cell assays or fixed-cell assays. Images were acquired using Fusion software (Andor Technology, version 2.0.0.15). For live-cell imaging, cells were imaged in their respective cell culture medium. DMEM with 10% NCS for U2-OS or DMEM with 10% FBS for HeLa, Cos-7 and MEF cells. Medium was pre-equilibrated at 37°C and 5% CO_2 before use. For actin burst and TMRE quantifications, cells were imaged at a single confocal slice at the medial region, approximate 2 μm above the basal surface, to avoid stress fibers. For live-cell drug treatments, cells were treated with 20μM CCCP, 20μM CCCP + 100μM CK666 simultaneously for media containing serum; or 1μM CCCP, 1μM CCCP + 100μM CK666 simultaneously for media free of serum at the start of

the fifth frame (~1min, with time interval set at 15s) during imaging and continued for another 9 min. To observe TMRE changes in WT, uridine treated or EtBr MEFs, cells were loaded with 20 nM TMRE for 30 min in culture medium at 37°C and 5% CO_2. After incubation, TMRE was washed off with fresh culture medium before imaging.

Image analysis and quantification

All image analysis was performed on ImageJ Fiji (version 1.51n, National Institutes of Health).

Immunofluorescence analysis. Cells with actin clouds were scored by visual analysis for the presence or absence of actin assembly in a given field and expressed as a percentage of the total number of cells for that field. Taking all the imaging fields into consideration for each condition, a bar graph showing the average percentage of cells, along with its respective errors bar in standard deviation (s.d.) or standard errors of the mean (s.e.m.) was plotted with Microsoft Excel. For human patient fibroblast dataset, imaging wells were blinded by P.W. Elonkirjo and imaged by R. Chakrabarti. Microscopy images from each well were subsequently combined and scrambled by R. Chakrabarti before given to TS. Fung for analysis. Final quantification was unscrambled by R. Chakrabarti and then decoded by P. W. Elonkirjo.

Quantification from live-cell imaging The ImageJ Fiji Time Series Analyzer (UCLA) plugin was used for analysis for live-cell imaging. Cells that shrunk during imaging or exhibited signs of phototoxicity such as blebbing or vacuolization were excluded from analysis (maximal amount 10% for any treatment).

ADA. Quantification methods for actin assembly after mitochondrial-damage were previously described[3]. For each cell, one ROI was chosen which encompasses the entire area of ADA around mitochondria after drug addition. Fluorescence values for each time point (F) were normalized with the mean initial fluorescence before drug treatment (first four frames−F_0) and plotted against time as F/F_0. For DMSO control or cells that did not exhibit an actin burst, the ROI was selected as the bulk region of the cytoplasm containing mitochondria using the mito–DsRed channel.

TMRE. Mean TMRE fluorescence was calculated from the entire mitochondrial area for each individual cell. TMRE fluorescence values for each time point (F) were normalized with the mean initial fluorescence before drug treatment (first four frames−F_0) and plotted against time as F/F_0.

Cytoplasmic ATP changes using GO-ATeam1 biosensor

Go-Ateam1 plasmid (kindly provided by Hiromi Imamura, Kyoto University) was transfected into MEF cells using Lipofectamine 2000. The cells were then seeded onto Mat-tek dishes and imaged by spinning disk confocal microscopy. To acquire GFP and FRET signals, live cells were

excited using a 488 nm laser and signals collected using a 525-50 nm band pass filter (GFP) and 600-50 nm band pass filter (OFP/FRET). Cells were imaged at a medial focal plane (i.e. not in the basal region of the cell) for 1-min at 15 s intervals to establish baseline fluorescence, then perfused with indicated drugs and continuously imaged for another 9-min. Mean fluorescence for GFP and OFP(FRET) channels, as well as OFP/GFP ratio, for a particular ROI (square of 50 μm^2) from each cell (near the nucleus) were calculated for all time points using ImageJ. Ratios of each time point after drug treatment (F) were normalized with the mean initial ratio (first 5 frames before drug treatment) (F_0) and plotted against time as F/F_0. For oligomycin treated samples, data points were normalized to DMSO control curve.

L-Lactate assay from extracellular medium

An assay kit based on the NADH-coupled reduction of tetrazolium salt to formazan (BMR service, University of Buffalo, SUNY, A-108) was used to measure the amount of L-lactate in the extracellular medium.

Drug treatment. For MEFs (wild type, uridine treated, NDUFS4 KO or EtBr) given drug treatments, cells were seeded at 75,000 cells per well in a 96 well plate and allowed to adhere overnight in culture medium. The following day, overnight medium was removed and cells were washed and equilibrated for 1 hour with either 1) high glucose medium - DMEM (Gibco, A1443001) with 25 mM D-glucose, 4 mM L-glutamine, supplemented with no serum or 2) low glucose medium - DMEM (Gibco, A1443001) with 2 mM D-glucose, 4 mM L-glutamine, supplemented with no serum. Next, cells were treated with 1μM CCCP; 1μM CCCP + 100μM CK666; 2.5μM AA; 2.5μM AA + 100μM CK666; 5μM Rotenone; 5μM Rotenone + 100μM CK666 for wild type cells. 100μM CK666 versus volume equivalent DMSO was used for wild type, NDUFS4 KO, uridine treated and EtBr cells. Cell culture medium was withdrawn at various timepoints (1-6 hours) and deproteinized in PEG solution. Samples were assayed with the L-lactate kit according to manufacturer's instruction and OD 492nm was measured using a microplate reader (TECAN infinite M1000). A standard curve ranging from 0 to 1mM L-lactate was plotted for each experiment.

Hypoxia. For hypoxia experiments, MEFs were plated at 100,000 cells per well in a 96 well plate and allowed to adhere overnight at 37°C and 5% CO_2 normoxia conditions while an aliquot of high/low glucose medium was placed inside the 1% O_2 hypoxia chamber for oxygen depletion overnight. The following day, cells were brought into the hypoxia chamber, their pre-existing medium removed and treated with 100μM CK666 or DMSO containing hypoxic high/low glucose medium. Samples were taken at various timepoints (1-6 hours), deproteinized and assayed for L-lactate concentration.

For T_{eff} in hypoxic conditions, 400,000 cells were seeded per well in a poly-D-lysine treated 96 well plate and allowed to adhere and equilibrate for 1 hour at 37°C and 5% CO_2 normoxia in high/low glucose medium (with additional 1mM sodium pyruvate) before being brought inside the hypoxia chamber. Cells were then treated with either CK666 or DMSO containing hypoxic high/low glucose medium. An additional condition with 5mM D-glucose also performed for T_{eff}.

ATP assays from cell extracts

A luciferase-based assay was used (BMR service, University of Buffalo, SUNY, A-125). MEFs were plated at 1×10^6 cells per well in 60mm cell culture dishes and incubated for two days in standard medium (Corning DMEM containing 25 mM glucose, 10% FBS), resulting in 5.75 x 10^6 cells/dish for MEFs. On the day of extraction, cells were washed and incubated for 1 hour in Agilent Seahorse XF DMEM (103575-100, with 4mM L-glutamine, no sodium pyruvate or serum) supplemented with 25mM glucose (high glucose condition) or 1mM glucose (low glucose condition) before treatment with: DMSO, 1μM CCCP; 100μM CK666 + 1μM CCCP; or 100μM CK666 for 2 mins. Cells were lysed immediately with 10% TCA and washed 3 times with 1:1 ether pre-saturated in TE (10mM Tris-HCl and 1mM EDTA, pH 8) for sample deproteinization. Samples were diluted 8-fold in water and ATP assay then assays conducted followed manufacturer's instructions. The luminescence intensity was measured in a microplate reader (BioTek Synergy Neo2). A standard curve with ATP standards ranging from 0 -10μM was plotted for every experiment. The μM value of ATP determined in each assay was converted to a mM cellular value using the cell number stated above and an estimated cellular volume of 6 pL, obtained for Cos7 cells [609].

Seahorse assay

A Seahorse XFe96 Bioanalyser (Agilent) was used to determine oxygen consumption rate (OCR) and extracellular acidification rate (ECAR) for MEFs and activated $CD8^+$ cells. MEFs, taken from a T75 flask at 70-80% confluency and in culture for three days, were plated at 40,000 per well onto an Agilent XF microplate (101085-004) in DMEM (Corning; 10-013-CV) + 10% FBS medium, 24 hr before the experiment. Medium was changed 1-hour before the start of readout into 180 μL serum-free assay medium (Agilent Seahorse XF DMEM; 103575-100) supplemented with 4mM L-glutamine (Corning; 25-005-CI) and a variable amount of glucose (Agilent; 103577-100). The reading and injection regime was as follows: 1) Baseline OCR and ECAR were measured for 15min (6 measurements); 2) injection of CCCP (1μM final), CK666 (100μM final), or CK666 + CCCP; 3) measuring for 38 min (15 measurements); 4) injection of 50mM final 2-DG (Sigma Aldrich; D3179); 5) measuring for 18 minutes (7 measurements). Measurement parameters: 30 sec mix, 0 wait and 2 mins measure. For each experiment, three wells were done for CCCP or CK666 alone and four wells for CCCP + CK666. Stock concentrations: 10 mM

CCCP (in DMSO), 20 mM CK666 (in DMSO), 500 mM 2-DG (in glucose free medium). CCCP and CK666 were diluted to 10x stocks in the appropriate medium and 20 mL injected (final DMSO concentration 0.5%). 22 mL 2-DG injected. "ΔECAR initial" represents the difference between the first measurement after the first injection and the last measurement before the injection, which represents a time span of approximately 2.5 min post-injection. "ΔECAR 40 min" represent the difference between the last measurement after the first injection and the last measurement before the first injection, which represents a time span of approximately 38 min post-injection.

For MEF treated with rotenone (Sigma; R8875) and antimycin A (Sigma; A8674), the reading and injection regime was as follows: 1) Baseline OCR and ECAR were measured for 30min (12 measurements); 2) injection of antimycin A (2.5μM final), CK666 (100μM final), or CK666 + antimycin A, rotenone (5μM final), or CK666 + rotenone or DMSO (volume equivalent to CK666); 3) measuring for 3 hours 22 mins (45 measurements); 4) injection of 50mM final 2-DG; 5) measuring for 30 minutes (12 measurements). Measurement parameters: 30 sec mix, 0 wait and 2 mins measure for baseline and 2-DG treatments, 30 sec mix, 0 wait and 4 mins measure for drug treatment. For each experiment, at least three wells were done for each condition. Stock concentrations for antimycin A and rotenone: 10 mM (in ethanol) and 10mM (in DMSO) respectively.

For MEF treated with oligomycin (Sigma; 75351) and CGP-37157 (CGP, Sigma; C8874), the reading and injection regime was as follows: 1) Baseline OCR and ECAR were measured for 24min (6 measurements); 2) injection of oligomycin (1.5μM final), CK666 (100μM final), or CK666 + oligomycin, CGP (80μM final), CGP + oligomycin, CCCP (1μM final), CK666 + CCCP, CGP + CCCP or DMSO (volume equivalent to oligomycin); 3) measuring for 1 hours 15 mins (15 measurements); 4) injection of 50mM final 2-DG; 5) measuring for 24 minutes (6 measurements). Measurement parameters: 2 min mix, 0 wait and 2 mins measure for baseline, drug and 2-DG treatments. For each experiment, at least three wells were done for each condition. Stock concentrations for oligomycin and CGP: 10mM (in DMSO) respectively.

For T_{eff}, 150,000 cells (activated with anti-CD3 and anti-CD28 antibodies 48 hours prior) were plated into individual wells of a poly-D-lysine coated seahorse cell culture microplate (Agilent; 101085-004). T cell culture medium was changed 1 hour before the start of readout into 180μL serum-free assay medium (Agilent Seahorse XF DMEM; 103575-100) supplemented with 4mM L-glutamine, 1mM sodium pyruvate and either 2mM or 25mM glucose. The reading and injection regime was as follows: 1) Baseline OCR and ECAR were measured for 42min (12 measurements); 2) injection of various treatments, with the concentration same as MEFs: CCCP, CK666, CK666 + CCCP, antimycin A, CK666 + antimycin A, rotenone, CK666 + rotenone or

DMSO (volume equivalent to CK666); 3) measuring for 2 hours 38 min (45 measurements); 4) injection of 50mM final 2-DG; 5) measuring for 42 minutes (12 measurements). Measurement parameters: 30 sec mix, 0 wait and 3 mins measure. For each experiment, at least three wells were done for each condition.

Statistical analysis and graph plotting software

All statistical analyses and P value determinations were conducted using GraphPad Prism QuickCalcs or GraphPad Prism 9 (version 9.2.0, GraphPad Software). For P values in multiple comparisons (two way unpaired t-test; one or two-way ANOVA), Tukey's multiple comparisons test was performed in GraphPad Prism 9. Scatter plots for TMRE, L-lactate assays were plotted with GraphPad Prism 9. ECAR and OCR curves, along with the standard deviation (s.d.); live-cell actin burst, along with the standard errors of the mean (s.e.m.) were all plotted using Microsoft Excel for Office 365 (version 16.0.11231.20164, Microsoft Corporation). Exact P values, sample size N and the number of independent experiments for each analysis are provided in Supplementary Table 1 on the preprint server (https://doi.org/10.1101/2022.06.03.494723).

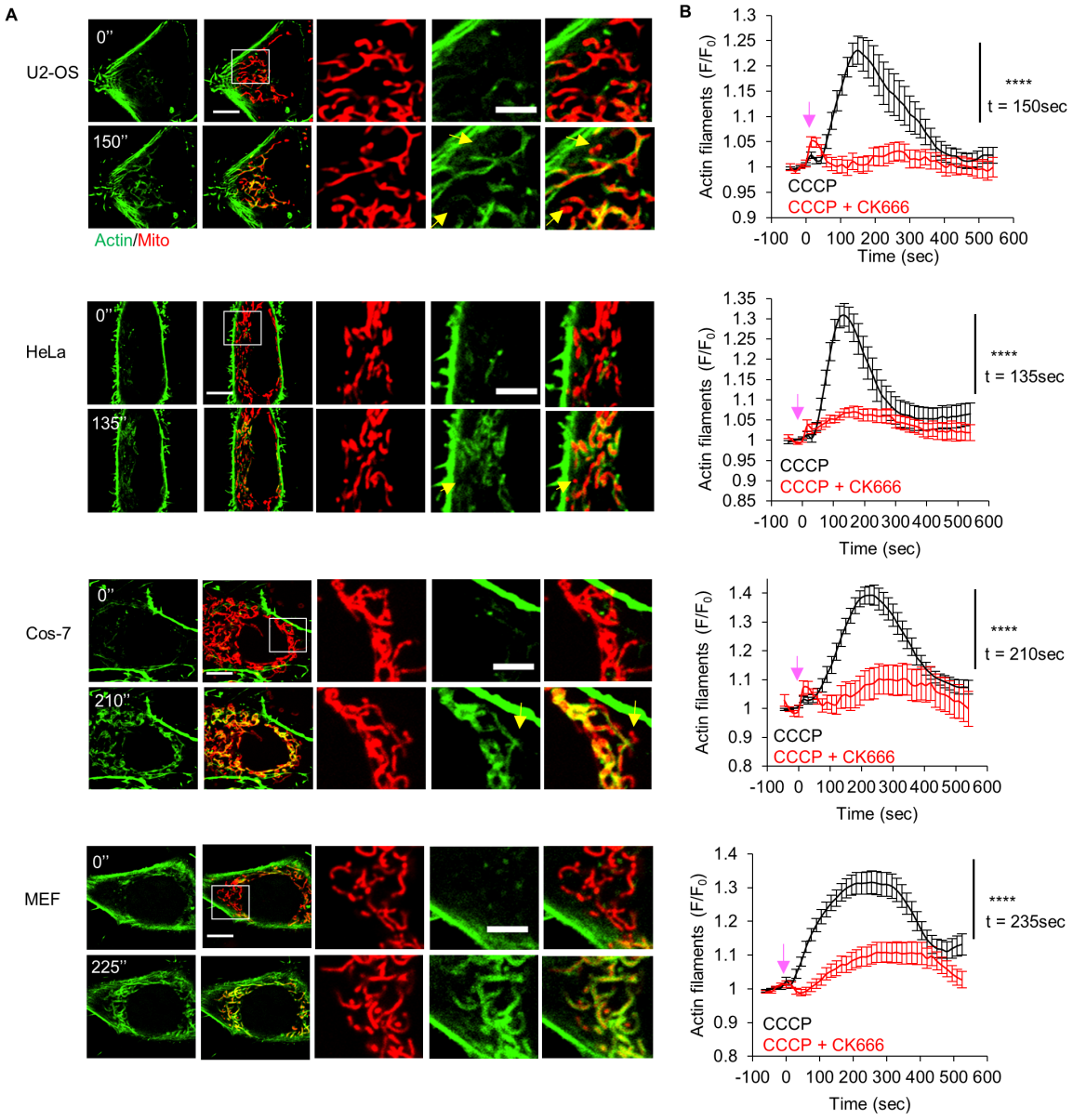

Figure 4.1: ADA in multiple cell types. A) Micrographs of live-cell imaging for U2-OS, HeLa, Cos-7 and MEF cell before (0 sec) and at their peak ADA timepoints after 20µM CCCP addition (150sec – U2-OS; 135sec -HeLa; 210sec – Cos-7; 225sec – MEF). All cells were transfected with markers for actin filaments (GFP-Ftractin, green) and mitochondria (mito-DsRed, red). Scale bars are 10 µm (full cell), 5 µm (inset). Yellow arrow indicates punctate mitochondrion without actin assembly. **B)** Graph of actin intensity (± s.e.m.) around mitochondria in U2-OS, HeLa, Cos7 and MEF cells as a function of time of 20µM CCCP or 100µM CK666 + 20µM CCCP simultaneous treatment. Cells per condition: U2-OS, n = 31; HeLa, n = 32; Cos-7, n ≥ 17; MEF, n ≥ 22. Arrows indicate time of treatment. **** $P < 0.0001$. Experiments done in 25mM glucose with serum.

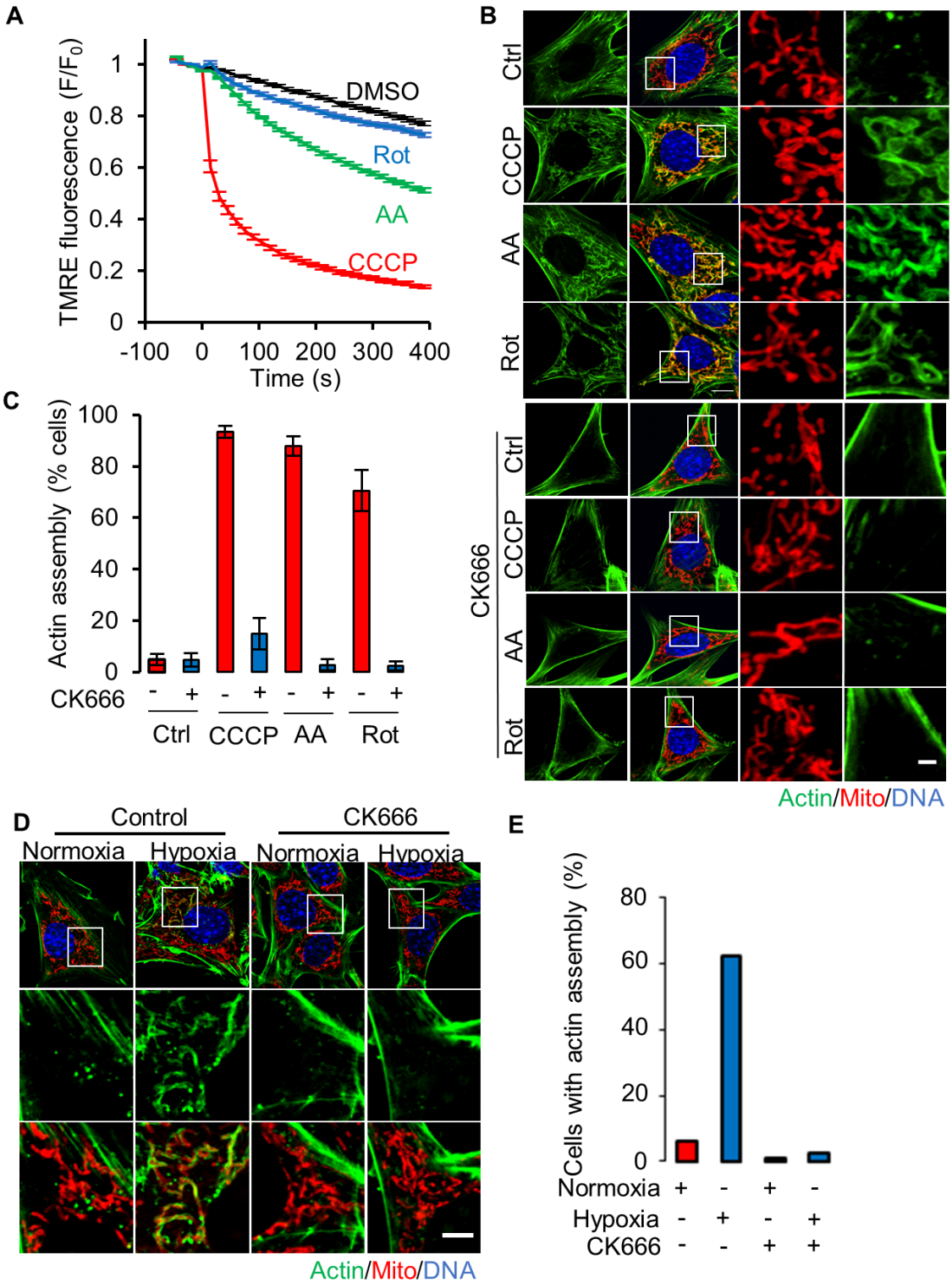
A
TMRE fluorescence (F/F0)
1
0.8
0.6
0.4
0.2
0
-100
0
100
200
300
400
Time (s)
DMSO
Rot
AA
CCCP
B
Ctrl
CCCP
AA
Rot
CK666
Ctrl
CCCP
AA
Rot
Actin/Mito/DNA
C
Actin assembly (% cells)
100
80
60
40
20
0
CK666
- + - + - + - +
Ctrl
CCCP
AA
Rot
D
Control
CK666
Normoxia
Hypoxia
Normoxia
Hypoxia
Actin/Mito/DNA
E
Cells with actin assembly (%)
80
60
40
20
0
Normoxia + - + -
Hypoxia - + - +
CK666 - - + +

Figure 4.2: ADA stimulation by mitochondrial depolarization or ETC inhibition. A) Mitochondrial depolarization (assessed by TMRE fluorescence) in MEFs with DMSO, CCCP, antimycin A or rotenone (± s.e.m.) treatments. n ≥ 98 cells per group. Experiments done in 25mM glucose with serum. **B)** MEFs stained for actin filaments (TRITC-phalloidin, green), mitochondria (Tom20, red) and DNA (DAPI, blue) after 3 min treatment with DMSO, 20μM CCCP, 25μM antimycin A or 50μM rotenone in the absence (top) or presence (bottom) of 100μM CK666. Right images are zooms of boxed regions. Scale bar: 5 μm. **C)** % cells (± s.d.) displaying ADA for the conditions shown in (**B**). n ≥ 62/18 cells/fields of view (FOV) per group. Experiments done in 25mM glucose with serum. **D)** MEFs stained similarly to B, in normoxia or hypoxia for 30 min, in presence of absence of 100μM CK-666. Scale bar: 5 μm. **E)** % cells displaying ADA after 30 min normoxia or hypoxia, in the absence or presence of 100μM CK-666. n ≥ 174/20 cells/FOV per group. Experiments done in 25mM glucose without serum.

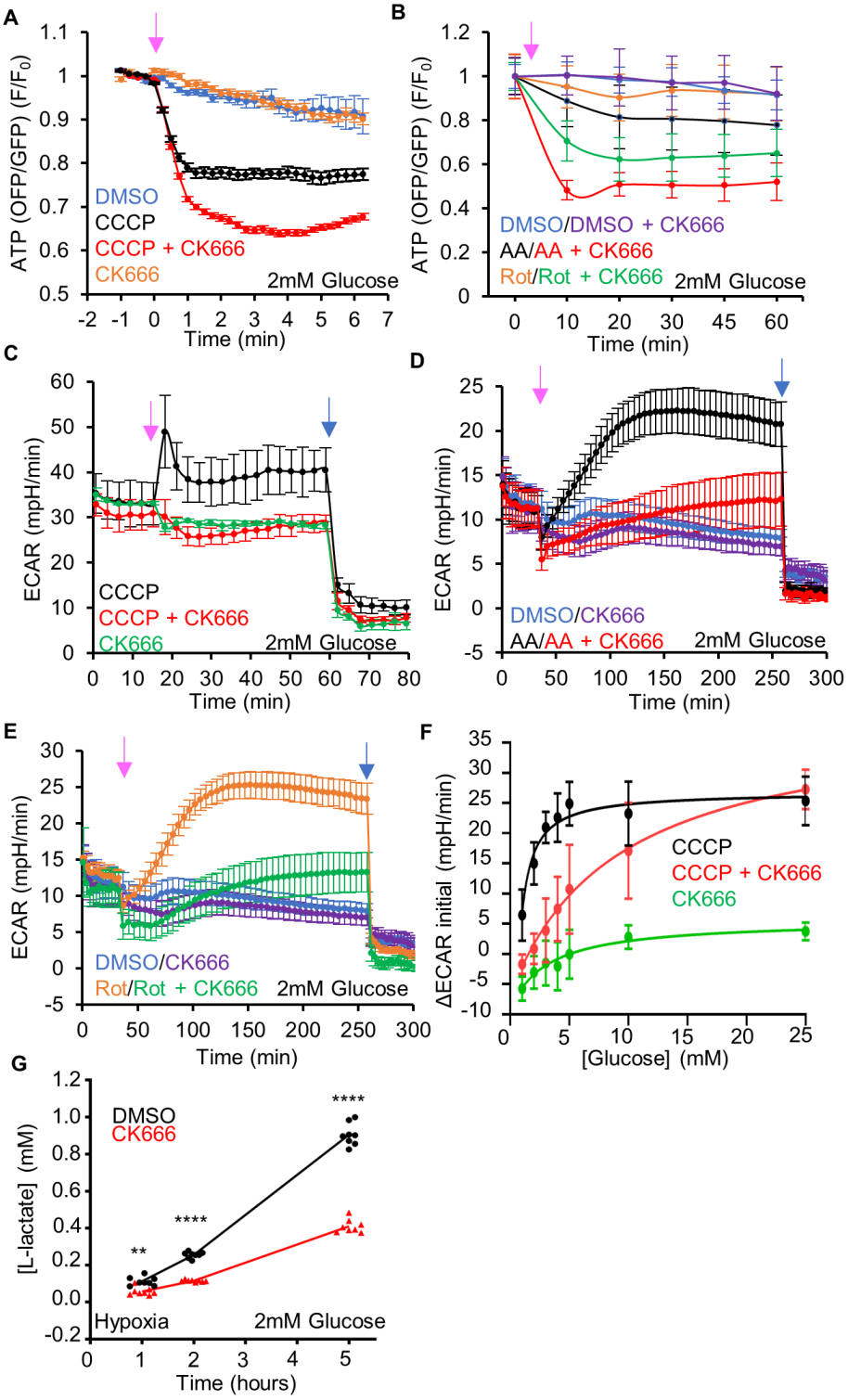
A
ATP (OFP/GFP) (F/F0)
DMSO
CCCP
CCCP + CK666
CK666
2mM Glucose
Time (min)
B
ATP (OFP/GFP) (F/F0)
DMSO/DMSO + CK666
AA/AA + CK666
Rot/Rot + CK666
2mM Glucose
Time (min)
C
ECAR (mpH/min)
CCCP
CCCP + CK666
CK666
2mM Glucose
Time (min)
D
ECAR (mpH/min)
DMSO/CK666
AA/AA + CK666
2mM Glucose
Time (min)
E
ECAR (mpH/min)
DMSO/CK666
Rot/Rot + CK666
2mM Glucose
Time (min)
F
ΔECAR initial (mpH/min)
CCCP
CCCP + CK666
CK666
[Glucose] (mM)
G
[L-lactate] (mM)
DMSO
CK666
**
****
****
Hypoxia
2mM Glucose
Time (hours)

Figure 4.3: ADA is required for glycolytic activation upon mitochondrial perturbation in MEFs. A) Cytoplasmic ATP levels (± s.e.m.) after 20μM CCCP in the absence or presence of 100μM CK666, using GO-ATeam1. n ≥ 35 cells per group. P values graphed in **Figure S4.3A**. Arrow indicates time of treatment. Experiments done in 2mM glucose with serum. **B)** Cytoplasmic ATP levels (± s.e.m.) after 25μM antimycin A or 50μM rotenone in the absence or presence of 100μM CK666, using GO-ATeam1. n ≥ 24 cells per group. P values graphed in **Figure S4.3C**. Arrow indicates time of treatment. Experiments done in 2mM glucose with serum. **C)** ECAR (± s.d.) upon 100μM CK666, 1μM CCCP or 1μM CCCP + 100μM CK666 addition (15 min), followed by 50mM 2-deoxyglucose (2-DG) (59 min) in 2mM glucose medium without serum. Pink arrow indicates drug treatment and blue arrow indicate 2-DG treatment. **D)** ECAR (± s.d.) upon DMSO, 100μM CK666, 2.5μM antimycin A or 2.5μM antimycin A + 100μM CK666 addition (33 min), then 50mM 2-DG (258 min) in 2mM glucose medium without serum. Pink arrow indicates drug treatment and blue arrow indicate 2-DG treatment. **E)** ECAR (± s.d.) upon DMSO, 100μM CK666, 5μM rotenone or 5μM rotenone + 100μM CK666 addition (33 min), then 50mM 2-DG (258 min) in 2mM glucose medium without serum. Pink arrow indicates drug treatment and blue arrow indicate 2-DG treatment. **F)** Effect of glucose concentration on ECAR spike (± s.d.) induced by 3 min 1μM CCCP, with and without 100μM CK666. P values graphed in **Figure S4.4D**. **G)** Effect of 100μM CK666 on lactate production in hypoxia (1% O_2) in MEFs at 2mM glucose without serum. Points indicate individual well measurements starting with 100,000 cells/well. ** P = 0.0018. **** P < 0.0001.

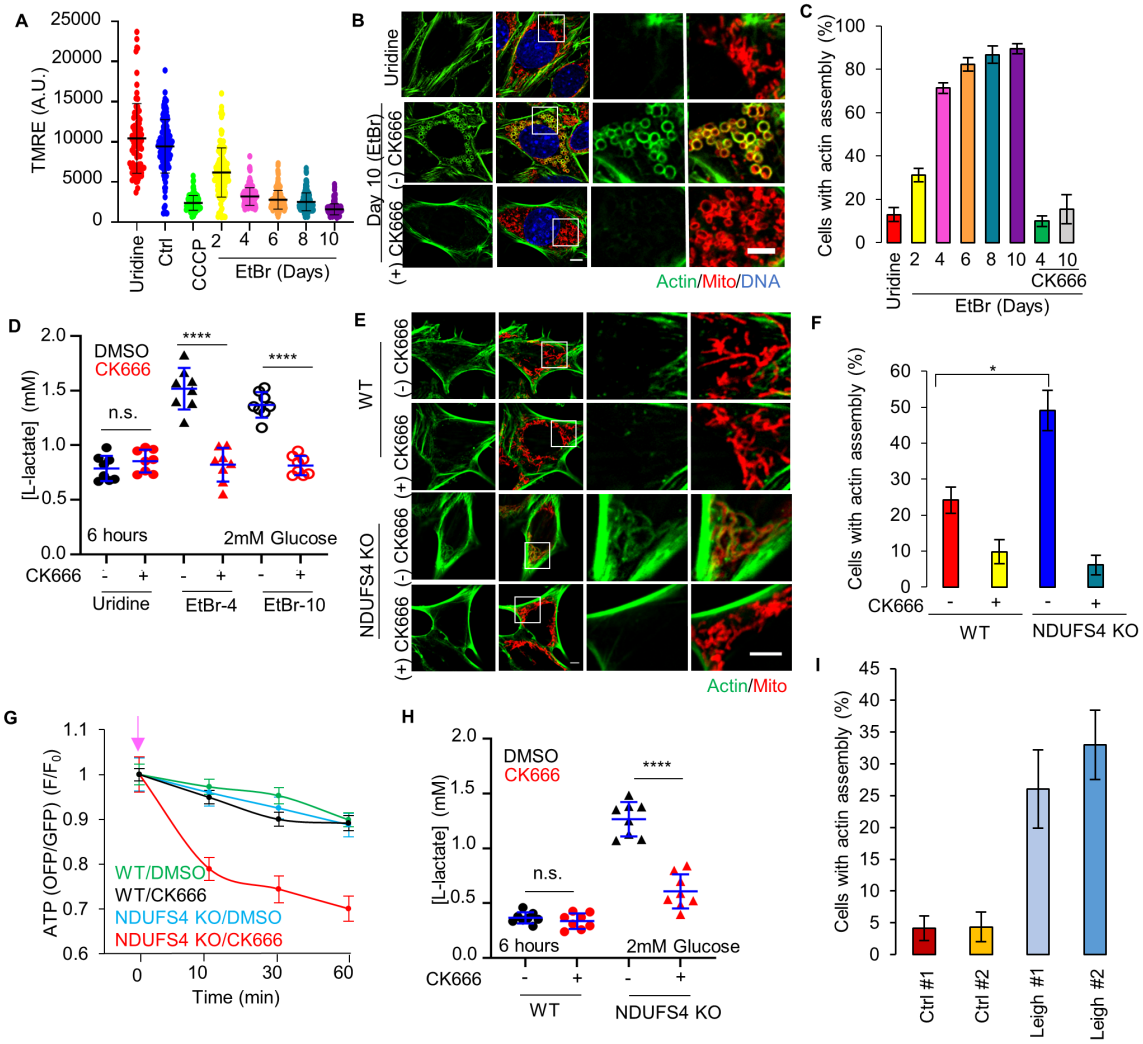
A
TMRE (A.U.)
Uridine
Ctrl
CCCP
EtBr (Days)
B
Uridine
Day 10 (EtBr)
(-) CK666
(+) CK666
Actin/Mito/DNA
C
Cells with actin assembly (%)
Uridine
EtBr (Days)
CK666
D
[L-lactate] (mM)
DMSO
CK666
n.s.
****
6 hours
2mM Glucose
CK666
Uridine
EtBr-4
EtBr-10
E
WT
NDUFS4 KO
(-) CK666
(+) CK666
Actin/Mito
F
Cells with actin assembly (%)
CK666
WT
NDUFS4 KO
G
ATP (OFP/GFP) (F/F0)
WT/DMSO
WT/CK666
NDUFS4 KO/DMSO
NDUFS4 KO/CK666
Time (min)
H
[L-lactate] (mM)
DMSO
CK666
n.s.
****
6 hours
2mM Glucose
CK666
WT
NDUFS4 KO
I
Cells with actin assembly (%)
Ctrl #1
Ctrl #2
Leigh #1
Leigh #2

Figure 4.4: Actin assembly in ETC protein depleted cells. A) Mitochondrial polarization in MEFs (± s.d.) after 0.2 μg/ml ethidium bromide (EtBr)/50 μg/ml uridine treatment. Ctrl, untreated. Uridine, uridine treatment alone (10 days). CCCP - 10 min 20μM CCCP treated Ctrl cells. Circles indicate individual cell measurements (n ≥ 86 cells per group). Experiments done in 25mM glucose with serum. **B)** MEFs under uridine alone or ethidium bromide/uridine treatment (EtBr) for 10 days, stained for actin filaments (green) and mitochondria (red). Scale bar: 5 μm. **C)** % cells (± s.d.) displaying actin assembly after time in ethidium bromide/uridine, with and without 100μM CK666. n ≥ 98/15 cells/fields of view (FOV) per group. Experiments done in 25mM glucose with serum. **D)** Lactate production (± s.d.) in ethidium bromide cells (4 days, EtBr-4; 10 days, EtBr-10) and uridine-treated control (10 days), with and without 100μM CK666 after 6 hours. Points indicate individual well measurements starting with 75,000 cells/well. n.s. $P > 0.05$. **** $P < 0.0001$. Experiments done in 2mM glucose without serum. **E)** WT and NDUFS4 KO MEFs stained for actin filaments (green) and mitochondria (red). Scale bar: 5 μm. **F)** % cells (± s.d.) displaying actin assembly in WT and NDUFS4 KO MEFs, with and without 10 minutes of 100μM CK666 treatment. n ≥ 70/12 cells/FOVs per group. * $P=0.018$. Experiments done in 25mM glucose with serum. **G)** Cytosolic ATP levels in WT or NDUFS4 KO MEFs upon 100μM CK666 treatment. n ≥ 30 cells per group. Arrow indicates drug treatment. Experiments done in 25mM glucose with serum. **H)** Lactate production (± s.d.) in WT and NDUFS4 KO cells, with and without 100μM CK666 after 6 hours. n.s. $P > 0.05$. **** $P < 0.0001$. Points indicate individual well measurements starting with 75,000 cells/well. Experiments done in 2mM glucose without serum. **I)** % cells (± s.e.m.) displaying actin assembly in control or Leigh syndrome patient fibroblasts. n ≥ 76/13 cells/FOVs per group. Experiments done in 25mM glucose with serum. Statistical tests are tabled in **Figure S4.10B**.

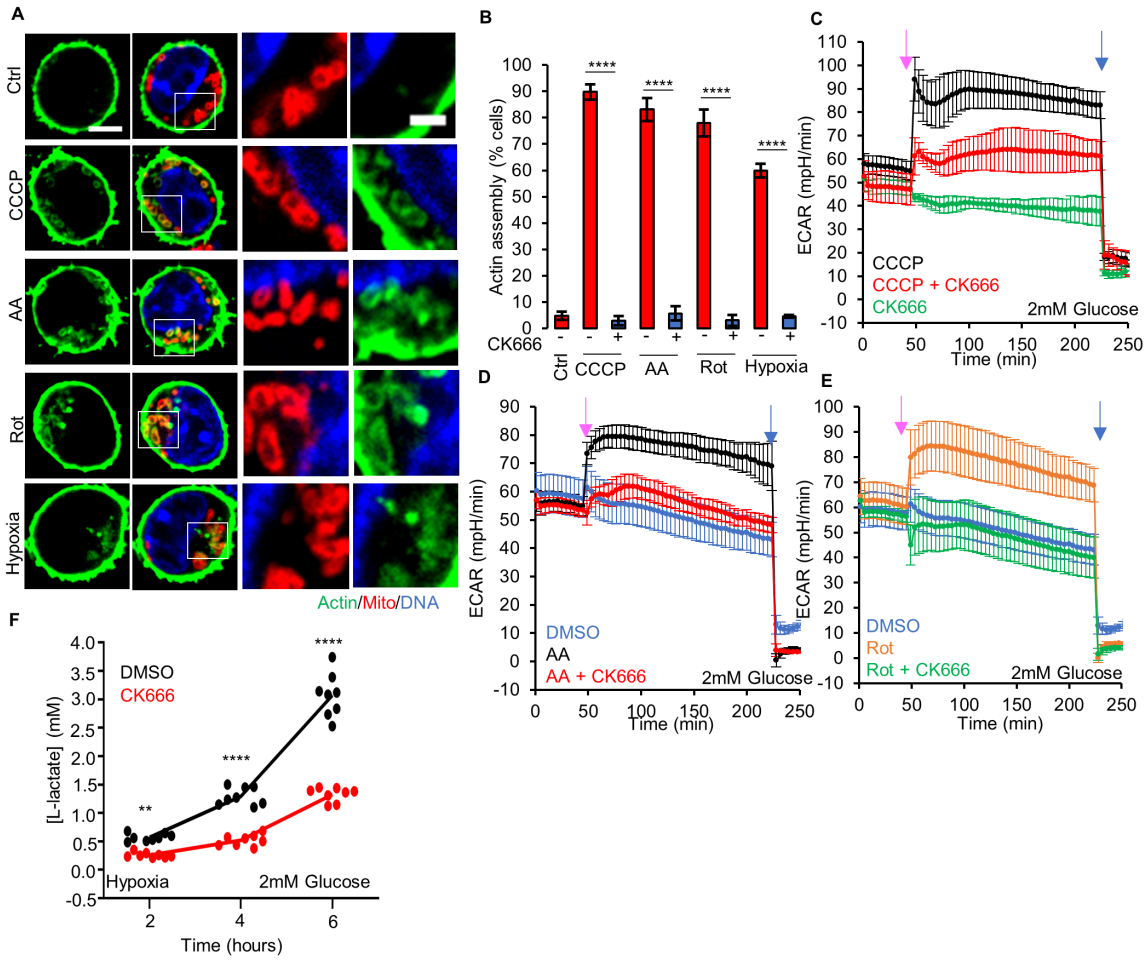
A
Ctrl
CCCP
AA
Rot
Hypoxia
Actin/Mito/DNA
B
Actin assembly (% cells)
CK666
Ctrl
CCCP
AA
Rot
Hypoxia
C
ECAR (mpH/min)
CCCP
CCCP + CK666
CK666
2mM Glucose
Time (min)
D
ECAR (mpH/min)
DMSO
AA
AA + CK666
2mM Glucose
Time (min)
E
ECAR (mpH/min)
DMSO
Rot
Rot + CK666
2mM Glucose
Time (min)
F
[L-lactate] (mM)
DMSO
CK666
Hypoxia
2mM Glucose
Time (hours)

Figure 4.5: Effector T lymphocytes (T_{eff}) require ADA for glycolytic activation. A) T_{eff} stained for actin filaments (TRITC-phalloidin, green), mitochondria (Tom20, red) and DNA (DAPI, blue) under un-stimulated conditions, or after treatment with 3 min 1μM CCCP, 5min 2.5μM antimycin A, 5 5μM min rotenone, or 60 min hypoxia in 2mM glucose medium. Right images are zooms of boxed regions. Scale bars: 5μm (full cell) and 2μm (inset). **B)** % cells (±s.e.m.) displaying ADA in treatments described in A, n ≥ 61/5 cells/FOV per group. **** P<0.0001. Experiments done in 2mM glucose without serum. **C)** ECAR (±s.d.) in T_{eff} upon addition of 100μM CK666, 1μM CCCP or 1μM CCCP + 100μM CK666 (45 min), followed by 50mM 2-deoxyglucose (2-DG)(223 min) in 2mM glucose medium without serum. Pink arrow indicates drug treatment and blue arrow indicate 2-DG treatment. **D)** ECAR (±s.d.) in T_{eff} upon addition of DMSO, 2.5μM antimycin A or 2.5μM antimycin A + 100μM CK666 (45 min), followed by 50mM 2-DG (223 min) in 2mM glucose medium without serum. Pink arrow indicates drug treatment and blue arrow indicate 2-DG treatment. **E)** ECAR (±s.d.) in T_{eff} upon addition of DMSO, 5μM rotenone or 5μM rotenone + 100μM CK666 (45 min), followed by 50mM 2-DG (223 min) in 2mM glucose medium without serum. Pink arrow indicates drug treatment and blue arrow indicate 2-DG treatment. **F)** Lactate production (2mM glucose without serum) induced by hypoxia (1% oxygen) in T_{eff} in the presence or absence of 100μM CK666 addition. Circles indicate individual well measurements starting with 400,000 cells/well. ** P=0.0013. **** P<0.0001.

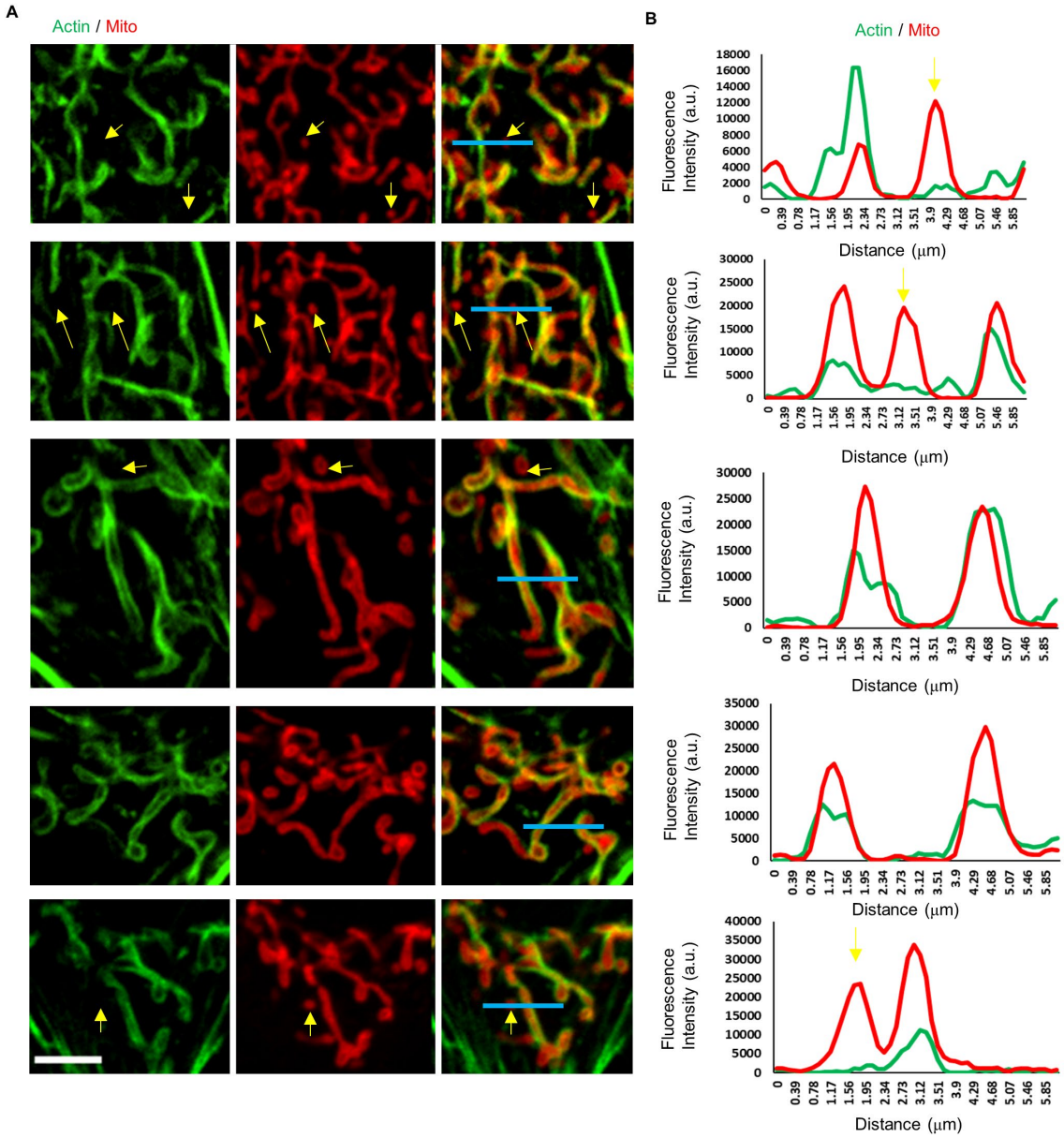

Figure S4.1: Line scans of ADA MEFs. A) Micrographs of actin assembly around mitochondria in fixed MEFs, stained for actin (green) and mitochondria (red). Scale bar: 5μm. Blue lines represent the region for line scans in **(B)**. Yellow arrows indicate punctate mitochondria without actin assembly. **B)** Line scans showing the fluorescent intensity for actin and mitochondria signal across each mitochondrion as shown in **(A)**.

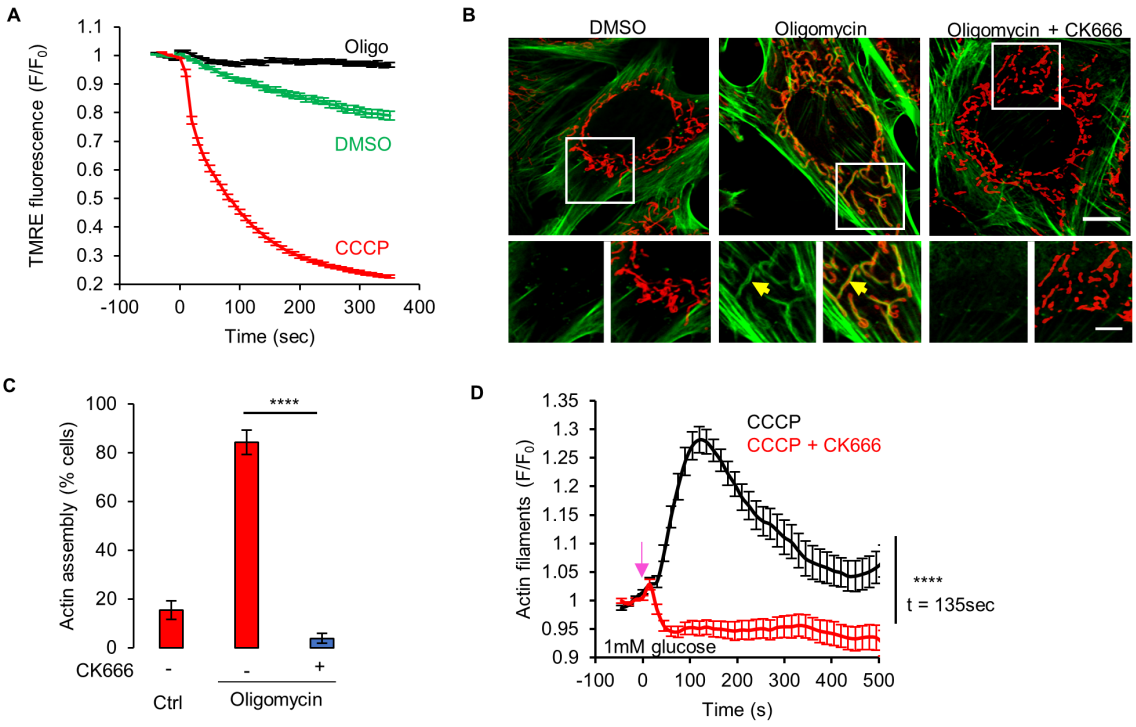

Figure S4.2: Oligomycin-induced ADA in MEFs. A) Mitochondrial polarization (assessed by TMRE fluorescence) in MEFs with DMSO, 1µM CCCP or 1.5µM oligomycin (± s.e.m.) treatment. n ≥ 118 cells per group. Experiments done in 2mM glucose without serum. **B)** MEFs stained for actin filaments (TRITC-phalloidin, green), mitochondria (Tom20, red) and DNA (DAPI, blue) after 5 min treatment with DMSO, 1.5µM oligomycin or 1.5µM oligomycin with 100µM CK666. Bottom images are zooms of boxed regions. Experiments done in 2mM glucose without serum. Scale bars: 10 µm and 5 µm. Arrow indicate actin assembly. **C)** % cells (± s.e.m.) displaying ADA for the conditions shown in (**B**). n ≥ 65/14 cells/fields of view (FOV) per group. **** P<0.0001. Experiments done in 2mM glucose without serum. **D)** Graph of actin intensity (± s.e.m.) around mitochondria in MEF cells as a function of time for 1µM CCCP or 100µM CK666 + 1µM CCCP simultaneous treatment. Cells were cultured in Agilent seahorse DMEM supplemented with 1mM glucose and 4mM glutamine but without serum for 1 hour before imaging. n ≥ 35 cells per condition. Arrow indicates time of treatment. **** P<0.0001.

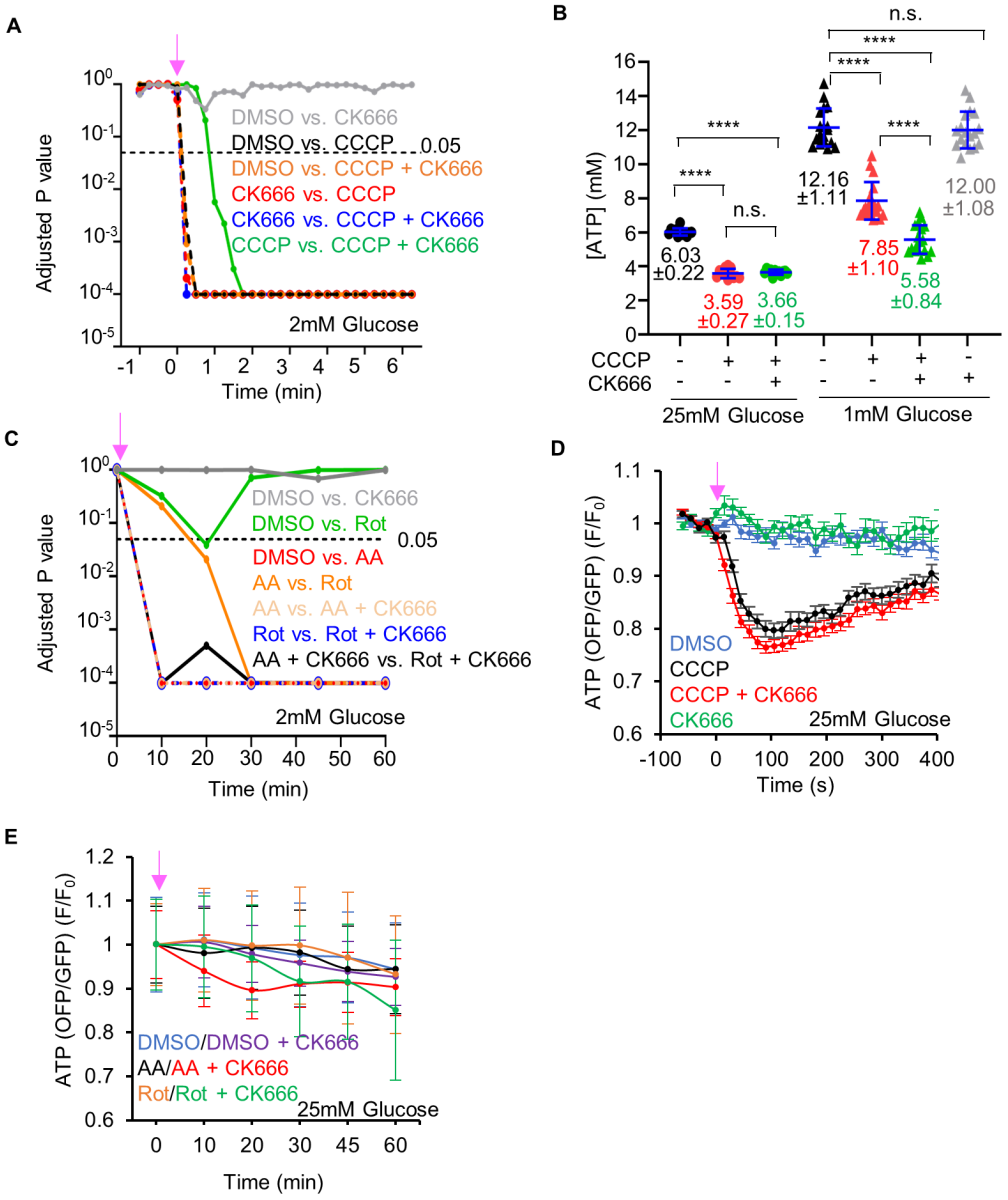
A
Adjusted P value
DMSO vs. CK666
DMSO vs. CCCP
0.05
DMSO vs. CCCP + CK666
CK666 vs. CCCP
CK666 vs. CCCP + CK666
CCCP vs. CCCP + CK666
2mM Glucose
Time (min)
B
[ATP] (mM)
n.s.
****
****
****
****
****
n.s.
6.03 ±0.22
3.59 ±0.27
3.66 ±0.15
12.16 ±1.11
7.85 ±1.10
5.58 ±0.84
12.00 ±1.08
CCCP
CK666
25mM Glucose
1mM Glucose
C
Adjusted P value
DMSO vs. CK666
DMSO vs. Rot
0.05
DMSO vs. AA
AA vs. Rot
AA vs. AA + CK666
Rot vs. Rot + CK666
AA + CK666 vs. Rot + CK666
2mM Glucose
Time (min)
D
ATP (OFP/GFP) (F/F0)
DMSO
CCCP
CCCP + CK666
CK666
25mM Glucose
Time (s)
E
ATP (OFP/GFP) (F/F0)
DMSO/DMSO + CK666
AA/AA + CK666
Rot/Rot + CK666
25mM Glucose
Time (min)

Figure S4.3: ATP levels changes by complex I or III inhibition. A) Graph of P values for comparisons of GO-ATeam1 timecourses in Fig 3 A (CCCP or CCCP/CK666 treatment of MEFs in 2mM glucose). **B)** ATP levels (± s.d.) in MEFs upon DMSO, 1µM CCCP or 1µM CCCP + 100µM CK666 treatments in medium containing either 1mM or 25mM glucose without serum, assayed from cell extracts. Points indicate individual measurements starting with 10^6 cells/dish. n ≥ 12 measurements for each group. n.s. $P > 0.05$. **** $P < 0.0001$. **C)** Graph of P values for comparisons of GO-ATeam1 timecourses in **Figure 4.3B** (antimycin A and rotenone treatments of MEFs in 2mM glucose). **D)** Graph of change in ATP levels (± s.e.m.) in live MEFs stimulated with 20µM CCCP in the absence or presence of 100µM CK666, using GO-ATeam1 biosensor. Cells cultured in medium containing 25mM glucose with serum. n ≥ 20 cells for each group. Arrow indicates time of treatment. **E)** Graph of change in ATP levels (± s.e.m.) in live MEFs stimulated with 25µM antimycin A or 50µM rotenone in the absence or presence of 100µM CK666, using GO-ATeam1 biosensor. Cells cultured in medium containing 25mM glucose with serum. n ≥ 33 cells for each group. Arrow indicates time of treatment.

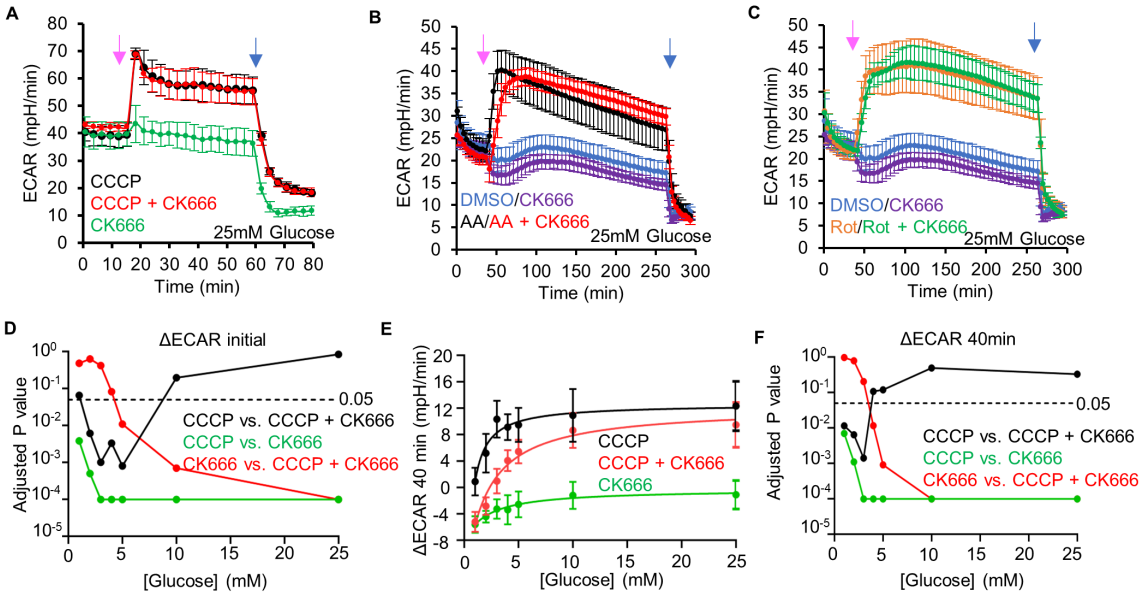

Figure S4.4: Changes in ECAR in MEFs after mitochondrial inhibitor treatments. A) ECAR (± s.d.) upon 100µM CK666, 1µM CCCP or 1µM CCCP + 100µM CK666 addition (15 min), followed by 50mM 2-DG (59 min) in 25mM glucose medium without serum. Pink arrow indicates drug treatment and blue arrow indicate 2-DG treatment. **B)** ECAR (± s.d.) upon DMSO, 100µM CK666, 2.5µM antimycin A or 2.5µM antimycin A + 100µM CK666 addition (33 min), then 50mM 2-DG (258 min) in 25mM glucose medium without serum. Pink arrow indicates drug treatment and blue arrow indicate 2-DG treatment. **C)** ECAR (± s.d.) upon DMSO, 100µM CK666, 5µM rotenone or 5µM rotenone + 100µM CK666 addition (33 min), then 50mM 2-DG (258 min) in 25mM glucose medium without serum. Pink arrow indicates drug treatment and blue arrow indicate 2-DG treatment. **D)** P values for comparisons between individual curves in **Figure 4.3F**. **E)** Effect of glucose concentration (± s.d.) on prolonged ECAR increase (after 40 min) induced by 1µM CCCP or 1µM CCCP + 100µM CK666 in MEFs. P values graphed in (**F**). **F)** P values for comparisons between individual curves in (**E**).

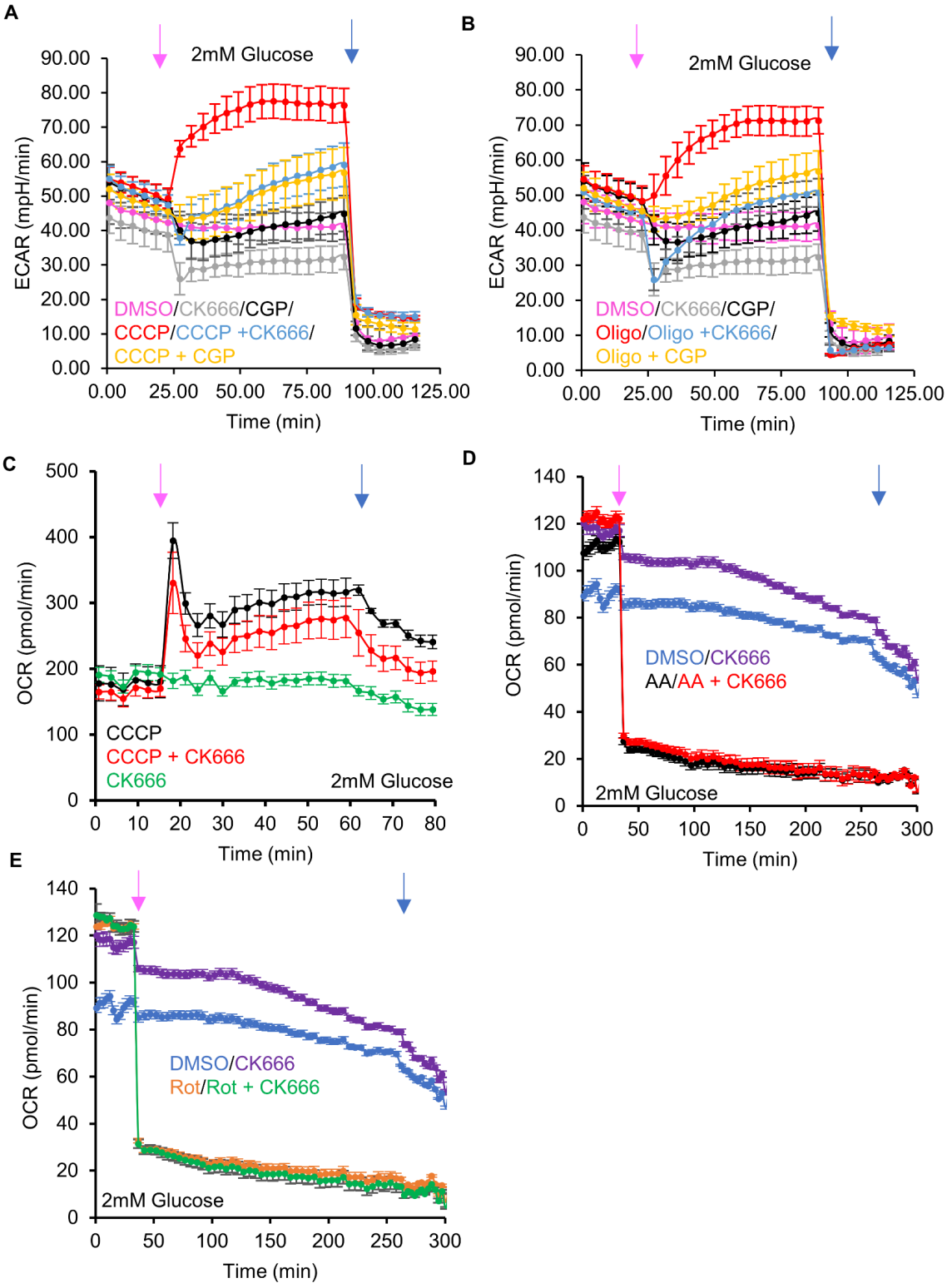
A
2mM Glucose
ECAR (mpH/min)
Time (min)
DMSO/CK666/CGP/
CCCP/CCCP +CK666/
CCCP + CGP
B
2mM Glucose
ECAR (mpH/min)
Time (min)
DMSO/CK666/CGP/
Oligo/Oligo +CK666/
Oligo + CGP
C
OCR (pmol/min)
Time (min)
CCCP
CCCP + CK666
CK666
2mM Glucose
D
OCR (pmol/min)
Time (min)
DMSO/CK666
AA/AA + CK666
2mM Glucose
E
OCR (pmol/min)
Time (min)
DMSO/CK666
Rot/Rot + CK666
2mM Glucose

Figure S4.5 Effect of NCLX inhibition on CCCP- and oligomycin-activated glycolysis. A) ECAR (± s.d.) upon DMSO, 100μM CK666, 80 μM CGP37157, 1μM CCCP, 1μM CCCP + 100μM CK666 addition or 1μM CCCP + 80μM CGP37157 addition (at 23 min, pink arrow), followed by 50mM 2-DG (at 89 min, blue arrow) in 2mM glucose medium without serum. **B)** ECAR (± s.d.) upon DMSO, 100μM CK666, 80 μM CGP37157, 1.5μM oligomycin, 1μM oligomycin + 100μM CK666 addition or 1μM oligomycin + 80μM CGP37157 addition (at 23 min, pink arrow), followed by 50mM 2-DG (at 89 min, blue arrow) in 2mM glucose medium without serum. **C)** OCR (± s.d.) in MEFs (in 2mM glucose without serum) upon 100μM CK666, 1μM CCCP or 1μM CCCP + CK666 addition at 15 min, then 50mM 2-DG at 59 min. Pink arrow indicates drug treatment and blue arrow indicates 2-DG treatment. **D)** OCR (± s.d.) in MEFs (in 2mM glucose without serum) upon DMSO, 100μM CK666, 2.5μM antimycin A or 2.5μM antimycin A + 100μM CK666 addition at 33 min, then 50mM 2-DG at 258 min. Pink arrow indicates drug treatment and blue arrow indicates 2-DG treatment. **E)** OCR (± s.d.) in MEFs (in 2mM glucose without serum) upon DMSO, 100μM CK666, 2.5μM rotenone or 2.5μM rotenone + 100μM CK666 addition at 33 min, then 50mM 2-DG at 258 min. Pink arrow indicates drug treatment and blue arrow indicates 2-DG treatment.

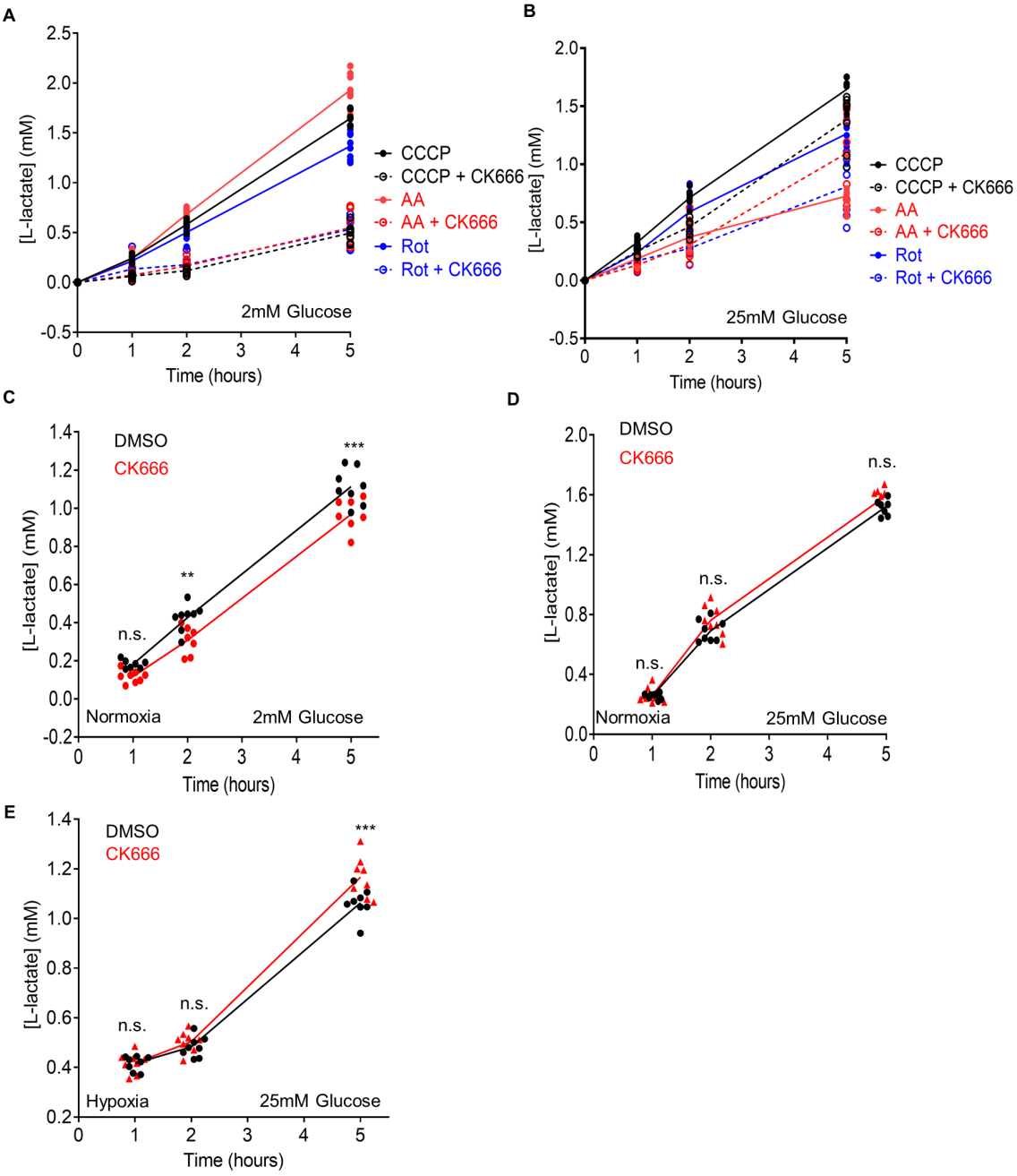
A
[L-lactate] (mM)
Time (hours)
2mM Glucose
CCCP
CCCP + CK666
AA
AA + CK666
Rot
Rot + CK666
B
[L-lactate] (mM)
Time (hours)
25mM Glucose
CCCP
CCCP + CK666
AA
AA + CK666
Rot
Rot + CK666
C
DMSO
CK666
n.s.
**
***
Normoxia
2mM Glucose
[L-lactate] (mM)
Time (hours)
D
DMSO
CK666
n.s.
n.s.
n.s.
Normoxia
25mM Glucose
[L-lactate] (mM)
Time (hours)
E
DMSO
CK666
n.s.
n.s.
***
Hypoxia
25mM Glucose
[L-lactate] (mM)
Time (hours)

Figure S4.6. Changes in lactate production induced by mitochondrial inhibitors and hypoxia in MEFs. A) Effect of 100μM CK666 on lactate production upon 1μM CCCP, 2.5μM antimycin A, or 5μM rotenone treatment of MEFs in 2mM glucose without serum. Points indicate individual well measurements starting with 75,000 cells/well. **B)** Effect of 100μM CK666 on lactate production upon 1μM CCCP, 2.5μM antimycin A, or 5μM rotenone treatment of MEFs in 25mM glucose without serum. Points indicate individual well measurements starting with 75,000 cells/well. **C)** Effect of 100μM CK666 on lactate production in normoxia (21% O_2) in MEFs at 2mM glucose without serum. Points indicate individual well measurements starting with 100,000 cells/well. n.s. $P > 0.05$. ** $P = 0.002$. *** $P = 0.0002$. **D)** Effect of 100μM CK666 on lactate production in normoxia in MEFs at 25mM glucose without serum. Points indicate individual well measurements starting with 100,000 cells/well. n.s. $P > 0.05$. **E)** Effect of 100μM CK666 on lactate production in hypoxia in MEFs at 25mM glucose without serum. Points indicate individual well measurements starting with 100,000 cells/well. n.s. $P > 0.05$. *** $P = 0.0003$.

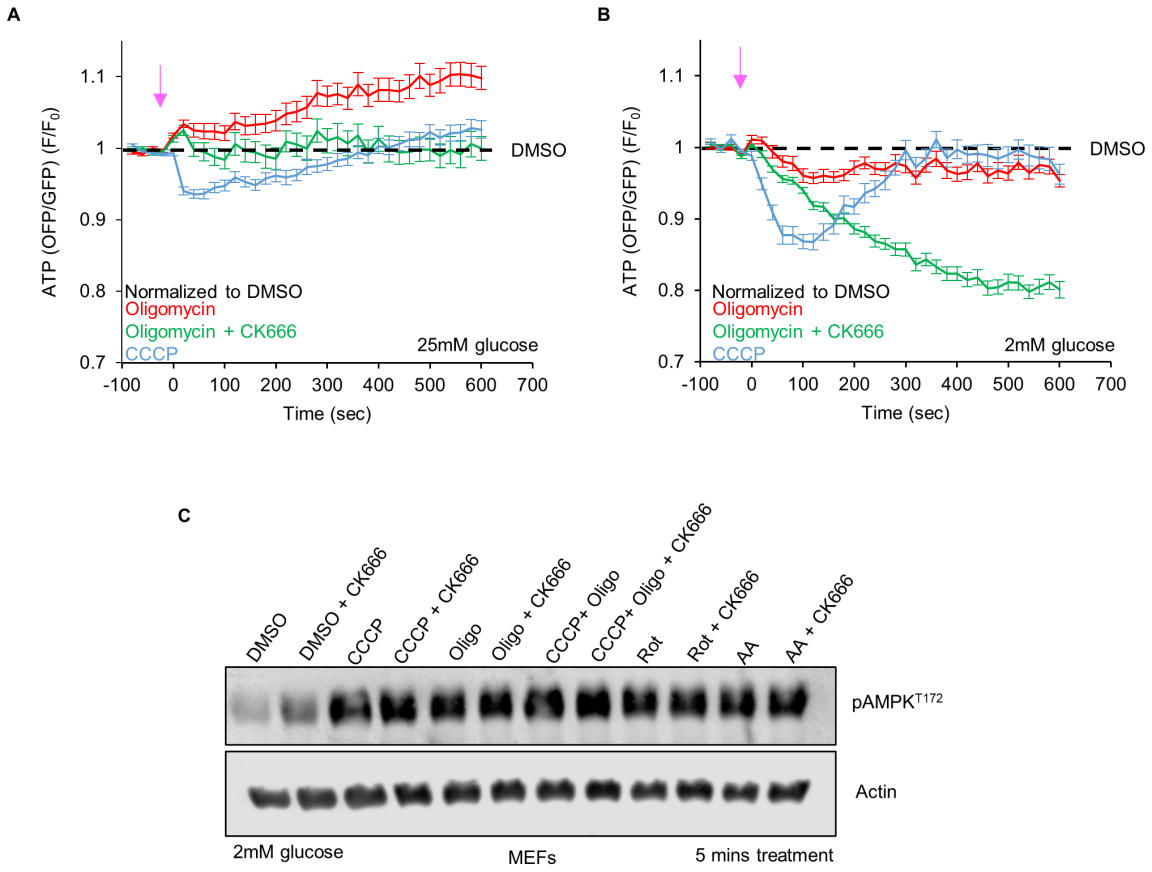

Figure S4.7. Cytoplasmic ATP changes induced by ATP synthase inhibition. A) Cytoplasmic ATP levels (± s.e.m.) after 1.5μM oligomycin in the absence or presence of 100μM CK666, or 1μM CCCP using GO-ATeam1. Data were normalized to DMSO control. n ≥ 24 cells per group. Arrow indicates time of treatment. Experiments done in 25mM glucose without serum. **B)** Cytoplasmic ATP levels (± s.e.m.) after 1.5μM oligomycin in the absence or presence of 100μM CK666, or 1μM CCCP using GO-ATeam1. Data were normalized to DMSO control. n ≥ 24 cells per group. Arrow indicates time of treatment. Experiments done in 2mM glucose without serum. **C)** AMPK activation after 5 min treatment of MEFs with ETC or ATP synthase inhibition. Actin is used as a loading control. Experiments done in 2mM glucose without serum.

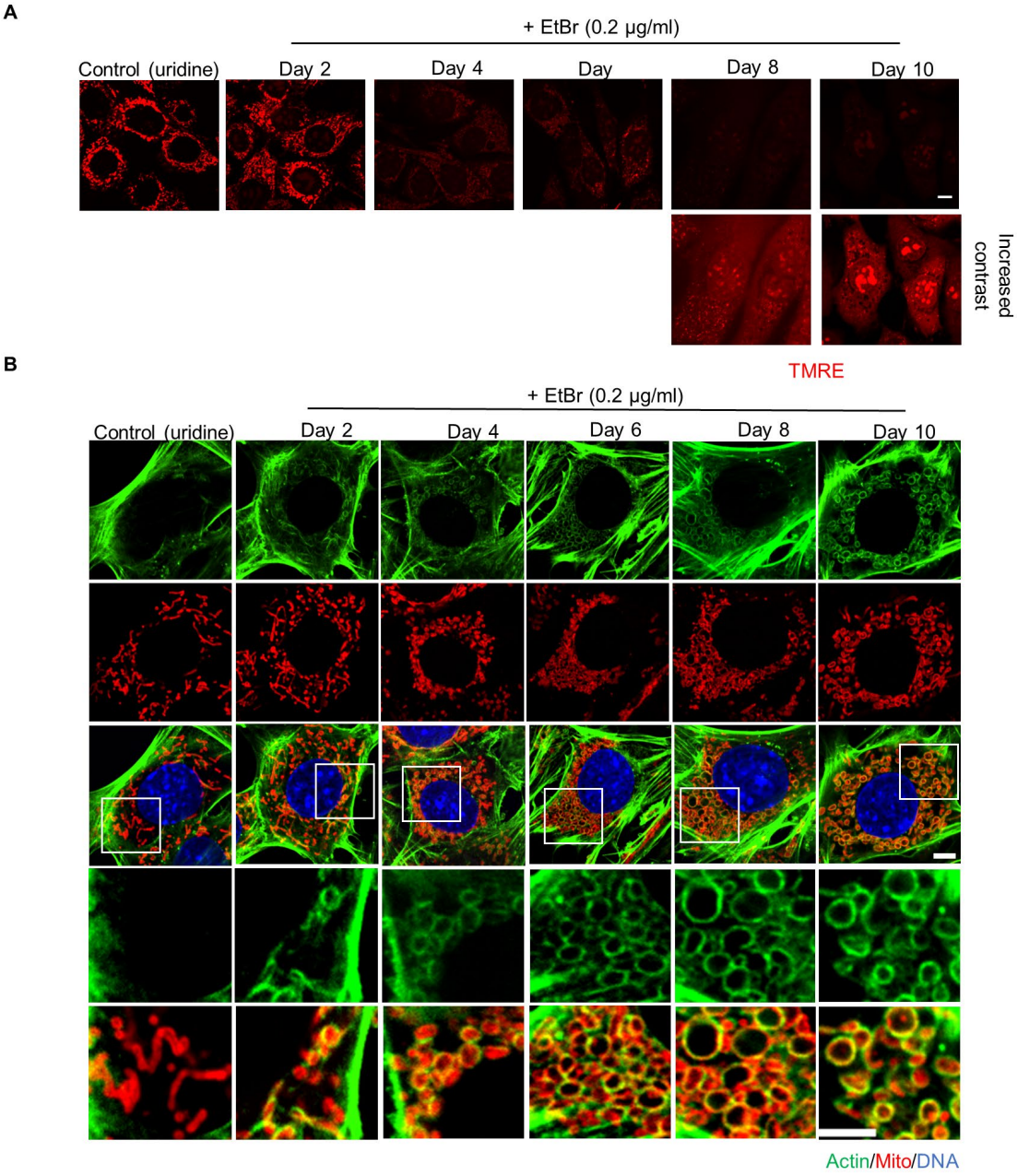
A
+ EtBr (0.2 μg/ml)
Control (uridine)
Day 2
Day 4
Day
Day 8
Day 10
Increased contrast
TMRE
B
+ EtBr (0.2 μg/ml)
Control (uridine)
Day 2
Day 4
Day 6
Day 8
Day 10
Actin/Mito/DNA
C
MEF-EtBr (Day 10)
(-) CK666
(+) CK666- 5 min
Actin/Mito

Figure S4.8: ADA and mitochondrial depolarization in EtBr-treated cells. A) Micrographs of TMRE staining of EtBr-treated cells at varying days post-treatment or control cells treated with uridine for 10 days. For days 8 and 10 post-EtBr treatment, the images below represent increased processing to reveal the presence of cells. Scale bar: 5 μm. **B)** Micrographs of actin staining (TRITC-phalloidin, green) around mitochondria (Tom20, red) at different days of EtBr treatment. DNA is stained with DAPI (blue). Images at the bottom are zooms of the boxed region. Scale bars: 5 μm. **C)** Micrographs of actin staining (TRITC-phalloidin, green) around mitochondria (Tom20, red) at day 10 of EtBr treatment with or without 100μM CK666 for 5min before fixation. Images at the right are zooms of the boxed region. Scale bars: 5 μm.

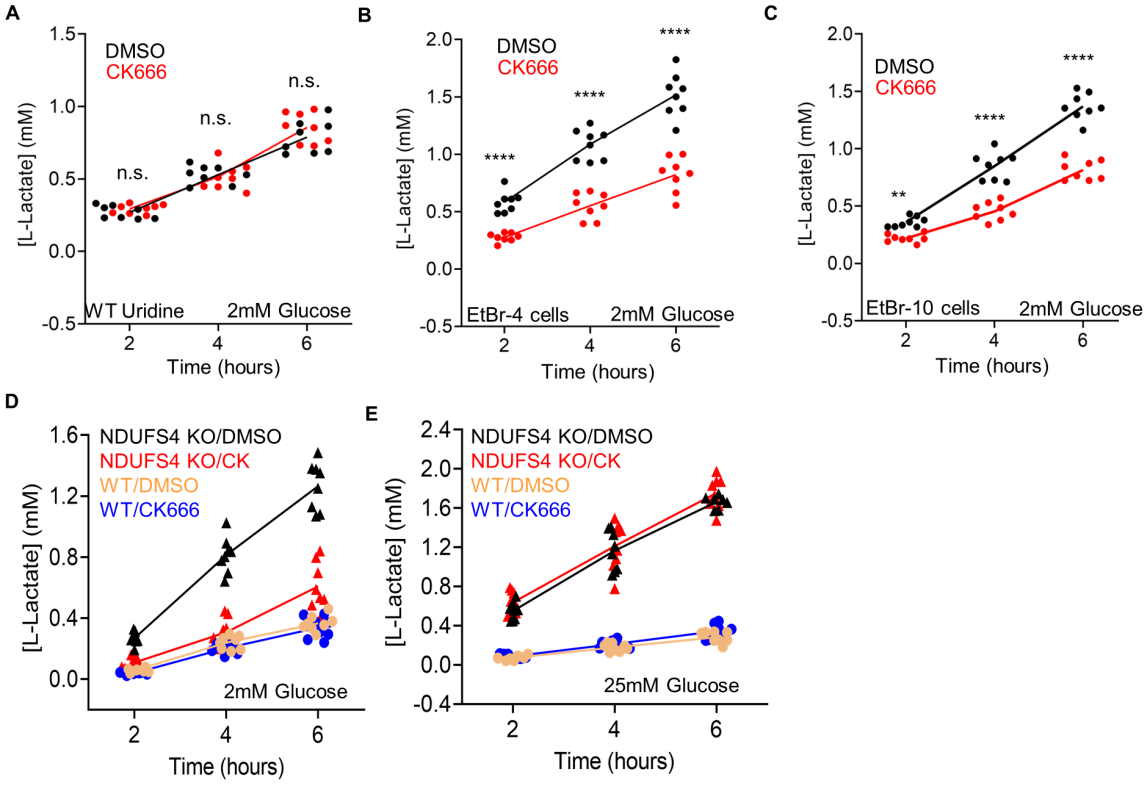

Figure S4.9: Changes in lactate production in EtBr or NDUFS4 KO MEFs. A) Time course of lactate production from control cells (uridine-treated and in 2mM glucose without serum) in the presence or absence of 100µM CK666. Points indicate individual well measurements starting with 75,000 cells/well. n.s. $P > 0.05$. **B)** Time course of lactate production from EtBr-4 cells (in 2mM glucose without serum) in the presence or absence of 100µM CK666. Points indicate individual well measurements starting with 75,000 cells/well. **** $P < 0.0001$. **C)** Time course of lactate production from EtBr-10 cells (in 2mM glucose without serum) in the presence or absence of 100µM CK666. Points indicate individual well measurements starting with 75,000 cells/well. ** $P = 0.0024$. **** $P < 0.0001$. **D)** Time course of lactate production from WT and NDUFS4 KO cells (in 2mM glucose without serum) in the presence or absence of 100µM CK666. Points indicate individual well measurements starting with 75,000 cells/well. **E)** Time course of lactate production from WT and NDUFS4 KO cells (in 25mM glucose without serum) in the presence or absence of 100µM CK666. Points indicate individual well measurements starting with 75,000 cells/well.

A

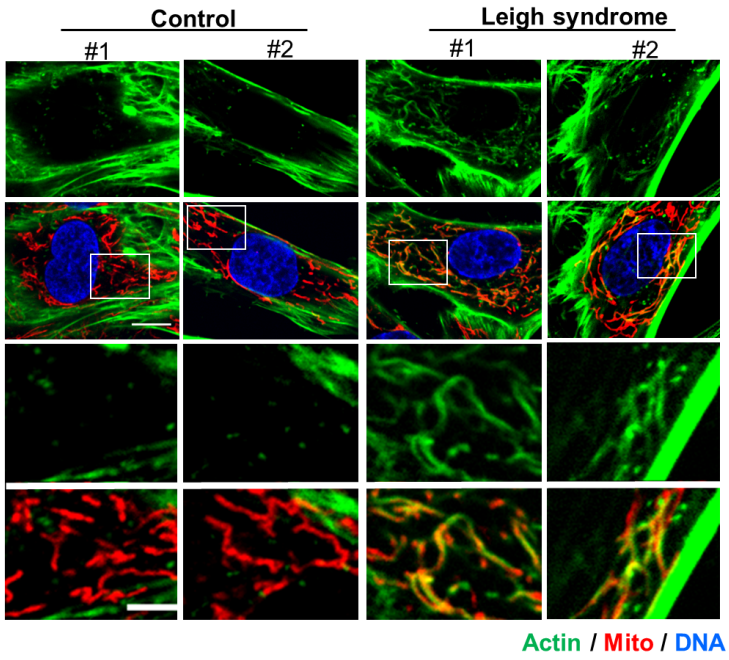

B

	Mean Diff.	t,df	95% CI of diff.	Summary	P Value
Control vs. Leigh #1	21.80 ± 5.80	t=3.761, df=47	10.14 to 33.46	***	0.0005
Control vs. Leigh #2	28.77 ± 4.91	t=5.863, df=14	18.88 to 38.65	****	<0.0001

Figure S4.10: Actin assembly in Leigh syndrome fibroblasts. A) Micrographs of actin staining (TRITC-phalloidin, green) around mitochondria (Tom20, red) for control and Leigh syndrome fibroblasts. Scale bars are 10µm (full cell) and 5µm (inset). **B)** Table giving P values for comparisons of graph in **Figure 4.4I** using unpaired student's t test. Ctrl #1-2 were combined for analysis.

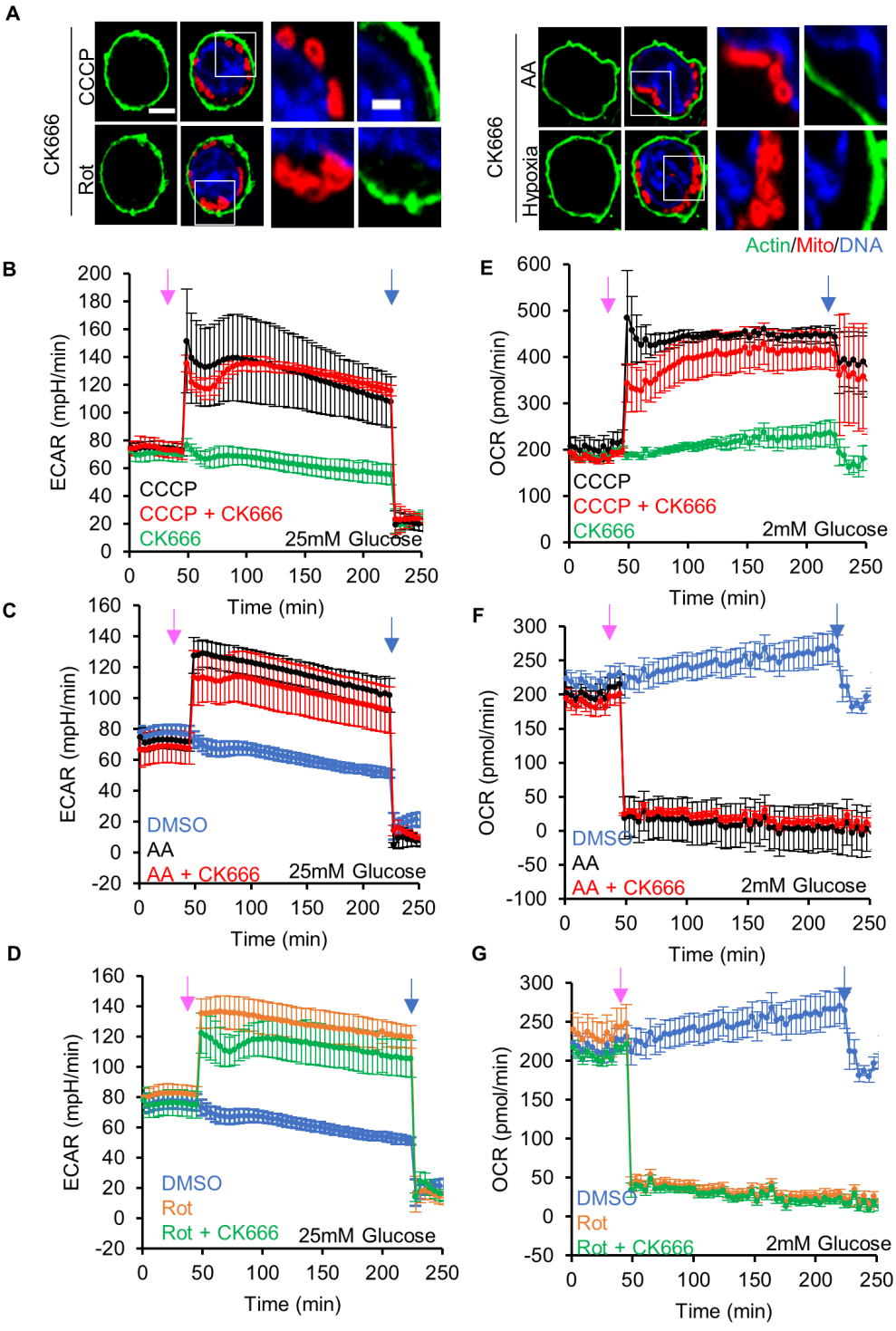
A
CK666
CCCP
Rot
CK666
AA
Hypoxia
Actin/Mito/DNA
B
ECAR (mpH/min)
CCCP
CCCP + CK666
CK666
25mM Glucose
Time (min)
E
OCR (pmol/min)
CCCP
CCCP + CK666
CK666
2mM Glucose
Time (min)
C
ECAR (mpH/min)
DMSO
AA
AA + CK666
25mM Glucose
Time (min)
F
OCR (pmol/min)
DMSO
AA
AA + CK666
2mM Glucose
Time (min)
D
ECAR (mpH/min)
DMSO
Rot
Rot + CK666
25mM Glucose
Time (min)
G
OCR (pmol/min)
DMSO
Rot
Rot + CK666
2mM Glucose
Time (min)

Figure S4.11: Effect of CK666 on ADA and glycolytic activation in T_{eff}. A) T_{eff} stained for actin filaments (TRITC-phalloidin, green), mitochondria (Tom20, red) and DNA (DAPI, blue) after CCCP, antimycin A, rotenone, or hypoxia in the presence of CK666 for 2mM glucose medium without serum (1μM CCCP + 100μM CK666, 3 min; 2.5μM antimycin A + 100μM CK666 and 5μM rotenone + 100μM CK666, 5 min; hypoxia with 100μM CK666, 60 min). Images at right are zooms of boxed regions. Scale bars: 5μm (full cell) and 2μm (inset). **B)** ECAR (± s.d.) in 25mM glucose without serum upon 100μM CK666, 1μM CCCP or 1μM CCCP + 100μM CK666 addition at 45 min, then 50mM 2-deoxyglucose (2-DG) at 223 min. Pink arrow indicates drug treatment and blue arrow indicates 2-DG treatment. **C)** ECAR (± s.d.) in 25mM glucose without serum upon DMSO, 2.5μM antimycin A or 2.5μM antimycin A + 100μM CK666 addition at 45 min, then 50mM 2-DG at 223 min. Pink arrow indicates drug treatment and blue arrow indicates 2-DG treatment. **D)** ECAR (± s.d.) in 25 mM glucose without serum upon DMSO, 5μM rotenone or 5μM rotenone + 100μM CK666 addition at 45 min, then 50mM 2-DG at 223 min. Pink arrow indicates drug treatment and blue arrow indicates 2-DG treatment. **E)** OCR (± s.d.) in 2mM glucose without serum upon 100μM CK666, 1μM CCCP or 1μM CCCP + 100μM CK666 addition at 45 min, then 50mM 2-DG at 223 min. Pink arrow indicates drug treatment and blue arrow indicates 2-DG treatment. **F)** OCR (± s.d.) in 2mM glucose without serum upon DMSO, 2.5μM antimycin A or 2.5μM antimycin A + 100μM CK666 addition at 45 min, then 50mM 2-DG at 223 min. Pink arrow indicates drug treatment and blue arrow indicates 2-DG treatment. **G)** OCR (± s.d.) in 2 mM glucose without serum upon DMSO, 5μM rotenone or 5μM rotenone + 100μM CK666 addition at 45 min, then 50mM 2-DG at 223 min. Pink arrow indicates drug treatment and blue arrow indicates 2-DG treatment.

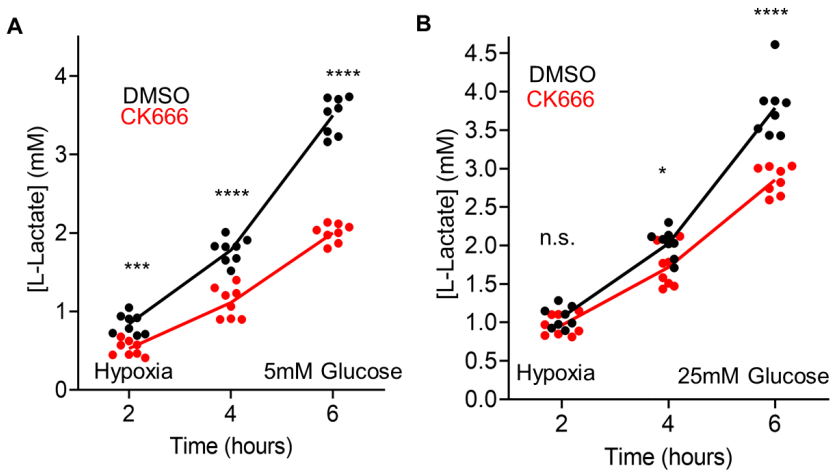

Figure S4.12: Effect of CK666 on hypoxia-induced lactate production in T_{eff}. A) Lactate production induced by hypoxia (1% oxygen) in T_{eff} in the presence or absence of 100µM CK666 addition (5 mM glucose without serum). Circles indicate individual well measurements starting with 400,000 cells/well. *** P = 0.0003. **** P < 0.0001. **B)** Lactate production induced by hypoxia (1% oxygen) in T_{eff} in the presence or absence of 100µM CK666 addition (25mM glucose without serum). Circles indicate individual well measurements starting with 400,000 cells/well. n.s. P > 0.05. * P = 0.0136. **** P <0.0001.

Chapter V:

Peri-mitochondrial actin delays Parkin recruitment in damaged mitochondria

Chapter V

Acute actin polymerization at depolarized mitochondria delays Parkin recruitment.

Tak Shun Fung[1], Rajarshi Chakrabarti[1,2], Henry N. Higgs[1]

[1]Department of Biochemistry and Cell Biology, Geisel School of Medicine at Dartmouth College, Hanover NH, USA

[2]MitoCare Center, Department of Pathology, Anatomy and Cell Biology, Thomas Jefferson University, Philadelphia PA, USA.

Manuscript in preparation.

T.S.F. and R.C. designed and performed experiments, interpreted and analyzed data, and wrote the manuscript.

H.N.H. supervised the project, designed experiments, interpreted and analyzed data, and wrote the manuscript.

5.1 Abstract

Mitochondrial depolarization results in damage to the organelle, which induces a variety of cellular responses. Rapid responses to mitochondrial depolarization (<30mins) include actin polymerization around the depolarized mitochondrion (ADA, acute damaged-induced actin), upregulation of glycolysis, and rearrangement of the inner mitochondrial membrane by a process known as circularization. At longer timepoints (1-2 hours), depolarized mitochondria are eliminated through PINK1/Parkin mitophagy. The relationship between ADA and mitophagy is poorly understood. We show here that ADA inhibits PINK1/Parkin-mediated mitophagy by delaying Parkin recruitment to mitochondria. Conditions that prolong ADA, such as culturing cells in galactose-containing medium to necessitate oxidative phosphorylation, also prolong the delay in Parkin recruitment in a manner overcome by ADA inhibition. The mechanism of this effect may be ADA-mediated disruption of mitochondrial-endoplasmic reticulum contact sites (MERCs), suggested by: 1) ADA causes an acute drop in MERCs, and 2) over-expression of MERC-inducing protein VAP-B overcomes the delay in Parkin recruitment. Lastly, we show that ADA is distinct from a second wave of actin polymerization that occurs after 1-2 hours after mitochondrial depolarization, which we call prolonged damage-induced actin (PDA), in that ADA is independent of two PDA activators: myosin VI and N-WASP. These results suggest that ADA is a first responder after mitochondrial damage, transiently delaying mitophagy by disrupting MERCs, possibly allowing time for mitochondrial recovery.

5.2 Introduction

A major function of mitochondria is to oxidize organic molecules for ATP production, using the mitochondrial membrane potential ($\Delta\psi_m$) generated by the electron transport chain (ETC) across the inner mitochondrial membrane (IMM) to drive ATP synthase [234, 235, 237]. Mitochondria are also important signaling hubs [77, 222, 644], participating in apoptosis, gene expression, host-pathogen response and calcium signaling. $\Delta\psi_m$ is a critical marker of mitochondrial health, and disruption of $\Delta\psi_m$ results in multiple cellular responses that, when severe, lead to pathological consequences [645-647]. Therefore, monitoring and maintaining the $\Delta\psi_m$ is important for cellular health.

Loss of $\Delta\psi_m$ ('mitochondrial depolarization') can occur in several forms. Local depolarization leads to transient mitochondrial contractions [532], which may prevent excessive mitochondrial fusion [648]. Brief episodes of $\Delta\psi_m$ loss also coincide with opening of mitochondrial permeability transition pores (mPTP), which allows cation release from mitochondria but does not lead to significant change in mitochondrial function [649]. However, not all depolarization events are synced with PTP opening [650, 651]. Sustained loss of $\Delta\psi_m$, on the other hand, is considered a cellular crisis and triggers mitochondrial turnover by mitophagy - involving a cascade of reactions including the protein kinase PINK1 and the E3 ubiquitin ligase Parkin [406, 408].

A growing number of studies have documented several important roles for actin filaments in regulation of mitochondrial homeostasis and dynamics (**Chapter II-IV**) [12, 16, 154, 429, 430, 530, 531]. Acute dissipation of $\Delta\psi_m$ using uncouplers like FCCP and CCCP generates a cloud of actin filaments around the depolarized mitochondria within 5 min of depolarization, which we term ADA (acute damage-induced actin) (**Chapter II-IV**) [16]. In addition, prolonged dissipation of the $\Delta\psi_m$, or mitochondrial damage, causes a second round of mitochondrial actin polymerization 1-2 hours after, which we term (prolonged damage-induced actin, PDA) [432, 433].

Both ADA and PDA have been shown to have multiple effects. ADA transiently suppresses mitochondrial dynamics (**Chapter II**). These dynamics involve rearrangement of the inner mitochondrial membrane (IMM) dependent on the IMM protease Oma1, resulting in circularization of the IMM within an intact outer mitochondrial membrane (OMM). ADA inhibits both mitochondrial circularization and proteolytic processing of the Oma1 substrate Opa1. A second ADA function is to rapidly stimulate glycolysis

(**Chapter IV**). PDA on the other hand, inhibits fusion of damaged mitochondria after $\Delta\psi_m$ loss [432], which seals the fate of the damaged mitochondrion through mitophagy. In addition, PDA causes dispersion of mitochondrial clusters, aiding mitophagic engulfment [433].

Both ADA (**Chapter II**) [16] and PDA [432, 433] depend on the actin nucleation factor Arp2/3 complex, but the signaling pathways activating Arp2/3 complex may differ. For ADA, increased cytoplasmic calcium causes protein kinase C-dependent activation of Rac1, in turn activating the Arp2/3 complex activator WAVE (**Chapter III**). In addition to Arp2/3 complex, ADA also requires formin proteins of the FMNL family. Interestingly, PDA depends on myosin VI, a unique actin-based motor protein that moves toward the minus end of actin filaments [652]. Silencing myosin VI resulted in cells with dysfunctional mitochondrial and hampered mitophagy. These cells are unable to proliferate on carbon sources (galactose) that necessitate oxidative phosphorylation (oxphos) [432, 653, 654]. Whether ADA depends on myosin VI as well is currently unknown.

While the cellular roles of PDA appear to enhance mitophagy, the effects of ADA on mitophagy are unknown. In this study, we show that ADA's effect on mitophagy is distinct from PDA. ADA transiently disrupts endoplasmic reticulum (ER)-mitochondrial contacts (MERCs) and this disruption delays Parkin recruitment. Cells grown in galactose also have a more robust ADA response, and delayed Parkin response. These results suggest that ADA serves a contrasting function to PDA, in that it delays mitophagy**.**

5.3 Results

5.3.1 ADA disrupts ER-mitochondrial contact

We have previously shown that ADA occurs around mitochondria within 2 mins of treatment with depolarizing agents like CCCP. Since ADA involves a meshwork of filaments closely associated with mitochondria, we wondered whether ADA might displace other structures in close proximity to mitochondria. Using live-cell microscopy in U2-OS cells expressing fluorescent markers for ER, mitochondria and actin, we find that the actin filaments formed during ADA often occur between mitochondria and ER (**Figure 5.1A; Figure S5.1A**). Moreover, there is a reduction in the overlap between ER and mitochondria during ADA (**Figure 5.1A, B**) suggesting that ADA disrupts ER-mitochondrial interaction. This decrease in ER-mitochondrial overlap correlates temporally with the ADA timecourse, with a transient nadir at ~2min after CCCP addition and returning to near-baseline by 5-min (**Figure 5.1B**). In addition, the effect of CCCP on ER-mitochondrial overlap is disrupted by treatment with the Arp2/3 complex inhibitor CK666 (**Figure 5.1A, B**), suggesting that ADA is responsible for the disruption.

We also tested whether mitochondrial depolarization affected mitochondrial association with another organelle, lysosomes. ADA does not appear to disrupt mitochondrial-lysosomal contacts (**Figure S5.1B, C**), suggesting that ADA's disruption of MERCs is not generalizable for all mitochondrial interactions with other organelle.

We next asked if ADA serves as a diffusive barrier to impede access of cytoplasmic proteins to mitochondria. To test this possibility, we utilized an rapamycin-inducible mitochondrial recruitment system by expressing cytosolic CFP-$(FRB)_5$ (a 82kDa protein) and mitochondrially targeted AKAP1-FKBP-YFP. Upon rapamycin addition, CFP-$(FRB)_5$ is recruited to the OMM in 15-30 sec (**Figure S5.1D, E**). We tested the effect of ADA on recruitment of CFP-$(FRB)_5$ by adding rapamycin at ~100 sec after CCCP addition (corresponds to peak ADA). The rate of CFP-$(FRB)_5$ recruitment is not measurably influenced by ADA (**Figure S5.1F, G**) These results suggest that the actin filaments polymerized during ADA do not physically block access to mitochondria.

We also asked whether inhibiting the two actin polymerization factors required for ADA, Arp2/3 complex and FMNL formins, causes an increased number of MERCs in cells not stimulated with CCCP. For this purpose, we used the SPLICS construct [655], which

fluorescently labels MERCs of 8-10nm or less. Interestingly, knock-down (KD) of either Arp2/3 complex or FMNL formins in U2-OS cells enhanced mitochondrial-ER interactions (**Figure 5.1C, D**). This effect is similar to that produced by over-expressing (OE) the ER-mitochondrial tethering protein VAP-B [656], which we used as a positive control. VAP-B overexpression does not alter CCCP-induced ADA (**Figure S5.2A, B**).

The increase in MERCs caused by KD of ADA activators would be predicted to enhance downstream effects of MERCs. To test MERCs functionally, we performed mitochondrial calcium uptake experiments. Histamine stimulation triggers calcium release from the ER [12, 657] and a subsequent increase in mitochondrial calcium if mitochondria are in close contact [376, 658](**Figure 5.1E; Figure S5.2C**). In both U2-OS and HeLa cells, mitochondrial calcium uptake is increased after Arp2 KD, suggesting Arp2/3 complex-mediated actin inhibits MERCs.

5.3.2 ADA delays Parkin recruitment to depolarized mitochondria

CCCP treatment induces large-scale mitophagy of depolarized mitochondria [407, 412]. Though the final steps of mitophagy occur much later than the initial depolarization (>8 hrs) [659], the early events prepare mitochondria for downstream clearance. One early step is Parkin recruitment, which leads to outer mitochondrial membrane (OMM) protein ubiquitination and recruitment of autophagy receptors [406, 408]. Importantly, previous reports have suggested that a sub-set of Parkin recruitment occurs at MERCs [660, 661]. Since ADA disrupts MERCs, we asked if ADA influences Parkin recruitment.

We examined mitochondrial recruitment kinetics of GFP-Parkin in control, Arp2/3 complex-inhibited and FMNL KD cells by live-cell microscopy, quantifying in two ways: 1) by visual assessment of mitochondrial Parkin intensity deviation from baseline in individual cells, and 2) by trendline analysis of averaged curves. Both methods give similar results (**Table 5.1**), and times listed here are from the first method.

Parkin recruitment to mitochondria in control U2-OS cells starts at 45.5 min ± 10.7 min (mean ± s.d. - first time point which mitochondrial Parkin noticeably deviates from baseline) after 20μM CCCP treatment. All methods of ADA inhibition cause an acceleration of Parkin recruitment, including CK666 (29.4 min ± 9.0 min) (**Figure 5.2A-C**), FMNL DKD (consisting of knocking down FMNL1 and FMNL3 [621]) (32.6 min ±

8.7 min) (**Figure 5.2D-F**), Arp2 KD (31.6 min ± 8.3 min) and WRC KD (33.4 min ± 10.3 min) respectively (**Figure 5.3A-C**). We also evaluated these effects in HeLa cells where CK666 treatment, Arp2 KD or FMNL DKD (consisting of FMNL1 and FMNL2 silencing [621]) causes significantly faster CCCP-induced Parkin recruitment (25.2 min ± 10.9 min, 28.7min ± 6.0 min, and 29.0 min ± 6.1 min, respectively) than control cells (46.3 min ± 12.2 min) (**Figure S5.3**). These results suggest that ADA plays an important role in delaying the initial events in Parkin-mediated mitophagy.

If the mechanism of ADA-mediated Parkin delay involves ADA's role on MERCs, VAP-B OE would be expected to counter-act this effect. Indeed, VAP-B OE accelerates mitochondrial recruitment of Parkin upon CCCP treatment (**Figure 5.3D-F**), to a similar rate to that caused by ADA inhibition. Taken together, these results suggest that MERCs facilitate mitochondrial Parkin recruitment, and that ADA delays Parkin recruitment by transiently disrupting these contacts.

We also tested the effect of ADA on Parkin recruitment in cells that have mitochondria chronically defective in oxphos. We have previously shown that cells treated with Ethidium Bromide (EtBr) for a set duration (4-10 days) exhibit persistent actin polymerization around their mitochondria, similar to ADA (**Chapter IV**). While this mitochondrially-associated actin is present for days, it is removed by a 5 min treatment with CK666, suggesting that the actin must be maintained constantly by active Arp2/3 complex. EtBr leads to drastic depolarization of the mitochondria network (**Chapter IV**). Therefore, we asked whether the ADA-like filaments might prevent Parkin recruitment around the mitochondria, preventing their disposal through mitophagy. Our GFP-Parkin marker is cytosolic in mouse embryonic fibroblasts (MEFs) treated with EtBr (10 days) (**Figure 5.4**), suggesting a block in recruitment despite mitochondria being largely depolarized. However, CK666 treatment results in Parkin accumulation around the mitochondria (**Figure 5.4**). These results suggest that the persistent actin filaments around chronically compromised mitochondria, like ADA, inhibit Parkin recruitment.

5.3.3 Galactose-primed cells have sustained ADA and delayed Parkin recruitment

Cells rely on both oxphos and glycolysis to provide ATP for cellular processes. Although oxphos is the most efficient pathway for energy production, many cultured cell lines, especially those procured from human tumors (U2-OS and HeLa), exhibit high aerobic

glycolysis [662]. Therefore, studies conducted using standard culture media (with supraphysiological glucose) carry the risk of tracking mitochondrial function and mitophagy against a background of upregulated aerobic glycolysis and suppressed oxphos [538]. We wondered what happens to ADA if cells are forced to rely heavily on oxphos for its ATP production. Shifting cellular energy dependency can be achieved by growing cells in galactose media [148, 663], instead of standard glucose-based media. In galactose media, the production of pyruvate via glycolytic metabolism yields no net ATP and the cells are forced to use oxphos of pyruvate or of glutamine for ATP production [653, 654, 664].

We cultured U2-OS and HeLa in glucose-free media containing 10mM galactose, 4mM glutamine, 1mM sodium pyruvate and 10% serum for at least 10 days before experimentation. After 10 days, cells proliferate slower and eventually stops growing after 4-5 passages (data not shown). To assess mitochondrial function in galactose-primed cells, we performed bioenergetic profiling via seahorse assays. Both HeLa and U2-OS cells grown on glucose mainly utilized aerobic glycolysis, as they exhibited a relatively lower basal oxygen consumption rate (OCR) and a relatively higher basal extracellular acidification rate (ECAR) (**Figure S5.4A, B**). In contrast, cells grown on galactose have a significantly higher basal OCR and lower ECAR, which suggest a greater dependence on oxphos (**Figure S5.4A, B**). The maximal OCR for cells in galactose media is also higher than those grown in glucose media, suggesting that the mitochondria have adapted to the absence of extracellular glucose (**Figure S5.4A, B**). We also performed the glycolytic stress test for these two culture conditions. HeLa cells show slight variation in glucose uptake between those in galactose versus those in glucose; but the glycolytic changes for U2-OS are almost the same for both conditions (**Figure S5.4C, D**). We also assessed mitochondrial polarization in both glucose- and galactose-grown HeLa cells, and found that TMRE fluorescence is essentially unchanged (**Figure 5.5A**), suggesting that mitochondria maintain appreciable $\Delta\psi_m$ in both cases.

We followed up with ADA assessment for cells grown in galactose-based media. Curiously, we found that ADA is more robust and sustains for a longer duration in both HeLa and U2-OS cells (**Figure 5.5B-D; Figure S5.5**). For both cell types, actin assembly peaks at a higher level in galactose and persists at an elevated level even after eight minutes (**Figure 5.5B-D; Figure S5.5**).

We next evaluated Parkin recruitment in galactose-primed cells. Similar to findings from earlier studies [548, 665], we found that cells grown in galactose displays a slower Parkin response (**Figure 5.6A, B**) after 25μM CCCP treatment. To address whether lethargic Parkin recruitment is due to sustained ADA, we depolarized the mitochondria in galactose-primed Arp2 KD HeLa cells. In this scenario, we found that Parkin recruitment is sped up once again, having mitochondrial Parkin accumulation on par with their glucose-based counterparts (**Figure 5.6C-E**). These results suggest that ADA assumes greater importance in delaying Parkin recruitment in cells that rely on oxphos for ATP production.

5.3.4 Myosin VI, N-WASP, Spire1C and mDia formins are not required for ADA

In addition to ADA, another round of polymerization (prolonged damaged-induced actin, PDA) occurs after sustained mitochondrial depolarization, within 1-2 hrs. The reported effects of PDA have been to assist mitophagy [432, 433].

In HEK-293 cells transfected with mCherry-Parkin in an OE system, we found PDA assembly around mitochondria after one hour of CCCP treatment (**Figure 5.7A, B**). These actin assembly coincide with Parkin recruitment on the same mitochondrial population. The morphology of mitochondria also became smaller discrete units after long hours of treatment, similar to what others have seen [149]. PDA also assembles readily in HeLa cells, and a higher abundance of Parkin (Parkin OE) promotes PDA formation (**Figure 5.7C, D**).

While PDA requires Arp2/3 complex, the reported activators for PDA are different compared to ADA. We tested whether two activators for PDA, myosin VI and the Arp2/3 complex activator N-WASP, are also relevant for ADA. Myosin VI KD (**Figure 5.8A**) does not alter the kinetics or amplitude of ADA (**Figure 5.8B, C**). In addition, we found that wiskostatin, a chemical inhibitor targeting the NPF N-WASP [666], did not affect ADA in U2-OS cells either (**Figure 5.8D, E**). In contrast, KD of WAVE regulatory complex (WRC) abolished ADA (**Figure 5.8D, E**), similar to our previous findings (**Chapter III**). These results suggest that ADA and PDA use distinct activation pathways.

We also tested another actin polymerization factor linked to mitochondrial function, Spire1C, for its involvement in ADA. Spire1C is a splice variant of the Spire1 protein, a

tandem WH2 motif-containing nucleation factor, that is mitochondrially associated and has been shown to mediate actin assembly around the mitochondria [20]. Spire1 KD cells, using three distinct siRNAs, have elongated mitochondria (**Figure S5.6A, B**), suggesting effective KD (an anti-Spire1 antibody was unavailable for confirmation of KD). However, CCCP-induced actin assembly is unaffected by Spire1 KD (**Figure S5.6C, D**).

Similarly, formins have been shown to be involved in PDA, as suggested by the application of the pan-formin inhibitor SMIFH2 [432]. However, the specific formin involved in this context is an open question and further confounded by the finding that SMIFH2 is also a myosin inhibitor [667]. We were interested to see if formins in addition to the FMNL family were required for ADA. We tested the mDia family formins, since they represent a major class of formins involved in multiple cellular processes [4]. We found that silencing mDia1 or mDia2 in U2-OS cells did not disrupt ADA (**Figure S5.7**). We have previously shown that other formins like INF2 are not involved in ADA (**Chapter II)**. Our current conclusion is that only the FMNL formins, in addition to Arp2/3 complex, are needed for ADA.

5.4 Discussion

In this chapter, we show that ADA delays the recruitment of Parkin onto depolarized mitochondria. Actin filaments do not merely form a barrier to prevent Parkin access (which at ~50kDa is smaller than the 82kDa CFP-$(FRB)_5$ component used in our experiments). Instead, we found an acute reduction in ER-mitochondrial interaction upon actin assembly. Conversely, overexpression of VAP-B, an ER-mitochondrial tether, accelerates depolarization-induced Parkin assembly, suggesting that MERC facilitates Parkin recruitment to depolarized mitochondria. From a broader perspective, MERCs are vital for a host of other cellular functions like lipid transfer [668] and the unfolded protein response (UPR) [669]. The disruptive effects of ADA on these processes are still unclear at this moment. Likewise, PINK1/Parkin mitophagy represents just one major route for mitophagy, it is unexplored whether ADA has an effect on other forms of mitophagy that are mediated by FUNDC1 [670] or BNIP3/NIX [671].

When we shift cells to be oxphos-reliant (galactose medium), ADA is prolonged and causes a delay in Parkin recruitment upon depolarization, suggesting that cells adapt to protect mitochondria once they become the sole ATP provider. This effect could be cell type specific. Previous reports showed that CCCP-induced Parkin accumulation is delayed in galactose-grown HeLa [665] or U2-OS [548]; but another study found similar recruitment rates for RPE1 cells in a variety of culture conditions [538].

The role of glycolysis in regulating ADA under glucose media is also unclear. Tackling how aerobic glycolysis influences ADA might be vital, especially in the context of cancer, where malignant cells regulate their bioenergetic pathways and mitochondrial morphology based on the availability of nutrients [672].

As for long-term mitochondrial depolarization, it is fascinating that EtBr-treated cells retain their mitochondrial population despite the loss of $\Delta\psi_m$, which might suggest that mitochondria are now rewired to sustain biomolecular synthesis or support calcium signaling, rather than ATP production. Peri-mitochondrial actin assembly might be one method by which cells insulate this organelle from Parkin to preserve them. More experiments are certainly required to establish the nature and role of actin assembly for this context. Furthermore, it would be exciting to test if the inhibition of Parkin recruitment through actin dynamics holds true in pathophysiological models (e.g. Leigh

syndrome [673], ischemia [195] or cytotoxic T cell exhaustion [674, 675]); or in brown adipocytes, which can naturally depolarize mitochondria for heat generation (~70-80% depolarization after adrenergic stimulation) [244, 676].

Finally, it is fascinating that at least two distinct actin filament populations assemble around depolarized mitochondria at different times and for different purposes. Both ADA and PDA are Arp2/3-dependent but use distinct NPFs. ADA occurs acutely (within 5 min) and is dependent on the activity of the WRC and FMNL formins, delaying mitophagy. PDA occurs 1-2 hours after the initial damage, is dependent on N-WASP and myosin VI, and helps promote mitophagy. At even further timepoints, actin filaments are required again, this time to assist actual autophagosome assembly through a variety of Arp2/3 complex activators, WHAMM, JMY, and WASH [470, 471, 474, 479, 480, 677]. Hence, this diversity of function in mitophagy makes it difficult to label the actin cytoskeleton strictly as a facilitator or an impediment to mitophagy, but rather a multifaceted modulator of the entire process.

5.5 Material and Methods

Cell culture

Wild-type human osteosarcoma U2-OS (U2-OS-WT), human cervical cancer HeLa cells and human kidney HEK-293 cells were procured from American Type Culture Collection (ATCC) and grown in DMEM (Corning, 10-013-CV) supplemented with 10% newborn calf serum (NCS, Hyclone, SH30118.03) for U2-OS or 10% fetal bovine serum (FBS, Sigma-Aldrich F4135) at 37°C with 5% CO_2 for HeLa and HEK-293. Mouse Embryonic Fibroblasts were gift from David C. Chan (California Institute of Technology) and grown in DMEM supplemented with or 10% FBS at 37°C with 5% CO_2.

For galactose medium, cells were grown in 10mM galactose in DMEM (Gibco, A1443001) media supplemented with 4mM L-glutamine and 1 mM sodium pyruvate with 10% FBS for at least ten days before experiments.

DNA transfections, plasmids, and siRNA

For plasmid transfections, cells were seeded at 4×10^5 cells per well in a 35 mm dish at ~16h before transfection. Transfections were performed in OPTI-MEM medium (Gibco, 31985062) using lipofectamine 2000 (Invitrogen, 11668) as per manufacturer's protocol, followed by trypsinization and re-plating onto glass-bottomed dishes (MatTek Corporation, P35G-1.5-14-C) at $\sim1\times10^5$ cells per well. Cells were imaged ~16–24 h after transfection except for VAP-B overexpressing cells which were imaged within 8-12 hours after transfections.

mApple-F-tractin and GFP-F-tractin plasmid were gifts from C. Waterman and A. Pasapera (National Institutes of Health, Bethesda, MD) and were on a GFP-N1 backbone (Clonetech), as described previously [556]. Mito-DsRed and mito-BFP (GFP-N1 backbone) constructs were previously described [423] and consist of amino acids 1–22 of S. cerevisiae COX4 N terminal to the respective fusion protein. ERtagRFP (modified GFP-N1 backbone) was a gift from E. Snapp (Albert Einstein College of Medicine, New York, NY), with prolactin signal sequence at 5′ of the fluorescent protein and KDEL sequence at3′. Myc-VAP-B was a gift from C.C.J. Miller (King's College, London, UK) and described elsewhere [656]. pLAMP1-mCherry on pcDNA3.1 was from Addgene (#45147). Cyto-CFP-$FRBX_5$ was from Addgene (#103776). AKAP1-YFP-FKBP was a kind gift from Gyorgy Haznoczky (Thomas Jefferson University, Philadelphia, USA). pEGFP-parkin WT was from Addgene (#45875). mCherry-Parkin WT was from Addgene (#23956). OMM-$GFP_{1\text{-}10}$ and ER-Short β_{11} coexpression ($SPLICS_S$) constructs to reconstitute GFP fluorescene were gifts from Tito Cali (University of Padova). Mito-R-GECO1 (K_d = 0.48 μM for calcium) is a gift from Y.M. Usachev (University of Iowa Carver College of Medicine,

Iowa City, IA). The following amounts of DNA were transfected per well (individually or combined for co-transfection): 500 ng for mito–BFP, Mito–DsRed, mApple-F-tractin, GFP–F-tractin, pLAMP1-mCherry, Mito-R-GECO1; 100 ng for the mCherry-Parkin WT, pEGFP-parkin WT, AKAP1-YFP-FKBP, OMM-GFP_{1-10} and ER-Short β_{11}; 800 ng for ER-RFP; 750ng for Cyto-CFP-FRBX5; 400 ng for myc-VAP-B.

For all siRNA transfections except Nap1 and Arp2, 1×10^5 cells were plated onto a 35mm dish and 2µl RNAimax (Invitrogen, 13778) with 63pmol siRNA were used per well. Cells were analyzed 72-96h post siRNA transfection. For Nap1 and Arp2 siRNA transfections, 1×10^5 cells were plated directly onto glass-bottomed dishes (MatTek Corporation, P35G-1.5-14-C) and 2µl RNAimax (Invitrogen, 13778) with 63pg siRNA were used per dish. Cells were analyzed 96h post siRNA transfection for Nap1 and 48h for Arp2. For live-cell imaging, plasmids containing fluorescent markers were transfected into siRNA-treated cells 18–24 h prior to imaging, as described above. siRNAs: human FMNL1 (IDT, hs.Ri.FMNL1.13.5, 5'-GTGGTACATTCGGTGGATCATGTTCTCCACCGAAT-3'); FMNL2 (IDT, hs.Ri.FMNL2.13.1, 5'-CATGATGCAGTTTAGTAA-3'); FMNL3 (Ambion, s40551, 5'-GCATCAAGGAGACATATGA-3'); INF2 (IDT, 5'-GGATCAACCTGGAGATCATCCGC-3') Spire1 (IDT, #1: hs.Ri.SPIRE1.13.1, 5'-GGTATGCTTACAAATGACTTGGTTAGTCATTTGTAA-3'; #2: hs.Ri.SPIRE1.13.2, 5'-GGGGTAAAACTTAAGAACTTGGACCTTCTTAAGTT-3'; #3: hs.Ri.SPIRE1.13.3, 5'-AATCTAGCACAGACTTGGAGCTCTTCCAAGTCTGTG-3'); mDia1 (Ambion, s4092, 5'-GGAGTTACGATAGCCGGAA-3'); mDia2 (IDT, 5'-GGCAAAGATTAATGAGCTTCAAGCA-3'); Myosin6 (IDT, hs.Ri.MYO6.13.1, 5'-AUCUUGUCCAAGUUGUUUCAUUGAT-3'); Nap1 (IDT, hs.Ri.NCKAP1.13.1, 5'-AAUACGCUUUACCAAGUCAAUUGUU-3'); Arp2 (IDT, custom synthesized, HSC.RNAI.N001005386.12.6, 5'- GGAUAUAAUAUUGAGCAAGAGCAGA-3'); and negative control (IDT, #51-01-14-04, 5′-CGUUAAUCGCGUAUAAUACGCGUAU-3′).

For U2-OS cells, FMNL DKD involves silencing FMNL1 and FMNL3 while for HeLa cells, FMNL DKD involves silencing FMNL1 and FMNL2 [621].

Western blotting

For preparation of whole cell extracts in MEFs and NIH 3T3 cells, cells were washed 3x with ice-cold PBS, lysed using SDS-lysis-buffer (2% SDS, 10% glycerol, 63 mM Tris-HCl pH 6.8, 0.01% bromophenol blue, 5% β-mercaptoethanol), boiled for 5 min at 95°C and sonicated to shear genomic DNA. Western blotting was carried out according to standard techniques and

chemiluminescence signals were obtained upon incubation with ECL Prime Western Blotting Detection Reagent (GE Healthcare) and were recorded with ECL Chemocam imager (Intas).

For U2-OS and HeLa samples, cells from a 35mm dish were trypsinized, pelleted by centrifugation at 300 g for 5min and resuspended in 400µl of 1× DB (50mM Tris-HCl, pH 6.8, 2mM EDTA, 20% glycerol, 0.8% SDS, 0.02% Bromophenol Blue, 1000mM NaCl, 4M urea). Proteins were separated by SDS-PAGE in a Bio-Rad mini-gel system (7×8.4cm) and transferred onto polyvinylidene fluoride membrane (EMD Millipore, IPFL00010). The membrane was blocked with TBS-T (20 mM Tris-HCl, pH 7.6, 136 mM NaCl, 0.1% Tween-20) containing 3% BSA (VWR Life Science, VWRV0332) for 1h, then incubated with primary antibody solution at 4°C overnight. After washing with TBS-T, the membrane was either incubated with HRP-conjugated secondary antibody or fluorescently tagged LiCor antibody for 1h at 23°C. Signals were detected by chemiluminescence or using LiCOR fluorescent imager.

Antibodies used

GAPDH (Calbiochem; clone 6C5; #CB1001; 1:10,000; mouse monoclonal) and (Santa Cruz: clone C9; sc-365062; 1:1500; mouse monoclonal). mDia1 (1:1000; chicken polyclonal) [63]. mDia2 antibody is a rabbit polyclonal raised by Covance against amino acids 1-520 of mouse mDia2 (bacterially-expressed and purified). Serum from the 13-week bleed was used at 1:2000. Myosin VI (kindly provided by Antonina J. Kruppa & Folma Buss, University of Cambridge, UK; 1:1000; rabbit polyclonal) (Buss et al., 1998). For ECL: HRP-conjugated secondary antibodies used were anti-mouse IgG (Dianova; #115-035-062; 1:10,000; goat) and (Bio-Rad; 1705047; 1:2000; goat), anti-rabbit IgG (Dianova; #111-035-045; 1:10,000; goat) and (Bio-Rad; 1706515; 1:5000; goat), anti-guinea pig IgG (Jackson Immuno Research Laboratories; #106-035-003; 1:5000; goat) and anti-Chicken/Turkey IgG (Invitrogen; #613120; 1:5000; Rabbit). Li-COR antibodies used were: anti-rabbit IRDye 800CW (#926-32211; 1:15000; goat) and anti-mouse IRDye 680RD (#926-68070; 1:15000; goat).

EtBr treatment of MEFs

This treatment followed published protocols showing mtDNA depletion [630]. 2 x10^4 MEFs were plated directly onto Mat-tek imaging dishes and incubated in DMEM + 10% FBS overnight. 24 hours later, overnight media was replaced either with EtBr-containing media (DMEM + 10% FBS + 0.2 µg/ml EtBr (VWR life science, X328) + 50 µg/ml uridine) or control media (DMEM + 10% FBS + 50 µg/ml uridine).

Immunofluorescence

For all cell types and conditions, cells were fixed with 1% glutaraldehyde (Electron Microscopy Sciences, 16020) for 10 mins and subsequently washed three times with sodium borohydride (Fisher Chemical, S678)(1mg/ml, 15 mins interval) and then permeabilized with 0.25% TritonX-100 for 10 min. After permeabilization, they were washed thrice again with PBS and incubated in blocking buffer (10% NCS in PBS) for 30 min. The cells were then incubated with anti-Tom20 (Abcam, ab78547 1:500) antibody prepared in 0.1% blocking solution for 90 min. Following PBS washes, the cells were incubated with secondary antibody against Tom20 (Alexa Fluor 488-coupled anti-rabbit; Invitrogen #A11037; 1:200) mixed with TRITC-phalloidin (Sigma, P1951 1:400), 1X DAPI (Sigma, D9542) and incubated for 60 min. The cells were then washed with PBS, resuspended in 2 ml PBS and imaged on the same or following day.

Drug treatment. For drug treatments, cells were seeded onto Mat-tek dishes at 200,000 cells/well and incubated at 37°C incubator overnight. Cells were fixed at various timepoints after 20μM CCCP (Sigma, C2759) treatment.

Microscopy

Microscopy of fixed samples was performed on an inverted Axiovert S100TV (Carl Zeiss) epifluorescence microscope equipped with electronic shutters (Uniblitz Electronic 35 mm including driver Model VMMD-1, BFI Optilas), a filter wheel (LUDL Electronic products LTD), filter cubes (Chroma Technology Corp. Rockingham), and epifluorescence illumination (light source HXP 120, Zeiss). Imaging was performed using a 100x/1.4-NA plan apochromatic oil objective. Images were acquired with a back-illuminated, cooled, charge-coupled-device (CCD) camera (CoolSnap HQ2, Photometrics) driven by VisiView software (Visitron Systems).

Live cell imaging was conducted in DMEM (Gibco, 21063-029) with 25 mM D-glucose, 4 mM L-glutamine and 25 mM Hepes, supplemented with 10% newborn calf serum and no sodium pyruvate, hence referred to as “live cell imaging media”. For galactose and glucose comparisons, the live cell imaging was done in their culture media respectively and not the live cell imaging media.

Cells (~$3.5x10^5$) were plated onto MatTek dishes 16 hrs prior to imaging. Medium was pre-equilibrated at 37°C and 5% CO_2 before use. Dishes were imaged using the Dragonfly 302 spinning disk confocal (Andor Technology) on a Nikon Ti-E base and equipped with an iXon Ultra 888 EMCCD camera, a Zyla 4.2 Mpixel sCMOS camera, and a Tokai Hit stage-top incubator set at 37°C. A solid-state 405 smart diode 100 mW laser, solid state 560 OPSL smart laser 50 mW laser, and solid state 637 OPSL smart laser 140 mW laser were used. Objectives used were the CFI Plan Apochromat Lambda 100X/1.45 NA oil (Nikon, MRD01905) for all drug

treatment live-cell assays; and CFI Plan Apochromat 60X/1.4 NA oil (Nikon, MRD01605) to observe transient depolarization events or Parkin recruitment during live-cell imaging. Images were acquired using Fusion software (Andor Technology, version 2.0.0.15). For actin burst and TMRE quantifications, cells were imaged at a single confocal slice at the medial region, approximate 2 μm above the basal surface, to avoid stress fibers. Parkin recruitment was also imaged at the same medial region.

For CCCP (Sigma-Aldrich, C2759) treatments, cells were treated with 20μM CCCP (from a 100mM stock in DMSO) at the start of the fifth frame (~1min, with time interval set at 15s) during imaging and continued for another 5-8min. Equal volume DMSO (Invitrogen, D12345) was used as negative control. For histamine (Sigma-Aldrich, H7125) treatments, cells were treated with 100 μM histamine (from a 100mM stock in DMSO) at the start of the fifth frame (~1min, with time interval set at 15s) during imaging and continued for another 3-5min.

For TMRE (Sigma-Aldrich, 87917) staining before CCCP treatment, cells were loaded with 20nM TMRE (from 30mM stock in DMSO) for 30min in live-cell imaging medium. Cells were subsequently washed twice with live-cell medium and fresh live-cell medium added prior to imaging.

For Parkin recruitment assay with drug treatments, cells were pre-treated with 1ml of live-cell medium containing 100μM CK666 (Sigma-Aldrich, SML006) (from a 20mM stock in DMSO) for 30min before imaging. During imaging, cells were treated with 1ml live-cell medium containing 40μM CCCP at the start of the third frame (4min, time interval set at 2min). Imaging was continued at least 1.5 hours with cells in medium containing a final concentration of 20μM CCCP and 50μM CK666. Control cells were pretreated with an equal volume of DMSO (replacing CK666) and stimulated with 20μM CCCP during imaging. To visualize more cells in the field, the 60×1.4 NA objective was used. For glucose versus galactose-grown cells, imaging plates were stimulated with 25μM CCCP instead.

Parkin recruitment assay in KD cells was similar, except without the pre-treatment step, acquisition time interval was either 1.5 or 2min. Parkin recruitment assay in glucose and galactose-grown cells was also similar, except without the pre-treatment step and the acquisition time interval was just 1.5min interval for an hour duration.

For cyto-CFP-FRBX5 recruitment studies, cells were transfected with respective plasmids, pre-treated with 1 ml of live cell media and imaged for 5 frames at 12 sec/frame, following which either DMSO (Invitrogen, D12345) or CCCP (final 40 μM) was added and imaged for another

100 sec following which 1 ml of rapamycin (Sigma 553210) (final 10 μM)-containing live cell media was added and imaged for another 150 sec.

Image analysis and quantification

Unless otherwise stated, all image analysis was performed on ImageJ Fiji (version 1.51n, National Institutes of Health). Cells that shrunk during imaging or exhibited signs of phototoxicity such as blebbing or vacuolization were excluded from analysis (maximal amount 10% for any treatment).

ADA. Quantification methods for actin assembly after CCCP treatment in live-cell imaging were previously described [560]. For each cell, one ROI was chosen which encompasses the entire area of ADA around mitochondria after drug addition. Fluorescence values for each time point (F) were normalized with the mean initial fluorescence before drug treatment (first four frames−F_0) and plotted against time as F/F_0. For DMSO control or cells that did not exhibit actin burst, the ROI was selected as the bulk region of the cytoplasm containing mitochondria using the mito–BFP channel.

For fixed cell assays, cells positive with actin clouds were scored by visual analysis for the presence or absence of actin assembly in a given field and expressed as a percentage of the total number of cells for that field. Taking all the imaging fields into consideration for each condition, a bar graph showing the average percentage of cells, along with its respective errors bar in standard deviation (s.d.) or standard errors of the mean (s.e.m.) was plotted with Microsoft Excel.

Mitochondria calcium uptake. Quantification methods for mitochondrial calcium increase after 100μ histamine treatment in live-cell imaging were previously described [12]. For each cell, one ROI was chosen which encompasses the entire mitochondria network after drug addition. Fluorescence values for each time point (F) were normalized with the mean initial fluorescence before drug treatment (first four frames−F_0) and plotted against time as F/F_0.

Depolarization. Mean TMRE fluorescence was calculated from the entire mitochondrial area for each individual cell. TMRE fluorescence values for each time point (F) were normalized with the mean initial fluorescence before drug treatment (first four frames−F_0) and plotted against time as F/F_0.

Parkin recruitment. Parkin association with mitochondria was analyzed in Fiji using the Colocalization and Time series analyzer V3 ImageJ plugin. Firstly, GFP-Parkin (rolling ball 30.0) and mito-BFP images (rolling ball 20.0) were background-subtracted and converted into 8-bit files. Parkin-associated mitochondria were thresholded using the Colocalization ImageJ plugin

with the following parameters: ratio, 25% (0–100%); threshold channel 1, 25 (0–255); threshold channel 2, 25 (0–255); and display value, 255 (0–255) for U2-OS; and ratio, 50% (0–100%); threshold channel 1, 50 (0–255); threshold channel 2, 50 (0–255); and display value, 255 (0–255) for HeLa. ROIs were drawn for individual cells in the overlapped pixel stack and analyzed using Time series analyzer V3. The ROI was selected as the bulk region of the cell containing mitochondria using the mito-BFP signal. Mean colocalized signal of Parkin on mitochondria was plotted with respect to imaging duration (1.5 hr) at 2min or 1.5min intervals.

To calculate the time of initial Parkin onset, the time of clear deviation from the pre-treatment intensity was manually read from the individual curve of each cell. For trendline analysis, data points from the linear portion of the averaged kinetic curve were extracted and a trendline was calculated using Excel. The time for the trendline to cross the point where $y = 0$ was determined as the average time for Parkin onset.

Parkin recruitment (fixed cells). Fixed cells were visually assessed for clear Parkin recruitment on mitochondrial population and manually counted. The percentage of cells positive for Parkin on mitochondria was calculated for each imaging field of view.

PDA (fixed cells). Fixed cells were visually assessed for clear actin assembly on mitochondrial population after one hour of 20μM CCCP treatment and manually counted. The percentage of cells positive for PDA was calculated for the total number of cells overall.

ER-Mitochondria, lysosome-mitochondria and FRB-mitochondria overlap. U2-OS cells transiently transfected with the respective markers were imaged live by spinning disc confocal fluorescence microscopy at 15-s intervals in a single focal plane at the medial section 2-4 μm from the base. ROIs in the peri-nuclear region (ER-mitochondria, lysosome-mitochondria) or for the whole mitochondrial network (FRB-mitochondria) were background-subtracted using “rolling ball radius” plugin of Image J with a value of 20.0. The respective channels were further processed for bleach correction in Image J using “simple ratio” and converted to 8-bit images. The channels were then analyzed using the colocalization plugin in ImageJ with the following parameters: ratio 50% (0–100%); threshold channel 1: 30 (0–255); threshold channel 2: 1: 30 (0–255); display value: 255 (0–255) to obtain the overlapping pixels. The overlap intensity was then normalized to the pre-treatment frames (1-5) and plotted over time.

SPLICS overlap with mito. Images were converted to 8 bits and binarized. Overlapping pixels between Splics and mitochondria were measured using co-localization plugin in ImageJ. Overlapped pixel area was normalized with the respective mitochondrial area from each cell and graphed out as a scatter plot for each condition

Seahorse assay

A Seahorse XFe96 Bioanalyser (Agilent) was used to determine oxygen consumption rate (OCR) and extracellular acidification rate (ECAR) for HeLa and U2-OS cells. Hela or U2-OS taken from a T75 flask at 70-80% confluency and in culture for three days, were plated at 20,000 per well onto an Agilent XF microplate (101085-004) in galactose-rich or glucose-rich media + 10% FBS medium, 24 hr before the experiment. Medium was changed 1-hour before the start of readout into 180 µL serum-free assay medium (Agilent Seahorse XF DMEM; 103575-100) supplemented with 4mM L-glutamine (Corning; 25-005-CI) and galactose or glucose. The reading and injection regime was as follows for mito-stress test: 1) Baseline OCR and ECAR were measured first (6 measurements – 3 min mix and 3 min measure); 2) injection of Oligomycin (1.5µM final) (3 measurements – 3min mix and 3 min measure); 3) injection of CCCP (5 µM final)(3 measurements – 3min mix and 3 min measure) ; 4) injection of Rotenone and Antimycin A (5 µM final each) (3 measurements – 3min mix and 3 min measure). Measurement parameters: 30 sec mix, 0 wait and 2 mins measure. For each experiment, At least three technical repeats were done for each condition.

For glycolytic flux test, medium was changed 1-hour before the start of readout into 180 µL serum-free assay medium (Agilent Seahorse XF DMEM; 103575-100) supplemented with 4mM L-glutamine (Corning; 25-005-CI) without any glucose or galactose. The reading and injection regime was as follows: 1) Baseline OCR and ECAR were measured first (6 measurements – 3 min mix and 3 min measure); 2) injection of glucose (10mM final) (3 measurements – 3min mix and 3 min measure); 3) injection of Oligomycin (1.5 µM final)(3 measurements – 3min mix and 3 min measure) ; 4) injection of 2-DG (50mM final) (3 measurements – 3min mix and 3 min measure). Measurement parameters: 30 sec mix, 0 wait and 2 mins measure. For each experiment, At least three technical repeats were done for each condition.

Statistical analysis and graph plotting software

All statistical analyses and P-value determinations were conducted using GraphPad Prism QuickCalcs or GraphPad Prism 8 (version 8.3.0, GraphPad Software). To determine P-values, an unpaired Student's t-test was performed between two groups of data, comparing full datasets as stated in the figure legends. For P-values in multiple comparisons (unpaired), Tukey's multiple comparisons test was performed in GraphPad Prism 8. Live-cell actin burst and parkin curves, along with the standard errors of the mean (s.e.m.) were plotted using Microsoft Excel for Office 365 (version 16.0.11231.20164, Microsoft Corporation).

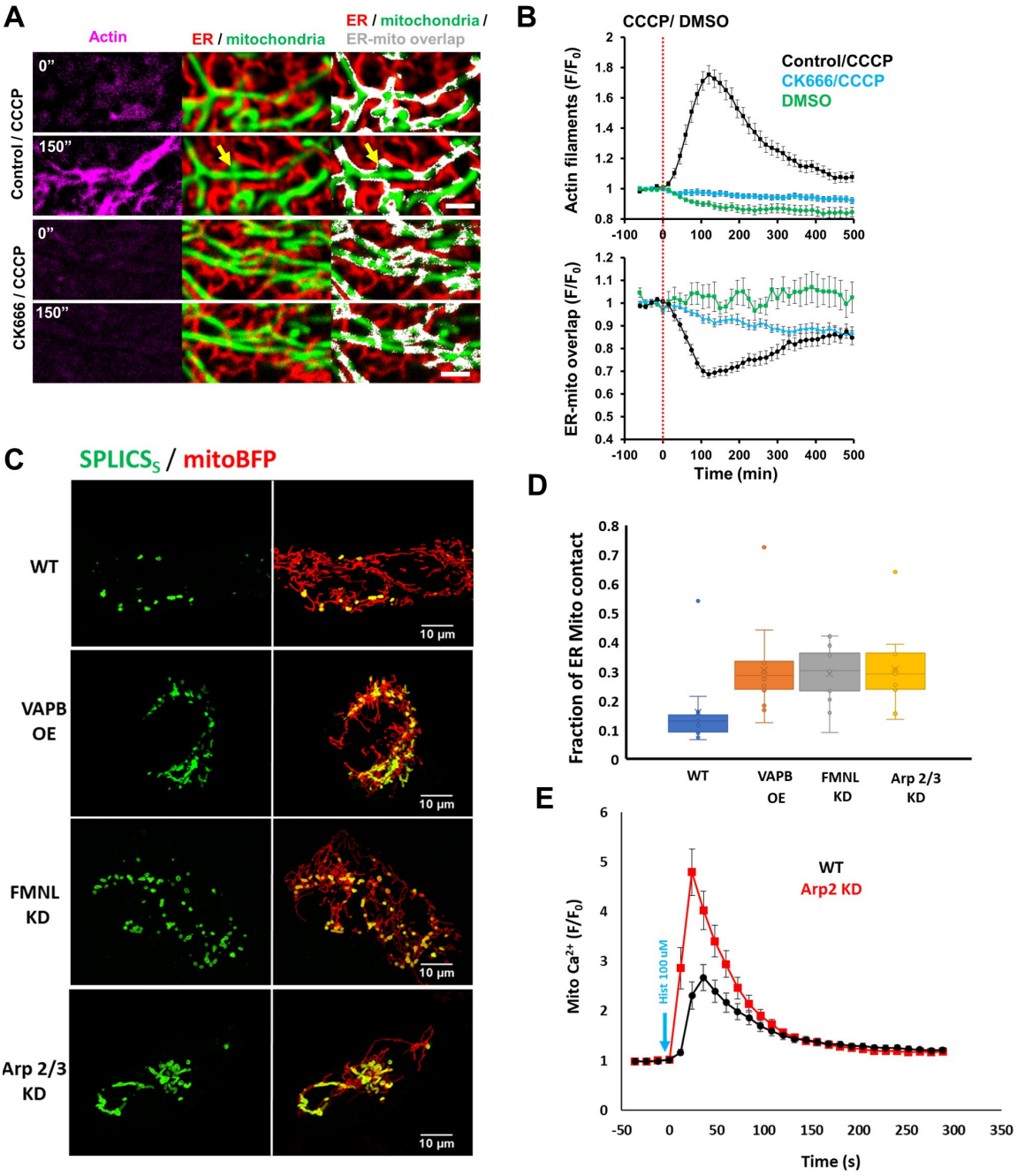
A
Actin
ER / mitochondria
ER / mitochondria / ER-mito overlap
Control / CCCP
CK666 / CCCP
0"
150"
B
CCCP/ DMSO
Control/CCCP
CK666/CCCP
DMSO
Actin filaments (F/F0)
ER-mito overlap (F/F0)
Time (min)
C
SPLICSS / mitoBFP
WT
VAPB OE
FMNL KD
Arp 2/3 KD
10 µm
D
Fraction of ER Mito contact
WT
VAPB OE
FMNL KD
Arp 2/3 KD
E
WT
Arp2 KD
Hist 100 uM
Mito Ca2+ (F/F0)
Time (s)

Figure 5.1: ADA transiently disrupts MERCs. A) Time lapse montages of CCCP-induced actin polymerization and ER-mitochondrial overlap in U2-OS cells transfected with ER-RFP (ER; red), mito-BFP (mitochondria; blue) and GFP-F tractin (actin filaments; green) and pre-treated with either DMSO or CK666 (100 μM; 30 min). Yellow arrows indicate the disruption of ER-mitochondrial contact. **B)** Quantification of CCCP-induced actin polymerization and ER-mitochondrial overlap in U2-OS cells transfected with ER-RFP (ER; red), mito-BFP (mitochondria; blue) and GFP-F tractin (actin filaments; green) and pre-treated with either DMSO or CK666 (100 μM; 30 min). N= 45 cells (CCCP), 34 cells (CK666/CCCP) and 19 cells (DMSO). **C**) Representative micrographs of U2-OS cells expressing the split-GFP-based contact site sensor ($SPLICS_S$ -with ER short spacer [655]) along with mito-BFP for WT control, VAP-B overexpression, FMNL family KD and Arp2 KD conditions. **D**) Quantification of mitochondrial population that is in close proximity to the ER for **C**. N >20 cells per condition. 2 independent experiments. (**E**) Mitochondrial calcium uptake after 100μM histamine stimulation for Arp2 KD or WT U2-OS cells. N > 20 cells per condition. 2 independent experiments.

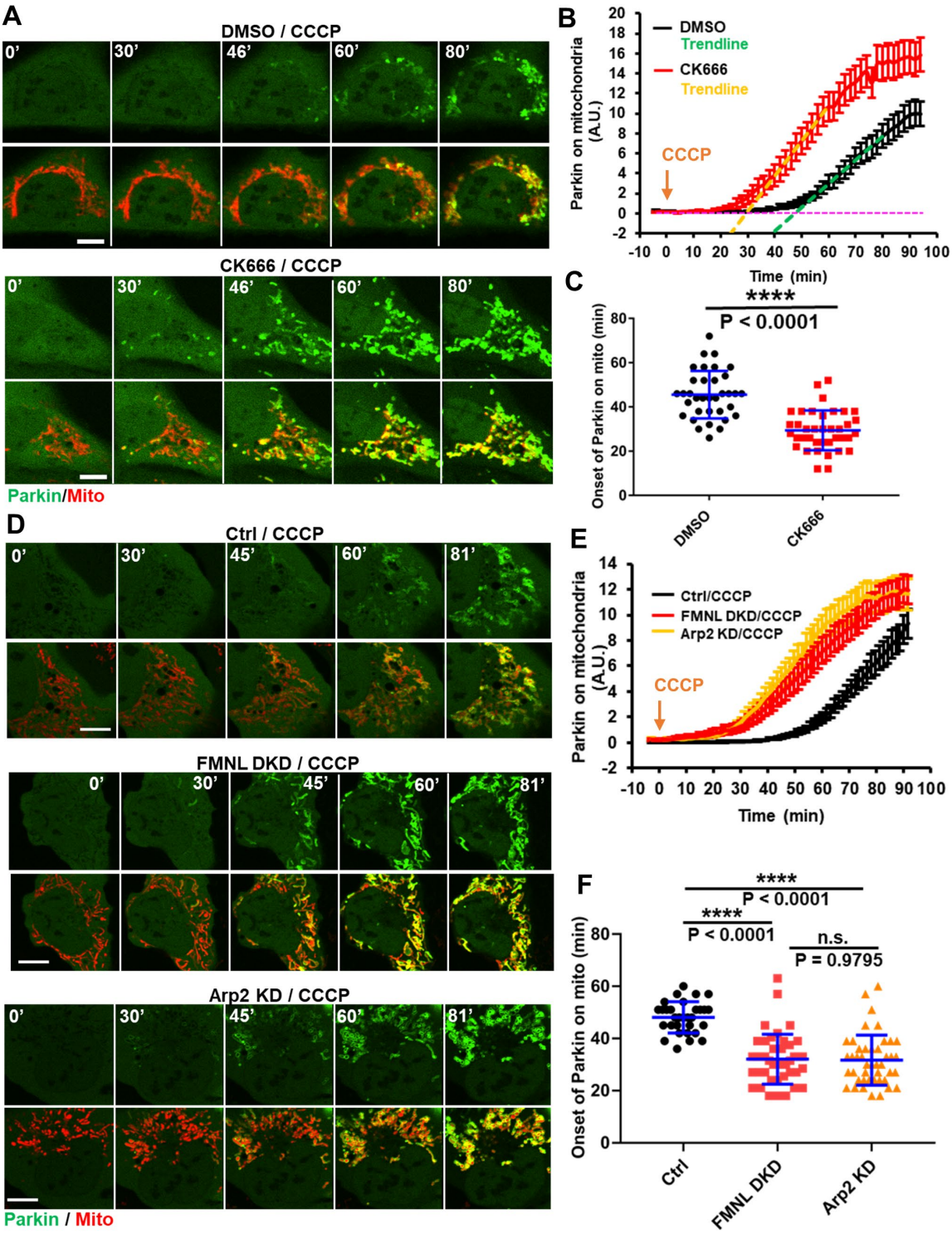
A
DMSO / CCCP
0'
30'
46'
60'
80'
CK666 / CCCP
0'
30'
46'
60'
80'
Parkin/Mito
B
DMSO
Trendline
CK666
Trendline
CCCP
Parkin on mitochondria (A.U.)
Time (min)
C
****
P < 0.0001
Onset of Parkin on mito (min)
DMSO
CK666
D
Ctrl / CCCP
0'
30'
45'
60'
81'
FMNL DKD / CCCP
0'
30'
45'
60'
81'
Arp2 KD / CCCP
0'
30'
45'
60'
81'
Parkin / Mito
E
Ctrl/CCCP
FMNL DKD/CCCP
Arp2 KD/CCCP
CCCP
Parkin on mitochondria (A.U.)
Time (min)
F
****
P < 0.0001
****
P < 0.0001
n.s.
P = 0.9795
Onset of Parkin on mito (min)
Ctrl
FMNL DKD
Arp2 KD

Figure 5.2: ADA delays mitochondrial Parkin recruitment in CK666 treated and FMNL family KD U2-OS cells. A) Time lapse montages of WT U2-OS cells transfected with GFP-Parkin (green) and Mito-BFP (red) pre-treated with 30 mins 100µM CK666 or DMSO before treatment with 20µM CCCP treatment during live-cell imaging at time 0. Imaging conduced at the medial cell section. Scale: 10µm. Time in mins. **B**) Quantification of colocalized Parkin signal with mitochondrial signal in live-cell imaging after 20µM treatment of CCCP at time 0 for 30 mins DMSO (black) or 100µM CK666 (red) pre-treated U2-OS cells. N = 35 cells for DMSO/CCCP and 38 for CK666/CCCP. 4 independent experiments. Error ± S.E.M. Trendline for DMSO (green) and CK666 (gold) were drawn using datapoints in the linear range: 60-80 mins (11 datapoints) for DMSO and 40-60 mins (11 datapoints) for CK666. Time taken for the trendline to cross the y = 0 (magenta) are: 47.4 mins for DMSO and 29.4 mins for CK666 respectively. **C**) Scatter plot of Parkin signal onset on mitochondria for DMSO or 100µM CK666 treated U2-OS cells. Parkin onset time = 45.54 min ± 10.74 (mean ± s.d.) for DMSO/CCCP and 29.42 ± 10.74 for CK666/CCCP. ****. P< 0.0001. Student's unpaired t-test. **D**) Time lapse montages of ctrl, Arp2 KD and FMNL1/3 DKD U2-OS cells transfected with GFP-Parkin (green) and Mito-BFP (red) treated with 20µM CCCP treatment at time 0 during live-cell imaging. Imaging conduced at the medial cell section. Scale: 10µm. Time in mins. **E**) Quantification of colocalized Parkin signal with mitochondrial signal in live-cell imaging after 20µM treatment of CCCP at time 0 for ctrl (black), FMNL1/3 DKD (red) or Arp2 KD (gold) U2-OS cells. N = 31 cells for ctrl; 42 for FMNL1/3 DKD and 44 for Arp2 KD. 2 independent experiments. Error ± S.E.M. **F**) Scatter plot of Parkin signal onset on mitochondria for ctrl, FMNL1/3 DKD or Arp2 KD in U2-OS cells. Parkin onset time = 46.97 min ± 8.86 (mean ± s.d.) for ctrl; 32.61 ± 8.75 for FMNL 1/3 DKD and 32.06 ± 9.03 for Arp2 KD cells. **** P< 0.0001 for ctrl vs FMNL1/3 DKD and ctrl vs Arp2 KD; n.s. P = 0.9795 for FMNL1/3 DKD vs Arp2 KD. Tukey's multiple comparisons test used.

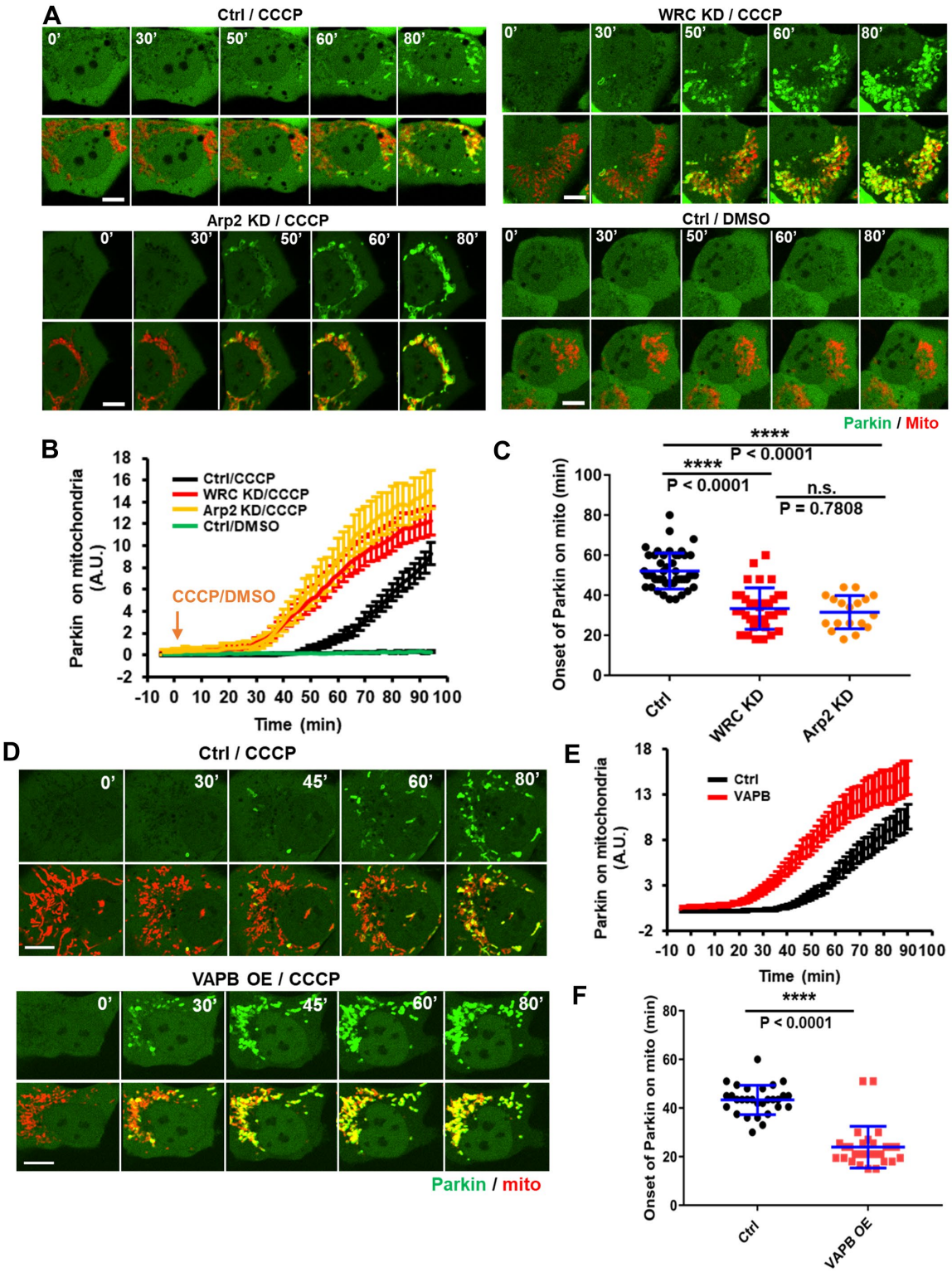
A
Ctrl / CCCP
WRC KD / CCCP
Arp2 KD / CCCP
Ctrl / DMSO
0'
30'
50'
60'
80'
Parkin / Mito
B
Parkin on mitochondria (A.U.)
Ctrl/CCCP
WRC KD/CCCP
Arp2 KD/CCCP
Ctrl/DMSO
CCCP/DMSO
Time (min)
C
Onset of Parkin on mito (min)
****
P < 0.0001
****
P < 0.0001
n.s.
P = 0.7808
Ctrl
WRC KD
Arp2 KD
D
Ctrl / CCCP
0'
30'
45'
60'
80'
VAPB OE / CCCP
Parkin / mito
E
Parkin on mitochondria (A.U.)
Ctrl
VAPB
Time (min)
F
Onset of Parkin on mito (min)
****
P < 0.0001
Ctrl
VAPB OE

Figure 5.3: ADA delays mitochondrial Parkin recruitment in WRC KD and VAP-B OE U2-OS cells. A) Time lapse montages of ctrl, Arp2 KD and WRC complex KD U2-OS cells transfected with GFP-Parkin (green) and Mito-BFP (red) treated with 20μM CCCP treatment or DMSO during live-cell imaging at time 0. Imaging conducted at the medial cell section. Scale: 10μm. Time in mins. **B)** Quantification of colocalized Parkin signal with mitochondrial signal in live-cell imaging after DMSO or 20μM treatment of CCCP at time 0 for ctrl (black) WRC KD (red) or Arp2 KD (gold) U2-OS cells. N = 48 cells for ctrl/CCCP; 35 for WRC KD/CCCP; 18 for Arp2 KD/CCCP and 30 for ctrl/DMSO. 2 independent experiments. Error ± S.E.M. **C)** Scatter plot of Parkin signal onset on mitochondria for ctrl, WRC KD or Arp2 KD in U2-OS cells. Parkin onset time = 52.08 min ± 8.934 (mean ± s.d.) for ctrl; 33.37 ± 10.30 for WRC KD and 31.56 ± 8.31 for Arp2 KD cells. **** P< 0.0001for ctrl *vs* WRC KD and ctrl *vs* Arp2 KD; n.s. P = 0.7808 for WRC KD *vs* Arp2 KD. Tukey's multiple comparisons test used. **D)** Time lapse montages of control and myc-VAP-B-overexpressing U2-OS cells transfected with GFP-Parkin (green) and Mito-BFP (red), and treated with 20μM CCCP treatment at time 0 during live-cell imaging. Imaging conduced at the medial cell section. Scale: 10μm. Time in mins. **E**) Quantification of colocalized Parkin signal with mitochondrial signal in live-cell imaging after 20μM treatment of CCCP at time 0 for control (black) and myc-VAP-B-overexpressing (red) U2-OS cells. N = 29 cells for ctrl and 28 for VAPB overexpression. 2 independent experiments. Error ± S.E.M. **F)** Scatter plot of Parkin signal onset on mitochondria for control and myc-VAP-B-overexpressing U2-OS cells. Parkin onset time = 43.34 min ± 6.02 (mean ± s.d.) for control and 23.95 ± 8.578 for myc-VAP-B overexpression. **** P< 0.0001. Student’s unpaired t-test.

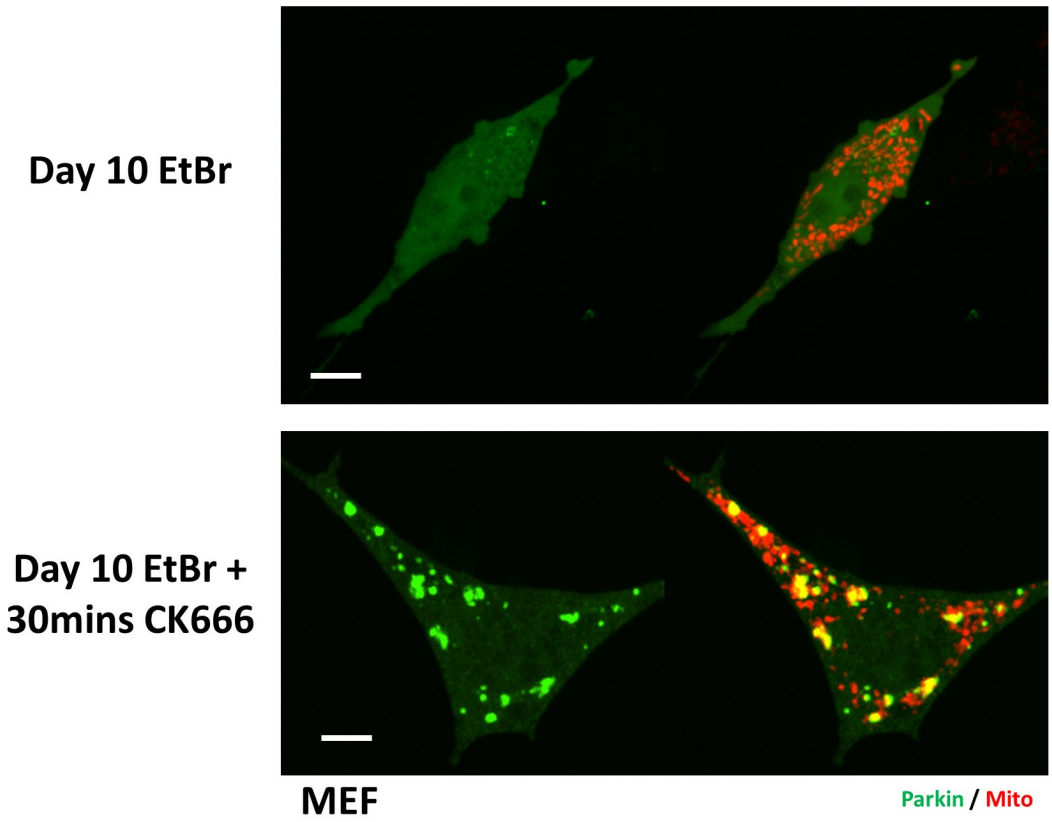

Figure 5.4: Parkin recruitment is inhibited by dynamic actin in EtBr-treated MEF. Micrographs of mouse embryonic fibroblasts transfected with GFP-Parkin (green) and Mito-BFP (red) and treated with EtBr for 10 days. Top cell shows cytosolic Parkin with no treatment while bottom cell is treated with 100μM CK666 for 30minutes. Scale: 10 μm.

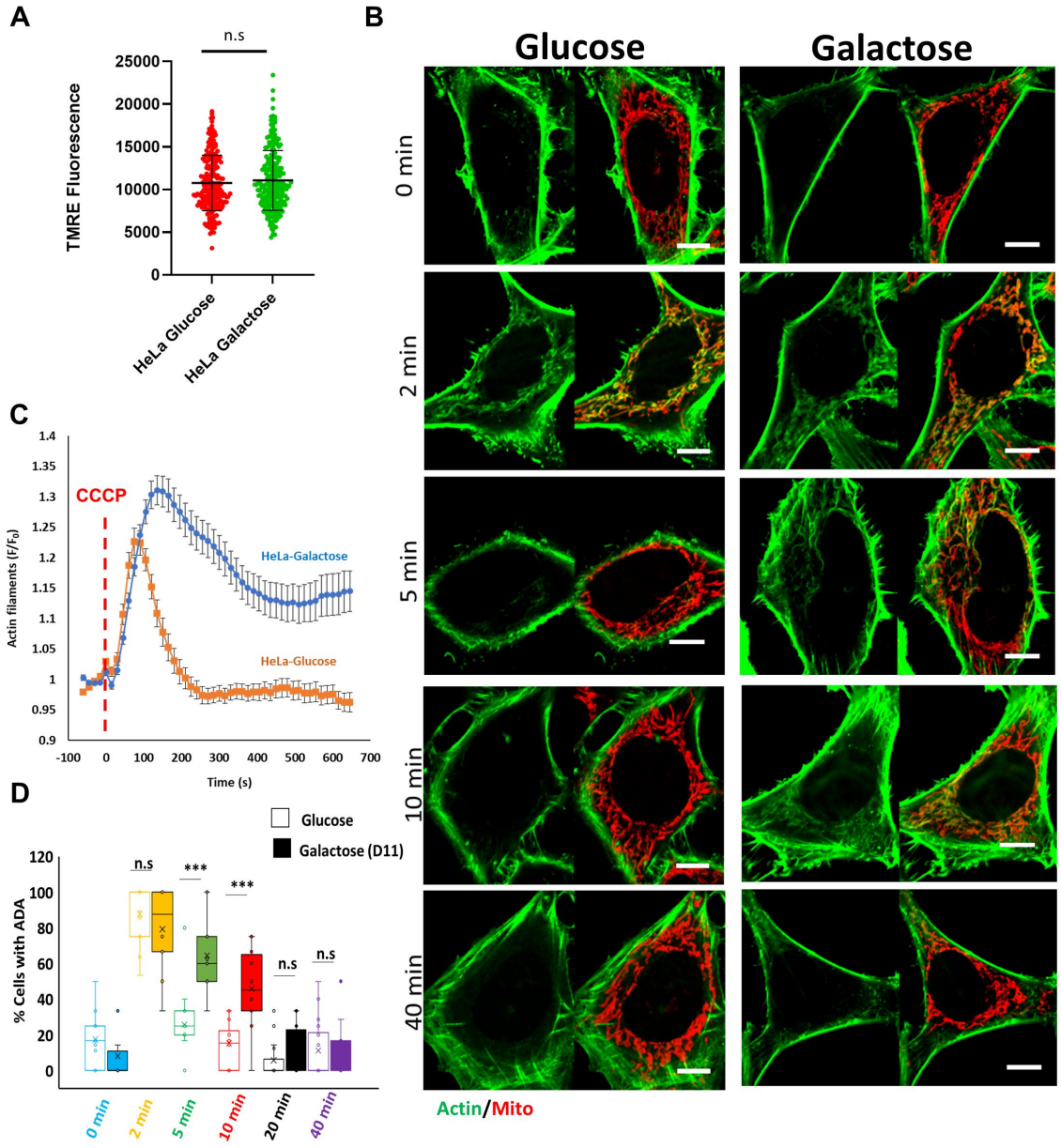

Figure 5.5: ADA is sustained in galactose-grown HeLa cells. A) Scatter plot of TMRE intensity for glucose versus galactose-primed HeLa cells. N > 50 cells per condition. 2 independent experiments. Error ± s.d. P-values were obtained from an unpaired Student's t test. n.s. P>0.05. **B**) Representative montages of actin assembly between glucose and Day 11 galactose-primed HeLas. Cells were fixed at different timepoints and stained for actin (Phalloidin) and mitochondria (Tom20). Scale: 10 µm. **C)** Quantification of CCCP-induced actin polymerization in glucose control and galactose-primed HeLa cells in live-cell imaging. N > 50 cells per condition. 2 independent experiments. Error ± S.E.M. **D**) Quantification of percentage of cells with actin assembly for conditions in **B**. N > 50 cells per condition. Error ± s.d. P-values were obtained from an unpaired Student's t test. n.s. P>0.05. *** P=0.0001. 2 independent experiments

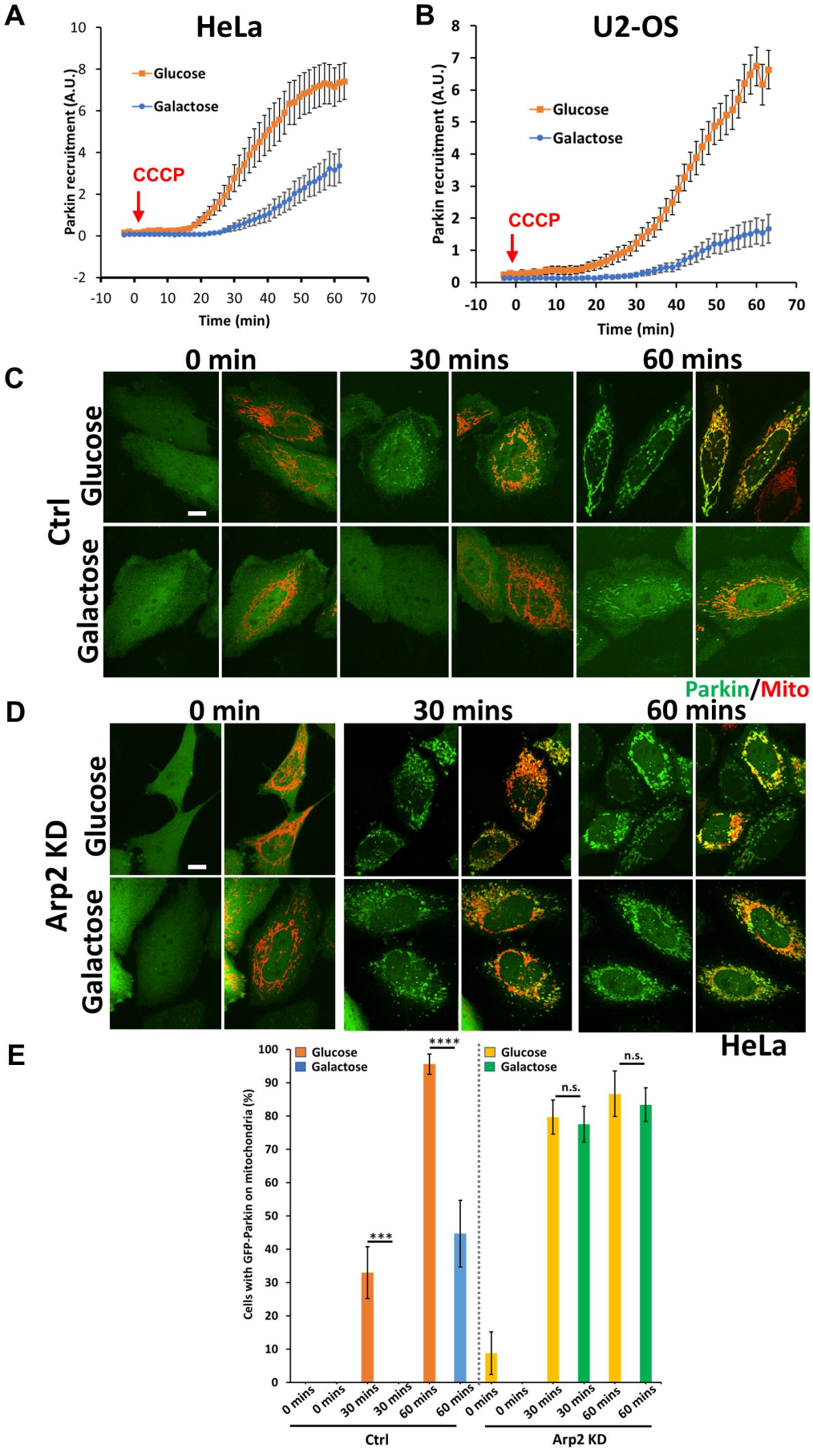
A
HeLa
Glucose
Galactose
CCCP
Parkin recruitment (A.U.)
Time (min)
B
U2-OS
Glucose
Galactose
CCCP
Parkin recruitment (A.U.)
Time (min)
C
0 min
30 mins
60 mins
Ctrl
Glucose
Galactose
Parkin/Mito
D
0 min
30 mins
60 mins
Arp2 KD
Glucose
Galactose
HeLa
E
Glucose
Galactose
Cells with GFP-Parkin on mitochondria (%)
***
****
n.s.
n.s.
0 mins
30 mins
60 mins
Ctrl
Arp2 KD

Figure 5.6: Parkin recruitment is delayed in galactose-grown cells. A) Quantification of colocalized Parkin signal with mitochondrial signal in live-cell imaging after 25µM treatment of CCCP at time 0 for glucose control versus galactose-primed HeLa cells. N > 20 cells for each condition. 2 independent experiments. Error ± S.E.M. **B**) Quantification of colocalized Parkin signal with mitochondrial signal in live-cell imaging after 20µM treatment of CCCP at time 0 for glucose control versus galactose-primed U2-OS cells. N > 20 cells for each condition. 2 independent experiments. Error ± S.E.M. **C**) Representative montages of glucose versus galactose grown HeLa transfected with GFP-Parkin (green) and Mito-BFP (red) for scrambled siRNA control fixed and imaged at different time points. Scale: 10 µm. **D**) Representative montages of glucose versus galactose grown Arp2 KD HeLa transfected with GFP-Parkin (green) and Mito-BFP (red) fixed and imaged at different time points. Scale: 10 µm. **E**) Quantification of fixed cells with Parkin signal accumulation on mitochondria after 25µM treatment of CCCP for glucose control versus galactose-primed HeLa cells. N > 20 cells/ >10 fields of view (FOVs) for each condition. 2 independent experiments. Error ± S.E.M. P-values were obtained from an unpaired Student's t test. n.s. P>0,05. *** P=0.0023. ****P<0.0001.

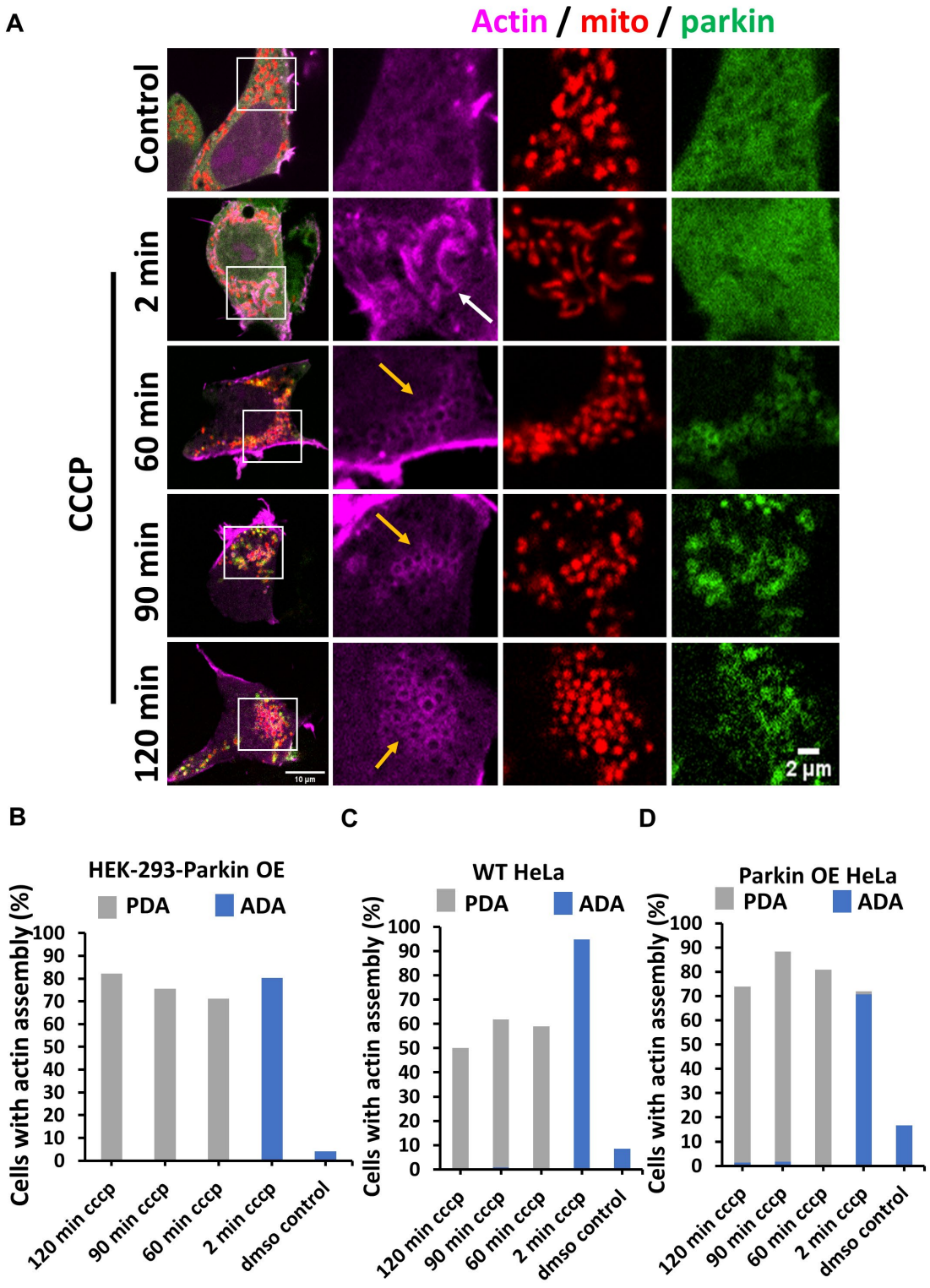
A
Actin / mito / parkin
Control
2 min
60 min
90 min
120 min
CCCP
10 µm
2 µm
B
HEK-293-Parkin OE
PDA
ADA
Cells with actin assembly (%)
120 min cccp
90 min cccp
60 min cccp
2 min cccp
dmso control
C
WT HeLa
D
Parkin OE HeLa

Figure 5.7: PDA in HEK-293 and HeLa cells. A) Representative montages of fixed HEK-293 cells showing actin filaments (GFP-F-tractin; magenta), mitochondria (mito BFP; red) and Parkin (mCherry-Parkin, green) treated with 20μM CCCP for respective timepoints. Control was DMSO-treated for 60 min. Imaging conducted at the medial cell section. White arrow denotes ADA and yellow arrows denote PDA. Scale bar: 10 μm and 2 μm (inset). **B)** Quantification of cells with PDA (grey) and ADA (blue) after 20μM CCCP in **A**. N > 40 cells for each condition. **C)** Quantification of HeLa cells with PDA (grey) and ADA (blue) after 20μM CCCP for respective timepoints. Cells were only transfected with GFP-F-tractin and mito BFP. DMSO control were treated for 60 min. N > 50 cells for each condition. **D)** Quantification of HeLa cells with PDA (grey) and ADA (blue) after 20μM CCCP for respective timepoints. For OE, cells were transfected with GFP-F-tractin, mito BFP and mCherry-Parkin. DMSO control were treated for 60 min. N > 50 cells for each condition.

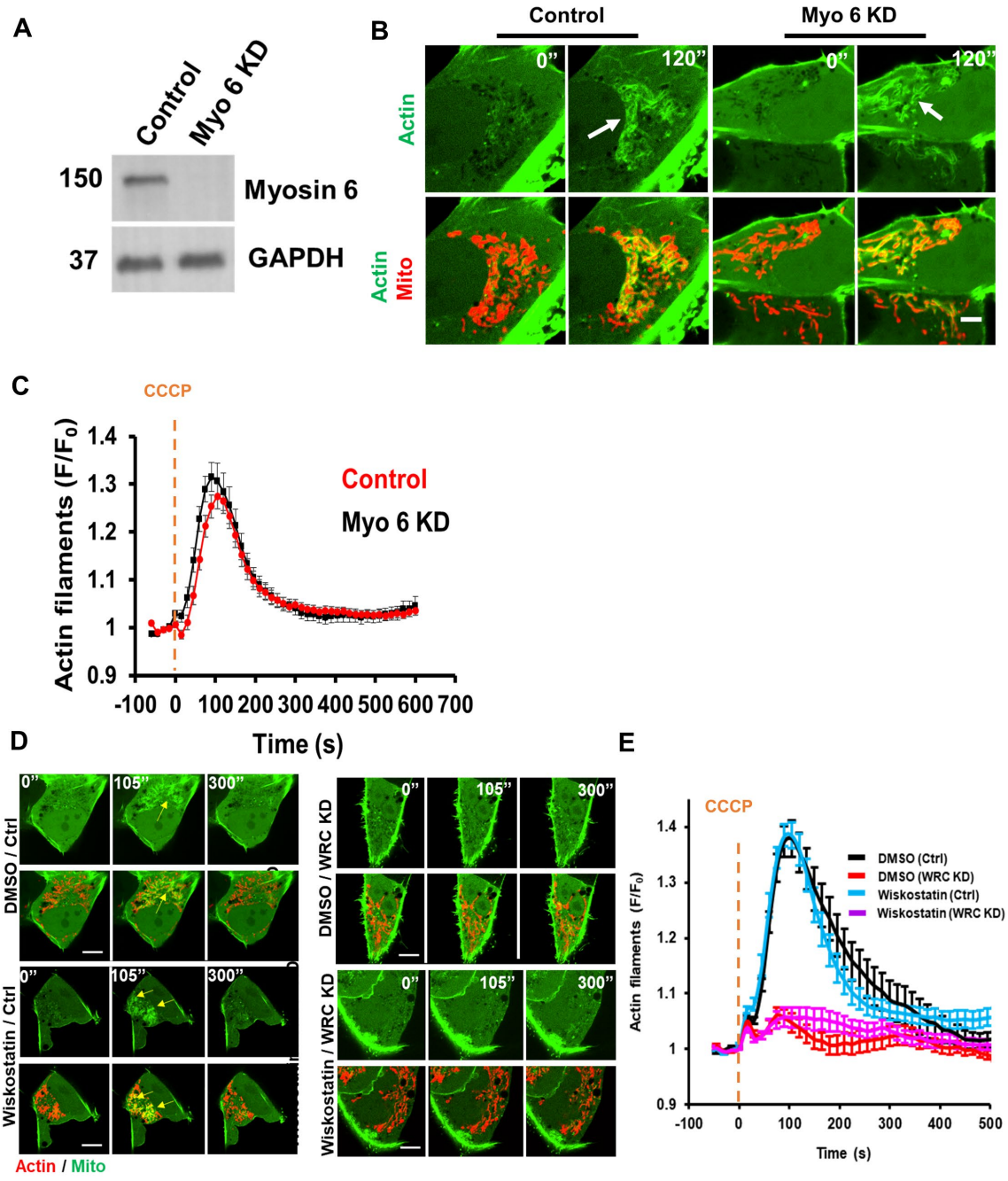
A
Control
Myo 6 KD
150
Myosin 6
37
GAPDH
B
Control
Myo 6 KD
0”
120”
Actin
Actin
Mito
C
CCCP
Actin filaments (F/F0)
Control
Myo 6 KD
Time (s)
D
0”
105”
300”
DMSO / Ctrl
Wiskostatin / Ctrl
DMSO / WRC KD
Wiskostatin / WRC KD
Actin / Mito
E
CCCP
DMSO (Ctrl)
DMSO (WRC KD)
Wiskostatin (Ctrl)
Wiskostatin (WRC KD)
Actin filaments (F/F0)
Time (s)

Figure 5.8: Myosin VI silencing does not affect ADA in U2-OS cells. A) Western blot for myosin 6 upon siRNA mediated suppression of myosin 6 in U2-OS cells to confirm respective KD. GAPDH used as loading control. **B)** Time-lapse montages of control and myosin 6 KD U2-OS cells showing actin filaments (GFP-F-tractin; green) and mitochondria (mito BFP; red) treated with 20μM CCCP at time 0 (sec). Imaging conducted at the medial cell section. Arrows denote ADA. Scale bar: 5 μm. **C)** Quantification of CCCP-induced actin polymerization in control and myosin 6 KD. N = 22 cells (control); 25 cells (myosin VI KD); 2 independent experiments. Error ± S.E.M. **D**) Time-lapse image montage of DMSO or 1-hour 5μM Wiskostatin pre-treated ctrl U2-OS or WRC KD U2-OS cells followed by 20μM CCCP-induced actin polymerization. Cells were transfected with GFP–F-tractin (green) and mito–BFP (red). Imaging conducted at the medial cell section. CCCP was added at time point 0. Scale bars: 10 μm. Arrow denotes actin assembly. **E**) Quantification of CCCP-induced actin polymerization in either 1 hour 5μM Wiskostatin pre-treated or DMSO pre-treated U2-OS-ctrl and U2-OS-WRC KD cells (15 s intervals); N = 40 cells for DMSO/ctrl, 40 cells for Wiskostatin/ctrl, 40 cells for DMSO/WRC KD and 40 cells for Wiskostatin/WRC KD; 3 independent experiments. Error ± S.E.M.

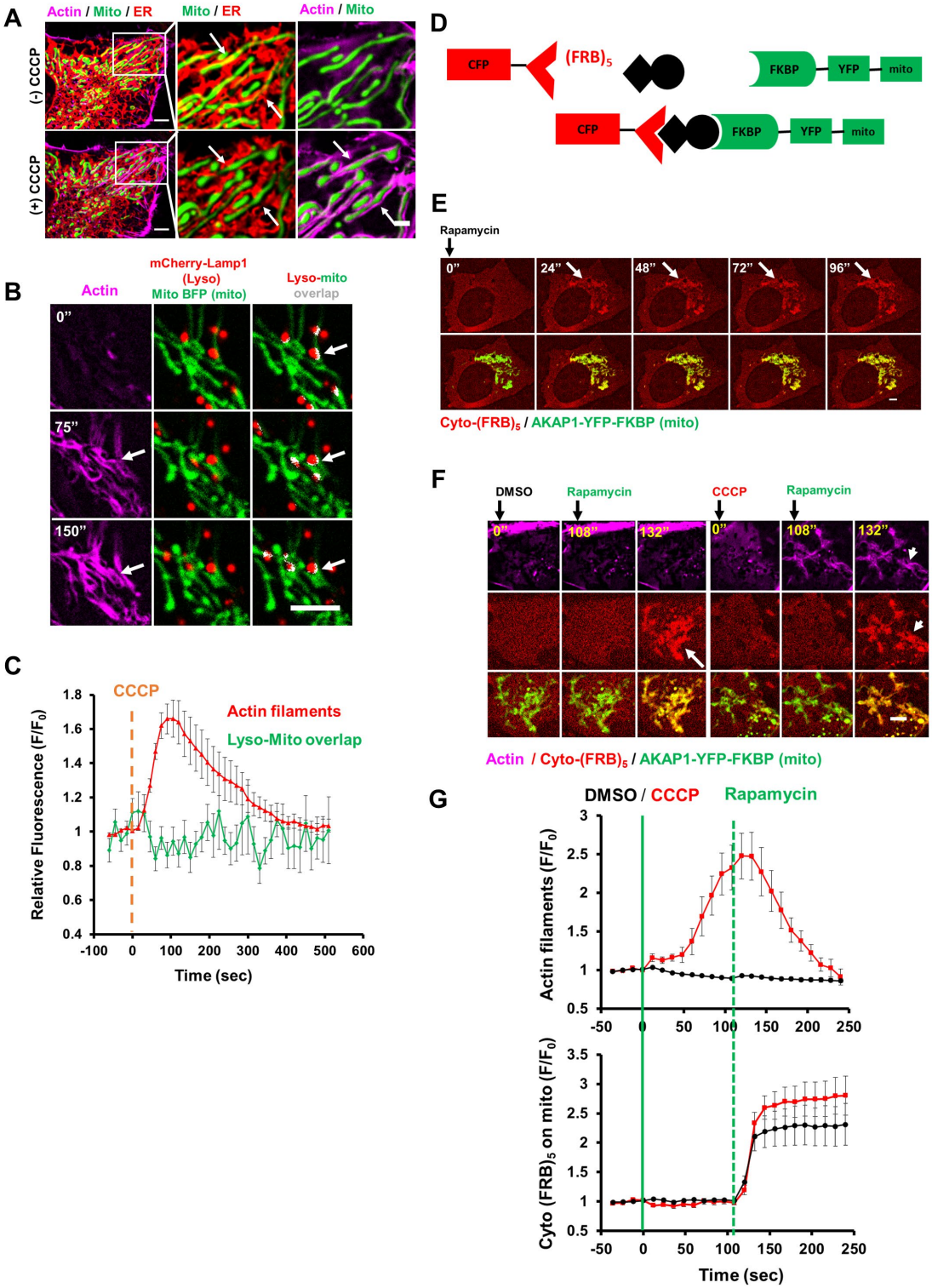
A
Actin / Mito / ER
Mito / ER
Actin / Mito
(-) CCCP
(+) CCCP
B
Actin
mCherry-Lamp1 (Lyso)
Mito BFP (mito)
Lyso-mito overlap
0”
75”
150”
C
CCCP
Actin filaments
Lyso-Mito overlap
Relative Fluorescence (F/F0)
Time (sec)
D
CFP
(FRB)5
FKBP
YFP
mito
E
Rapamycin
0”
24”
48”
72”
96”
Cyto-(FRB)5 / AKAP1-YFP-FKBP (mito)
F
DMSO
Rapamycin
CCCP
Rapamycin
0”
108”
132”
Actin / Cyto-(FRB)5 / AKAP1-YFP-FKBP (mito)
G
DMSO / CCCP
Rapamycin
Actin filaments (F/F0)
Cyto (FRB)5 on mito (F/F0)
Time (sec)

Figure S5.1: ADA does not inhibit protein arrival or mitochondrial-lysosomal interactions. **A**) Micrographs from U2-OS cells transfected with ER-RFP (ER; red), mito-BFP (mitochondria; green) and GFP-F tractin (actin filaments; magenta) after 100 seconds of CCCP treatment. **B**) Time-lapse montages of CCCP-induced actin polymerization and lysosomal-mitochondrial overlap in U2-OS cells transfected with mCherry-Lamp1 (lysosomes; red), mito-BFP (mitochondria; green) and GFP-F tractin (actin filaments; magenta). **C**) Quantification of CCCP-induced actin polymerization and Lysosome-mitochondrial overlap in U2-OS cells transfected with mCherry-Lamp1 (lysosome; red), mito-BFP (mitochondria; green) and GFP-F tractin (actin filaments; magenta) N= 20 cells from 2 independent experiments. **D)** Model for cytosolic CFP-$(FRB)_5$ and OMM bound FKBP-YFP-mito tethering after the Rapamycin introduction (black). **E**) Time lapse montage of U2-OS cells transfected with cyto-$(FRB)_5$ and AKAP1-YFP-FKBP and treated with 10 μM Rapamycin at time 0 as indicated. Scale bar: 5 μm. **F**) Time lapse montage of U2-OS cells transfected with cyto-$(FRB)_5$, AKAP1-YFP-FKBP CCCP and GFP-Ftractin and treated with either DMSO or CCCP for 100 seconds followed by rapamycin (final 10 μM). **G**) Quantification of actin filaments (upper) and mitochondrially associated CFP-$(FRB)_5$ (lower) after the following treatments: DMSO or CCCP at time 0 followed by rapamycin (final 10 μM) treatment after 100 seconds of initial treatment. N= 9 cells from 2 independent experiments.

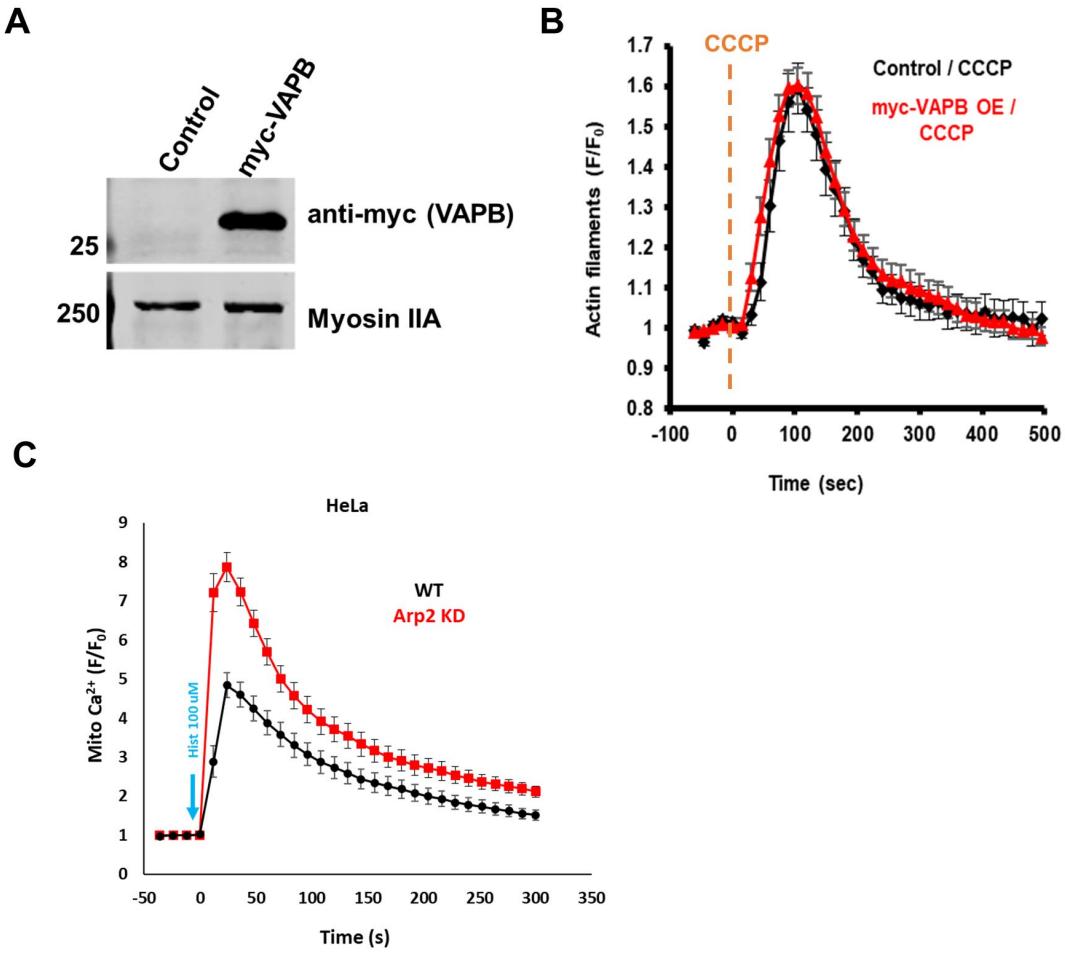

Figure S5.2: VAP-B OE does not inhibit ADA. **A**) Western blot for myc tag showing VAP-B expression in control and myc-VAP-B overexpressed U2-OS cells. Myosin IIA is used as loading control. **B**) Quantification of CCCP-induced actin polymerization in control and myc-VAP-B-overexpressing U2-OS cells. N= 20 cells (control) and 45 cells (overexpressing myc-VAP-B). 2 independent experiments. Error ± S.E.M. **C**) Mitochondrial calcium uptake after 100µM histamine stimulation for Arp2 KD or WT HeLa cells. N > 20 cells per condition. 2 independent experiments.

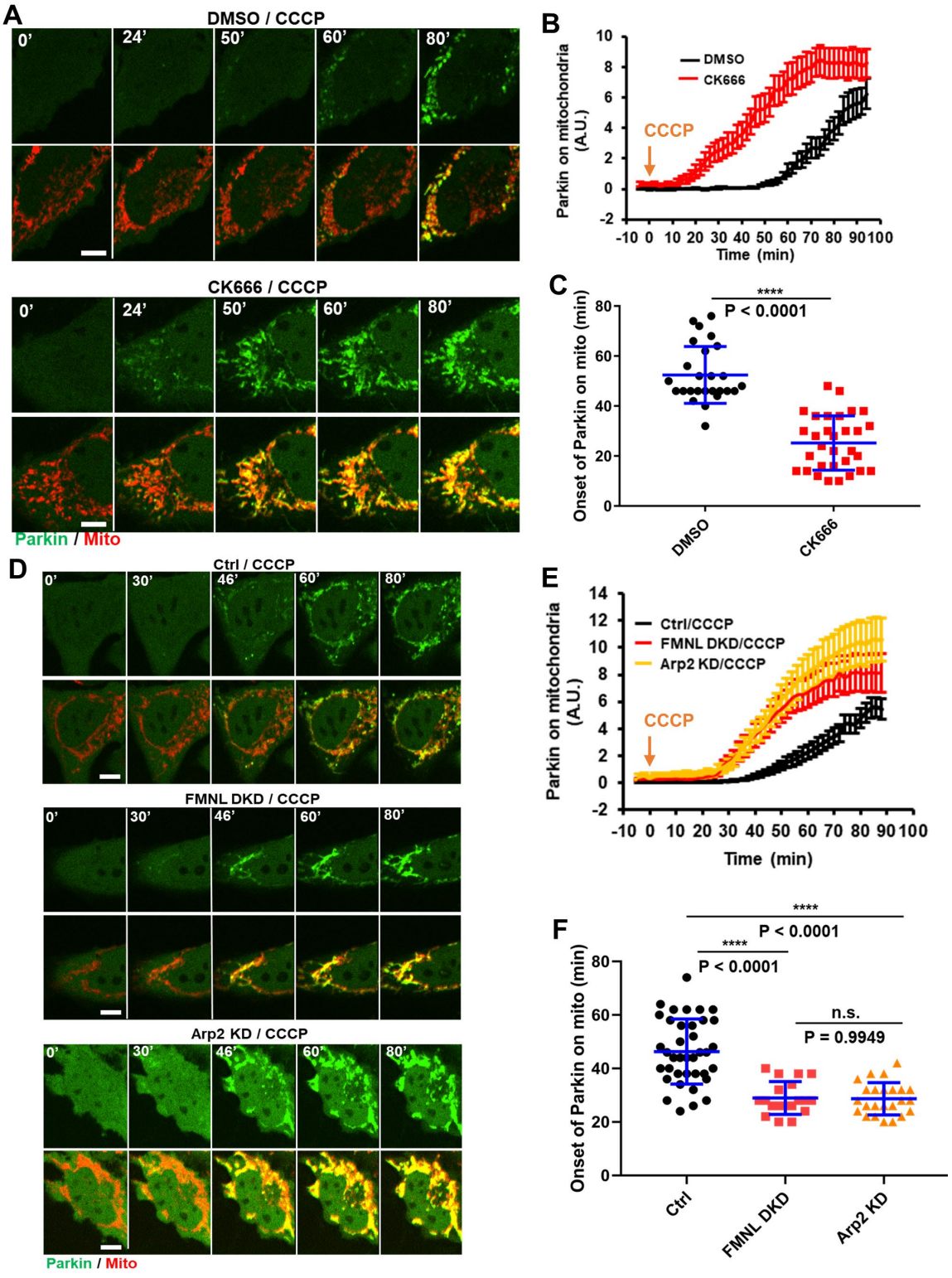
A
DMSO / CCCP
0'
24'
50'
60'
80'
CK666 / CCCP
Parkin / Mito
B
DMSO
CK666
CCCP
Parkin on mitochondria (A.U.)
Time (min)
C
****
P < 0.0001
Onset of Parkin on mito (min)
DMSO
CK666
D
Ctrl / CCCP
30'
46'
FMNL DKD / CCCP
Arp2 KD / CCCP
Parkin / Mito
E
Ctrl/CCCP
FMNL DKD/CCCP
Arp2 KD/CCCP
F
P < 0.0001
n.s.
P = 0.9949
Ctrl
FMNL DKD
Arp2 KD

Figure S5.3: ADA delays mitochondrial Parkin recruitment in CK666 treated and FMNL family KD in HeLa cells. A) Time lapse montages of WT HeLa cells transfected with GFP-Parkin (green) and Mito-BFP (red) pre-treated with 30 mins 100µM CK666 or DMSO before treatment with 20µM CCCP treatment during live-cell imaging at time 0. Imaging conducted at the medial cell section. Scale: 10µm. Time in mins. **B**) Quantification of colocalized Parkin signal with mitochondrial signal in live-cell imaging after 20µM treatment of CCCP at time 0 for 30 mins DMSO (black) or 100µM CK666 (red) pre-treated HeLa cells. N = 26 cells for DMSO/CCCP and 31 for CK666/CCCP. 4 independent experiments. Error ± S.E.M. **C**) Scatter plot of Parkin signal onset on mitochondria for DMSO or 100µM CK666 treated HeLa cells. Parkin onset time = 52.64 min ± 11.35 (mean ± s.d.) for DMSO/CCCP and 25.23 ± 10.89 for CK666/CCCP. **** P< 0.0001. Student's unpaired t-test. **D)** Time lapse montages of ctrl, Arp2 KD and FMNL1/2 DKD HeLa cells transfected with GFP-Parkin (green) and Mito-BFP (red) treated with 20µM CCCP treatment at time 0 during live-cell imaging. Imaging conduced at the medial cell section. Scale: 10µm. Time in mins. **E)** Quantification of colocalized Parkin signal with mitochondrial signal in live-cell imaging after 20µM treatment of CCCP at time 0 for ctrl (black), FMNL1/2 DKD (red) or Arp2 KD (gold) HeLa cells. N = 38 cells for ctrl; 19 for FMNL1/2 DKD and 24 for Arp2 KD. 2 independent experiments. Error ± S.E.M. **F)** Scatter plot of Parkin signal onset on mitochondria for ctrl, FMNL 1/2 DKD or Arp2 KD in HeLa cells. Parkin onset time = 46.32 min ± 12.16 (mean ± s.d.) for ctrl; 28.95 ± 6.12 for FMNL 1/2 DKD and 28.67 ± 6.01 for Arp2 KD cells. **** P< 0.0001for ctrl *vs* FMNL 1/2 DKD and ctrl *vs* Arp2 KD; n.s. P = 0.9949 for FMNL 1/2 DKD *vs* Arp2 KD. Tukey's multiple comparisons test used.

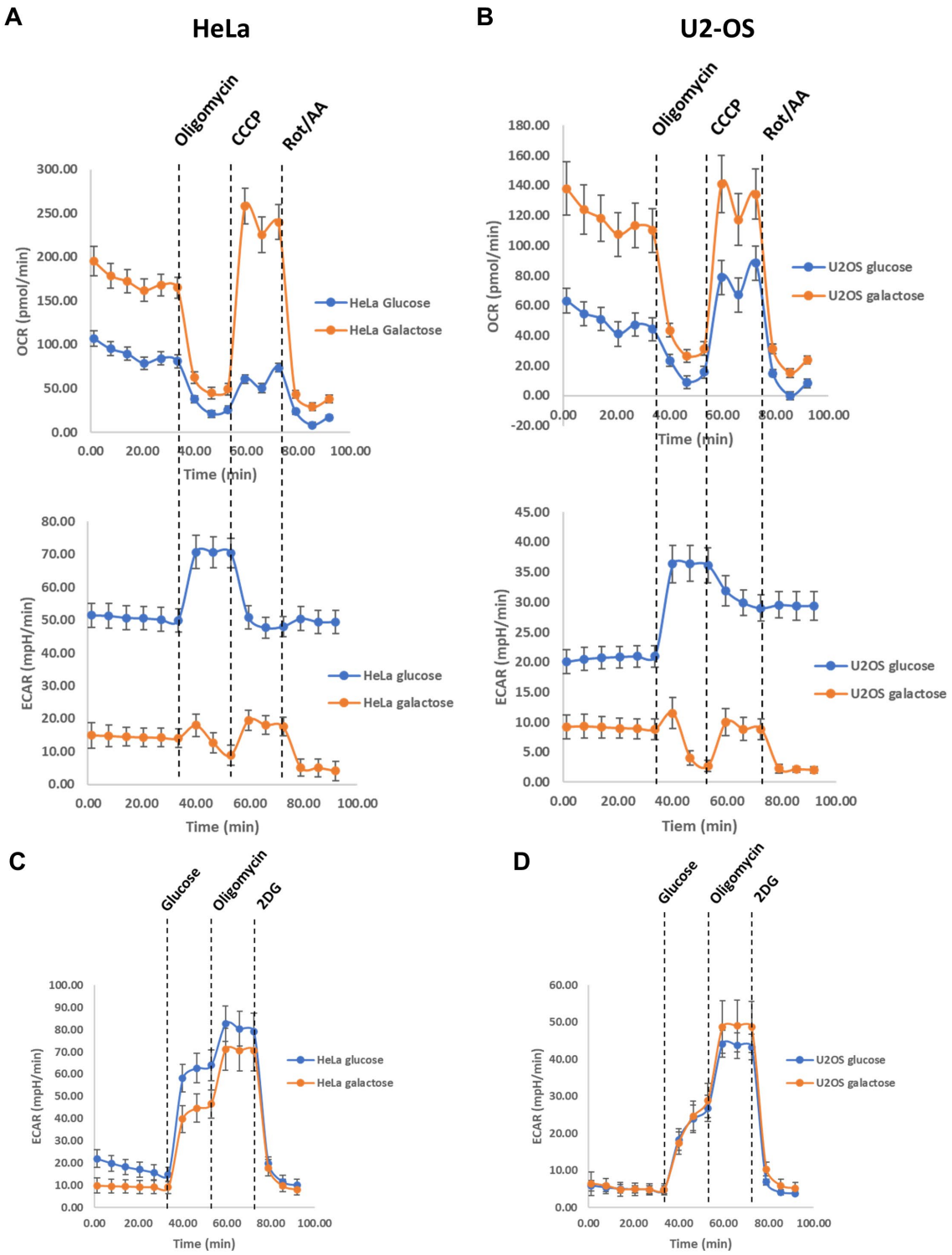
A
HeLa
Oligomycin
CCCP
Rot/AA
OCR (pmol/min)
HeLa Glucose
HeLa Galactose
Time (min)
ECAR (mpH/min)
HeLa glucose
HeLa galactose
Time (min)
B
U2-OS
Oligomycin
CCCP
Rot/AA
OCR (pmol/min)
U2OS glucose
U2OS galactose
Time (min)
ECAR (mpH/min)
U2OS glucose
U2OS galactose
Tiem (min)
C
Glucose
Oligomycin
2DG
ECAR (mpH/min)
HeLa glucose
HeLa galactose
Time (min)
D
Glucose
Oligomycin
2DG
ECAR (mpH/min)
U2OS glucose
U2OS galactose
Time (min)

Figure S5.4: Bioenergetic profiling of glucose versus galactose-grown cells. A) Oxygen consumption rate (OCR) and extracellular acidification rate (ECAR) for glucose control versus Day 11 galactose-primed HeLa cells. After basal readout, 1.5μM Oligomycin was added followed by 5μM of CCCP and finally 5μM/5μM of Rotenone/Antimycin A together. At least 3 technical repeats for each condition. Errors bars represent s.d. **B**) OCR and ECAR for glucose control versus Day 11 galactose-primed U2-OS cells. Same treatment regimen as **A**. At least 3 technical repeats for each condition. Errors bars represent s.d. **C**) ECAR readout for glycolytic flux assay for both glucose and Day 11 galactose-primed HeLa cells. Cells were first cultured in glucose-free media before glucose concentration was brought to 10mM. Next, cells were treated with 1.5μM Oligomycin and 50mM 2-DG (final concentration) to inhibit glycolysis. At least 3 technical repeats for each condition. Errors bars represent s.d. **D**) ECAR readout for glycolytic flux assay for both glucose and Day 11 galactose-primed U2-OS cells. Same treatment regimen as **C**. At least 3 technical repeats for each condition. Errors bars represent s.d.

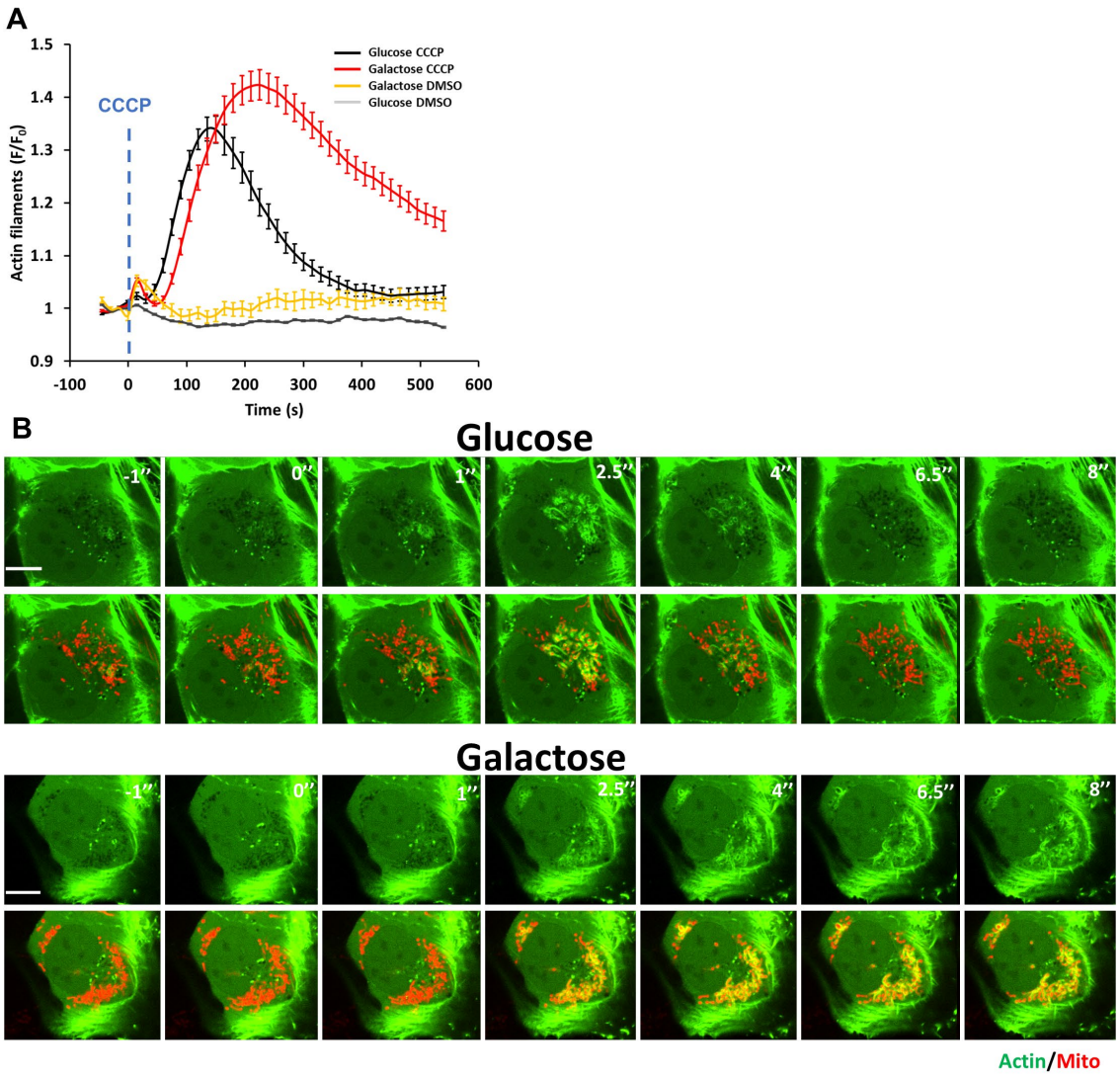

Figure S5.5: ADA is sustained in galactose-grown U2-OS cells. A) Quantification of CCCP-induced actin polymerization in glucose control and galactose-primed U2-OS cells. N = 47 cells for glucose CCCP; 93 cells for galactose CCCP; 19 cells for glucose DMSO and 8 cells for galactose DMSO. 3 independent experiments. Error ± S.E.M. **B**) Time-lapse montages of control and Day 14 galactose-primed U2-OS cells showing actin filaments (GFP-F-tractin; green) and mitochondria (mito BFP; red) treated with 20μM CCCP at time 0 (min). Imaging conducted at the medial cell section. Time in mins. Scale bar: 10 μm.

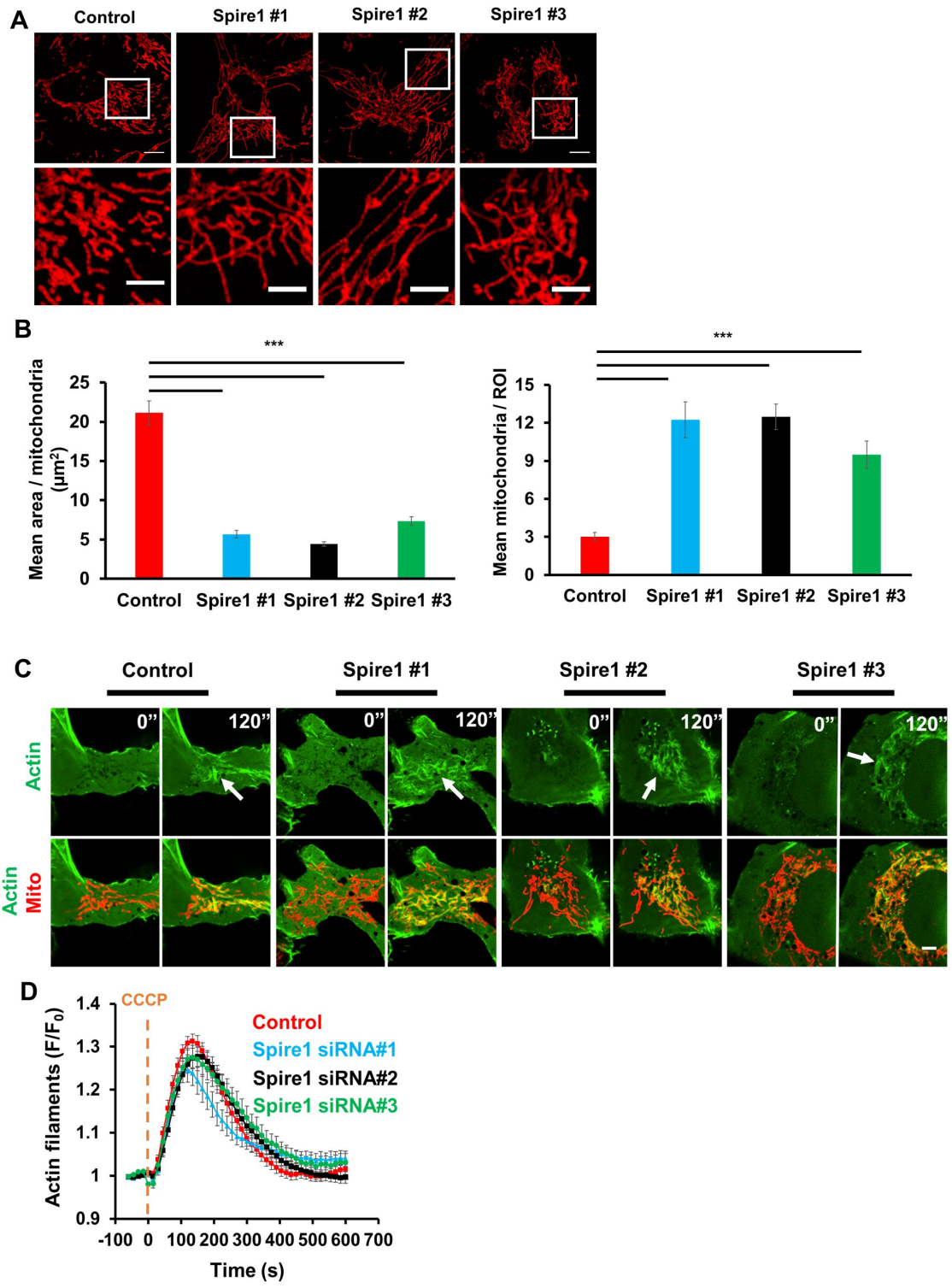
A
Control
Spire1 #1
Spire1 #2
Spire1 #3
B
***
Mean area / mitochondria (μm²)
25
20
15
10
5
0
Control
Spire1 #1
Spire1 #2
Spire1 #3
***
Mean mitochondria / ROI
15
12
9
6
3
0
Control
Spire1 #1
Spire1 #2
Spire1 #3
C
Control
Spire1 #1
Spire1 #2
Spire1 #3
Actin
Actin
Mito
0”
120”
D
CCCP
Control
Spire1 siRNA#1
Spire1 siRNA#2
Spire1 siRNA#3
Actin filaments (F/F0)
1.4
1.3
1.2
1.1
1
0.9
-100
0
100
200
300
400
500
600
700
Time (s)

Figure S5.6: Spire1 KD does not inhibit ADA in U2-OS cells. A) U2-OS cells were transfected with scrambled siRNA (control) and three spire1 siRNA (#1, #2, #3) for 96 hrs. Cells were then fixed and mitochondria stained using anti-Tom20 (red). ROIs of fixed dimension were analyzed for mitochondrial length and number as described in Materials and methods. Images of control and spire1 KD are shown. Bars: (main) 5 μm; (insets) 2 μm. **B)** Mean mitochondrial length quantification represented as area (square micrometers) per mitochondrion (left) and mean mitochondrial number quantification (right) for control and spire 1 KD cells. Errors bars represent s.d. P-values were obtained from an unpaired Student's t test. *** *P*=0.0001. **C**) Time-lapse montages of control and spire 1c KD U2-OS cells (using three different siRNA(s)) showing actin filaments (GFP-F-tractin; green) and mitochondria (mito BFP; red) treated with 20μM CCCP at time 0 (sec). Imaging conducted at the medial cell section. Arrows denote robust ADIA in CCCP-stimulated condition. Scale bar: 5 μm. **D)** Quantification of CCCP-induced actin polymerization in control and spire 1c KD U2-OS cells using three different siRNA(s). N= 27 cells (control), 27 cells (spire1 siRNA#1), 50 cells (spire1 siRNA#2), 30 cells (Spire1 siRNA #3); 3 independent experiments. Error ± S.E.M.

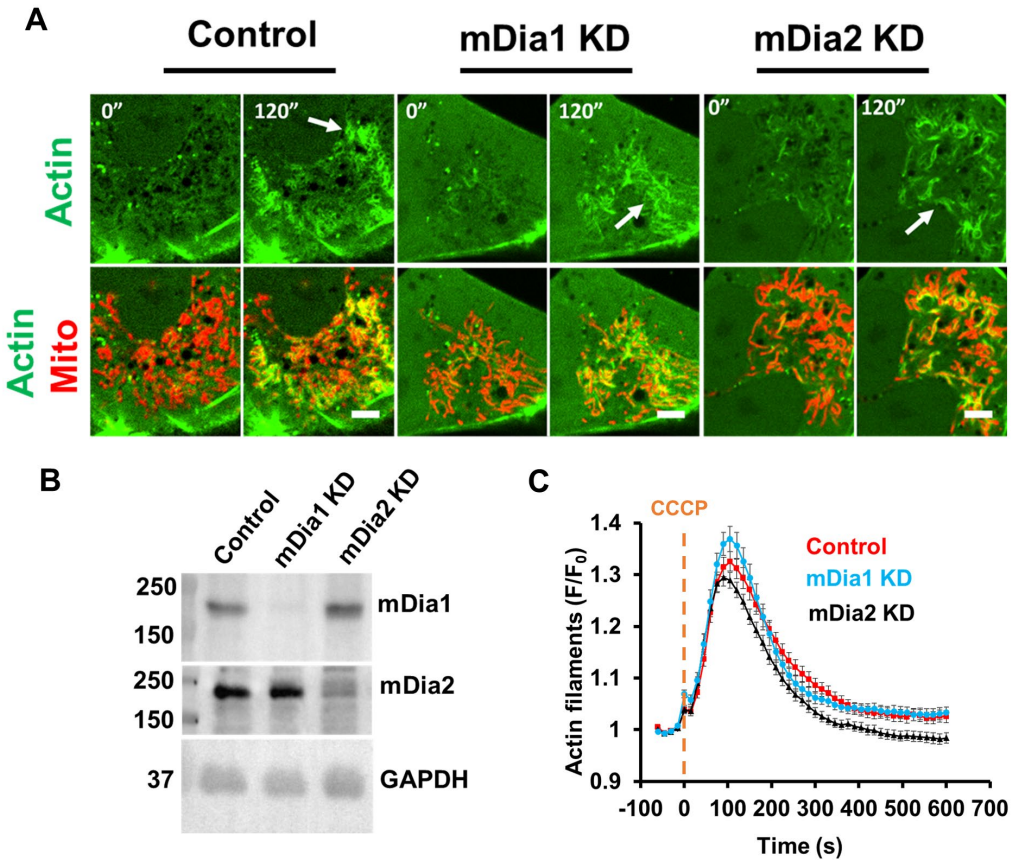

Figure S5.7: mDia family silencing does not inhibit ADA in U2-OS cells. A) Time-lapse montages of control and respective mDia KD U2-OS cells showing actin filaments (GFP-F-tractin; green) and mitochondria (mito BFP; red) treated with 20µM CCCP at time 0 (sec). Imaging conducted at the medial cell section. Arrows denote robust ADIA in CCCP-stimulated condition. Scale bar: 5 µm. **B)** Western blot for mDia1 and mDia2 upon siRNA-mediated suppression of respective mDia proteins in U2-OS cells to confirm respective KD. GAPDH used as loading control. **C**) Quantification of CCCP-induced actin polymerization in control and respective mDia1 KD U2-OS cells. N= 67 cells (control); 55 cells (mDia1 KD); 74 cells (mDia2 KD); 3 independent experiments. Error ± S.E.M.

Table 5.1: Parkin recruitment times after CCCP-depolarization

Condition	Cell type	Parkin onset (min ± S.D.)	Trendline analysis (min)	Number of cells
DMSO^	U2OS	45.4 ± 10.7	47.4	35
CK666^	U2OS	29.4 ± 9.0	29.4	38
Ctrl KD*	U2OS	47.0 ± 8.9	51.8	31
FMNL DKD[%]	U2OS	32.6 ± 8.7	26.3	42
Arp2 KD	U2OS	32.1 ± 9.0	25.3	44
Ctrl KD*	U2OS	52.1 ± 8.9	56.4	48
WRC KD	U2OS	33.4 ± 10.3	27.0	35
Arp2 KD	U2OS	31.6 ± 8.3	28.7	18
Ctrl OE*	U2OS	43.3 ± 6.0	42.7	29
VAPB OE	U2OS	24.0 ± 8.6	21.8	28
DMSO^	HeLa	52.5 ± 11.4	51.0	26
CK666^	HeLa	25.2 ± 10.9	18.4	31
Ctrl KD*	HeLa	46.3 ± 12.2	42.6	38
FMNL DKD[$]	HeLa	29.0 ± 6.1	21.7	19
Arp2 KD	HeLa	28.7 ± 6.0	24.8	24

All imaging done in live cell imaging media: 25mM glucose in DMEM, 4mM L-glutamine, 25 mM Hepes, supplemented with 10% newborn calf serum and no sodium pyruvate.

*each control (Ctrl) represents that for the treatment that follows (knock-down (KD) or over-expression (OE))s.

^Cells were pre-treated for 30mins before imaging starts.

[%]FMNL1 and FMNL3 double KD.

[$]FMNL1 and FMNL2 double KD.

Chapter VI:

Future directions

The future directions of this project point in multiple directions . Although it is difficult to list them all here, and careful readers would come up with interesting ideas of their own, but here are some of the next steps I see the project maturing in the lab.

- **Understanding the tethering between mitochondria and actin**

At this stage, it would be super informative to understand how and what molecular tethers bind the actin together with the mitochondrial population. A couple of approaches may bring this to fruition. 1) TurboID analysis or other assays to label proteins of interest. 2) Better imaging techniques to understand the ultrastructure of actin filaments. For example, could we get better resolution of what the actin filaments around the mitochondria really looked like with STED imaging or FIB-SEM imaging? 3) Investigate and screen if there are motor proteins like myosins (or other known actin binding proteins) involved that brings actin filaments close to the mitochondria.

- **Understanding the glycolytic step involved in ADA**

The relationship between actin and glycolysis remains one of the most interesting mechanisms to unravel. Here, metabolomics or carbon tracing experiments would come in handy to understand which steps of glycolysis might be regulated by ADA. In addition, an understand the NADH/NAD^+ changes that happen with/out actin assembly will bring clues to the metabolic rewiring. Figuring this out would be a major step forward in the field, as the idea that glycolytic enzymes require localization to organelles to form 'hubs' is starting to emerge and the actin cytoskeleton can be one potential bringing proteins in place.

- **The broad picture and therapeutic potential?**

Although this is still speculative at this stage, but ADA can be a therapeutic option. Probes can be generated to promote ADA without depolarizing the mitochondria. For example, a mitochondrial-localizing Arp2/3 complex activating probe can be developed. We will first test if this probe promotes glycolysis in both the seahorse and the lactate production assays. If the initial characterizations are promising, we can use the probe in T-cells or other immune cells and test the relevant effects (cancer- or pathogen fighting properties). In the end, we would really like to establish the importance of actin cytoskeleton and mitochondrial communication and how this interaction is imperative for cellular health, homeostasis, as well as a crucial stress response.

Chapter VII:

Literature cited

1. Kage F, Vicente-Manzanares M, McEwan BC, Kettenbach AN, Higgs HN. Myosin II proteins are required for organization of calcium-induced actin networks upstream of mitochondrial division. Molecular biology of the cell. 2022;33(7):ar63. Epub 2022/04/16. doi: 10.1091/mbc.E22-01-0005. PubMed PMID: 35427150.

2. A M, Fung TS, Francomacaro LM, Huynh T, Kotila T, Svindrych Z, et al. Regulation of INF2-mediated actin polymerization through site-specific lysine acetylation of actin itself. Proceedings of the National Academy of Sciences of the United States of America. 2020;117(1):439-47. Epub 2019/12/25. doi: 10.1073/pnas.1914072117. PubMed PMID: 31871199; PubMed Central PMCID: PMCPMC6955303.

3. Hatch AL, Ji WK, Merrill RA, Strack S, Higgs HN. Actin filaments as dynamic reservoirs for Drp1 recruitment. Molecular biology of the cell. 2016;27(20):3109-21. Epub 2016/08/26. doi: 10.1091/mbc.E16-03-0193. PubMed PMID: 27559132; PubMed Central PMCID: PMCPMC5063618.

4. Valencia DA, Quinlan ME. Formins. Current biology : CB. 2021;31(10):R517-r22. Epub 2021/05/26. doi: 10.1016/j.cub.2021.02.047. PubMed PMID: 34033783.

5. Blanchoin L, Boujemaa-Paterski R, Sykes C, Plastino J. Actin dynamics, architecture, and mechanics in cell motility. Physiological reviews. 2014;94(1):235-63. Epub 2014/01/03. doi: 10.1152/physrev.00018.2013. PubMed PMID: 24382887.

6. Aiken J, Holzbaur ELF. Cytoskeletal regulation guides neuronal trafficking to effectively supply the synapse. Current biology : CB. 2021;31(10):R633-r50. Epub 2021/05/26. doi: 10.1016/j.cub.2021.02.024. PubMed PMID: 34033795; PubMed Central PMCID: PMCPMC8360495.

7. Pollard TD. Actin and Actin-Binding Proteins. Cold Spring Harbor perspectives in biology. 2016;8(8). Epub 2016/03/19. doi: 10.1101/cshperspect.a018226. PubMed PMID: 26988969; PubMed Central PMCID: PMCPMC4968159.

8. Stoddard PR, Lynch EM, Farrell DP, Dosey AM, DiMaio F, Williams TA, et al. Polymerization in the actin ATPase clan regulates hexokinase activity in yeast. Science (New York, NY). 2020;367(6481):1039-42. Epub 2020/02/29. doi: 10.1126/science.aay5359. PubMed PMID: 32108112; PubMed Central PMCID: PMCPMC7846450.

9. Dominguez R, Holmes KC. Actin Structure and Function. Annual Review of Biophysics. 2011;40(1):169-86. doi: 10.1146/annurev-biophys-042910-155359.

10. Holmes KC, Popp D, Gebhard W, Kabsch W. Atomic model of the actin filament. Nature. 1990;347(6288):44-9. Epub 1990/09/06. doi: 10.1038/347044a0. PubMed PMID: 2395461.

11. Pollard TD. Assembly and dynamics of the actin filament system in nonmuscle cells. Journal of Cellular Biochemistry. 1986;31(2):87-95. doi: https://doi.org/10.1002/jcb.240310202.

12. Chakrabarti R, Ji WK, Stan RV, de Juan Sanz J, Ryan TA, Higgs HN. INF2-mediated actin polymerization at the ER stimulates mitochondrial calcium uptake, inner membrane constriction, and division. The Journal of cell biology. 2018;217(1):251-68. Epub 2017/11/17. doi: 10.1083/jcb.201709111. PubMed PMID: 29142021; PubMed Central PMCID: PMCPMC5748994.

13. Shao X, Li Q, Mogilner A, Bershadsky Alexander D, Shivashankar GV. Mechanical stimulation induces formin-dependent assembly of a perinuclear actin rim. Proceedings of the National Academy of Sciences. 2015;112(20):E2595-E601. doi: 10.1073/pnas.1504837112.

14. Wales P, Schuberth CE, Aufschnaiter R, Fels J, García-Aguilar I, Janning A, et al. Calcium-mediated actin reset (CaAR) mediates acute cell adaptations. eLife. 2016;5:e19850. doi: 10.7554/eLife.19850.

15. Gautreau AM, Fregoso FE, Simanov G, Dominguez R. Nucleation, stabilization, and disassembly of branched actin networks. Trends in cell biology. 2022;32(5):421-32. Epub 2021/11/28. doi: 10.1016/j.tcb.2021.10.006. PubMed PMID: 34836783; PubMed Central PMCID: PMCPMC9018471.

16. Li S, Xu S, Roelofs BA, Boyman L, Lederer WJ, Sesaki H, et al. Transient assembly of F-actin on the outer mitochondrial membrane contributes to mitochondrial fission. The Journal of cell biology. 2015;208(1):109-23. Epub 2014/12/31. doi: 10.1083/jcb.201404050. PubMed PMID: 25547155; PubMed Central PMCID: PMCPMC4284235.

17. Higgs HN, Peterson KJ. Phylogenetic analysis of the formin homology 2 domain. Molecular biology of the cell. 2005;16(1):1-13. Epub 2004/10/29. doi: 10.1091/mbc.e04-07-0565. PubMed PMID: 15509653; PubMed Central PMCID: PMCPMC539145.

18. Breitsprecher D, Goode BL. Formins at a glance. Journal of cell science. 2013;126(Pt 1):1-7. Epub 2013/03/22. doi: 10.1242/jcs.107250. PubMed PMID: 23516326; PubMed Central PMCID: PMCPMC3603506.

19. Dominguez R. The WH2 Domain and Actin Nucleation: Necessary but Insufficient. Trends in biochemical sciences. 2016;41(6):478-90. Epub 2016/04/14. doi: 10.1016/j.tibs.2016.03.004. PubMed PMID: 27068179; PubMed Central PMCID: PMCPMC4884163.

20. Manor U, Bartholomew S, Golani G, Christenson E, Kozlov M, Higgs H, et al. A mitochondria-anchored isoform of the actin-nucleating spire protein regulates mitochondrial division. Elife. 2015;4. Epub 2015/08/26. doi: 10.7554/eLife.08828. PubMed PMID: 26305500; PubMed Central PMCID: PMCPMC4574297.

21. Faix J, Rottner K. Ena/VASP proteins in cell edge protrusion, migration and adhesion. Journal of cell science. 2022;135(6). Epub 2022/03/15. doi: 10.1242/jcs.259226. PubMed PMID: 35285496.

22. Mockrin SC, Korn ED. Acanthamoeba profilin interacts with G-actin to increase the rate of exchange of actin-bound adenosine 5'-triphosphate. Biochemistry. 1980;19(23):5359-62. Epub 1980/11/11. doi: 10.1021/bi00564a033. PubMed PMID: 6893804.

23. Vinson VK, De La Cruz EM, Higgs HN, Pollard TD. Interactions of Acanthamoeba profilin with actin and nucleotides bound to actin. Biochemistry. 1998;37(31):10871-80. Epub 1998/08/07. doi: 10.1021/bi980093l. PubMed PMID: 9692980.

24. Safer D, Elzinga M, Nachmias VT. Thymosin beta 4 and Fx, an actin-sequestering peptide, are indistinguishable. The Journal of biological chemistry. 1991;266(7):4029-32. Epub 1991/03/05. PubMed PMID: 1999398.

25. Wiggan O, Bernstein BW, Bamburg JR. A phosphatase for cofilin to be HAD. Nature cell biology. 2005;7(1):8-9. Epub 2005/01/06. doi: 10.1038/ncb0105-8. PubMed PMID: 15632942.

26. Arber S, Barbayannis FA, Hanser H, Schneider C, Stanyon CA, Bernard O, et al. Regulation of actin dynamics through phosphorylation of cofilin by LIM-kinase. Nature. 1998;393(6687):805-9. Epub 1998/07/09. doi: 10.1038/31729. PubMed PMID: 9655397.

27. Rehklau K, Hoffmann L, Gurniak CB, Ott M, Witke W, Scorrano L, et al. Cofilin1-dependent actin dynamics control DRP1-mediated mitochondrial fission. Cell death & disease. 2017;8(10):e3063. Epub 2017/10/06. doi: 10.1038/cddis.2017.448. PubMed PMID: 28981113; PubMed Central PMCID: PMCPMC5680571.

28. Hoffmann L, Rust MB, Culmsee C. Actin(g) on mitochondria - a role for cofilin1 in neuronal cell death pathways. Biological chemistry. 2019;400(9):1089-97. Epub 2019/07/01. doi: 10.1515/hsz-2019-0120. PubMed PMID: 31256058.

29. Svitkina TM, Borisy GG. Arp2/3 complex and actin depolymerizing factor/cofilin in dendritic organization and treadmilling of actin filament array in lamellipodia. The Journal of cell biology. 1999;145(5):1009-26. Epub 1999/06/03. doi: 10.1083/jcb.145.5.1009. PubMed PMID: 10352018; PubMed Central PMCID: PMCPMC2133125.

30. Chakrabarti R, Lee M, Higgs HN. Multiple roles for actin in secretory and endocytic pathways. Current biology : CB. 2021;31(10):R603-r18. Epub 2021/05/26. doi: 10.1016/j.cub.2021.03.038. PubMed PMID: 34033793.

31. Jansen S, Collins A, Yang C, Rebowski G, Svitkina T, Dominguez R. Mechanism of actin filament bundling by fascin. The Journal of biological chemistry. 2011;286(34):30087-96. Epub 2011/06/21. doi: 10.1074/jbc.M111.251439. PubMed PMID: 21685497; PubMed Central PMCID: PMCPMC3191048.

32. Winkelman JD, Suarez C, Hocky GM, Harker AJ, Morganthaler AN, Christensen JR, et al. Fascin- and α-Actinin-Bundled Networks Contain Intrinsic Structural Features that Drive Protein Sorting. Current biology : CB. 2016;26(20):2697-706. Epub 09/22. doi: 10.1016/j.cub.2016.07.080. PubMed PMID: 27666967.

33. Nakamura F, Osborn TM, Hartemink CA, Hartwig JH, Stossel TP. Structural basis of filamin A functions. The Journal of cell biology. 2007;179(5):1011-25. Epub 2007/12/07. doi: 10.1083/jcb.200707073. PubMed PMID: 18056414; PubMed Central PMCID: PMCPMC2099194.

34. Gurel PS, Ge P, Grintsevich EE, Shu R, Blanchoin L, Zhou ZH, et al. INF2-mediated severing through actin filament encirclement and disruption. Current biology :

CB. 2014;24(2):156-64. Epub 01/09. doi: 10.1016/j.cub.2013.12.018. PubMed PMID: 24412206.

35. Fehon RG, McClatchey AI, Bretscher A. Organizing the cell cortex: the role of ERM proteins. Nature reviews Molecular cell biology. 2010;11(4):276-87. Epub 2010/03/24. doi: 10.1038/nrm2866. PubMed PMID: 20308985; PubMed Central PMCID: PMCPMC2871950.

36. Gunning PW, Hardeman EC, Lappalainen P, Mulvihill DP. Tropomyosin - master regulator of actin filament function in the cytoskeleton. Journal of cell science. 2015;128(16):2965-74. Epub 2015/08/05. doi: 10.1242/jcs.172502. PubMed PMID: 26240174.

37. Titus MA. Myosin-Driven Intracellular Transport. Cold Spring Harbor perspectives in biology. 2018;10(3). Epub 2018/03/03. doi: 10.1101/cshperspect.a021972. PubMed PMID: 29496823; PubMed Central PMCID: PMCPMC5830894.

38. Sellers JR, Heissler SM. Nonmuscle myosin-2 isoforms. Current biology : CB. 2019;29(8):R275-r8. Epub 2019/04/25. doi: 10.1016/j.cub.2019.03.022. PubMed PMID: 31014482.

39. Vicente-Manzanares M, Ma X, Adelstein RS, Horwitz AR. Non-muscle myosin II takes centre stage in cell adhesion and migration. Nature Reviews Molecular Cell Biology. 2009;10(11):778-90. doi: 10.1038/nrm2786.

40. McIntosh BB, Ostap EM. Myosin-I molecular motors at a glance. Journal of cell science. 2016;129(14):2689-95. Epub 2016/07/13. doi: 10.1242/jcs.186403. PubMed PMID: 27401928; PubMed Central PMCID: PMCPMC4958297.

41. Altman D, Sweeney HL, Spudich JA. The Mechanism of Myosin VI Translocation and Its Load-Induced Anchoring. Cell. 2004;116(5):737-49. doi: 10.1016/S0092-8674(04)00211-9.

42. Rottner K, Stradal TEB, Chen B. WAVE regulatory complex. Current biology : CB. 2021;31(10):R512-r7. Epub 2021/05/26. doi: 10.1016/j.cub.2021.01.086. PubMed PMID: 34033782; PubMed Central PMCID: PMCPMC8882368.

43. Machesky LM, Insall RH. Scar1 and the related Wiskott-Aldrich syndrome protein, WASP, regulate the actin cytoskeleton through the Arp2/3 complex. Current

biology : CB. 1998;8(25):1347-56. Epub 1999/01/16. doi: 10.1016/s0960-9822(98)00015-3. PubMed PMID: 9889097.

44. Chen Z, Borek D, Padrick SB, Gomez TS, Metlagel Z, Ismail AM, et al. Structure and control of the actin regulatory WAVE complex. Nature. 2010;468(7323):533-8. doi: 10.1038/nature09623.

45. Stahnke S, Döring H, Kusch C, de Gorter DJJ, Dütting S, Guledani A, et al. Loss of Hem1 disrupts macrophage function and impacts migration, phagocytosis, and integrin-mediated adhesion. Current biology : CB. 2021;31(10):2051-64.e8. Epub 2021/03/13. doi: 10.1016/j.cub.2021.02.043. PubMed PMID: 33711252.

46. Schaks M, Singh SP, Kage F, Thomason P, Klünemann T, Steffen A, et al. Distinct Interaction Sites of Rac GTPase with WAVE Regulatory Complex Have Non-redundant Functions in Vivo. Current biology : CB. 2018;28(22):3674-84.e6. Epub 2018/11/06. doi: 10.1016/j.cub.2018.10.002. PubMed PMID: 30393033; PubMed Central PMCID: PMCPMC6264382.

47. Koronakis V, Hume PJ, Humphreys D, Liu T, Hørning O, Jensen ON, et al. WAVE regulatory complex activation by cooperating GTPases Arf and Rac1. Proceedings of the National Academy of Sciences of the United States of America. 2011;108(35):14449-54. Epub 2011/08/17. doi: 10.1073/pnas.1107666108. PubMed PMID: 21844371; PubMed Central PMCID: PMCPMC3167530.

48. Lebensohn AM, Kirschner MW. Activation of the WAVE complex by coincident signals controls actin assembly. Molecular cell. 2009;36(3):512-24. Epub 2009/11/18. doi: 10.1016/j.molcel.2009.10.024. PubMed PMID: 19917258; PubMed Central PMCID: PMCPMC2818508.

49. Chen B, Brinkmann K, Chen Z, Pak CW, Liao Y, Shi S, et al. The WAVE regulatory complex links diverse receptors to the actin cytoskeleton. Cell. 2014;156(1-2):195-207. Epub 2014/01/21. doi: 10.1016/j.cell.2013.11.048. PubMed PMID: 24439376; PubMed Central PMCID: PMCPMC4059610.

50. Leng Y, Zhang J, Badour K, Arpaia E, Freeman S, Cheung P, et al. Abelson-interactor-1 promotes WAVE2 membrane translocation and Abelson-mediated tyrosine phosphorylation required for WAVE2 activation. Proceedings of the National Academy of Sciences of the United States of America. 2005;102(4):1098-103. Epub 2005/01/20. doi:

10.1073/pnas.0409120102. PubMed PMID: 15657136; PubMed Central PMCID: PMCPMC545868.

51. Oikawa T, Yamaguchi H, Itoh T, Kato M, Ijuin T, Yamazaki D, et al. PtdIns(3,4,5)P3 binding is necessary for WAVE2-induced formation of lamellipodia. Nature cell biology. 2004;6(5):420-6. doi: 10.1038/ncb1125.

52. Yamazaki D, Suetsugu S, Miki H, Kataoka Y, Nishikawa S, Fujiwara T, et al. WAVE2 is required for directed cell migration and cardiovascular development. Nature. 2003;424(6947):452-6. Epub 2003/07/25. doi: 10.1038/nature01770. PubMed PMID: 12879075.

53. Cook SA, Comrie WA, Poli MC, Similuk M, Oler AJ, Faruqi AJ, et al. HEM1 deficiency disrupts mTORC2 and F-actin control in inherited immunodysregulatory disease. Science (New York, NY). 2020;369(6500):202-7. Epub 2020/07/11. doi: 10.1126/science.aay5663. PubMed PMID: 32647003; PubMed Central PMCID: PMCPMC8383235.

54. Scita G, Nordstrom J, Carbone R, Tenca P, Giardina G, Gutkind S, et al. EPS8 and E3B1 transduce signals from Ras to Rac. Nature. 1999;401(6750):290-3. Epub 1999/09/28. doi: 10.1038/45822. PubMed PMID: 10499589.

55. Innocenti M, Gerboth S, Rottner K, Lai FP, Hertzog M, Stradal TE, et al. Abi1 regulates the activity of N-WASP and WAVE in distinct actin-based processes. Nature cell biology. 2005;7(10):969-76. Epub 2005/09/13. doi: 10.1038/ncb1304. PubMed PMID: 16155590.

56. Block J, Breitsprecher D, Kühn S, Winterhoff M, Kage F, Geffers R, et al. FMNL2 drives actin-based protrusion and migration downstream of Cdc42. Current biology : CB. 2012;22(11):1005-12. Epub 2012/05/23. doi: 10.1016/j.cub.2012.03.064. PubMed PMID: 22608513; PubMed Central PMCID: PMCPMC3765947.

57. Harris ES, Gauvin TJ, Heimsath EG, Higgs HN. Assembly of filopodia by the formin FRL2 (FMNL3). Cytoskeleton (Hoboken). 2010;67(12):755-72. Epub 11/02. doi: 10.1002/cm.20485. PubMed PMID: 20862687.

58. Harris ES, Li F, Higgs HN. The Mouse Formin, FRLα, Slows Actin Filament Barbed End Elongation, Competes with Capping Protein, Accelerates

Polymerization from Monomers, and Severs Filaments *. Journal of Biological Chemistry. 2004;279(19):20076-87. doi: 10.1074/jbc.M312718200.

59. Harris ES, Higgs HN. Biochemical analysis of mammalian formin effects on actin dynamics. Methods in enzymology. 2006;406:190-214. Epub 2006/02/14. doi: 10.1016/s0076-6879(06)06015-0. PubMed PMID: 16472659.

60. Kage F, Winterhoff M, Dimchev V, Mueller J, Thalheim T, Freise A, et al. FMNL formins boost lamellipodial force generation. Nature communications. 2017;8:14832. Epub 2017/03/23. doi: 10.1038/ncomms14832. PubMed PMID: 28327544; PubMed Central PMCID: PMCPMC5364437.

61. Kage F, Steffen A, Ellinger A, Ranftler C, Gehre C, Brakebusch C, et al. FMNL2 and -3 regulate Golgi architecture and anterograde transport downstream of Cdc42. Scientific reports. 2017;7(1):9791. Epub 2017/08/31. doi: 10.1038/s41598-017-09952-1. PubMed PMID: 28852060; PubMed Central PMCID: PMCPMC5575334.

62. Pfisterer K, Levitt J, Lawson CD, Marsh RJ, Heddleston JM, Wait E, et al. FMNL2 regulates dynamics of fascin in filopodia. The Journal of cell biology. 2020;219(5). Epub 2020/04/16. doi: 10.1083/jcb.201906111. PubMed PMID: 32294157; PubMed Central PMCID: PMCPMC7199847.

63. Young LE, Heimsath EG, Higgs HN. Cell type–dependent mechanisms for formin-mediated assembly of filopodia. Molecular biology of the cell. 2015;26(25):4646-59. doi: 10.1091/mbc.E15-09-0626.

64. Young LE, Latario CJ, Higgs HN. Roles for Ena/VASP proteins in FMNL3-mediated filopodial assembly. Journal of cell science. 2018;131(21):jcs220814. doi: 10.1242/jcs.220814.

65. Gauvin TJ, Young LE, Higgs HN. The formin FMNL3 assembles plasma membrane protrusions that participate in cell-cell adhesion. Molecular biology of the cell. 2015;26(3):467-77. Epub 2014/11/28. doi: 10.1091/mbc.E14-07-1247. PubMed PMID: 25428984; PubMed Central PMCID: PMCPMC4310738.

66. Gardberg M, Heuser VD, Koskivuo I, Koivisto M, Carpén O. FMNL2/FMNL3 formins are linked with oncogenic pathways and predict melanoma outcome. The journal of pathology Clinical research. 2016;2(1):41-52. Epub 2016/08/09. doi: 10.1002/cjp2.34. PubMed PMID: 27499915; PubMed Central PMCID: PMCPMC4858127.

67. Zhu XL, Liang L, Ding YQ. Overexpression of FMNL2 is closely related to metastasis of colorectal cancer. International journal of colorectal disease. 2008;23(11):1041-7. Epub 2008/07/31. doi: 10.1007/s00384-008-0520-2. PubMed PMID: 18665374.

68. Liu J, Chen S, Chen Y, Geng N, Feng C. High expression of FMNL3 associates with cancer cell migration, invasion, and unfavorable prognosis in tongue squamous cell carcinoma. Journal of oral pathology & medicine : official publication of the International Association of Oral Pathologists and the American Academy of Oral Pathology. 2019;48(6):459-67. Epub 2019/04/08. doi: 10.1111/jop.12857. PubMed PMID: 30955218.

69. Perfettini JL, Roumier T, Kroemer G. Mitochondrial fusion and fission in the control of apoptosis. Trends in cell biology. 2005;15(4):179-83. Epub 2005/04/09. doi: 10.1016/j.tcb.2005.02.005. PubMed PMID: 15817372.

70. Scorrano L, Ashiya M, Buttle K, Weiler S, Oakes SA, Mannella CA, et al. A distinct pathway remodels mitochondrial cristae and mobilizes cytochrome c during apoptosis. Developmental cell. 2002;2(1):55-67. Epub 2002/01/10. doi: 10.1016/s1534-5807(01)00116-2. PubMed PMID: 11782314.

71. Liu X, Kim CN, Yang J, Jemmerson R, Wang X. Induction of apoptotic program in cell-free extracts: requirement for dATP and cytochrome c. Cell. 1996;86(1):147-57. Epub 1996/07/12. doi: 10.1016/s0092-8674(00)80085-9. PubMed PMID: 8689682.

72. Rizzuto R, De Stefani D, Raffaello A, Mammucari C. Mitochondria as sensors and regulators of calcium signalling. Nature reviews Molecular cell biology. 2012;13(9):566-78. Epub 2012/08/02. doi: 10.1038/nrm3412. PubMed PMID: 22850819.

73. Biswas G, Adebanjo OA, Freedman BD, Anandatheerthavarada HK, Vijayasarathy C, Zaidi M, et al. Retrograde Ca2+ signaling in C2C12 skeletal myocytes in response to mitochondrial genetic and metabolic stress: a novel mode of inter-organelle crosstalk. The EMBO journal. 1999;18(3):522-33. Epub 1999/02/02. doi: 10.1093/emboj/18.3.522. PubMed PMID: 9927412; PubMed Central PMCID: PMCPMC1171145.

74. Martinus RD, Garth GP, Webster TL, Cartwright P, Naylor DJ, Høj PB, et al. Selective induction of mitochondrial chaperones in response to loss of the mitochondrial

genome. European journal of biochemistry. 1996;240(1):98-103. Epub 1996/08/15. doi: 10.1111/j.1432-1033.1996.0098h.x. PubMed PMID: 8797841.

75. Moehlman AT, Youle RJ. Mitochondrial Quality Control and Restraining Innate Immunity. Annual review of cell and developmental biology. 2020;36:265-89. Epub 2020/10/07. doi: 10.1146/annurev-cellbio-021820-101354. PubMed PMID: 33021820.

76. West AP, Shadel GS, Ghosh S. Mitochondria in innate immune responses. Nature reviews Immunology. 2011;11(6):389-402. Epub 2011/05/21. doi: 10.1038/nri2975. PubMed PMID: 21597473; PubMed Central PMCID: PMCPMC4281487.

77. West AP, Shadel GS. Mitochondrial DNA in innate immune responses and inflammatory pathology. Nature reviews Immunology. 2017;17(6):363-75. Epub 2017/04/11. doi: 10.1038/nri.2017.21. PubMed PMID: 28393922; PubMed Central PMCID: PMCPMC7289178.

78. Ward PS, Thompson CB. Metabolic reprogramming: a cancer hallmark even warburg did not anticipate. Cancer cell. 2012;21(3):297-308. Epub 2012/03/24. doi: 10.1016/j.ccr.2012.02.014. PubMed PMID: 22439925; PubMed Central PMCID: PMCPMC3311998.

79. Pavlova NN, Zhu J, Thompson CB. The hallmarks of cancer metabolism: Still emerging. Cell metabolism. 2022;34(3):355-77. Epub 2022/02/07. doi: 10.1016/j.cmet.2022.01.007. PubMed PMID: 35123658; PubMed Central PMCID: PMCPMC8891094.

80. Chandel NS. Metabolism of Proliferating Cells. Cold Spring Harbor perspectives in biology. 2021;13(10). Epub 2021/10/03. doi: 10.1101/cshperspect.a040618. PubMed PMID: 34598925; PubMed Central PMCID: PMCPMC8485748.

81. Xu J, Huang X. Lipid Metabolism at Membrane Contacts: Dynamics and Functions Beyond Lipid Homeostasis. Frontiers in cell and developmental biology. 2020;8:615856. Epub 2021/01/12. doi: 10.3389/fcell.2020.615856. PubMed PMID: 33425923; PubMed Central PMCID: PMCPMC7786193.

82. Funai K, Summers SA, Rutter J. Reign in the membrane: How common lipids govern mitochondrial function. Current opinion in cell biology. 2020;63:162-73. Epub

2020/02/28. doi: 10.1016/j.ceb.2020.01.006. PubMed PMID: 32106003; PubMed Central PMCID: PMCPMC7484982.

83. Kühlbrandt W. Structure and function of mitochondrial membrane protein complexes. BMC Biol. 2015;13:89. Epub 20151029. doi: 10.1186/s12915-015-0201-x. PubMed PMID: 26515107; PubMed Central PMCID: PMCPMC4625866.

84. Lemasters JJ. Modulation of mitochondrial membrane permeability in pathogenesis, autophagy and control of metabolism. Journal of gastroenterology and hepatology. 2007;22 Suppl 1:S31-7. Epub 2007/08/25. doi: 10.1111/j.1440-1746.2006.04643.x. PubMed PMID: 17567461.

85. Daum G. Lipids of mitochondria. Biochimica et Biophysica Acta (BBA) - Reviews on Biomembranes. 1985;822(1):1-42. doi: https://doi.org/10.1016/0304-4157(85)90002-4.

86. Giacomello M, Pyakurel A, Glytsou C, Scorrano L. The cell biology of mitochondrial membrane dynamics. Nature reviews Molecular cell biology. 2020;21(4):204-24. Epub 2020/02/20. doi: 10.1038/s41580-020-0210-7. PubMed PMID: 32071438.

87. Chandel NS. Mitochondria as signaling organelles. BMC Biol. 2014;12:34. Epub 20140527. doi: 10.1186/1741-7007-12-34. PubMed PMID: 24884669; PubMed Central PMCID: PMCPMC4035690.

88. Gilkerson RW, Selker JM, Capaldi RA. The cristal membrane of mitochondria is the principal site of oxidative phosphorylation. FEBS letters. 2003;546(2-3):355-8. Epub 2003/07/02. doi: 10.1016/s0014-5793(03)00633-1. PubMed PMID: 12832068.

89. Mannella CA. Structure and dynamics of the mitochondrial inner membrane cristae. Biochimica et biophysica acta. 2006;1763(5-6):542-8. Epub 2006/05/30. doi: 10.1016/j.bbamcr.2006.04.006. PubMed PMID: 16730811.

90. Cogliati S, Enriquez JA, Scorrano L. Mitochondrial Cristae: Where Beauty Meets Functionality. Trends in biochemical sciences. 2016;41(3):261-73. Epub 2016/02/10. doi: 10.1016/j.tibs.2016.01.001. PubMed PMID: 26857402.

91. Nicholls DG, Ferguson SJ. Bioenergetics: Academic Press; 2013.

92. Wiedemann N, Pfanner N. Mitochondrial Machineries for Protein Import and Assembly. Annual review of biochemistry. 2017;86:685-714. Epub 2017/03/17. doi: 10.1146/annurev-biochem-060815-014352. PubMed PMID: 28301740.

93. Bennett CF, Latorre-Muro P, Puigserver P. Mechanisms of mitochondrial respiratory adaptation. Nature Reviews Molecular Cell Biology. 2022. doi: 10.1038/s41580-022-00506-6.

94. Rath S, Sharma R, Gupta R, Ast T, Chan C, Durham TJ, et al. MitoCarta3.0: an updated mitochondrial proteome now with sub-organelle localization and pathway annotations. Nucleic acids research. 2021;49(D1):D1541-d7. Epub 2020/11/12. doi: 10.1093/nar/gkaa1011. PubMed PMID: 33174596; PubMed Central PMCID: PMCPMC7778944.

95. Rensvold JW, Shishkova E, Sverchkov Y, Miller IJ, Cetinkaya A, Pyle A, et al. Defining mitochondrial protein functions through deep multiomic profiling. Nature. 2022;606(7913):382-8. Epub 2022/05/26. doi: 10.1038/s41586-022-04765-3. PubMed PMID: 35614220.

96. Fazal FM, Han S, Parker KR, Kaewsapsak P, Xu J, Boettiger AN, et al. Atlas of Subcellular RNA Localization Revealed by APEX-Seq. Cell. 2019;178(2):473-90.e26. Epub 2019/06/25. doi: 10.1016/j.cell.2019.05.027. PubMed PMID: 31230715; PubMed Central PMCID: PMCPMC6786773.

97. Birky CW, Jr. The inheritance of genes in mitochondria and chloroplasts: laws, mechanisms, and models. Annual review of genetics. 2001;35:125-48. Epub 2001/11/09. doi: 10.1146/annurev.genet.35.102401.090231. PubMed PMID: 11700280.

98. Kaguni LS. DNA polymerase gamma, the mitochondrial replicase. Annual review of biochemistry. 2004;73:293-320. Epub 2004/06/11. doi: 10.1146/annurev.biochem.72.121801.161455. PubMed PMID: 15189144.

99. Tyynismaa H, Sembongi H, Bokori-Brown M, Granycome C, Ashley N, Poulton J, et al. Twinkle helicase is essential for mtDNA maintenance and regulates mtDNA copy number. Human molecular genetics. 2004;13(24):3219-27. Epub 2004/10/29. doi: 10.1093/hmg/ddh342. PubMed PMID: 15509589.

100. Korhonen JA, Pham XH, Pellegrini M, Falkenberg M. Reconstitution of a minimal mtDNA replisome in vitro. The EMBO journal. 2004;23(12):2423-9. Epub 2004/05/29.

doi: 10.1038/sj.emboj.7600257. PubMed PMID: 15167897; PubMed Central PMCID: PMCPMC423294.

101. Campbell CT, Kolesar JE, Kaufman BA. Mitochondrial transcription factor A regulates mitochondrial transcription initiation, DNA packaging, and genome copy number. Biochimica et biophysica acta. 2012;1819(9-10):921-9. Epub 2012/04/03. doi: 10.1016/j.bbagrm.2012.03.002. PubMed PMID: 22465614.

102. Alam TI, Kanki T, Muta T, Ukaji K, Abe Y, Nakayama H, et al. Human mitochondrial DNA is packaged with TFAM. Nucleic acids research. 2003;31(6):1640-5. Epub 2003/03/11. doi: 10.1093/nar/gkg251. PubMed PMID: 12626705; PubMed Central PMCID: PMCPMC152855.

103. Kazak L, Reyes A, Holt IJ. Minimizing the damage: repair pathways keep mitochondrial DNA intact. Nature reviews Molecular cell biology. 2012;13(10):659-71. Epub 2012/09/21. doi: 10.1038/nrm3439. PubMed PMID: 22992591.

104. Peeva V, Blei D, Trombly G, Corsi S, Szukszto MJ, Rebelo-Guiomar P, et al. Linear mitochondrial DNA is rapidly degraded by components of the replication machinery. Nature communications. 2018;9(1):1727. Epub 2018/05/02. doi: 10.1038/s41467-018-04131-w. PubMed PMID: 29712893; PubMed Central PMCID: PMCPMC5928156.

105. Nissanka N, Bacman SR, Plastini MJ, Moraes CT. The mitochondrial DNA polymerase gamma degrades linear DNA fragments precluding the formation of deletions. Nature communications. 2018;9(1):2491. Epub 2018/06/29. doi: 10.1038/s41467-018-04895-1. PubMed PMID: 29950568; PubMed Central PMCID: PMCPMC6021392.

106. Silva-Pinheiro P, Minczuk M. The potential of mitochondrial genome engineering. Nature reviews Genetics. 2022;23(4):199-214. Epub 2021/12/04. doi: 10.1038/s41576-021-00432-x. PubMed PMID: 34857922.

107. Björkholm P, Harish A, Hagström E, Ernst AM, Andersson SG. Mitochondrial genomes are retained by selective constraints on protein targeting. Proceedings of the National Academy of Sciences of the United States of America. 2015;112(33):10154-61. Epub 2015/07/22. doi: 10.1073/pnas.1421372112. PubMed PMID: 26195779; PubMed Central PMCID: PMCPMC4547212.

108. Lackner LL. Shaping the dynamic mitochondrial network. BMC Biol. 2014;12:35. Epub 2014/06/03. doi: 10.1186/1741-7007-12-35. PubMed PMID: 24884775; PubMed Central PMCID: PMCPMC4035697.

109. Hollenbeck PJ, Saxton WM. The axonal transport of mitochondria. Journal of cell science. 2005;118(Pt 23):5411-9. Epub 2005/11/25. doi: 10.1242/jcs.02745. PubMed PMID: 16306220; PubMed Central PMCID: PMCPMC1533994.

110. Schwarz TL. Mitochondrial trafficking in neurons. Cold Spring Harbor perspectives in biology. 2013;5(6). Epub 2013/06/05. doi: 10.1101/cshperspect.a011304. PubMed PMID: 23732472; PubMed Central PMCID: PMCPMC3660831.

111. Liesa M, Palacín M, Zorzano A. Mitochondrial dynamics in mammalian health and disease. Physiological reviews. 2009;89(3):799-845. Epub 2009/07/09. doi: 10.1152/physrev.00030.2008. PubMed PMID: 19584314.

112. Hoppins S, Lackner L, Nunnari J. The machines that divide and fuse mitochondria. Annual review of biochemistry. 2007;76:751-80. Epub 2007/03/17. doi: 10.1146/annurev.biochem.76.071905.090048. PubMed PMID: 17362197.

113. Moore AS, Holzbaur ELF. Mitochondrial-cytoskeletal interactions: dynamic associations that facilitate network function and remodeling. Current opinion in physiology. 2018;3:94-100. Epub 2018/12/18. doi: 10.1016/j.cophys.2018.03.003. PubMed PMID: 30555978; PubMed Central PMCID: PMCPMC6289269.

114. Meeusen S, McCaffery JM, Nunnari J. Mitochondrial fusion intermediates revealed in vitro. Science (New York, NY). 2004;305(5691):1747-52. Epub 2004/08/07. doi: 10.1126/science.1100612. PubMed PMID: 15297626.

115. Detmer SA, Chan DC. Functions and dysfunctions of mitochondrial dynamics. Nature reviews Molecular cell biology. 2007;8(11):870-9. Epub 2007/10/12. doi: 10.1038/nrm2275. PubMed PMID: 17928812.

116. McBride HM, Neuspiel M, Wasiak S. Mitochondria: more than just a powerhouse. Current biology : CB. 2006;16(14):R551-60. Epub 2006/07/25. doi: 10.1016/j.cub.2006.06.054. PubMed PMID: 16860735.

117. Senft D, Ronai ZA. Regulators of mitochondrial dynamics in cancer. Current opinion in cell biology. 2016;39:43-52. Epub 2016/02/21. doi: 10.1016/j.ceb.2016.02.001. PubMed PMID: 26896558; PubMed Central PMCID: PMCPMC4828329.

118. Chan DC. Fusion and fission: interlinked processes critical for mitochondrial health. Annual review of genetics. 2012;46:265-87. Epub 2012/09/01. doi: 10.1146/annurev-genet-110410-132529. PubMed PMID: 22934639.

119. Baker N, Patel J, Khacho M. Linking mitochondrial dynamics, cristae remodeling and supercomplex formation: How mitochondrial structure can regulate bioenergetics. Mitochondrion. 2019;49:259-68. doi: https://doi.org/10.1016/j.mito.2019.06.003.

120. Kleele T, Rey T, Winter J, Zaganelli S, Mahecic D, Perreten Lambert H, et al. Distinct fission signatures predict mitochondrial degradation or biogenesis. Nature. 2021;593(7859):435-9. Epub 2021/05/07. doi: 10.1038/s41586-021-03510-6. PubMed PMID: 33953403.

121. Smirnova E, Griparic L, Shurland DL, van der Bliek AM. Dynamin-related protein Drp1 is required for mitochondrial division in mammalian cells. Molecular biology of the cell. 2001;12(8):2245-56. Epub 2001/08/22. doi: 10.1091/mbc.12.8.2245. PubMed PMID: 11514614; PubMed Central PMCID: PMCPMC58592.

122. Toyama EQ, Herzig S, Courchet J, Lewis TL, Jr., Losón OC, Hellberg K, et al. Metabolism. AMP-activated protein kinase mediates mitochondrial fission in response to energy stress. Science (New York, NY). 2016;351(6270):275-81. Epub 2016/01/28. doi: 10.1126/science.aab4138. PubMed PMID: 26816379; PubMed Central PMCID: PMCPMC4852862.

123. Palmer CS, Osellame LD, Laine D, Koutsopoulos OS, Frazier AE, Ryan MT. MiD49 and MiD51, new components of the mitochondrial fission machinery. EMBO reports. 2011;12(6):565-73. Epub 2011/04/22. doi: 10.1038/embor.2011.54. PubMed PMID: 21508961; PubMed Central PMCID: PMCPMC3128275.

124. Otera H, Miyata N, Kuge O, Mihara K. Drp1-dependent mitochondrial fission via MiD49/51 is essential for apoptotic cristae remodeling. The Journal of cell biology. 2016;212(5):531-44. Epub 2016/02/24. doi: 10.1083/jcb.201508099. PubMed PMID: 26903540; PubMed Central PMCID: PMCPMC4772499.

125. Losón OC, Song Z, Chen H, Chan DC. Fis1, Mff, MiD49, and MiD51 mediate Drp1 recruitment in mitochondrial fission. Molecular biology of the cell. 2013;24(5):659-67. Epub 2013/01/04. doi: 10.1091/mbc.E12-10-0721. PubMed PMID: 23283981; PubMed Central PMCID: PMCPMC3583668.

126. Otera H, Wang C, Cleland MM, Setoguchi K, Yokota S, Youle RJ, et al. Mff is an essential factor for mitochondrial recruitment of Drp1 during mitochondrial fission in mammalian cells. The Journal of cell biology. 2010;191(6):1141-58. Epub 2010/12/15. doi: 10.1083/jcb.201007152. PubMed PMID: 21149567; PubMed Central PMCID: PMCPMC3002033.

127. Bleazard W, McCaffery JM, King EJ, Bale S, Mozdy A, Tieu Q, et al. The dynamin-related GTPase Dnm1 regulates mitochondrial fission in yeast. Nature cell biology. 1999;1(5):298-304. Epub 1999/11/13. doi: 10.1038/13014. PubMed PMID: 10559943; PubMed Central PMCID: PMCPMC3739991.

128. Wasiak S, Zunino R, McBride HM. Bax/Bak promote sumoylation of DRP1 and its stable association with mitochondria during apoptotic cell death. The Journal of cell biology. 2007;177(3):439-50. Epub 2007/05/02. doi: 10.1083/jcb.200610042. PubMed PMID: 17470634; PubMed Central PMCID: PMCPMC2064824.

129. Shen Q, Yamano K, Head BP, Kawajiri S, Cheung JT, Wang C, et al. Mutations in Fis1 disrupt orderly disposal of defective mitochondria. Molecular biology of the cell. 2014;25(1):145-59. Epub 2013/11/08. doi: 10.1091/mbc.E13-09-0525. PubMed PMID: 24196833; PubMed Central PMCID: PMCPMC3873885.

130. Osellame LD, Singh AP, Stroud DA, Palmer CS, Stojanovski D, Ramachandran R, et al. Cooperative and independent roles of the Drp1 adaptors Mff, MiD49 and MiD51 in mitochondrial fission. Journal of cell science. 2016;129(11):2170-81. Epub 2016/04/15. doi: 10.1242/jcs.185165. PubMed PMID: 27076521; PubMed Central PMCID: PMCPMC6919635.

131. Simpson CL, Tokito MK, Uppala R, Sarkar MK, Gudjonsson JE, Holzbaur ELF. NIX initiates mitochondrial fragmentation via DRP1 to drive epidermal differentiation. Cell reports. 2021;34(5):108689. Epub 2021/02/04. doi: 10.1016/j.celrep.2021.108689. PubMed PMID: 33535046; PubMed Central PMCID: PMCPMC7888979.

132. Friedman JR, Lackner LL, West M, DiBenedetto JR, Nunnari J, Voeltz GK. ER tubules mark sites of mitochondrial division. Science (New York, NY).

2011;334(6054):358-62. Epub 2011/09/03. doi: 10.1126/science.1207385. PubMed PMID: 21885730; PubMed Central PMCID: PMCPMC3366560.

133. Csordás G, Weaver D, Hajnóczky G. Endoplasmic Reticulum-Mitochondrial Contactology: Structure and Signaling Functions. Trends in cell biology. 2018;28(7):523-40. Epub 2018/03/29. doi: 10.1016/j.tcb.2018.02.009. PubMed PMID: 29588129; PubMed Central PMCID: PMCPMC6005738.

134. Scorrano L, De Matteis MA, Emr S, Giordano F, Hajnóczky G, Kornmann B, et al. Coming together to define membrane contact sites. Nature communications. 2019;10(1):1287. Epub 2019/03/22. doi: 10.1038/s41467-019-09253-3. PubMed PMID: 30894536; PubMed Central PMCID: PMCPMC6427007.

135. Csordás G, Renken C, Várnai P, Walter L, Weaver D, Buttle KF, et al. Structural and functional features and significance of the physical linkage between ER and mitochondria. The Journal of cell biology. 2006;174(7):915-21. Epub 2006/09/20. doi: 10.1083/jcb.200604016. PubMed PMID: 16982799; PubMed Central PMCID: PMCPMC2064383.

136. Lewis SC, Uchiyama LF, Nunnari J. ER-mitochondria contacts couple mtDNA synthesis with mitochondrial division in human cells. Science (New York, NY). 2016;353(6296):aaf5549. Epub 2016/07/16. doi: 10.1126/science.aaf5549. PubMed PMID: 27418514; PubMed Central PMCID: PMCPMC5554545.

137. Wong YC, Ysselstein D, Krainc D. Mitochondria-lysosome contacts regulate mitochondrial fission via RAB7 GTP hydrolysis. Nature. 2018;554(7692):382-6. Epub 2018/01/25. doi: 10.1038/nature25486. PubMed PMID: 29364868; PubMed Central PMCID: PMCPMC6209448.

138. Wong YC, Peng W, Krainc D. Lysosomal Regulation of Inter-mitochondrial Contact Fate and Motility in Charcot-Marie-Tooth Type 2. Developmental cell. 2019;50(3):339-54.e4. Epub 2019/06/25. doi: 10.1016/j.devcel.2019.05.033. PubMed PMID: 31231042; PubMed Central PMCID: PMCPMC6726396.

139. Boutry M, Kim PK. ORP1L mediated PI(4)P signaling at ER-lysosome-mitochondrion three-way contact contributes to mitochondrial division. Nature communications. 2021;12(1):5354. doi: 10.1038/s41467-021-25621-4.

140. Nagashima S, Tábara LC, Tilokani L, Paupe V, Anand H, Pogson JH, et al. Golgi-derived PI(4)P-containing vesicles drive late steps of mitochondrial division. Science (New York, NY). 2020;367(6484):1366-71. Epub 2020/03/21. doi: 10.1126/science.aax6089. PubMed PMID: 32193326.

141. Taguchi N, Ishihara N, Jofuku A, Oka T, Mihara K. Mitotic phosphorylation of dynamin-related GTPase Drp1 participates in mitochondrial fission. The Journal of biological chemistry. 2007;282(15):11521-9. Epub 2007/02/16. doi: 10.1074/jbc.M607279200. PubMed PMID: 17301055.

142. Kashatus DF, Lim KH, Brady DC, Pershing NL, Cox AD, Counter CM. RALA and RALBP1 regulate mitochondrial fission at mitosis. Nature cell biology. 2011;13(9):1108-15. Epub 2011/08/09. doi: 10.1038/ncb2310. PubMed PMID: 21822277; PubMed Central PMCID: PMCPMC3167028.

143. Ishihara N, Nomura M, Jofuku A, Kato H, Suzuki SO, Masuda K, et al. Mitochondrial fission factor Drp1 is essential for embryonic development and synapse formation in mice. Nature cell biology. 2009;11(8):958-66. Epub 2009/07/07. doi: 10.1038/ncb1907. PubMed PMID: 19578372.

144. Shields LY, Kim H, Zhu L, Haddad D, Berthet A, Pathak D, et al. Dynamin-related protein 1 is required for normal mitochondrial bioenergetic and synaptic function in CA1 hippocampal neurons. Cell death & disease. 2015;6(4):e1725. Epub 2015/04/17. doi: 10.1038/cddis.2015.94. PubMed PMID: 25880092; PubMed Central PMCID: PMCPMC4650558.

145. Rey T, Zaganelli S, Cuillery E, Vartholomaiou E, Croisier M, Martinou JC, et al. Mitochondrial RNA granules are fluid condensates positioned by membrane dynamics. Nature cell biology. 2020;22(10):1180-6. Epub 2020/09/30. doi: 10.1038/s41556-020-00584-8. PubMed PMID: 32989247; PubMed Central PMCID: PMCPMC7610405.

146. Yamashita SI, Jin X, Furukawa K, Hamasaki M, Nezu A, Otera H, et al. Mitochondrial division occurs concurrently with autophagosome formation but independently of Drp1 during mitophagy. The Journal of cell biology. 2016;215(5):649-65. Epub 2016/12/03. doi: 10.1083/jcb.201605093. PubMed PMID: 27903607; PubMed Central PMCID: PMCPMC5147001.

147. Burman JL, Pickles S, Wang C, Sekine S, Vargas JNS, Zhang Z, et al. Mitochondrial fission facilitates the selective mitophagy of protein aggregates. The

Journal of cell biology. 2017;216(10):3231-47. Epub 2017/09/13. doi: 10.1083/jcb.201612106. PubMed PMID: 28893839; PubMed Central PMCID: PMCPMC5626535.

148. Soubannier V, McLelland GL, Zunino R, Braschi E, Rippstein P, Fon EA, et al. A vesicular transport pathway shuttles cargo from mitochondria to lysosomes. Current biology : CB. 2012;22(2):135-41. Epub 2012/01/10. doi: 10.1016/j.cub.2011.11.057. PubMed PMID: 22226745.

149. Fu D, Lippincott-Schwartz J. Monitoring the Effects of Pharmacological Reagents on Mitochondrial Morphology. Current protocols in cell biology. 2018;79(1):e45. Epub 2018/06/21. doi: 10.1002/cpcb.45. PubMed PMID: 29924486.

150. Legros F, Lombès A, Frachon P, Rojo M. Mitochondrial fusion in human cells is efficient, requires the inner membrane potential, and is mediated by mitofusins. Molecular biology of the cell. 2002;13(12):4343-54. Epub 2002/12/12. doi: 10.1091/mbc.e02-06-0330. PubMed PMID: 12475957; PubMed Central PMCID: PMCPMC138638.

151. Li GB, Zhang HW, Fu RQ, Hu XY, Liu L, Li YN, et al. Mitochondrial fission and mitophagy depend on cofilin-mediated actin depolymerization activity at the mitochondrial fission site. Oncogene. 2018;37(11):1485-502. Epub 2018/01/13. doi: 10.1038/s41388-017-0064-4. PubMed PMID: 29321664.

152. Mageswaran SK, Grotjahn DA, Zeng X, Barad BA, Medina M, Hoang MH, et al. Nanoscale details of mitochondrial fission revealed by cryo-electron tomography. bioRxiv. 2021:2021.12.13.472487. doi: 10.1101/2021.12.13.472487.

153. Minamikawa T, Williams DA, Bowser DN, Nagley P. Mitochondrial permeability transition and swelling can occur reversibly without inducing cell death in intact human cells. Experimental cell research. 1999;246(1):26-37. Epub 1999/01/12. doi: 10.1006/excr.1998.4290. PubMed PMID: 9882512.

154. De Vos KJ, Allan VJ, Grierson AJ, Sheetz MP. Mitochondrial function and actin regulate dynamin-related protein 1-dependent mitochondrial fission. Current biology : CB. 2005;15(7):678-83. Epub 2005/04/13. doi: 10.1016/j.cub.2005.02.064. PubMed PMID: 15823542.

155. Liu X, Hajnóczky G. Altered fusion dynamics underlie unique morphological changes in mitochondria during hypoxia-reoxygenation stress. Cell death and differentiation. 2011;18(10):1561-72. Epub 2011/03/05. doi: 10.1038/cdd.2011.13. PubMed PMID: 21372848; PubMed Central PMCID: PMCPMC3172112.

156. Miyazono Y, Hirashima S, Ishihara N, Kusukawa J, Nakamura K-i, Ohta K. Uncoupled mitochondria quickly shorten along their long axis to form indented spheroids, instead of rings, in a fission-independent manner. Scientific reports. 2018;8(1):350. doi: 10.1038/s41598-017-18582-6.

157. Malka F, Guillery O, Cifuentes-Diaz C, Guillou E, Belenguer P, Lombès A, et al. Separate fusion of outer and inner mitochondrial membranes. EMBO reports. 2005;6(9):853-9. Epub 2005/08/23. doi: 10.1038/sj.embor.7400488. PubMed PMID: 16113651; PubMed Central PMCID: PMCPMC1369163.

158. Ishihara N, Eura Y, Mihara K. Mitofusin 1 and 2 play distinct roles in mitochondrial fusion reactions via GTPase activity. Journal of cell science. 2004;117(Pt 26):6535-46. Epub 2004/12/02. doi: 10.1242/jcs.01565. PubMed PMID: 15572413.

159. Song Z, Ghochani M, McCaffery JM, Frey TG, Chan DC. Mitofusins and OPA1 mediate sequential steps in mitochondrial membrane fusion. Molecular biology of the cell. 2009;20(15):3525-32. Epub 2009/05/30. doi: 10.1091/mbc.e09-03-0252. PubMed PMID: 19477917; PubMed Central PMCID: PMCPMC2719570.

160. Ban T, Ishihara T, Kohno H, Saita S, Ichimura A, Maenaka K, et al. Molecular basis of selective mitochondrial fusion by heterotypic action between OPA1 and cardiolipin. Nature cell biology. 2017;19(7):856-63. Epub 2017/06/20. doi: 10.1038/ncb3560. PubMed PMID: 28628083.

161. Chen H, Detmer SA, Ewald AJ, Griffin EE, Fraser SE, Chan DC. Mitofusins Mfn1 and Mfn2 coordinately regulate mitochondrial fusion and are essential for embryonic development. The Journal of cell biology. 2003;160(2):189-200. Epub 2003/01/16. doi: 10.1083/jcb.200211046. PubMed PMID: 12527753; PubMed Central PMCID: PMCPMC2172648.

162. Chen Y, Liu Y, Dorn GW, 2nd. Mitochondrial fusion is essential for organelle function and cardiac homeostasis. Circulation research. 2011;109(12):1327-31. Epub 2011/11/05. doi: 10.1161/circresaha.111.258723. PubMed PMID: 22052916; PubMed Central PMCID: PMCPMC3237902.

163. Chen H, Chan DC. Mitochondrial dynamics--fusion, fission, movement, and mitophagy--in neurodegenerative diseases. Human molecular genetics. 2009;18(R2):R169-76. Epub 2009/10/08. doi: 10.1093/hmg/ddp326. PubMed PMID: 19808793; PubMed Central PMCID: PMCPMC2758711.

164. Chen H, Vermulst M, Wang YE, Chomyn A, Prolla TA, McCaffery JM, et al. Mitochondrial fusion is required for mtDNA stability in skeletal muscle and tolerance of mtDNA mutations. Cell. 2010;141(2):280-9. Epub 2010/04/21. doi: 10.1016/j.cell.2010.02.026. PubMed PMID: 20403324; PubMed Central PMCID: PMCPMC2876819.

165. Hermann GJ, Thatcher JW, Mills JP, Hales KG, Fuller MT, Nunnari J, et al. Mitochondrial fusion in yeast requires the transmembrane GTPase Fzo1p. The Journal of cell biology. 1998;143(2):359-73. Epub 1998/10/24. doi: 10.1083/jcb.143.2.359. PubMed PMID: 9786948; PubMed Central PMCID: PMCPMC2132826.

166. Chen H, McCaffery JM, Chan DC. Mitochondrial fusion protects against neurodegeneration in the cerebellum. Cell. 2007;130(3):548-62. Epub 2007/08/19. doi: 10.1016/j.cell.2007.06.026. PubMed PMID: 17693261.

167. Abrisch RG, Gumbin SC, Wisniewski BT, Lackner LL, Voeltz GK. Fission and fusion machineries converge at ER contact sites to regulate mitochondrial morphology. The Journal of cell biology. 2020;219(4). Epub 2020/04/25. doi: 10.1083/jcb.201911122. PubMed PMID: 32328629; PubMed Central PMCID: PMCPMC7147108.

168. Mishra P, Carelli V, Manfredi G, Chan DC. Proteolytic cleavage of Opa1 stimulates mitochondrial inner membrane fusion and couples fusion to oxidative phosphorylation. Cell metabolism. 2014;19(4):630-41. Epub 2014/04/08. doi: 10.1016/j.cmet.2014.03.011. PubMed PMID: 24703695; PubMed Central PMCID: PMCPMC4018240.

169. Amchenkova AA, Bakeeva LE, Chentsov YS, Skulachev VP, Zorov DB. Coupling membranes as energy-transmitting cables. I. Filamentous mitochondria in fibroblasts and mitochondrial clusters in cardiomyocytes. The Journal of cell biology. 1988;107(2):481-95. Epub 1988/08/01. doi: 10.1083/jcb.107.2.481. PubMed PMID: 3417757; PubMed Central PMCID: PMCPMC2115217.

170. Skulachev VP. Mitochondrial filaments and clusters as intracellular power-transmitting cables. Trends in biochemical sciences. 2001;26(1):23-9. Epub 2001/02/13. doi: 10.1016/s0968-0004(00)01735-7. PubMed PMID: 11165513.

171. Mitra K, Wunder C, Roysam B, Lin G, Lippincott-Schwartz J. A hyperfused mitochondrial state achieved at G1-S regulates cyclin E buildup and entry into S phase. Proceedings of the National Academy of Sciences of the United States of America. 2009;106(29):11960-5. Epub 2009/07/21. doi: 10.1073/pnas.0904875106. PubMed PMID: 19617534; PubMed Central PMCID: PMCPMC2710990.

172. Tondera D, Grandemange S, Jourdain A, Karbowski M, Mattenberger Y, Herzig S, et al. SLP-2 is required for stress-induced mitochondrial hyperfusion. The EMBO journal. 2009;28(11):1589-600. Epub 2009/04/11. doi: 10.1038/emboj.2009.89. PubMed PMID: 19360003; PubMed Central PMCID: PMCPMC2693158.

173. Yao CH, Wang R, Wang Y, Kung CP, Weber JD, Patti GJ. Mitochondrial fusion supports increased oxidative phosphorylation during cell proliferation. Elife. 2019;8. Epub 2019/01/30. doi: 10.7554/eLife.41351. PubMed PMID: 30694178; PubMed Central PMCID: PMCPMC6351101.

174. Hardie DG. Keeping the home fires burning: AMP-activated protein kinase. Journal of the Royal Society, Interface. 2018;15(138). Epub 2018/01/19. doi: 10.1098/rsif.2017.0774. PubMed PMID: 29343628; PubMed Central PMCID: PMCPMC5805978.

175. Murphy MP, O'Neill LAJ. How should we talk about metabolism? Nature immunology. 2020;21(7):713-5. Epub 2020/05/16. doi: 10.1038/s41590-020-0691-8. PubMed PMID: 32409776.

176. Goodman RP, Calvo SE, Mootha VK. Spatiotemporal compartmentalization of hepatic NADH and NADPH metabolism. The Journal of biological chemistry. 2018;293(20):7508-16. Epub 2018/03/09. doi: 10.1074/jbc.TM117.000258. PubMed PMID: 29514978; PubMed Central PMCID: PMCPMC5961030.

177. Lewis CA, Parker SJ, Fiske BP, McCloskey D, Gui DY, Green CR, et al. Tracing compartmentalized NADPH metabolism in the cytosol and mitochondria of mammalian cells. Molecular cell. 2014;55(2):253-63. Epub 2014/06/03. doi: 10.1016/j.molcel.2014.05.008. PubMed PMID: 24882210; PubMed Central PMCID: PMCPMC4106038.

178. Luengo A, Li Z, Gui DY, Sullivan LB, Zagorulya M, Do BT, et al. Increased demand for NAD(+) relative to ATP drives aerobic glycolysis. Molecular cell. 2021;81(4):691-707.e6. Epub 2021/01/01. doi: 10.1016/j.molcel.2020.12.012. PubMed PMID: 33382985; PubMed Central PMCID: PMCPMC8315838.

179. Lautrup S, Sinclair DA, Mattson MP, Fang EF. NAD(+) in Brain Aging and Neurodegenerative Disorders. Cell metabolism. 2019;30(4):630-55. Epub 2019/10/03. doi: 10.1016/j.cmet.2019.09.001. PubMed PMID: 31577933; PubMed Central PMCID: PMCPMC6787556.

180. Imamura H, Nhat KP, Togawa H, Saito K, Iino R, Kato-Yamada Y, et al. Visualization of ATP levels inside single living cells with fluorescence resonance energy transfer-based genetically encoded indicators. Proceedings of the National Academy of Sciences of the United States of America. 2009;106(37):15651-6. Epub 2009/09/02. doi: 10.1073/pnas.0904764106. PubMed PMID: 19720993; PubMed Central PMCID: PMCPMC2735558.

181. Tantama M, Martínez-François JR, Mongeon R, Yellen G. Imaging energy status in live cells with a fluorescent biosensor of the intracellular ATP-to-ADP ratio. Nature communications. 2013;4(1):2550. doi: 10.1038/ncomms3550.

182. Hu Q, Wu D, Walker M, Wang P, Tian R, Wang W. Genetically encoded biosensors for evaluating NAD(+)/NADH ratio in cytosolic and mitochondrial compartments. Cell reports methods. 2021;1(7). Epub 2021/12/14. doi: 10.1016/j.crmeth.2021.100116. PubMed PMID: 34901920; PubMed Central PMCID: PMCPMC8659198.

183. Zhao Y, Wang A, Zou Y, Su N, Loscalzo J, Yang Y. In vivo monitoring of cellular energy metabolism using SoNar, a highly responsive sensor for NAD(+)/NADH redox state. Nature protocols. 2016;11(8):1345-59. Epub 2016/07/01. doi: 10.1038/nprot.2016.074. PubMed PMID: 27362337.

184. Zou Y, Wang A, Huang L, Zhu X, Hu Q, Zhang Y, et al. Illuminating NAD(+) Metabolism in Live Cells and In Vivo Using a Genetically Encoded Fluorescent Sensor. Developmental cell. 2020;53(2):240-52.e7. Epub 2020/03/21. doi: 10.1016/j.devcel.2020.02.017. PubMed PMID: 32197067; PubMed Central PMCID: PMCPMC7323873.

185. Chandel NS. Glycolysis. Cold Spring Harbor perspectives in biology. 2021;13(5). Epub 2021/05/05. doi: 10.1101/cshperspect.a040535. PubMed PMID: 33941515; PubMed Central PMCID: PMCPMC8091952.

186. Tirosh A, Shai I, Tekes-Manova D, Israeli E, Pereg D, Shochat T, et al. Normal Fasting Plasma Glucose Levels and Type 2 Diabetes in Young Men. New England Journal of Medicine. 2005;353(14):1454-62. doi: 10.1056/NEJMoa050080.

187. Expert Committee on the D, Classification of Diabetes M. Follow-up Report on the Diagnosis of Diabetes Mellitus. Diabetes Spectrum. 2004;17(1):51-9. doi: 10.2337/diaspect.17.1.51.

188. Ancey PB, Contat C, Meylan E. Glucose transporters in cancer - from tumor cells to the tumor microenvironment. The FEBS journal. 2018;285(16):2926-43. Epub 2018/06/13. doi: 10.1111/febs.14577. PubMed PMID: 29893496.

189. Chen LQ, Cheung LS, Feng L, Tanner W, Frommer WB. Transport of sugars. Annual review of biochemistry. 2015;84:865-94. Epub 2015/03/10. doi: 10.1146/annurev-biochem-060614-033904. PubMed PMID: 25747398.

190. Pelley JW. 6 - Glycolysis and Pyruvate Oxidation. In: Pelley JW, editor. Elsevier's Integrated Review Biochemistry (Second Edition). Philadelphia: W.B. Saunders; 2012. p. 49-55.

191. Houtkooper RH, Cantó C, Wanders RJ, Auwerx J. The secret life of NAD+: an old metabolite controlling new metabolic signaling pathways. Endocrine reviews. 2010;31(2):194-223. Epub 2009/12/17. doi: 10.1210/er.2009-0026. PubMed PMID: 20007326; PubMed Central PMCID: PMCPMC2852209.

192. Martin JL, Costa ASH, Gruszczyk AV, Beach TE, Allen FM, Prag HA, et al. Succinate accumulation drives ischaemia-reperfusion injury during organ transplantation. Nature Metabolism. 2019;1(10):966-74. doi: 10.1038/s42255-019-0115-y.

193. Li Z, Ji BW, Dixit PD, Tchourine K, Lien EC, Hosios AM, et al. Cancer cells depend on environmental lipids for proliferation when electron acceptors are limited. Nat Metab. 2022;4(6):711-23. Epub 2022/06/24. doi: 10.1038/s42255-022-00588-8. PubMed PMID: 35739397.

194. Halestrap AP, Wilson MC. The monocarboxylate transporter family--role and regulation. IUBMB life. 2012;64(2):109-19. Epub 2011/12/14. doi: 10.1002/iub.572. PubMed PMID: 22162139.

195. Gruszczyk AV, Casey AM, James AM, Prag HA, Burger N, Bates GR, et al. Mitochondrial metabolism and bioenergetic function in an anoxic isolated adult mouse cardiomyocyte model of in vivo cardiac ischemia-reperfusion injury. Redox biology. 2022;54:102368. Epub 2022/06/25. doi: 10.1016/j.redox.2022.102368. PubMed PMID: 35749842; PubMed Central PMCID: PMCPMC9234472.

196. Rabinowitz JD, Enerbäck S. Lactate: the ugly duckling of energy metabolism. Nat Metab. 2020;2(7):566-71. Epub 2020/07/23. doi: 10.1038/s42255-020-0243-4. PubMed PMID: 32694798; PubMed Central PMCID: PMCPMC7983055.

197. Watson MJ, Vignali PDA, Mullett SJ, Overacre-Delgoffe AE, Peralta RM, Grebinoski S, et al. Metabolic support of tumour-infiltrating regulatory T cells by lactic acid. Nature. 2021;591(7851):645-51. doi: 10.1038/s41586-020-03045-2.

198. Karagiannis A, Gallopin T, Lacroix A, Plaisier F, Piquet J, Geoffroy H, et al. Lactate is an energy substrate for rodent cortical neurons and enhances their firing activity. eLife. 2021;10:e71424. doi: 10.7554/eLife.71424.

199. Brooks GA. Role of the Heart in Lactate Shuttling. Frontiers in nutrition. 2021;8:663560. Epub 2021/05/11. doi: 10.3389/fnut.2021.663560. PubMed PMID: 33968972; PubMed Central PMCID: PMCPMC8101701.

200. Li VL, He Y, Contrepois K, Liu H, Kim JT, Wiggenhorn AL, et al. An exercise-inducible metabolite that suppresses feeding and obesity. Nature. 2022;606(7915):785-90. Epub 2022/06/16. doi: 10.1038/s41586-022-04828-5. PubMed PMID: 35705806.

201. Zhang D, Tang Z, Huang H, Zhou G, Cui C, Weng Y, et al. Metabolic regulation of gene expression by histone lactylation. Nature. 2019;574(7779):575-80. Epub 2019/10/28. doi: 10.1038/s41586-019-1678-1. PubMed PMID: 31645732; PubMed Central PMCID: PMCPMC6818755.

202. Liu S, Fu S, Wang G, Cao Y, Li L, Li X, et al. Glycerol-3-phosphate biosynthesis regenerates cytosolic NAD(+) to alleviate mitochondrial disease. Cell metabolism. 2021;33(10):1974-87.e9. Epub 2021/07/17. doi: 10.1016/j.cmet.2021.06.013. PubMed PMID: 34270929.

203. Vander Heiden MG, Cantley LC, Thompson CB. Understanding the Warburg effect: the metabolic requirements of cell proliferation. Science (New York, NY). 2009;324(5930):1029-33. Epub 2009/05/23. doi: 10.1126/science.1160809. PubMed PMID: 19460998; PubMed Central PMCID: PMCPMC2849637.

204. Ohashi K, Kawai S, Murata K. Identification and characterization of a human mitochondrial NAD kinase. Nature communications. 2012;3(1):1248. doi: 10.1038/ncomms2262.

205. Zhu J, Schwörer S, Berisa M, Kyung YJ, Ryu KW, Yi J, et al. Mitochondrial NADP(H) generation is essential for proline biosynthesis. Science (New York, NY). 2021;372(6545):968-72. Epub 2021/04/24. doi: 10.1126/science.abd5491. PubMed PMID: 33888598; PubMed Central PMCID: PMCPMC8241437.

206. Campbell S, Mesaros C, Izzo L, Affronti H, Noji M, Schaffer BE, et al. Glutamine deprivation triggers NAGK-dependent hexosamine salvage. Elife. 2021;10. Epub 2021/12/01. doi: 10.7554/eLife.62644. PubMed PMID: 34844667; PubMed Central PMCID: PMCPMC8631944.

207. Wellen KE, Lu C, Mancuso A, Lemons JM, Ryczko M, Dennis JW, et al. The hexosamine biosynthetic pathway couples growth factor-induced glutamine uptake to glucose metabolism. Genes & development. 2010;24(24):2784-99. Epub 2010/11/26. doi: 10.1101/gad.1985910. PubMed PMID: 21106670; PubMed Central PMCID: PMCPMC3003197.

208. Hart GW, Slawson C, Ramirez-Correa G, Lagerlof O. Cross talk between O-GlcNAcylation and phosphorylation: roles in signaling, transcription, and chronic disease. Annual review of biochemistry. 2011;80:825.

209. Chandel NS. Carbohydrate Metabolism. Cold Spring Harbor perspectives in biology. 2021;13(1). Epub 2021/01/06. doi: 10.1101/cshperspect.a040568. PubMed PMID: 33397651; PubMed Central PMCID: PMCPMC7778149.

210. Park G, Jung S, Wellen KE, Jang C. The interaction between the gut microbiota and dietary carbohydrates in nonalcoholic fatty liver disease. Experimental & molecular medicine. 2021;53(5):809-22. Epub 2021/05/22. doi: 10.1038/s12276-021-00614-x. PubMed PMID: 34017059; PubMed Central PMCID: PMCPMC8178320.

211. Tappy L, Lê KA. Metabolic effects of fructose and the worldwide increase in obesity. Physiological reviews. 2010;90(1):23-46. Epub 2010/01/21. doi: 10.1152/physrev.00019.2009. PubMed PMID: 20086073.

212. Kennedy EP, Lehninger AL. Oxidation of fatty acids and tricarboxylic acid cycle intermediates by isolated rat liver mitochondria. The Journal of biological chemistry. 1949;179(2):957-72. Epub 1949/06/01. PubMed PMID: 18150026.

213. Ernster L, Schatz G. Mitochondria: a historical review. Journal of Cell Biology. 1981;91(3):227s-55s. doi: 10.1083/jcb.91.3.227s.

214. Elia I, Rowe JH, Johnson S, Joshi S, Notarangelo G, Kurmi K, et al. Tumor cells dictate anti-tumor immune responses by altering pyruvate utilization and succinate signaling in CD8(+) T cells. Cell metabolism. 2022. Epub 2022/07/13. doi: 10.1016/j.cmet.2022.06.008. PubMed PMID: 35820416.

215. Krebs HA, Johnson WA. Metabolism of ketonic acids in animal tissues. The Biochemical journal. 1937;31(4):645-60. Epub 1937/04/01. doi: 10.1042/bj0310645. PubMed PMID: 16746382; PubMed Central PMCID: PMCPMC1266984.

216. Krebs HA, Eggleston LV. The oxidation of pyruvate in pigeon breast muscle. The Biochemical journal. 1940;34(3):442-59. Epub 1940/03/01. doi: 10.1042/bj0340442. PubMed PMID: 16747180; PubMed Central PMCID: PMCPMC1265297.

217. Chandel NS. Mitochondria. Cold Spring Harbor perspectives in biology. 2021;13(3). Epub 2021/03/03. doi: 10.1101/cshperspect.a040543. PubMed PMID: 33649187; PubMed Central PMCID: PMCPMC7919390.

218. Zhao W-N, McAlister-Henn L. Assembly and Function of a Cytosolic Form of NADH-specific Isocitrate Dehydrogenase in Yeast (∗). Journal of Biological Chemistry. 1996;271(17):10347-52.

219. Glancy B, Balaban RS. Role of mitochondrial Ca2+ in the regulation of cellular energetics. Biochemistry. 2012;51(14):2959-73. Epub 2012/03/27. doi: 10.1021/bi2018909. PubMed PMID: 22443365; PubMed Central PMCID: PMCPMC3332087.

220. Williams GS, Boyman L, Lederer WJ. Mitochondrial calcium and the regulation of metabolism in the heart. Journal of molecular and cellular cardiology. 2015;78:35-45.

Epub 2014/12/03. doi: 10.1016/j.yjmcc.2014.10.019. PubMed PMID: 25450609; PubMed Central PMCID: PMCPMC6534814.

221. Rich PR, Maréchal A. The mitochondrial respiratory chain. Essays in biochemistry. 2010;47:1-23. Epub 2010/06/11. doi: 10.1042/bse0470001. PubMed PMID: 20533897.

222. Spinelli JB, Haigis MC. The multifaceted contributions of mitochondria to cellular metabolism. Nature cell biology. 2018;20(7):745-54. Epub 2018/06/29. doi: 10.1038/s41556-018-0124-1. PubMed PMID: 29950572; PubMed Central PMCID: PMCPMC6541229.

223. Birsoy K, Wang T, Chen WW, Freinkman E, Abu-Remaileh M, Sabatini DM. An Essential Role of the Mitochondrial Electron Transport Chain in Cell Proliferation Is to Enable Aspartate Synthesis. Cell. 2015;162(3):540-51. Epub 2015/08/02. doi: 10.1016/j.cell.2015.07.016. PubMed PMID: 26232224; PubMed Central PMCID: PMCPMC4522279.

224. Sullivan LB, Gui DY, Hosios AM, Bush LN, Freinkman E, Vander Heiden MG. Supporting Aspartate Biosynthesis Is an Essential Function of Respiration in Proliferating Cells. Cell. 2015;162(3):552-63. Epub 2015/08/02. doi: 10.1016/j.cell.2015.07.017. PubMed PMID: 26232225; PubMed Central PMCID: PMCPMC4522278.

225. Arnold PK, Jackson BT, Paras KI, Brunner JS, Hart ML, Newsom OJ, et al. A non-canonical tricarboxylic acid cycle underlies cellular identity. Nature. 2022;603(7901):477-81. Epub 2022/03/11. doi: 10.1038/s41586-022-04475-w. PubMed PMID: 35264789; PubMed Central PMCID: PMCPMC8934290.

226. Hatzivassiliou G, Zhao F, Bauer DE, Andreadis C, Shaw AN, Dhanak D, et al. ATP citrate lyase inhibition can suppress tumor cell growth. Cancer cell. 2005;8(4):311-21. Epub 2005/10/18. doi: 10.1016/j.ccr.2005.09.008. PubMed PMID: 16226706.

227. Srere PA. The citrate cleavage enzyme. I. Distribution and purification. The Journal of biological chemistry. 1959;234:2544-7. Epub 1959/10/01. PubMed PMID: 13833535.

228. Bauer DE, Hatzivassiliou G, Zhao F, Andreadis C, Thompson CB. ATP citrate lyase is an important component of cell growth and transformation. Oncogene.

2005;24(41):6314-22. Epub 2005/07/12. doi: 10.1038/sj.onc.1208773. PubMed PMID: 16007201.

229. Sivanand S, Viney I, Wellen KE. Spatiotemporal Control of Acetyl-CoA Metabolism in Chromatin Regulation. Trends in biochemical sciences. 2018;43(1):61-74. Epub 2017/11/28. doi: 10.1016/j.tibs.2017.11.004. PubMed PMID: 29174173; PubMed Central PMCID: PMCPMC5741483.

230. Zhao S, Torres A, Henry RA, Trefely S, Wallace M, Lee JV, et al. ATP-Citrate Lyase Controls a Glucose-to-Acetate Metabolic Switch. Cell reports. 2016;17(4):1037-52. Epub 2016/10/21. doi: 10.1016/j.celrep.2016.09.069. PubMed PMID: 27760311; PubMed Central PMCID: PMCPMC5175409.

231. Koveal D, Díaz-García CM, Yellen G. Fluorescent Biosensors for Neuronal Metabolism and the Challenges of Quantitation. Current opinion in neurobiology. 2020;63:111-21. Epub 2020/06/20. doi: 10.1016/j.conb.2020.02.011. PubMed PMID: 32559637; PubMed Central PMCID: PMCPMC7646541.

232. Jang C, Chen L, Rabinowitz JD. Metabolomics and Isotope Tracing. Cell. 2018;173(4):822-37. Epub 2018/05/05. doi: 10.1016/j.cell.2018.03.055. PubMed PMID: 29727671; PubMed Central PMCID: PMCPMC6034115.

233. Trefely S, Liu J, Huber K, Doan MT, Jiang H, Singh J, et al. Subcellular metabolic pathway kinetics are revealed by correcting for artifactual post harvest metabolism. Molecular Metabolism. 2019;30:61-71. doi: https://doi.org/10.1016/j.molmet.2019.09.004.

234. Mitchell P. Coupling of phosphorylation to electron and hydrogen transfer by a chemi-osmotic type of mechanism. Nature. 1961;191:144-8. Epub 1961/07/08. doi: 10.1038/191144a0. PubMed PMID: 13771349.

235. Mitchell P. Chemiosmotic coupling in oxidative and photosynthetic phosphorylation. 1966. Biochimica et biophysica acta. 2011;1807(12):1507-38. Epub 2011/11/16. doi: 10.1016/j.bbabio.2011.09.018. PubMed PMID: 22082452.

236. Slater EC. Peter Dennis Mitchell, 29 September 1920-10 April 1992. The Royal Society London; 1994.

237. Mitchell PD. Chemiosmotic coupling and energy transduction: Glynn Research; 1968.

238. Racker E, Stoeckenius W. Reconstitution of purple membrane vesicles catalyzing light-driven proton uptake and adenosine triphosphate formation. Journal of Biological Chemistry. 1974;249(2):662-3.

239. Mitchell P. Keilin's respiratory chain concept and its chemiosmotic consequences. Science (New York, NY). 1979;206(4423):1148-59. Epub 1979/12/07. doi: 10.1126/science.388618. PubMed PMID: 388618.

240. Brand MD, Nicholls DG. Assessing mitochondrial dysfunction in cells. The Biochemical journal. 2011;435(2):297-312. Epub 2011/07/06. doi: 10.1042/bj20110162. PubMed PMID: 21726199; PubMed Central PMCID: PMCPMC3076726.

241. Santo-Domingo J, Demaurex N. The renaissance of mitochondrial pH. Journal of General Physiology. 2012;139(6):415-23. doi: 10.1085/jgp.201110767.

242. Rieger B, Junge W, Busch KB. Lateral pH gradient between OXPHOS complex IV and F0F1 ATP-synthase in folded mitochondrial membranes. Nature communications. 2014;5(1):3103. doi: 10.1038/ncomms4103.

243. Wolf DM, Segawa M, Kondadi AK, Anand R, Bailey ST, Reichert AS, et al. Individual cristae within the same mitochondrion display different membrane potentials and are functionally independent. The EMBO journal. 2019;38(22):e101056. doi: https://doi.org/10.15252/embj.2018101056.

244. Nicholls DG. Mitochondrial proton leaks and uncoupling proteins. Biochimica et biophysica acta Bioenergetics. 2021;1862(7):148428. Epub 2021/04/03. doi: 10.1016/j.bbabio.2021.148428. PubMed PMID: 33798544.

245. Divakaruni AS, Brand MD. The regulation and physiology of mitochondrial proton leak. Physiology (Bethesda, Md). 2011;26(3):192-205. Epub 2011/06/15. doi: 10.1152/physiol.00046.2010. PubMed PMID: 21670165.

246. Jastroch M, Divakaruni AS, Mookerjee S, Treberg JR, Brand MD. Mitochondrial proton and electron leaks. Essays in biochemistry. 2010;47:53-67. doi: 10.1042/bse0470053. PubMed PMID: 20533900.

247. Nicholls DG. A history of UCP1. Biochemical Society transactions. 2001;29(Pt 6):751-5. Epub 2001/11/16. doi: 10.1042/bst0290751. PubMed PMID: 11709069.

248. Bertholet AM, Chouchani ET, Kazak L, Angelin A, Fedorenko A, Long JZ, et al. H(+) transport is an integral function of the mitochondrial ADP/ATP carrier. Nature. 2019;571(7766):515-20. Epub 2019/07/26. doi: 10.1038/s41586-019-1400-3. PubMed PMID: 31341297; PubMed Central PMCID: PMCPMC6662629.

249. White JS, von Heijne G, Engelman D. Cell Boundaries: How Membranes and Their Proteins Work: CRC Press; 2022.

250. Murphy MP, Chouchani ET. Why succinate? Physiological regulation by a mitochondrial coenzyme Q sentinel. Nature chemical biology. 2022;18(5):461-9. Epub 2022/04/29. doi: 10.1038/s41589-022-01004-8. PubMed PMID: 35484255; PubMed Central PMCID: PMCPMC9150600.

251. Gu J, Liu T, Guo R, Zhang L, Yang M. The coupling mechanism of mammalian mitochondrial complex I. Nature structural & molecular biology. 2022;29(2):172-82. Epub 2022/02/12. doi: 10.1038/s41594-022-00722-w. PubMed PMID: 35145322.

252. Hirst J. Mitochondrial complex I. Annual review of biochemistry. 2013;82:551-75. Epub 2013/03/27. doi: 10.1146/annurev-biochem-070511-103700. PubMed PMID: 23527692.

253. Pryde KR, Hirst J. Superoxide is produced by the reduced flavin in mitochondrial complex I: a single, unified mechanism that applies during both forward and reverse electron transfer. The Journal of biological chemistry. 2011;286(20):18056-65. Epub 2011/03/12. doi: 10.1074/jbc.M110.186841. PubMed PMID: 21393237; PubMed Central PMCID: PMCPMC3093879.

254. Murphy MP. How mitochondria produce reactive oxygen species. The Biochemical journal. 2009;417(1):1-13. doi: 10.1042/BJ20081386. PubMed PMID: 19061483.

255. Brand MD. Mitochondrial generation of superoxide and hydrogen peroxide as the source of mitochondrial redox signaling. Free Radical Biology and Medicine. 2016;100:14-31. doi: https://doi.org/10.1016/j.freeradbiomed.2016.04.001.

256. Fato R, Bergamini C, Bortolus M, Maniero AL, Leoni S, Ohnishi T, et al. Differential effects of mitochondrial Complex I inhibitors on production of reactive oxygen species. Biochimica et biophysica acta. 2009;1787(5):384-92. Epub 2008/12/09. doi:

10.1016/j.bbabio.2008.11.003. PubMed PMID: 19059197; PubMed Central PMCID: PMCPMC2724837.

257. Wheaton WW, Weinberg SE, Hamanaka RB, Soberanes S, Sullivan LB, Anso E, et al. Metformin inhibits mitochondrial complex I of cancer cells to reduce tumorigenesis. Elife. 2014;3:e02242. Epub 2014/05/21. doi: 10.7554/eLife.02242. PubMed PMID: 24843020; PubMed Central PMCID: PMCPMC4017650.

258. LaMoia TE, Shulman GI. Cellular and Molecular Mechanisms of Metformin Action. Endocrine reviews. 2021;42(1):77-96. doi: 10.1210/endrev/bnaa023.

259. González-Rodríguez P, Zampese E, Stout KA, Guzman JN, Ilijic E, Yang B, et al. Disruption of mitochondrial complex I induces progressive parkinsonism. Nature. 2021;599(7886):650-6. doi: 10.1038/s41586-021-04059-0.

260. Scharping NE, Rivadeneira DB, Menk AV, Vignali PDA, Ford BR, Rittenhouse NL, et al. Mitochondrial stress induced by continuous stimulation under hypoxia rapidly drives T cell exhaustion. Nature immunology. 2021;22(2):205-15. Epub 2021/01/06. doi: 10.1038/s41590-020-00834-9. PubMed PMID: 33398183; PubMed Central PMCID: PMCPMC7971090.

261. Karamanlidis G, Lee CF, Garcia-Menendez L, Kolwicz SC, Jr., Suthammarak W, Gong G, et al. Mitochondrial complex I deficiency increases protein acetylation and accelerates heart failure. Cell metabolism. 2013;18(2):239-50. Epub 2013/08/13. doi: 10.1016/j.cmet.2013.07.002. PubMed PMID: 23931755; PubMed Central PMCID: PMCPMC3779647.

262. Spinelli JB, Rosen PC, Sprenger HG, Puszynska AM, Mann JL, Roessler JM, et al. Fumarate is a terminal electron acceptor in the mammalian electron transport chain. Science (New York, NY). 2021;374(6572):1227-37. Epub 2021/12/03. doi: 10.1126/science.abi7495. PubMed PMID: 34855504; PubMed Central PMCID: PMCPMC8803114.

263. Selak MA, Armour SM, MacKenzie ED, Boulahbel H, Watson DG, Mansfield KD, et al. Succinate links TCA cycle dysfunction to oncogenesis by inhibiting HIF-alpha prolyl hydroxylase. Cancer cell. 2005;7(1):77-85. Epub 2005/01/18. doi: 10.1016/j.ccr.2004.11.022. PubMed PMID: 15652751.

264. Mitchell P. Possible molecular mechanisms of the protonmotive function of cytochrome systems. Journal of theoretical biology. 1976;62(2):327-67. Epub 1976/10/21. doi: 10.1016/0022-5193(76)90124-7. PubMed PMID: 186667.

265. Hunte C, Palsdottir H, Trumpower BL. Protonmotive pathways and mechanisms in the cytochrome bc1 complex. FEBS letters. 2003;545(1):39-46. Epub 2003/06/06. doi: 10.1016/s0014-5793(03)00391-0. PubMed PMID: 12788490.

266. Starkov AA, Fiskum G. Myxothiazol induces H(2)O(2) production from mitochondrial respiratory chain. Biochemical and biophysical research communications. 2001;281(3):645-50. Epub 2001/03/10. doi: 10.1006/bbrc.2001.4409. PubMed PMID: 11237706.

267. Hernansanz-Agustín P, Choya-Foces C, Carregal-Romero S, Ramos E, Oliva T, Villa-Piña T, et al. Na(+) controls hypoxic signalling by the mitochondrial respiratory chain. Nature. 2020;586(7828):287-91. Epub 07/29. doi: 10.1038/s41586-020-2551-y. PubMed PMID: 32728214.

268. Korge P, Calmettes G, John SA, Weiss JN. Reactive oxygen species production induced by pore opening in cardiac mitochondria: The role of complex III. The Journal of biological chemistry. 2017;292(24):9882-95. Epub 2017/04/30. doi: 10.1074/jbc.M116.768317. PubMed PMID: 28450391; PubMed Central PMCID: PMCPMC5473241.

269. Kaila VRI, Verkhovsky MI, Wikström M. Proton-Coupled Electron Transfer in Cytochrome Oxidase. Chemical Reviews. 2010;110(12):7062-81. doi: 10.1021/cr1002003.

270. LaMoia TE, Butrico GM, Kalpage HA, Goedeke L, Hubbard BT, Vatner DF, et al. Metformin, phenformin, and galegine inhibit complex IV activity and reduce glycerol-derived gluconeogenesis. Proceedings of the National Academy of Sciences of the United States of America. 2022;119(10):e2122287119. Epub 2022/03/04. doi: 10.1073/pnas.2122287119. PubMed PMID: 35238637; PubMed Central PMCID: PMCPMC8916010.

271. Katyal G, Ebanks B, Lucassen M, Papetti C, Chakrabarti L. Sequence and structure comparison of ATP synthase F0 subunits 6 and 8 in notothenioid fish. PloS one. 2021;16(10):e0245822-e. doi: 10.1371/journal.pone.0245822. PubMed PMID: 34613983.

272. Walker John E. The ATP synthase: the understood, the uncertain and the unknown. Biochemical Society transactions. 2013;41(1):1-16. doi: 10.1042/BST20110773.

273. Nirody JA, Budin I, Rangamani P. ATP synthase: Evolution, energetics, and membrane interactions. The Journal of general physiology. 2020;152(11). Epub 2020/09/24. doi: 10.1085/jgp.201912475. PubMed PMID: 32966553; PubMed Central PMCID: PMCPMC7594442.

274. Walker JE, Dickson VK. The peripheral stalk of the mitochondrial ATP synthase. Biochimica et biophysica acta. 2006;1757(5-6):286-96. Epub 2006/05/16. doi: 10.1016/j.bbabio.2006.01.001. PubMed PMID: 16697972.

275. Davies KM, Anselmi C, Wittig I, Faraldo-Gómez JD, Kühlbrandt W. Structure of the yeast F1Fo-ATP synthase dimer and its role in shaping the mitochondrial cristae. Proceedings of the National Academy of Sciences of the United States of America. 2012;109(34):13602-7. Epub 2012/08/07. doi: 10.1073/pnas.1204593109. PubMed PMID: 22864911; PubMed Central PMCID: PMCPMC3427116.

276. Blum Thorsten B, Hahn A, Meier T, Davies Karen M, Kühlbrandt W. Dimers of mitochondrial ATP synthase induce membrane curvature and self-assemble into rows. Proceedings of the National Academy of Sciences. 2019;116(10):4250-5. doi: 10.1073/pnas.1816556116.

277. Lardy HA, Johnson D, Mc MW. Antibiotics as tools for metabolic studies. I. A survey of toxic antibiotics in respiratory, phosphorylative and glycolytic systems. Archives of biochemistry and biophysics. 1958;78(2):587-97. Epub 1958/12/01. doi: 10.1016/0003-9861(58)90383-7. PubMed PMID: 13618041.

278. Racker E. A mitochondrial factor conferring oligomycin sensitivity on soluble mitochondrial ATPase. Biochemical and biophysical research communications. 1963;10:435-9. Epub 1963/03/25. doi: 10.1016/0006-291x(63)90375-9. PubMed PMID: 13972927.

279. Symersky J, Osowski D, Walters DE, Mueller DM. Oligomycin frames a common drug-binding site in the ATP synthase. Proceedings of the National Academy of Sciences of the United States of America. 2012;109(35):13961-5. Epub 08/06. doi: 10.1073/pnas.1207912109. PubMed PMID: 22869738.

280. Hirst J. Open questions: respiratory chain supercomplexes-why are they there and what do they do? BMC Biol. 2018;16(1):111. Epub 2018/11/02. doi: 10.1186/s12915-018-0577-5. PubMed PMID: 30382836; PubMed Central PMCID: PMCPMC6211484 PUBLISHER'S NOTE: Springer Nature remains neutral with regard to jurisdictional claims in published maps and institutional affiliations.

281. Milenkovic D, Blaza JN, Larsson NG, Hirst J. The Enigma of the Respiratory Chain Supercomplex. Cell metabolism. 2017;25(4):765-76. Epub 2017/04/06. doi: 10.1016/j.cmet.2017.03.009. PubMed PMID: 28380371.

282. Letts JA, Fiedorczuk K, Sazanov LA. The architecture of respiratory supercomplexes. Nature. 2016;537(7622):644-8. Epub 2016/09/23. doi: 10.1038/nature19774. PubMed PMID: 27654913.

283. Davies Karen M, Blum Thorsten B, Kühlbrandt W. Conserved in situ arrangement of complex I and III2 in mitochondrial respiratory chain supercomplexes of mammals, yeast, and plants. Proceedings of the National Academy of Sciences. 2018;115(12):3024-9. doi: 10.1073/pnas.1720702115.

284. Cogliati S, Frezza C, Soriano ME, Varanita T, Quintana-Cabrera R, Corrado M, et al. Mitochondrial cristae shape determines respiratory chain supercomplexes assembly and respiratory efficiency. Cell. 2013;155(1):160-71. Epub 2013/09/24. doi: 10.1016/j.cell.2013.08.032. PubMed PMID: 24055366; PubMed Central PMCID: PMCPMC3790458.

285. Muhleip A, Flygaard RK, Haapanen O, Baradaran R, Gruhl T, Tobiasson V, et al. Structural basis of mitochondrial membrane bending by I-II-III2-IV2 supercomplex. bioRxiv. 2022:2022.06.26.497646. doi: 10.1101/2022.06.26.497646.

286. Ast T, Mootha VK. Oxygen and mammalian cell culture: are we repeating the experiment of Dr. Ox? Nat Metab. 2019;1(9):858-60. Epub 2020/07/23. doi: 10.1038/s42255-019-0105-0. PubMed PMID: 32694740.

287. Cantor JR, Abu-Remaileh M, Kanarek N, Freinkman E, Gao X, Louissaint A, Jr., et al. Physiologic Medium Rewires Cellular Metabolism and Reveals Uric Acid as an Endogenous Inhibitor of UMP Synthase. Cell. 2017;169(2):258-72.e17. doi: 10.1016/j.cell.2017.03.023.

288. Pekkurnaz G, Trinidad JC, Wang X, Kong D, Schwarz TL. Glucose regulates mitochondrial motility via Milton modification by O-GlcNAc transferase. Cell. 2014;158(1):54-68. Epub 2014/07/06. doi: 10.1016/j.cell.2014.06.007. PubMed PMID: 24995978; PubMed Central PMCID: PMCPMC4224014.

289. Kasianowicz J, Benz R, McLaughlin S. The kinetic mechanism by which CCCP (carbonyl cyanide m-chlorophenylhydrazone) transports protons across membranes. The Journal of membrane biology. 1984;82(2):179-90. Epub 1984/01/01. doi: 10.1007/bf01868942. PubMed PMID: 6096547.

290. Benz R, McLaughlin S. The molecular mechanism of action of the proton ionophore FCCP (carbonylcyanide p-trifluoromethoxyphenylhydrazone). Biophysical journal. 1983;41(3):381-98. Epub 1983/03/01. doi: 10.1016/s0006-3495(83)84449-x. PubMed PMID: 6838976; PubMed Central PMCID: PMCPMC1329191.

291. TAINTER ML, STOCKTON AB, CUTTING WC. DINITROPHENOL IN THE TREATMENT OF OBESITY: FINAL REPORT. Journal of the American Medical Association. 1935;105(5):332-7. doi: 10.1001/jama.1935.02760310006002.

292. Colman E. Dinitrophenol and obesity: an early twentieth-century regulatory dilemma. Regulatory toxicology and pharmacology : RTP. 2007;48(2):115-7. Epub 2007/05/04. doi: 10.1016/j.yrtph.2007.03.006. PubMed PMID: 17475379.

293. Parascandola J. Dinitrophenol and bioenergetics: an historical perspective. Molecular and cellular biochemistry. 1974;5(1-2):69-77. Epub 1974/11/15. doi: 10.1007/bf01874175. PubMed PMID: 4610359.

294. Grundlingh J, Dargan PI, El-Zanfaly M, Wood DM. 2,4-dinitrophenol (DNP): a weight loss agent with significant acute toxicity and risk of death. Journal of medical toxicology : official journal of the American College of Medical Toxicology. 2011;7(3):205-12. Epub 2011/07/09. doi: 10.1007/s13181-011-0162-6. PubMed PMID: 21739343; PubMed Central PMCID: PMCPMC3550200.

295. Zhang C, Liu Z, Bunker E, Ramirez A, Lee S, Peng Y, et al. Sorafenib targets the mitochondrial electron transport chain complexes and ATP synthase to activate the PINK1-Parkin pathway and modulate cellular drug response. The Journal of biological chemistry. 2017;292(36):15105-20. Epub 2017/07/05. doi: 10.1074/jbc.M117.783175. PubMed PMID: 28673964; PubMed Central PMCID: PMCPMC5592685.

296. Perry SW, Norman JP, Barbieri J, Brown EB, Gelbard HA. Mitochondrial membrane potential probes and the proton gradient: a practical usage guide. BioTechniques. 2011;50(2):98-115. Epub 2011/04/14. doi: 10.2144/000113610. PubMed PMID: 21486251; PubMed Central PMCID: PMCPMC3115691.

297. Rego AC, Vesce S, Nicholls DG. The mechanism of mitochondrial membrane potential retention following release of cytochrome c in apoptotic GT1-7 neural cells. Cell death and differentiation. 2001;8(10):995-1003. Epub 2001/10/13. doi: 10.1038/sj.cdd.4400916. PubMed PMID: 11598797.

298. Connolly NMC, Theurey P, Adam-Vizi V, Bazan NG, Bernardi P, Bolaños JP, et al. Guidelines on experimental methods to assess mitochondrial dysfunction in cellular models of neurodegenerative diseases. Cell death and differentiation. 2018;25(3):542-72. Epub 2017/12/13. doi: 10.1038/s41418-017-0020-4. PubMed PMID: 29229998; PubMed Central PMCID: PMCPMC5864235.

299. Nicholls DG, Darley-Usmar VM, Wu M, Jensen PB, Rogers GW, Ferrick DA. Bioenergetic profile experiment using C2C12 myoblast cells. Journal of visualized experiments : JoVE. 2010(46). Epub 2010/12/30. doi: 10.3791/2511. PubMed PMID: 21189469; PubMed Central PMCID: PMCPMC3159644.

300. Ruas JS, Siqueira-Santos ES, Rodrigues-Silva E, Castilho RF. High glycolytic activity of tumor cells leads to underestimation of electron transport system capacity when mitochondrial ATP synthase is inhibited. Scientific reports. 2018;8(1):17383. Epub 2018/11/28. doi: 10.1038/s41598-018-35679-8. PubMed PMID: 30478338; PubMed Central PMCID: PMCPMC6255871.

301. Ruas JS, Siqueira-Santos ES, Amigo I, Rodrigues-Silva E, Kowaltowski AJ, Castilho RF. Underestimation of the Maximal Capacity of the Mitochondrial Electron Transport System in Oligomycin-Treated Cells. PloS one. 2016;11(3):e0150967. Epub 2016/03/08. doi: 10.1371/journal.pone.0150967. PubMed PMID: 26950698; PubMed Central PMCID: PMCPMC4780810.

302. Galber C, Minervini G, Cannino G, Boldrin F, Petronilli V, Tosatto S, et al. The f subunit of human ATP synthase is essential for normal mitochondrial morphology and permeability transition. Cell reports. 2021;35(6):109111. Epub 2021/05/13. doi: 10.1016/j.celrep.2021.109111. PubMed PMID: 33979610.

303. Bertholet AM, Natale AM, Bisignano P, Suzuki J, Fedorenko A, Hamilton J, et al. Mitochondrial uncouplers induce proton leak by activating AAC and UCP1. Nature. 2022;606(7912):180-7. Epub 2022/05/26. doi: 10.1038/s41586-022-04747-5. PubMed PMID: 35614225.

304. Trefts E, Shaw RJ. AMPK: restoring metabolic homeostasis over space and time. Molecular cell. 2021;81(18):3677-90. Epub 2021/09/22. doi: 10.1016/j.molcel.2021.08.015. PubMed PMID: 34547233; PubMed Central PMCID: PMCPMC8549486.

305. Herzig S, Shaw RJ. AMPK: guardian of metabolism and mitochondrial homeostasis. Nature Reviews Molecular Cell Biology. 2018;19(2):121-35. doi: 10.1038/nrm.2017.95.

306. Hawley SA, Davison M, Woods A, Davies SP, Beri RK, Carling D, et al. Characterization of the AMP-activated Protein Kinase Kinase from Rat Liver and Identification of Threonine 172 as the Major Site at Which It Phosphorylates AMP-activated Protein Kinase *. Journal of Biological Chemistry. 1996;271(44):27879-87. doi: 10.1074/jbc.271.44.27879.

307. Hawley SA, Boudeau J, Reid JL, Mustard KJ, Udd L, Mäkelä TP, et al. Complexes between the LKB1 tumor suppressor, STRADα/β and MO25α/β are upstream kinases in the AMP-activated protein kinase cascade. Journal of Biology. 2003;2(4):28. doi: 10.1186/1475-4924-2-28.

308. Vara-Ciruelos D, Russell FM, Hardie DG. The strange case of AMPK and cancer: Dr Jekyll or Mr Hyde? (†). Open biology. 2019;9(7):190099. Epub 2019/07/11. doi: 10.1098/rsob.190099. PubMed PMID: 31288625; PubMed Central PMCID: PMCPMC6685927.

309. Chen L, Jiao Z-H, Zheng L-S, Zhang Y-Y, Xie S-T, Wang Z-X, et al. Structural insight into the autoinhibition mechanism of AMP-activated protein kinase. Nature. 2009;459(7250):1146-9. doi: 10.1038/nature08075.

310. Gu X, Yan Y, Novick SJ, Kovach A, Goswami D, Ke J, et al. Deconvoluting AMP-activated protein kinase (AMPK) adenine nucleotide binding and sensing. Journal of Biological Chemistry. 2017;292(30):12653-66. doi: 10.1074/jbc.M117.793018.

311. Hardie DG, Schaffer BE, Brunet A. AMPK: An Energy-Sensing Pathway with Multiple Inputs and Outputs. Trends in cell biology. 2016;26(3):190-201. Epub 2015/12/01. doi: 10.1016/j.tcb.2015.10.013. PubMed PMID: 26616193; PubMed Central PMCID: PMCPMC5881568.

312. Hawley SA, Pan DA, Mustard KJ, Ross L, Bain J, Edelman AM, et al. Calmodulin-dependent protein kinase kinase-β is an alternative upstream kinase for AMP-activated protein kinase. Cell metabolism. 2005;2(1):9-19.

313. Woods A, Dickerson K, Heath R, Hong S-P, Momcilovic M, Johnstone SR, et al. Ca2+/calmodulin-dependent protein kinase kinase-β acts upstream of AMP-activated protein kinase in mammalian cells. Cell metabolism. 2005;2(1):21-33.

314. Toyama Erin Q, Herzig S, Courchet J, Lewis Tommy L, Losón Oliver C, Hellberg K, et al. AMP-activated protein kinase mediates mitochondrial fission in response to energy stress. Science (New York, NY). 2016;351(6270):275-81. doi: 10.1126/science.aab4138.

315. Hung C-M, Lombardo Portia S, Malik N, Brun Sonja N, Hellberg K, Van Nostrand Jeanine L, et al. AMPK/ULK1-mediated phosphorylation of Parkin ACT domain mediates an early step in mitophagy. Science Advances.7(15):eabg4544. doi: 10.1126/sciadv.abg4544.

316. Pasteur L. Expériences et vues nouvelles sur la nature des fermentations1861.

317. Pasteur L. The Physiological Theory of Fermentation: CreateSpace Independent Publishing Platform; 2018.

318. Corrado M, Pearce EL. Targeting memory T cell metabolism to improve immunity. The Journal of clinical investigation. 2022;132(1). Epub 2022/01/05. doi: 10.1172/jci148546. PubMed PMID: 34981777; PubMed Central PMCID: PMCPMC8718135 Therapeutics and a founder of Rheos Medicines.

319. Zhao S, Peralta RM, Avina-Ochoa N, Delgoffe GM, Kaech SM. Metabolic regulation of T cells in the tumor microenvironment by nutrient availability and diet. Seminars in immunology. 2021;52:101485. Epub 2021/09/01. doi: 10.1016/j.smim.2021.101485. PubMed PMID: 34462190; PubMed Central PMCID: PMCPMC8545851.

320. Warburg O. Uber den stoffwechsel der karzinomezellen. Biochem Z. 1924;152:309-44.

321. Racker E. Bioenergetics and the problem of tumor growth. American scientist. 1972;60(1):56-63. Epub 1972/01/01. PubMed PMID: 4332766.

322. Crabtree HG. Observations on the carbohydrate metabolism of tumours. The Biochemical journal. 1929;23(3):536-45. Epub 1929/01/01. doi: 10.1042/bj0230536. PubMed PMID: 16744238; PubMed Central PMCID: PMCPMC1254097.

323. Warburg O. On the Origin of Cancer Cells. Science (New York, NY). 1956;123(3191):309-14. doi: 10.1126/science.123.3191.309.

324. Warburg O. On respiratory impairment in cancer cells. Science (New York, NY). 1956;124(3215):269-70. Epub 1956/08/10. PubMed PMID: 13351639.

325. Otto AM. Warburg effect(s)—a biographical sketch of Otto Warburg and his impacts on tumor metabolism. Cancer & Metabolism. 2016;4(1):5. doi: 10.1186/s40170-016-0145-9.

326. Barros LF, Ruminot I, San Martín A, Lerchundi R, Fernández-Moncada I, Baeza-Lehnert F. Aerobic Glycolysis in the Brain: Warburg and Crabtree Contra Pasteur. Neurochemical Research. 2021;46(1):15-22. doi: 10.1007/s11064-020-02964-w.

327. Devic S. Warburg Effect - a Consequence or the Cause of Carcinogenesis? Journal of Cancer. 2016;7(7):817-22. Epub 2016/05/11. doi: 10.7150/jca.14274. PubMed PMID: 27162540; PubMed Central PMCID: PMCPMC4860798.

328. DeBerardinis RJ, Chandel NS. We need to talk about the Warburg effect. Nat Metab. 2020;2(2):127-9. Epub 2020/07/23. doi: 10.1038/s42255-020-0172-2. PubMed PMID: 32694689.

329. Koppenol WH, Bounds PL, Dang CV. Otto Warburg's contributions to current concepts of cancer metabolism. Nature reviews Cancer. 2011;11(5):325-37. Epub 2011/04/22. doi: 10.1038/nrc3038. PubMed PMID: 21508971.

330. Christofk HR, Vander Heiden MG, Harris MH, Ramanathan A, Gerszten RE, Wei R, et al. The M2 splice isoform of pyruvate kinase is important for cancer metabolism and tumour growth. Nature. 2008;452(7184):230-3. doi: 10.1038/nature06734.

331. Nolop KB, Rhodes CG, Brudin LH, Beaney RP, Krausz T, Jones T, et al. Glucose utilization in vivo by human pulmonary neoplasms. Cancer. 1987;60(11):2682-9. Epub 1987/12/01. doi: 10.1002/1097-0142(19871201)60:11<2682::aid-cncr2820601118>3.0.co;2-h. PubMed PMID: 3499969.

332. Barletta JA, Hornick JL. Succinate dehydrogenase-deficient tumors: diagnostic advances and clinical implications. Advances in anatomic pathology. 2012;19(4):193-203. Epub 2012/06/14. doi: 10.1097/PAP.0b013e31825c6bc6. PubMed PMID: 22692282.

333. Lane N. Transformer: The Deep Chemistry of Life and Death: Profile; 2022.

334. Vyas S, Zaganjor E, Haigis MC. Mitochondria and Cancer. Cell. 2016;166(3):555-66. Epub 2016/07/30. doi: 10.1016/j.cell.2016.07.002. PubMed PMID: 27471965; PubMed Central PMCID: PMCPMC5036969.

335. Chandel NS, Schumacker PT. Cellular oxygen sensing by mitochondria: old questions, new insight. Journal of applied physiology (Bethesda, Md : 1985). 2000;88(5):1880-9. Epub 2000/05/08. doi: 10.1152/jappl.2000.88.5.1880. PubMed PMID: 10797153.

336. Li S, Li W, Yuan J, Bullova P, Wu J, Zhang X, et al. Impaired oxygen-sensitive regulation of mitochondrial biogenesis within the von Hippel-Lindau syndrome. Nat Metab. 2022;4(6):739-58. Epub 2022/06/28. doi: 10.1038/s42255-022-00593-x. PubMed PMID: 35760869; PubMed Central PMCID: PMCPMC9236906.

337. Denko NC. Hypoxia, HIF1 and glucose metabolism in the solid tumour. Nature reviews Cancer. 2008;8(9):705-13. Epub 2009/01/15. doi: 10.1038/nrc2468. PubMed PMID: 19143055.

338. Lu H, Forbes RA, Verma A. Hypoxia-inducible Factor 1 Activation by Aerobic Glycolysis Implicates the Warburg Effect in Carcinogenesis*. Journal of Biological Chemistry. 2002;277(26):23111-5. doi: https://doi.org/10.1074/jbc.M202487200.

339. Lee P, Chandel NS, Simon MC. Cellular adaptation to hypoxia through hypoxia inducible factors and beyond. Nature reviews Molecular cell biology. 2020;21(5):268-83. Epub 2020/03/08. doi: 10.1038/s41580-020-0227-y. PubMed PMID: 32144406; PubMed Central PMCID: PMCPMC7222024.

340. Potter M, Newport E, Morten KJ. The Warburg effect: 80 years on. Biochemical Society transactions. 2016;44(5):1499-505. doi: 10.1042/BST20160094.

341. Lim AR, Rathmell WK, Rathmell JC. The tumor microenvironment as a metabolic barrier to effector T cells and immunotherapy. eLife. 2020;9:e55185. doi: 10.7554/eLife.55185. PubMed PMID: 32367803.

342. O'Sullivan D, Sanin DE, Pearce EJ, Pearce EL. Metabolic interventions in the immune response to cancer. Nature reviews Immunology. 2019;19(5):324-35. Epub 2019/03/02. doi: 10.1038/s41577-019-0140-9. PubMed PMID: 30820043.

343. Stine ZE, Schug ZT, Salvino JM, Dang CV. Targeting cancer metabolism in the era of precision oncology. Nature Reviews Drug Discovery. 2022;21(2):141-62. doi: 10.1038/s41573-021-00339-6.

344. Cercek A, Lumish M, Sinopoli J, Weiss J, Shia J, Lamendola-Essel M, et al. PD-1 Blockade in Mismatch Repair-Deficient, Locally Advanced Rectal Cancer. The New England journal of medicine. 2022;386(25):2363-76. Epub 2022/06/07. doi: 10.1056/NEJMoa2201445. PubMed PMID: 35660797.

345. DePeaux K, Delgoffe GM. Metabolic barriers to cancer immunotherapy. Nature reviews Immunology. 2021;21(12):785-97. Epub 2021/05/01. doi: 10.1038/s41577-021-00541-y. PubMed PMID: 33927375; PubMed Central PMCID: PMCPMC8553800.

346. Kumagai S, Koyama S, Itahashi K, Tanegashima T, Lin YT, Togashi Y, et al. Lactic acid promotes PD-1 expression in regulatory T cells in highly glycolytic tumor microenvironments. Cancer cell. 2022;40(2):201-18.e9. Epub 2022/01/30. doi: 10.1016/j.ccell.2022.01.001. PubMed PMID: 35090594.

347. Kaestner L. Perspective. In: Kaestner L, editor. Calcium signalling: Approaches and Findings in the Heart and Blood. Berlin, Heidelberg: Springer Berlin Heidelberg; 2013. p. 29-34.

348. Dittman JS, Ryan TA. The control of release probability at nerve terminals. Nature reviews Neuroscience. 2019;20(3):177-86. Epub 2019/01/17. doi: 10.1038/s41583-018-0111-3. PubMed PMID: 30647451.

349. Nicholls DG. The Pancreatic β-Cell: A Bioenergetic Perspective. Physiological reviews. 2016;96(4):1385-447. Epub 2016/09/02. doi: 10.1152/physrev.00009.2016. PubMed PMID: 27582250.

350. Berridge MJ, Bootman MD, Roderick HL. Calcium signalling: dynamics, homeostasis and remodelling. Nature reviews Molecular cell biology. 2003;4(7):517-29. Epub 2003/07/03. doi: 10.1038/nrm1155. PubMed PMID: 12838335.

351. Rizzuto R, Brini M, Murgia M, Pozzan T. Microdomains with high Ca2+ close to IP3-sensitive channels that are sensed by neighboring mitochondria. Science (New York, NY). 1993;262(5134):744-7. Epub 1993/10/29. doi: 10.1126/science.8235595. PubMed PMID: 8235595.

352. Lanner JT, Georgiou DK, Joshi AD, Hamilton SL. Ryanodine receptors: structure, expression, molecular details, and function in calcium release. Cold Spring Harbor perspectives in biology. 2010;2(11):a003996. Epub 2010/10/22. doi: 10.1101/cshperspect.a003996. PubMed PMID: 20961976; PubMed Central PMCID: PMCPMC2964179.

353. Rossi CS, Lehninger AL. STOICHIOMETRIC RELATIONSHIPS BETWEEN ACCUMULATION OF IONS BY MITOCHONDRIA AND THE ENERGY-COUPLING SITES IN THE RESPIRATORY CHAIN. Biochem Z. 1963;338:698-713. Epub 1963/01/01. PubMed PMID: 14087335.

354. Abramov AY, Canevari L, Duchen MR. Changes in intracellular calcium and glutathione in astrocytes as the primary mechanism of amyloid neurotoxicity. The Journal of neuroscience : the official journal of the Society for Neuroscience. 2003;23(12):5088-95. Epub 2003/07/02. doi: 10.1523/jneurosci.23-12-05088.2003. PubMed PMID: 12832532; PubMed Central PMCID: PMCPMC6741151.

355. Celsi F, Pizzo P, Brini M, Leo S, Fotino C, Pinton P, et al. Mitochondria, calcium and cell death: a deadly triad in neurodegeneration. Biochimica et biophysica acta. 2009;1787(5):335-44. Epub 2009/03/10. doi: 10.1016/j.bbabio.2009.02.021. PubMed PMID: 19268425; PubMed Central PMCID: PMCPMC2696196.

356. de Juan-Sanz J, Holt GT, Schreiter ER, de Juan F, Kim DS, Ryan TA. Axonal Endoplasmic Reticulum Ca(2+) Content Controls Release Probability in CNS Nerve Terminals. Neuron. 2017;93(4):867-81.e6. Epub 2017/02/07. doi: 10.1016/j.neuron.2017.01.010. PubMed PMID: 28162809; PubMed Central PMCID: PMCPMC5325711.

357. Demaurex N, Frieden M. Measurements of the free luminal ER Ca(2+) concentration with targeted "cameleon" fluorescent proteins. Cell calcium.

2003;34(2):109-19. Epub 2003/06/18. doi: 10.1016/s0143-4160(03)00081-2. PubMed PMID: 12810053.

358. Caridha D, Yourick D, Cabezas M, Wolf L, Hudson TH, Dow GS. Mefloquine-induced disruption of calcium homeostasis in mammalian cells is similar to that induced by ionomycin. Antimicrobial agents and chemotherapy. 2008;52(2):684-93. Epub 2007/11/15. doi: 10.1128/aac.00874-07. PubMed PMID: 17999964; PubMed Central PMCID: PMCPMC2224738.

359. Morgan AJ, Jacob R. Ionomycin enhances Ca2+ influx by stimulating store-regulated cation entry and not by a direct action at the plasma membrane. The Biochemical journal. 1994;300 (Pt 3)(Pt 3):665-72. Epub 1994/06/15. doi: 10.1042/bj3000665. PubMed PMID: 8010948; PubMed Central PMCID: PMCPMC1138219.

360. Clapham DE. Calcium Signaling. Cell. 2007;131(6):1047-58. doi: 10.1016/j.cell.2007.11.028.

361. Cooper D, Dimri M. Biochemistry, Calcium Channels. StatPearls. Treasure Island (FL): StatPearls Publishing

362. Chemaly ER, Troncone L, Lebeche D. SERCA control of cell death and survival. Cell calcium. 2018;69:46-61. Epub 2017/07/28. doi: 10.1016/j.ceca.2017.07.001. PubMed PMID: 28747251; PubMed Central PMCID: PMCPMC5748262.

363. Daverkausen-Fischer L, Pröls F. Regulation of calcium homeostasis and flux between the endoplasmic reticulum and the cytosol. The Journal of biological chemistry. 2022;298(7):102061. Epub 2022/05/25. doi: 10.1016/j.jbc.2022.102061. PubMed PMID: 35609712; PubMed Central PMCID: PMCPMC9218512.

364. Brini M, Carafoli E. The plasma membrane Ca²+ ATPase and the plasma membrane sodium calcium exchanger cooperate in the regulation of cell calcium. Cold Spring Harbor perspectives in biology. 2011;3(2). Epub 2011/03/23. doi: 10.1101/cshperspect.a004168. PubMed PMID: 21421919; PubMed Central PMCID: PMCPMC3039526.

365. Shattock MJ, Ottolia M, Bers DM, Blaustein MP, Boguslavskyi A, Bossuyt J, et al. Na+/Ca2+ exchange and Na+/K+-ATPase in the heart. The Journal of physiology.

2015;593(6):1361-82. Epub 2015/03/17. doi: 10.1113/jphysiol.2014.282319. PubMed PMID: 25772291; PubMed Central PMCID: PMCPMC4376416.

366. Calvo-Rodriguez M, Hou SS, Snyder AC, Kharitonova EK, Russ AN, Das S, et al. Increased mitochondrial calcium levels associated with neuronal death in a mouse model of Alzheimer's disease. Nature communications. 2020;11(1):2146. Epub 2020/05/03. doi: 10.1038/s41467-020-16074-2. PubMed PMID: 32358564; PubMed Central PMCID: PMCPMC7195480.

367. Wolf SG, Mutsafi Y, Dadosh T, Ilani T, Lansky Z, Horowitz B, et al. 3D visualization of mitochondrial solid-phase calcium stores in whole cells. eLife. 2017;6:e29929. doi: 10.7554/eLife.29929.

368. Hunter DR, Haworth RA, Southard JH. Relationship between configuration, function, and permeability in calcium-treated mitochondria. The Journal of biological chemistry. 1976;251(16):5069-77. Epub 1976/08/25. PubMed PMID: 134035.

369. Hunter DR, Haworth RA. The Ca2+-induced membrane transition in mitochondria. I. The protective mechanisms. Archives of biochemistry and biophysics. 1979;195(2):453-9. Epub 1979/07/01. doi: 10.1016/0003-9861(79)90371-0. PubMed PMID: 383019.

370. Haworth RA, Hunter DR. The Ca2+-induced membrane transition in mitochondria. II. Nature of the Ca2+ trigger site. Archives of biochemistry and biophysics. 1979;195(2):460-7. Epub 1979/07/01. doi: 10.1016/0003-9861(79)90372-2. PubMed PMID: 38751.

371. Walker JE, Carroll J, He J. Reply to Bernardi: The mitochondrial permeability transition pore and the ATP synthase. Proceedings of the National Academy of Sciences of the United States of America. 2020;117(6):2745-6. Epub 2020/01/30. doi: 10.1073/pnas.1921409117. PubMed PMID: 31992647; PubMed Central PMCID: PMCPMC7022154.

372. Csordás G, Renken C, Várnai P, Walter L, Weaver D, Buttle KF, et al. Structural and functional features and significance of the physical linkage between ER and mitochondria. The Journal of cell biology. 2006;174(7):915-21. Epub 09/18. doi: 10.1083/jcb.200604016. PubMed PMID: 16982799.

373. Csordás G, Várnai P, Golenár T, Roy S, Purkins G, Schneider TG, et al. Imaging interorganelle contacts and local calcium dynamics at the ER-mitochondrial interface. Molecular cell. 2010;39(1):121-32. Epub 2010/07/07. doi: 10.1016/j.molcel.2010.06.029. PubMed PMID: 20603080; PubMed Central PMCID: PMCPMC3178184.

374. Giacomello M, Drago I, Bortolozzi M, Scorzeto M, Gianelle A, Pizzo P, et al. Ca2+ hot spots on the mitochondrial surface are generated by Ca2+ mobilization from stores, but not by activation of store-operated Ca2+ channels. Molecular cell. 2010;38(2):280-90. Epub 2010/04/27. doi: 10.1016/j.molcel.2010.04.003. PubMed PMID: 20417605.

375. Rizzuto R, Pinton P, Carrington W, Fay FS, Fogarty KE, Lifshitz LM, et al. Close contacts with the endoplasmic reticulum as determinants of mitochondrial Ca2+ responses. Science (New York, NY). 1998;280(5370):1763-6. Epub 1998/06/20. doi: 10.1126/science.280.5370.1763. PubMed PMID: 9624056.

376. Rizzuto R, Marchi S, Bonora M, Aguiari P, Bononi A, De Stefani D, et al. Ca2+ transfer from the ER to mitochondria: When, how and why. Biochimica et Biophysica Acta (BBA) - Bioenergetics. 2009;1787(11):1342-51. doi: https://doi.org/10.1016/j.bbabio.2009.03.015.

377. Booth DM, Várnai P, Joseph SK, Hajnóczky G. Oxidative bursts of single mitochondria mediate retrograde signaling toward the ER. Molecular cell. 2021;81(18):3866-76.e2. Epub 2021/08/06. doi: 10.1016/j.molcel.2021.07.014. PubMed PMID: 34352204; PubMed Central PMCID: PMCPMC8455442.

378. Garbincius JF, Elrod JW. Mitochondrial calcium exchange in physiology and disease. Physiological reviews. 2022;102(2):893-992. Epub 2021/10/27. doi: 10.1152/physrev.00041.2020. PubMed PMID: 34698550; PubMed Central PMCID: PMCPMC8816638.

379. Gincel D, Zaid H, Shoshan-Barmatz V. Calcium binding and translocation by the voltage-dependent anion channel: a possible regulatory mechanism in mitochondrial function. The Biochemical journal. 2001;358(Pt 1):147-55. Epub 2001/08/04. doi: 10.1042/0264-6021:3580147. PubMed PMID: 11485562; PubMed Central PMCID: PMCPMC1222042.

380. Deniaud A, Rossi C, Berquand A, Homand J, Campagna S, Knoll W, et al. Voltage-dependent anion channel transports calcium ions through biomimetic

membranes. Langmuir : the ACS journal of surfaces and colloids. 2007;23(7):3898-905. Epub 2007/02/24. doi: 10.1021/la063105+. PubMed PMID: 17315898.

381. Tan W, Colombini M. VDAC closure increases calcium ion flux. Biochimica et biophysica acta. 2007;1768(10):2510-5. Epub 2007/07/10. doi: 10.1016/j.bbamem.2007.06.002. PubMed PMID: 17617374; PubMed Central PMCID: PMCPMC2220155.

382. Nicholls DG. Mitochondria and calcium signaling. Cell calcium. 2005;38(3-4):311-7. Epub 2005/08/10. doi: 10.1016/j.ceca.2005.06.011. PubMed PMID: 16087232.

383. Kirichok Y, Krapivinsky G, Clapham DE. The mitochondrial calcium uniporter is a highly selective ion channel. Nature. 2004;427(6972):360-4. Epub 2004/01/23. doi: 10.1038/nature02246. PubMed PMID: 14737170.

384. De Stefani D, Raffaello A, Teardo E, Szabò I, Rizzuto R. A forty-kilodalton protein of the inner membrane is the mitochondrial calcium uniporter. Nature. 2011;476(7360):336-40. Epub 2011/06/21. doi: 10.1038/nature10230. PubMed PMID: 21685888; PubMed Central PMCID: PMCPMC4141877.

385. Baughman JM, Perocchi F, Girgis HS, Plovanich M, Belcher-Timme CA, Sancak Y, et al. Integrative genomics identifies MCU as an essential component of the mitochondrial calcium uniporter. Nature. 2011;476(7360):341-5. Epub 2011/06/21. doi: 10.1038/nature10234. PubMed PMID: 21685886; PubMed Central PMCID: PMCPMC3486726.

386. Chaudhuri D, Sancak Y, Mootha VK, Clapham DE. MCU encodes the pore conducting mitochondrial calcium currents. Elife. 2013;2:e00704. Epub 2013/06/12. doi: 10.7554/eLife.00704. PubMed PMID: 23755363; PubMed Central PMCID: PMCPMC3673318.

387. Woods JJ, Nemani N, Shanmughapriya S, Kumar A, Zhang M, Nathan SR, et al. A Selective and Cell-Permeable Mitochondrial Calcium Uniporter (MCU) Inhibitor Preserves Mitochondrial Bioenergetics after Hypoxia/Reoxygenation Injury. ACS Central Science. 2019;5(1):153-66. doi: 10.1021/acscentsci.8b00773.

388. Sancak Y, Markhard AL, Kitami T, Kovács-Bogdán E, Kamer KJ, Udeshi ND, et al. EMRE is an essential component of the mitochondrial calcium uniporter complex. Science (New York, NY). 2013;342(6164):1379-82. Epub 2013/11/16. doi:

10.1126/science.1242993. PubMed PMID: 24231807; PubMed Central PMCID: PMCPMC4091629.

389. Mallilankaraman K, Cárdenas C, Doonan PJ, Chandramoorthy HC, Irrinki KM, Golenár T, et al. MCUR1 is an essential component of mitochondrial Ca2+ uptake that regulates cellular metabolism. Nature cell biology. 2012;14(12):1336-43. Epub 2012/11/28. doi: 10.1038/ncb2622. PubMed PMID: 23178883; PubMed Central PMCID: PMCPMC3511605.

390. Perocchi F, Gohil VM, Girgis HS, Bao XR, McCombs JE, Palmer AE, et al. MICU1 encodes a mitochondrial EF hand protein required for Ca(2+) uptake. Nature. 2010;467(7313):291-6. Epub 2010/08/10. doi: 10.1038/nature09358. PubMed PMID: 20693986; PubMed Central PMCID: PMCPMC2977980.

391. Plovanich M, Bogorad RL, Sancak Y, Kamer KJ, Strittmatter L, Li AA, et al. MICU2, a paralog of MICU1, resides within the mitochondrial uniporter complex to regulate calcium handling. PloS one. 2013;8(2):e55785. Epub 2013/02/15. doi: 10.1371/journal.pone.0055785. PubMed PMID: 23409044; PubMed Central PMCID: PMCPMC3567112 laboratory (based at Massachusetts General Hospital/Harvard Medical School) collaborated with Alnylam Pharmaceuticals (co-authors include JDG, L. Speciner, NT, JO, VK). As employees, they received compensation/stock from Alnylam. The authors do not believe that the fact that they are employees of a company, receiving salary/equity from this company, represents a competing interest that compromises the objectivity of the work. This does not alter the authors' adherence to all the PLOS ONE policies on data sharing and materials.

392. Patron M, Granatiero V, Espino J, Rizzuto R, De Stefani D. MICU3 is a tissue-specific enhancer of mitochondrial calcium uptake. Cell death and differentiation. 2019;26(1):179-95. Epub 2018/05/05. doi: 10.1038/s41418-018-0113-8. PubMed PMID: 29725115; PubMed Central PMCID: PMCPMC6124646.

393. Berezhnaya E, Hajnóczky G. How do MICUs gate the mitochondrial calcium uniporter? Cell calcium. 2021;100:102497. Epub 2021/11/15. doi: 10.1016/j.ceca.2021.102497. PubMed PMID: 34775300.

394. Ashrafi G, de Juan-Sanz J, Farrell RJ, Ryan TA. Molecular Tuning of the Axonal Mitochondrial Ca(2+) Uniporter Ensures Metabolic Flexibility of Neurotransmission. Neuron. 2020;105(4):678-87.e5. Epub 2019/12/22. doi: 10.1016/j.neuron.2019.11.020. PubMed PMID: 31862210; PubMed Central PMCID: PMCPMC7035162.

395. Phillips CB, Tsai C-W, Tsai M-F. The conserved aspartate ring of MCU mediates MICU1 binding and regulation in the mitochondrial calcium uniporter complex. Elife. 2019;8:e41112.

396. Palty R, Silverman WF, Hershfinkel M, Caporale T, Sensi SL, Parnis J, et al. NCLX is an essential component of mitochondrial Na+/Ca2+ exchange. Proceedings of the National Academy of Sciences of the United States of America. 2010;107(1):436-41. Epub 2009/12/19. doi: 10.1073/pnas.0908099107. PubMed PMID: 20018762; PubMed Central PMCID: PMCPMC2806722.

397. Kostic M, Sekler I. Functional properties and mode of regulation of the mitochondrial Na(+)/Ca(2+) exchanger, NCLX. Seminars in cell & developmental biology. 2019;94:59-65. Epub 2019/01/19. doi: 10.1016/j.semcdb.2019.01.009. PubMed PMID: 30658153.

398. Katoshevski T, Ben-Kasus Nissim T, Sekler I. Recent studies on NCLX in health and diseases. Cell calcium. 2021;94:102345. Epub 2021/01/29. doi: 10.1016/j.ceca.2020.102345. PubMed PMID: 33508514.

399. Kostic M, Katoshevski T, Sekler I. Allosteric Regulation of NCLX by Mitochondrial Membrane Potential Links the Metabolic State and Ca(2+) Signaling in Mitochondria. Cell reports. 2018;25(12):3465-75.e4. Epub 2018/12/20. doi: 10.1016/j.celrep.2018.11.084. PubMed PMID: 30566870.

400. Luongo TS, Lambert JP, Gross P, Nwokedi M, Lombardi AA, Shanmughapriya S, et al. The mitochondrial Na(+)/Ca(2+) exchanger is essential for Ca(2+) homeostasis and viability. Nature. 2017;545(7652):93-7. Epub 2017/04/27. doi: 10.1038/nature22082. PubMed PMID: 28445457; PubMed Central PMCID: PMCPMC5731245.

401. Islam MM, Takeuchi A, Matsuoka S. Membrane current evoked by mitochondrial Na(+)-Ca(2+) exchange in mouse heart. The journal of physiological sciences : JPS. 2020;70(1):24. Epub 2020/05/02. doi: 10.1186/s12576-020-00752-3. PubMed PMID: 32354321.

402. García-Casas P, Alvarez-Illera P, Gómez-Orte E, Cabello J, Fonteriz RI, Montero M, et al. The Mitochondrial Na(+)/Ca(2+) Exchanger Inhibitor CGP37157 Preserves Muscle Structure and Function to Increase Lifespan and Healthspan in Caenorhabditis elegans. Frontiers in pharmacology. 2021;12:695687. Epub 2021/07/03. doi:

10.3389/fphar.2021.695687. PubMed PMID: 34211399; PubMed Central PMCID: PMCPMC8241105.

403. Wacquier B, Combettes L, Dupont G. Cytoplasmic and Mitochondrial Calcium Signaling: A Two-Way Relationship. Cold Spring Harbor perspectives in biology. 2019;11(10). Epub 2019/05/22. doi: 10.1101/cshperspect.a035139. PubMed PMID: 31110132; PubMed Central PMCID: PMCPMC6771369.

404. Glancy B, Willis WT, Chess DJ, Balaban RS. Effect of Calcium on the Oxidative Phosphorylation Cascade in Skeletal Muscle Mitochondria. Biochemistry. 2013;52(16):2793-809. doi: 10.1021/bi3015983.

405. Territo PR, Mootha VK, French SA, Balaban RS. Ca2+ activation of heart mitochondrial oxidative phosphorylation: role of the F0/F1-ATPase. American Journal of Physiology-Cell Physiology. 2000;278(2):C423-C35.

406. Pickles S, Vigié P, Youle RJ. Mitophagy and Quality Control Mechanisms in Mitochondrial Maintenance. Current biology : CB. 2018;28(4):R170-r85. Epub 2018/02/21. doi: 10.1016/j.cub.2018.01.004. PubMed PMID: 29462587; PubMed Central PMCID: PMCPMC7255410.

407. Palikaras K, Lionaki E, Tavernarakis N. Mechanisms of mitophagy in cellular homeostasis, physiology and pathology. Nature cell biology. 2018;20(9):1013-22. Epub 2018/08/30. doi: 10.1038/s41556-018-0176-2. PubMed PMID: 30154567.

408. Harper JW, Ordureau A, Heo JM. Building and decoding ubiquitin chains for mitophagy. Nature reviews Molecular cell biology. 2018;19(2):93-108. Epub 2018/01/24. doi: 10.1038/nrm.2017.129. PubMed PMID: 29358684.

409. Kane LA, Lazarou M, Fogel AI, Li Y, Yamano K, Sarraf SA, et al. PINK1 phosphorylates ubiquitin to activate Parkin E3 ubiquitin ligase activity. The Journal of cell biology. 2014;205(2):143-53. Epub 2014/04/23. doi: 10.1083/jcb.201402104. PubMed PMID: 24751536; PubMed Central PMCID: PMCPMC4003245.

410. Koyano F, Okatsu K, Kosako H, Tamura Y, Go E, Kimura M, et al. Ubiquitin is phosphorylated by PINK1 to activate parkin. Nature. 2014;510(7503):162-6. Epub 2014/05/03. doi: 10.1038/nature13392. PubMed PMID: 24784582.

411. Kondapalli C, Kazlauskaite A, Zhang N, Woodroof HI, Campbell DG, Gourlay R, et al. PINK1 is activated by mitochondrial membrane potential depolarization and

stimulates Parkin E3 ligase activity by phosphorylating Serine 65. Open biology. 2012;2(5):120080. Epub 2012/06/23. doi: 10.1098/rsob.120080. PubMed PMID: 22724072; PubMed Central PMCID: PMCPMC3376738.

412. Narendra DP, Jin SM, Tanaka A, Suen DF, Gautier CA, Shen J, et al. PINK1 is selectively stabilized on impaired mitochondria to activate Parkin. PLoS biology. 2010;8(1):e1000298. Epub 2010/02/04. doi: 10.1371/journal.pbio.1000298. PubMed PMID: 20126261; PubMed Central PMCID: PMCPMC2811155.

413. Vives-Bauza C, Zhou C, Huang Y, Cui M, de Vries RL, Kim J, et al. PINK1-dependent recruitment of Parkin to mitochondria in mitophagy. Proceedings of the National Academy of Sciences of the United States of America. 2010;107(1):378-83. Epub 2009/12/08. doi: 10.1073/pnas.0911187107. PubMed PMID: 19966284; PubMed Central PMCID: PMCPMC2806779.

414. Lazarou M, Sliter DA, Kane LA, Sarraf SA, Wang C, Burman JL, et al. The ubiquitin kinase PINK1 recruits autophagy receptors to induce mitophagy. Nature. 2015;524(7565):309-14. Epub 2015/08/13. doi: 10.1038/nature14893. PubMed PMID: 26266977; PubMed Central PMCID: PMCPMC5018156.

415. Stolz A, Ernst A, Dikic I. Cargo recognition and trafficking in selective autophagy. Nature cell biology. 2014;16(6):495-501.

416. Matheoud D, Sugiura A, Bellemare-Pelletier A, Laplante A, Rondeau C, Chemali M, et al. Parkinson's Disease-Related Proteins PINK1 and Parkin Repress Mitochondrial Antigen Presentation. Cell. 2016;166(2):314-27. Epub 2016/06/28. doi: 10.1016/j.cell.2016.05.039. PubMed PMID: 27345367.

417. Matheoud D, Cannon T, Voisin A, Penttinen AM, Ramet L, Fahmy AM, et al. Intestinal infection triggers Parkinson's disease-like symptoms in Pink1(-/-) mice. Nature. 2019;571(7766):565-9. Epub 2019/07/19. doi: 10.1038/s41586-019-1405-y. PubMed PMID: 31316206.

418. Pickrell Alicia M, Youle Richard J. The Roles of PINK1, Parkin, and Mitochondrial Fidelity in Parkinson’s Disease. Neuron. 2015;85(2):257-73. doi: https://doi.org/10.1016/j.neuron.2014.12.007.

419. Liu L, Feng D, Chen G, Chen M, Zheng Q, Song P, et al. Mitochondrial outer-membrane protein FUNDC1 mediates hypoxia-induced mitophagy in mammalian cells.

Nature cell biology. 2012;14(2):177-85. Epub 2012/01/24. doi: 10.1038/ncb2422. PubMed PMID: 22267086.

420. Novak I, Kirkin V, McEwan DG, Zhang J, Wild P, Rozenknop A, et al. Nix is a selective autophagy receptor for mitochondrial clearance. EMBO reports. 2010;11(1):45-51. doi: https://doi.org/10.1038/embor.2009.256.

421. Yang C, Svitkina TM. Ultrastructure and dynamics of the actin−myosin II cytoskeleton during mitochondrial fission. Nature cell biology. 2019;21(5):603-13. doi: 10.1038/s41556-019-0313-6.

422. Korobova F, Ramabhadran V, Higgs HN. An actin-dependent step in mitochondrial fission mediated by the ER-associated formin INF2. Science (New York, NY). 2013;339(6118):464-7. Epub 2013/01/26. doi: 10.1126/science.1228360. PubMed PMID: 23349293; PubMed Central PMCID: PMCPMC3843506.

423. Korobova F, Gauvin TJ, Higgs HN. A role for myosin II in mammalian mitochondrial fission. Current biology : CB. 2014;24(4):409-14. Epub 2014/02/04. doi: 10.1016/j.cub.2013.12.032. PubMed PMID: 24485837; PubMed Central PMCID: PMCPMC3958938.

424. Lin S, Huang C, Gunda V, Sun J, Chellappan SP, Li Z, et al. Fascin Controls Metastatic Colonization and Mitochondrial Oxidative Phosphorylation by Remodeling Mitochondrial Actin Filaments. Cell reports. 2019;28(11):2824-36.e8. Epub 2019/09/12. doi: 10.1016/j.celrep.2019.08.011. PubMed PMID: 31509745; PubMed Central PMCID: PMCPMC6759858.

425. Ji WK, Chakrabarti R, Fan X, Schoenfeld L, Strack S, Higgs HN. Receptor-mediated Drp1 oligomerization on endoplasmic reticulum. The Journal of cell biology. 2017;216(12):4123-39. Epub 2017/11/22. doi: 10.1083/jcb.201610057. PubMed PMID: 29158231; PubMed Central PMCID: PMCPMC5716263.

426. Ji WK, Hatch AL, Merrill RA, Strack S, Higgs HN. Actin filaments target the oligomeric maturation of the dynamin GTPase Drp1 to mitochondrial fission sites. Elife. 2015;4:e11553. Epub 2015/11/27. doi: 10.7554/eLife.11553. PubMed PMID: 26609810; PubMed Central PMCID: PMCPMC4755738.

427. Liu A, Kage F, Higgs HN. Mff oligomerization is required for Drp1 activation and synergy with actin filaments during mitochondrial division. Molecular biology of the cell.

2021;32(20):ar5. Epub 2021/08/05. doi: 10.1091/mbc.E21-04-0224. PubMed PMID: 34347505; PubMed Central PMCID: PMCPMC8684745.

428. Basu H, Pekkurnaz G, Falk J, Wei W, Chin M, Steen J, et al. FHL2 anchors mitochondria to actin and adapts mitochondrial dynamics to glucose supply. The Journal of cell biology. 2021;220(10). Epub 2021/08/04. doi: 10.1083/jcb.201912077. PubMed PMID: 34342639; PubMed Central PMCID: PMCPMC8340551.

429. Moore AS, Wong YC, Simpson CL, Holzbaur EL. Dynamic actin cycling through mitochondrial subpopulations locally regulates the fission-fusion balance within mitochondrial networks. Nature communications. 2016;7:12886. Epub 2016/10/01. doi: 10.1038/ncomms12886. PubMed PMID: 27686185; PubMed Central PMCID: PMCPMC5056443.

430. Moore AS, Coscia SM, Simpson CL, Ortega FE, Wait EC, Heddleston JM, et al. Actin cables and comet tails organize mitochondrial networks in mitosis. Nature. 2021;591(7851):659-64. doi: 10.1038/s41586-021-03309-5.

431. Lamason RL, Welch MD. Actin-based motility and cell-to-cell spread of bacterial pathogens. Current opinion in microbiology. 2017;35:48-57. Epub 2016/12/21. doi: 10.1016/j.mib.2016.11.007. PubMed PMID: 27997855; PubMed Central PMCID: PMCPMC5474209.

432. Kruppa AJ, Kishi-Itakura C, Masters TA, Rorbach JE, Grice GL, Kendrick-Jones J, et al. Myosin VI-Dependent Actin Cages Encapsulate Parkin-Positive Damaged Mitochondria. Developmental cell. 2018;44(4):484-99.e6. Epub 2018/02/06. doi: 10.1016/j.devcel.2018.01.007. PubMed PMID: 29398621; PubMed Central PMCID: PMCPMC5932465.

433. Hsieh C-W, Yang WY. Omegasome-proximal PtdIns(4,5)P2 couples F-actin mediated mitoaggregate disassembly with autophagosome formation during mitophagy. Nature communications. 2019;10(1):969. doi: 10.1038/s41467-019-08924-5.

434. Hu H, Juvekar A, Lyssiotis CA, Lien EC, Albeck JG, Oh D, et al. Phosphoinositide 3-Kinase Regulates Glycolysis through Mobilization of Aldolase from the Actin Cytoskeleton. Cell. 2016;164(3):433-46. doi: 10.1016/j.cell.2015.12.042. PubMed PMID: 26824656.

435. Park JS, Burckhardt CJ, Lazcano R, Solis LM, Isogai T, Li L, et al. Mechanical regulation of glycolysis via cytoskeleton architecture. Nature. 2020;578(7796):621-6. Epub 2020/02/14. doi: 10.1038/s41586-020-1998-1. PubMed PMID: 32051585; PubMed Central PMCID: PMCPMC7210009.

436. Kondo H, Ratcliffe CDH, Hooper S, Ellis J, MacRae JI, Hennequart M, et al. Single-cell resolved imaging reveals intra-tumor heterogeneity in glycolysis, transitions between metabolic states, and their regulatory mechanisms. Cell reports. 2021;34(7):108750. Epub 2021/02/18. doi: 10.1016/j.celrep.2021.108750. PubMed PMID: 33596424; PubMed Central PMCID: PMCPMC7900713.

437. Chhabra ES, Higgs HN. The many faces of actin: matching assembly factors with cellular structures. Nature cell biology. 2007;9(10):1110-21. Epub 2007/10/03. doi: 10.1038/ncb1007-1110. PubMed PMID: 17909522.

438. MacVicar T, Langer T. OPA1 processing in cell death and disease - the long and short of it. Journal of cell science. 2016;129(12):2297-306. Epub 2016/05/18. doi: 10.1242/jcs.159186. PubMed PMID: 27189080.

439. Chakrabarti R, Higgs HN. Revolutionary view of two ways to split a mitochondrion. Nature. 2021;593(7859):346-7. Epub 2021/05/07. doi: 10.1038/d41586-021-01173-x. PubMed PMID: 33953387.

440. Patel MS, Nemeria NS, Furey W, Jordan F. The pyruvate dehydrogenase complexes: structure-based function and regulation. The Journal of biological chemistry. 2014;289(24):16615-23. Epub 2014/05/07. doi: 10.1074/jbc.R114.563148. PubMed PMID: 24798336; PubMed Central PMCID: PMCPMC4059105.

441. Utter MF, Keech DB. PYRUVATE CARBOXYLASE. I. NATURE OF THE REACTION. The Journal of biological chemistry. 1963;238:2603-8. Epub 1963/08/01. PubMed PMID: 14063279.

442. Yang L, Venneti S, Nagrath D. Glutaminolysis: A Hallmark of Cancer Metabolism. Annual Review of Biomedical Engineering. 2017;19(1):163-94. doi: 10.1146/annurev-bioeng-071516-044546.

443. Strzyz P. Alternative cycle for citrate. Nature Reviews Molecular Cell Biology. 2022;23(5):305-. doi: 10.1038/s41580-022-00475-w.

444. Alberts B, Johnson A, Wilson J, Lewis J, Hunt T, Roberts K, et al. Molecular Biology of the Cell: Garland Science; 2008.

445. Jin SM, Lazarou M, Wang C, Kane LA, Narendra DP, Youle RJ. Mitochondrial membrane potential regulates PINK1 import and proteolytic destabilization by PARL. The Journal of cell biology. 2010;191(5):933-42. Epub 2010/12/01. doi: 10.1083/jcb.201008084. PubMed PMID: 21115803; PubMed Central PMCID: PMCPMC2995166.

446. Higgs HN, Pollard TD. Activation by Cdc42 and PIP(2) of Wiskott-Aldrich syndrome protein (WASp) stimulates actin nucleation by Arp2/3 complex. The Journal of cell biology. 2000;150(6):1311-20. Epub 2000/09/20. doi: 10.1083/jcb.150.6.1311. PubMed PMID: 10995437; PubMed Central PMCID: PMCPMC2150692.

447. Rohatgi R, Ma L, Miki H, Lopez M, Kirchhausen T, Takenawa T, et al. The interaction between N-WASP and the Arp2/3 complex links Cdc42-dependent signals to actin assembly. Cell. 1999;97(2):221-31. Epub 1999/04/29. doi: 10.1016/s0092-8674(00)80732-1. PubMed PMID: 10219243.

448. Rohatgi R, Nollau P, Ho HY, Kirschner MW, Mayer BJ. Nck and phosphatidylinositol 4,5-bisphosphate synergistically activate actin polymerization through the N-WASP-Arp2/3 pathway. The Journal of biological chemistry. 2001;276(28):26448-52. Epub 2001/05/08. doi: 10.1074/jbc.M103856200. PubMed PMID: 11340081.

449. Torres E, Rosen MK. Contingent phosphorylation/dephosphorylation provides a mechanism of molecular memory in WASP. Molecular cell. 2003;11(5):1215-27. Epub 2003/05/29. doi: 10.1016/s1097-2765(03)00139-4. PubMed PMID: 12769846.

450. Miki H, Sasaki T, Takai Y, Takenawa T. Induction of filopodium formation by a WASP-related actin-depolymerizing protein N-WASP. Nature. 1998;391(6662):93-6. doi: 10.1038/34208.

451. Tsuboi S, Meerloo J. Wiskott-Aldrich syndrome protein is a key regulator of the phagocytic cup formation in macrophages. The Journal of biological chemistry. 2007;282(47):34194-203. Epub 2007/09/25. doi: 10.1074/jbc.M705999200. PubMed PMID: 17890224.

452. Sasahara Y, Rachid R, Byrne MJ, de la Fuente MA, Abraham RT, Ramesh N, et al. Mechanism of recruitment of WASP to the immunological synapse and of its activation following TCR ligation. Molecular cell. 2002;10(6):1269-81. Epub 2002/12/31. doi: 10.1016/s1097-2765(02)00728-1. PubMed PMID: 12504004.

453. Linder S, Nelson D, Weiss M, Aepfelbacher M. Wiskott-Aldrich syndrome protein regulates podosomes in primary human macrophages. Proceedings of the National Academy of Sciences. 1999;96(17):9648. doi: 10.1073/pnas.96.17.9648.

454. Lorenz M, Yamaguchi H, Wang Y, Singer RH, Condeelis J. Imaging sites of N-wasp activity in lamellipodia and invadopodia of carcinoma cells. Current biology : CB. 2004;14(8):697-703. Epub 2004/04/16. doi: 10.1016/j.cub.2004.04.008. PubMed PMID: 15084285.

455. Kessels MM, Qualmann B. Syndapins integrate N-WASP in receptor-mediated endocytosis. The EMBO journal. 2002;21(22):6083-94. Epub 2002/11/12. doi: 10.1093/emboj/cdf604. PubMed PMID: 12426380; PubMed Central PMCID: PMCPMC137196.

456. Lommel S, Benesch S, Rottner K, Franz T, Wehland J, Kuhn R. Actin pedestal formation by enteropathogenic Escherichia coli and intracellular motility of Shigella flexneri are abolished in N-WASP-defective cells. EMBO reports. 2001;2(9):850-7. Epub 2001/09/18. doi: 10.1093/embo-reports/kve197. PubMed PMID: 11559594; PubMed Central PMCID: PMCPMC1084051.

457. Egile C, Loisel TP, Laurent V, Li R, Pantaloni D, Sansonetti PJ, et al. Activation of the CDC42 effector N-WASP by the Shigella flexneri IcsA protein promotes actin nucleation by Arp2/3 complex and bacterial actin-based motility. The Journal of cell biology. 1999;146(6):1319-32. Epub 1999/09/24. doi: 10.1083/jcb.146.6.1319. PubMed PMID: 10491394; PubMed Central PMCID: PMCPMC2156126.

458. Kobayashi K, Kuroda S, Fukata M, Nakamura T, Nagase T, Nomura N, et al. p140Sra-1 (specifically Rac1-associated protein) is a novel specific target for Rac1 small GTPase. The Journal of biological chemistry. 1998;273(1):291-5. Epub 1998/02/07. doi: 10.1074/jbc.273.1.291. PubMed PMID: 9417078.

459. Chen Z, Borek D, Padrick SB, Gomez TS, Metlagel Z, Ismail AM, et al. Structure and control of the actin regulatory WAVE complex. Nature. 2010;468(7323):533-8. Epub

2010/11/26. doi: 10.1038/nature09623. PubMed PMID: 21107423; PubMed Central PMCID: PMCPMC3085272.

460. Miki H, Yamaguchi H, Suetsugu S, Takenawa T. IRSp53 is an essential intermediate between Rac and WAVE in the regulation of membrane ruffling. Nature. 2000;408(6813):732-5. Epub 2000/12/29. doi: 10.1038/35047107. PubMed PMID: 11130076.

461. Kitamura T, Kitamura Y, Yonezawa K, Totty NF, Gout I, Hara K, et al. Molecular cloning of p125Nap1, a protein that associates with an SH3 domain of Nck. Biochemical and biophysical research communications. 1996;219(2):509-14. Epub 1996/02/15. doi: 10.1006/bbrc.1996.0264. PubMed PMID: 8605018.

462. Suetsugu S, Yamazaki D, Kurisu S, Takenawa T. Differential Roles of WAVE1 and WAVE2 in Dorsal and Peripheral Ruffle Formation for Fibroblast Cell Migration. Developmental cell. 2003;5(4):595-609. doi: https://doi.org/10.1016/S1534-5807(03)00297-1.

463. Yan C, Martinez-Quiles N, Eden S, Shibata T, Takeshima F, Shinkura R, et al. WAVE2 deficiency reveals distinct roles in embryogenesis and Rac-mediated actin-based motility. The EMBO journal. 2003;22(14):3602-12. Epub 2003/07/11. doi: 10.1093/emboj/cdg350. PubMed PMID: 12853475; PubMed Central PMCID: PMCPMC165620.

464. Derivery E, Sousa C, Gautier JJ, Lombard B, Loew D, Gautreau A. The Arp2/3 activator WASH controls the fission of endosomes through a large multiprotein complex. Developmental cell. 2009;17(5):712-23. Epub 2009/11/20. doi: 10.1016/j.devcel.2009.09.010. PubMed PMID: 19922875.

465. Jia D, Gomez TS, Metlagel Z, Umetani J, Otwinowski Z, Rosen MK, et al. WASH and WAVE actin regulators of the Wiskott–Aldrich syndrome protein (WASP) family are controlled by analogous structurally related complexes. Proceedings of the National Academy of Sciences. 2010;107(23):10442-7. doi: 10.1073/pnas.0913293107.

466. Hao YH, Fountain MD, Jr., Fon Tacer K, Xia F, Bi W, Kang SH, et al. USP7 Acts as a Molecular Rheostat to Promote WASH-Dependent Endosomal Protein Recycling and Is Mutated in a Human Neurodevelopmental Disorder. Molecular cell. 2015;59(6):956-69. Epub 2015/09/15. doi: 10.1016/j.molcel.2015.07.033. PubMed PMID: 26365382; PubMed Central PMCID: PMCPMC4575888.

467. Gomez TS, Billadeau DD. A FAM21-containing WASH complex regulates retromer-dependent sorting. Developmental cell. 2009;17(5):699-711. Epub 2009/11/20. doi: 10.1016/j.devcel.2009.09.009. PubMed PMID: 19922874; PubMed Central PMCID: PMCPMC2803077.

468. Duleh SN, Welch MD. WASH and the Arp2/3 complex regulate endosome shape and trafficking. Cytoskeleton (Hoboken). 2010;67(3):193-206. Epub 2010/02/23. doi: 10.1002/cm.20437. PubMed PMID: 20175130; PubMed Central PMCID: PMCPMC2887680.

469. Rottner K, Hanisch J, Campellone KG. WASH, WHAMM and JMY: regulation of Arp2/3 complex and beyond. Trends in cell biology. 2010;20(11):650-61. Epub 2010/10/05. doi: 10.1016/j.tcb.2010.08.014. PubMed PMID: 20888769.

470. King JS, Gueho A, Hagedorn M, Gopaldass N, Leuba F, Soldati T, et al. WASH is required for lysosomal recycling and efficient autophagic and phagocytic digestion. Molecular biology of the cell. 2013;24(17):2714-26. Epub 2013/07/26. doi: 10.1091/mbc.E13-02-0092. PubMed PMID: 23885127; PubMed Central PMCID: PMCPMC3756923.

471. Xia P, Wang S, Du Y, Zhao Z, Shi L, Sun L, et al. WASH inhibits autophagy through suppression of Beclin 1 ubiquitination. The EMBO journal. 2013;32(20):2685-96. Epub 2013/08/27. doi: 10.1038/emboj.2013.189. PubMed PMID: 23974797; PubMed Central PMCID: PMCPMC3801434.

472. Russo AJ, Mathiowetz AJ, Hong S, Welch MD, Campellone KG. Rab1 recruits WHAMM during membrane remodeling but limits actin nucleation. Molecular biology of the cell. 2016;27(6):967-78. doi: 10.1091/mbc.E15-07-0508.

473. Campellone KG, Webb NJ, Znameroski EA, Welch MD. WHAMM Is an Arp2/3 Complex Activator That Binds Microtubules and Functions in ER to Golgi Transport. Cell. 2008;134(1):148-61. doi: 10.1016/j.cell.2008.05.032.

474. Kast DJ, Zajac AL, Holzbaur EL, Ostap EM, Dominguez R. WHAMM Directs the Arp2/3 Complex to the ER for Autophagosome Biogenesis through an Actin Comet Tail Mechanism. Current biology : CB. 2015;25(13):1791-7. Epub 2015/06/23. doi: 10.1016/j.cub.2015.05.042. PubMed PMID: 26096974; PubMed Central PMCID: PMCPMC4489997.

475. Zuchero JB, Belin B, Mullins RD. Actin binding to WH2 domains regulates nuclear import of the multifunctional actin regulator JMY. Molecular biology of the cell. 2012;23(5):853-63. doi: 10.1091/mbc.e11-12-0992.

476. Zuchero JB, Coutts AS, Quinlan ME, Thangue NBL, Mullins RD. p53-cofactor JMY is a multifunctional actin nucleation factor. Nature cell biology. 2009;11(4):451-9. doi: 10.1038/ncb1852.

477. Schlüter K, Waschbüsch D, Anft M, Hügging D, Kind S, Hänisch J, et al. JMY is involved in anterograde vesicle trafficking from the trans-Golgi network. European Journal of Cell Biology. 2014;93(5):194-204. doi: https://doi.org/10.1016/j.ejcb.2014.06.001.

478. Lin Z, Xu Y-N, Namgoong S, Kim N-H. JMY Functions as Actin Nucleation-Promoting Factor and Mediator for p53-Mediated DNA Damage in Porcine Oocytes. PloS one. 2014;9(10):e109385. doi: 10.1371/journal.pone.0109385.

479. Coutts AS, La Thangue NB. Actin nucleation by WH2 domains at the autophagosome. Nature communications. 2015;6(1):7888. doi: 10.1038/ncomms8888.

480. Hu X, Mullins RD. LC3 and STRAP regulate actin filament assembly by JMY during autophagosome formation. The Journal of cell biology. 2019;218(1):251-66. Epub 2018/11/14. doi: 10.1083/jcb.201802157. PubMed PMID: 30420355; PubMed Central PMCID: PMCPMC6314544.

481. Shikama N, Lee CW, France S, Delavaine L, Lyon J, Krstic-Demonacos M, et al. A novel cofactor for p300 that regulates the p53 response. Molecular cell. 1999;4(3):365-76. Epub 1999/10/13. doi: 10.1016/s1097-2765(00)80338-x. PubMed PMID: 10518217.

482. Kluge F, Weissbach J, Weber A, Stradal T, Posern G. Regulation of MRTF-A by JMY via a nucleation-independent mechanism. Cell Communication and Signaling. 2018;16(1):86. doi: 10.1186/s12964-018-0299-x.

483. Firat-Karalar EN, Hsiue PP, Welch MD. The actin nucleation factor JMY is a negative regulator of neuritogenesis. Molecular biology of the cell. 2011;22(23):4563-74. doi: 10.1091/mbc.e11-06-0585.

484. Lim CS, Kim SH, Jung JG, Kim JK, Song WK. Regulation of SPIN90 phosphorylation and interaction with Nck by ERK and cell adhesion. The Journal of

biological chemistry. 2003;278(52):52116-23. Epub 2003/10/16. doi: 10.1074/jbc.M310974200. PubMed PMID: 14559906.

485. Cho IH, Lee MJ, Kim DH, Kim B, Bae J, Choi KY, et al. SPIN90 dephosphorylation is required for cofilin-mediated actin depolymerization in NMDA-stimulated hippocampal neurons. Cellular and Molecular Life Sciences. 2013;70(22):4369-83. doi: 10.1007/s00018-013-1391-4.

486. Kim DJ, Kim SH, Lim CS, Choi KY, Park CS, Sung BH, et al. Interaction of SPIN90 with the Arp2/3 Complex Mediates Lamellipodia and Actin Comet Tail Formation. Journal of Biological Chemistry. 2006;281(1):617-25. doi: 10.1074/jbc.M504450200.

487. Fukuoka M, Suetsugu S, Miki H, Fukami K, Endo T, Takenawa T. A Novel Neural Wiskott-Aldrich Syndrome Protein (N-Wasp) Binding Protein, Wish, Induces Arp2/3 Complex Activation Independent of Cdc42. Journal of Cell Biology. 2001;152(3):471-82. doi: 10.1083/jcb.152.3.471.

488. Basu R, Chang F. Characterization of dip1p reveals a switch in Arp2/3-dependent actin assembly for fission yeast endocytosis. Current biology : CB. 2011;21(11):905-16. Epub 2011/05/31. doi: 10.1016/j.cub.2011.04.047. PubMed PMID: 21620704; PubMed Central PMCID: PMCPMC3121306.

489. MacGrath SM, Koleske AJ. Cortactin in cell migration and cancer at a glance. Journal of cell science. 2012;125(7):1621. doi: 10.1242/jcs.093781.

490. Hutchcroft JE, Slavik JM, Lin H, Watanabe T, Bierer BE. Uncoupling activation-dependent HS1 phosphorylation from nuclear factor of activated T cells transcriptional activation in Jurkat T cells: differential signaling through CD3 and the costimulatory receptors CD2 and CD28. Journal of immunology (Baltimore, Md : 1950). 1998;161(9):4506-12. Epub 1998/10/30. PubMed PMID: 9794375.

491. Brunati AM, Donella-Deana A, Ruzzene M, Marin O, Pinna LA. Site specificity of p72 syk protein tyrosine kinase: efficient phosphorylation of motifs recognized by Src homology 2 domains of the Src family. FEBS letters. 1995;367(2):149-52. doi: 10.1016/0014-5793(95)00555-N.

492. Yamanashi Y, Okada M, Semba T, Yamori T, Umemori H, Tsunasawa S, et al. Identification of HS1 protein as a major substrate of protein-tyrosine kinase(s) upon B-

cell antigen receptor-mediated signaling. Proceedings of the National Academy of Sciences. 1993;90(8):3631. doi: 10.1073/pnas.90.8.3631.

493. Campbell DH, Sutherland RL, Daly RJ. Signaling pathways and structural domains required for phosphorylation of EMS1/cortactin. Cancer research. 1999;59(20):5376-85. Epub 1999/10/28. PubMed PMID: 10537323.

494. Martinez-Quiles N, Ho H-YH, Kirschner MW, Ramesh N, Geha RS. Erk/Src Phosphorylation of Cortactin Acts as a Switch On-Switch Off Mechanism That Controls Its Ability To Activate N-WASP. Molecular and Cellular Biology. 2004;24(12):5269. doi: 10.1128/MCB.24.12.5269-5280.2004.

495. Zhang X, Yuan Z, Zhang Y, Yong S, Salas-Burgos A, Koomen J, et al. HDAC6 modulates cell motility by altering the acetylation level of cortactin. Molecular cell. 2007;27(2):197-213. Epub 2007/07/24. doi: 10.1016/j.molcel.2007.05.033. PubMed PMID: 17643370; PubMed Central PMCID: PMCPMC2684874.

496. Lettau M, Kabelitz D, Janssen O. SDF1α-induced interaction of the adapter proteins Nck and HS1 facilitates actin polymerization and migration in T cells. European Journal of Immunology. 2015;45(2):551-61. doi: 10.1002/eji.201444473.

497. El Sayegh TY, Arora PD, Laschinger CA, Lee W, Morrison C, Overall CM, et al. Cortactin associates with N-cadherin adhesions and mediates intercellular adhesion strengthening in fibroblasts. Journal of cell science. 2004;117(21):5117. doi: 10.1242/jcs.01385.

498. Bryce NS, Clark ES, Leysath JML, Currie JD, Webb DJ, Weaver AM. Cortactin Promotes Cell Motility by Enhancing Lamellipodial Persistence. Current Biology. 2005;15(14):1276-85. doi: 10.1016/j.cub.2005.06.043.

499. Huang Y, Biswas C, Klos Dehring DA, Sriram U, Williamson EK, Li S, et al. The actin regulatory protein HS1 is required for antigen uptake and presentation by dendritic cells. Journal of immunology (Baltimore, Md : 1950). 2011;187(11):5952-63. Epub 2011/10/28. doi: 10.4049/jimmunol.1100870. PubMed PMID: 22031761; PubMed Central PMCID: PMCPMC3221870.

500. Gomez TS, McCarney SD, Carrizosa E, Labno CM, Comiskey EO, Nolz JC, et al. HS1 functions as an essential actin-regulatory adaptor protein at the immune synapse.

Immunity. 2006;24(6):741-52. Epub 2006/06/20. doi: 10.1016/j.immuni.2006.03.022. PubMed PMID: 16782030; PubMed Central PMCID: PMCPMC1779661.

501. Wagner AR, Luan Q, Liu SL, Nolen BJ. Dip1 defines a class of Arp2/3 complex activators that function without preformed actin filaments. Current biology : CB. 2013;23(20):1990-8. Epub 2013/10/15. doi: 10.1016/j.cub.2013.08.029. PubMed PMID: 24120641; PubMed Central PMCID: PMCPMC3930447.

502. Watanabe S, Ando Y, Yasuda S, Hosoya H, Watanabe N, Ishizaki T, et al. mDia2 induces the actin scaffold for the contractile ring and stabilizes its position during cytokinesis in NIH 3T3 cells. Molecular biology of the cell. 2008;19(5):2328-38. Epub 2008/02/22. doi: 10.1091/mbc.e07-10-1086. PubMed PMID: 18287523; PubMed Central PMCID: PMCPMC2366861.

503. Eng CH, Huckaba TM, Gundersen GG. The formin mDia regulates GSK3beta through novel PKCs to promote microtubule stabilization but not MTOC reorientation in migrating fibroblasts. Molecular biology of the cell. 2006;17(12):5004-16. Epub 2006/09/22. doi: 10.1091/mbc.e05-10-0914. PubMed PMID: 16987962; PubMed Central PMCID: PMCPMC1679669.

504. Vicente-Manzanares M, Rey M, Pérez-Martínez M, Yáñez-Mó M, Sancho D, Cabrero JR, et al. The RhoA effector mDia is induced during T cell activation and regulates actin polymerization and cell migration in T lymphocytes. Journal of immunology (Baltimore, Md : 1950). 2003;171(2):1023-34. Epub 2003/07/09. doi: 10.4049/jimmunol.171.2.1023. PubMed PMID: 12847276.

505. Lakha R, Montero AM, Jabeen T, Costeas CC, Ma J, Vizcarra CL. Variable Autoinhibition among Deafness-Associated Variants of Diaphanous 1 (DIAPH1). Biochemistry. 2021;60(29):2320-9. Epub 07/19. doi: 10.1021/acs.biochem.1c00170. PubMed PMID: 34279089.

506. Lu Q, Lu L, Chen W, Chen H, Xu X, Zheng Z. RhoA/mDia-1/profilin-1 signaling targets microvascular endothelial dysfunction in diabetic retinopathy. Graefe's archive for clinical and experimental ophthalmology = Albrecht von Graefes Archiv fur klinische und experimentelle Ophthalmologie. 2015;253(5):669-80. Epub 2015/03/21. doi: 10.1007/s00417-015-2985-3. PubMed PMID: 25791356.

507. Ercan-Sencicek AG, Jambi S, Franjic D, Nishimura S, Li M, El-Fishawy P, et al. Homozygous loss of DIAPH1 is a novel cause of microcephaly in humans. European Journal of Human Genetics. 2015;23(2):165-72. doi: 10.1038/ejhg.2014.82.

508. Gombos R, Migh E, Antal O, Mukherjee A, Jenny A, Mihály J. The Formin DAAM Functions as Molecular Effector of the Planar Cell Polarity Pathway during Axonal Development in Drosophila. The Journal of neuroscience : the official journal of the Society for Neuroscience. 2015;35(28):10154-67. Epub 2015/07/17. doi: 10.1523/jneurosci.3708-14.2015. PubMed PMID: 26180192; PubMed Central PMCID: PMCPMC4502256.

509. Szikora S, Földi I, Tóth K, Migh E, Vig A, Bugyi B, et al. The formin DAAM is required for coordination of the actin and microtubule cytoskeleton in axonal growth cones. Journal of cell science. 2017;130(15):2506-19. Epub 2017/06/14. doi: 10.1242/jcs.203455. PubMed PMID: 28606990.

510. Grobe H, Wüstenhagen A, Baarlink C, Grosse R, Grikscheit K. A Rac1-FMNL2 signaling module affects cell-cell contact formation independent of Cdc42 and membrane protrusions. PloS one. 2018;13(3):e0194716. doi: 10.1371/journal.pone.0194716.

511. Zhang M-F, Li Q-L, Yang Y-F, Cao Y, Zhang CZ. FMNL1 Exhibits Pro-Metastatic Activity via CXCR2 in Clear Cell Renal Cell Carcinoma. Frontiers in Oncology. 2020;10. doi: 10.3389/fonc.2020.564614.

512. Wang Y, Sherrard A, Zhao B, Melak M, Trautwein J, Kleinschnitz E-M, et al. GPCR-induced calcium transients trigger nuclear actin assembly for chromatin dynamics. Nature communications. 2019;10(1):5271. doi: 10.1038/s41467-019-13322-y.

513. Subramanian B, Chun J, Perez-Gill C, Yan P, Stillman IE, Higgs HN, et al. FSGS-Causing INF2 Mutation Impairs Cleaved INF2 N-Fragment Functions in Podocytes. Journal of the American Society of Nephrology : JASN. 2020;31(2):374-91. Epub 2020/01/12. doi: 10.1681/asn.2019050443. PubMed PMID: 31924668; PubMed Central PMCID: PMCPMC7003299.

514. Boyer O, Nevo F, Plaisier E, Funalot B, Gribouval O, Benoit G, et al. INF2 mutations in Charcot-Marie-Tooth disease with glomerulopathy. The New England journal of medicine. 2011;365(25):2377-88. Epub 2011/12/23. doi: 10.1056/NEJMoa1109122. PubMed PMID: 22187985.

515. Schulze N, Graessl M, Blancke Soares A, Geyer M, Dehmelt L, Nalbant P. FHOD1 regulates stress fiber organization by controlling the dynamics of transverse arcs and dorsal fibers. Journal of cell science. 2014;127(Pt 7):1379-93. Epub 2014/02/01. doi: 10.1242/jcs.134627. PubMed PMID: 24481812.

516. Antoku S, Wu W, Joseph LC, Morrow JP, Worman HJ, Gundersen GG. ERK1/2 Phosphorylation of FHOD Connects Signaling and Nuclear Positioning Alternations in Cardiac Laminopathy. Developmental cell. 2019;51(5):602-16.e12. Epub 2019/12/04. doi: 10.1016/j.devcel.2019.10.023. PubMed PMID: 31794718; PubMed Central PMCID: PMCPMC7561008.

517. Miyagi Y, Yamashita T, Fukaya M, Sonoda T, Okuno T, Yamada K, et al. Delphilin: a novel PDZ and formin homology domain-containing protein that synaptically colocalizes and interacts with glutamate receptor delta 2 subunit. The Journal of neuroscience : the official journal of the Society for Neuroscience. 2002;22(3):803-14. doi: 10.1523/JNEUROSCI.22-03-00803.2002. PubMed PMID: 11826110.

518. Liu R, Linardopoulou EV, Osborn GE, Parkhurst SM. Formins in development: Orchestrating body plan origami. Biochimica et Biophysica Acta (BBA) - Molecular Cell Research. 2010;1803(2):207-25. doi: https://doi.org/10.1016/j.bbamcr.2008.09.016.

519. Belin BJ, Lee T, Mullins RD. DNA damage induces nuclear actin filament assembly by Formin -2 and Spire-½ that promotes efficient DNA repair. [corrected]. eLife. 2015;4:e07735-e. doi: 10.7554/eLife.07735. PubMed PMID: 26287480.

520. Leader B, Leder P. Formin-2, a novel formin homology protein of the cappuccino subfamily, is highly expressed in the developing and adult central nervous system. Mechanisms of development. 2000;93(1-2):221-31. Epub 2000/04/27. doi: 10.1016/s0925-4773(00)00276-8. PubMed PMID: 10781961.

521. Gorukmez O, Gorukmez O, Ekici AA. A Novel Nonsense FMN2 Mutation in Nonsyndromic Autosomal Recessive Intellectual Disability Syndrome. Fetal and Pediatric Pathology. 2020;40:702 - 6.

522. Fex M, Nicholas LM, Vishnu N, Medina A, Sharoyko VV, Nicholls DG, et al. The pathogenetic role of β-cell mitochondria in type 2 diabetes. The Journal of endocrinology. 2018;236(3):R145-r59. Epub 2018/02/13. doi: 10.1530/joe-17-0367. PubMed PMID: 29431147.

523. Pagliarini DJ, Rutter J. Hallmarks of a new era in mitochondrial biochemistry. Genes & development. 2013;27(24):2615-27. Epub 2013/12/20. doi: 10.1101/gad.229724.113. PubMed PMID: 24352419; PubMed Central PMCID: PMCPMC3877752.

524. Chandel NS, Maltepe E, Goldwasser E, Mathieu CE, Simon MC, Schumacker PT. Mitochondrial reactive oxygen species trigger hypoxia-induced transcription. Proceedings of the National Academy of Sciences of the United States of America. 1998;95(20):11715-20. Epub 1998/09/30. PubMed PMID: 9751731; PubMed Central PMCID: PMCPMC21706.

525. Al-Mehdi AB, Pastukh VM, Swiger BM, Reed DJ, Patel MR, Bardwell GC, et al. Perinuclear mitochondrial clustering creates an oxidant-rich nuclear domain required for hypoxia-induced transcription. Science signaling. 2012;5(231):ra47. Epub 2012/07/06. doi: 10.1126/scisignal.2002712. PubMed PMID: 22763339; PubMed Central PMCID: PMCPMC3565837.

526. Head B, Griparic L, Amiri M, Gandre-Babbe S, van der Bliek AM. Inducible proteolytic inactivation of OPA1 mediated by the OMA1 protease in mammalian cells. The Journal of cell biology. 2009;187(7):959-66. Epub 2009/12/30. doi: 10.1083/jcb.200906083. PubMed PMID: 20038677; PubMed Central PMCID: PMCPMC2806274.

527. Ehses S, Raschke I, Mancuso G, Bernacchia A, Geimer S, Tondera D, et al. Regulation of OPA1 processing and mitochondrial fusion by m-AAA protease isoenzymes and OMA1. The Journal of cell biology. 2009;187(7):1023-36. Epub 2009/12/30. doi: 10.1083/jcb.200906084. PubMed PMID: 20038678; PubMed Central PMCID: PMCPMC2806285.

528. Ishihara N, Fujita Y, Oka T, Mihara K. Regulation of mitochondrial morphology through proteolytic cleavage of OPA1. The EMBO journal. 2006;25(13):2966-77. Epub 2006/06/17. doi: 10.1038/sj.emboj.7601184. PubMed PMID: 16778770; PubMed Central PMCID: PMCPMC1500981.

529. Utsumi T, Sakurai N, Nakano K, Ishisaka R. C-terminal 15 kDa fragment of cytoskeletal actin is posttranslationally N-myristoylated upon caspase-mediated cleavage and targeted to mitochondria. FEBS letters. 2003;539(1-3):37-44. Epub 2003/03/26. PubMed PMID: 12650923.

530. Chua BT, Volbracht C, Tan KO, Li R, Yu VC, Li P. Mitochondrial translocation of cofilin is an early step in apoptosis induction. Nature cell biology. 2003;5(12):1083-9. Epub 2003/11/25. doi: 10.1038/ncb1070. PubMed PMID: 14634665.

531. DuBoff B, Gotz J, Feany MB. Tau promotes neurodegeneration via DRP1 mislocalization in vivo. Neuron. 2012;75(4):618-32. Epub 2012/08/28. doi: 10.1016/j.neuron.2012.06.026. PubMed PMID: 22920254; PubMed Central PMCID: PMCPMC3428596.

532. Lee H, Yoon Y. Transient contraction of mitochondria induces depolarization through the inner membrane dynamin OPA1 protein. The Journal of biological chemistry. 2014;289(17):11862-72. Epub 2014/03/15. doi: 10.1074/jbc.M113.533299. PubMed PMID: 24627489; PubMed Central PMCID: PMCPMC4002095.

533. Kwon D, Park E, Sesaki H, Kang SJ. Carbonyl cyanide 3-chlorophenylhydrazone (CCCP) suppresses STING-mediated DNA sensing pathway through inducing mitochondrial fission. Biochemical and biophysical research communications. 2017;493(1):737-43. Epub 2017/09/02. doi: 10.1016/j.bbrc.2017.08.121. PubMed PMID: 28859978.

534. Song Z, Chen H, Fiket M, Alexander C, Chan DC. OPA1 processing controls mitochondrial fusion and is regulated by mRNA splicing, membrane potential, and Yme1L. The Journal of cell biology. 2007;178(5):749-55. Epub 2007/08/22. doi: 10.1083/jcb.200704110. PubMed PMID: 17709429; PubMed Central PMCID: PMCPMC2064540.

535. Anand R, Wai T, Baker MJ, Kladt N, Schauss AC, Rugarli E, et al. The i-AAA protease YME1L and OMA1 cleave OPA1 to balance mitochondrial fusion and fission. The Journal of cell biology. 2014;204(6):919-29. Epub 2014/03/13. doi: 10.1083/jcb.201308006. PubMed PMID: 24616225; PubMed Central PMCID: PMCPMC3998800.

536. Patten DA, Wong J, Khacho M, Soubannier V, Mailloux RJ, Pilon-Larose K, et al. OPA1-dependent cristae modulation is essential for cellular adaptation to metabolic demand. The EMBO journal. 2014;33(22):2676-91. Epub 2014/10/10. doi: 10.15252/embj.201488349. PubMed PMID: 25298396; PubMed Central PMCID: PMCPMC4282575.

537. Varanita T, Soriano ME, Romanello V, Zaglia T, Quintana-Cabrera R, Semenzato M, et al. The OPA1-dependent mitochondrial cristae remodeling pathway controls atrophic, apoptotic, and ischemic tissue damage. Cell metabolism. 2015;21(6):834-44. Epub 2015/06/04. doi: 10.1016/j.cmet.2015.05.007. PubMed PMID: 26039448; PubMed Central PMCID: PMCPMC4457892.

538. MacVicar TD, Lane JD. Impaired OMA1-dependent cleavage of OPA1 and reduced DRP1 fission activity combine to prevent mitophagy in cells that are dependent on oxidative phosphorylation. Journal of cell science. 2014;127(Pt 10):2313-25. Epub 2014/03/19. doi: 10.1242/jcs.144337. PubMed PMID: 24634514; PubMed Central PMCID: PMCPMC4021475.

539. Pruyne D. Revisiting the Phylogeny of the Animal Formins: Two New Subtypes, Relationships with Multiple Wing Hairs Proteins, and a Lost Human Formin. PloS one. 2016;11(10):e0164067. Epub 2016/10/04. doi: 10.1371/journal.pone.0164067. PubMed PMID: 27695129; PubMed Central PMCID: PMCPMC5047451.

540. A M, Fung TS, Kettenbach AN, Chakrabarti R, Higgs HN. A complex containing lysine-acetylated actin inhibits the formin INF2. Nature cell biology. 2019;21(5):592-602. Epub 2019/04/10. doi: 10.1038/s41556-019-0307-4. PubMed PMID: 30962575; PubMed Central PMCID: PMCPMC6501848.

541. Campellone KG, Welch MD. A nucleator arms race: cellular control of actin assembly. Nature reviews Molecular cell biology. 2010;11(4):237-51. Epub 2010/03/20. doi: 10.1038/nrm2867. PubMed PMID: 20237478; PubMed Central PMCID: PMCPMC2929822.

542. Matsuda N, Sato S, Shiba K, Okatsu K, Saisho K, Gautier CA, et al. PINK1 stabilized by mitochondrial depolarization recruits Parkin to damaged mitochondria and activates latent Parkin for mitophagy. The Journal of cell biology. 2010;189(2):211-21. Epub 2010/04/21. doi: 10.1083/jcb.200910140. PubMed PMID: 20404107; PubMed Central PMCID: PMCPMC2856912.

543. Tanaka A, Cleland MM, Xu S, Narendra DP, Suen DF, Karbowski M, et al. Proteasome and p97 mediate mitophagy and degradation of mitofusins induced by Parkin. The Journal of cell biology. 2010;191(7):1367-80. Epub 2010/12/22. doi: 10.1083/jcb.201007013. PubMed PMID: 21173115; PubMed Central PMCID: PMCPMC3010068.

544. Park YS, Choi SE, Koh HC. PGAM5 regulates PINK1/Parkin-mediated mitophagy via DRP1 in CCCP-induced mitochondrial dysfunction. Toxicology letters. 2018;284:120-8. Epub 2017/12/16. doi: 10.1016/j.toxlet.2017.12.004. PubMed PMID: 29241732.

545. Coutts AS, La Thangue NB. Actin nucleation by WH2 domains at the autophagosome. Nature communications. 2015;6:7888. Epub 2015/08/01. doi: 10.1038/ncomms8888. PubMed PMID: 26223951; PubMed Central PMCID: PMCPMC4532831.

546. Yamano K, Wang C, Sarraf SA, Munch C, Kikuchi R, Noda NN, et al. Endosomal Rab cycles regulate Parkin-mediated mitophagy. Elife. 2018;7. Epub 2018/01/24. doi: 10.7554/eLife.31326. PubMed PMID: 29360040; PubMed Central PMCID: PMCPMC5780041.

547. Okatsu K, Uno M, Koyano F, Go E, Kimura M, Oka T, et al. A dimeric PINK1-containing complex on depolarized mitochondria stimulates Parkin recruitment. The Journal of biological chemistry. 2013;288(51):36372-84. Epub 2013/11/06. doi: 10.1074/jbc.M113.509653. PubMed PMID: 24189060; PubMed Central PMCID: PMCPMC3868751.

548. McLelland GL, Goiran T, Yi W, Dorval G, Chen CX, Lauinger ND, et al. Mfn2 ubiquitination by PINK1/parkin gates the p97-dependent release of ER from mitochondria to drive mitophagy. Elife. 2018;7. Epub 2018/04/21. doi: 10.7554/eLife.32866. PubMed PMID: 29676259; PubMed Central PMCID: PMCPMC5927771.

549. Durcan TM, Tang MY, Perusse JR, Dashti EA, Aguileta MA, McLelland GL, et al. USP8 regulates mitophagy by removing K6-linked ubiquitin conjugates from parkin. The EMBO journal. 2014;33(21):2473-91. Epub 2014/09/14. doi: 10.15252/embj.201489729. PubMed PMID: 25216678; PubMed Central PMCID: PMCPMC4283406.

550. Lee Y, Stevens DA, Kang SU, Jiang H, Lee YI, Ko HS, et al. PINK1 Primes Parkin-Mediated Ubiquitination of PARIS in Dopaminergic Neuronal Survival. Cell reports. 2017;18(4):918-32. Epub 2017/01/26. doi: 10.1016/j.celrep.2016.12.090. PubMed PMID: 28122242; PubMed Central PMCID: PMCPMC5312976.

551. Hoppins S, Edlich F, Cleland MM, Banerjee S, McCaffery JM, Youle RJ, et al. The soluble form of Bax regulates mitochondrial fusion via MFN2 homotypic complexes.

Molecular cell. 2011;41(2):150-60. Epub 2011/01/25. doi: 10.1016/j.molcel.2010.11.030. PubMed PMID: 21255726; PubMed Central PMCID: PMCPMC3072068.

552. Duvezin-Caubet S, Jagasia R, Wagener J, Hofmann S, Trifunovic A, Hansson A, et al. Proteolytic processing of OPA1 links mitochondrial dysfunction to alterations in mitochondrial morphology. The Journal of biological chemistry. 2006;281(49):37972-9. Epub 2006/09/28. doi: 10.1074/jbc.M606059200. PubMed PMID: 17003040.

553. Sekine S, Wang C, Sideris DP, Bunker E, Zhang Z, Youle RJ. Reciprocal Roles of Tom7 and OMA1 during Mitochondrial Import and Activation of PINK1. Molecular cell. 2019;73(5):1028-43.e5. Epub 2019/02/09. doi: 10.1016/j.molcel.2019.01.002. PubMed PMID: 30733118.

554. Desmurs M, Foti M, Raemy E, Vaz FM, Martinou JC, Bairoch A, et al. C11orf83, a mitochondrial cardiolipin-binding protein involved in bc1 complex assembly and supercomplex stabilization. Mol Cell Biol. 2015;35(7):1139-56. Epub 2015/01/22. doi: 10.1128/mcb.01047-14. PubMed PMID: 25605331; PubMed Central PMCID: PMCPMC4355537.

555. Zhang K, Li H, Song Z. Membrane depolarization activates the mitochondrial protease OMA1 by stimulating self-cleavage. EMBO reports. 2014;15(5):576-85. Epub 2014/04/11. doi: 10.1002/embr.201338240. PubMed PMID: 24719224; PubMed Central PMCID: PMCPMC4210089.

556. Johnson HW, Schell MJ. Neuronal IP3 3-kinase is an F-actin-bundling protein: role in dendritic targeting and regulation of spine morphology. Molecular biology of the cell. 2009;20(24):5166-80. Epub 2009/10/23. doi: 10.1091/mbc.E09-01-0083. PubMed PMID: 19846664; PubMed Central PMCID: PMCPMC2793293.

557. Wu J, Prole DL, Shen Y, Lin Z, Gnanasekaran A, Liu Y, et al. Red fluorescent genetically encoded Ca2+ indicators for use in mitochondria and endoplasmic reticulum. The Biochemical journal. 2014;464(1):13-22. Epub 2014/08/29. doi: 10.1042/bj20140931. PubMed PMID: 25164254; PubMed Central PMCID: PMCPMC4214425.

558. Nam HS, Benezra R. High levels of Id1 expression define B1 type adult neural stem cells. Cell stem cell. 2009;5(5):515-26. Epub 2009/11/10. doi: 10.1016/j.stem.2009.08.017. PubMed PMID: 19896442; PubMed Central PMCID: PMCPMC2775820.

559. Ramabhadran V, Korobova F, Rahme GJ, Higgs HN. Splice variant-specific cellular function of the formin INF2 in maintenance of Golgi architecture. Molecular biology of the cell. 2011;22(24):4822-33. Epub 2011/10/15. doi: 10.1091/mbc.E11-05-0457. PubMed PMID: 21998196; PubMed Central PMCID: PMCPMC3237625.

560. Fung TS, Ji WK, Higgs HN, Chakrabarti R. Two distinct actin filament populations have effects on mitochondria, with differences in stimuli and assembly factors. Journal of cell science. 2019;132(18). Epub 2019/08/16. doi: 10.1242/jcs.234435. PubMed PMID: 31413070; PubMed Central PMCID: PMCPMC6765187.

561. Siton-Mendelson O, Bernheim-Groswasser A. Functional Actin Networks under Construction: The Cooperative Action of Actin Nucleation and Elongation Factors. Trends in biochemical sciences. 2017;42(6):414-30. Epub 2017/04/05. doi: 10.1016/j.tibs.2017.03.002. PubMed PMID: 28372857.

562. Goley ED, Welch MD. The ARP2/3 complex: an actin nucleator comes of age. Nature reviews Molecular cell biology. 2006;7(10):713-26. Epub 2006/09/23. doi: 10.1038/nrm2026. PubMed PMID: 16990851.

563. Rotty JD, Wu C, Bear JE. New insights into the regulation and cellular functions of the ARP2/3 complex. Nature reviews Molecular cell biology. 2013;14(1):7-12. Epub 2012/12/06. doi: 10.1038/nrm3492. PubMed PMID: 23212475.

564. Schnoor M, Stradal TE, Rottner K. Cortactin: Cell Functions of A Multifaceted Actin-Binding Protein. Trends in cell biology. 2018;28(2):79-98. Epub 2017/11/23. doi: 10.1016/j.tcb.2017.10.009. PubMed PMID: 29162307.

565. Schaks M, Giannone G, Rottner K. Actin dynamics in cell migration. Essays in biochemistry. 2019;63(5):483-95. Epub 2019/09/26. doi: 10.1042/ebc20190015. PubMed PMID: 31551324; PubMed Central PMCID: PMCPMC6823167.

566. El-Mir MY, Nogueira V, Fontaine E, Avéret N, Rigoulet M, Leverve X. Dimethylbiguanide inhibits cell respiration via an indirect effect targeted on the respiratory chain complex I. The Journal of biological chemistry. 2000;275(1):223-8. Epub 2000/01/05. doi: 10.1074/jbc.275.1.223. PubMed PMID: 10617608.

567. Owen MR, Doran E, Halestrap AP. Evidence that metformin exerts its anti-diabetic effects through inhibition of complex 1 of the mitochondrial respiratory chain.

The Biochemical journal. 2000;348 Pt 3(Pt 3):607-14. Epub 2000/06/07. PubMed PMID: 10839993; PubMed Central PMCID: PMCPMC1221104.

568. Lai FP, Szczodrak M, Oelkers JM, Ladwein M, Acconcia F, Benesch S, et al. Cortactin promotes migration and platelet-derived growth factor-induced actin reorganization by signaling to Rho-GTPases. Molecular biology of the cell. 2009;20(14):3209-23. Epub 2009/05/22. doi: 10.1091/mbc.e08-12-1180. PubMed PMID: 19458196; PubMed Central PMCID: PMCPMC2710823.

569. Steffen A, Rottner K, Ehinger J, Innocenti M, Scita G, Wehland J, et al. Sra-1 and Nap1 link Rac to actin assembly driving lamellipodia formation. The EMBO journal. 2004;23(4):749-59. Epub 02/05. doi: 10.1038/sj.emboj.7600084. PubMed PMID: 14765121.

570. Litschko C, Linkner J, Brühmann S, Stradal TEB, Reinl T, Jänsch L, et al. Differential functions of WAVE regulatory complex subunits in the regulation of actin-driven processes. Eur J Cell Biol. 2017;96(8):715-27. Epub 2017/09/12. doi: 10.1016/j.ejcb.2017.08.003. PubMed PMID: 28889942.

571. Steffen A, Ladwein M, Dimchev GA, Hein A, Schwenkmezger L, Arens S, et al. Rac function is crucial for cell migration but is not required for spreading and focal adhesion formation. Journal of cell science. 2013;126(20):4572-88. doi: 10.1242/jcs.118232.

572. Bagur R, Hajnoczky G. Intracellular Ca(2+) Sensing: Its Role in Calcium Homeostasis and Signaling. Molecular cell. 2017;66(6):780-8. Epub 2017/06/18. doi: 10.1016/j.molcel.2017.05.028. PubMed PMID: 28622523; PubMed Central PMCID: PMCPMC5657234.

573. Wolf SG, Mutsafi Y, Dadosh T, Ilani T, Lansky Z, Horowitz B, et al. 3D visualization of mitochondrial solid-phase calcium stores in whole cells. eLife. 2017;6. Epub 2017/11/07. doi: 10.7554/eLife.29929. PubMed PMID: 29106371; PubMed Central PMCID: PMCPMC5703638.

574. Zeng L, Webster SV, Newton PM. The biology of protein kinase C. Adv Exp Med Biol. 2012;740:639-61. Epub 2012/03/29. doi: 10.1007/978-94-007-2888-2_28. PubMed PMID: 22453963.

575. Müller PM, Rademacher J, Bagshaw RD, Wortmann C, Barth C, van Unen J, et al. Systems analysis of RhoGEF and RhoGAP regulatory proteins reveals spatially organized RAC1 signalling from integrin adhesions. Nature cell biology. 2020;22(4):498-511. Epub 2020/03/24. doi: 10.1038/s41556-020-0488-x. PubMed PMID: 32203420.

576. Price LS, Langeslag M, ten Klooster JP, Hordijk PL, Jalink K, Collard JG. Calcium signaling regulates translocation and activation of Rac. The Journal of biological chemistry. 2003;278(41):39413-21. Epub 2003/07/31. doi: 10.1074/jbc.M302083200. PubMed PMID: 12888567.

577. Drake JC, Wilson RJ, Laker RC, Guan Y, Spaulding HR, Nichenko AS, et al. Mitochondria-localized AMPK responds to local energetics and contributes to exercise and energetic stress-induced mitophagy. Proceedings of the National Academy of Sciences of the United States of America. 2021;118(37). Epub 2021/09/09. doi: 10.1073/pnas.2025932118. PubMed PMID: 34493662; PubMed Central PMCID: PMCPMC8449344.

578. Wu J, Rowart P, Jouret F, Gassaway BM, Rajendran V, Rinehart J, et al. Mechanisms involved in AMPK-mediated deposition of tight junction components to the plasma membrane. Am J Physiol Cell Physiol. 2020;318(3):C486-C501. Epub 2020/01/09. doi: 10.1152/ajpcell.00422.2019. PubMed PMID: 31913699; PubMed Central PMCID: PMCPMC7099514.

579. Kühn S, Erdmann C, Kage F, Block J, Schwenkmezger L, Steffen A, et al. The structure of FMNL2-Cdc42 yields insights into the mechanism of lamellipodia and filopodia formation. Nature communications. 2015;6:7088. Epub 2015/05/13. doi: 10.1038/ncomms8088. PubMed PMID: 25963737; PubMed Central PMCID: PMCPMC4432619.

580. Ding WX, Ni HM, Li M, Liao Y, Chen X, Stolz DB, et al. Nix is critical to two distinct phases of mitophagy, reactive oxygen species-mediated autophagy induction and Parkin-ubiquitin-p62-mediated mitochondrial priming. The Journal of biological chemistry. 2010;285(36):27879-90. Epub 2010/06/25. doi: 10.1074/jbc.M110.119537. PubMed PMID: 20573959; PubMed Central PMCID: PMCPMC2934655.

581. Yoshii SR, Kishi C, Ishihara N, Mizushima N. Parkin mediates proteasome-dependent protein degradation and rupture of the outer mitochondrial membrane. The Journal of biological chemistry. 2011;286(22):19630-40. Epub 2011/04/02. doi:

10.1074/jbc.M110.209338. PubMed PMID: 21454557; PubMed Central PMCID: PMCPMC3103342.

582. Griparic L, Kanazawa T, van der Bliek AM. Regulation of the mitochondrial dynamin-like protein Opa1 by proteolytic cleavage. The Journal of cell biology. 2007;178(5):757-64. Epub 2007/08/22. doi: 10.1083/jcb.200704112. PubMed PMID: 17709430; PubMed Central PMCID: PMCPMC2064541.

583. Baker MJ, Lampe PA, Stojanovski D, Korwitz A, Anand R, Tatsuta T, et al. Stress-induced OMA1 activation and autocatalytic turnover regulate OPA1-dependent mitochondrial dynamics. The EMBO journal. 2014;33(6):578-93. Epub 2014/02/20. doi: 10.1002/embj.201386474. PubMed PMID: 24550258; PubMed Central PMCID: PMCPMC3989652.

584. Harris ES, Rouiller I, Hanein D, Higgs HN. Mechanistic differences in actin bundling activity of two mammalian formins, FRL1 and mDia2. The Journal of biological chemistry. 2006;281(20):14383-92. Epub 2006/03/25. doi: 10.1074/jbc.M510923200. PubMed PMID: 16556604.

585. Heimsath EG, Jr., Higgs HN. The C terminus of formin FMNL3 accelerates actin polymerization and contains a WH2 domain-like sequence that binds both monomers and filament barbed ends. The Journal of biological chemistry. 2012;287(5):3087-98. Epub 2011/11/19. doi: 10.1074/jbc.M111.312207. PubMed PMID: 22094460; PubMed Central PMCID: PMCPMC3270965.

586. Kage F, Steffen A, Ellinger A, Ranftler C, Gehre C, Brakebusch C, et al. FMNL2 and -3 regulate Golgi architecture and anterograde transport downstream of Cdc42. Scientific Reports. 2017;7(1):9791. doi: 10.1038/s41598-017-09952-1.

587. Gomez TS, Kumar K, Medeiros RB, Shimizu Y, Leibson PJ, Billadeau DD. Formins regulate the actin-related protein 2/3 complex-independent polarization of the centrosome to the immunological synapse. Immunity. 2007;26(2):177-90. Epub 2007/02/20. doi: 10.1016/j.immuni.2007.01.008. PubMed PMID: 17306570; PubMed Central PMCID: PMCPMC2836258.

588. Colón-Franco JM, Gomez TS, Billadeau DD. Dynamic remodeling of the actin cytoskeleton by FMNL1γ is required for structural maintenance of the Golgi complex. Journal of cell science. 2011;124(Pt 18):3118-26. Epub 08/24. doi: 10.1242/jcs.083725. PubMed PMID: 21868368.

589. Endo M. Calcium-induced calcium release in skeletal muscle. Physiological reviews. 2009;89(4):1153-76. Epub 2009/10/01. doi: 10.1152/physrev.00040.2008. PubMed PMID: 19789379.

590. Giannini G, Conti A, Mammarella S, Scrobogna M, Sorrentino V. The ryanodine receptor/calcium channel genes are widely and differentially expressed in murine brain and peripheral tissues. Journal of Cell Biology. 1995;128(5):893-904. doi: 10.1083/jcb.128.5.893.

591. Bennett DL, Cheek TR, Berridge MJ, De Smedt H, Parys JB, Missiaen L, et al. Expression and Function of Ryanodine Receptors in Nonexcitable Cells (∗). Journal of Biological Chemistry. 1996;271(11):6356-62. doi: 10.1074/jbc.271.11.6356.

592. van Rijssel J, van Buul JD. The many faces of the guanine-nucleotide exchange factor trio. Cell adhesion & migration. 2012;6(6):482-7. Epub 2012/10/19. doi: 10.4161/cam.21418. PubMed PMID: 23076143; PubMed Central PMCID: PMCPMC3547891.

593. Klems A, van Rijssel J, Ramms AS, Wild R, Hammer J, Merkel M, et al. The GEF Trio controls endothelial cell size and arterial remodeling downstream of Vegf signaling in both zebrafish and cell models. Nature communications. 2020;11(1):5319. Epub 2020/10/23. doi: 10.1038/s41467-020-19008-0. PubMed PMID: 33087700; PubMed Central PMCID: PMCPMC7578835.

594. Gu J, Yang Z, Yuan L, Guo S, Wang D, Zhao N, et al. Rho-GEF trio regulates osteoclast differentiation and function by Rac1/Cdc42. Experimental cell research. 2020;396(1):112265. Epub 2020/09/09. doi: 10.1016/j.yexcr.2020.112265. PubMed PMID: 32898553.

595. Egorov MV, Capestrano M, Vorontsova OA, Di Pentima A, Egorova AV, Mariggiò S, et al. Faciogenital Dysplasia Protein (FGD1) Regulates Export of Cargo Proteins from the Golgi Complex via Cdc42 Activation. Molecular biology of the cell. 2009;20(9):2413-27. doi: 10.1091/mbc.e08-11-1136.

596. Egorov M, Polishchuk R. Identification of CDC42 Effectors Operating in FGD1-Dependent Trafficking at the Golgi. Frontiers in cell and developmental biology. 2019;7(7). doi: 10.3389/fcell.2019.00007.

597. Pedigo NG, Van Delden D, Walters L, Farrell CL. Minireview: Role of genetic changes of faciogenital dysplasia protein 1 in human disease. Physiological genomics. 2016;48(7):446-54. Epub 2016/05/21. doi: 10.1152/physiolgenomics.00101.2015. PubMed PMID: 27199457.

598. Orrico A, Galli L, Cavaliere ML, Garavelli L, Fryns JP, Crushell E, et al. Phenotypic and molecular characterisation of the Aarskog-Scott syndrome: a survey of the clinical variability in light of FGD1 mutation analysis in 46 patients. European journal of human genetics : EJHG. 2004;12(1):16-23. Epub 2003/10/16. doi: 10.1038/sj.ejhg.5201081. PubMed PMID: 14560308.

599. Oshima T, Fujino T, Ando K, Hayakawa M. Role of FGD1, a Cdc42 guanine nucleotide exchange factor, in epidermal growth factor-stimulated c-Jun NH2-terminal kinase activation and cell migration. Biological & pharmaceutical bulletin. 2011;34(1):54-60. Epub 2011/01/08. doi: 10.1248/bpb.34.54. PubMed PMID: 21212517.

600. Hornbeck PV, Zhang B, Murray B, Kornhauser JM, Latham V, Skrzypek E. PhosphoSitePlus, 2014: mutations, PTMs and recalibrations. Nucleic acids research. 2015;43(Database issue):D512-20. Epub 2014/12/18. doi: 10.1093/nar/gku1267. PubMed PMID: 25514926; PubMed Central PMCID: PMCPMC4383998.

601. Wai T, Saita S, Nolte H, Müller S, König T, Richter-Dennerlein R, et al. The membrane scaffold SLP2 anchors a proteolytic hub in mitochondria containing PARL and the i-AAA protease YME1L. EMBO reports. 2016;17(12):1844-56. Epub 2016/10/16. doi: 10.15252/embr.201642698. PubMed PMID: 27737933; PubMed Central PMCID: PMCPMC5283581.

602. Gandre-Babbe S, van der Bliek AM. The novel tail-anchored membrane protein Mff controls mitochondrial and peroxisomal fission in mammalian cells. Molecular biology of the cell. 2008;19(6):2402-12. Epub 2008/03/21. doi: 10.1091/mbc.e07-12-1287. PubMed PMID: 18353969; PubMed Central PMCID: PMCPMC2397315.

603. Kruppa AJ, Kishi-Itakura C, Masters TA, Rorbach JE, Grice GL, Kendrick-Jones J, et al. Myosin VI-Dependent Actin Cages Encapsulate Parkin-Positive Damaged Mitochondria. Developmental Cell. 2018;44(4):484-99.e6. doi: https://doi.org/10.1016/j.devcel.2018.01.007.

604. Mathiowetz AJ, Baple E, Russo AJ, Coulter AM, Carrano E, Brown JD, et al. An Amish founder mutation disrupts a PI(3)P-WHAMM-Arp2/3 complex–driven

autophagosomal remodeling pathway. Molecular biology of the cell. 2017;28(19):2492-507. doi: 10.1091/mbc.e17-01-0022.

605. Kast DJ, Dominguez R. The Cytoskeleton-Autophagy Connection. Current biology : CB. 2017;27(8):R318-r26. Epub 2017/04/26. doi: 10.1016/j.cub.2017.02.061. PubMed PMID: 28441569; PubMed Central PMCID: PMCPMC5444402.

606. Kage F, Döring H, Mietkowska M, Schaks M, Grüner F, Stahnke S, et al. Lamellipodia-like actin networks in cells lacking WAVE Regulatory Complex. bioRxiv. 2021:2021.06.18.449030. doi: 10.1101/2021.06.18.449030.

607. Wu J, Prole David L, Shen Y, Lin Z, Gnanasekaran A, Liu Y, et al. Red fluorescent genetically encoded Ca2+ indicators for use in mitochondria and endoplasmic reticulum. Biochemical Journal. 2014;464(1):13-22. doi: 10.1042/BJ20140931.

608. Kaksonen M, Peng HB, Rauvala H. Association of cortactin with dynamic actin in lamellipodia and on endosomal vesicles. Journal of cell science. 2000;113(24):4421-6. doi: 10.1242/jcs.113.24.4421.

609. Valm AM, Cohen S, Legant WR, Melunis J, Hershberg U, Wait E, et al. Applying systems-level spectral imaging and analysis to reveal the organelle interactome. Nature. 2017;546(7656):162-7. Epub 2017/05/26. doi: 10.1038/nature22369. PubMed PMID: 28538724; PubMed Central PMCID: PMCPMC5536967.

610. Nesvizhskii AI, Keller A, Kolker E, Aebersold R. A statistical model for identifying proteins by tandem mass spectrometry. Analytical chemistry. 2003;75(17):4646-58. Epub 2003/11/25. doi: 10.1021/ac0341261. PubMed PMID: 14632076.

611. Graw S, Tang J, Zafar MK, Byrd AK, Bolden C, Peterson EC, et al. proteiNorm - A User-Friendly Tool for Normalization and Analysis of TMT and Label-Free Protein Quantification. ACS omega. 2020;5(40):25625-33. Epub 2020/10/20. doi: 10.1021/acsomega.0c02564. PubMed PMID: 33073088; PubMed Central PMCID: PMCPMC7557219.

612. Huber W, von Heydebreck A, Sültmann H, Poustka A, Vingron M. Variance stabilization applied to microarray data calibration and to the quantification of differential expression. Bioinformatics (Oxford, England). 2002;18 Suppl 1:S96-104. Epub 2002/08/10. doi: 10.1093/bioinformatics/18.suppl_1.s96. PubMed PMID: 12169536.

613. Ritchie ME, Phipson B, Wu D, Hu Y, Law CW, Shi W, et al. limma powers differential expression analyses for RNA-sequencing and microarray studies. Nucleic acids research. 2015;43(7):e47. Epub 2015/01/22. doi: 10.1093/nar/gkv007. PubMed PMID: 25605792; PubMed Central PMCID: PMCPMC4402510.

614. Chawade A, Alexandersson E, Levander F. Normalyzer: a tool for rapid evaluation of normalization methods for omics data sets. Journal of proteome research. 2014;13(6):3114-20. Epub 2014/04/29. doi: 10.1021/pr401264n. PubMed PMID: 24766612; PubMed Central PMCID: PMCPMC4053077.

615. Storey AJ, Naceanceno KS, Lan RS, Washam CL, Orr LM, Mackintosh SG, et al. ProteoViz: a tool for the analysis and interactive visualization of phosphoproteomics data. Molecular omics. 2020;16(4):316-26. Epub 2020/04/30. doi: 10.1039/c9mo00149b. PubMed PMID: 32347222; PubMed Central PMCID: PMCPMC7423749.

616. Deutsch EW, Bandeira N, Sharma V, Perez-Riverol Y, Carver JJ, Kundu DJ, et al. The ProteomeXchange consortium in 2020: enabling 'big data' approaches in proteomics. Nucleic acids research. 2020;48(D1):D1145-d52. Epub 2019/11/07. doi: 10.1093/nar/gkz984. PubMed PMID: 31686107; PubMed Central PMCID: PMCPMC7145525.

617. Perez-Riverol Y, Bai J, Bandla C, García-Seisdedos D, Hewapathirana S, Kamatchinathan S, et al. The PRIDE database resources in 2022: a hub for mass spectrometry-based proteomics evidences. Nucleic acids research. 2022;50(D1):D543-d52. Epub 2021/11/02. doi: 10.1093/nar/gkab1038. PubMed PMID: 34723319; PubMed Central PMCID: PMCPMC8728295.

618. Nunnari J, Suomalainen A. Mitochondria: in sickness and in health. Cell. 2012;148(6):1145-59. Epub 2012/03/20. doi: 10.1016/j.cell.2012.02.035. PubMed PMID: 22424226; PubMed Central PMCID: PMCPMC5381524.

619. Kasahara A, Scorrano L. Mitochondria: from cell death executioners to regulators of cell differentiation. Trends in cell biology. 2014;24(12):761-70. Epub 2014/09/06. doi: 10.1016/j.tcb.2014.08.005. PubMed PMID: 25189346.

620. Sturdik E, Cully J, Sturdikova M, Durcova E. Stimulation of glycolysis in Ehrlich ascites carcinoma cells with phenylhydrazonopropanedinitrile and others uncouplers of oxidative phosphorylation. Neoplasma. 1986;33(5):575-82. Epub 1986/01/01. PubMed PMID: 3785464.

621. Fung TS, Chakrabarti R, Kollasser J, Rottner K, Stradal TEB, Kage F, et al. Parallel kinase pathways stimulate actin polymerization at depolarized mitochondria. Current biology : CB. 2022;32(7):1577-92.e8. Epub 2022/03/16. doi: 10.1016/j.cub.2022.02.058. PubMed PMID: 35290799; PubMed Central PMCID: PMCPMC9078333.

622. Nolen BJ, Tomasevic N, Russell A, Pierce DW, Jia Z, McCormick CD, et al. Characterization of two classes of small molecule inhibitors of Arp2/3 complex. Nature. 2009;460(7258):1031-4. Epub 2009/08/04. doi: 10.1038/nature08231. PubMed PMID: 19648907; PubMed Central PMCID: PMCPMC2780427.

623. Nakano M, Imamura H, Nagai T, Noji H. Ca(2)(+) regulation of mitochondrial ATP synthesis visualized at the single cell level. ACS Chem Biol. 2011;6(7):709-15. Epub 2011/04/15. doi: 10.1021/cb100313n. PubMed PMID: 21488691.

624. Silver IA, Erecińska M. Extracellular glucose concentration in mammalian brain: continuous monitoring of changes during increased neuronal activity and upon limitation in oxygen supply in normo-, hypo-, and hyperglycemic animals. The Journal of neuroscience : the official journal of the Society for Neuroscience. 1994;14(8):5068-76. Epub 1994/08/01. doi: 10.1523/jneurosci.14-08-05068.1994. PubMed PMID: 8046468; PubMed Central PMCID: PMCPMC6577171.

625. Krebs HA. The Pasteur effect and the relations between respiration and fermentation. Essays in biochemistry. 1972;8:1-34. Epub 1972/01/01. PubMed PMID: 4265190.

626. Racker E. History of the Pasteur effect and its pathobiology. Molecular and cellular biochemistry. 1974;5(1-2):17-23. Epub 1974/11/15. doi: 10.1007/BF01874168. PubMed PMID: 4279327.

627. Mookerjee SA, Gerencser AA, Nicholls DG, Brand MD. Quantifying intracellular rates of glycolytic and oxidative ATP production and consumption using extracellular flux measurements. The Journal of biological chemistry. 2017;292(17):7189-207. Epub 2017/03/09. doi: 10.1074/jbc.M116.774471. PubMed PMID: 28270511; PubMed Central PMCID: PMCPMC5409486.

628. Pike Winer LS, Wu M. Rapid analysis of glycolytic and oxidative substrate flux of cancer cells in a microplate. PloS one. 2014;9(10):e109916. Epub 2014/11/02. doi: 10.1371/journal.pone.0109916. PubMed PMID: 25360519; PubMed Central PMCID:

PMCPMC4215881 North Billerica, MA, USA. Min Wu was an employee at Seahorse Bioscience at the time of this work, North Billerica, MA, USA. However, this does not alter the authors' adherence to PLOS ONE policies on sharing data and materials.

629. Vafai SB, Mootha VK. Mitochondrial disorders as windows into an ancient organelle. Nature. 2012;491(7424):374-83. Epub 2012/11/16. doi: 10.1038/nature11707. PubMed PMID: 23151580.

630. Fernández-Moreno M, Hermida-Gómez T, Gallardo ME, Dalmao-Fernández A, Rego-Pérez I, Garesse R, et al. Generating Rho-0 Cells Using Mesenchymal Stem Cell Lines. PloS one. 2016;11(10):e0164199. Epub 2016/10/21. doi: 10.1371/journal.pone.0164199. PubMed PMID: 27764131; PubMed Central PMCID: PMCPMC5072612.

631. Rahman S, Thorburn D. Nuclear Gene-Encoded Leigh Syndrome Spectrum Overview. In: Adam MP, Ardinger HH, Pagon RA, Wallace SE, Bean LJH, Mirzaa G, et al., editors. GeneReviews. Seattle (WA): University of Washington, Seattle; 1993.

632. Lake NJ, Compton AG, Rahman S, Thorburn DR. Leigh syndrome: One disorder, more than 75 monogenic causes. Annals of neurology. 2016;79(2):190-203. Epub 2015/10/28. doi: 10.1002/ana.24551. PubMed PMID: 26506407.

633. Quintana A, Kruse SE, Kapur RP, Sanz E, Palmiter RD. Complex I deficiency due to loss of Ndufs4 in the brain results in progressive encephalopathy resembling Leigh syndrome. Proceedings of the National Academy of Sciences of the United States of America. 2010;107(24):10996-1001. Epub 2010/06/11. doi: 10.1073/pnas.1006214107. PubMed PMID: 20534480; PubMed Central PMCID: PMCPMC2890717.

634. van der Windt GJ, Everts B, Chang CH, Curtis JD, Freitas TC, Amiel E, et al. Mitochondrial respiratory capacity is a critical regulator of CD8+ T cell memory development. Immunity. 2012;36(1):68-78. Epub 2011/12/31. doi: 10.1016/j.immuni.2011.12.007. PubMed PMID: 22206904; PubMed Central PMCID: PMCPMC3269311.

635. Sena LA, Li S, Jairaman A, Prakriya M, Ezponda T, Hildeman DA, et al. Mitochondria are required for antigen-specific T cell activation through reactive oxygen species signaling. Immunity. 2013;38(2):225-36. Epub 2013/02/19. doi:

10.1016/j.immuni.2012.10.020. PubMed PMID: 23415911; PubMed Central PMCID: PMCPMC3582741.

636. Geltink RIK, Kyle RL, Pearce EL. Unraveling the Complex Interplay Between T Cell Metabolism and Function. Annual review of immunology. 2018;36:461-88. Epub 2018/04/21. doi: 10.1146/annurev-immunol-042617-053019. PubMed PMID: 29677474; PubMed Central PMCID: PMCPMC6323527.

637. Reina-Campos M, Scharping NE, Goldrath AW. CD8(+) T cell metabolism in infection and cancer. Nature reviews Immunology. 2021;21(11):718-38. Epub 2021/05/14. doi: 10.1038/s41577-021-00537-8. PubMed PMID: 33981085; PubMed Central PMCID: PMCPMC8806153.

638. Chang CH, Curtis JD, Maggi LB, Jr., Faubert B, Villarino AV, O'Sullivan D, et al. Posttranscriptional control of T cell effector function by aerobic glycolysis. Cell. 2013;153(6):1239-51. Epub 2013/06/12. doi: 10.1016/j.cell.2013.05.016. PubMed PMID: 23746840; PubMed Central PMCID: PMCPMC3804311.

639. Menk AV, Scharping NE, Moreci RS, Zeng X, Guy C, Salvatore S, et al. Early TCR Signaling Induces Rapid Aerobic Glycolysis Enabling Distinct Acute T Cell Effector Functions. Cell reports. 2018;22(6):1509-21. Epub 2018/02/10. doi: 10.1016/j.celrep.2018.01.040. PubMed PMID: 29425506; PubMed Central PMCID: PMCPMC5973810.

640. Chang CH, Qiu J, O'Sullivan D, Buck MD, Noguchi T, Curtis JD, et al. Metabolic Competition in the Tumor Microenvironment Is a Driver of Cancer Progression. Cell. 2015;162(6):1229-41. Epub 2015/09/01. doi: 10.1016/j.cell.2015.08.016. PubMed PMID: 26321679; PubMed Central PMCID: PMCPMC4864363.

641. Gautreau AM, Fregoso FE, Simanov G, Dominguez R. Nucleation, stabilization, and disassembly of branched actin networks. Trends in cell biology. 2021. Epub 2021/11/28. doi: 10.1016/j.tcb.2021.10.006. PubMed PMID: 34836783.

642. Hu H, Juvekar A, Lyssiotis CA, Lien EC, Albeck JG, Oh D, et al. Phosphoinositide 3-Kinase Regulates Glycolysis through Mobilization of Aldolase from the Actin Cytoskeleton. Cell. 2016;164(3):433-46. Epub 2016/01/30. doi: 10.1016/j.cell.2015.12.042. PubMed PMID: 26824656; PubMed Central PMCID: PMCPMC4898774.

643. Espinoza-Simón E, Chiquete-Félix N, Morales-García L, Pedroza-Dávila U, Pérez-Martínez X, Araiza-Olivera D, et al. In Saccharomyces cerevisiae, withdrawal of the carbon source results in detachment of glycolytic enzymes from the cytoskeleton and in actin reorganization. Fungal Biology. 2020;124(1):15-23. doi: https://doi.org/10.1016/j.funbio.2019.10.005.

644. Kamer KJ, Sancak Y, Mootha VK. The uniporter: from newly identified parts to function. Biochemical and biophysical research communications. 2014;449(4):370-2. Epub 2014/05/13. doi: 10.1016/j.bbrc.2014.04.143. PubMed PMID: 24814702.

645. Zorov DB, Juhaszova M, Sollott SJ. Mitochondrial reactive oxygen species (ROS) and ROS-induced ROS release. Physiological reviews. 2014;94(3):909-50. Epub 2014/07/06. doi: 10.1152/physrev.00026.2013. PubMed PMID: 24987008; PubMed Central PMCID: PMCPMC4101632.

646. Izyumov DS, Avetisyan AV, Pletjushkina OY, Sakharov DV, Wirtz KW, Chernyak BV, et al. “Wages of Fear”: transient threefold decrease in intracellular ATP level imposes apoptosis. Biochimica et Biophysica Acta (BBA) - Bioenergetics. 2004;1658(1):141-7. doi: https://doi.org/10.1016/j.bbabio.2004.05.007.

647. Zamzami N, Marchetti P, Castedo M, Zanin C, Vayssière JL, Petit PX, et al. Reduction in mitochondrial potential constitutes an early irreversible step of programmed lymphocyte death in vivo. The Journal of experimental medicine. 1995;181(5):1661-72. Epub 1995/05/01. doi: 10.1084/jem.181.5.1661. PubMed PMID: 7722446; PubMed Central PMCID: PMCPMC2192017.

648. Murata D, Yamada T, Tokuyama T, Arai K, Quirós PM, López-Otín C, et al. Mitochondrial Safeguard: a stress response that offsets extreme fusion and protects respiratory function via flickering-induced Oma1 activation. The EMBO journal. 2020;39(24):e105074. Epub 2020/11/18. doi: 10.15252/embj.2020105074. PubMed PMID: 33200421; PubMed Central PMCID: PMCPMC7737612.

649. Zorova LD, Popkov VA, Plotnikov EY, Silachev DN, Pevzner IB, Jankauskas SS, et al. Mitochondrial membrane potential. Analytical biochemistry. 2018;552:50-9. Epub 2017/07/18. doi: 10.1016/j.ab.2017.07.009. PubMed PMID: 28711444; PubMed Central PMCID: PMCPMC5792320.

650. Gerencser AA, Chinopoulos C, Birket MJ, Jastroch M, Vitelli C, Nicholls DG, et al. Quantitative measurement of mitochondrial membrane potential in cultured cells:

calcium-induced de- and hyperpolarization of neuronal mitochondria. The Journal of physiology. 2012;590(12):2845-71. Epub 2012/04/13. doi: 10.1113/jphysiol.2012.228387. PubMed PMID: 22495585; PubMed Central PMCID: PMCPMC3448152.

651. Kamo N, Muratsugu M, Hongoh R, Kobatake Y. Membrane potential of mitochondria measured with an electrode sensitive to tetraphenyl phosphonium and relationship between proton electrochemical potential and phosphorylation potential in steady state. The Journal of membrane biology. 1979;49(2):105-21. doi: 10.1007/BF01868720.

652. Wells AL, Lin AW, Chen LQ, Safer D, Cain SM, Hasson T, et al. Myosin VI is an actin-based motor that moves backwards. Nature. 1999;401(6752):505-8. Epub 1999/10/16. doi: 10.1038/46835. PubMed PMID: 10519557.

653. Melser S, Chatelain EH, Lavie J, Mahfouf W, Jose C, Obre E, et al. Rheb regulates mitophagy induced by mitochondrial energetic status. Cell metabolism. 2013;17(5):719-30. Epub 2013/04/23. doi: 10.1016/j.cmet.2013.03.014. PubMed PMID: 23602449.

654. Reitzer LJ, Wice BM, Kennell D. Evidence that glutamine, not sugar, is the major energy source for cultured HeLa cells. The Journal of biological chemistry. 1979;254(8):2669-76. Epub 1979/04/25. PubMed PMID: 429309.

655. Cieri D, Vicario M, Giacomello M, Vallese F, Filadi R, Wagner T, et al. SPLICS: a split green fluorescent protein-based contact site sensor for narrow and wide heterotypic organelle juxtaposition. Cell death and differentiation. 2018;25(6):1131-45. Epub 2017/12/13. doi: 10.1038/s41418-017-0033-z. PubMed PMID: 29229997; PubMed Central PMCID: PMCPMC5988678.

656. Gomez-Suaga P, Paillusson S, Stoica R, Noble W, Hanger DP, Miller CCJ. The ER-Mitochondria Tethering Complex VAPB-PTPIP51 Regulates Autophagy. Current biology : CB. 2017;27(3):371-85. Epub 2017/01/31. doi: 10.1016/j.cub.2016.12.038. PubMed PMID: 28132811; PubMed Central PMCID: PMCPMC5300905.

657. Aguilar-Maldonado B, Gómez-Viquez L, García La, Del Angel RM, Arias-Montaño JA, Guerrero-Hernández An. Histamine potentiates IP3-mediated Ca2+ release via thapsigargin-sensitive Ca2+ pumps. Cellular Signalling. 2003;15(7):689-97. doi: https://doi.org/10.1016/S0898-6568(03)00012-3.

658. Szabadkai G, Simoni AM, Rizzuto R. Mitochondrial Ca2+ uptake requires sustained Ca2+ release from the endoplasmic reticulum. The Journal of biological chemistry. 2003;278(17):15153-61. Epub 2003/02/15. doi: 10.1074/jbc.M300180200. PubMed PMID: 12586823.

659. McWilliams TG, Muqit MM. PINK1 and Parkin: emerging themes in mitochondrial homeostasis. Current opinion in cell biology. 2017;45:83-91. Epub 2017/04/25. doi: 10.1016/j.ceb.2017.03.013. PubMed PMID: 28437683.

660. Gelmetti V, De Rosa P, Torosantucci L, Marini ES, Romagnoli A, Di Rienzo M, et al. PINK1 and BECN1 relocalize at mitochondria-associated membranes during mitophagy and promote ER-mitochondria tethering and autophagosome formation. Autophagy. 2017;13(4):654-69. Epub 2017/04/04. doi: 10.1080/15548627.2016.1277309. PubMed PMID: 28368777; PubMed Central PMCID: PMCPMC5388214.

661. Van Laar VS, Roy N, Liu A, Rajprohat S, Arnold B, Dukes AA, et al. Glutamate excitotoxicity in neurons triggers mitochondrial and endoplasmic reticulum accumulation of Parkin, and, in the presence of N-acetyl cysteine, mitophagy. Neurobiology of disease. 2015;74:180-93. Epub 2014/12/06. doi: 10.1016/j.nbd.2014.11.015. PubMed PMID: 25478815; PubMed Central PMCID: PMCPMC4322770.

662. Bensinger SJ, Christofk HR. New aspects of the Warburg effect in cancer cell biology. Seminars in cell & developmental biology. 2012;23(4):352-61. Epub 2012/03/13. doi: 10.1016/j.semcdb.2012.02.003. PubMed PMID: 22406683.

663. Benard G, Bellance N, James D, Parrone P, Fernandez H, Letellier T, et al. Mitochondrial bioenergetics and structural network organization. Journal of cell science. 2007;120(Pt 5):838-48. Epub 2007/02/15. doi: 10.1242/jcs.03381. PubMed PMID: 17298981.

664. Aguer C, Gambarotta D, Mailloux RJ, Moffat C, Dent R, McPherson R, et al. Galactose enhances oxidative metabolism and reveals mitochondrial dysfunction in human primary muscle cells. PloS one. 2011;6(12):e28536. Epub 2011/12/24. doi: 10.1371/journal.pone.0028536. PubMed PMID: 22194845; PubMed Central PMCID: PMCPMC3240634.

665. Van Laar VS, Arnold B, Cassady SJ, Chu CT, Burton EA, Berman SB. Bioenergetics of neurons inhibit the translocation response of Parkin following rapid

mitochondrial depolarization. Human molecular genetics. 2011;20(5):927-40. Epub 2010/12/15. doi: 10.1093/hmg/ddq531. PubMed PMID: 21147754; PubMed Central PMCID: PMCPMC3033183.

666. Peterson JR, Bickford LC, Morgan D, Kim AS, Ouerfelli O, Kirschner MW, et al. Chemical inhibition of N-WASP by stabilization of a native autoinhibited conformation. Nature structural & molecular biology. 2004;11(8):747-55. doi: 10.1038/nsmb796.

667. Nishimura Y, Shi S, Zhang F, Liu R, Takagi Y, Bershadsky AD, et al. The formin inhibitor SMIFH2 inhibits members of the myosin superfamily. Journal of cell science. 2021;134(8). Epub 2021/02/17. doi: 10.1242/jcs.253708. PubMed PMID: 33589498; PubMed Central PMCID: PMCPMC8121067.

668. Vance JE. Newly made phosphatidylserine and phosphatidylethanolamine are preferentially translocated between rat liver mitochondria and endoplasmic reticulum. The Journal of biological chemistry. 1991;266(1):89-97. Epub 1991/01/05. PubMed PMID: 1898727.

669. Carreras-Sureda A, Kroemer G, Cardenas Julio C, Hetz C. Balancing energy and protein homeostasis at ER-mitochondria contact sites. Science signaling.15(741):eabm7524. doi: 10.1126/scisignal.abm7524.

670. Chen M, Chen Z, Wang Y, Tan Z, Zhu C, Li Y, et al. Mitophagy receptor FUNDC1 regulates mitochondrial dynamics and mitophagy. Autophagy. 2016;12(4):689-702. Epub 2016/04/07. doi: 10.1080/15548627.2016.1151580. PubMed PMID: 27050458; PubMed Central PMCID: PMCPMC4836026.

671. Zhang J, Ney PA. Role of BNIP3 and NIX in cell death, autophagy, and mitophagy. Cell death and differentiation. 2009;16(7):939-46. Epub 2009/02/21. doi: 10.1038/cdd.2009.16. PubMed PMID: 19229244; PubMed Central PMCID: PMCPMC2768230.

672. Bergers G, Fendt SM. The metabolism of cancer cells during metastasis. Nature reviews Cancer. 2021;21(3):162-80. Epub 2021/01/20. doi: 10.1038/s41568-020-00320-2. PubMed PMID: 33462499; PubMed Central PMCID: PMCPMC8733955.

673. van de Wal MAE, Adjobo-Hermans MJW, Keijer J, Schirris TJJ, Homberg JR, Wieckowski MR, et al. Ndufs4 knockout mouse models of Leigh syndrome: pathophysiology and intervention. Brain : a journal of neurology. 2022;145(1):45-63.

Epub 2021/12/02. doi: 10.1093/brain/awab426. PubMed PMID: 34849584; PubMed Central PMCID: PMCPMC8967107.

674. Yu Y-R, Imrichova H, Wang H, Chao T, Xiao Z, Gao M, et al. Disturbed mitochondrial dynamics in CD8+ TILs reinforce T cell exhaustion. Nature immunology. 2020;21(12):1540-51. doi: 10.1038/s41590-020-0793-3.

675. Lisci M, Barton Philippa R, Randzavola Lyra O, Ma Claire Y, Marchingo Julia M, Cantrell Doreen A, et al. Mitochondrial translation is required for sustained killing by cytotoxic T cells. Science (New York, NY).374(6565):eabe9977. doi: 10.1126/science.abe9977.

676. Wikstrom JD, Mahdaviani K, Liesa M, Sereda SB, Si Y, Las G, et al. Hormone-induced mitochondrial fission is utilized by brown adipocytes as an amplification pathway for energy expenditure. The EMBO journal. 2014;33(5):418-36. Epub 2014/01/17. doi: 10.1002/embj.201385014. PubMed PMID: 24431221; PubMed Central PMCID: PMCPMC3983686.

677. Mi N, Chen Y, Wang S, Chen M, Zhao M, Yang G, et al. CapZ regulates autophagosomal membrane shaping by promoting actin assembly inside the isolation membrane. Nature cell biology. 2015;17(9):1112-23. Epub 2015/08/04. doi: 10.1038/ncb3215. PubMed PMID: 26237647.